

Natural Gas Hydrates – from the Microstructure towards a Geological Understanding

Dissertation

Zur Erlangung des
Doktorgrades der Naturwissenschaften
(Dr. rer. nat.)

im Fachbereich Geowissenschaften
der Universität Bremen

vorgelegt von
Stephan A. Klapp

Bremen, August 2009

Gutachter:

Prof. Dr. Gerhard Bohrmann

Prof. Dr. Werner F. Kuhs

“If there is magic on this planet, it is contained in water.”
Loren Eiseley, *The Immense Journey*, 1957

PREFACE

This PhD thesis was written at the 'MARUM – Center for Marine Environmental Sciences' and Department of Geosciences at the University of Bremen, Germany. The thesis work has been carried out from September 2006 until August 2009. The thesis was funded by a private scholarship of the 'HGM Energy GmbH' in Bremen. The graduate education was embedded into 'GLOMAR – Bremen International Graduate School for Marine Sciences'. The gas hydrate samples researched in this thesis were retrieved during the R/V SONNE Cruise SO 174 in the Gulf of Mexico in 2003, R/V PROFESSOR LOGACHEV Cruise TTR 15 in the Black Sea in 2005, R/V METEOR Cruise M67/2 in the Gulf of Mexico in 2006 and R/V METEOR Cruise M72/3a+b in the Black Sea in 2007. The collaborating institutes and laboratories are the 'Abteilung Kristallographie' of the 'Geowissenschaftliches Zentrum' at the University of Göttingen (GZG), Germany, the 'Deutsches Elektronen-Synchrotron' (DESY) and 'Hamburger Synchrotronstrahlungslabor' (HASYLAB) in Hamburg, Germany, the Geochemistry Group from the Department of Geosciences at the University of Mainz, Germany, the Paul-Scherrer-Institute (PSI) and Swiss Light Source (SLS) in Villigen, Switzerland, and the Monterey Bay Aquarium Research Institute (MBARI), California, USA.

The thesis comprises six research papers in the main text attempting to better understand gas hydrates in natural submarine environments. Accordingly, the Introduction Chapter is subdivided into a geological part and a mineralogical part, both focusing on gas hydrates. The motivation for this thesis is given after the introduction on hydrate mineralogy. The second Chapter briefly describes the analytical methods and sampling locations. The research papers start in Chapter 3 with a methodological paper describing the technique for obtaining crystal sizes of gas hydrates. The results of these investigations are interpreted in the geological context in Chapter 4. The relations of gas chemistry, crystallographic structure, microstructure and thermodynamic stability for hydrates from the Gulf of Mexico are presented in Chapter 5. μ -computer tomography is introduced as a novel technology for gas hydrate research with first results in Chapter 6. Chapter 7 reports on the co-existence of two gas hydrate structures at the Chapopote asphalt volcano in the southern Gulf of Mexico. In Chapter 7 the assessment of the gas hydrate inventory of the Batumi gas seep in the eastern Black Sea is presented along with a discussion on possible transport mechanisms to the sea surface. The thesis closes with a Chapter drawing conclusions from the outcomes of the research presented here and offering future perspectives.

CONTENTS

	Abbreviations	IV
	Abstract	V
	Kurzfassung	VII
CHAPTER 1	INTRODUCTION	1
1.1	Gas hydrates in marine sediments	1
1.1.1	Introduction	1
1.1.2	Gas hydrates on Earth	2
1.1.2.1	Gas hydrate occurrence	2
1.1.2.2	Hydrocarbon gas sources	3
1.1.3	Parameters for hydrate formation in marine sediments	4
1.1.3.1	Pressure and temperature	4
1.1.3.2	Methane solubility	5
1.1.3.3	Influence of salinity	5
1.1.3.4	Effect of methane oxidation on the gas hydrate interface in sediments	6
1.1.4	Marine environments promoting gas seepage and gas hydrate formation	6
1.1.4.1	Cold seeps	6
1.1.4.2	Gas seepage – is there an effect on the atmosphere?	7
1.1.5	Occurrence of gas hydrates in marine sediments	9
1.1.5.1	Hydrate fabric and relation to burial depth	9
1.1.5.2	Shapes of shallow gas hydrates in marine deposits	11
1.1.6	Gas hydrates and energy industry	12
1.2	Mineralogical aspects of gas hydrates	13
1.2.1	Structure of gas hydrates	13
1.2.1.1	Crystallographic structures	13
1.2.1.2	Hydration number	14
1.2.1.3	Relation of gases and hydrate structures	16
1.2.1.4	Incipient structure and long-term stability	18
1.2.1.5	Volatility	19
1.2.2	Microstructure	20
1.2.2.1	Sub-micrometer-sized porosity	20
1.2.2.2	Microstructure and anomalous self-preservation	21
1.2.2.3	Microstructure imaging of decomposing hydrates	21
1.2.2.4	Developments for microstructure characterization of hydrates	22
1.2.3	Grain growth	23
1.2.3.1	Ostwald ripening	23
1.2.3.2	Static grain growth	24
1.3	Motivation and main questions	25
CHAPTER 2	METHODS AND SAMPLING LOCATIONS	27
2.1	Methods	27
2.1.1	Recovery of samples	27
2.1.2	Gas chemistry	27
2.1.3	X-ray diffraction	28
2.1.3.1	Phase analysis	28
2.1.3.2	Crystallite size analyses	29
2.1.4	X-ray computer tomography	31

2.1.4.1	Medical computer tomography	31
2.1.4.2	Microscale computerized tomography	31
2.1.5	FE - Scanning Environmental Electron Microscopy	33
2.1.6	Raman spectroscopy	34
2.2	Sampling locations	35
2.2.1	Gulf of Mexico	35
2.2.1.1	Northern Gulf of Mexico	36
2.2.1.2	Southern Gulf of Mexico	37
2.2.2	Study sites offshore Georgia in the eastern Black Sea	37
CHAPTER 3	MANUSCRIPT 1: Crystallite size distributions of marine gas hydrates.	39
	Klapp, S.A. , S. Hemes, H. Klein, G. Bohrmann, W.F. Kuhs, Abegg, F. (2008) In: Englezos, P. and Ripmeester, J., Eds., <i>Proceedings of the 6th International Conference on Gas Hydrates (ICGH 2008)</i> , July 6-10, 2008, Vancouver, BC, Canada, 13 pp.	
CHAPTER 4	MANUSCRIPT 2: Grain size measurements of natural gas hydrates.	53
	Klapp, S.A. , Hemes, S., Klein, H., Bohrmann, G., MacDonald, I.R., Kuhs, W.F. (submitted May 5, 2009) <i>Marine Geology</i> .	
CHAPTER 5	MANUSCRIPT 3: Microstructures of structure I and II gas hydrates from the Gulf of Mexico.	67
	Klapp, S.A. , Bohrmann, G., Kuhs, W.F., Murshed, M.M., Pape, T., Klein, H., Techmer, K.S., Heeschen, K.U., Abegg, F. (in press) <i>Marine and Petroleum Geology</i> , doi:10.1016/j.marpetgeo.2009.03.004.	
CHAPTER 6	MANUSCRIPT 4: Natural gas hydrate investigations by synchrotron radiation X-ray cryo-tomographic microscopy.	83
	Murshed, M.M., Klapp, S.A. , Enzmann, F., Szeder, T., Huthwelker, T., Stampanoni, M., Marone, F., Hintermüller, C., Bohrmann, G., Kuhs, W.F., Kersten, M. (2008) <i>Geophysical Research Letters</i> , 35, L23612, doi:10.1029/2008GL035460.	
CHAPTER 7	MANUSCRIPT 5: Mixed gas hydrate structures on the Chapopote asphalt volcano, southern Gulf of Mexico.	91
	Klapp, S.A. , Murshed, M.M., Pape, T., Klein, H., Bohrmann, G., Kuhs, W.F., Brewer, P.G., manuscript in preparation.	
CHAPTER 8	MANUSCRIPT 6: High-intensity gas seepage feeds shallow gas hydrate deposits in the eastern Black Sea.	111
	Pape T., Bahr A., Klapp S.A. , Abegg F., Bohrmann G. (submitted June 25, 2009) <i>Earth and Planetary Science Letters</i> .	
CHAPTER 9	CONCLUSIONS AND PERSPECTIVES	127
9.1	Conclusions	127
9.1.1	sl/sII structure co-occurrence	127
9.1.2	Relation between the gas chemical composition, crystallographic structure and microstructure	127
9.1.3	Crystallite sizes and size distributions of hydrates	128
9.1.4	Dissociation of gas hydrates	129
9.1.5	Gas hydrate occurrence at a constrained seep site and possible transport mechanisms to the sea surface	129
9.2	Perspectives	130
9.2.1	Porosity and grain boundaries of different hydrate structures	130
9.2.2	Crystallite sizes	130

9.2.3	Co-occurrence of two structures	131
9.2.4	Hydrate transport through water by means of seafloor rafting	132
	References	133
	Acknowledgements	155
APPENDICES		157
Appendix I	Feseker, T., Pape, T., Wallmann, K., Klapp, S.A. , Schmidt-Schierhorn, F., Bohrmann, G. (in press) The thermal structure of the Dvurechenskii mud volcano and its implications for gas hydrate stability and eruption dynamics. <i>Marine and Petroleum Geology</i> . doi:10.1016/j.marpetgeo.2009.01.021	
Appendix II	Sahling H., Bohrmann G., Artemov Y.G, Bahr A., Brüning M., Klapp S.A. , Klauke I., Kozlova E., Nikolovska A., Pape T., Reitz A., Wallmann K. (2009) Vodyanitskii Mud Volcano, Sorokin Trough, Black Sea: Geological characterization and quantification of gas bubble streams. <i>Marine and Petroleum Geology</i> . doi:10.1016/j.marpetgeo.2009.01.010	
Appendix III	Pape T., Bahr A., Rethemeyer J., Kessler J.D., Sahling H., Hinrichs K.-U., Klapp S.A. , Reeburgh W.S., Bohrmann G. (in revision) Molecular and isotopic partitioning of low molecular weight hydrocarbons during migration and gas hydrate precipitation in deposits of a high-flux seepage site. <i>Marine Chemistry</i> .	
Appendix IV	Bohrmann, G., Kuhs, W.F., Klapp, S.A. , Techmer, K.S., Klein, H., Murshed, M.M., Abegg, F. (2007) Appearance and preservation of natural gas hydrate from Hydrate Ridge sampled during ODP Leg 204 drilling. <i>Marine Geology</i> , 244, 1-14, doi:10.1016/j.margeo.2007.05.003	
Appendix V	Klapp, S.A. , H. Klein, W.F. Kuhs (2009) Gas hydrate crystallite size investigations with high-energy synchrotron radiation, in: D. Long, M.A. Lovell, J.G. Rees, C.A. Rochelle, (Eds), <i>Sediment-Hosted Gas Hydrates: New Insights on Natural and Synthetic Systems</i> . 319, The Geological Society, London, Special Publications, London, pp. 161-170.	

ABBREVIATIONS

2D	Two-dimensional	LC	Large cage
3D	Three-dimensional	m	Number of faces of a cage
AOM	Anaerobic oxidation of methane	mbsf	Meters below seafloor
BGHS	Base of gas hydrate stability	mbsl	Meters below sea level
b	Number of edges of a cage face m	μ CT	Microscale computerized tomography
C_1 or CH_4	Methane	n	Hydration number / Growth exponent (<i>Ostwald-ripening</i>)
C_2 or C_2H_6	Ethane	N_2	Nitrogen molecule
C_{2+}	Non-methane low-molecular weight hydrocarbons	P	Pressure
C_3 or C_3H_8	Propane	R_c	Mean crystallite size
C_4 or C_4H_{10}	Butane isomers (<i>n-/ iso-butane</i>)	SC	Small cage
C_5 or C_5H_{12}	Pentane isomers	SCXRTM	Synchrotron radiation X-ray cryo-tomographic microscopy
CO_2	Carbon dioxide	SEM	Scanning Electron Microscopy
CT	Computerized tomography	sl	Gas hydrate structure I
DESY	Deutsches Elektronen-Synchrotron	slI	Gas hydrate structure II
EDX	Energy-dispersive X-ray micro-analysis	sH	Gas hydrate structure H
FE-SEM	Field-Emission Scanning Electron Microscopy	SMI	Sulfate-methane interface
GC	Gas chromatograph	SLS	Swiss Light Source
GHOZ	Gas hydrate occurrence zone	t	Time
GHSZ	Gas hydrate stability zone	T	Temperature
GOM	Gulf of Mexico	TOMCAT	<u>T</u> Omographic <u>M</u> icroscopy and <u>C</u> oherent <u>r</u> adiology experimen <u>I</u> s beamline
Gt	Giga-tons (10^{12} [kg])	θ	Cage occupancy
HASYLAB	Hamburger Synchrotronstrahlungs-laborator	ν	frequency
I_h	Hexagonal Ice	ν_k	Internal vibrations of a molecule
K	Growth rate	wt. %	Weight percent
		XRD	X-ray diffraction

ABSTRACT

In gas hydrate research, hydrates are often studied according to their geological occurrence or to their chemical and physical properties; this PhD thesis combines both approaches using the example of gas hydrate microstructure. The main objective of this thesis is to investigate mineralogical characteristics of gas hydrates from cold seeps in the Gulf of Mexico and the eastern Black Sea.

The investigated gas hydrate properties are the crystal structure, the crystallite sizes and size distributions, the compositions of the hydrate-forming gases, the hydrate porosity as well as the grain boundary networks. That was accomplished by using X-ray diffraction, gas chromatography, Raman-spectroscopy, and scanning electron microscopy. Furthermore, the 'moving area detector method' or 'Bragg tomography' was applied for size measurements of hydrate crystallites as a new method, and computer tomography using Synchrotron radiation was used for the first time for gas hydrate inspections on a micro-scale.

The crystallite sizes of natural hydrates are governed by the velocity of crystal growth, therefore time is an important factor. One important result of this thesis is that the gas hydrate crystallite size evolution is also affected by more factors, which are impurities in the grain boundary network such as oil and salts, as well as possibly the presence of a second hydrate structure. The mean crystallite sizes of the investigated hydrates ranged between 190 and 400 μm . Hydrate crystals from different Black Sea oil and gas seeps with similar pressure/temperature conditions have similar mean grain sizes. For those hydrates, corresponding grain size distributions suggest continuous normal grain growth. Oil coatings were found on the grain boundaries of hydrates retrieved along the continental margin of the northern Gulf of Mexico. Spatially limited oil occurrence inside the hydrate matrix is considered as a factor accounting for different grain sizes on short distances. The oil migrates along the grain boundaries, where it retards diffusive mass exchange between the grains.

Gas hydrates from the northern Gulf of Mexico crystallize to structure type II hydrate (sII) from methane and a fraction of up to 30 mol% of C_2 through C_5 hydrocarbons. Since the C_2 – C_5 hydrocarbons are less volatile than methane, less subcooling of these gases is required to form hydrates. Therefore, the hydrates occur at moderate pressure/temperature conditions, where methane structure type I hydrate (sI) is unstable. One important result of this thesis is that the lower molecular mobility of C_2 – C_5 hydrocarbons compared to methane incorporated in hydrates is displayed phenomenologically by dense, non-porous surfaces of the gas hydrates on a micrometer scale. Instead, hydrates which were formed from volatiles like methane, often crystallizing to sI, are characterized by a micro-porosity.

A further objective of this thesis was to investigate the coexistence of sI and sII at the Chapopote asphalt volcano in the southern Gulf of Mexico. Methane is the prevailing gas constituent in the gas mixture but C_2 – C_5 hydrocarbons, which are incorporated into sII, are also present. Patches of viscous and ductile asphalts partially covering the seafloor trap the gas ascending from below and prevent gas discharge into the water. sI and sII hydrates trapped below the asphalt are intimately associated on short distances within individual crystallite-agglomerates. Areas within individual agglomerates where hydrate cages are only partially filled by gases cannot be ascribed to a certain hydrate structure and are considered as the transition between the structures. sII hydrates at the Chapopote asphalt volcano had larger crystallite sizes than sI and the sII grain size distributions indicated a steady-state crystal growth. In contrast, the distributions of the smaller sI crystals were skewed towards

smaller sizes in two of three samples and suggested that the grain growth was not in steady-state. Different formation mechanisms are presented which may explain the coexistence of the two structures and are supported by the analytical results of the investigation. Here, the simultaneous crystallization of sI and sII from the gas phase is the favored explanation. The preferred incorporation of less volatiles into sII is considered as the key to understanding the co-occurrence. Also, a limiting factor facilitating the sI/sII co-existence is the impermeable asphalt layer (or matrix), where the gas phase is denuded of certain components and accordingly relatively enriched in others during hydrate formation.

Micro-computer tomograms of the Chapopote hydrates showed small bubbles as well as genetic changes of the hydrate outside hydrate stability. The presence of bubbles indicates that free gas co-occurs together with the gas hydrate. Furthermore, ice was found in the sample originating both from decomposed hydrates and from pore water, which was frozen during the subsequent sample preservation in liquid nitrogen. An important outcome is that also well-preserved hydrates can be accompanied by an ice fraction not deriving from hydrate dissociation; accordingly, ice is not an exclusive indicator for hydrate decomposition.

The potential effect hydrates may exert on climate was investigated at the Batumi gas seep, eastern Black Sea. In the study area (0.5 km²) the hydrate-bound carbon within the upper 2.65 m below seafloor was estimated on 10.7 kt. It is unlikely that the hydrates decompose in the near future due to changes in the thermodynamic stability conditions. Instead, the rough seafloor topography suggests episodic detachment of gas hydrate chunks from the seafloor, which float upwards due to the positive buoyancy.

KURZFASSUNG

In der Gashydrat-Forschung werden Hydrate einerseits oft hinsichtlich ihres geologischen Vorkommens untersucht und andererseits hinsichtlich ihrer chemischen und physikalischen Eigenschaften. In dieser Dissertation wird versucht, beides am Beispiel der Gashydrat-Mikrostruktur zu vereinen. In der vorliegenden Arbeit wurden mineralogische Merkmale von Gashydraten, die von fokussierten Gasaustrittsstellen aus dem Golf von Mexiko und dem östlichen Schwarzen Meer geborgen wurden, beschrieben und interpretiert.

Untersucht wurden die Kristallstruktur, die Korngrößen und deren Verteilungen, die Zusammensetzung hydratbildender Gase sowie die Oberflächenporosität und das Korngrenzen-Netzwerk. Hierzu wurden Röntgen-Diffraktometrie, Gas-Chromatographie, Raman-Spektroskopie und Elektronenmikroskopie angewendet. Darüber hinaus wurde eine neue Methode zur Bestimmung der Gashydrat-Kristallitgrößen eingesetzt, das so genannte 'Moving area detector'-Verfahren oder 'Bragg Tomographie'. Computertomographische Analysen mithilfe von Synchrotron-Röntgenstrahlung wurden erstmals im Mikro-Maßstab an Gashydratproben durchgeführt.

Die Kristallitgrößen natürlicher Gashydrate werden durch die Geschwindigkeit des Kristallwachstums gesteuert, daher ist Zeit ein wesentlicher Faktor für das Kristallwachstum. Weitere Faktoren wie Fremdpartikel, zum Beispiel Salze und Öl im Korngrenzen-Netzwerk der Gashydrate, und möglicherweise die Anwesenheit einer weiteren Gashydrat-Kristallstruktur bestimmen ebenfalls das Wachstum. Die mittleren Kristallitgrößen der Hydrate betragen zwischen 190 und 400 μm . Gashydrat-Kristalle verschiedener Öl- und/oder Gas-Seeps im Schwarzen Meer weisen bei jeweils ähnlichen Druck/Temperaturbedingungen ähnliche mittlere Korngrößen auf. Die Korngrößenverteilungen lassen auf ein kontinuierliches Normal-Wachstum schließen. Öl-Filme wurden an den Korngrenzen von Gashydraten des nördlichen Kontinentalabhangs im Golf von Mexiko nachgewiesen. Ein wesentliches Resultat ist, dass trotz gleicher Bildungsbedingungen Öl an einer Lokation zu unterschiedlichen Kristallitgrößen der Gashydrate führt, indem es in die Räume zwischen Gashydrat-Kristalliten eindringt und so den diffusiven Stoff-Transport zwischen den Kristallen verlangsamt.

Gashydrate am nördlichen Golf von Mexiko bilden aus Methan und einem Anteil von bis zu 30 mol% $\text{C}_2\text{—C}_5$ Kohlenwasserstoff-Komponenten den Struktur-Typ II (sII). Aufgrund ihrer im Vergleich zu Methan geringeren Flüchtigkeit müssen die $\text{C}_2\text{—C}_5$ Kohlenwasserstoffe weniger stark unterkühlt werden, um mit Wasser Gashydrate zu bilden und kommen daher bei moderaten Druck/Temperaturbedingungen vor, bei denen die aus Methan gebildete Hydrat-Struktur I (sI) instabil ist. Die geringere molekulare Mobilität von $\text{C}_2\text{—C}_5$ Kohlenwasserstoffen in Hydraten im Vergleich zu Methan drückt sich neben der höheren thermodynamischen Stabilität phänomenologisch in einer massiv erscheinenden, nicht-porösen Oberfläche der Gashydrate im Mikrometer-Bereich aus. Gashydrate, die von flüchtigen Komponenten wie Methan dominiert werden und häufig zu sI kristallisieren, sind hingegen durch eine Mikroporosität charakterisiert.

Ein Schwerpunkt dieser Dissertation war die Untersuchung koexistierender sI/sII Gashydratstrukturen am Chapopote Asphalt Vulkan im südlichen Golf von Mexiko: Beide Strukturen sind eng miteinander assoziiert und kommen sehr kleinräumig innerhalb einzelner Kristallit-Agglomerate vor. Die Gaszusammensetzung beider Strukturen ist von Methan dominiert, und weitere Kohlenwasserstoffe sind präsent, die in sII inkorporiert werden. Asphalte, die

partiell den Meeresboden bedecken, bieten Hohlräume, in denen sich aufsteigende Gasblasen sammeln und dort im Kontakt mit Wasser unmittelbar Hydrate bilden. Bereiche innerhalb eines Kristallit-Agglomerats mit geringer Käfig-Besetzung können keiner Kristallit-Struktur zugeordnet werden und werden als Übergang zwischen sI und sII interpretiert. sII Hydrate haben am Chapopote Asphalt Vulkan größere Kristallitgrößen als sI und die Korngrößenverteilungen deuteten auf ein kontinuierliches Gleichgewichtswachstum in sII hin. Dagegen sind die Verteilungen der kleineren sI Kristallite in zwei von drei Untersuchungen zu kleineren Größen verschoben, so dass nicht von einem Gleichgewichtswachstum ausgegangen werden kann. Verschiedene Bildungsmechanismen werden diskutiert, die zur sI/sII-Koexistenz führen können und durch die analytischen Befunde gestützt werden. Präferiert wird hier eine simultane Kristallisation beider Strukturen aus der Gasphase. Die Diskriminierung von Methan gegenüber weniger flüchtigen Komponenten, die zu sII kristallisieren, wird als ein Schlüsselprozess gesehen. Ein limitierender Faktor für das gemeinsame Auftreten von sI und sII ist die Präsenz des Asphalts als Deckschicht oder Matrix, in der der Gasphase Komponenten nur durch Gashydratbildung entzogen und andere Komponenten entsprechend angereichert werden.

Mikro-computertomographische Untersuchungen der Gashydrate des Chapopote Asphalt Vulkans zeigten kleine Hohlräume innerhalb der Gashydrate sowie genetische Veränderungen der Hydrate außerhalb der Hydrat-Stabilität. Die Präsenz der Gasblasen belegt, dass freies Gas neben Gashydraten vorkommen kann. Neben Eis von dissoziiertem Gashydrat lag auch Eis aus gefrorenem Porenwasser vor. Das zeigt, dass wenig zersetzte Gashydrate von Eis umgeben sein können, das nicht aus der Gashydrat-Zersetzung stammt, und Eis nicht als exklusiver Indikator für Gashydrat-Zersetzung angesehen werden kann.

Im Batumi Seep Gebiet im östlichen Schwarzen Meer wurde untersucht, welchen Effekt dissoziierende Gashydrate auf das Klima haben könnten. Für das Untersuchungsgebiet von ca. 0,5 km² wurde die Masse des hydratgebundenen Kohlenstoffs in den oberen 2,65 m Sedimenttiefe mit ca. 10,7 kt quantifiziert. Eine massive Gashydrat-Zersetzung aufgrund thermodynamischer Instabilität ist bei den gegenwärtigen Druck/Temperaturbedingungen unwahrscheinlich. Hingegen lässt die unruhige Meeresboden-Topographie auf episodisches Ablösen von Gashydrat-Brocken schließen, die aufgrund ihrer Dichte im Meerwasser auf-treiben.

CHAPTER 1

INTRODUCTION

1.1 Gas hydrates in marine sediments

1.1.1 Introduction on gas hydrates

Gas hydrates are solid, non-stoichiometric compounds, which crystallize from water and guests, often gas molecules. Water molecules create cages by van-der-Waals-forces, which are stabilized by the guest molecules. Gas hydrates form under elevated pressure (P) and low temperature (T).

It is likely that the first artificial hydrates were produced in 1790 by Sir Joseph Priestley. The researcher observed enhanced “ice” formation when cold water was brought into contact with sulfur dioxide (Priestley, 1790). 20 years later Sir Humphry Davy reported on chlorine hydrates as a form of solid water (Davy, 1811). Michael Faraday continued research on the composition of chlorine hydrate (Faraday, 1823). For the next more than 100 years, research on gas hydrates centered on the identification of more gases, which combine with water to hydrate.

Gas hydrates became subject of economic interest in the 1930s when their potential to clog gas and oil pipelines became evident (Hammerschmidt, 1934; Wilcox et al., 1941). In the 1960s, Soviet scientists calculated that large quantities of methane-rich gas hydrate supposedly existed in arctic permafrost regions (Makogon, 1965) as well as in marine sediments (Makogon et al., 1971). The first gas hydrates were discovered in the Siberian permafrost in 1971 (Makogon et al., 1971), followed by recoveries in the Caspian and Black Sea (Yefremova & Zhizhchenko, 1974). In 1982, the Deep Sea Drilling Project targeted gas hydrate recovery (Shiple & Didyk, 1982). Since then, marine and permafrost gas hydrate deposits have been explored at many locations worldwide (Kvenvolden, 1993).

Besides scientific curiosity in gas hydrate as a mineral precipitate in nature, the interest in hydrates funds on the notion that hydrates store gases in a compressed form. Four fundamental questions arose from this awareness, which have both driven research and fueled debates since the early gas hydrate discoveries:

1. Is there a feedback between gas hydrate stability and climate (e.g., Dickens et al., 1997a; Katz et al., 1999; Kennett et al., 2003)?
2. How much does gas hydrate contribute to seafloor stability on continental slopes (e.g., Dunlap & Hooper, 1990; Henriot & Mienert, 1998; Nisbet & Piper, 1998)?
3. Could gas hydrates represent a future energy resource (e.g., Collet, 2002; Kvenvolden, 1998)?
4. What is the role of methane hydrate in the carbon cycle (e.g., Kvenvolden, 2002; Zeebe et al., 2009)?

Today, hundreds of molecules and elements have been identified to form gas hydrates. In addition to the fundamental aspects, gas hydrates haven been considered for applications like seawater desalination (Max, 2006) or transport of hydrogen gas (Lee et al., 2005; Mao & Mao, 2004).

Natural gas hydrates also occur outside permafrost or marine sediments and possibly even on other celestial bodies. In Greenland and Antarctic continental ice sheets, air hydrates form from recrystallization of ice and air bubble inclusions in deeply buried ice (Shoji & Langway, 1982). On Mars, the presence of large amounts of atmospheric carbon

dioxide together with water or ice near the poles may combine to carbon dioxide hydrates in the subsurface (Falenty & Kuhs, 2008; Longhi, 2006; Milton, 1974). Also, for Saturn's moon Titan it is suggested that large amounts of methane were stored in hydrate form and account for an admixing of methane to Titan's atmosphere (Osegovic & Max, 2005; Tobie et al., 2006). Because hydrates can be formed by many different molecules and elements, in this thesis the term "gas hydrates" or simply "hydrates" means hydrocarbon hydrates, which are dominated by methane (CH₄).

This thesis focuses on naturally occurring gas hydrates formed from hydrocarbon gases in shallow marine sediments, which are considered the dominant gas hydrates on Earth (Kvenvolden, 1993). It is shown that the mineralogy of hydrate crystals reflects the formation conditions and therefore helps to understand hydrate deposits in sediments.

1.1.2 Gas hydrates on Earth

Deposits of gas hydrate have been identified on Earth at many locations and the number of reported occurrences has been increasing significantly over the recent years: from 2005 to 2008 the number of known hydrate sites rose from ca. 70 to more than 90 (e.g., Hester & Brewer, 2009; Klauda & Sandler, 2005; Milkov, 2005).

1.1.2.1 Gas hydrate occurrence

Worldwide hydrate deposits are shown in Figure 1.1 (modified after Hester & Brewer, 2009). Deposits marked in red are inferred from indirect methods such as seismic reflectors and pore water anomalies in sediment cores. Direct evidence from sampled gas hydrates is mapped in yellow.

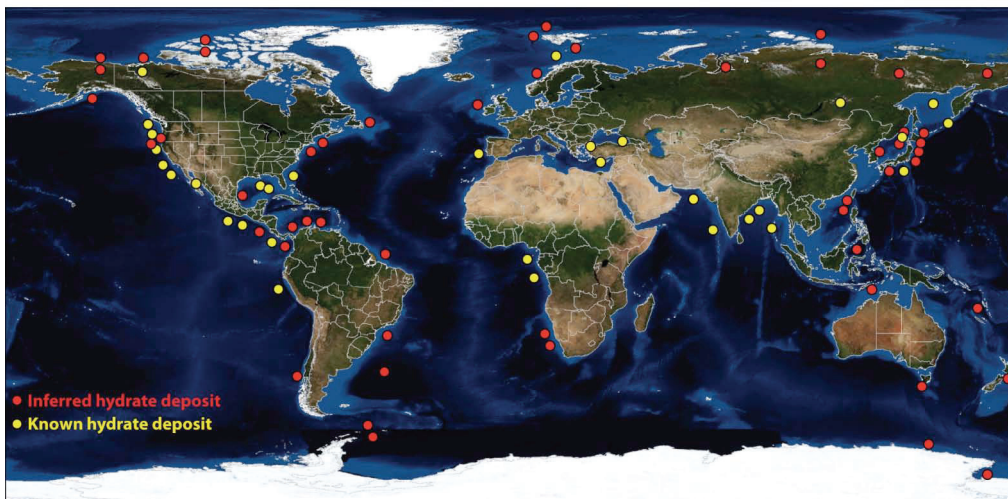


Figure 1.1: Known and inferred gas hydrate deposits in the world (after Hester & Brewer, 2009). Additional data from Bialas et al. (2007), Bohrmann and Pape (2007), Bohrmann and Spiess (2008), Bourry et al. (2009), and Pape et al. (submitted).

Gas hydrates in sediments can only form under elevated P and at low T, which for marine environments means that they occur in at least 300 m water depths but often deeper (Kvenvolden, 1993). However, to facilitate hydrate precipitation the formation waters need to be supersaturated with hydrate forming gases such as CH₄. Copious CH₄ production and appropriate P,T conditions are commonly found in continental margin sediments where the

slopes fall off into ocean basins and input of nutrients and organic material from continents is large. The nutrients fuel the production of organic matter, which is degraded in the sediments to various products, finally to hydrate forming gases such as CH₄ or carbon dioxide (CO₂).

The quantification of hydrate-bound carbon is in the focus of ongoing research. As the assessment relies on assumptions and models, their accuracy directly affects the precision of the calculations. One control of hydrate occurrence models is how good a model predicts already known hydrate deposits (Sloan & Koh, 2007). Klauda and Sandler's (2005) model is considered state-of-the-art as it allows prediction of almost all known hydrate deposits (see Sloan & Koh, 2007). According to their model, 74,400 Gt of CH₄ is stored as hydrates. Other estimations figure lower values for the amount of hydrate-bound carbon, Buffett and Archer (2004) calculated 3,000 Gt carbon stored in hydrates. 10,000 Gt is the most widely cited mass of hydrate-bound carbon (Kvenvolden, 1993), which is in several publications considered as a "consensus value" (Milkov, 2004; Klauda & Sandler, 2005).

1.1.2.2 Hydrocarbon gas sources

For natural gas hydrates, light hydrocarbons are the major guest molecules (Kvenvolden, 1993; Buffett, 2000). Two fundamentally different sources exist for hydrocarbon gas molecules:

Thermogenic CH₄ and higher hydrocarbons are generated by catagenesis deep in anoxic sediments. In the temperature range of 50 to 200 °C, organic matter is cracked and shorter hydrocarbons are produced (Killops & Killops, 2004; Tissot & Welte, 1984). These temperatures are typically met in sediment depths of at least 2 km depending on the local geotherm. Accordingly, the incorporation of thermogenic hydrocarbons in hydrates allows concluding on the presence of hydrocarbon pathways in the subsurface.

CH₄ from biogenic sources is produced by methanogenic archaea, which occur in anoxic sediments and produce CH₄ by organic matter degradation (Whiticar, 1999). The organisms are capable of surviving in a broad range of physical and chemical conditions (salinity, pH, P, T), which implies that CH₄ hydrates can be found at a wide range of living conditions, provided that the physical parameters for the stability are met.

The ratio of CH₄ (C₁) to heavier hydrocarbons provides some information on the hydrocarbon source. Low molecular weight hydrocarbons (C₂₊) are sometimes expressed as the sum of ethane and propane (C₂ + C₃) (Whiticar et al., 1995), but butane isomers (C₄) or pentanes (C₅) are sometimes also included in the ratio (Chapter 7; Chapter 8; Appendix III). Although both biogenic and thermogenic hydrocarbons are dominated by CH₄, biogenic hydrocarbons consist predominantly of CH₄ resulting in a C₁/C₂₊ ratio greater than 100. For thermogenic hydrocarbons the ratio is less than 100 (Bernard et al., 1976).

Chemical and isotopic analyses are used to discriminate between biogenic and thermogenic sources of light hydrocarbons. Biological hydrocarbons are dominantly composed of CH₄ which is depleted in ¹³C relative to thermogenic CH₄ due to kinetic fractionation (Whiticar, 1999). Usually, it is assumed that a δ¹³C—CH₄ value less than -50 ‰ (V-PDB) standard indicates biogenic CH₄, whereas values greater than -50 ‰ point to thermogenic CH₄ origin (Claypool & Kvenvolden, 1983; Schoell, 1988).

The stable hydrogen isotope ratio, i.e. the fraction of deuterium (D/H) gives some more information on the metabolism used for biogenic CH₄ production: hydrogen atoms in CH₄

produced from acetate fermentation yield a δD value lower than -250 ‰ Standard Mean Ocean Water (SMOW; Vienna standard), whereas carbonate fermentation leads to δD values from -150 to -250 ‰ (Whiticar et al., 1986).

The hydrate samples presented in this study are retrieved from the Gulf of Mexico and Black Sea. Current studies on chemical analyses of gas hydrates from different locations show that biogenic CH_4 production seems to be the dominant origin of hydrate forming CH_4 in most marine environments, for instance at the Hydrate Ridge (Suess et al., 2001), Congo-Angola basin (Charlou et al., 2004), Blake Ridge (Dickens et al., 1997b), Nankai Trough (Takahashi et al., 2001), and the Sea of Okhotsk (Ginsburg et al. 1993). Hydrates with thermogenic CH_4 have been recovered from the Gulf of Mexico (Brooks et al., 1984), Barkley Canyon (Chapman et al., 2004), Marmara Sea (Bourry et al., 2009), Caspian Sea (Ginsburg et al., 1992) and from the Lake Baikal (Kida et al., 2006).

In this thesis, the distinction between thermogenic and biogenic hydrate forming gases is significant and is discussed in Chapters 5 and 7 with respect to the microstructural findings (Section 1.2.2) and different crystallographic structures (Section 1.2.1).

1.1.3 Parameters for hydrate formation in marine sediments

The controlling parameters for gas hydrate formation and persistence in sediments are P, T, gas composition and saturation, and dissolved ions in the pore water. These parameters are briefly described in this section. The gas hydrate stability zone (GHSZ) is the area in the phase diagram (Figure 1.2) where these parameters allow for gas hydrate occurrence.

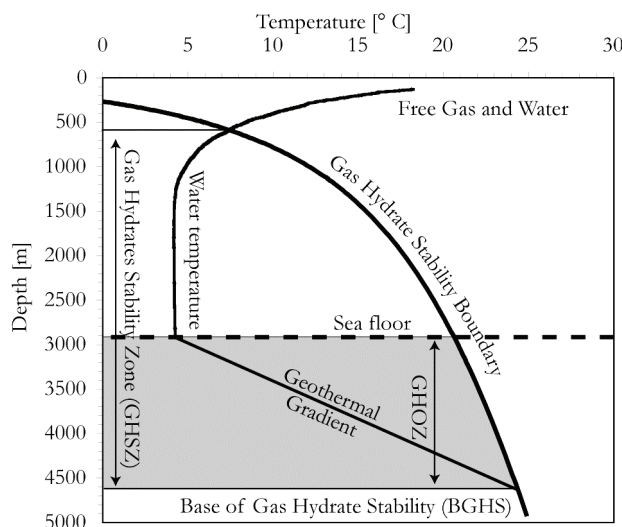


Figure 1.2: Gas hydrate stability diagram. The stability for CH_4 dominated hydrate (structure I; Section 1.2.1) in the southern Gulf of Mexico (Chapters 5, 6, 7) is displayed. GHOZ: Gas hydrate occurrence zone.

1.1.3.1 Pressure and temperature

Temperature and pressure conditions spanning the gas hydrate stability horizon occur at the seafloor nearly everywhere on Earth at water depths of several hundred meters, depending on local seawater temperature. Figure 1.2 gives an example from the southern Gulf of Mexico. The lower limit of hydrate stability within the sediments is often determined by the temperature increase following the regional geothermal gradient, which can be

overprinted by local thermal perturbations caused by fluid flow or heat focusing (e.g., at mud volcanoes; Kopf, 2002; Sauter et al., 2006; Appendices I; II). The base of gas hydrate stability (BGHS) is defined by the coordinate in the P, T diagram where the geotherm crosses the hydrate stability curve. At a given location, P and T are static on short timescales but become dynamic on longer timescales, as they are affected by changes in sea level and changes in ocean and sediment temperature, by tectonic activity as well as by sedimentation (Bahr et al., 2008; Bangs et al., 2005; Kennett et al., 2003; Mienert et al., 2005; Pecher et al., 1998, 2001; Xu, 2004). Short-term changes in bottom water temperature and pressure due to tides, currents, or deep eddies can also affect gas hydrate deposits (e.g., MacDonald et al., 1994, 2005; Ruppel, 2000). In this thesis, the role of past sea level and water temperature changes on gas hydrate deposits is exemplarily discussed in Chapter 8 for the Batumi seep area offshore Georgia in the Black Sea.

1.1.3.2 Methane solubility

An essential premise in precipitation of gas hydrates is the supersaturation of hydrate forming gases in the sediment pore water (Figure 1.3; Kashchiev & Firoozabadi, 2002), which is a function of temperature and pressure (Claypool & Kaplan, 1974), dissolved ions (Masoudi & Tohidi, 2005), and the presence (Duan & Mao, 2006; Sun & Duan, 2007) or the absence of gas hydrates in the solution (Tishchenko et al., 2005). Hydrate will only form when the concentration of the hydrate former (i.e., CH₄) exceeds solubility. The deficiency of hydrate in shallow marine sediments within the GHSZ can result from escape of CH₄ into the ocean, which is much under-saturated with CH₄. The anaerobic oxidation of methane is a further cause for a lack of CH₄ in shallow sediments (AOM; see Section 1.1.3.4). Of all seas in the world, the Black Sea has the highest amount of CH₄ dissolved in the water, which is ca. 15 µmol/l (Kessler et al., 2006). This value is far below saturation (ca. 100 mmol/l; Pape et al., 2008).

Figure 1.3 illustrates the GHZO in relation to the CH₄ solubility and concentration: In shallow sediments within the GHSZ, CH₄ concentration is below saturation values. The CH₄ concentration increases with depth, because the influence of both AOM and seawater undersaturated in CH₄ declines. Once the CH₄ concentration reaches solubility, gas hydrates flocculate defining the upper onset of the GHZO. The depth in which the CH₄ concentration falls below the solubility value marks the base of hydrate occurrence. The relationship shows that as the CH₄ flux increases or decreases the GHZO will expand or contract, respectively.

1.1.3.3 Influence of salinity

The GHSZ is affected by dissolved ions from salts in the formation waters in that dissolved ions decrease hydrate stability. This is because the ions interchange with polar water molecules decreasing the probability of water molecules to arrange in a cage structure. Also, dissolved ions from salts affect the solubility of gas molecules (Duan and Mao, 2006; Masoudi et al., 2004). Salts sometimes have a major effect on hydrates and inhibit hydrate formation, even though sufficient guest molecule concentrations and adequate P,T conditions are established (Masoudi & Tohidi, 2005; Østergaard et al., 2002; Ruppel et al., 2005). In this thesis, examples of salts in gas hydrate microstructure are

shown in Chapter 6 as well as in Appendix IV. The possible effect salt brines may have on gas hydrate crystal growth is discussed in Chapter 4.

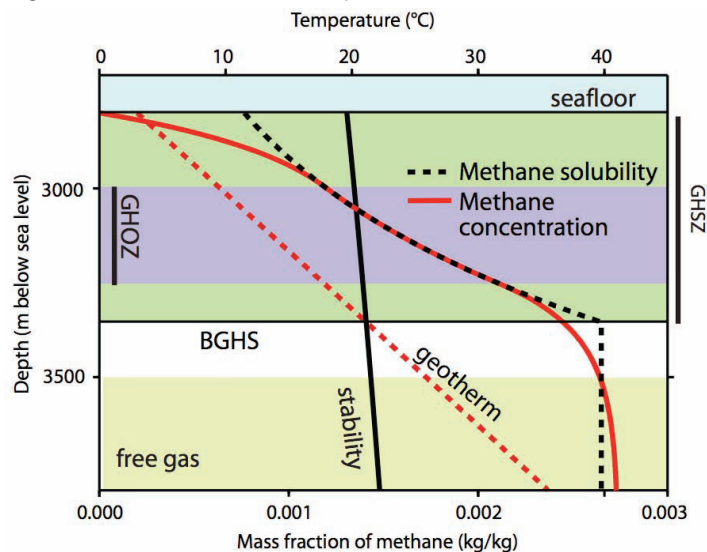


Figure 1.3: Gas hydrate occurrence zone (GHOZ) defined by the mass fraction of methane (example from Tréhu et al., 2006a). Gas hydrates flocculate when the CH_4 concentration reaches solubility.

1.1.3.4 Effect of methane oxidation on the gas hydrate interface in sediments

Microbial CH_4 consumption within the sulfate-methane interface zone (SMI) can lower the CH_4 concentration to levels below solubility (Borowski et al., 1996) and accounts for the offset between the upper limit of the GHSZ in the sediments and the gas hydrate occurrence zone (GHOZ; Figure 1.3). The thickness of the methane-depleted zone between the seafloor and the onset of CH_4 and methane hydrates is governed by the activity of microbial consortia performing anaerobic oxidation of methane (AOM) coupled to sulfate reduction (Boetius et al., 2000; Orphan et al., 2001). Hence, outcropping gas hydrates at the seafloor are uncommon. However, gas hydrate deposits near the seafloor or even outcropping are known at the Bush Hill site in the Gulf of Mexico (e.g., MacDonald et al., 1994; 2005) or at Barkley Canyon (Chapman et al., 2004). These hydrate outcrops are explained by thermogenic hydrocarbons as well as by rapid CH_4 flux (MacDonald et al., 2005; Chapman et al., 2004). Suess et al. (2001) report on outcropping gas hydrates at Hydrate Ridge, which are dominated by biogenic CH_4 and characterized by high CH_4 flux (Torres et al., 2004), such that the methane consumption is outbalanced by the high gas flux from below.

1.1.4 Marine environments promoting gas seepage and gas hydrate formation

1.1.4.1 Cold seeps

The mineralogical investigations on the hydrates presented in this study help to better understand so-called cold seep systems, where the hydrates were retrieved. Cold seeps are sites of localized fluid escape on the seafloor, which is not related to geothermal activity (Bohrmann & Torres, 2006). Cold seeps are characterized by fluid fluxes transporting gases, oil or fresh water and are typically found at locations where the structure of the subsurface fosters fluid flow from deep reservoirs towards the sediment surface (Ding et al., 2008; Judd & Hovland, 2007; Tréhu et al., 1999). Depending on the escaping fluids and on the oxygen concentrations in the bottom waters, cold seeps are frequently accompanied by seep fauna

(Sahling et al., 2003), which is adapted to nutrient cycles often related to the CH₄ flux (Sahling et al., 2002). Fluid migration and fluid discharge into open water can be forced from deep sediments by landsliding, sediment compaction, tectonic compression, and more geological processes or a combination of those (Bohrmann et al., 2002; Judd & Hovland, 2007). Hence, practically every regime with sedimentation, plate tectonics, salt-diapirism induced tectonics, eustatic rebound or ground water movement can foster cold seeps. Accordingly, seeps occur both on land and in marine settings. Within the GHSZ in marine environments, most cold seeps are found along continental margins but they also occur near abyssal plains (Sahling et al., 2008). Seeps can be identified by various techniques. Rising gas bubbles in the water column (gas flares) indicate gas seepage at the seafloor (Greinert et al., 2006; Sahling et al., 2008). Anomalous reflections of hydro-acoustic echo sounders point to shallow gas hydrates if AOM is limited to shallow sediment depths (Section 1.1.3.4) (Klaucke et al., 2006; Paull et al., 2008). Video observations of deep-towed TV-sleds can identify cold seeps basing on seep fauna (Bohrmann et al., 2002).

Hydrocarbon seeps can be categorized according to the hydrocarbon homologs, i.e., the hydrocarbon chain lengths or the viscosity. Some eastern Black Sea hydrocarbon seeps such as the Colkheti Seep or the Pechori Mound are characterized by both gas and oil seepage (Akhmetzhanov et al., 2007; Bohrmann & Pape, 2007). Such seeps can be categorized as oil seeps. Oil seeps are also frequent in the Gulf of Mexico (MacDonald et al., 1989, 1996; Sassen et al., 1999), where gas hydrates form from thermogenic gases (Brooks et al., 1984), which migrate together with oil from deep reservoirs to shallow sediment depths (e.g., Chen and Cathles, 2003; Sassen et al., 2001a, 2001c).

Similar to cold seeps, mud volcanoes (MV) expel significant amounts of fluidized mud, (Kopf, 2002, 2003) and hydrocarbons (Feseker et al., 2008; Sauter et al., 2006). The formation and decomposition of gas hydrates at MV is more dynamic than at cold seeps, e.g., at the Dvurechenski MV in the Black Sea (Bohrmann et al., 2003; Wallmann et al., 2006a; Appendix I) or the Vodyanitskii MV in the Black Sea (Appendix II).

1.1.4.2 Gas seepage – is there an effect on the atmosphere?

In Chapter 8 of this study gas hydrate occurrence in the Batumi seep area in the Black Sea is described. Possible mechanisms are discussed in how far hydrocarbons from these hydrates may break the sea surface. In this section a brief discussion is provided on the fate of gas bubbles released from seeps into the water. This section also provides a background for Chapter 7, where the coexistence of different gas hydrate structures (introduced in Chapter 1.2.1) is reported. One possibility for the co-occurrence lies in the presence of bubbles with different gas compositions.

It has repeatedly been suggested that hydrocarbons and carbon dioxide (CO₂) discharged as gas bubbles from seeps into the ocean water may travel all the way from the seafloor to the surface of the ocean and from there into the atmosphere, where they act as greenhouse gases and contribute to global warming (e.g., Etiope et al., 2008a, 2008b; Judd, 2002; Judd & Hovland, 2007; Kopf, 2003; Milkov et al., 2003a; Solomon et al., 2009). This gas flux has been acknowledged as a source of atmospheric carbon in the fourth assessment report of the Intergovernmental Panel on Climate Change (Denman et al., 2007). The total annual flux from marine seeps to the atmosphere is 20 Tg of CH₄, 0.45 Tg of ethane and 0.09 Tg of

propane (Etiope & Ciccioli, 2009; Judd, 2004). The effect of offshore gas seepage on climate change is, however, still debated controversially, as calculations (McGinnis et al., 2006; Rehder et al., 2009; Yamoto et al., 2009) and open sea experiments (Brewer et al., 2002; Rehder et al., 2002) suggest that rising gas bubbles dissolve or exchange the gases during their ascent due to the undersaturation of CH₄ in seawater (Leifer & MacDonald, 2003; Leifer & Patro, 2002; Rehder et al., 2004). While traveling a few tens of meters upwards in the ocean, gas bubbles without a hydrate skin lose about half their volume to the surrounding water (Rehder et al., 2002). If the distance from seafloor to sea surface is longer than a few tens of meters, the gas from the bubble is dissolved completely. McGinnis et al. (2006) and Schmale et al. (2005) conclude from both calculations and field observations, respectively, that only CH₄ emitted from less than 100 m water depth reaches the atmosphere at all. CH₄ emissions from deeper located seeps will be dissolved while rising upwards in the water column.

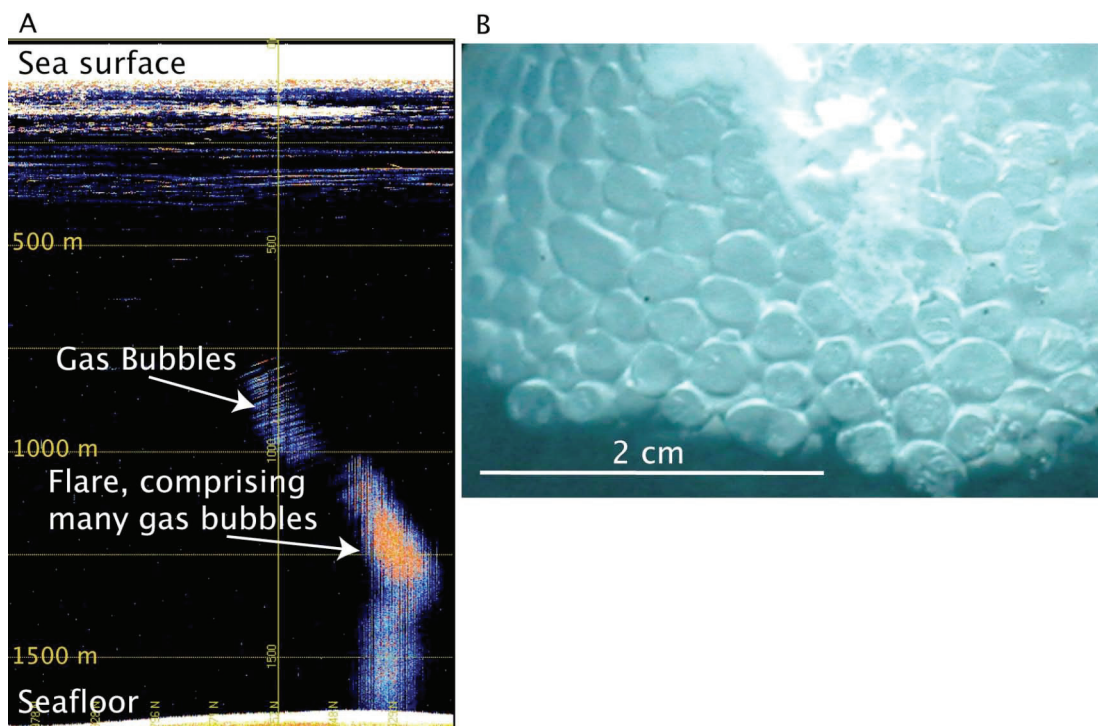


Figure 1.4: Gas seepage. **A.** Hydro-acoustic echo-sounder image of a gas flare (Flare no. 7; Makran accretionary wedge offshore Pakistan, ca. 1600 meters below sea level (mbsl); Nov./Dec. 2007; R/V Meteor cruise M74/3; Bohrmann et al., 2008). **B.** Gas bubbles coated by a hydrate skin; the bubbles were caught in a transparent plastic funnel (Kobuleti Ridge, Black Sea, offshore Georgia, ca. 1100 mbsl; R/V Meteor cruise M72/3; Bohrmann & Pape, 2007).

In contrast, emissions of CH₄ inside the GHSZ reach further upwards into the water column. CH₄ bubbles within the GHSZ have been observed to form a hydrate rim on the surface of the bubble (e.g., Appendix II), which forms from the combination of water with the gas (Maini & Bishnoi, 1981). Although hydrates dissolve in open water (Rehder et al., 2004), the traveling distance until half of the bubble volume is dissolved in the water is almost four times longer than without a hydrate skin (Rehder et al., 2002). Figure 1.4A shows an image of a gas flare from the Makran area in the northwest Indian Ocean. There, hydrate-coated bubbles from gas discharge are imaged by acoustic tools. Figure 1.4B shows hydrate-coated gas bubbles in high resolution from a seep in the Black Sea. Greinert et al. (2006) observed gas flares originating from gas emanation at seepage sites in the Black Sea rising 1300 m

high into the water up to ca. 720 m water depth. The authors related the dissolution of the gas bubbles in that depth to the disintegration of the hydrate skins on the bubble surface, as the calculated methane hydrate stability limit in the Black Sea is in about the same depth (Bohrmann et al., 2003).

From the current information available in the literature the picture emerges that even high gas flux seepage deeper than 100 m water depth in marine basins does not significantly contribute to the atmospheric CH₄ concentration, because the gas is dissolved in the water before it can reach the atmosphere (Judd, 2004; Leifer & Patro, 2002; McGinnis et al., 2006; Greinert et al., 2006; Rehder et al., 2002; Yamoto et al., 2009).

An alternative CH₄ transport mechanism through the water is discussed in Chapter 8. MacDonald et al. (1994) discussed the possibility of massive gas hydrate chunk detachment from the seafloor in the Gulf of Mexico. Such gas hydrate rafting has been observed on Hydrate Ridge at the Cascadia Margin (Suess et al., 2001). At the Batumi seep area in 840 m water depth near-seafloor gas hydrates were investigated, as shallow hydrates are more easily affected by changes in the environmental conditions than deeper-seated hydrates. Video-documented massive gas ebullition co-occurred with fresh fractures in the sediments on the scale of meters, which were interpreted as the results of gas hydrate rafting, i.e., detached chunks of hydrate that drifted from the seafloor due to their buoyancy (Chapter 8; Suess et al., 2001; MacDonald et al., 1994). Large chunks of massive hydrates have a much bigger chance of breaking the sea surface than hydrate skinned-bubbles (Brewer et al., 2002; Paull et al., 2003).

1.1.5 Occurrence of gas hydrates in marine sediments

Gas hydrates precipitate as authigenic minerals in marine sediments. They occur in different fabrics in the sediments, which are related to the lithology and porosity, gas flux, water content and overburden pressure (Bohrmann & Torres, 2006).

1.1.5.1 Hydrate fabric and relation to burial depth

In the cores of the ODP Leg 204 drillings (Tréhu et al., 2006b) crystal sizes of deep-seated hydrates seemed to be larger than the shallower ones (Klapp et al., 2007; Appendix V). During the ODP Leg 204 drilling campaign a relation between burial depth and the fabric of the gas hydrates was recognized (Abegg et al., 2006; 2007; Bohrmann & Torres, 2006).

The gas hydrate system at Hydrate Ridge is fed by rising gas bubbles from below (Haeckel et al., 2004; Milkov et al., 2005) precipitating as hydrates in the upper ca. 180 m of the sediment column in the pore space of the sediment (e.g., Torres et al., 2002; Tréhu et al., 2004). If the hydrates form in shallow sediment depths, accumulating and growing hydrates will displace the sediment in order to gain space. This is impossible at greater depth due to the overburden; at Hydrate Ridge the approximate sediment depth at which the force of gas hydrate crystallization (see Torres et al., 2004) cannot overcome the overburden pressure is 25 meters below seafloor (mbsf) (Torres et al., 2004). Accordingly, in the deeper sediments gas hydrates form only along surfaces of cracks and fissures (Abegg et al., 2007) and have distinctly different fabrics than the shallower hydrates (Abegg et al., 2006; Bohrmann et al., 1998). It has been suggested that the bubble fabric of the gas hydrates gradually decreases with increasing depth down to that particular horizon where the

pressure from the overlying sediments exceeds the force of crystallization to displace sediment particles in order to grow (Torres et al., 2002; 2004).

Gas hydrates can be classified into disseminated, nodular, layered and massive hydrates (Malone, 1985) according to the size of hydrate occurrences. Bohrmann et al. (1998) and Suess et al. (1999; 2002) described gas hydrates from Hydrate Ridge occurring in layers or joints with thickness from millimeters to decimeters. The classification of Malone (1985) combined with a hydrate size characterization allowed to describe the gas hydrate fabric within the host sediments of ODP 204 cores and therefore to relate the formation of gas hydrates to their host environment (Abegg et al., 2006). The relation of gas hydrate fabric, dipping angle of gas hydrate layers and the respective burial depth revealed that deep-seated gas hydrate layers have very steep dipping angles ($60^\circ - 90^\circ$), whereas shallow hydrates have a flat dipping (Abegg et al., 2007). A graphical description of the relation of depth and dipping of hydrate layers as measured in sediment cores by computer tomography analyses is shown in Figure 1.5.

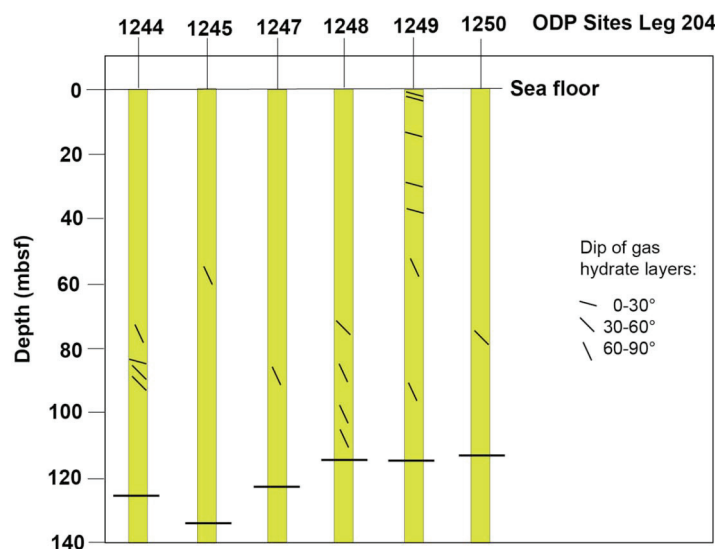


Figure 1.5: Relation of dipping of gas hydrates and burial depth at ODP Leg 204 drilling sites (after Abegg et al., 2007).

Abegg et al. (2006; 2007) and Bohrmann et al. (1998) showed that gas hydrate occurrence on Hydrate Ridge could be classified into two major groups with respect to the burial depth: In shallow depths massive hydrates, hydrate nodules and hydrates which were intercalated with the sediments occurred, the layers formed (sub-)parallel to the bedding. The size of such hydrates varied from millimeters to decimeters, the transition to massive hydrates occurred gradually. At depths greater than the horizon where the overburden pressure overcomes the gas hydrate crystallization force to displace sediment grains, massive hydrates only occurred if large spaces and cavities were present in the sediments. Otherwise, hydrates were found in veins and veinlets with steep dipping angles (Figure 1.5). This is due to upwards-migrating gases and hydrate precipitation along fractures and faults within the sediments (Abegg et al., 2007; Bohrmann & Torres, 2006; Torres et al., 2004; Tréhu et al., 2004).

The focus of the gas hydrate investigations presented in this thesis was laid on hydrates from shallow sediment depths of a few mbsf in order to better understand near seafloor

hydrate deposits. An exception is one hydrate piece from the Indian drilling campaign (Collett et al., 2008a) as well as the ODP Leg 204 hydrates (Appendices IV, V).

1.1.5.2 Shapes of shallow gas hydrates in marine deposits

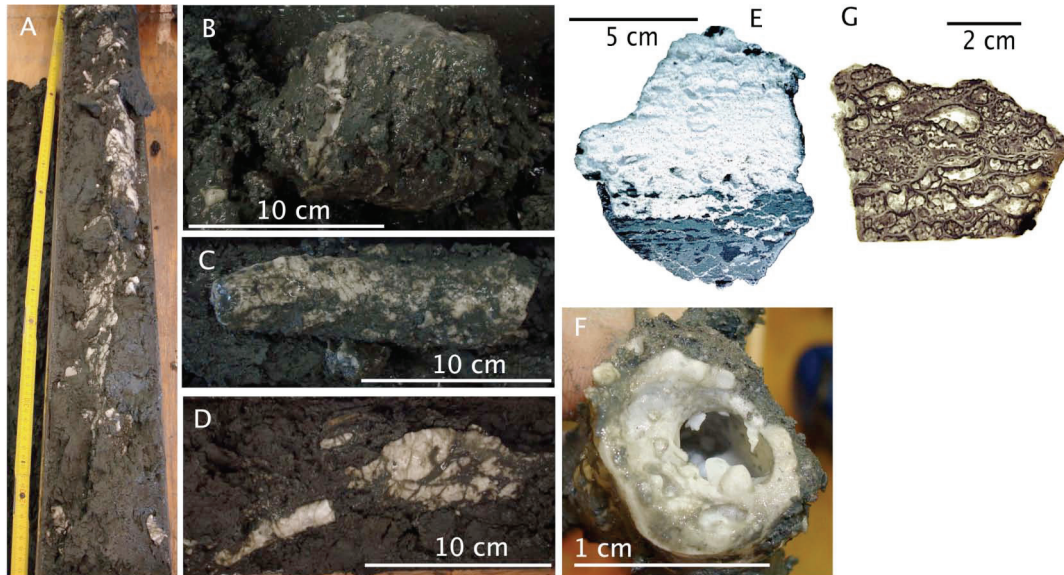


Figure 1.6: Shapes of gas hydrate in shallow marine sediments. **A.** Vein, several centimeters thick and on a length scale of a meter. **B.** Hydrate layer. **C.** Massive, elongated nodule or a thick hydrate tube. **D.** Tube-shaped hydrate piece and a nodule. **E.** Massive gas hydrate layer parallel to the stratification. **F.** Inside view of a hydrate tube: the hydrate precipitated on the inside of the tube, which is in contact to host sediments. The conduit in the center of the tube facilitates gas transport. **G:** Thin Section of pure gas hydrate layer; the globular structure of gas hydrate shows that it is formed from gas bubbles. Figures A, B, C, D, F: R/V Meteor expedition M74/3a, African continental margin offshore Congo river; courtesy T. Pape. Figures E, G: changed from Bohrmann et al., 1998.

Diverse shapes and fabrics of shallow gas hydrates are known (Figure 1.6). Shallow hydrates can be quite massive and deposits can have large sizes near the seafloor. At the Bush Hill in the northern Gulf of Mexico (GOM) and at the Barkley Canyon in the northeast Pacific Ocean massive hydrate deposits several meters in size crop out at the seafloor (MacDonald et al., 1994; Chapman et al., 2004, respectively). At the Chapopote asphalt volcano (short: Chapopote) in the southern GOM hydrate layers of some centimeters in thickness are trapped below layers of asphalt (MacDonald et al., 2004; Chapter 7). Figure 1.6 shows typical examples of shallow gas hydrates. Veins (Figure 1.6 A) typically form when gas is transported vertically along conduits and combines with water to hydrate. When hydrates in shallow sediments force their own space during growth by fracturing or pushing apart the sediment framework (Suess et al., 1999; 2001), they typically form veins (Figure 1.6A), layers (1.6B), tubes (1.6C) and nodules (1.6D) of pure gas hydrate (Abegg et al., 2006; Tréhu et al., 2006a). Nodules can be spherical or elongated (Figure 1.6C, D) depending on gas flux, bedding and fractures in the sediment. Figure 1.6F shows the inside of a tube of gas hydrate; it indicates a high gas flux site where gas both precipitates as hydrate but is also transported further upwards in the sediments through the GHSZ. Occasionally, matrices of massive gas hydrate can encase small sediment clasts. Shallow hydrates can be tightly intercalated with soft and fine-grained sediments, e.g. at Hydrate Ridge. Thin sections of pure hydrate layers and cross sections perpendicular to stratification

revealed dense interfingering of hydrates and sediments (Figure 1.6 E; Bohrmann et al., 1998). Hydrates occurring in layers dominantly form parallel to the bedding but sometimes cross-cut the bedding obliquely (Suess et al., 1999). The fabric of hydrates from Hydrate Ridge was characterized by a spongy structure filled by small bubbles from millimeters to several centimeters, which are elongated parallel to the bedding (Figure 1.6E, G; Bohrmann et al., 1998; Suess et al., 1999).

Shallow gas hydrates from Hydrate Ridge are reported to have a globular fabric, which is formed from trapped gas bubbles under an impermeable layer in which subsequent addition of free gas leads to the formation of globular gas hydrate (Figure 1.6 G; Bohrmann et al., 1998). A similar situation is proposed to exist underneath the asphalt layers at the Chapopote (see MacDonald et al., 2004) for the gas hydrate samples presented in Chapter 7. Impermeable layers can be mandatory in a geological environment to facilitate unusual gas hydrate structural compositions (Chapter 7).

1.1.6 Gas hydrates and energy industry

Gas hydrates are interesting for industry, in particular for the energy industry for several reasons.

Flow assurance: Hydrates cause problems in gas or oil transport, as they can clog pipelines (Wilcox, 1934; Koh, 2002; Sloan & Koh, 2007). Faster flow rates, answering to higher energy demand, cause higher pressures in pipelines, evoking increased hydrate formation (Sloan & Koh, 2007). The economic damage seems to be severe enough that in the major oil companies much work is dedicated to inhibit gas hydrate formation during gas and oil recovery and transport.

Energy/ gas production: Hydrocarbons from hydrates are considered as a potentially significant energy resource (e.g., Max et al., 2006). In a conceptual study Walsh et al. (2009) showed that the range of gas prices necessary to produce gas from hydrates is not significantly higher than it already is in the North American energy market. In Canadian and US-American permafrost, production tests and reservoir models have been conducted at several sites over the past years, such as the Mallik 5L-field test (Dallimore and Collett, 2005), the Mt. Albert stratigraphic test well (Anderson et al., 2008; Collett et al., 2008b), and more (see Anderson et al., 2008). Still, for North America energy production from conventional gas reservoirs in the Arctic is economically more attractive than from gas hydrate reservoirs, therefore Walsh et al. (2009) conclude that the production from gas hydrates will commence once unique market conditions exist.

Gas production from marine hydrate resources on the other hand may proceed even earlier although financial and technological efforts will be greater (Max et al., 2006; Walsh et al., 2009). This can happen if no conventional gas resources exist, diversification of energy supply becomes a concern, or the security of supply becomes part of the political agenda of a country. For those reasons, several countries have launched national gas hydrate programs targeting marine resources. For instance, India launched the National Gas Hydrate Program Expedition 01 (Collett et al., 2008a); China started the Chinese Guangzhou Marine Geological Survey Expedition 1 (Zhang et al., 2007; Han et al., 2008); South Korean scientists currently investigate the Ulleung back-arc basin for gas hydrates (Chun et al., 2008; Ryu et al., 2009) and Japanese scientists explore the Japanese Sea for hydrate deposits (Matsumoto et al., 2009). Various contributions to the 6th International Conference

on Gas Hydrates report on the efforts of those mentioned and more countries to assess their gas hydrate provinces (Englezos & Ripmeester, 2008).

Methane production and simultaneous CO₂ sequestration: Carbon capture and sequestration (CCS) into deep strata reduces carbon emissions and has been done for years (e.g., Lackner, 2003; WBGU, 2006). One option currently being discussed is the incorporation of CO₂ in hydrates, as CO₂ is a hydrate forming gas (e.g., Brewer et al., 1999; House et al., 2006; Rochelle et al., 2009). A variation of CO₂ sequestration by incorporation into gas hydrates is to replace existing gas hydrate deposits in natural systems and sequester CO₂ while simultaneously recovering CH₄ from the hydrates. Experiments eventually targeting such large-scale gas replacement strategies are currently being carried out (Stevens et al., 2008; Husebø et al., 2008; Erslund et al., in press; J. Howard, pers. comm., July and August 2008). In Germany, which has no own gas hydrate resources, the SUGAR project (short for Submarine Gas Hydrate Reservoirs), launched in 2008, targets the prospection, exploration and quantification of suitable methane hydrate deposits, where CH₄ is planned to be replaced by CO₂, and the transportation of methane hydrate.

Further applications: Gas hydrate is an interesting material for more applications due to the high volumetric density of guest molecules compared to free gas. Currently, companies and academia are testing methods to safely transport reactive gases bound in hydrates, for instance hydrogen (Mao and Mao, 2004; Lee et al., 2005; Strobel et al., 2006). Because gas hydrates only form from water and gas and thereby expel other substances dissolved in the water, for instance salts in the case of seawater (e.g., Chapter 6), hydrates can be used for desalination or water purification (Max, 2002; 2006).

1.2 Mineralogical aspects of gas hydrates

Most of the attention gas hydrates receive is due to the volumetric density of gas molecules in the hydrate structure. Often a ratio of 1:164 is quoted, which returns the volumetric ratio of CH₄ gas under standard conditions to an ideally saturated CH₄ hydrate (sl, Section 1.2.1). This ratio was first reported by Davidson et al. (1978). The maximum amount of CH₄ that a hydrate unit cell can store is fixed by the geometry of the water molecules, which span different cage structures.

In the following section different hydrate structures and hydrate forming gases are explained (1.2.1). In section 1.2.2 the microstructure of gas hydrates is introduced. A background on crystallite sizes, growth and ripening of crystals is provided in section 1.2.3.

1.2.1 Structure of gas hydrates

1.2.1.1 Crystallographic structures

Gas hydrates are mostly classified according to their crystallographic structure, which is governed by the local P,T conditions as well as by the gas chemical composition, particularly by the diameter of the gas molecule. Three hydrate structures are known in nature, which are the structures I, II and H (von Stackelberg & Müller, 1951; 1954; Ripmeester et al., 1987). They are typically abbreviated sl, sII and sH, respectively. The unit cells of the hydrate structures comprise different polyhedral cages, and these cage types occur in a certain ratio in a unit cell (Figure 1.7). The cages are described according to the number of faces [*m*], which form the cage, and the number of edges [*b*] in the form [*b*^{*m*}]. For instance,

the large cage (LC) of sI (top left in Figure 1.7) comprises 12 pentagons (5^{12}) and 2 hexagons (6^2), therefore the cage is named $5^{12}6^2$. Six LC and two small cages (5^{12} ; SC) form a sI unit cell. sII is formed from 16 SC and 8 LC, the LC of sII ($5^{12}6^4$) are bigger than those of sI. The diameters of the cages are given in Table 1.1. sH comprises 3 different cage types: 3 SC, which are the same small cages as for sI and sII, 2 medium sized cages, comprising of 3 different crystal planes ($4^35^66^3$), and 1 very large cage ($5^{12}6^8$).

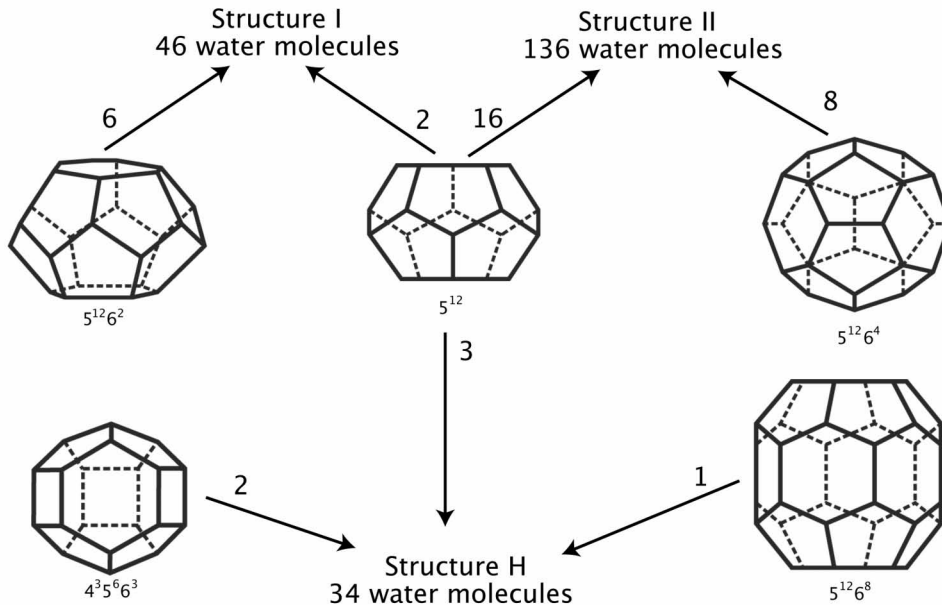


Figure 1.7: Relation of cages and crystal structure of gas hydrates. Depicted are the five different cages, which form three different crystallographic hydrate structures discovered in nature. The smallest cage (5^{12}), shown in the center of the upper three cage types, occurs in all three structures (after Bohrmann and Torres, 2006).

Parameters describing the gas hydrate structures sI, sII and sH are listed in Table 1.1. The SC of sI are connected in space by the vertices of the cages, for sII the faces are shared. For both structures, the spaces between the SC are formed by the LC (Figure 1.7). In sH, face sharing occurs in two dimensions, such that a layer of SC connects to a layer of medium and LC (Sloan & Koh, 2007; Ribeiro & Lage, 2008). All three structures can incorporate different guest molecules into a single unit cell, but sH needs two different-sized molecules to form: one small molecule as a helping gas (Ripmeester et al., 1987) such as CH_4 filling the SC, and a large molecule.

1.2.1.2 Hydration number

Each hydrate cage is formed from water molecules which are hydrogen-bonded. The guests, which are mostly gas molecules, stabilize the cage. To remain stable the ratio of guest and cage diameter needs to be within certain thresholds to assure stability. As gas hydrates are non-stoichiometric compounds, not all cages need to be filled with guest molecules, but if too many cages are empty the structure becomes fragile. However, it has been observed that some cages are occupied by more than one guest molecule. N_2 forms sII hydrate, but due to the small molecule diameter, two N_2 molecules are incorporated into the LC of sII (Kuhs et al., 1997). Also, for hydrogen transport, experiments were conducted

trying to implement as many as 6 H₂ molecules into the LC of sH (Susilo, 2008; R. Susilo, pers. comm. July 2006; July 2008).

The hydration number (n) expresses the ratio of water molecules to gas molecules within a unit cell, assuming single occupancy. It is directly correlated to the cage occupancy (θ), as each unoccupied cage adds more water but no gas molecule to the equation, therefore a high n implies a low θ . sI can host a maximum of 8 guest molecules (Figure 1.7), assuming single occupancy. Because the SC and LC of sI comprise a total of 46 water molecules, the ideal n would be 5.750. For both sII and sH, n ideally would be 5.667. This means that for natural hydrates, n could never drop below this value, otherwise multiple cage occupancy would occur.

The cage occupancy θ is important to determine the amount of gas captured in hydrates. Early gas hydrate assessments assumed an ideal hydration number (Table 1.1), with all cages occupied (Kvenvolden, 1995; 1999). However, literature from various oceanic locations shows that full occupancy so far has never been observed in nature (Kida et al., 2009 and references therein; review in Sloan & Koh, 2007). Udachin et al. (2007) presented the first single crystal data from marine hydrates from two locations, and reported that the LC of both sI and sII were fully occupied. The SC were occupied only by CH₄ and were filled to 89.8%, which agrees to earlier publications (Koh, 2002). Laboratory studies on CH₄ and CO₂ hydrates showed that θ is dependent on P in that n decreases with increasing P, i.e., more cages are occupied at higher P and constant T (Klapproth et al., 2003). That was also observed for other gases, such as H₂S (Cady, 1983). Laboratory investigations on CH₄ hydrate over a wide range of P,T conditions but always close to hydrate dissociation showed that the hydration number for pure CH₄ hydrate remained constant at 5.99 ± 0.07 (Circone et al., 2005). Theoretical calculations for gas hydrate from the Batumi Seep area in the Black Sea comprising mostly CH₄ revealed that at fixed T, θ would increase with increasing P (Figure 1.8). This aspect needs to be considered in quantifications of gas captured in gas hydrates. Chapter 8 addresses the quantification of gas hydrate at the Batumi Seep area.

Table 1.1: Structures of gas hydrate cells (from Sloan & Koh, 2007). Space group reference numbers from the International Tables of Crystallography.

Structure	I		II		H		
Crystal system	Cubic		Cubic		Hexagonal		
Space group	Pm3n (No. 223)		Fd3m (No. 227)		P6/mmm (No. 191)		
Lattice parameters	a = 11.88 Å		a = 17.3 Å		a = 12.2 Å; c = 10.1 Å		
	$\alpha = \beta = \gamma = 90^\circ$		$\alpha = \beta = \gamma = 90^\circ$		$\alpha = \beta = 90^\circ$; $\gamma = 120^\circ$		
Ideal unit cell	$2(5^{12}) \times 6(5^{12}6^2) \times 46 \text{ H}_2\text{O}$		$16(5^{12}) \times 8(5^{12}6^4) \times 136 \text{ H}_2\text{O}$		$3(5^{12}) \times 2(4^35^66^3) \times 18(5^{12}6^8) \times 34 \text{ H}_2\text{O}$		
Ideal hydration number	5.750		5.667		5.667		
Cages	small	large	small	large	small	medium	large
Average cavity radius [Å]	3.95	4.33	3.91	4.73	3.94	4.04	5.79
Variation in radius [%]	3.4	14.4	5.5	1.73	4.0	8.5	15.1
Water molecules per cavity	20	24	20	28	20	20	36

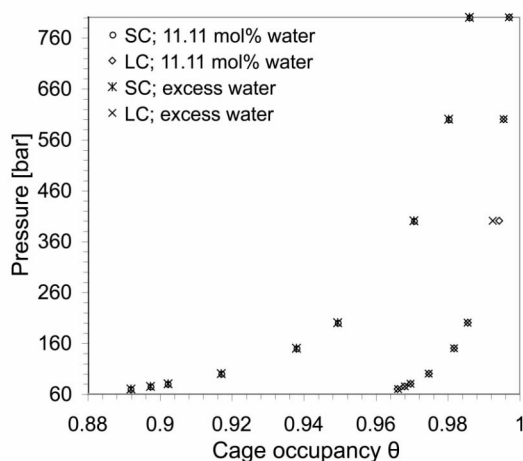


Figure 1.8: Isothermal cage occupancy (θ) against pressure. Calculations were done by the Colorado School of Mines Gibbs Energy Minimization software (CSMGem) (Sloan & Koh, 2007), using gas chemistry data of a gas hydrate piece retrieved from the Batumi seep area during R/V METEOR expedition M72/3 (Bohrmann & Pape, 2007; core GeoB 11925; CH₄: 99.93 mol%; C₂H₆: 0.02 mol%; CO₂: 0.04 mol%. T = 9.0 °C).

1.2.1.3 Relation of gases and hydrate crystal structures

The formation of a discrete gas hydrate structure is determined by the P,T conditions as well as by the size of the guest molecule. Many guests from H₂ to tetrahydrofuran are known to form hydrates (Sloan & Koh, 2007). Not only molecules can be incorporated into hydrates but also noble gases, i.e. elements. Hydrocarbons were most important for the samples presented in this thesis. Also, in the studied marine environments, the P,T field is constrained by $P \leq 300$ bar and T in the range of 0 to 20 °C.

At most known marine hydrate deposits, CH₄ is the prevailing hydrate forming gas (Hester and Brewer, 2009 and references therein; Kvenvolden, 1993), which is due to the fact that microbial degradation of organic material produces CH₄. CH₄ is incorporated into the SC of sI and sII and into the LC of sI. Other than from CH₄, sI also forms from small gas molecules such as H₂S and CO₂ (Figure 1.9; Table 1.2). sII hydrate forms when larger guest molecules, e.g. propane (C₃H₈), *iso*- and *n*-butane (C₄H₁₀) are present in the feeding gas (Figure 1.9; Table 1.2). The ratios of guest molecule sizes and cavity diameters (Table 1.2) help to estimate whether a certain cage type of a crystal structure is likely to be formed from the respective gas molecule. The ratios were calculated using the cage radii given in Table 1.1 (Sloan & Koh, 2007). At guest/cavity ratios >1 (Table 1.2) the incorporation of the respective guest is unlikely under natural conditions on Earth, however laboratory experiments using various gases showed that this is possible under more extreme P,T conditions (e.g., Chou et al., 2000; Moudrakovski et al., 2001).

The samples of the present thesis contain several hydrocarbon species (Chapters 5, 8; Appendix III). If two or more gases are present, the crystal structure is governed both by the size of the largest guest molecule present and by the concentrations of the guests. Ethane (C₂H₆) fits into the LC of both sI and sII. As single guests CH₄ as well as C₂H₆ both form sI hydrate, but when occurring together, either sI or sII can form depending on P,T and the relative concentrations of the potential guests. A CH₄—C₂H₆ mixed hydrate persists at various P,T conditions as sI if the CH₄ concentration stays below 72.2 – 75.0 mol% (Subramanian et al., 2000a) or above 99.2 – 99.4 mol% (Subramanian et al., 2000b). At

Table 1.2: Guest molecules and hydrate cages; ratio of guest molecule diameter versus cavity diameter (from Sloan and Koh, 2007).

Ratio: Guest molecule diameter / cavity diameter					
Guest molecule		Structure I		Structure II	
Molecule	Diameter [Å]	SC	LC	SC	LC
N ₂	4.1	0.804	0.7	0.817	0.616
O ₂	4.2	0.824	0.717	0.837	0.631
CH ₄	4.36	0.855	0.744	0.868	0.655
H ₂ S	4.58	0.898	0.782	0.912	0.687
CO ₂	5.12	1.00	0.834	1.02	0.769
C ₂ H ₆	5.5	1.08	0.939	1.10	0.826
C ₃ H ₈	6.28	1.23	1.07	1.25	0.943
<i>i</i> -C ₄ H ₁₀	6.5	1.27	1.11	1.29	0.976
<i>n</i> -C ₄ H ₁₀	7.1	1.39	1.21	1.41	1.07

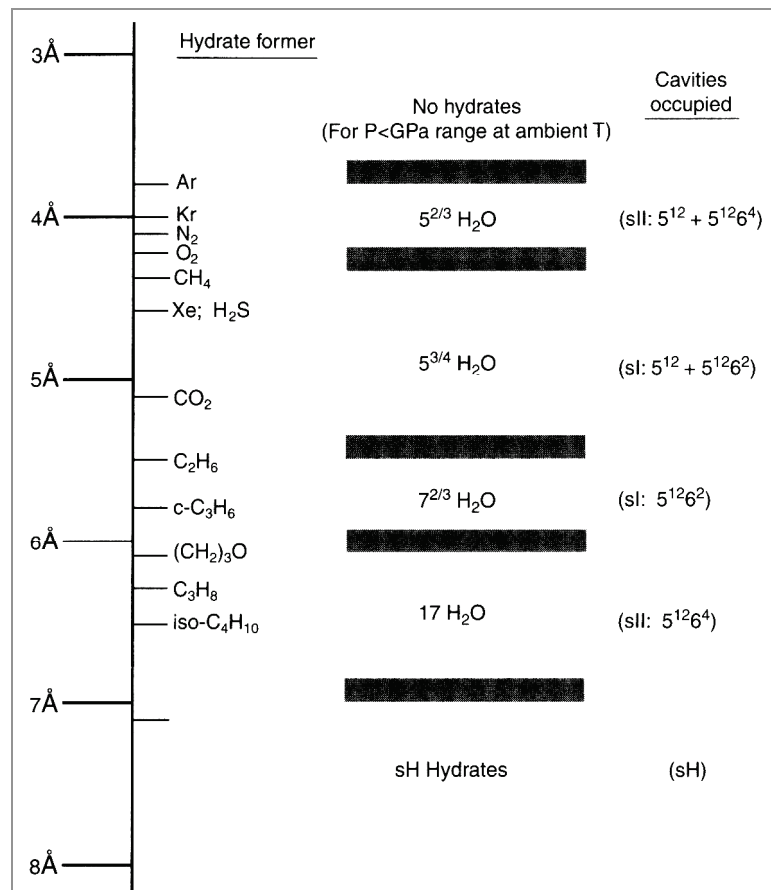


Figure 1.9: Hydrate-forming gases and element/molecule diameters (left column) and the respective cages, where they occur (right column). Depending on the size, some molecules fit only into one cage type, therefore the hydration number (middle column) is high, given that no other molecules are present. Molecules smaller than 3.5 Å do not form hydrates under natural conditions on Earth, and molecules larger than 7.1 Å are incorporated into sH (note that sH needs also small molecules to stabilize the SC) (from Sloan & Koh, 2007).

concentrations between these thresholds, sII hydrate forms. Ballard and Sloan (2001) calculated for a broader P range at 3-4 °C, that depending on P and the relative gas concentrations sI, sII or a mix of both can be expected. The results were confirmed in laboratory experiments by Takeya et al. (2003).

The structural change from sI to sII and sII to sI with mole fractions of ca. 75 and ca. 99 mol% CH₄ and the balance being C₂H₆ can be understood as a structural transition and is explained by the guest molecule diameter/cavity diameter ratio (Ballard & Sloan, 2001; Table 1.2) and the relative abundances of the LC and SC in each structure type (Figure 1.7). At low CH₄ and high C₂H₆ concentrations, sI is the preferred phase because it contains three times as many LC than SC (Figure 1.7; Table 1.1) and in both structures C₂H₆ occupies the LC. At higher CH₄ concentrations the transition to sII occurs because CH₄ is more abundant and is incorporated into the SC of sII, of which sII has twice as many as of the LC. At very high CH₄ concentrations sI is the incipient hydrate structure (Subramanian et al., 2000b). It has been shown that CH₄ and C₂H₆ compositions close to the transition points can coexist in a metastable state (Ballard & Sloan, 2001; Ohno et al., 2009; Subramanian et al., 2000a, 2000b; Yeon et al., 2006). However, recent long-term observations of CH₄—C₂H₆ sI/sII hydrate (95 mol% CH₄; P=50 bar; T= -3 °C) lasting almost six months demonstrated that eventually the coexistence might not be a transient, metastable state but that instead miscibility gaps exist and both structures are stable (Murshed & Kuhs, 2009).

1.2.1.4 Incipient structure and long-term stability

The literature reviewed in this section is important for understanding the coexistence of two closely associated gas hydrate structures. Chapter 7 addresses the co-occurrence of sI and sII gas hydrates from the Chapopote asphalt volcano, which are formed by C₁ to C₅ hydrocarbons.

Under marine conditions, pure CH₄ and water combine to sI hydrate which remains stable in that no structural conversion occurs. However, in recent years researchers have observed that some hydrates undergo transformation, that is, they crystallize in an incipient structure and then transform either completely or partly into another structure. Single guest experiments showed that CO₂ hydrate formed incipiently both as sI and sII mix (Klapproth et al., 2003; T = -1 °C, P = 20 bar; from ice powder, after Kuhs et al., 1992; and Stern et al., 1996). CO₂-sII had initially higher formation kinetics, forming faster than sI. After ca. five hours of reaction, sI formation was faster than sII and sII transformed into sI. The time lapse between the completed formation of sII crystals and the transformation to sI was considered as a transient existence of sII (Klapproth et al., 2003).

Likewise, metastable transient coexistences of sI and sII were observed for CH₄ and C₂H₆ mixes (Ohno et al., 2009). In their experiments, mixed hydrate structures coexisted for a gas composition with 65 mol% CH₄ for one week, while for a gas mix comprising 93 mol% CH₄, all hydrate transformed into sII after three hours. Ohno et al. (2009) proposed that the metastability depended on the gas composition, as the structural conversion happened faster for the higher CH₄ concentration. That was explained by the degree of guest-gas redistribution and the water molecule rearrangement, as well as by differences the driving force for the conversion (Ohno et al., 2009). The driving force is the difference in the chemical potential of water in the liquid and in the hydrate phase (Kashchiev & Firoozabadi, 2002). It is also an important factor in the induction time for gas hydrate nucleation of

different compositions and at different P,T conditions (Ribeiro & Lage, 2008; Skovborg et al., 1993).

Structural transitions of gas hydrate were observed by exposing C₂H₆ sl hydrate to a CH₄ atmosphere (Murshed & Kuhs, 2007; Murshed et al., submitted). A gas replacement reaction occurred in combination with a structural change from sl to sII starting at the surface of the preexisting hydrate with a shrinking core (see Kuhs et al., 2006) of yet unreacted parent material. Murshed and Kuhs (2007) and Murshed et al. (submitted) concluded that a regrowth process of gas hydrate crystals, which is stimulated by a change in the feeding gas composition must be limited by diffusion control of the reacted shell towards the core. This implies that at any given time different structures may coexist, controlled by a change in the feeding gas, which can be stable over long time periods (Murshed & Kuhs, 2009). Similar to the experiment, hydrocarbon feeds from different sources were reported for hydrate deposits in the Kukuy Canyon in Lake Baikal and were related to different hydrate structures, which were found in the canyon (Kida et al., 2006, 2009). A sl and sII hydrate mix was also found in bulk samples of outcropping gas hydrates at Barkley Canyon; the hydrates were characterized by heterogeneous CH₄ dominated gas compositions (Hester et al., 2007a). To study the structure co-occurrence, the authors grew sl and sII hydrates, which formed simultaneously from an artificial gas mixture (92.5 mol% C₁, 7.5 mol% C₂—C₅) in natural settings. 65 days after the reaction, the authors found a heterogeneous mix of sl and sII, which Hester et al. (2007a) ascribed to a formation mechanism that allowed for hydrate growth in isolated pockets and reactors such as gas bubbles coated by hydrate skins (Mori and Mochizuki, 1997; Tophan, 1984; see also Figure 1.4B). Also at Barkley Canyon, a sII-sH hydrate mix was found (Lu et al., 2007). The co-occurrence was ascribed to the circumstance that the gases captured in the hydrate mix would neither all fit into sII nor into sH, such that a coexistence of both structures emerged (Lu et al., 2007). This interpretation corresponds to the observation of a miscibility gap for CH₄ and C₂H₆ (Murshed & Kuhs, 2009). An equilibrating system seeks to reduce the Gibbs free energy (Lasaga, 1998), and from the cited studies it emerges that for hydrocarbon compositions of C₁—C₅ and P,T conditions relevant for marine hydrate systems a coexistence of more than one structure may provide the lowest intrinsic energy and stabilize the system.

Isobaric subcooling from outside to inside of the CH₄ sl stability horizon de-mixed a sII hydrate formed from CH₄, C₂H₆ and C₃H₈ into a coexistence of CH₄ dominated sl and C₂H₆- and C₃H₈-rich sII hydrate (Schicks et al., 2006). During the transition process, all crystals first decomposed and then regrew. It is unknown how stable the coexistence is for longer time periods, but the de-mixing process was reversible and commenced rapidly (Schicks et al., 2006). The reversibility of the structure conversion is remarkable as it suggests that the transition comprising rapid decomposition and regrowth into different structures, as observed by Schicks et al. (2006), is a thermodynamically stable process instead of a metastable phenomenon.

1.2.1.5 Volatility

The volatility of hydrate guest molecules is not only relevant for hydrate formation but is also considered to be important for certain microstructural features, in particular the porosity or non-porosity of gas hydrates. In Chapter 5 the microstructure of gas hydrates is discussed in relation to the crystallographic structure and gas composition.

During gas hydrate formation the incipient hydrate structure provides the greatest reduction of Gibbs free energy coming from the vapor and water phase (Ballard & Sloan, 2001). Also, the frequently used modeling software CSMGem, used here to obtain information on phase boundaries and flash calculations for incipient hydrate structures, uses convergence criteria to minimize the Gibbs free energy in hydrate/water/ice/vapor systems (Ballard & Sloan, 2001; Sloan & Koh, 2007). The greatest reduction in free energy can be achieved with a high cage occupancy θ , i.e. optimal filling of the available cages for the given hydrocarbons. Critical reviews of different proposed hydrate nucleation models are given by Ribeiro & Lage (2008) and Sloan & Koh (2007). The actual P,T coordinates for the phase transition into the hydrate stability also depend on the volatility of the hydrate forming gases. This is because in either of the models for hydrate nucleation, gas molecules need to be captured in cages of water molecules. More volatile gases are more fugitive, therefore, volatile gases require more subcooling compared to less volatiles. At P,T conditions relevant for marine seep environments, CH₄ has a vapor pressure 10 to 20 times higher than C₂H₆, which has a vapor pressure more than 10 times higher than C₃H₈. C₃H₈ has a vapor pressure about 8 times higher than C₄H₁₀ (Perry & Green, 1997).

1.2.2 Microstructure

The microstructure is understood as the structure of a sample at high magnifications (Goldstein et al., 2003). It implies surface characteristics of a material (Chapter 5; Appendix IV) as well as the three-dimensional architecture (Friis et al., 2007; Medalia et al., 2002; Chapter 6), structural effects of compositional changes in composite materials, the inclusion or exclusion of components in multi-component systems (e.g., liquids, gases or solids; Chapter 5), crystallographic phases forming the material (although there, the transition passes over into the nanostructure, e.g., Wang et al., 2008), the fabric of the material, and properties of the grains or crystals forming the material. The properties of grains and crystals are subdivided into the texture and orientation of grains, assemblages of crystallites to agglomerates, and the crystallite sizes and size distributions. The microstructure of a material can influence physical properties such as strength and behavior at different temperatures and pressures (e.g., Durham et al., 2003). Several of these aspects with respect to gas hydrates are described in the following sections.

1.2.2.1 Sub-micrometer sized porosity

The meso- or microporosity of hydrates is a characteristic that has been investigated over the past ten years: Artificially formed hydrates from CH₄, argon (Ar), N₂ and CO₂ are known to feature a porous microstructure (Genov et al., 2004; Klapproth et al., 2003; Kuhs et al., 2000a, 2004a, 2004b; Staykova et al., 2003). Also, sl hydrates recovered from marine and permafrost deposits show the same porous microstructure. All mesopores have almost the same size, irrespective of burial depth, transfer during recovery (given that the hydrates did not decompose completely), hydrate forming P,T conditions and pore water composition (Kuhs et al., 2004a, 2004b; Suess et al., 2002; Techmer et al., 2005; Chapters 3, 4, 5; Appendices IV, V). Except for CO₂, the pores have diameters in range from ca. 200 to 400 nm and therefore are named micro- or mesopores. CO₂ hydrate pores have diameters of less than 100 nm (Kuhs et al., 2000a; Genov et al., 2004).

Dense hydrate surfaces have been synthesized for sl hydrates above the ice point by Falenty et al. (2007), Klapproth et al. (2007) and Stern et al. (2004; 2005), but they were not distinguished in relation to the crystal structure or gas composition. In Chapter 5 dense, i.e. non-porous sII hydrates from the Gulf of Mexico are described comprising significant amounts of C₂—C₅ molecules. There, microstructural observations are discussed regarding the volatility of the gases, the thermodynamic stability and the crystal structure.

1.2.2.2 Microstructure and anomalous self-preservation

Microstructure observations on gas hydrates helped to shed light on the anomalous self-preservation of gas hydrates (Kuhs et al., 2004b; Stern et al., 2001; Takeya et al., 2001). Intense studies over the past years on decomposition and dissociation kinetics (Falenty et al., 2007; Circone et al., 2003), particularly aided by neutron diffraction (Falenty & Kuhs, 2008; Kuhs et al., 2004b; Kuhs & Hansen, 2006), helped to define certain isobaric temperature and isothermal pressure ranges (so-called “islands”) of meta-stability, where the decomposition of hydrates is slowed down. For instance, at atmospheric pressure and -5 °C CH₄ hydrate is metastable such that the time that passes to decompose 50% of the hydrate is almost one month (Stern et al., 2001). Stern et al. (2002) suggested that ice, which is produced from the endothermic decomposition, shields the still intact hydrate temporarily. The self-preservation seems to be related to the ice cover. Defects in the ice are supposed to facilitate the diffusion of gas molecules through the ice during the decomposition (Kuhs et al., 2004b; Falenty & Kuhs, 2008). Microstructure inspections on partly dissociated hydrates with well constrained and monitored decomposition histories revealed differences in the microstructure of ice and hydrate. Samples, which were decomposed at comparatively high temperatures were covered by large ice crystals with well defined grain boundaries (Falenty & Kuhs, 2008). Apparently the ice anneals faster at warmer temperatures due to higher water molecule mobility (e.g., Devlin, 2000). Instead, open pores from degassing were found in samples which decomposed at lower temperatures (Falenty & Kuhs, 2008). These results on the microstructure show that the anomalous preservation is not only controlled by the temperature gradient shifting hydrates outside of the stability but also by the degree of annealing of the ice coverage, which seals open pores where the hydrate degasses.

1.2.2.3 Microstructure imaging of decomposing hydrates

Awareness of the decomposition history is mandatory when dealing with gas hydrate samples, as it was for this thesis. Bohrmann et al. (Appendix IV) investigated systematically the grade of decomposition of samples from the Hydrate Ridge (ODP Leg 204). For samples with large ice fractions and little hydrate left over, extensive decomposition pores in the micrometer range were observed by Scanning Electron Microscope investigations (Section 2.1.5). In contrast, well-preserved samples with large hydrate fractions and little ice were characterized by typical monotonous mesoporosity (Kuhs et al., 2000a; Appendix IV). Clear differences exist between the dissociation-derived pores and the intrinsic porous microstructure of hydrates (Section 1.2.2.1).

In contrast to the almost mono-disperse mesopores, as a result of dissociation every decomposition pore has a different diameter. Dissociation pores are much larger than mesopores and often have a pore diameter of more than 10 µm, sometimes even 50 to 100

μm (see Appendix IV). Also, the dissociation-derived pores are fewer than mesopores (unless the hydrate is completely dissociated), i.e. there are larger dense parts of the sample between the pores. EDX analyses tell that the matrices in which the dissociation pores are found comprise ice, indicating a dissociation of the hydrate accompanied by the release of the gas. Bohrmann et al. (Appendix IV) showed that the quantitative ice-hydrate ratio corresponds well to the observations of the surface of the specimen covered by dissociation pores, suggesting that the large pores in the ice matrix are dissociation features, as was suggested by Kuhs et al. (2004a) and Stern and Kirby (2007).

Macroscopic inspections of hydrate samples indicated that some pores, or rather bubbles, are inclusions of free gas in the hydrate matrix. Such free gas bubbles can be considered as the original part of the in situ structure (Bohrmann et al., 1998), whereas decomposition pores are secondary alterations. These gas bubbles would add to the porosity estimation (e.g., Suess et al., 2002). Recent experiments both in laboratory (Schicks et al., 2006) and in open water (Hester et al., 2007a) showed that occluded gas (small bubbles of a few micrometers size) co-occurs with gas hydrates in samples, which confirms previous gas bubble observations in microanalysis.

1.2.2.4 Developments for microstructure characterization of hydrates

Presently, research in gas hydrate microstructures focuses on imaging and recording different stages in gas hydrate formation and decomposition under various conditions (Camps et al., 2008; Falenty & Kuhs, 2008; Murshed et al., submitted; Stern & Kirby, 2008; Stern et al., in press). Recent advances in microstructure work tried to overcome certain limitations; for once, by studying time-resolved subsamples with constrained P,T and gas composition backgrounds, where processes could be resolved (e.g., Falenty & Kuhs, 2008; Murshed & Kuhs, 2009; Murshed et al., submitted), and also by implementing modern computer-tomographic techniques into hydrate research (Chapter 6), which allows to image three dimensions of the sample.

On a microscale, for natural samples the identification of ice from hydrate decomposition and from frozen pore water can be made on the basis of salt crusts, which are excluded during the formation of ice from pore water (Stern & Kirby, 2008; Chapter 6; Appendix IV). Also, tunnel-like structures connecting intact gas hydrate and areas of decomposition were interpreted as the beginning of hydrate decomposition. The progression of so-called decomposition fronts can be traced by these proxies and has been done both by SEM (Techmer et al., 2005; Appendix IV) and micro-computer tomography (Chapter 6).

Since in natural deposits gas hydrates form from gas bubbles (Clennell et al., 1999; Leifer & Judd, 2002; see Topham, 1984) microstructure analysis of gas bubbles can be used to investigate hydrate formation. Similar to time-resolved studies of hydrate decomposition kinetics (Falenty & Kuhs, 2008; Kuhs et al., 2004b), time-resolved formation experiments can be performed in open ocean (unpublished data), in that hydrates, which are sampled at different time intervals, and are studied onshore by microstructure analyses tools. Evaluation and interpretation of underwater experiments, conducted in the Monterey Canyon offshore California together with the Monterey Bay Aquarium Research Institute in summer 2008, are underway.

Microstructure analyses have been found helpful to distinguish between different hydrate structures and volatile hydrocarbons forming these structures. Chapter 5 describes how

SEMs were used to identify porous and non-porous microstructure on hydrates having discretely different gas chemical composition and crystallographic structures.

1.2.3 Grain growth

Air hydrates have been observed in polar ice (Shoji & Langway, 1982), where these hydrates crystallize from air inclusions and ice (Pauer et al., 1999). Initially, many small hydrate crystallites form from one air bubble in the ice (primary air hydrates) and subsequently regrow to a single hydrate crystal (secondary air hydrate) (Kipfstuhl et al., 2001; Ohno et al., 2004; Pauer et al., 2000; Salamatin et al., 2003). In an earlier publication (Klapp et al., 2007), which preceded this thesis and the publications herein, it was assumed that similar recrystallization processes happen in marine settings, where freshly flocculated hydrate crystallites regrow (Appendix V).

In this thesis the terms *grains*, *crystals* and *crystallites* are used to describe a single hydrate crystallite. Technically, crystallite sizes of gas hydrates belong to the microstructure characterization (Section 1.2.2). However, because grain growth is an important subject of this thesis, it is introduced here in an own section.

Crystallite size distributions can help to understand gas hydrate formation and subsequent evolution. The crystal size evolution is mainly governed by the free energy differences between grains, that is, the grain boundary surface energy and the contribution of deformational work to the free energy (Ricard & Bercovici, 2009).

1.2.3.1 Ostwald ripening

Ostwald ripening is considered as the underlying process governing the crystal growth of the hydrates presented in this thesis. Ostwald ripening is discussed in Chapter 4 in particular, but also in Chapters 3 and 7 as well as in Appendix V.

The regrowth process from small to large crystallites can be described as grain coarsening. If the mobilities of present water and gas molecules are high, such as at relatively warm temperatures, grains can grow in a process called “normal grain growth” or “Ostwald ripening”. In those coarsening processes large grains grow on the expense of smaller grains in order to decrease the free energy in the system by lowering the total surface or grain boundary energy. This is considered as one of the major driving forces in regrowth of marine gas hydrates (Klapp et al., 2007; Appendix V) and is also supposed to be the driving force in the regrowth of primary to secondary air hydrates in polar ice (Kipfstuhl et al., 2001). Normal grain growth is controlled by a diffusive mass transfer from small to large grains, which also implies that the presence of impurities or particles within the grain boundary network could hinder the coarsening or slow it down (Doherty et al., 1997).

Originally, Ostwald ripening was considered as a process occurring in liquids. According to Wagner (1961), Ostwald ripening occurred in an emulsion in which diffusive mass transfer happens between droplets of one phase through a second liquid phase. Thereby, mass is transported from small droplets to the increasing surface of larger droplets. The higher solubility of small droplets of one liquid within a second liquid is the driving force for Ostwald ripening (Wagner, 1961). A further reason is the minimization of the interfacial energy which is accomplished by the reduction of the contact area to the surrounding medium (Lasaga, 1998; Lifshitz & Slyozov, 1961). This second argument does not only apply for liquid phases.

Instead, minimization of the interfacial energy also occurs in gases or solid materials (Lasaga, 1998), for instance in ice. Legagneux (2003) explained the metamorphosis of snow by Ostwald ripening of ice crystals. For solid materials Ostwald ripening means coarsening of larger particles by dissolution of small particles and diffusive transport through the media, driven by the reduction of the interfacial energy.

Assuming that in a model (see Lasaga, 1998; Wagner, 1961) all particles were spherical and disconnected from others then the diffusion field of each particle would be also spherical. Every molecule hitting a surface of a particle is incorporated into the lattice. The system is developing into a dynamical steady-state. This implies that the shape of the particle size distribution stays the same if it is normalized with the mean crystallite size. It also means that the model can be described using a growth equation:

$$R_c^n - R_0^n = Kt \quad (1)$$

with R_c = mean crystallite size; R_0 = mean crystallite size at $t = 0$; n = growth exponent; und K = growth rate. Models suggest a growth exponent of 2 (Wagner, 1961) or 3 (Lifshitz and Slyozov, 1961).

The growth rate K depends on the shape of the particles (Humphreys & Hatherley, 2004). Impurities between the crystals can hamper mass transport, which is known as Zener-pinning (Doherty et al., 1997). This might be relevant for gas hydrate crystal growth because while water molecules from pore waters form hydrate cages, ions which were dissolved in the water are excluded and salts crystallize from those ions in the interspaces between crystals. Also, larger hydrocarbons, which occur at oil and asphalt seeps and cannot be incorporated into the hydrate lattice, can stay occluded between crystals. Salts or oil between crystals might act as impurities between grains in that they slow down diffusive mass transfer Chapter 3; 4).

1.2.3.2 Static grain growth

The steady-state grain sizes are balanced by normal grain growth and dynamic grain size reduction (Austin & Evans, 2007). Contribution of grain damage to the free energy is important if stress affects grain growth or reduction. Austin & Evans suggested that crystals grow to a stable size, which would be constrained by the deformation conditions, given that all other microstructural controls are either in steady-state or otherwise do not affect the partitioning work.

For interpreting crystallite sizes of gas hydrates, it is important that normal grain growth and dynamic grain size reduction work independently (Austin & Evans, 2007). A static grain size will occur when grain growth and reduction are equal. The grain growth equals the static grain growth when the grains are not under deformation stress. As the soft sediments hosting gas hydrates in shallow marine deposits are not rigid enough to transfer stress on hydrate crystals, which would damage the grains, the grain growth of hydrates can be considered as static (see Austin & Evans, 2007; Ricard & Bercovici, 2009). However, deformational stress might be relevant for gas hydrates in greater sediment depth (see Section 1.1.5.1; Torres et al., 2004).

Crystallite sizes of gas hydrates are discussed throughout Chapters 3 to 9. Chapter 3 provides an introduction to the methods how hydrate crystal size information were acquired, about the challenges, and reports crystallite sizes of natural gas hydrate samples. Chapter 4 provides further data and interpretation; the data are discussed in respect of the geological hydrate environment and implications. Chapter 6 shows how microstructural features can be imaged by micro-computer tomography and thereby highlights a novel approach of how hydrate crystallite sizes might be obtained in future. Chapters 7 and 8 discuss grain size information as one factor of several in a broader context: Chapter 7 reports on co-occurrence of hydrate structures which have different grain sizes; and Chapter 8 describes shallow hydrate accumulations in a high gas flux seepage area, where grain sizes are interpreted as one proxy of several in describing the dynamics of the system. The interpretations of these chapters are reviewed in Chapter 9, where also future perspectives are presented.

1.3 Motivation and main questions

It has become clear over the past years that considerable delicacy and complexity exist in the relationship between crystal structure and size of hydrate formers if more than one gas species is present. This emphasizes the need to obtain structural information together with thermodynamic parameters, especially in multicomponent systems. Current interest in hydrate persistence and decomposition requires the application of new techniques that allow acquiring high-resolved structural and statistically significant crystallite size information. A better comprehension of the growth of hydrate crystals and of the crystallite size evolution, as well as understanding of interfacial properties, is the key to understanding hydrates in natural environments.

The driving force for this thesis was to learn more about how gas hydrates occur on Earth, in particular in high magnification, at which the basic properties are discernable that govern the evolution of large hydrate deposits. The main question was not how they nucleate in the subsurface, but rather how they persist, how they change over time, whether a second structure forms, and how the gases could reach the atmosphere when the hydrates decompose.

What is the relation between the guest molecules, the prevailing crystallographic structure and the microstructure?

When the thesis was started in September 2006, it was assumed that gas hydrates in general feature a microporous microstructure. There was good evidence for that: whatever gases were used to produce hydrates, and no matter which hydrates from natural occurrences were studied – all samples had micropores. Occasionally, some samples also revealed dense parts but dense hydrates had rarely been observed in nature. Therefore, the questions raised here are: How and when do porous and non-porous hydrates form, how does the (lacking) porosity relate to the ambient thermodynamic stability, and how does it relate to the crystallographic structure and gas chemical composition?

What do hydrate crystallite sizes and size distributions reveal?

Early results of grain size analyses from Hydrate Ridge (ODP Leg 204) preceding this thesis showed that the sizes of gas hydrate crystals from Hydrate Ridge were quite large

and much larger than synthetic samples prepared in the lab. That were very exciting results. Of course these first results urged investigating the crystallite sizes of more hydrate samples from other locations. The questions asked for this study are: What are the crystallite sizes of hydrates from other places? How much do they vary? How are the crystallite size distributions shaped and what does this reveal about particular hydrate deposits? What factors could possibly control the grain sizes and how are time and ripening processes involved?

How do two gas hydrate structures form at one geological site?

The first report on the coexistence of two hydrate structures in a natural deposit was published half a year after this thesis started and it described the coexistence of sI and sII in one gravity core in Lake Baikal (Kida et al., 2006). In 2007, a paper was launched reporting on intimately associated sII/sH hydrates from Barkley Canyon, which was also the first publication showing evidence of natural sH hydrates (Lu et al., 2007). From a mineralogical point of view it is quite likely that at a thermogenic gas seep discharging methane and higher hydrocarbons not only one structure is formed. Both laboratory experiments and free energy minimization calculations show that miscibility gaps are possible in the case of hydrates under certain P,T conditions and gas mixtures. In this thesis, the Chapopote asphalt volcano in the Gulf of Mexico was identified as a third location where two structures co-occur. The questions asked are: How did the two structures form? Did one structure form first? What is the role of the environment where the hydrates precipitated? These questions are still largely unanswered in the case of Lake Baikal and are also the reason for ongoing research at the Barkley Canyon.

Amount of gas hydrate at the Batumi seep and possible transport mechanisms to the sea surface

In order to look beyond the microstructure of gas hydrates, an approach to constrain the extend of a gas hydrate province related to an area of active, at some spots ferocious seepage was conducted at the Batumi seep area (Black Sea) by integrating different methods. The extent of the seepage area was obtained by hydro-acoustic techniques and the gas was quantified by controlled degassing of pressurized sediment cores. Calculations on the amount of hydrates were done by considering pore volume, salinity, solubilities of the gases, dissolved and free gas as well as hydrate-bound gas. The questions are: How much gas is stored in hydrates within the constrained area? Which mechanisms can be considered for transporting the gas to the sea surface?

CHAPTER 2

METHODS AND SAMPLING LOCATIONS

2.1 Methods

2.1.1 Recovery of samples

The gas hydrates presented in this thesis were retrieved either with gravity corers or video-guided grab sampler (TV-grabs). The gravity corers were deployed with a 6 m or a 3.5 m-core barrel with an inner diameter of 13.2 cm. For the deployment the winch speed was commonly set to 1.0 m/s to slack and 1.3 m/s to heave the gravity corers in the water column. Heaving of the sediment-loaded gravity corers out of the subsurface was done with 0.2 to 0.5 m/s. The head of the gravity corers was burdened with approximately 0.8 to 2.5 t of lead. The coring was conducted with a soft plastic hose inside the barrel, which allowed rapid access to the hydrates on deck minimizing their dissociation after recovery. The gas hydrates were swiftly carried into liquid nitrogen ($-196\text{ }^{\circ}\text{C}$), where they are stable for long-term storage (Tulk et al., 1999). Gravity corers were used for gas hydrate recovery during all research cruises relevant for this thesis.

The TV-grab was used to recover large sample volumes ($\leq 0.8\text{ m}^3$) from a defined sampling location in the sediment. In contrast to gravity cores, due to the operation of the TV-grab, the samples are not oriented within their sediment matrix after the release from the grab on the ship's deck. The TV-grab was operated during the R/V SONNE expedition SO 174 in 2003 (Bohrmann & Schenk, 2004).

2.1.2 Gas chemistry

The molecular compositions of the hydrate-bound gas were obtained by gas chromatography. For all samples presented in this study, in total two gas chromatographs (GC) were used.

During the R/V SONNE expedition SO 174, for analyzing C_1 – C_5 hydrocarbons, a Thermo-Electron GC equipped with a capillary column (Alltech AT-Q; 30 m length; 0.32 mm inside diameter) and a flame ionization detector was used, as described in Heeschen et al. (2007). For hydrates from all other expeditions a two-channel GC from Agilent Technologies type 6890N was employed. C_1 – C_6 hydrocarbons were quantified with a capillary column (OPTIMA-5; 50 m length; 0.32 mm inside diameter) connected to a flame ionization detector, whereas O_2 , N_2 , and CO_2 as well as CH_4 and C_2H_6 were determined using a packed (molecular sieve) stainless steel column coupled to a thermal conductivity detector. Further details on the CGs are described in Heeschen et al. (2007) and Pape et al. (submitted).

The molar ratios of hydrocarbons were used to relate the hydrate-bound components to thermogenic or biogenic sources (section 1.1.2.2; Bernard et al., 1976), to estimate the crystallographic structure (section 1.2.1), and to calculate the hydrate thermodynamic stability. That was accomplished using the HWHYD software (HWHYD, 2005), which is a commercial program from Heriot-Watt-University; as well as CSMGem software (Ballard & Sloan, 2001; Sloan & Koh, 2007). CSMGem is a multi-phase flash program for hydrate prediction. It is a Gibbs energy minimization program, which incorporates the mechanical model for hydrates of Van der Waals and Platteeuw (1959) and funds on spectroscopic and diffraction measurements (Ballard & Sloan, 2001).

2.1.3 X-ray diffraction

X-ray diffraction (XRD) is one of the key methods in this thesis. It was used both to analyze and quantify the hydrate phases present in a sample and to measure the sizes of hydrate crystallites.

The XRD data were obtained either at a high-energy Synchrotron facility or – only in the case of phase analyses – also with a laboratory powder diffractometer. The Synchrotron beamlines BW 5 and HARWI II of the ‘Hamburger Synchrotronstrahlungslabor’ (HASYLAB) at the ‘Deutsches Elektronenstrahl-Synchrotron’ (DESY) were used. The storage ring of the HASYLAB provides high beam energy (ca. 100 keV) corresponding to a short wavelength of ca. 0.12 Å (see Nielsen & McMorrow, 2001). An imperfect Silicon single crystal was used as a monochromator. The high beam energy provides deep sample penetration and hence is well suited for bulk sample investigations. Synchrotron radiation is also advantageous over conventional laboratory X-ray sources as the X-ray beam is very parallel and therefore allows for a high angular resolution. The diffraction patterns obtained by Synchrotron XRD were recorded on a two-dimensional area detector (type mar345). For more details on the XRD measurements at the BW5 beamline see Bunge et al. (2002, 2003), Klein et al. (2004), Wcislak et al. (2003) and also Chapter 3 of this thesis. A general overview of X-ray diffraction is given in Nielson and McMorrow (2001).

During the measurements, the gas hydrate samples were kept stable by using a cryostat cooled by a closed helium cycle. The temperature was set to 80 K (–193 °C) and was monitored by a ‘Lake Shore’ temperature controller.

2.1.3.1 Phase analysis

Phase analyses comprised of several successive steps: For the data processing, the two-dimensional diffracted Debye-Scherrer-rings from the Synchrotron measurements were transformed into a digital format displaying the recorded diffracted X-ray intensity as a function of the diffraction angle (Figure 2.1). That was done using the software *fit2d* (Hammerley et al., 1996), which provides tools to integrate the diffracted Debye-Scherrer-cones as well as a masking tool to hide (or exclude) high-intensity spots on the Debye-Scherrer-cones, which can derive from large crystallites in the sample. The masking function is convenient tool when samples are X-rayed both to obtain the phase composition and the crystallite sizes, such that the sample cannot be crushed prior to the measurements and accordingly comprises larger crystals.

In addition to Synchrotron measurements also a laboratory diffractometer was used for phase analyses. The diffractometer is a Philipps Materials Research Diffractometer cryogoniometer operating at a wavelength of 0.7093 Å from a molybdenum anode. It is equipped with a closed-cycle helium-cryostat facilitating cold-temperature measurements and is located in the laboratories of the ‘Abteilung Kristallographie’ at the University of Göttingen. A temperature of 80 K (–193 °C) was maintained during measurements, monitored by a ‘Lake Shore’ temperature controller.

For quantitative phase analyses, the diffraction data of both laboratory diffractometer and Synchrotron facilities are treated with the Rietveld method, which is a least square method allowing to iteratively fit the structural data of the sample with the structural data of the anticipated phases the sample is supposed to contain (Allmann & Kern, 2002). For this thesis,

the Rietveld software GSAS (Larson & Von Dreele, 1994) was used within the software environment of EXPGUI (Toby, 2001). The crystal structure parameters for sI were taken from Klapproth (2002), for sII modified from Rawn et al. (2002) (M.M. Murshed, pers. comm., Sept. 2006) and for sH from Kirchner et al. (2004). The crystal structure parameters for hexagonal ice (I_h) were modified from Leadbetter et al. (1985). For the Rietveld refinement, a Chebychev background function of 6 polynomial terms was assumed and subsequently refined. The Rietveld refinement also included the weight fractions of the phase constituents as well as their lattice parameters (see Table 1.1; Section 1.2.1), the zero point on the detector and three Gaussian profile parameters (GU, GV and GW) to fit the shapes of the peaks.

Ideal powder diffractions of the three known crystallographic structures occurring in nature are shown in Figure 2.1 (A, B, C). A XRD pattern of sH is shown for completeness, although the structure was not found in any sample investigated in this thesis. sI hydrate was identified by the characteristic reflections (321), (320) and (210) (Figure 2.1 A); the characteristic peaks to identify sII gas hydrate are the strong (531) and (440) signals (Figure 2.1 B). However, in the mixed sI/sII hydrate (Chapter 7), where sII was not the dominant hydrate phase, sII could be clearly identified by the (400) and (111) reflections, which do not overlap with reflections from other phases. Typically, during Synchrotron measurements the diffraction angles in the 2 θ spectrum from 0° to 3.0° 2 θ are refined for gas hydrate analyses due to reflections of the sample containers at higher diffraction angles. For completeness, Figure 2.1 displays the spectrum up to 7.2° 2 θ .

2.1.3.2 Crystallite size analyses

Investigating crystallite size was a major objective of this thesis. The 'moving area detector method' applied on gas hydrates is a new technology to obtain crystallite size information in a statistically significant quantity and provides the crystallite size distributions, which allows to draw conclusions on the crystallite size evolutions of gas hydrates.

The crystallite sizes were measured by the use of Synchrotron XRD. However, in contrast to phase analyses measurements, both the detector and the sample were moved in order to obtain two dimensions of the crystals. The two dimensions are the orientation coordinates of the crystal on the respective Debye-Scherrer-ring, also known as the orientation angle [γ] (Bunge et al., 2003), of which the crystallites are measured, and the lengths of the reflections. The 'moving area detector method' was developed for material science purposes (Bunge et al., 2002, 2003; Klein et al., 2004; Wcislak et al., 2003). Because Bragg diffraction is used to obtain information on the internal structure of a sample – i.e. the grain sizes –, the name 'Bragg tomography' is used synonymously with 'moving area detector method'. This emphasizes that the method is in fact a tomographic technique, operating with XRD instead of absorption as most tomographic techniques do (e.g., Chapter 6).

Detailed accounts on the experimental set up of the 'moving area detector method', the requirements on sample and beam quality, and on data processing are given in Chapter 3, which is considered as a methodological manuscript describing the 'moving area detector method' with respect to gas hydrate analysis. Also, the manuscript in Appendix V gives a description of the method.

Other than Bragg tomography, further methods exist to obtain some crystallite size information of gas hydrates, including calculating the crystallite size from the spot size on a Debye-Scherrer-ring (Klapproth, 2002; Rodriguez-Navarro et al., 2006; S. Hemes, W.F. Kuhs, H. Klein, pers. comm. July 2009) or electron microscopy (Falenty & Kuhs, 2008; Staykova et

al., 2003). Optical microscopy is used to observe hydrates during formation experiments (Makogon, 1994; Ohmura et al., 2004; Schicks et al., 2006; Smelik & King, 1997; Tohidi et al., 2001), or investigating hydrates from air molecules (Pauer et al., 1999; Kipfstuhl et al., 2001).

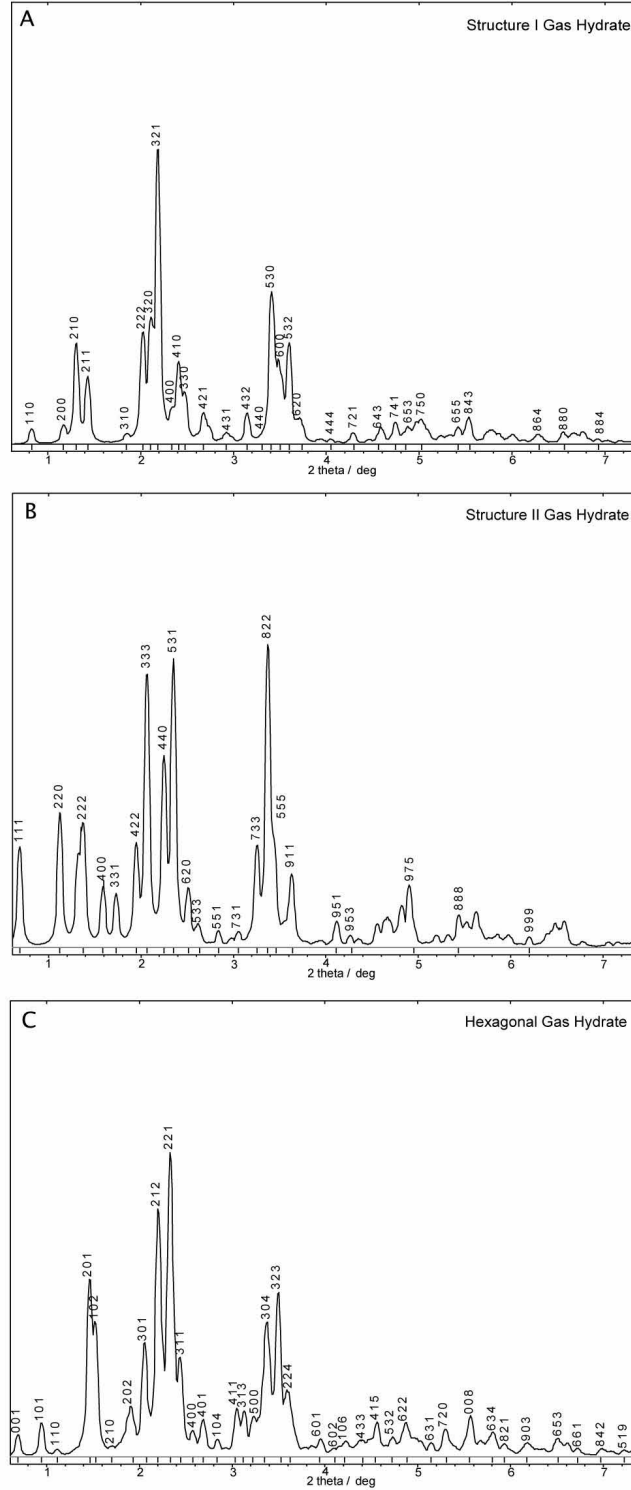


Figure 2.1: Ideal powder XRD patterns of sI (A), sII (B) and sH hydrate (C). The XRD patterns were calculated using the software PowderCell (2006) assuming a wavelength of 0.12 Å.

2.1.4 X-ray computer tomography

Computerized Tomography (CT) is becoming popular with geoscientists but was originally developed for medical purposes, because it is a rapid, non-destructive technique to image objects three-dimensionally. CT allows to image samples with minimal preparation and hence requires no change in the state of the sample, which is important for gas hydrates. As the technology is primarily based on density contrasts of the different sample components, free gas, gas hydrate, sediments including frozen pore water as well as the fabric of the constituents inside any sample can be visualized. CT-inspections of sediment cores related to gas hydrate occurrence or core-scale laboratory experiments were carried out by Abegg et al. (2007; 2008), Freifeld et al. (2006), Jones et al. (2007), Kneafsey et al. (2007), and were also conducted in the context of both the ocean drilling programs at Hydrate Ridge (Abegg et al., 2006; Tréhu et al., 2006a, b) and the Indian and Corean gas hydrate programs (Collett et al., 2008a; Holland et al., 2008; Priest et al., 2008). Parallel to CT, Magnetic Resonance Imaging tomography has been adapted in geosciences as a three-dimensional imaging method (Erslund et al., 2008).

In CT imaging, every slice represents a two dimensional (2D) matrix of digital values, which is used to construct the image. The digital values are directly related to X-ray attenuation of a small volume element of the scanned sample: A volume element is equivalent to a pixel multiplied by the slice thickness and is termed a 'voxel'. Although several factors influence the X-ray attenuation, the primary control is the bulk density of the material in a voxel. Thus the matrix of digital values, with suitable calibration, is interpreted as a matrix of bulk density values.

2.1.4.1 Medical computer tomography

Sediment cores containing hydrate samples investigated in this thesis were three-dimensionally reconstructed by using the MARUM medical CT scanner (type General Electric Pro Speed SX Power). The aim of the scans was to investigate the cores for gas hydrate and for sedimentary structures. The scans were used to locate core sections with massive hydrate occurrence. To accomplish this purpose, scans of 1.0 mm resolution were sufficient to obtain an overview over larger sample volumes as demonstrated in Figure 2.2. An overview scan of a core section is shown in Figure 2.2A; the core section is 55 cm long and stems from 1.65 (top) to 2.20 mbsf (bottom). The central part indicated by the scale bar comprises gas hydrate. Figure 2.2B shows a top view of a slice through the hydrate section in 2.2 A. The grey shaded material is gas hydrate; black patches are cavities with low X-ray absorption, such as gas fillings. The very bright material comprises high-absorbing minerals of the hosting sediment.

2.1.4.2 Microscale computerized tomography

The TOMCAT beamline is the first powerful microscale X-ray computerized tomography (μ CT) beamline suitable for gas hydrates, which resolves on a micrometer scale and provides full volumetric (three dimensional – 3D) information. In contrast to medical X-ray scanners, synchrotron X-ray micro-tomography at the TOMCAT beamline (short for Tomographic Microscopy and Coherent radiology experimenTs) at the Swiss Light Source (SLS), Paul-

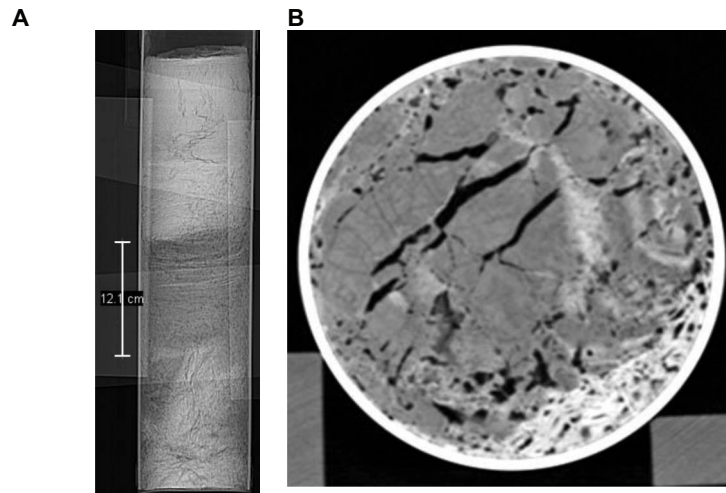


Figure 2.2: Example of a CT scan from the gravity core GeoB 11946 retrieved at the Batumi seep in the eastern Black Sea. **(A)** Overview of a core section. The location of the massive gas hydrate layer is indicated. **(B)** Single slice from the massive hydrate showing fractures and bubbles inside.

Scherrer-Institute in Villigen, Switzerland, facilitates very high resolution; pixel sizes are equivalent to a few hundred nanometers (370 nm – 6 μm) (Donogue et al., 2006; Stampanoni et al., 2006). The beamline is in operation since 2006 (Stampanoni et al., 2006).

Most of the tomograms were recorded at the SLS using a beam energy of 20 keV, taking 1501 projections with each projection lasting mostly 375 milliseconds exposure time to the beam. Typically, an aluminum filter of 250 μm thickness was applied, reducing the beam energy. The voxel size was mostly set to an edge length of 740 nm. The tomography data were processed by MATLAB® and Amira® Visage Imaging® software packages. The combination of the software allows both visualizing certain compounds of the samples (for instance, pores or solid gas hydrate crystals, see Figure 2.3, or salt crystals, Figure 2.4) and also calculating the corresponding properties of the compounds, e.g. volumes of pores within certain thresholds.

In this thesis it is shown that synchrotron radiation X-ray cryo-tomographic microscopy (SCXRTM) is a well-suited method to analyze natural gas hydrate samples (Chapter 6). The X-ray attenuation contrast allows to distinguish crystallites and to establish their spatial distribution in the samples. As an example, Figure 2.3 shows a gas hydrate crystal from the Colkheti oil seep in the eastern Black Sea. In the image, parts of the matrix in which the hydrate was embedded are blanked out such that only gas hydrate within certain density thresholds is displayed.

The obtained SCXRTM images (Chapter 6; see also Figures 2.3, 2.4) demonstrate the feasibility of the method to address a variety of missing information such as internal surface area, the individual volume of each inclusion, and the morphology of the voids of natural gases in a specified volume. Likewise, SCXRTM can give access to the crystallite shapes, crystallite sizes and grain boundary network topology; quantities which are of prime importance for understanding any coarsening processes related to gas hydrates. However, the first μCT on gas hydrates at the SLS were measured in the middle of this thesis project such that no routine has been established yet to process SCXRTM data on gas hydrates.

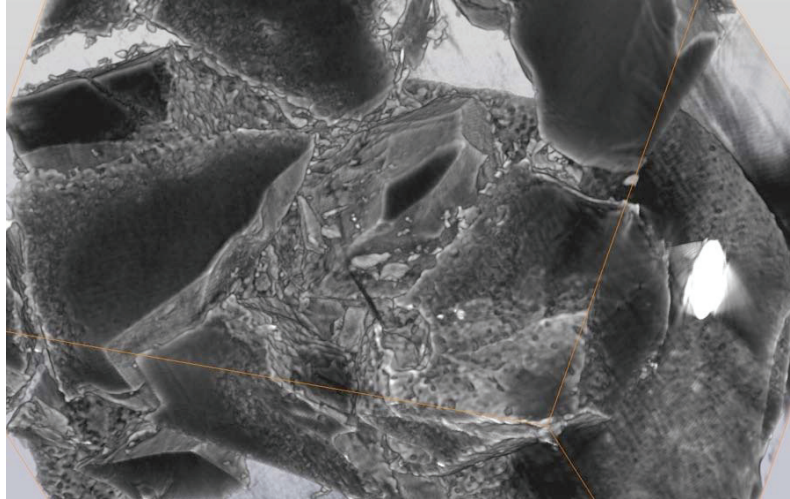


Figure 2.3: 3D, gray scale image generated by SCXRTM of a gas hydrate crystal from the Colkhetti oil seep in the eastern Black Sea. The orange bounding box marks the scanned sample volume. It is shown for orientation; the edge length of the box is 1.1 mm.

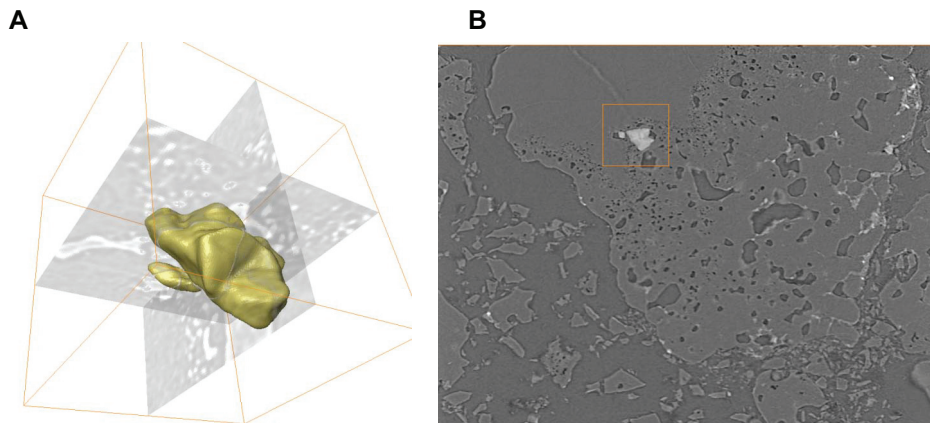


Figure 2.4: Sample *GeoB10618*, Chapopote asphalt volcano, Gulf of Mexico: Salt grain embedded in gas hydrate matrix. (A) Salt grain in 3D (yellow); (B) Grain in hydrate matrix (2D gray scale image). The edge length of the orange bounding box is 150 μm .

2.1.5 FE - Scanning Environmental Electron Microscopy

Field-Emission Scanning Electron Microscopy (FE-SEM, further abbreviated: SEM) is one of the fundamental methods for studying gas hydrate microstructure (Camps et al., 2008; Kuhs et al., 2000a, 2004a,b; Suess et al., 2001; Stern et al., 2004, 2005). Accordingly, it has been used in this thesis for several publications, including Chapters 3 and 4 as well as Appendix V; however, SEM is in the focus of Chapter 5 as well as Appendix IV. Compared to tomography SEM has the advantage to accomplish element analysis with the onboard energy-dispersive X-ray micro-analysis (EDX) unit. Both SEMs used for this thesis facilitate this option. EDX allows analyzing the chemical compounds within a defined 'area of interest'. The EDX units helped significantly to uncover small hydrate patches in largely decomposed samples (Appendix IV) based on small carbon signals; and to constrain oil (carbon-rich) patches and dense gas hydrate structures from oil seeps in the Gulf of Mexico (Chapter 5).

Both SEMs are located in the 'Geowissenschaftliches Zentrum' at the University of Göttingen (GZG). One is a Cryo-Field-Emission-Environmental-Scanning Electron-Microscope (FEI Quanta 200 FEG) (located in the 'Abteilung Kristallographie' of the GZG), the other a

Cryo-Field-Emission Scanning Electron Microscope (FE-SEM) Zeiss Leo 1530 Gemini (located in the Applied Geology group of the GZG). The SEMs are equipped with cryo-stages, cooled by liquid N₂ allowing for cold-temperature analyses. The sample stages are evacuated during the analyses ($P \approx 10^{-5}$ bar), therefore, in order to keep the hydrates stable, the temperature was constantly kept below -175 °C. The SEM images were taken by secondary electrons (see Goldstein et al., 2003) with an acceleration voltage of 1.7 – 2.3 kV to avoid edging effects on the sample surface (e.g., Stern et al., 2004). For EDX measurements the energy needs to be increased to 5.0 kV, hence the EDX spectra are taken once the SEM pictures are saved. The hydrate specimens had sizes up to 0.5×0.5×0.5 cm and are uncoated. More details on the SEM investigations are given in Chapter 5 and Appendix IV.

2.1.6 Raman spectroscopy

Raman spectroscopy has been widely used as a powerful tool for identifying the hydrate structure type and relative cage occupancy of guests enclathrated in the hydrates. With respect to the description of natural gas hydrate samples, which often stem from larger sampling volumes, Raman spectroscopy provides small-scale (local) information. Unlike powder diffraction and gas chromatography, it does not necessarily allow concluding on the mineralogy of larger piece of a sample. Therefore, a suitable combination of investigating tools for both local and bulk representation will help provide useful information for the description of natural gas hydrates. More details for the application of laser Raman spectroscopy on gas hydrates can be found elsewhere (Brewer et al., 2004; Murshed & Kuhs, 2009; Sum et al., 1997; Tulk et al., 2000; Uchida et al., 2002).

The laser Raman spectroscopy is a light scattering technique. From a classical point of view, Raman light scattering can be thought of as a coupling between the electromagnetic fields of the incident light with the polarizability tensor of the scattering material. The incident laser light induces oscillating dipoles that are modulated by molecular or lattice vibrations within the material. If the light is scattered elastically (i.e., the frequency of the scattered light is the similar to that of incident light), the process is known as Rayleigh scattering. But light is scattered inelastically when lattice or internal molecular vibrations [ν_k] are involved, and the process is then known as Raman scattering. When an electrical field is applied from a laser beam with the frequency [ν], the induced dipole oscillates at the induced frequency of the laser (Rayleigh scattering) and also at additional frequencies ($[\nu - \nu_k]$, Stokes scattering; $[\nu + \nu_k]$, Anti-Stokes scattering) arising from the Raman effect. Raman scattering occurs when the derived polarizability tensor changes during the molecular oscillation. For molecules like CH₄, this can happen when the nuclei of the molecules are displaced from their equilibrium positions as in the case during a molecular vibration. An in-depth description of the method can be found in Long (1977) and McCreery (2000).

The vibrational modes of molecules shift in frequency depending on the local environment of the molecules. The electrical fields produced by water molecules forming the hydrate cages are considered responsible for changing the electronic structure of the guest molecules such that the force constants (Tulk et al., 2000) of the trapped molecules in each of the cage types are slightly different. Therefore, the frequency shift measured by Raman spectroscopy allows the discrimination between a molecule in the gas phase and in a discrete form in different hydrate cages (Subramanian et al., 2000b). It has been also reported that the host-guest interaction changes due to presence of a different guest in the adjacent

cages. For example, CO₂ in the neighboring cages perturbs the C—H bond length (also the relative Raman scattering cross section) of methane in the hydrate cages, which affects the polarizability derivatives as well as the relative intensities of the Raman spectra (Wilson et al., 2002; Chazallon et al., 2007).

The totally symmetric C—H stretching of methane [ν_1] is helpful for investigating natural hydrates. The ν_1 frequencies at ca. 2905 cm⁻¹, 2915 cm⁻¹ and 2917 cm⁻¹ are assigned to methane in the SC (5¹²), LC (sI-5¹²6²; sII-5¹²6⁴) of hydrates and methane in the gas phase, respectively. The frequencies of ν_1 in sI cages differ as much as 1 cm⁻¹ from those of sII hydrate and hence can help discriminate methane enclathration in different structure types.

It is worthwhile to note that the O—H stretching modes cannot distinguish the different hydrate structures although liquid water can be clearly distinguished from that of solid water phases (ice). Therefore, the stretching modes of the hydrate guests have been usually used for the assignment of hydrate structure, cage occupancy [θ] and quantification.

The Raman spectra obtained in this study were interpreted comprehensively using the references cited earlier in this section. Further information on Raman scattering of hydrocarbon molecules was obtained from Charlou et al. (2004), Evans and Bernstein (1956), Herzberg (1945) and Prasad et al. (2008). For Raman spectroscopy presented in Chapter 7, a Horiba Jobin Yvon HR800 UV Micro-Raman spectrometer was used, which was equipped with an air-cooled Ar-laser working at 488 nm with a laser power of less than 20 mW. For the microscope laser a long distance objective (brand *Olympus*) with 50x magnification was used. Raman spectra were collected in the range from 200 cm⁻¹ to 4000 cm⁻¹ with a spectral resolution of ca. 2.2 cm⁻¹ using a grating of 600 grooves/mm and a Peltier-cooled charge-coupled device (CCD) detector (brand *Andor*, 1024x256 pixels). For the calibrations of the spectral positions the Raman mode of silicon was used, which was calibrated against the Rayleigh line, both before and after the measurements. A more detailed description of the laser Raman spectrometer and the measuring conditions can be found in Murshed and Kuhs (2009) and Murshed et al. (submitted). The spectrometer is furnished with a freezing stage (type *Linkam* THMS600), where the hydrate samples are investigated at liquid N₂ temperature and atmospheric pressure. These conditions allow for investigations over several hours on the same specimen. The sample stage can be moved in lateral (X, Y) and horizontal directions (Z), allowing for a spatial resolution. The focus spot has a diameter of about 1.1 μ m and a depth resolution of about 15 μ m (confocal length). The spectra were baseline corrected and fitted with the *dmfit* software (Massiot et al., 2002).

2.2 Sampling Locations

The samples investigated in this thesis were retrieved from both the northern and southern Gulf of Mexico (Figure 2.5) and from the eastern Black Sea (Figure 2.6). The following site descriptions provide information on the geological environments of the seeps.

2.2.1 Gulf of Mexico

The Gulf of Mexico basin had its origin in the Late Triassic as the result of rifting within the North American Plate as it began to crack and drift away from the African and South American plates (Bartolini et al., 2002). The rifting phase continued until the Middle Jurassic (Humphris, 1979; Worrall & Snelson, 1989). The progression of the sea into the continental

area during late Middle Jurassic resulted in the formation of the extensive salt deposits (Watkins et al., 1978). The time after the formation of the salt deposits in the Late Jurassic is considered as main drifting episode, during which the Yucatan block was separated from the North American Plate and moved southwards (Bartolini et al., 2002). During that period oceanic crust formed in the central part of the basin. Since the Late Jurassic, the basin has been a stable geologic province characterized by the persistent subsidence of its central part, due to sediment loading as the basin filled with thick clastic sediments along its northwestern and northern margins, particularly during the Cenozoic (Bartolini et al., 2002).

2.2.1.1 Northern Gulf of Mexico

The study site of this thesis in the northern GOM is the Green Canyon; there, two locations were probed (Figure 2.5): Bush Hill (GC185) and GC415.

The northern Gulf of Mexico (GOM) is a prolific hydrocarbon province. The seafloor is covered by siliciclastic sediments overlying Jurassic salt sheets (Humphris, 1979; Worrall & Snelson, 1989). Salt domes intruding into more shallow sediments generate faults, which serve as pathways for oil, gas, and brine migration from sub-bottom reservoirs to the seafloor (Macgregor, 1993; Reilly et al., 1996). The fluxes of hydrocarbons from below evoke the formation of localized seeps at the seafloor, where the hydrocarbons are discharged into the water (Brooks et al., 1984; Kennicutt et al., 1988; Roberts & Carney, 1997; Sassen et al., 1999; MacDonald et al., 1989, 2003; Sager et al., 2003). Light hydrocarbons form shallowly buried hydrate deposits near the seafloor, which locally crop out (MacDonald et al., 1994). The hydrate deposits are reported to generate an irregular bathymetry (MacDonald et al., 2003) and to support seep fauna, such as annelid “ice worms” (Fisher et al., 2000). SI and SII hydrate are known in the northern GOM (Brooks et al., 1984; Rawn et al., 2008).

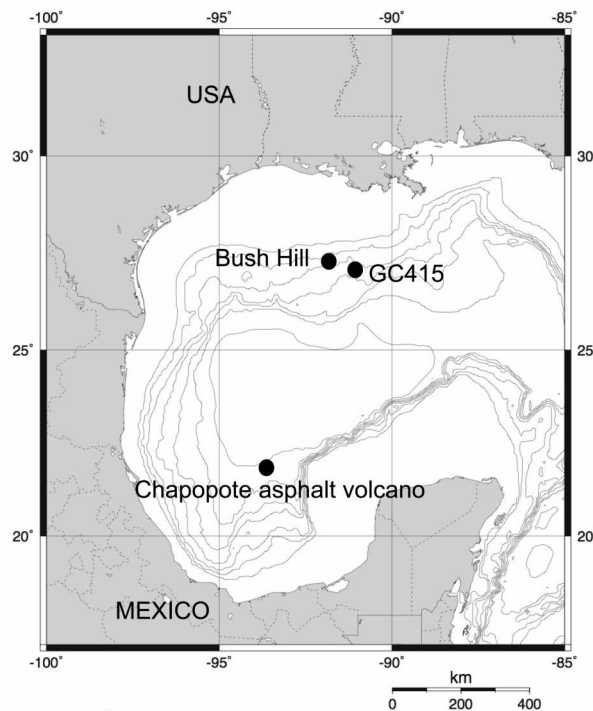


Figure 2.5: Study sites in the Gulf of Mexico (GOM). In the northern GOM, Bush Hill and GC415 were sampled, in the southern GOM the Chapopote asphalt volcano. Map produced by Generic Mapping Tools; M. Weinelt, <http://www.aquarius.ifm-geomar.de/>.

Bush Hill is a mound located 550 mbsl, aligned along a N—S antithetic fault (Reilly et al., 1996) and is covered with up to 30 cm of hemipelagic mud (e.g., Roberts & Aharon, 1994; Sassen et al., 1994; MacDonald et al., 2003). Gas originates from the Jolliet gas field (Chen & Cathles, 2003; MacDonald et al., 1994) and is discharged from the Bush Hill into the water (MacDonald et al., 1989). The total gas hydrate volume at the Bush Hill is estimated on 6.2 to $15.6 \times 10^6 \text{ m}^3$, which has supposedly accumulated over the past 10,000 years (Chen & Cathles, 2003).

Site GC415 is a hydrate deposit in 1000 mbsl. The seep is characterized by strong oil and gas discharge. The location was inferred from oil-slicks at the sea surface (MacDonald et al., 1996), by hydro-acoustic imaging of gas flares in the water column, and by typical seep fauna communities at the seafloor evidenced by deep-towed TV-sleds (Bohrmann & Schenck, 2004). Pore water profiles indicate strong fluid migration (Reitz et al., 2007). Site GC415 comprises two main seep locations, which are found 950 mbsl (GC415 west) and 1050 mbsl (GC415 east) and host large amounts of gas hydrates.

2.2.1.2 Southern Gulf of Mexico

The study site in the southern GOM was the Chapopote asphalt volcano (in the following: Chapopote; Figure 2.5). The Chapopote is part of the Campeche Knolls province. These knolls are formed from uplifted salt domes; the uplifting is considered to be analogue to the halokinetic activity at the Texas/Louisiana shelf in the northern GOM (Garrison & Martin, 1973). Likewise to the northern GOM, the salt has Jurassic age (Watkins et al., 1978) and was deposited during the rifting phase of the Gulf (Bartolini et al., 2002). The source rocks for petroleum are of late Jurassic and Cretaceous age (Magoon et al., 2002; Santamaria-Orozco et al., 1998) and are covered by 5–10 km thick Cenozoic sediments.

The Chapopote is a cold seep in almost 3000 mbsl extruding hydrocarbons from molecular sizes of CH_4 to very long chain lengths and hosting seep communities (MacDonald et al., 2004). It was detected with the help of satellite data, which imaged oil slicks on the sea surface (Bohrmann & Schenck, 2004; MacDonald et al., 2004). The asphalt cover at the Chapopote comprises many individual patches distributed over several hundred of square meters (Brüning et al., submitted). ROV-based video documentations showed that the asphalt flows apparently have different ages and could be used to identify the center of the asphalt volcano (Brüning et al., submitted). Shallow gas hydrates were found beneath the asphalt cover on the seafloor. High-resolution 2D seismic profiles revealed that a shallow hydrocarbon reservoir is located beneath the area of asphalt extrusion, and that hydrocarbons invaded shallow sediments beyond the area of known asphalt occurrence (Bohrmann & Spiess, 2008; Ding et al., 2008).

2.2.2 Study sites offshore Georgia in the eastern Black Sea

The Black Sea is a back-arc basin formed in the Cretaceous/Palaeogene (Starostenko et al. 2004), and is in the current tectonic regime being subjected to deformation by compression due to the northwards movement of the Arabian plate and the westwards movement of the Anatolian plate (McClusky et al., 2000). The Black Sea is separated into a western and an eastern sub-basin by the Andrusov Ridge. Both sub-basins are covered with 12–16 km thick organic-rich sediments (Starostenko et al., 2004). Of those, the Late Oligocene/Lower

Miocene Maikopian formation comprising organic rich clay sediments 4–5 km in thickness is of major interest for oil and gas supply (Starostenko et al., 2004).

Deep-water cold seeps were discovered at many sites in the Black Sea (see Pape et al., 2008), including the study sites on the continental slope offshore Georgia, eastern Black Sea (Figure 2.6). The study area offshore Georgia comprises a system of W-E striking canyons and ridges (Klaucke et al., 2006; Wagner-Friedrichs, 2007). The investigated cold seeps are the Batumi seep area, the Colkhети Seep, and the Pechori Mound (Figure 2.6). They are located between 850 and 1200 mbsl on the tops and flanks of ridge structures. Gas flares in the water column as well as localized and focused seafloor gas emissions were detected by hydro-acoustic measurements and video observations, sidescan sonar mapping as well as seismic surveys (Brüning et al., pers. comm. Aug. 2009; Klaucke et al., 2006; Wagner-Friedrichs, 2007, respectively).

The Colkhети Seep and Pechori Mound are characterized by gas seepage, gas hydrate occurrence, oil-stained sediments, and authigenic carbonates (Akhmetzhanov et al., 2007; Bohrmann & Pape, 2007). At the Batumi seep area intense gas seepage, shallow gas hydrate accumulations, and authigenic carbonates were found; oil seepage was not observed (Akhmetzhanov et al., 2007; Bohrmann & Pape, 2007; Chapter 8; Appendix III). The Batumi seep area is characterized by a rugged seafloor (M. Brüning & H. Sahling, pers. comm. July 2009; Chapter 8).

The hydrocarbons discharged from the investigated seep sites most likely originate from the organic-rich sediments of the Maikopian formation (Akhmetzhanov et al., 2007; Bohrmann & Pape, 2007). Seepage at the Batumi seep area seems to be related to fluid migration along faults (Akhmetzhanov et al., 2007; Wagner-Friedrichs, 2007). The presence of higher hydrocarbons in the seepage fluids at oil seeps point to the admixture of hydrocarbons from deeper sources (Heeschen et al. 2007; A. Reitz & T. Pape, pers. comm. July 2009; Appendix III). Cold seeps and decomposing gas hydrates are considered to contribute to 86–91% of the Black Sea CH₄ budget (Kessler et al. 2006), which comprises a total of 96 Tg of dissolved CH₄ (Reeburgh et al., 1991).

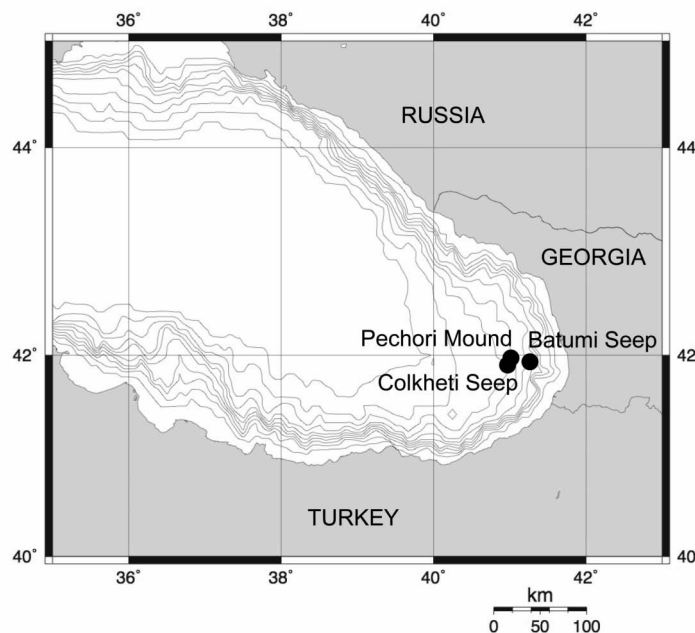


Figure 2.6: Eastern Black Sea and seep locations discussed in this thesis. Map produced by Generic Mapping Tool; M. Weinelt, <http://www.aquarius.ifm-geomar.de/>.

CHAPTER 3
MANUSCRIPT 1
CRYSTALLITE SIZE DISTRIBUTIONS OF MARINE GAS HYDRATES

Stephan A. Klapp^{1*}, Susanne Hemes², Helmut Klein²,
Gerhard Bohrmann¹, Werner F. Kuhs², Fritz Abegg¹

Proceedings of the 6th International Conference on Gas Hydrates (ICGH 2008), ed. by
P. Englezos, J. Ripmeester, Vancouver, British Columbia, Canada, July 6-10, 2008.

¹ MARUM – Center for Marine and Environmental Sciences and Department of
Geoscience, University of Bremen, P.O. 330440, D-28334 Bremen, Germany

² Abteilung Kristallographie, Geowissenschaftliches Zentrum der Universität
Göttingen, Goldschmidtstrasse 1, D-37077 Göttingen, Germany

3.1 Abstract

Due to experimental difficulties, size distributions of gas hydrate crystallites are largely unknown in natural samples. For the first time, we were able to determine crystallite size distributions of several natural gas hydrates for samples retrieved from the Gulf of Mexico, the Black Sea and from Hydrate Ridge offshore Oregon from varying depth below the sea floor. High-energy synchrotron radiation provides high photon fluxes as well as high penetration depth and thus allows the investigation of bulk sediment samples. The gas hydrate crystallite sizes measured with a newly developed diffraction technique, utilizing the excellent beam collimation, appear to be (log-) normally distributed in the natural samples and to be of roughly globular shape. The mean crystallite sizes are typically in the range from 200-400 μm for hydrates recovered from the sea floor while a tendency for bigger grains was noticed in greater depth for the Hydrate Ridge samples, indicating a difference in the formation age or formation process. Laboratory produced methane hydrate, starting from ice and aged for 3 weeks, shows half a lognormal curve with a mean value in the order of 40 μm . This one order-of-magnitude smaller grain sizes suggests that care must be taken when transposing crystallite-size sensitive (petro-) physical data from laboratory-made gas hydrates to natural settings.

3.2 Introduction

Gas hydrates are materials which crystallize under inclusion of gas molecules into rigid cages of water molecules. On Earth, gas hydrates form in polar environments, particularly in onshore and offshore sediments, as well as on continental margins (Kvenvolden et al., 1993). Hydrates need elevated pressure and cold temperature to form; in marine environments gas concentrations must exceed solubility in interstitial waters (Kashchiev & Firoozabadi, 2002). Ambient gas composition governs the crystallizing gas hydrate structures. Methane and small fractions of ethane form structure I gas hydrate. Methane and hydrocarbon molecules up to the size of butane (C_4) form structure II gas hydrate. C_5

molecules within the gas mixture of hydrates would lead to the formation of a hexagonal gas hydrate (structure H).

Gas hydrates are considered a large hydrocarbon reservoir on Earth (Collett, 2002; Dickens et al., 1997a; Max et al., 2006). The absolute quantity of carbon stored in gas hydrates is uncertain, yet Buffett and Archer (2004) figure 3000 Gt carbon being stored in gas hydrates. Klauda and Sandler (Klauda & Sandler, 2005) report 74,400 Gt of methane being stored as hydrates; their model is regarded state-of-the-art as it enables prediction of almost all known hydrate occurrences (Sloan & Koh, 2007). The significance of hydrates as reservoirs for methane and other hydrocarbons lies in their potential role as a source for greenhouse gases and consequently as a probable driving force for global warming (Kennett et al., 2000; Archer & Buffett, 2005; Zachos et al., 2008). Additionally, hydrates might turn into hydrocarbon sources in the future satisfying the still increasing global demand in energy.

Many examinations on laboratory produced and natural gas hydrates as well as theoretical predictions involve crystallite-size dependent physical properties, whether they address glaciology (Kipfstuhl et al., 2001), rheology (Durham et al., 2003), chemical engineering (Sloan & Koh, 2007) or numerical modeling (Torres et al., 2004; Haeckel et al., 2004; Wallmann et al., 2006b; Bhatnagar et al., 2008).

For marine hydrate deposits, for instance at gas seeps, gas exchange reactions of free gas with gas hydrates are fundamental to understand the importance of gas hydrates in those systems. Laboratory experiments suggest that gas replacement occurs from methane to CO₂ (Yoon et al., 2004) or to ethane (Murshed & Kuhs, 2007) but little is known about gas substitution in nature. Scientific and economic interest, however, is large on such reaction kinetics due to anticipated CO₂ sequestration projects by gas replacement in hydrates. The mean crystal size of gas hydrates and the crystal size distribution (CSD) is a particularly crucial aspect: exchange reactions of gas hydrates to adjust their cage filling to changing p-T conditions are likely to take place along grain boundaries of gas hydrate crystallites and the exchange rates will differ depending on the grain size. Also, the mechanical properties, in particular concerning static and dynamic deformation of gas hydrate aggregates will depend on the crystallite size and may take place differently in nature than what is anticipated from laboratory experiments.

Sizes of gas hydrate crystallites are essentially unidentified particularly in nature despite their significance for our understanding of gas hydrate formation and the physical properties of gas hydrate aggregates. In this study, grains are understood as crystallites and vice versa. Crystallite sizes and shapes of gas hydrates yield insights relevant to geosciences, glaciology and chemical engineering: The understanding of gas hydrate crystal growth could be much enhanced by knowing the CSDs of gas hydrates. They could help identifying processes occurring during a possible time-dependent continued growth (Klapp et al., 2007): The growth of gas hydrate crystals may well resemble a ripening process similar to Ostwald ripening (Lifshitz & Slyozov, 1961; Wagner C, 1961). In such a process, big grains grow on the expense of smaller grains in order to minimize the free energy within a system. This happens both because of the higher solubility of smaller compared to bigger grains (Wagner C, 1961) and because the grain boundary energy of bigger particles is relatively less than that of smaller particles. Hydrate re-growth is witnessed from polar air hydrates, which occur in Greenland and Antarctic ice sheets and initially crystallize from air inclusions (Kipfstuhl et al., 2001).

Assessing the CSDs of gas hydrates is a notoriously difficult enterprise; all established methods for measuring grain sizes which geoscientists are familiar with fail when it comes to gas hydrates, which is mostly due to the thermodynamic conditions compulsory to preserve hydrates during the study.

Optical microscopy is inappropriate, because conditions to keep gas hydrates stable cannot easily be maintained during the preparation of thin sections. For short time and on a coarse length scale, however, photographs can be obtained for fabric inspections (Bohrmann et al., 1998) yet are not very suitable for identifying grain boundaries. Optical microscopy in cold room environments (below $-20\text{ }^{\circ}\text{C}$) is a very good tool for investigating ice thin sections containing polar air hydrates (e.g., Kipfstuhl et al., 2001). This only works for hydrates encased by ice acting as a pressure vessel but not for pure gas hydrate specimen. Also, tracking down grain boundaries by crossing polarizers would not work, as structure I and II gas hydrates crystallize in the cubic crystal system and thus behave isotropically in that no change in the crystal orientation would be discernable, adding to the difficulty of identifying grain boundaries. Further, the cooling of the samples would become difficult, since at atmospheric pressure methane hydrate is only stable at temperatures below $\sim -80\text{ }^{\circ}\text{C}$.

Electron microscopes with cryo-stages allow for low-temperature investigations and hence are excellent tools for gas hydrate microstructure assessment (Kuhs et al., 2000a, 2004; Techmer et al., 2005; Appendix IV). The advantage of electron microscopy lies in its excellent local resolution, which allows for sharp images at more than 24,000x magnification at cooled gas hydrate samples. Because electron microscopes can only image the surface of specimens but not their interior, the determination is a priori limited to what can be seen on the sample surface.

In our earlier work we reported on CSDs of gas hydrates obtained from synchrotron radiation measurements (Klapp et al., 2007). Here we present new data and describe the experiments in more detail.

3.3 Experimental

3.3.1 Sample origin and preservation

All new data presented in this work stem from hydrates recovered from shallow depths of the upper three meters of sediment at gas seepage systems. Samples described in this study are retrieved from the Eastern Black Sea (Pechori Mound, Colkhetti Seep, Samsun Seep) and from the Gulf of Mexico (Bush Hill area in the Northern Gulf and Campeche Knolls in the Southern Gulf). The Black Sea samples were retrieved during the TTR 15 cruise in 2005 with the R/V PROF. LOGACHEV. Samples from Pechori Mound and Samsun Seep were recovered by gravity-coring, from Colkhetti Seep by a TV-guided grab. Hydrates from Campeche Knolls were gravity-cored during R/V METEOR cruise in 2006, Bush Hill samples were retrieved by a TV grab during R/V SONNE cruise in 2003.

The samples were not pressure-cored, and despite immediate storage in liquid nitrogen to avoid decomposition after recovery, the outer parts of the hydrate could decompose during the transfer from sea floor to the research vessels. Consequently, for the CSD measurements we took care to only use unaltered or almost unaltered samples. All hydrate samples were comprehensively studied before actual crystal size investigations by x-ray computer tomography, x-ray diffraction and electron microscopy (for Gulf of Mexico

samples: (Chapter 5); for Black Sea: unpublished data). X-ray diffraction, combined with quantitative phase analysis, allows for choosing samples with high gas hydrate content. Electron microscopy visualizes the state of preservation of the samples (Kuhs et al., 2004b).

The crystallite sizes of gas hydrates are measured by imaging the length of the crystals with high-energy synchrotron radiation. In a first step, however, the specimens were investigated using two Cryo-Scanning Electron Microscopes.

3.3.2 Electron microscopy

One of the used electron microscopes is a Field-Emission Scanning Electron Microscope (FE-SEM), *Zeiss Leo 1530 Gemini*; the other one is a Cryo-Field-Emission-Environmental-Scanning Electron-Microscope (*FEI Quanta 200 FEG*). The FE-SEMs are designed for work at low acceleration voltages of less than 2 kV, which is mandatory for ice or gas hydrates in order to minimize sample alteration due to beam damage (Stern et al., 2004; Kuhs et al., 2004a). During the measurements, the samples are stored in a liquid-nitrogen cooled sample stage inside a vacuum chamber at temperatures of about 90 K (−183 °C) and at a pressure of about 1×10^{-6} bar.

The uncoated specimens are pieces of gas hydrate bearing samples with dimensions of about 0.5×0.5×0.5 cm. The SEM is equipped with a thin window EDX-detector (energy dispersive X-ray analysis) allowing for a local low-Z elemental analysis.

3.3.3 Sample preparation

One investigated gas hydrate sample was laboratory-produced following methods described in Kuhs et al. (1992) and Stern et al. (1996). It was synthesized from a sieved ice grain fraction of 200–400 μm, set under methane pressure of 60 bar and reacted for 3.5 weeks. The temperature was gradually increased from −5 °C to +2 °C. Each commencing step took place when the gas consumption by the specimen at the previous temperature step almost ceased.

The objective of this study is to find out the sizes of individual gas hydrate crystals. Therefore, it was important not to change the state of a sample, for instance by crushing. Instead, intact pieces of the sample of about one cubic centimeter were measured.

For the synchrotron measurements, pieces of pure hydrate were broken off each of the natural samples under visual inspection and then fixed into aluminum cans of 7 mm (Klapp et al., 2007) or 12 mm inner diameter and 40 mm length in an arbitrary orientation. In order to measure the natural sizes of the grains, only large pieces almost the size of the inner diameter of the cans were selected.

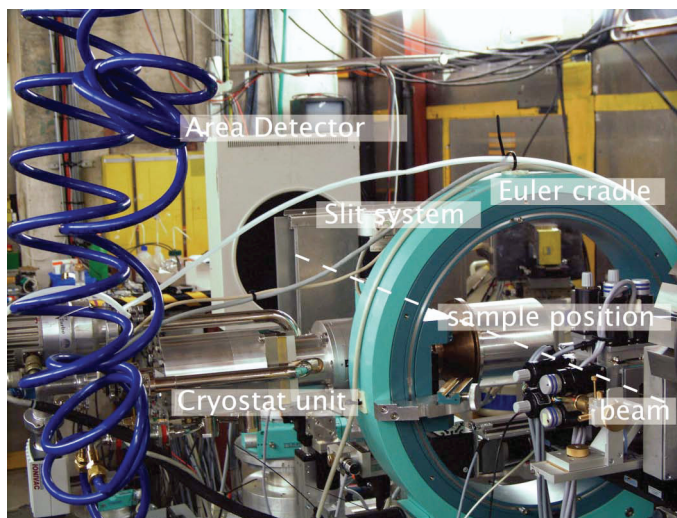
3.3.4 Synchrotron measurements

The gas hydrate grain sizes were measured at the beam line BW 5 at the *Hamburg Synchrotron Laboratory* (HASYLAB) of the *Deutsche Elektronen Synchrotron* (DESY).

High-energy synchrotron radiation provides a short X-ray wavelength ($\lambda \sim 0.12$ Å, the appropriate beam energy 100 keV) and thus allows investigating bulk sediment samples up to a thickness of some centimeters in X-ray diffraction experiments. The penetration

power is essential because the samples are 7 or 12 mm thick (inner diameter) and located in a cryostat with aluminum shields (Figure 3.1).

Figure 3.1. Set up at beam line BW5, HASYLAB, DESY. The broken white line shows the direction of the primary beam. The gas hydrate sample is stored during measurements in a cylindrical (12.7 mm outer diameter) aluminum can which is located within the cryostat.



Because the crystals of natural samples were possibly quite small, a particularly good angular and spatial resolution is needed. This is provided by high collimation, i.e. extremely low divergence of the high-energy synchrotron radiation and a high photon flux allowing for small beam diameters. During measurements, the cryostat stage is cooled by a closed cycle helium system to temperatures of ~ 70 K (-208 °C). A *Lake Shore* controller (Cryotronics Inc.) monitors the temperature of the sample. A vacuum of about 1×10^{-5} bar between the sample can and the shields of the cryostat prevents the heat flow from outside towards the sample.

The CSD measurements are performed with synchrotron radiation using the Moving Area Detector Method (Wcislak et al., 2003); this method was originally developed for material science purposes such as metals or ceramics (Bunge et al., 2002; Klein et al., 2004). In conventional powder diffraction experiments, the diffracted Debye-Scherrer-cones of individual crystal planes of sample crystallites are imaged as rings on a two-dimensional image plate detector. For this study, a *mar345* image plate detector was used. A diffraction image of a gas hydrate sample is shown in Figure 3.2; the exposure time for such images is circa 1 minute.

Using the Moving Area Detector Method to measure grain sizes, only one specific Debye-Scherrer-ring is used which is strong and shows no overlap with other reflection lines. For gas hydrate structure I the (321)-reflections, for structure II the (511)-reflections are used. In order to exclude all other reflections except the selected one, Bragg slits are positioned between sample and detector (Figure 3.3). A "location scan method" delivers grain sizes in scanning direction (Figure 3.3).

Both the sample and the detector are moved perpendicular to the beam; consequently, all crystal planes are imaged as streaks as long as they remain within the beam. The streaks correspond to individual crystallites, their lengths represent their diameters in scanning direction. Figure 3.3 schematically shows this method. Because of the large diffracted sample volume this method results in very good grain statistics.

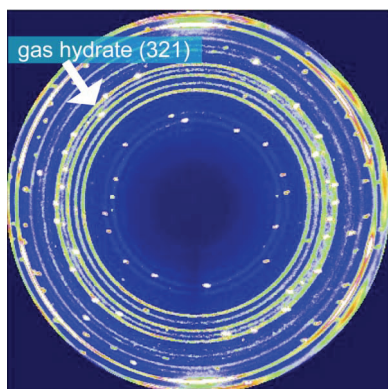


Figure 3.2. Debye-Scherrer-cones are imaged as rings on the area detector; each diffraction ring represents a (hkl)-crystal plane. One such ring is then selected for further grain size measurements (sample: TTR 15, Pechori Mound, eastern Black Sea). The sample was exposed to the synchrotron radiation for 90 seconds, beam energy was 100 keV.

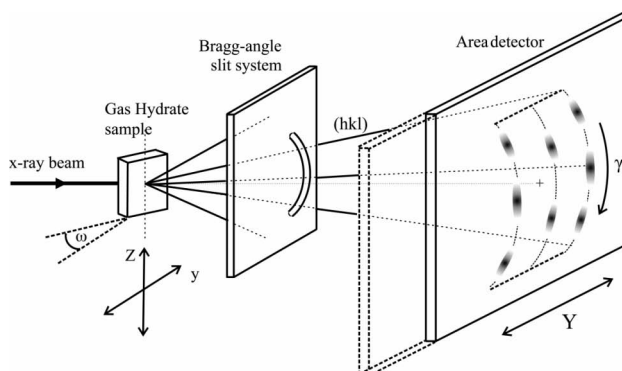


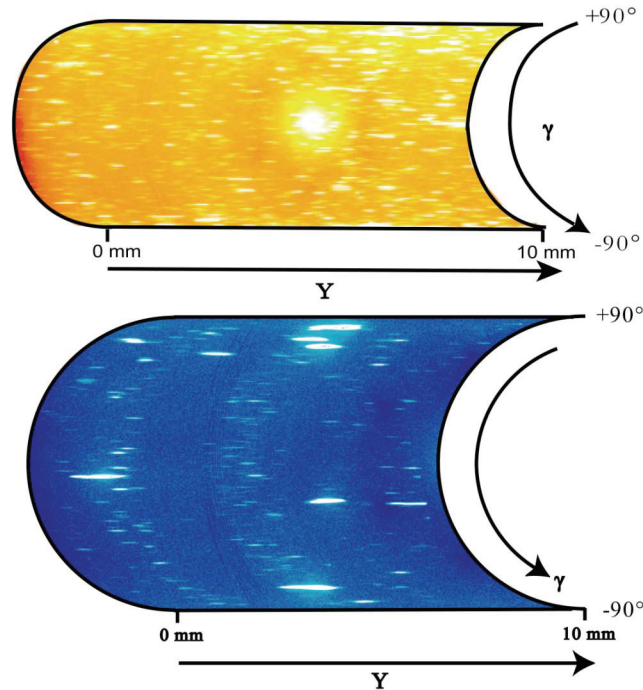
Figure 3.3. Schematic drawing of the Moving Area Detector Method: Sample and area detector are moved simultaneously during the measurement. Subsequently, the sample is moved in Y-direction through the locally fixed beam, the orientation angle ω stays in a fixed position. The Bragg-angle-slit lets pass only the chosen Debye-Scherrer-ring. The reflections of the crystallites reach the detector and a continuous image of the scanned volume is recorded (see Figure 3.4). In succeeding measurements the orientation angle ω is changed to another value.

Figure 3.4 depicts two orientation-location scans of natural gas hydrates from the Gulf of Mexico (Figure 3.4 A) and ODP Leg 204 (Figure 3.4 B); exposure times for these scans were circa 90 minutes. Typically, a central part of the 40 mm can was measured. In order to examine whether crystals might be elongated in one direction, a second set of measurements was carried out for one sample with the sample rotated by 90° so that the y-axis and z-axis were interchanged (see Figure 3.3). For these latter measurements, several sections through the diameter of the can were measured, each section 3.5 mm long, i.e. half of the inner diameter of the cylindrical can. In order to obtain reflections from differently oriented crystallites, two to six scans at different ω -positions (see Figure 3.3) were made for each sample. Between two scans, samples were rotated 0.2° about their length axis.

3.3.5 Data processing

Detector images were saved as digital images and processed by the *marView* software. Measuring and counting of the streaks was done by using the *Image-Pro* software, allowing an automatic detection and measurement of discrete features within an image. However, gas hydrates are weak scatterers unlike technical materials like metals, for which the Moving Area Detector Method was originally developed (Bunge et al., 2003). The detector image processing and the measurements of the streaks are time consuming, because two subsequent challenges need to be met: First, the data processing needs to enhance the contrast between background and reflections because the weak scattering of the synchrotron radiation by the gas hydrate crystal planes results in low intensities. Second, enhancing the displayed intensities produces artifacts on the image plate detector, which start resembling features from true reflections. Artifacts are pixels with intensities higher than the background, which do not belong to gas hydrate reflections.

Figure 3.4. Detector images of samples. The streaks correspond to individual crystals; only reflections from the crystal plane (321) are recorded. The samples were scanned 10 mm in Y-direction (see Figure 3.2). The total exposure time for this image was ca. 90 minutes, the beam energy was 100 keV. Different size of the images is due to slight differences in the orientation angle γ (a) GeoB 10618 (CT 2); Campeche Knolls, southern Gulf of Mexico (b) ODP 204 1249C-1H-CC, 0-10cm, Hydrate Ridge.



Unlike true reflections, they are not extended into the scanning direction nor do they have an increase in intensity at the rim of the reflection.

The problems were solved in three succeeding steps for each individual sample: First, the background noise of the raw data from the synchrotron beam line was reduced by the image processing software. In the next step, objects with high intensities were counted and measured on the whole detector image of the sample. By doing that, intense gas hydrate reflections were measured but no artifacts or weak gas hydrate reflections. To include streaks of gas hydrates with low intensities, the global detector image was segmented. For such segments, the intensity threshold was decreased which allowed adding weakly reflecting objects to the results. In a third step, the results were double-checked whether a measured object is a gas hydrate reflection or an artifact.

A reflected crystallite on the detector of just one pixel is equivalent to about 6 μm of crystal size. Theoretically, a crystal of that size could be imaged on the screen; practically, streak lengths starting at 4 pixels (which is equivalent to 24 μm) are included in the data. This is done to minimize the number of artifacts.

Three images were measured both automated and manually using the same images and the same software in order to scrutinize whether there are differences in results measured either by a scientist or an automatic program.

4. Results

The goal of SEM-imaging is to find boundaries between gas hydrate grains on the surface of the specimen. Gas hydrate could be distinguished from other phases like ice and sediments by typical homogeneously distributed sub- μm sized pores. These pores were described as a typical feature representing the gas hydrate phase in SEM studies (Kuks et al., 2000a; Techmer et al., 2005; Kuks et al., 2004a; Staykova et al., 2003; Appendix IV) and can be regarded as an established tool to identify gas hydrates. The

pores are largely not connected and have diameters ranging from 200 to 400 nm in methane hydrate (Kuhs et al., 2000a).

The SEM images depict porous gas hydrates in all samples except those from the Bush Hill area in the northern Gulf of Mexico. There, structure II gas hydrates were recovered with higher hydrocarbon content within the hydrate structure (Heeschen et al., 2007); those hydrates feature a smoother, brick- or tier-like microstructure on the surface (Figure 3.5A), details are given in Chapter 5.

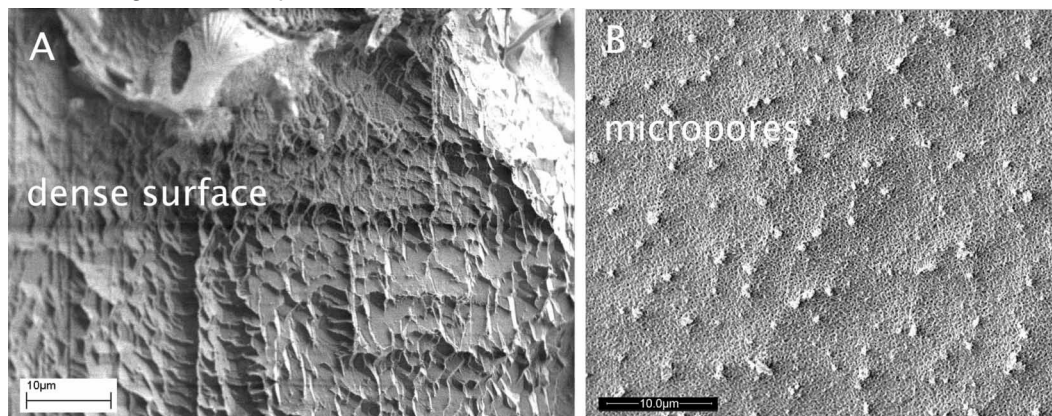


Figure 3.5. SEM images of gas hydrate samples. (a) dense gas hydrate; tier-like etch structures do not allow to draw conclusions on grain boundaries (Bush Hill, northern Gulf of Mexico). (b) in sub- μm porous gas hydrates: no grain boundaries are discernable (Samsun gas seep, eastern Black Sea).

Grain size information from SEM images could only be inferred from clearly discernable grain boundaries, but both micropores and brick-like surface structures do not allow deducing any conclusions regarding grain boundaries or grain sizes for the hydrates (Figure 3.5 A). Partially decomposed hydrates (though eventually, they were not used for synchrotron measurements) are recognizable from sub- μm porous hydrate patches surrounded by dense ice from hydrate decomposition (Appendix IV; Figure 3.6 A, B). It can be assumed that the decomposition of the hydrates progresses from the grain boundaries towards the interior; at least it is unlikely that decomposition starts inside a grain and advances outside. Accordingly, the size of these hydrate patches certainly cannot reflect the true, intrinsic crystal sizes, since decomposition already set in (see Figure 3.6).

In contrast to electron microscopy, the Moving Area Detector Method using high-energy synchrotron radiation allows to obtain crystal size information of gas hydrates. Moreover, it provides bulk information with good statistical precision rather than surface information from individual observations as in SEM.

All measurements of individual samples in different ω -positions (see Figure 3.3) add up to a total of several hundred data points per sample, which were plotted in histograms. For the synthetic sample $\sim 1,400$ data points are counted, which is due to the smaller grain sizes (Klapp et al., 2007). The distributions of the crystallite sizes from natural samples appear to be (log-) normally distributed; a clear distinction between normal and lognormal CSD cannot be made on the basis of the present data.

For all natural samples investigated here, crystals are on average a few hundred micrometers in diameter. Table 3.1 gives the mean crystal sizes for all gas hydrates samples; for comparison, it also includes data from an earlier publication (Klapp et al., 2007). The mean grain size of the synthetic gas hydrate sample is about $43 \pm 23 \mu\text{m}$. Since the grain sizes of the ice, which reacted with the methane gas to crystallize to synthetic

methane hydrate were much larger (a sieved fraction of 200 – 400 μm), there is confidence that the measurements are neither limited nor biased by the initial size of the ice grains. This demonstrates that the crystal sizes of fresh laboratory-produced hydrates lie in the range given by Klapproth (2002) and Staykova et al. (2003).

All three hydrate samples from different Black Sea seeps scatter around 220 μm (table 1); hydrates from the Campeche Knolls (Gulf of Mexico) range from ~ 190 to ~ 230 μm and Bush Hill hydrates from ~ 200 to ~ 300 μm . Crystals of gas hydrate specimens from the ODP 204 drillings on the Hydrate Ridge (Northwest Pacific) are larger, ranging between ~ 300 and ~ 600 μm in diameter.

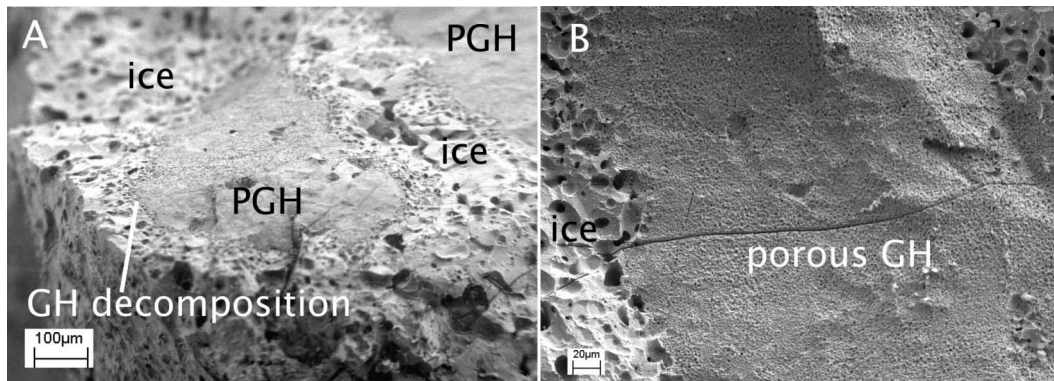


Figure 3.6. SEM images of gas hydrate sample (ODP 204 1247B-12H-2, 41-51cm) (a) Overview of patches of gas hydrate (PGH), characterized by sub-micrometer sized pores. The patches are limited by dense ice parts containing larger pores of tens of micrometer size in diameter. No information can be obtained about the actual size of crystallites within the patches, nor is it certain that larger pores within the dense matrix are forming grain boundaries between gas hydrate grains. (b) Boundary between sub-micrometer sized porous gas hydrate and decomposed hydrate (fewer and larger pores) seen in particular in the lower left part; a crack is seen in the porous hydrate.

5. Discussion

A comprehensive characterization of gas hydrates – whether in terms of mineralogical description or by modeling time-dependent exchange rates (Torres et al., 2004; Haeckel et al., 2004; Wallmann et al., 2006b) – needs information on the crystallite size and grain-boundary area. Still, previous attempts to obtain statistically sound CSDs of natural gas hydrates failed, because no adequate method was available. At best there was some information on individual crystallite sizes or on averaged hydrate crystallite sizes without access to the CSD; Klapproth (2002) and Staykova et al. (2003) quote crystal sizes of 15-40 μm from estimates based on the inhomogeneities of Debye-Scherrer rings for hydrates prepared by a reaction of methane gas with ice. Schicks et al. (2006) reacted water with pressured gas and produced larger single crystals up to the size of 100 μm . However, this technique is not as rapid (e.g., Tohidi et al., 2001) and generally not used for hydrate production. Using ice instead of water as a starting material is a popular method, but – as shown here – results in smaller crystal sizes than what is encountered in nature.

Scanning electron microscopy is an effective tool for investigating gas hydrates surfaces like studying the microstructure or phenomena related to the decomposition of gas hydrates (Stern et al., 2004; Techmer et al., 2005). Gas hydrate patches are identified by carbon signals in EDX analysis and sub-micrometer sized pores (see Figures 3.5 B; 3.6). The patches are surrounded by a dense matrix, which could lead to the impression that a

3. Crystallite size distributions of marine gas hydrates

single patch is a single grain. Actually, several single crystallites, which are connected to agglomerates, would have the same appearance in scanning electron microscopic images. Furthermore, the patches are likely to be shaped by partial decomposition of gas hydrates during retrieval; accordingly, single patches of hydrate cannot necessarily be addressed as single gas hydrate crystals. Yet, crystals, which are attached to each other, can be distinguished by different orientations of the crystals by diffraction. This principle is used in our synchrotron measurements (Figure 3.7 a).

Table 3.1. Mean grain sizes and standard-deviations of gas hydrate samples.

Provenience	sample	grain size [μm]	standard dev [μm]	
Gulf of Mexico	Bush Hill (SO 174 stat 157 TVG-10 GH 4)	204	89	<i>this study</i>
	Bush Hill (SO 174 stat 157 TVG-10 GH 1)	301	114	(Klapp et al., 2007)
	Campeche Knolls (GeoB 10618, CT 2)	227	99	<i>this study</i>
	Campeche Knolls (GeoB 10618, CT 2), manually	207	97	<i>this study</i>
	Campeche Knolls (GeoB 10618, CT 6)	187	109	<i>this study</i>
Black Sea	TTR 15, Colkhети Seep	223	101	<i>this study</i>
	TTR 15, Colkhети Seep, manually	214	130	<i>this study</i>
	TTR 15, Pechori Mound	213	89	<i>this study</i>
	TTR 15, Pechori Mound, manually	210	91	<i>this study</i>
	TTR 15, Samsun Seep	236	106	<i>this study</i>
Hydrate Ridge (ODP Leg 204)	204 1248C-8H-6, 68-87cm	361	79	(Klapp et al., 2007)
	204 1247B-12H-2, 41-51cm	592	374	(Klapp et al., 2007)
	204 1249C-1H-CC, 0-10cm	373	134	(Klapp et al., 2007)
	204 1248C 11H-5 (no tilt)	517	176	(Klapp et al., 2007)
	204 1248C 11H-5 (90° tilted)	569	342	(Klapp et al., 2007)
	204 1250C 2H-CC 0-1 cm	451	132	(Klapp et al., 2007)
Synthetic	CH ₄ -Hydrate	43	24	(Klapp et al., 2007)

In the following, the reliability of both methods applied to gas hydrate investigation is presented before the results themselves will be discussed. The Moving Area Detector Method is already regularly applied to materials like metals or ceramics (Bunge et al., 2003; Klein et al., 2004) and, as recently shown in (Klapp et al., 2007), it can successfully be used also for gas hydrates. Previous cursory studies on laboratory-made hydrates (Staykova et al., 2003; Klapproth, 2002; Schicks et al., 2006), are confirmed by the Moving Area Detector Method (Table 3.1).

Repeated measurements of one sample turned by 90° indicate that the crystallites are not elongated into a preferred sample direction. This gives confidence that the crystallites inside the sample have an approximately globular shape.

Unaltered crystallite sizes are granted by avoiding crushing of the hydrates and by investigating only hydrates with little decomposition. The latter is manifested in low ice fractions (checked by x-ray diffraction) of the investigated samples, pre-selected using scanning electron microscopy (details for Gulf of Mexico hydrate samples in Chapter 5; Black Sea: unpublished).

The grain sizes are not affected by any post-sampling re-arrangement. The time when a sample is transferred from a liquid nitrogen filled vessel to the pre-cooled sample holder is by far too short for any annealing effect due to the low mobility of water molecules at temperatures below 120K – the samples after recovery never experienced temperatures higher than this. Annealing effects are unlikely during the sample recovery, too, since no annealing effects have been observed on gas hydrate specimen which were sequestered in the ocean and recovered later (Stern et al., 2004).

Care was taken to include weak reflections of small grains and at the same time exclude artifacts. Figure 3.7 (B) shows a zoomed area of a diffraction image showing a small crystallite with low intensities. Such weak reflections would be outside thresholds during global image investigation, because its intensity is too close to that of the background. Including weak reflections during a global evaluation of the total detector image would unavoidably also include a significant number of artifacts. But due to adjusted thresholds within individual image segments, weaker streaks could successfully be added to the results.

In order to prove the reliability of the image processing method three selected images were evaluated manually by a scientist in addition to the automated measurements. The advantage of an interactive evaluation lies in the human ability to differentiate between shape and intensity simultaneously in that long streaks, even if they are just a little stronger than background values, are identified as reflections of hydrate crystals. No segmentation and no exclusion of artifacts are necessary. The good agreement of both human and computer measured grain sizes gives confidence into the reliability of the results obtained from automated image processing (see Table 3.1).

All determined grain sizes of gas hydrates recovered from natural environments are approximately an order of magnitude larger than those from synthetic samples. The crystal size of the synthetic product clearly documents that new gas hydrate crystals as prepared for various laboratory tests (Kuhs et al., 1992; Stern et al., 1996) are small in size and even smaller than what can be inferred about the size of single crystals from the methods used in (Schicks et al., 2006).

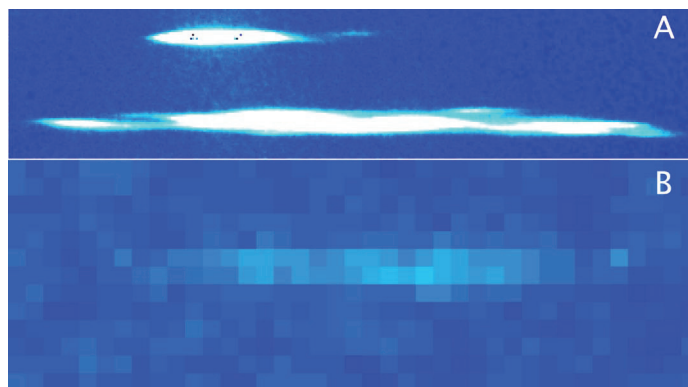


Figure 3.7. Close-ups of detector images of gas hydrate crystals. (a) Agglomerates of gas hydrate crystals (204 1247B-12H-2, 41-51cm). The length of the section is several hundred pixels. (b) A weak gas hydrate reflection, which would not be measured during global image analysis, because its intensities are close to those of artifacts, e.g. elevated background intensity. Individual pixels are visible.

The synchrotron measurements indicate that the sizes of different natural samples vary from 190 up to 600 μm . This allows concluding that larger natural gas hydrate crystals

have been undergoing a ripening process, considering that for polar air hydrates, which incorporate air molecules such as oxygen or nitrogen, such re-growth is known (Kipfstuhl et al., 2001).

However, care needs to be taken when comparing natural and synthetic gas hydrate grain sizes: Although mean crystallite sizes of natural hydrate samples are larger than freshly produced synthetic ones, this does not necessarily imply that in marine environments newly flocculated gas hydrates crystallites were similarly small. It appears that from pressurized gas and water crystallites of up to $\sim 100 \mu\text{m}$ are produced, although this number still needs to be put onto statistically firm grounds (Schicks et al., 2006).

Having pointed this out, it is interesting to note that the crystallite sizes of sub-samples from two sampling stations in the Gulf of Mexico in shallow sediment depths are different, which suggests grain size controls in marine environment working on short distance.

Two samples from different position from Bush Hill (TVG 10) show a difference of mean crystallite sizes of nearly $100 \mu\text{m}$ (Figure 3.8). These samples were recovered by TV-guided grab and stem from a volume of approximately 0.8 m^3 of almost pure gas hydrate (Bohrmann & Schenck, 2004). Since the hydrates were recovered from a water depth of 540 m and left the zone of gas hydrate stability in the water column in ca. 330 m water depth (Chapter 5), they stem from deep within the hydrate stability zone. The two sub-samples, which own different crystal sizes, come from different parts of the bulk TV-grab. The reason for the two varying grain sizes is unclear, yet several causes could account for the difference. First, given that ripening of crystals takes time (Lasaga, 1998), it would be consequent to reason that the sub-sample with the larger grains comprises older crystals. That, in turn, would suggest a very dynamic hydrate system, because the assumption implies that hydrates of different age were virtually neighboring. In fact, MacDonald et al. (MacDonald et al., 2005) find that the Bush Hill hydrates accumulate gradually on a yearly scale, which supports this thesis. Chen and Cathles (Chen & Cathles, 2003) figure that the Bush Hill deposit has been increasing in size since ca. 10,000 years. Yet, there are more arguments which might account for different grain sizes of these two sub-samples. Gas hydrate occurrence at Bush Hill has been described being massive (e.g., MacDonald et al., 1994). Hence, before being grabbed with a 0.8 m^3 TV-grab hydrate crystals could grow freely, because hydrate is encased and surrounded only by more hydrate but not much sediment. Using TV-guided grabs for hydrate recovery provides a large aggregate where to pick samples from, but a geological reconstruction is not possible due to disturbance of the structure during the grab.

Instead, the vertical orientation is known from the gravity cored samples, which were retrieved from the Campeche Knolls gas hydrates. The difference in crystallite size of the two Campeche Knolls sub-samples is not as large as from Bush Hill samples and amounts to $\sim 40 \mu\text{m}$. Hydrates at the site of sampling occur together with massive asphalts and highly viscous hydrocarbons (MacDonald et al., 2004), which might have affected the re-growth of hydrates on small scale. In any case, the distance of the two sub-samples is $\sim 40 \text{ cm}$, matching the grain size difference of the Bush Hill hydrates, which are more distant.

The three gas hydrate samples from the eastern Black Sea stem from different gas and oil seeps, which are far remote from one another (Akhmetzhanov et al., 2007). Their mean crystallite sizes (Figure 3.9) are in a similar range to those from the Campeche Knolls in the southern Gulf of Mexico. On the other hand, hydrates from ODP Leg 204 are larger

and scatter much more. One possible explanation for these differences could be ripening of the crystals:

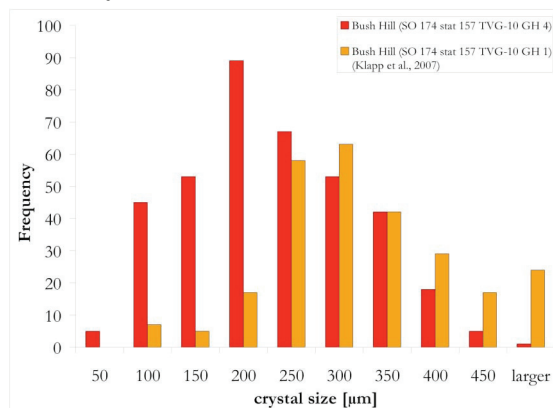


Figure 3.8. Crystal size distributions from two subsamples retrieved at the Bush Hill site in the Gulf of Mexico. The two samples stem from the same TV-grab.

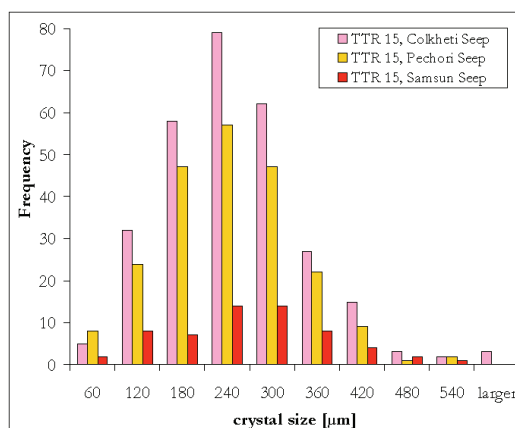


Figure 3.9. Crystal size distributions from hydrates sampled in eastern Black Sea seeps.

Klapp et al. (Klapp et al., 2007) suggested that ripening might happen to gas hydrates in oceanic environments, such that larger grains grow on the expense of smaller grains. Figure 3.4 A depicts a detector image of a sample from the Campeche Knolls in the Gulf of Mexico, Figure 3.4 B shows an detector image of a sample from the Hydrate Ridge; the mean grain size difference of the two samples is 146 μm. The detector image of the Hydrate Ridge sample displays larger reflections. Ripening, understood as a growth of the larger crystals on the expense of smaller ones, will ultimately lead to a CSD with larger mean values. Given similar CSDs upon hydrate formation, the samples from the Gulf of Mexico and from Black Sea seeps seem to be less ripened than those from Hydrate Ridge, if ripening is the cause for the different CSDs.

Ripening of crystals is a function of time, so larger grains may be older than smaller ones given that the initial crystal size and formation conditions are the same. Therefore, crystallite size information might possibly add to resolving formation ages of gas hydrates once the formation processes and conditions are constrained. What is needed to proceed further is the determination of the CSD of freshly grown marine gas hydrates, e.g. in dedicated sea-floor experiments.

6. Conclusions

Gas hydrate crystal sizes are difficult to measure, since previously, no adequate method existed to obtain statistically sound size distributions; a first approach was reported by Klapp et al. (Klapp et al., 2007). High-energy synchrotron radiation is an appropriate tool to investigate gas hydrate crystals, if combined with the Moving Area Detector Method (Klein et al., 2004; Bunge et al., 2003). Weak scattering of x-rays can be overcome by a multi-step image processing.

It turns out from our experiments that there are differences in crystallite size of natural and synthetic gas hydrate samples. Fresh, laboratory-produced hydrates are quite small with a mean grain size of near 40 μm. Shallow-buried, seepage associated marine gas hydrates from the Black Sea and Gulf of Mexico are 190-300 μm in size. Comparing the

latter to deeper buried, larger hydrates from the Hydrate Ridge, suggests that hydrate crystals in marine environments may well continue to grow. These results indicate that the sizes of gas hydrate crystals may add at least to qualitative constraining of formation ages.

With respect to the broad variety in the results of the measured grain sizes, modeling work (e.g., Luff & Wallmann, 2003), addressing diffusion or mechanical properties (in particular plastic deformation), should take the differences between natural and synthetic gas hydrates into account.

Acknowledgements

We thank Caterina Tommaseo and Lars Raue for support at the HASYLAB and Kirsten Techmer for help at the FE-SEM (all GZG Göttingen). We thank the captains and crews of the employed research vessels. Credits are due to HASYLAB at DESY for providing beam time and support. SAK thanks GLOMAR graduate school for Marine Sciences and the Vollkammer scholarship for support. This work was funded by the *German Research Foundation* (DFG) and the German Ministry of Education and Research (BMBF) in the programme GEOTECHNOLOGIEN.

CHAPTER 4
MANUSCRIPT 2
GRAIN SIZE MEASUREMENTS OF NATURAL GAS HYDRATES

Stephan A. Klapp^{1*}, Susanne Hemes², Helmut Klein²,
Gerhard Bohrmann¹, Ian R. MacDonald³, Werner F. Kuhs²

Submitted to *Marine Geology*, May 5th 2009.

¹ MARUM – Center for Marine and Environmental Sciences and Department of Geoscience, University of Bremen, P.O. 330440, D-28334 Bremen, Germany

² Abteilung Kristallographie, Geowissenschaftliches Zentrum der Universität Göttingen, Goldschmidtstrasse 1, D-37077 Göttingen, Germany

³ Texas A&M University, Corpus Christi, 6300 Ocean Dr. ST320, Corpus Christi, TX 78412, USA

4.1 Abstract

Methane hydrates are present in marine seep systems and occur within the gas hydrate stability zone. Very little is known about their crystallite sizes and size distributions as they are notoriously difficult to measure. Crystal size distributions are usually considered as one of the key petrophysical parameters as they influence mechanical properties and possible compositional changes, which may occur with changing environmental conditions. Variations in grain size are relevant for gas substitution in natural hydrates by replacing CH₄ with CO₂ for the purpose of carbon dioxide sequestration. Here we show that crystallite sizes of gas hydrates from some locations in the Indian Ocean, Gulf of Mexico and Black Sea are in the range of 200-400 μm; larger values were obtained for deeper-buried samples from ODP Leg 204. The crystallite sizes show generally a (log-) normal distribution and appear to vary sometimes rapidly with location.

Keywords

gas hydrates; grain sizes; crystallite size distribution; synchrotron radiation; Black Sea; Gulf of Mexico; Indian Ocean

4.2 Introduction

Gas hydrates are solid materials, which crystallized under inclusion of gas molecules into rigid cages of water molecules. On Earth, gas hydrates form in permafrost sediments as well as in the oceans predominantly along continental margins (Kvenvolden et al., 1993). Hydrates need elevated pressures and/or cold temperatures to form. The gas concentrations must exceed the solubility in interstitial waters (Kashchiev and Firoozabadi, 2002). The prevailing gas composition governs the crystal structure of the forming gas hydrate (Sloan and Koh, 2007).

It appears important to establish the crystallite size distributions as they have an influence on petrophysical properties like gas hydrate rheology (Durham et al., 2003), chemical engineering (Koh et al., 2002) or numerical modeling of geochemical processes (Torres et al., 2004; Haeckel et al., 2004; Wallmann et al., 2006b). For marine hydrate deposits, exchange reactions of free gas with existing gas hydrates of different composition may lead to re-growth processes and to changing gas composition, possibly influencing the hydrate stability. All exchange reactions can be expected to take place along the grain boundary network of gas hydrates, which is related to the crystallite size distributions. Laboratory experiments suggest that a gas replacement occurs exchanging methane by carbon dioxide (Yoon et al., 2004) or by ethane (Murshed and Kuhs, 2007) but little is known about gas substitution in nature. Scientific and economic interest, however, is large to better understand the replacement kinetics in particular in the context of carbon dioxide sequestration projects achieved by gas replacement in hydrates. The mean crystal sizes of gas hydrates and the crystallite size distributions are of particular interest here, as the exchange rates will be contingent on the extent of the grain boundary networks. Likewise, the mechanical properties, in particular the deformation of gas hydrate aggregates depend on the distributions of crystallite sizes. It turns out that synthetic samples often have smaller crystallite sizes than natural samples and mechanical laboratory tests may not reproduce faithfully the situation in natural settings (Klapp et al., 2007).

Gas hydrate crystallite size distributions are also important for our understanding of hydrate formation and evolution processes. The crystal size evolution is mainly governed by the free energy differences between grains, that is, the grain boundary surface energy and the contribution of deformational work to the free energy (Ricard and Bercovici, 2009). The latter is important if stress affects grain growth or grain size reduction, then the grain size evolution is determined by the rate of mechanical work (e.g., Austin and Evans, 2007). Mechanical deformation work on grains is typically found in tectonically active settings where tectonic stress forms crystal defects. As the soft sediments hosting gas hydrates in shallow marine deposits are not rigid enough to transfer stress on hydrate crystals, which would alter the grain sizes, the grain growth of hydrates can be considered as static (see Austin and Evans, 2007; Ricard and Bercovici, 2009). In that case, at elevated temperatures where local water and gas mobilities are high, a hydrate crystal coarsening may be expected in a process called “normal grain growth” or, for dispersed systems, “Ostwald ripening”. Corresponding models predict a change of mean crystallite size in time to the power of 2-3 dependency (Lifshitz and Slyozov, 1961; Wagner, 1961, summarized in Humphreys and Hatherly, 2004). In all these coarsening processes large grains grow on the cost of smaller grains in order to decrease the free energy in the system by lowering the total surface or grain boundary energy. Such a clathrate hydrate coarsening and re-growth is witnessed from polar air hydrates occurring in Greenland and Antarctic ice sheets and initially crystallizing from gaseous air inclusions (Pauer et al., 1999; Kipfstuhl et al., 2001). Normal grain growth is governed by a diffusive mass transfer from small to large grains, which also implies that the presence of impurities or particles within the grain boundary network could hinder the coarsening or slow it down (Doherty et al., 1997).

Establishing the crystallite size distributions of gas hydrates is a notoriously difficult enterprise; all optical standard methods for measuring grain sizes fail when it comes to gas

hydrates, mostly due to their thermodynamic instability during sampling, preparation or measurement.

Optical microscopy is inappropriate, because conditions to keep gas hydrates stable cannot easily be maintained during the preparation of thin sections. For short time and on a coarse length scale, however, photographs can be obtained for fabric inspections (Bohrmann et al., 1998) but are not suitable for identifying grain boundaries. Optical microscopy in cold room environments (below -20 °C) is a very good tool for investigating ice thin sections containing polar air hydrates (e.g., Kipfstuhl et al., 2001). This only works for hydrates encased by ice acting as a pressure vessel but not for pure gas hydrate specimen. Also, tracking down grain boundaries by crossing polarizers would not work, as structure I and II gas hydrates crystallize in the cubic crystal system and thus behave isotropically in that no change in the crystal orientation would be discernable, adding to the difficulty of identifying grain boundaries. Further, the cooling of the samples would become difficult, since at atmospheric pressure methane hydrate is only stable at temperatures below ~ -80 °C.

Scanning electron microscopy (SEM) at cryogenic temperatures allow for investigations of gas hydrates in their region of (meta)stability and hence are excellent tools for gas hydrate microstructural assessment (Kuhs et al., 2000a; Stern et al., 2004; Techmer et al., 2005; Appendix IV). The advantage of electron microscopy lies in its excellent local resolution, which allows for sharp images at more than 24,000x magnification at cooled gas hydrate samples. Yet, as electron microscopes can only image the surface of specimens but not their interior, the determination is a priori limited to what can be seen on the sample surface. Statistically relevant crystallite size distributions can hardly be expected from this technique. Recently, Murshed et al. (Chapter 6) showed first micro-scale computer-tomographic images of gas hydrate; grain size information was not communicated in this paper but might be inferred in the future from the grain boundary networks which were detected and discussed.

In our earlier work we reported the first crystal size analyses of gas hydrates as obtained from Bragg tomography (Klapp et al., 2007); here we present new data of natural marine hydrates of different locations from which a preliminary picture of typical gas hydrates crystallite size distributions emerges.

4.3 Materials and methods

All new data presented in this work stem from hydrates recovered from shallow burial-depths of the upper three meters of sediment in gas seepage systems, except one hydrate sample from offshore the Indian east coast. The Indian sample was retrieved during the Indian gas hydrate drilling campaign NGHP expedition 01 in 2006 from the Krishna-Godawari basin (Collett et al., 2008a). It stems from the drilling site 10D from 132,41 meters below the sea floor. The near-surface samples described in this study were retrieved from the Eastern Black Sea (Batumi Seep, Pechori Mound, Colkhetti Seep, Samsun Seep; Table 4.1) and from the Gulf of Mexico (Bush Hill area in the Northern Gulf and Chapopote Asphalt volcano in the Southern Gulf; Table 4.1). The Black Sea samples were recovered during the R/V Meteor cruise M72/3 in 2007 (Bohrmann and Pape, 2007) and during the TTR 15 cruise in 2005 with the R/V Prof. Logachev (Akhmetzhanov et al., 2007). Samples from the Batumi Seep, Pechori Mound and Samsun Seep were recovered by gravity-

coring and from Colkhetti Seep by a TV-guided grab. Hydrates from Chapopote were cored by a gravity corer during R/V Meteor cruise in 2006 (Bohrmann and Spiess, 2008), the Bush Hill samples were retrieved by a TV grab during R/V Sonne cruise in 2003 (Bohrmann and Schenk, 2004).

The samples were not pressure-cored, and despite immediate storage in liquid nitrogen to avoid decomposition after recovery, the outer parts of the hydrate could decompose already during the transfer from sea floor to the research vessels. Consequently, for the crystallite size distribution measurements we took care to only use largely unaltered samples from central parts of recovered cores, consisting for the most part of sediment-free aggregates of gas hydrate. All hydrate samples were comprehensively studied by X-ray diffraction and SEM before actual crystallite size distribution investigations using Bragg-tomography were undertaken: Quantitative X-ray phase analysis allowed to choose samples with high gas hydrate content, SEM visualizes the state of preservation of the samples (Kuhs et al., 2004a; Stern et al., 2004).

The gas hydrate crystallite size distributions were measured at the beam line BW 5 at the *Hamburg Synchrotron Laboratory* (HASYLAB) of the *Deutsches Elektronen Synchrotron* (DESY). High-energy synchrotron radiation at short X-ray wavelength ($\lambda \sim 0.12 \text{ \AA}$, corresponding to a beam energy of 100 keV) is used to investigate bulk samples. The actual gas hydrate grain sizes were measured using Bragg tomography in the Moving Area Detector Method (Wcislak et al., 2003); this method was originally developed for material science purposes such as metals or ceramics (Bunge et al., 2002; Klein et al., 2004). The data treatment was done by using the *MarView* software for the raw data as well as the *ImagePro Plus* and *ImageJ* packages for the size measurements of the gas hydrate crystallites. A detailed account of these procedures is given in Klapp et al. (2007; Appendix V).

4.4 Results

Gas hydrate grain sizes, obtained by synchrotron Bragg tomography, vary between less than 200 μm and more 500 μm for marine gas hydrates with good sample preservation. Other than checking the state of preservation, SEM was also applied in an attempt to detect grain boundaries on the 2-D surfaces. Gas hydrate sl could be distinguished from other phases like ice and sediments by typical homogeneously distributed sub- μm sized pores (diameter ranging from 200 to 400 nm in methane hydrate). These pores were described as a typical feature representing the sl gas hydrate phase in SEM studies (Kuhs et al., 2000a, 2004a; Staykova et al., 2003; Techmer et al., 2005; Appendix IV).

The SEM images depict porous gas hydrates in all samples except those from the Bush Hill area in the northern Gulf of Mexico. There, structure II hydrates were recovered with higher hydrocarbon content within the hydrate structure; those hydrates feature a smoother, tier-like microstructure on the surface (Figure 4.1a, b; see Chapter 5). Figure 4.1 gives an overview over the typical gas hydrate microstructure. The monotonous microstructure of intact (e.g., not dissociated) gas hydrate does not allow deducing any definite conclusions regarding grain boundaries or grain sizes for the hydrates, no matter whether the microstructure is dense and tier-like (Figure 4.1a, b) or porous (Figure 4.1c, d).

Partially decomposed hydrates (though eventually, they were not used for synchrotron measurements) are recognizable in SEM images by the sub- μm porous hydrate patches surrounded by dense ice (frozen water) resulting from hydrate decomposition (Kuhs et al.,

2004a; Appendix IV) and larger pores within the ice matrix (Figure 4.2a, b). It can be assumed that the decomposition of the hydrates progresses from the grain boundaries towards the interior. Accordingly, results from such partly decomposed hydrate patches may not reflect the true, intrinsic crystal sizes.

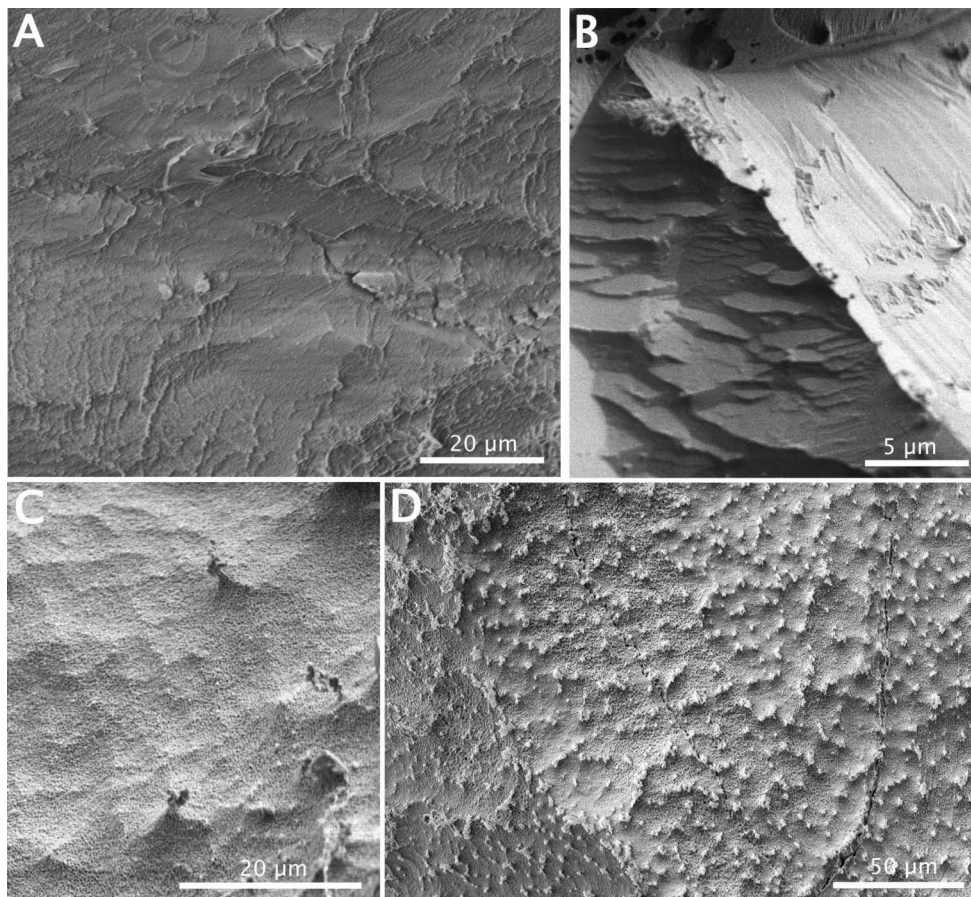


Figure 4.1: SEM images of gas hydrate samples. (A) Dense gas hydrate; tier-like surface structures do not allow to draw conclusions on grain boundaries (Bush Hill, northern Gulf of Mexico; TVG-10). (B) Higher resolution of dense, tier-like microstructure (Bush Hill, TVG-10). (C) In sub- μm porous gas hydrates are no grain boundaries discernible (Chapopote Asphalt volcano, Gulf of Mexico, GeoB 10618 CT6). (D) The monotonous porous fabric makes it impossible to detect any grain boundaries (Chapopote, GeoB 10618 CT6).

In contrast to optical methods, X-ray Bragg tomography provides bulk information with good statistical precision and accessing size information of several hundred grains in one experimental run, which can be plotted in histograms. The distributions of the crystallite sizes from natural samples appear to be in many cases (log-) normally distributed; a clear distinction between normal and lognormal crystallite size distribution cannot be made on the basis of the present data. Table 4.1 gives the mean crystal sizes for all gas hydrate samples. The arithmetic mean values of the two Batumi Seep hydrate samples are about 400 μm (Figure 4.3a, b), those of the other three hydrate samples from different Black Sea seep sites are centered around 220 μm (Table 4.1, Figure 4.3c-e); hydrates from the Chapopote (Gulf of Mexico) range from ~ 190 to ~ 230 μm and Bush Hill hydrates from ~ 200 to ~ 300 μm (Figure 4.4a, b). The hydrate sample from the Indian drilling campaign (NGHP-01) has an arithmetical mean crystallite size of 217 μm (Figure 4.4c). Crystals of gas hydrate specimens from the ODP 204 drilling campaign at Hydrate Ridge (Northwest

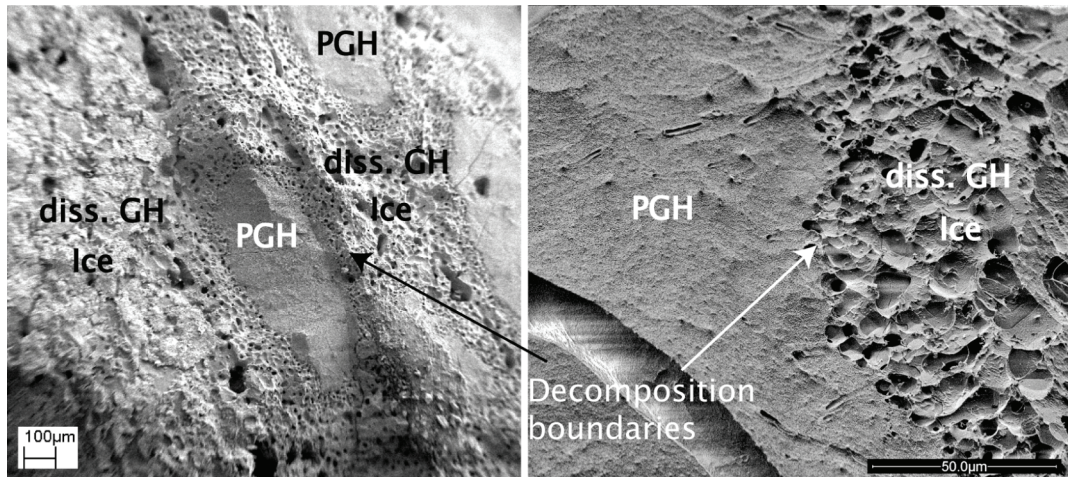


Figure 4.2: SEM images of gas hydrate samples. (A) Overview of patches of porous gas hydrate (PGH), characterized by sub-micrometer sized pores. The patches are surrounded by dense ice containing larger pores of tens of micrometer size in diameter. No information can be obtained about the actual size of crystallites within the patches, nor is it certain that larger pores within the dense matrix are forming grain boundaries between gas hydrate grains (ODP 204 1247B-12H-2, 41-51cm). (B) Boundary between sub-micrometer sized porous gas hydrate and decomposed hydrate (fewer and larger pores); a crack is seen in the porous hydrate (Batumi Seep, Black Sea, GeoB 11949). Abbreviation: PGH - porous gas hydrate; diss. GH - dissociated gas hydrate (frozen to ice).

Pacific) are larger, ranging from ~300 and ~600 μm in diameter with a tendency to increase with depth below the sea-floor (Klapp et al., 2007). In order to prove the reliability of the image processing method, three selected images were evaluated manually by a scientist in addition to the automated image analysis. The advantage of an interactive evaluation lies in the human ability to differentiate between signal and noise for small and thus very weak reflections using the shape of the trace of Bragg reflections; also the human brain is readily able to differentiate between accidentally overlapping and a single large grain; the software implementation of corresponding logical chains turned out to be difficult. Nevertheless, there is a very reasonable agreement of both human and computer measured grain sizes which gives us confidence into the reliability of the results obtained from the generally applied automated image processing (see Table 4.1).

4.5 Discussion

A comprehensive characterization of gas hydrates – whether in terms of mineralogical description or by modeling time-dependent exchange rates (Luff & Wallmann, 2003; Torres et al., 2004; Haeckel et al., 2004; Wallmann et al., 2006b) – needs information on the crystal size and grain-boundary area. Previous information on grain sizes was rudimentary. At best there were some data on individual crystallite sizes or on averaged hydrate crystallite sizes without information on the crystallite size distributions; Klapproth (2002) and Staykova et al. (2003) for example quote crystal sizes of 15-40 μm from estimates based on the inhomogeneities of X-ray Debye-Scherrer rings for laboratory-made hydrates prepared by an isothermal reaction of methane gas with ice close to 0°C, a method frequently applied for gas hydrate synthesis. Schicks et al. (2006) reacted water with pressured gas and produced larger single crystals up to the size of 100 μm. This and similar techniques (e.g., Tohidi et al., 2001) is not very rapid and generally not used for hydrate production in the laboratory. Clearly, synthetic gas hydrates prepared by a reaction of fine-grained ice with

gas results in crystal sizes smaller by an order of magnitude than what is encountered in nature as inferred from our Bragg tomography data which fully confirm our earlier estimates mentioned above. Care must therefore be exerted when comparing results from petrophysical lab tests to the natural settings when samples are prepared by the ice method.

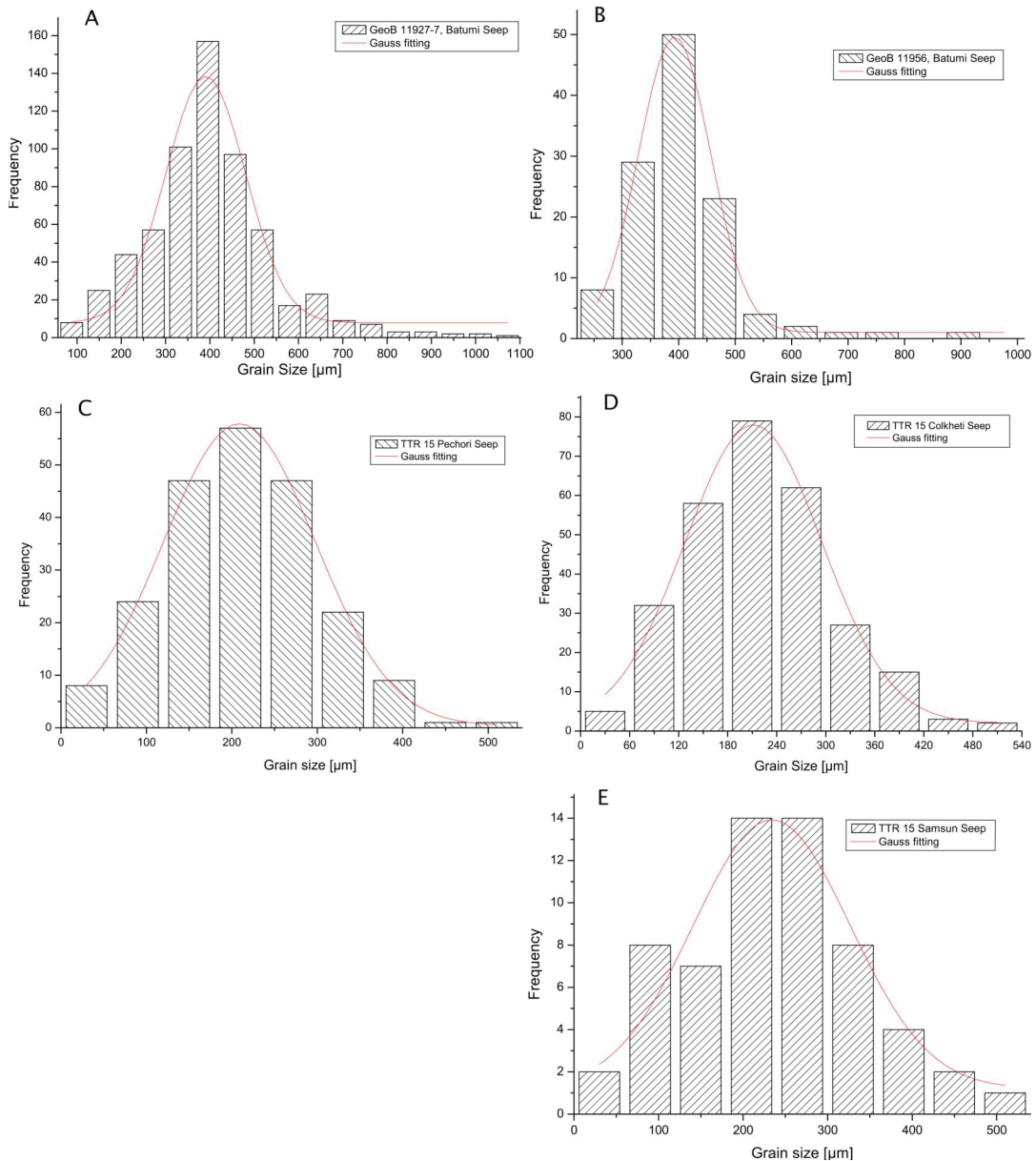


Figure 4.3: Crystal size distributions from hydrates sampled in eastern Black Sea seeps. **(A)** Batumi Seep, GeoB 11927-7; **(B)** Batumi Seep GeoB 11956; **(C)** Pechori Seep; **(D)** Colkhetti Seep; **(E)** Samsun Seep.

It is unlikely that the grain sizes are affected by any post-sampling re-arrangement. The time during sample transfer from a liquid nitrogen filled vessel to the pre-cooled sample holder is by far too short for any annealing effect due to the low mobility of water molecules at temperatures below 120K – the samples never experienced temperatures higher than this after recovery. Annealing effects are unlikely during the sample recovery, too, since no

Table 4.1 Mean grain sizes and standard-deviations of gas hydrate samples. Site conditions (water depth, meters below sea floor [mbsf] and temperature) are given for marine samples to provide information about the stability conditions for the hydrates.

sample	Mean grain size [μm]	standard dev [μm]	number of data points	Temp. [$^{\circ}\text{C}$]	water depth [m]	mbsf	Latitude	Longitude
Black Sea								
Colkheti Seep, BS 380GR	223	101	286	9.1 ^a	1142 ^a	< 1.00 ^a	41°58.08 N	41°06.17 E
Colkheti Seep, BS 380GR, manually	214	130	299	9.1 ^a	1142 ^a	< 1.00 ^a	41°58.08 N	41°06.17 E
Pechori Mound, BS 360G	213	89	217	9.1 ^a	1030 ^a	0.70-1.95 ^a	41°59.00 N	41°07.41 E
Pechori Mound, BS 360G, manually	210	91	63	9.1 ^a	1030 ^a	0.70-1.95 ^a	41°59.00 N	41°07.41 E
Samsun Seep, BS 383G	236	106	69	9.1 ^a	1431 ^a	4.65-4.75 ^a	41°28.46 N	37°35.83 E
Batumi Seep, GeoB 11927-7	400	146	613	9.0	843 ^b	1.50-3.30 ^b	41°57.41 N	41°17.32 E
Batumi Seep, GeoB 11956	410	95	119	9.0	856 ^b	0.80-0.90 ^b	41°57.45 N	41°17.44 E
Indian Ocean, NGHP Expedition 01								
Site 10D, Core 20X, Section 6, 52-59cm	217	99	189	11.5 ^g	1038 ^g	132.41 ^g	15°51.86 N	81°50.08 E
Gulf of Mexico								
Bush Hill (TVG-10 GH 4)	204	89	377	8.7 ^c	547 ^c	< 1.00 ^c	27°46.97 N	91°30.47 W
Bush Hill (TVG-10 GH 1)	301 ^d	114 ^d	261	8.7 ^c	547 ^c	< 1.00 ^c	27°46.97 N	91°30.47 W
Chapopote (GeoB 10618, CT 2)	227	99	672	4.4	2904 ^e	< 1.00 ^d	21°53.95 N	93°26.21 W
Chapopote (GeoB 10618, CT 2), manually	207	97	509	4.4	2904 ^d	< 1.00 ^d	21°53.95 N	93°26.21 W
Chapopote (GeoB 10618, CT 6)	187	109	743	4.4	2904 ^d	< 1.00 ^d	21°53.95 N	93°26.21 W
Hydrate Ridge (ODP Leg 204)								
1249C-1H-CC, 0-10cm	373 ^d	134 ^d	317	4.3 ^f	775 ^f	1.50 ^f	44°34.24 N	125°08.84 W
1250C 2H-CC 0-1 cm	451 ^d	132 ^d	124	4.4 ^f	792 ^f	5.06 ^f	44°34.13 N	125°09.02 W
1248C-8H-6, 68-87cm	361 ^d	79 ^d	99	8.8 ^f	828 ^f	74.46 ^f	44°34.45 N	125°09.15 W
1247B-12H-2, 41-51cm	592 ^d	374 ^d	40	8.5 ^f	845 ^f	93.01 ^f	44°34.66 N	125°09.08 W
1248C 11H-5 (no tilt)	517 ^d	176 ^d	231	9.9 ^f	828 ^f	100.89 ^f	44°34.45 N	125°09.15 W
1248C 11H-5 (90° tilted)	569 ^d	342 ^d	49	9.9 ^f	828 ^f	100.89 ^f	44°34.45 N	125°09.15 W
Synthetic CH₄-Hydrate	43 ^d	24 ^d	1793			<i>see text</i>		

Notes: a = Cruise TTR 15 R/V Prof. Logachev, Achmetzov et al., 2007; b = R/V Meteor cruise M72/3, Bohrmann and Pape, 2007; c = R/V Sonne cruise SO174, Bohrmann and Schenk, 2004; d = Klapp et al., 2007; e = R/V Meteor cruise M67/2, Bohrmann and Spiess, 2008; f = Tréhu et al., 2006b; g = Indian NGHP Expedition 01, Collett et al., 2008a.

annealing effects have been observed on gas hydrate specimen which were sequestered in the ocean and recovered later (Stern et al., 2004), thus we are very confident that the measured crystallite size distributions faithfully represent the situation of the natural settings. The synchrotron measurements indicate that the arithmetic mean grain sizes of different natural samples vary from 190 up to 600 μm (Figure 4.5). The much larger sizes when compared to synthetic material may have the following reason: either (1) the natural formation process yields distinctly larger grains than what is produced by any standard laboratory method or (2) gas hydrates with initially smaller crystallite sizes grow to larger grains by a coarsening process as observed in polar air hydrates (Kipfstuhl et al., 2001).

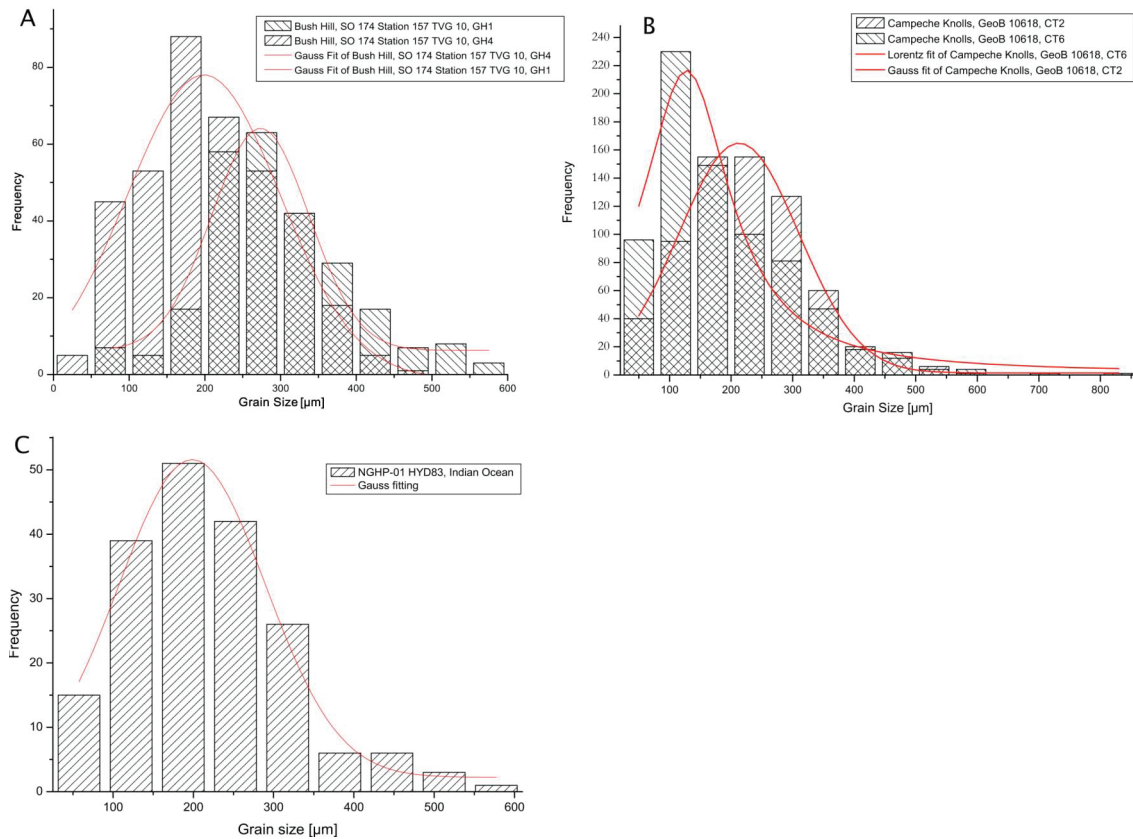


Figure 4.4: Crystal size distributions: **(A)** Two sub-samples retrieved at the Bush Hill site in the Gulf of Mexico. The two samples stem from the same TV-grab. **(B)** Two sub-samples from the gravity core GeoB 10618 at the Chapopote in the Southern Gulf of Mexico. One distribution shows the crystallite size distribution of sub-sample CT2, the other sub-sample CT6. **(C)** Crystal size distribution of a gas hydrate sample from the Indian NGHP expedition 01.

It is interesting to note that one of the samples (Chapopote, GeoB 10618 CT 6) shows a crystallite size distribution distinctly skewed towards smaller grains (Figure 4.3B) which is unexpected for a distribution growing in steady-state (see e.g., Humphreys and Hatherly, 2004). A possible explanation is the fairly recent formation of this hydrate with insufficient time to adjust to a better-equilibrated distribution by reducing the number of smaller grains. Alternatively, particles or impurities between the grains – inside the grain boundary network, see Chapter 6 – could have slowed down the grain coarsening. For normal grain growth mass is diffusively transported from small to large grains (Humphreys and Hatherly, 2004), therefore particles between two crystals could inhibit the diffusion between them (e.g., Doherty et al., 1997). In fact, hydrates at the sampling site occur together with mas-

sive asphalts and highly viscous hydrocarbons (MacDonald et al., 2004). It is plausible that heavy hydrocarbons act as inhibitors for hydrate crystal growth, if they are located in the grain boundary network. In oil seepage areas, oil and heavy hydrocarbons diffuse through massive hydrate layers (Bohrmann and Schenk, 2004; MacDonald et al., 2003; Sassen et al., 2001c) and are known to be in direct contact with the hydrate crystals on a microscopic scale (Chapter 5), emphasizing the possibility that at the Chapopote Asphalt volcano, asphalts might be stuck inside the grain boundary network. The difference in arithmetic mean crystallite size of the two Chapopote sub-samples amounts to $\sim 40 \mu\text{m}$. It is possible that the viscous hydrocarbons occurring at the location might have affected the coarsening of hydrates on a small local scale.

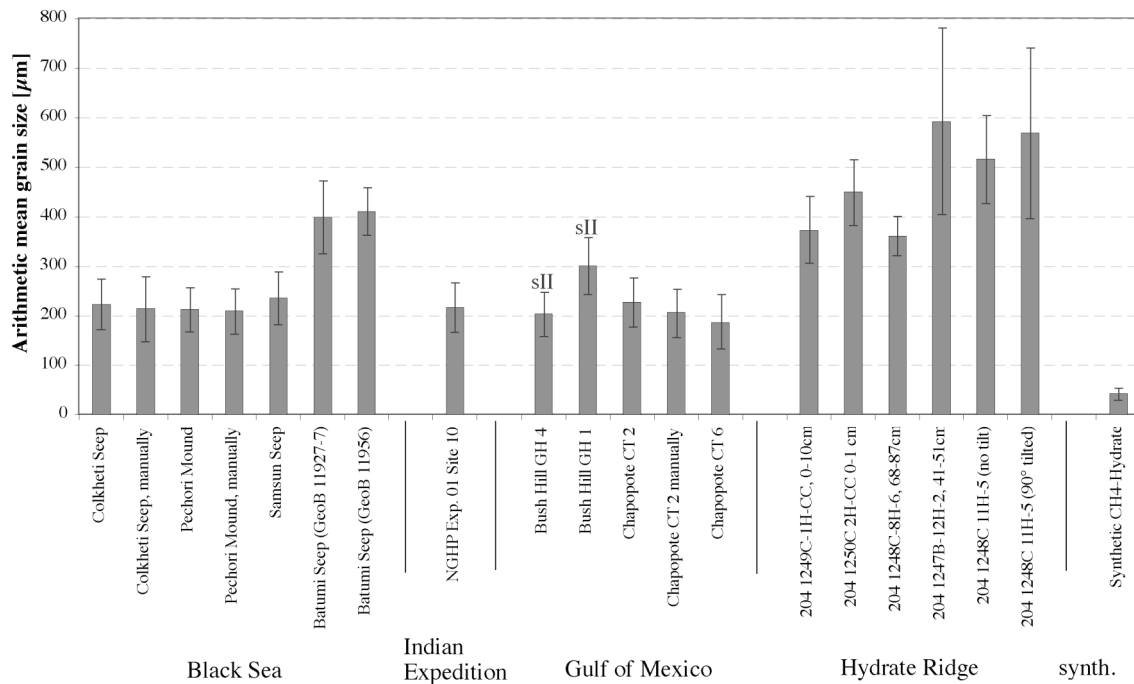


Figure 4.5: Bar diagram of the arithmetic mean crystal sizes given in Table 1. Geological locations are grouped. The two samples from Bush Hill/Gulf of Mexico are sII gas hydrates. Error bars indicate the standard deviation.

Remarkably, the crystallite sizes of two sub-samples from the Bush Hill sampling station in the Gulf of Mexico are different, suggesting that grain size controls in marine environment act differently over short distances: The two sub-samples from slightly different positions from Bush Hill (TVG 10) show a difference of mean crystallite sizes of nearly $100 \mu\text{m}$ (Figure 4.5). These samples were recovered by TV-guided grab and stem from a volume of approximately 0.8 m^3 of almost pure gas hydrate (Bohrmann and Schenk, 2004). The hydrates crystallized to structure II hydrate and were recovered from the sea floor in 540 m water depth and left the zone of gas hydrate stability in the water column in ca. 330 m water depth. The two sub-samples with different crystal sizes are from different parts of the bulk TV-grab. The reason for the two varying grain sizes is unclear, yet several causes could account for the difference. First, given that coarsening of crystals proceeds with time (see e.g. Lasaga, 1998), it would be consequent to argue that the sub-sample with the larger grains comprises older crystals. That, in turn, then suggests a very dynamic hydrate system, because the assumption implies that hydrates of different age are virtually neighboring. In fact, MacDonald et al. (2005) find that the Bush Hill hydrates accumulate gradu-

ally on a yearly scale, which supports this theory. Chen and Cathles (2003) propose that the Bush Hill deposit has been increasing in size since ~ 10,000 years. Yet, other reasons may account for the different grain sizes of these two sub-samples; differences in the thermodynamic conditions in terms of supersaturation or subcooling could lead to different conditions for nucleation and growth at different periods of time. Also, similar to the Chapopote site, the Bush Hill area is an oil seep with oil discharge into the water, such that oil and shallow gas hydrates occur together (MacDonald et al., 2005). That would allow for the possibility of oil affecting hydrate crystal growth.

The two Batumi Seep hydrates instead have almost identical arithmetic, mean grain sizes, although they were recovered from different stations (Table 4.1; Figure 4.5). The crystal size distributions are not skewed to one side, suggesting that normal grain growth occurs and that the grain size growth is static (see Austin and Evans, 2007; Ricard and Bercovici, 2009). Because the two samples originate from two different sites in the Batumi Seep area (Bohrmann and Pape, 2007; Chapter 8) and also have almost the same mean grain size and a similar grain size distribution (GeoB 11956 has fewer data points, accounting for the narrower distribution), one is tempted to assume that this would indicate very similar formation and growth conditions for hydrates at the Batumi Seep sites. Yet, the examples of the two sites in the Gulf of Mexico demonstrate that formation and growth can vary considerably over short distances.

The three other gas hydrate samples from the eastern Black Sea – originating from the Samsun Seep, Colkhети Seep and Pechori Mound – have much smaller mean crystal sizes than the Batumi Seep hydrates, scattering around 200 μm . These three seeps are far remote from one another (Akhmetzhanov et al., 2007). The mean crystallite sizes of the three samples (Figure 4.5) are in a similar range to those from the Chapopote in the southern Gulf of Mexico. Also similar to the Gulf of Mexico hydrates, the Colkhети Seep and Pechori Mound are oil seeps, which implies that if the presence of oil had an effect on the growth conditions of gas hydrates, this influence could affect the Black Sea oil seep hydrates as well.

The mean crystallite size of the hydrate sample from the Indian drilling campaign is similar to those Black Sea oil seeps and Chapopote hydrates (Figure 4.5). This sample was retrieved in an ocean drilling campaign from about 132 m below the sea floor (Collett et al., 2008a). Yet, the comparison with the existing grain size data of deep buried gas hydrates from ODP Leg 204 at Hydrate Ridge shows that the Indian samples does not fit into the pattern which emerges from the ODP 204 hydrates (Figure 4.5). For those hydrates a relationship of the arithmetical mean grain size and burial depth seems to be indicated (Table 4.1; Klapp et al., 2007), although more factors will affect the crystal size evolution. In particular, brines which are reported for the horizons where the Indian sample was retrieved (Collett et al., 2008a), could affect the gas hydrate crystal growth. Salts have an effect on the gas hydrate stability (Sloan and Koh, 2007) and one possibility could be that episodic brine-induced gas hydrate dissociation keeps the hydrate crystal growth in steady-state. More information, which is not yet available, will help to interpret the grain sizes. Another reason which could explain the differences between Hydrate Ridge samples and all other crystal sizes presented here could be again a coarsening of the crystals. Given a similar initial crystallite size distribution upon hydrate formation, the samples from the Indian ocean as well as from the Gulf of Mexico and from Black Sea seeps (except the Batumi Seep) seem to be younger than those from Hydrate Ridge, if time-dependent coarsening is

a major cause for the different crystallite size distributions and if the initial crystallite size distribution was at least similar.

The coarsening of air molecule hydrate crystals observed in polar ice (Pauer et al., 1999; Kipfstuhl et al., 2001) can be expected to be less affected by other factors than the coarsening of gas hydrates crystals in marine seep environments. As the presence of salts in hydrate formation waters can contribute to hinder hydrate formation, it can be speculated that salt brines within the strata slow down the hydrate crystal growth. Dissolved salts decrease the availability of water molecules and reduce the solubility of gas molecules in salt-rich solution (Duan and Mao, 2006; Masoudi et al., 2004). Mechanical hindrances would be asphalts, oil and other impurities, which may retard the grain growth, if they occur in the grain boundary network of oil seep hydrates. Several circumstances might decelerate but few factors could accelerate hydrate crystal growth. For instance, the presence of clay minerals such as montmorillonite together with quartz promotes the hydrate formation on mineral surfaces (Klapproth et al., 2007), but fostering hydrate formation is not necessarily related to stimulating crystal growth. Thus, the presence or absence of clay minerals could not explain grain size differences of marine hydrate samples investigated in this study (Figure 4.5). Instead, it is likely that coarsening is a major reason for the crystallite size evolution.

The crystal structure of the growing gas hydrates may also influence the hydrate crystal growth rate. The Bush Hill hydrates crystallize to structure II gas hydrate (Heeschen et al., 2007; Chapter 5), whereas the other samples presented here crystallized to structure I hydrate. However, it is likely that the growth kinetics of the two gas hydrate structures are similar, because both structures are cubic and form with the same small cage (5^{12}); it could only be the formation of the two large cages ($5^{12}6^2$ in sI and $5^{12}6^4$ in sII) in the two respective hydrate structures which may accelerate the crystal growth or slow it down. If there were differences in growth of the two structures (which we cannot identify at present) it would be likely that the diffusion was slowed down by larger hydrocarbon molecules such as butane (C_4H_{10}). From gas hydrate formation experiments (Staykova et al., 2003; Kuhs et al., 2006) we have good evidence that the rate-limiting step in hydrate growth for smaller molecules is the water mobility (and not the gas mobility); whether this also holds for large molecules like butane is a still open question. A better understanding of hydrate growth and regrowth, in particular its temperature and compositional dependency is needed to settle this issue.

4.6 Conclusions

The data presented here corroborate and extend information on of crystallite size distributions of gas hydrates (Table 4.1; Figure 4.5). Bragg tomography is at present the only tool to investigate gas hydrate crystallite size distributions systematically using the Moving Area Detector Method (Bunge et al., 2003; Klein et al., 2004).

It turns out that there is an order-of-magnitude difference in crystallite size of natural and most synthetic gas hydrate samples, although larger synthetic samples have been produced (Schicks et al., 2006). Shallow-buried, seepage associated marine gas hydrates from the Black Sea and Gulf of Mexico are 190-400 μm in size. Comparing the latter to deeper buried, larger hydrates from the Hydrate Ridge, suggests that hydrate crystals in marine environments may well be continuously growing. If the initial crystallite size distribu-

tions for a given p-T-x condition can be established, crystallite size information should give access to the formation ages of gas hydrates. Other factors that may influence the crystal size evolution are inhibitors such as salts/brines, particles or impurities in the grain boundary networks, or the crystal structure. What is needed to proceed further is a broader crystallite size distribution data base for various settings differing in their thermodynamic regime as well as the determination of the crystallite size distributions of freshly grown marine gas hydrates in designated sea-floor experiments and/or more realistic studies of gas hydrate crystal growth in laboratory work.

Acknowledgements

We thank Caterina Tommaseo and Lars Raue for support at the HASYLAB and Kirsten Techmer for help at the FE-SEM (all GZG Göttingen). Credits go to Barbara Teichert (now at the University of Münster, Germany) for providing the Indian Ocean gas hydrate sample. We thank the captains and crews of the employed research vessels. Credits go to HASYLAB at DESY for providing beam time and support. S.A. Klapp thanks GLOMAR graduate school for Marine Sciences and the Vollkammer scholarship for support. This work was funded by the *German Research Foundation* (DFG) and the German Ministry of Education and Research (BMBF) in the programme GEOTECHNOLOGIEN (Grants 03G064A, 03G0605B) of which it is publication number GEOTECH-xxx. This study received additional funding through the DFG-Research Center / Excellence Cluster "The Oceans in the Earth System".

CHAPTER 5
MANUSCRIPT 3

MICROSTRUCTURES OF STRUCTURE I AND II GAS HYDRATES FROM THE GULF OF MEXICO

Stephan A. Klapp^{a*}, Gerhard Bohrmann^a, Werner F. Kuhs^b, M. Mangir Murshed^b, Thomas Pape^a, Helmut Klein^b, Kirsten S. Techmer^b, Katja U. Heeschen^a and Friedrich Abegg^a

In press at *Marine and Petroleum Geology* (2009), doi:10.1016/j.marpetgeo.2009.03.004, available online since 5 April 2009.

^a MARUM – Center for Marine Environmental Sciences and Department of Geosciences, University of Bremen, P.O. 330440, D-28334 Bremen, Germany

^b GZG, Abt. Kristallographie, Universität Göttingen, Goldschmidtstr. 1, D-37077 Göttingen, Germany

5.1 Abstract

Gas hydrate samples from various locations in the Gulf of Mexico (GOM) differ considerably in their microstructure. Distinct microstructure characteristics coincide with discrete crystallographic structures, gas compositions and calculated thermodynamic stabilities. The crystallographic structures were established by X-ray diffraction, using both conventional X-ray sources and high-energy synchrotron radiation. The microstructures were examined by cryo-stage Field-Emission Scanning Electron Microscopy (FE-SEM). Good sample preservation was warranted by the low ice fractions shown from quantitative phase analyses.

Gas hydrate structure II samples from the Green Canyon in the northern GOM had methane concentrations of 70–80% and up to 30% of C₂–C₅ of measured hydrocarbons. Hydrocarbons in the crystallographic structure I hydrate from the Chapopote asphalt volcano in the southern GOM was comprised of more than 98% methane. Fairly different microstructures were identified for those different hydrates: Pores measuring 200–400 nm in diameter were present in structure I gas hydrate samples; no such pores but dense crystal surfaces instead were discovered in structure II gas hydrate. The stability of the hydrate samples is discussed regarding gas composition, crystallographic structure and microstructure.

Electron microscopic observations showed evidence of gas hydrate and liquid oil co-occurrence on a micrometer scale. That demonstrates that oil has direct contact to gas hydrates when it diffuses through a hydrate matrix.

Keywords: Gas hydrate; Gulf of Mexico; Microstructure; Structure II; Stability; Electron microscopy; X-ray diffraction; Porosity

5.2 Introduction

Gas hydrates are crystalline compounds of light hydrocarbons (methane, ethane, etc.) or non-hydrocarbon compounds (carbon dioxide, hydrogen sulfide, nitrogen) and water molecules which combine to build various hydrate structures (Sloan and Koh, 2007). The formation of gas hydrates is controlled by an array of physical and chemical parameters: Availabil-

ity of hydrate-forming gases is the prerequisite; hydrates only crystallize when the gas concentrations at least locally and temporarily exceed solubility (Kvenvolden, 1993). Hydrostatic pressure as given by the water depth, sediment temperature and pore water salinity are the limiting formation factors for marine gas hydrates which also govern the thickness of the gas hydrate stability zone.

Gas hydrates are considerable methane reservoirs (Collett, 2002; Max et al., 2006) and may turn into future sources of fossil fuels. The global methane hydrate inventory can be considered as a chemostat, which may partly control climate cycles (Kennett et al., 2003). The total amount of carbon stored in gas hydrates is still uncertain. Buffett and Archer (2004) figured 3000 Gt carbon being stored in gas hydrates; instead, Klauda and Sandler (2005) came up with 74,400 Gt of methane being stored as hydrates.

Hydrates form different crystallographic structures. Structure I (sI) gas hydrate is often addressed as methane hydrate because methane is the main guest molecule, sometimes amended by slight fractions of ethane and hydrogen sulfide. In many natural deposits like at several sites at the Hydrate Ridge offshore Oregon (Suess et al., 2001; Torres et al., 2004) or at the Blake Ridge (Dickens et al., 1997a; Matsumoto et al., 2000), methane originates predominantly, but not exclusively from microbial methane production. Because methane from biogenic origin is far more profuse than higher homologues predominantly derived from thermogenetic catalysis, gas hydrate sI is considered as the most abundant hydrate structure on earth (Kvenvolden, 1995), despite its greater limitations in stability conditions compared to the other two structures (Sloan and Koh, 2007; Lu et al., 2007). Structure II and structure H hydrates (sII and sH) derive hydrocarbons primarily from thermogenic origin; such compounds are methane through butanes for sII and methane through pentanes for sH. Thermogenic origin of hydrocarbons in gas hydrates has been reported for instance in the northern Gulf of Mexico (GOM) (Sassen et al., 2001a) and in the Barkley Canyon/Cascadia margin (Lu et al., 2007).

In general, hydrate structures are related to the molecule diameters of present hydrate-forming gases; however laboratory experiments have shown that before a long-term stable structure is equilibrated, transient existences of metastable structures are found (e.g., Klapproth et al., 2003). Gas hydrate structures I and II are quite distinguishable by their X-ray diffraction (XRD) pattern. Rietveld analysis (Toby, 2001) of the XRD data allow for quantitative analysis of different phases occurring within a sample, i.e. to assess the amounts of ice, different gas hydrate structures and other phases.

Microstructural observations of gas hydrates can be best obtained by electron microscopy. For convenience and in contrast to the usual nomenclature in material science, "mesopores" are understood here as pores in the range of hundreds of nanometers in diameter. A mesoporous microstructure is known for laboratory produced synthetic hydrates made of argon (Ar), nitrogen (N₂), carbon dioxide (CO₂) and methane (Kuhs et al., 2000a; Klapproth et al., 2003; Staykova et al., 2003) as well as natural sI hydrates (Kuhs et al., 2004a; Techmer et al., 2005). Mesoporous and nonporous hydrate microstructures are shown by (Stern et al., 2004) and (Stern et al., 2005), although there, the microstructure was not directly related to the crystallographic structure or the gas chemistry of the hydrates. Interestingly, for all investigated mesoporous hydrates the pore diameter has been observed in the same range of 200–400 nm (with the notable exception of CO₂ hydrates with pores below 100 nm as discussed in Kuhs et al., 2000a). It did not matter whether synthetic or natural hydrates were observed nor whether a hydrate sample stems from deep within the

gas hydrate stability nor whether it is close to the phase boundary. Macropores in the micrometer range were identified as originating from gas hydrate decomposition (Kuhs et al., 2004a and Stern and Kirby, 2007). Pores of tens of micrometers in diameter were found in methane-dominated SI gas hydrates from the Hydrate Ridge and were also attributed to gas hydrate dissociation upon recovery (Appendix IV). Each such decomposition pore has a different diameter in the few micrometer range, moreover, the size-normalized pore density is much smaller for decomposition pores than for mesopores. Some pores, or rather bubbles, could be inclusions of free gas into the gas hydrate matrix. Such free gas bubbles can be considered as the original part of the in situ structure or microstructure (Bohrmann et al., 1998), whereas decomposition pores are secondary alterations. These gas bubbles would add to the porosity estimation (e.g., Suess et al., 2002).

This paper assesses the relation between gas hydrate crystallographic structure and microstructure. We present new insights on the microstructure of natural SI and SII hydrates formed from methane through butane gases in the GOM. We combine results from XRD, gas chromatography and Field-Emission Scanning Electron Microscopy (FE-SEM) for individual samples from different locations in the GOM and attribute diverse microstructure observations to the corresponding gas chemical and crystallographic findings.

5.3 Geological setting and sampling in the Gulf of Mexico

Fluid migration in the GOM transports hydrocarbons from subsurface reservoirs to the seafloor at numerous sites. Thick sediment layers on the continental margin cover Early Jurassic salt sheets (Humphris, 1979), which create salt ridges and basins through halokinetic mobility (Rowan et al., 1999). Deeply buried oil and gas reservoirs are tapped by salt-tectonic-induced faults, which serve as pathways for hydrocarbons to shallower reservoirs and eventually to the seafloor. The depletion of heavy hydrocarbons or the stripping of light hydrocarbons (Chen et al., 2004; Whelan et al., 2005) results in gases ascending to near-surface sediments, where gas hydrates can form as part of seep related processes (Sassen et al., 2001a; MacDonald et al., 1994; MacDonald et al., 2003; Chen and Cathles, 2003). Gas hydrate presence in the northern GOM was first reported in 1984 (Brooks et al., 1984) and has been extensively studied henceforward. Collett and Kuuskraa (1998) calculated the total amount of hydrate-captured gas in the GOM area to be 70.1 Gt. Estimations should be treated carefully, though, since at individual sites elevated salinities and temperatures prevent hydrate formation despite high gas fluxes (Ruppel et al., 2005).

Samples investigated in this study were retrieved from the northern and southern GOM during the R/V Sonne cruise SO 174 in fall 2003 (Bohrmann and Schenck, 2004) and R/V Meteor cruise M67/2b in spring 2006 (Bohrmann and Spiess, 2008; Table 5.1). During the Sonne cruise, gas hydrates were recovered from three areas (Figure 5.1): From two different sites in the Green Canyon offshore Louisiana in the northern GOM (block CG415 as used by the United States Mineral Management Service) in about 1050 m water depth (named TVG-3 and TVG-12 in this paper; see Table 5.1); from two sites in the Bush Hill area (block GC185), which is part of the Green Canyon (these locations are called TVG-10 and GC-2); and from one site at the Chapopote asphalt volcano (sample TVG-6) in the Campeche Knolls area in the Southern GOM. On the M67/2b cruise additional hydrates were sampled at one gravity coring station from the Chapopote asphalt volcano (Figure 5.1). Samples from this cruise are named GC-6 with sub-samples.

5. Microstructures of structure I and II gas hydrates from the Gulf of Mexico

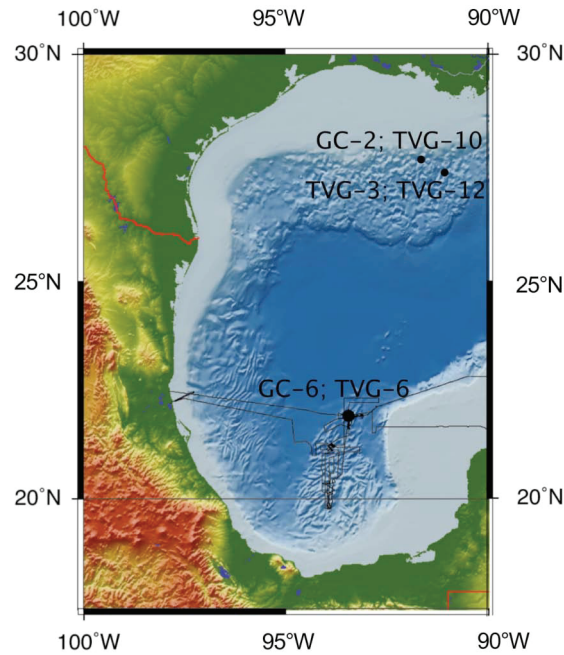


Figure 5.1: Map of sampling locations in the Gulf of Mexico. For station numbers see Table 5.1. Lines indicate the cruise track.

Table 5.1: Gas hydrate samples presented in this paper. TVG: TV-guided grab; GC: gravity corer. In the text, the short name is used.

Latitude [N]	Longitude [E]	Water depth [m]	Cruise, sampling station	Short name (in text)	Total core recovery [m]
Northern Gulf of Mexico					
Green Canyon Region					
<i>GC185 (Bush Hill)</i>					
27°46.95	91°30.44	547	SO 174, station 47; GC-2	GC-2	2.8
27°46.97	91°30.47	547	SO 174, station 157; TVG-10	TVG-10	
<i>GC415</i>					
27°32.61	90°59.55	1049	SO 174, Stat. 96; TVG-3	TVG-3	
27°33.47	90°58.85	951	SO 174 Stat 169; TVG-12	TVG-12	
Southern Gulf of Mexico					
Campeche Knolls Region					
21°54.00	93°26.24	2902	SO 174 Stat 140 TVG-6	TVG-6	
21°53.95	93°26.21	2904	M67/2 GeoB 10618; GC-6 #1	GC-6 #1	1
21°53.95	93°26.21	2904	M67/2 GeoB 10618; GC-6 #2	GC-6 #2 (sub-sample 1)	1
21°53.95	93°26.21	2904	M67/2 GeoB 10618, GC-6 #2	GC-6 #2 (sub-sample 2)	1

The Bush Hill area is located in relatively shallow water depths (500–600 m below sea level, mbsl) and is fed by gas from the Jolliet gas field (Chen and Cathles, 2003), from which free gas and oil discharges into the water (Sassen et al., 2001b; MacDonald et al., 2003). The oil-stained, gas-laden sediments host chemosynthetic communities (MacDonald et al., 2003). Compositions of light hydrocarbons (C₁–C₄) should result in the formation of sll gas hydrates, as suggested by many authors especially for the Bush Hill region (e.g., Sassen et al., 1994; Sassen et al., 2001b; Techmer et al., 2005; Chen and Cathles, 2003; MacDonald et al., 2005). Structure II gas hydrate was recently identified by XRD in Green Canyon block

GC234 (Rawn et al., 2008). Gas hydrates occur both as white precipitates as well as brownish-yellowish colored from oil perfusion through the hydrates (Figure 5.2; see MacDonald et al., 1994; 2003; Bohrmann and Schenck, 2004).

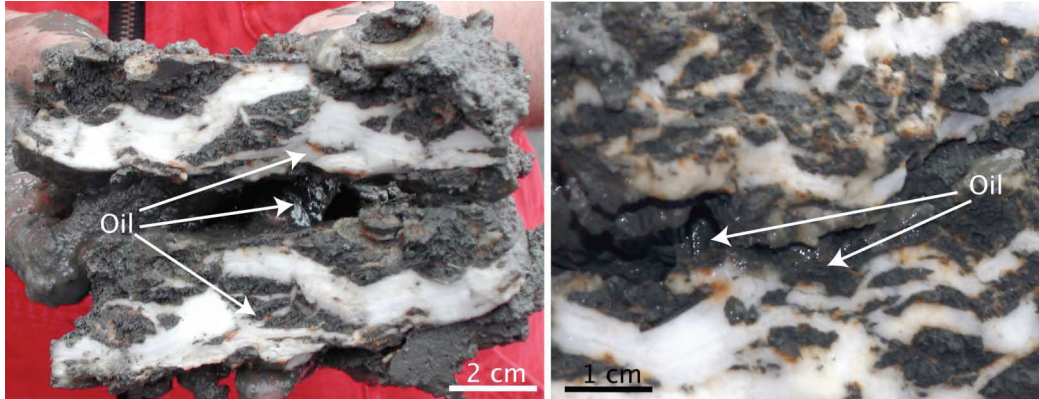


Figure 5.2: Gas hydrate specimen associated to oil-stained sediments (TVG-10 from Bush Hill).

The Chapopote asphalt volcano (in the following only Chapopote) is located in deep water (3000 mbsl) northwest of the Yucatán peninsula (Figure 5.1). The Chapopote is part of the Campeche Knolls salt diapirs, which are special due to the outflow of natural asphalt at the seafloor on top of the salt domes (MacDonald et al., 2004). The salt-tectonic-induced faults allow for fluid migration from subsurface hydrocarbon reservoirs (Ding et al., 2008) and seafloor seepage. Sufficient gas supply at the Chapopote seep sites evokes the formation of shallow gas hydrates.

5.4 Methods

Gas hydrate samples were recovered either by TV-guided grab or gravity corer (see Table 5.1). The Bush Hill samples were covered only by a very thin sediment layer, the other hydrate samples were retrieved from shallow sediment depths, such that the hydrates were not directly exposed to seawater. Immediately after recovery, the samples were quenched in liquid nitrogen (LN₂) to avoid further decomposition of the hydrates. Henceforward, the hydrates were always kept in LN₂ in a continuous cooling chain when transported or prepared for measurements in the home lab.

Bulk hydrate samples from each location were split into several sub-samples. They were prepared in LN₂ in a cold room (−10 °C to −20 °C) with air conditioning providing dry air to avoid condensation of atmospheric water as ice crystals on the surface of the specimen. The sub-samples were then used for electron microscopy and XRD. For the latter, sub-samples from each location were measured both with a laboratory diffractometer at the University of Göttingen, Germany as well as at high-energy synchrotron beam lines in Hamburg, Germany.

5.4.1 X-ray diffraction

XRD analysis was used for quantitative assessment of the major phases in the samples. For the in-house measurements in Göttingen, a Bragg-Brentano focusing Philips MRD (Materials Research Diffractometer) cryo-goniometer was used, which employs a wavelength of

0.7093 Å from a molybdenum anode. The synchrotron measurements were conducted with a wavelength of ~0.12 Å at the Beam Line BW 5 as well as at the HARWI II beam line at the Hamburg Synchrotron Laboratory (HASYLAB) of the Deutsche Elektronen Synchrotron (DESY) in Hamburg, Germany. The penetration power was sufficient to study larger samples in aluminum cans of 7 or 12 mm inner diameter, which were located in a cryostat with aluminum vacuum/heat shields. The short wavelength of the high-energy synchrotron radiation allowed for bulk sediment sample investigations. All synchrotron scans were performed exclusively at distinct locations of uncrushed gas hydrate pieces, comprising crystals of ca. 200–300 μm (Klapp et al., 2007) and not on powdered samples. Accordingly, structural information was obtained for the scanned volumes containing coarse crystals and not for the whole powder sample. In contrast, the cryo-MRD machine gave averages on the complete powder sample. Details of the XRD measurements are given in Appendix IV and Klapp et al. (2007). Phase fractions of the samples are then calculated from Rietveld refinement using the GSAS software (Larson and van Dreele, 1994) and the EXPGUI user interface (Toby, 2001).

5.4.2 FE-SEM investigations

Gas hydrate pieces, which were previously characterized by XRD, were analyzed by SEM. For electron microscopic investigations, two electron microscopes were applied; one is a Cryo-Field-Emission Scanning Electron Microscope (FE-SEM) Zeiss Leo 1530 Gemini, the other one is a Cryo-Field-Emission-Environmental-Scanning Electron Microscope (FEI Quanta 200 FEG). The FE-SEMs are designed for work at low acceleration voltages of less than 2 kV, which is well suited for ice or gas hydrates in order to minimize sample alteration due to beam damage (Kuhs et al., 2004a; Stern et al., 2004). The samples were kept in a LN₂ cooled sample stage inside a vacuum chamber at temperatures of about –188 °C and a pressure of about 1×10^{-6} bar during measurements.

The uncoated specimens were pieces of gas hydrate with dimensions of about 0.5 × 0.5 × 0.5 cm. The SEMs are equipped with thin window energy dispersive X-ray analysis (EDX) detectors allowing for small-scale analysis of low-Z elements. Both SEMs facilitate EDX analyses within distinct areas of interest as drawn into the SEM screen image. In standard practice, images are taken at a working distance ranging from 6 to 10 mm by secondary electrons with voltages between 1.7 and 2.4 kV; this is because gas hydrates are easily sublimation-etched even by slightly higher voltages. To obtain good results with the EDX unit, 5.0 kV voltages were applied; the working distance was raised to about 10–12 mm, due to the construction of the EDX detector in the sample chamber. The spot size for imaging normally is set to 3.0, for EDX investigations the spot size was raised to 4.0 or 5.0.

5.4.3 Gas chemical analyses

For all hydrate pieces recovered during cruise SO 174, gas chemical analyses were performed onboard by gas chromatography using a Thermo-Electron gas chromatograph (GC) equipped with a capillary column (Alltech AT-Q; 30 m length; 0.32 mm ID) and a flame ionization detector (FID) as described in Heeschen et al. (2007). Hydrate pieces from the gravity corer station GC-6 (sub-samples 1 and 2) from cruise M67/2 were dissociated onshore and analyzed with a two-channel GC (Agilent Technologies, 6890N). C₁–C₅ hydrocarbons were

separated, detected and quantified with a capillary column (OPTIMA-5; 0.32 mm ID, 50 m length) connected to a FID. In addition, permanent gas constituents (O_2 , N_2 , CO_2) as well as methane and ethane were determined using a packed (molecular sieve) stainless steel column coupled to a Thermal Conductivity Detector. While gas analyses of specimen GC-6 #1 and sub-sample 1 of specimen #2 were done after X-ray inspections, specimen GC-6 #2 (sub-sample 2) was not investigated by XRD. In the following we understand C_1 – C_5 hydrocarbons, which might be hydrate forming, as 'light' hydrocarbons. Abundances of light hydrocarbons are given as relative portion of the sum of C_1 – C_5 hydrocarbons in mol%.

The results of the gas chemical analyses together with salinity data and water temperature were used to calculate the stability boundaries of gas hydrates at the Bush Hill area (block GC185) and at the Chapopote. The salinity and temperature data were recorded on a CTD device by the Remotely Operated Vehicle *QUEST 4000 M* of the MARUM, Bremen, during dive no. 81 on the Chapopote on Meteor cruise M67/2 (Bohrmann and Spiess, 2008). The phase boundaries were calculated using the software HWHYD of the Heriot-Watt University, Edinburgh, UK (HWHYD, 2005).

5.5 Results

5.5.1 Phase analyses

XRD measurements revealed that all samples were comprised of cubic gas hydrates, i.e. either crystallographic structure type I or II. Additionally, all samples had fractions of ice as evidenced by their distinctive Bragg peaks. Structure I gas hydrate is identified by the major peaks (321) and (320) (Figure 5.3a) and type II by the major peaks (511), (531) and (440) (Figure 5.3b). Hexagonal ice (I_h) is present in all sub-samples, as confirmed by the three major ice I_h peaks (100), (002) and (101) (Figure 5.3).

Bush Hill gas hydrates were entirely composed of sII gas hydrate (Table 5.2). The samples GC-2 as well as TVG-10 were particularly well preserved with average ice fractions of <15% and ~13%, respectively (Table 5.2). Because of the small ice fractions, these samples allowed for observations of sII gas hydrate without much interfering ice. Also, samples from Green Canyon (TVG-3 and TVG-12) gave no indication on sI gas hydrate in this area, instead all gas hydrates in those samples is sII. In turn, the samples from the Chapopote contained sI gas hydrate (Table 5.2). The gas hydrate sI fractions range in these samples between 73 and 67 wt.%, with the balance being ice (I_h).

5.5.2 Gas chemical composition of the gas hydrates

The gas chemical compositions allowed for clear distinction between samples from different sites. Gas hydrates from the Bush Hill area yielded a methane portion of about 72.0 mol% of the measured light hydrocarbons, ethane portions of 7–13.0% and a propane fraction of 12.0 to almost 16.0% (Table 5.3; Heeschen et al., 2007). In addition, these gas hydrates had a significant fraction of butane isomers with 2.0–4.5% of *iso*-butane and 0.9–1.4% of *n*-butane.

Light hydrocarbons from the Green Canyon hydrates were composed of 75.0–82.0% methane, 9.0–11.0% ethane and 6.0–10.0% propane. The samples contained about 1.2–1.9% of *iso*-butane and 1.4–2.4% of *n*-butane.

Table 5.2: Gas hydrate structures found at individual sites in the Gulf of Mexico. Structures and phase fractions were determined by quantitative phase analyses of X-ray diffraction experiments (sI, sII: structure I, structure II, respectively). Numbers are in weight percent.

Region	sample station	sI	Ice	sII
Bush Hill	GC-2	0.0	7.7	92.3
		0.0	10.8	89.2
		0.0	34.5	65.5
		0.0	4.6	95.4
	<i>avg.</i>	0.0	14.4	85.6
	<i>st.-dev.</i>		11.8	11.8
	TVG-10	0.0	24.6	75.4
		0.0	12.0	88.0
		0.0	8.6	91.4
		0.0	7.4	92.6
<i>Avg.</i>	0.0	13.2	86.8	
<i>st.-dev.</i>		6.8	6.8	
GC 415	TVG-3	0.0	62.0	38.0
		0.0	77.2	22.8
		0.0	74.7	25.3
		<i>avg.</i>	0.0	71.3
	<i>st.-dev.</i>		6.7	6.7
	TVG-12	0.0	41.7	58.3
Chapopote	TVG-6	53.1	46.9	0.0
		87.5	12.5	0.0
		<i>avg.</i>	70.3	29.7
	<i>st.-dev.</i>	17.2	17.2	
	GC-6 #1	66.9	33.1	0.0
	GC-6 #2 (sub-sample 1)	72.9	27.1	0.0
<i>Avg.</i>	69.9	29.7	0.0	
<i>st.-dev.</i>	3.0	3.0		

Gas hydrate samples from the Chapopote differed significantly in the composition of enclathrated light hydrocarbons: they contained about 98.7% of methane and 1.1% of ethane and 0.1% of propane, while butane isomers were found in much smaller amounts in the hydrates recovered in sample TVG-6. A similar gas composition was obtained for specimen #1 from GC-6. Specimen of GC-6 #2 contained two hydrate sub-samples: One sub-sample was composed similarly to both specimen #1 and the hydrates from sample TVG-6 (see Table 5.3). The second sub-sample of hydrate specimen #2 comprised ca. 94.1% methane, ca. 2.6% ethane, 2.3% propane and ca. 1.0% butane isomers (Table 5.3). XRD analysis was not done for this sub-sample of specimen #2.

5.5.3 Microstructure inspections by Scanning Electron Microscopy

Electron microscopic observations showed clear differences in the microstructure between hydrate samples comprising sII and more than 20.0% of C₂–C₅ compared to methane-dominated sI gas hydrates (Figure 5.4; see Table 5.2 and Table 5.3).

The surface of sII hydrate from Bush Hill (Figure 5.4A) displays a solid and dense tier-like array of rectangular units, which becomes distinct at about 500× magnification (Figure 5.4B). Here, dense is used to describe the nonporous microstructure of the hydrate. No mesopores

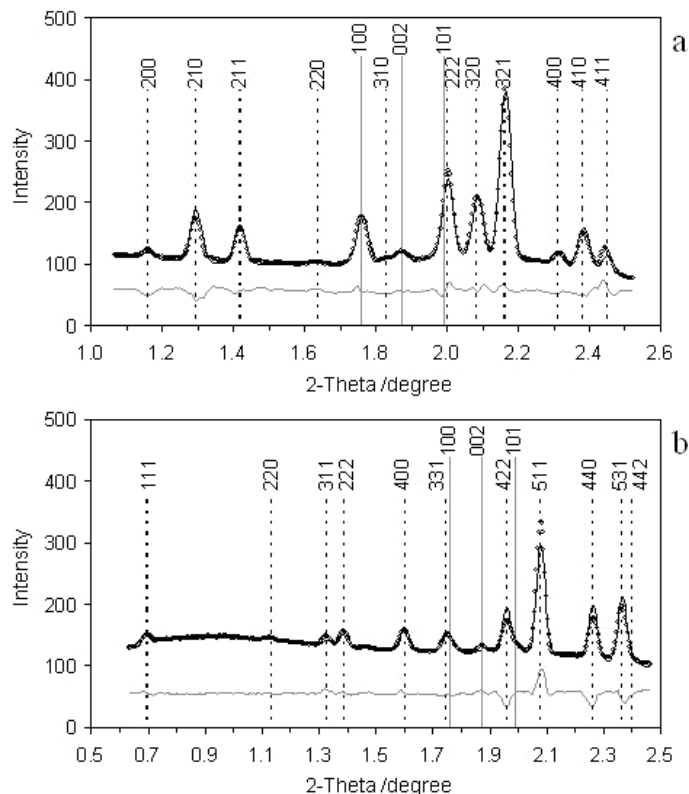


Figure 5.3: Rietveld plots of the synchrotron X-ray diffraction data of the hydrate samples (wavelength 0.1197314 Å). The solid black lines, open circles and solid grey lines represent the calculated pattern, the observed intensity data and the difference between observation and model calculation, respectively. The vertical solid and dashed lines show possible positions of Bragg reflections of hexagonal ice I_h and hydrate, respectively. Note different scaling for the x-axis. (a) The sample contains mainly sl hydrate (~88%, the remainder being ice I_h) collected from the Chapopote (SO 174; station 140, TVG-6). (b) Sample contains about 95% sII hydrate collected from the Bush Hill (SO 174; station 47, GC-2).

Table 5.3: Mol percent of C_1 – C_5 hydrocarbons measured from purposefully decomposed gas hydrate samples (in bold; below: standard-deviation). n gives back the number of measurements. C_5 -Isomers: Sum of unidentified C_5 -isomers.

Region	sample station	C_1	C_2	C_3	iC_4	nC_4	C_5 -Isomers	
Bush Hill (GC185)	GC-2	72.18	6.63	15.73	4.50	0.92	0.05	n=2
		0.24	0.64	0.69	0.17	0.03	0.02	
	TVG-10	71.69	13.09	11.85	2.01	1.35	0.02	n=7
		1.08	0.43	1.26	0.25	0.07	0.00	
GC415	TVG-3	74.61	11.10	9.95	1.88	2.43	0.03	n=2
		5.45	2.13	3.93	0.12	0.70	0.03	
	TVG-12	82.24	8.87	6.26	1.18	1.44	0.01	n=2
		0.05	0.23	0.29	0.06	0.07	0.01	
Chapopote	TVG-6	98.71	1.12	0.12	0.02	0.02	0.00	n=3
		0.07	0.13	0.05	0.01	0.01	0.00	
	GC-6 #1	98.08	1.65	0.16	0.03	0.06	0.03	n=5
		0.13	0.06	0.06	0.01	0.01	0.01	
	GC-6 #2 (sub-sample 1)	97.62	0.98	0.93	0.15	0.26	0.05	n=2
		0.05	0.65	0.42	0.07	0.10	0.01	
	GC-6 #2 (sub-sample 2)	94.10	2.61	2.25	0.32	0.64	0.07	n=3
		0.33	0.11	0.22	0.03	0.04	0.01	

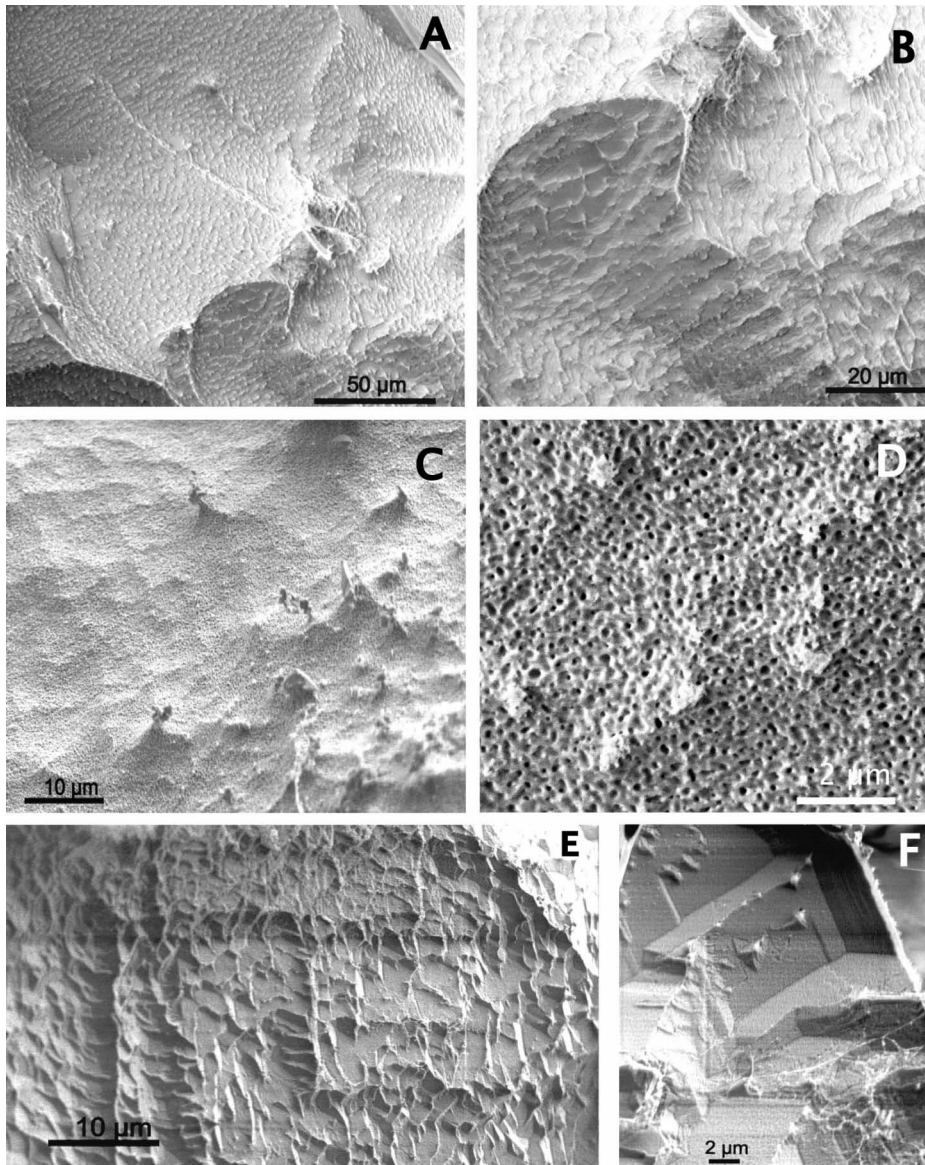


Figure 5.4: Electron microscopic pictures of gas hydrate samples (A, B, E, F: TVG-10, Bush Hill, sII hydrate. C, D: GC-6, Chapopote asphalt volcano, sI hydrate). **A.** Overview image of a Bush Hill sII gas hydrate: The surface appears dense and solid. **B.** Tier-like microstructure is clearly identifiable on a 20 μm scale. **C.** At about the same scale, mesopores are identifiable in Chapopote sI gas hydrates. **D.** Magnification of mesopores from Chapopote sI hydrates. **E.** Dense surface and tier-like shell are the typical and general microstructure of Bush Hill and Green Canyon sII gas hydrates. **F.** On very small scales, tiers in geometrical patterns become evident.

are discernable in samples which contain larger fractions of non-methane light hydrocarbon gases ($\text{C}_2\text{--C}_5$) and form sII gas hydrate. At somewhat greater magnification (ca. 1000 \times), sI hydrate from Chapopote (Figure 5.4C) shows a porous microstructure, which can be clearly discerned as 200–500 nm pores at extreme magnification (Figure 5.4D). Evidence of porosity is not visible in images of 5000 \times magnification of sII hydrate (Figure 5.4E). At very high magnifications, sII hydrate displays a tier-like array of layers (Figure 5.4F). The tier-like structure mimics a section across individual crystal planes and thereby forms tiers at the surface (Figure 5.4E, F). Geometrical patterns are visible at large magnifications (Figure 5.4F), i.e. parallel planes and distinct angles between them. In the porous hydrate samples, in contrast, geometrical patterns are not identifiable (Figure 5.4D).

EDX measurements reveal carbon signals in all gas hydrate samples. It turns out that the semi-quantitative EDX investigations show a constantly higher carbon content in the dense and tier-like structured material of the Bush Hill and Green Canyon sII hydrates than in the mesoporous sI hydrates from the Chapopote or in any other mesoporous hydrates, which were investigated in our earlier works (Kuhs et al., 2004a; Techmer et al., 2005; Appendix IV). These results were expected, as on average the sII gas hydrates presented in this study have more carbon atoms per hydrate cage than the sI hydrates. However, a fully quantitative evaluation is impossible due to the specimen's uneven surface, which deflects the electron beam.

SEM investigations also revealed that gas hydrates occur in direct contact with heavy hydrocarbons, i.e. they are soaked with petroleum. Figure 5.5A shows a SEM image of a sample with more than 85 wt.% gas hydrate content. Dense gas hydrate is visible in the right part of the image; in the left, a shimmering dark-looking material is discernable. The former liquid state of the material is suggested by its fabric, as the flowing was stopped by quenching of the sample in liquid nitrogen. The dark-looking material is characterized by a clear carbon peak as evidenced by EDX measurement. Although semi-quantitative, the EDX carbon signals of the oily dark patches in the images were much higher than those of the dense and tier-like material. Figure 5.5B shows a high magnification of the contact between a patch of higher hydrocarbon homologues and dense material. Figure 5.2 shows photographs of sediment samples on a centimeter scale, illustrating that hydrate-bearing sediments are soaked with petroleum, and discolor the hydrate in parts.

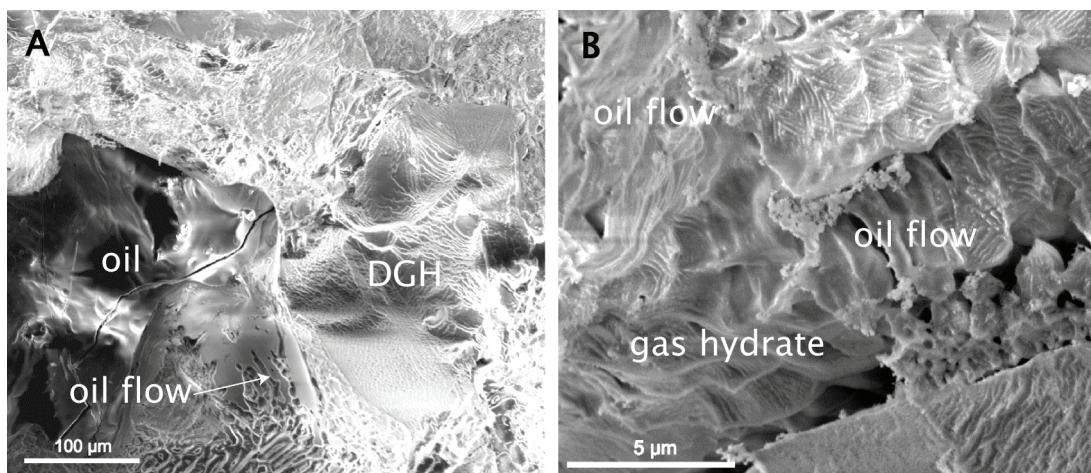


Figure 5.5: Electron microscopic pictures of gas hydrate samples. **A.** Oil patches are adjacent to dense gas hydrate (DGH). The flowing of the oil prior to deep freezing is discernable. In the image, the oil is flowing downwards, see the highly viscous flow in the central lower part of the image (sample TVG-10). **B.** Detail of the border between oil (top left) and gas hydrate (below) (sample TVG-3).

5.6 Discussion

5.6.1 Hydrocarbon composition and crystal structure

Gas chemical analyses revealed high abundances of light hydrocarbons and in particular of methane in all samples (Table 5.3; Heeschen et al., 2007). The fractions of methane, though, differ significantly between the samples from the Bush Hill (GC185) and Green Canyon (GC415) area, where roughly a fourth to a fifth of the measured hydrocarbons consist of C_2 to C_5 compounds, and Chapopote asphalt volcano hydrates, which host mostly more than

98% methane in hydrocarbons. The hydrocarbon compositions suggest gas hydrate sII formation in the Bush Hill and Green Canyon areas, because the larger molecules would not fit into the smaller cages of the structure I hydrate (Sloan and Koh, 2007). This agrees well with our results of XRD measurements and other published gas chemical data for the Bush Hill and Green Canyon. Sassen et al. (1994, 2001b), Suess et al. (2001) and Chen and Cathles (2003) reported on selective stripping of hydrocarbons from the thermogenic vent gas which crystallize to sII gas hydrate. They found hydrate-bound, light hydrocarbons in the same range of composition as reported here.

For Chapopote, both XRD investigations and compositions of light hydrocarbons reveal sI hydrate formation with almost exclusively methane as the hydrate-forming gas. The exception is one hydrate piece, which contained 94.1% methane and 5.9% C₂–C₅ of hydrate-forming hydrocarbons. This suggests that sII hydrate may sometimes occur in this area.

The dominance of strongly methane-rich sI forming hydrates was surprising because at Chapopote, seeping fluids comprise heavy oil, asphalt and light hydrocarbons (Bohrmann and Spiess, 2008; MacDonald et al., 2004), and in the sediments the C₁/C₂–C₅-ratio varied considerably with depth (Bohrmann and Schenck, 2004). This mélange of hydrocarbons would suggest that also light hydrocarbons other than methane were incorporated into the hydrates. Yet we found only one hydrate piece in which this seems to be the case. On the other hand, this piece was next to other hydrate pieces which contained more methane and crystallized to sI hydrate. This observation points to an inhomogeneous distribution of gases in the gas hydrates at Chapopote. To further explore the origin and distribution of Chapopote hydrate gases, more information on the hydrocarbon isotopic compositions and extent of biodegradation is needed. For this work, it is important to be aware of the hydrocarbon composition in the actual samples, which were investigated also by XRD and SEM.

XRD analyses confirm the interpretation of the gas analyses of the individual hydrate pieces. To the best of our knowledge, the results presented here are the first direct crystallographic structure identifications of gas hydrates from these locations in the GOM by XRD, together with a preliminary report by Rawn et al. (2008), who found sII hydrates by XRD in block GC234. In the many years of gas hydrate research in the GOM, often the hydrate structures were inferred from gas compositions. By interpreting compositions of hydrate-bound hydrocarbons, the most probable crystallographic hydrate structure could be predicted on thermodynamic grounds, but an experimental confirmation is still indicated due to remaining uncertainties, in particular close to stability limits, and possible metastable formations.

5.6.2 Hydrate stability

The onset of gas hydrate stability differs significantly at the Bush Hill area and Chapopote (Figure 5.6; calculation see Section 3.3). At the sampling site in the Bush Hill area in about 550 mbsl, sII hydrates are stable until about 310 mbsl, where the water is about 12.1 °C. At Chapopote, which is in about 2900 mbsl, hydrates would be stable up to a water depth of 620 m, where the water has a temperature of 7.4 °C (Figure 5.6), so Bush Hill sII hydrate would require an increase of about 10–11 °C above ambient and the Chapopote sI hydrates an increase of 14–15 °C above ambient to destabilize. The water temperature at Bush Hill is barely within the sI stability limit, which may explain why no sI hydrate is observed there. Moreover, MacDonald et al. (2005) show that temperature variations at Bush Hill would

regularly exceed the stability of sI hydrate. Little is known about temperature variations at Chapopote, but they are unlikely to challenge the stability of sI hydrate and even less likely to destabilize sII hydrate. Structure II gas hydrate with the given gas composition is clearly the more stable hydrate structure; the lack of sII hydrate at Chapopote is most probably a result of gas composition, not formation dynamics.

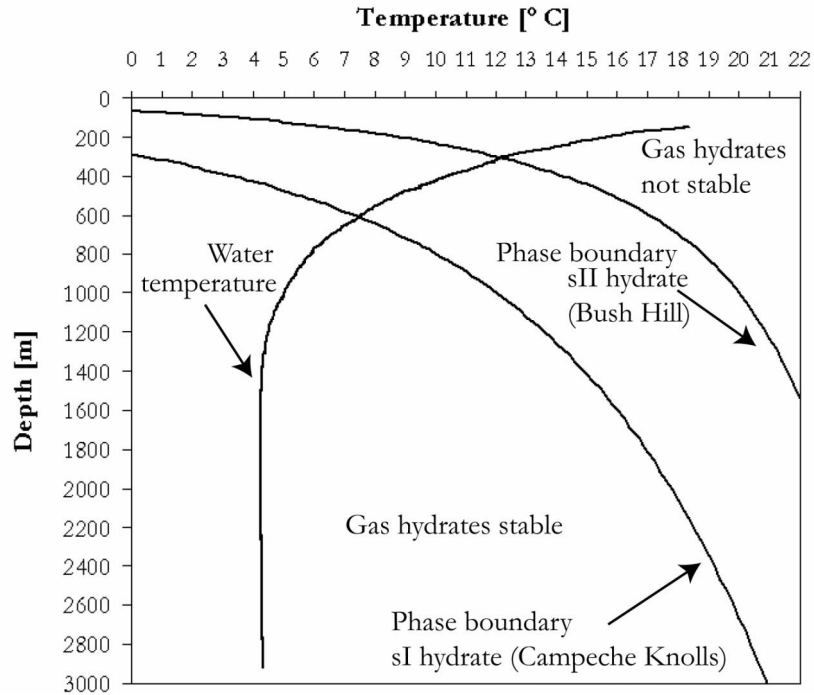


Figure 5.6: Stability models for gas hydrate occurrences in the Gulf of Mexico; Bush Hill, structure II hydrate (TVG-10); Chapopote, structure I hydrate (TVG-6). The phase boundaries were calculated using the Heriot-Watt-Hydrate software (HWHYD, 2005). The temperature was measured during ROV-diver 81 on M67/2.

5.6.3 Relation between crystal structure, microstructure, hydrocarbon composition and gas hydrate stability

It is noteworthy that the thermodynamically more stable hydrates lack mesoporosity but instead feature a dense and tier-like microstructure as evidenced by SEM. They form from a hydrocarbon mixture of about 70–80% of C_1 plus 20–30% C_2 – C_5 , and crystallize to structure II hydrate. Mesopores (200–500 nm diameter) have been considered as a typical characteristic for gas hydrate (Kuhs et al., 2000a, 2004a; Techmer et al., 2005; Appendix IV) and were identified in all Chapopote hydrates. There, only sI gas hydrates were found by XRD analyses and of those samples, the gas composition turns out to be 98% methane.

These observations point to a tight connection between significantly large fractions of light hydrocarbons (C_2 – C_5), sII hydrate formation, dense microstructure and greater gas hydrate stability. Hence it follows that the relation of microstructure and gas hydrate stability needs to be discussed.

It is likely that hydrate dissociation starts on the hydrate surface. Therefore, a larger surface area would lead to an accelerated decomposition. Given that the mesopores (200–500 nm) were not just a surface characteristic but an element of the internal structure of the mesoporous hydrates, it would be reasonable to assume a larger surface area for the mesoporous hydrates, because then the walls of the pores would add to the surface area.

Hydraulic compression and density experiments suggest that almost 20 vol.% of bulk methane hydrate samples exist as mesopores (200–500 nm) (Suess et al., 2002). However, area estimations from SEM inspections indicate that also larger pores of about 1 μm size or bubbles might have added to the calculated mesoporous volume (unpublished data), such that the true volume of mesopores might be significantly lower. Kuhs et al. (2004a) argue from specific surface area experiments that the mesopores of both laboratory-grown and submarine gas hydrates are predominantly closed. Thus, they may be a feature related to the grain boundary network of gas hydrates, as was suggested by recent synchrotron microtomographic work (Chapter 6). Hence it seems unlikely that the mesopores could contribute significantly to an accelerated bulk decomposition of the hydrates.

Most importantly, the stability of gas hydrates is primarily governed by the cage filling of adequate gases (Sloan and Koh, 2007) and consequently by the crystallographic structure type depending on the available gases at a geological site. The data presented here show that hydrocarbon mixtures comprising comparatively less volatile hydrocarbons like propane and butane prefer a structure II gas hydrate and form dense microstructures. Lower pressure or lower subcooling is needed to shift a gas assortment consisting of a larger fraction of less volatile hydrocarbons into the hydrate stability. This suggests that the volatility of the hydrate formers could be an important factor accounting for the observed hydrate microstructure. This suggestion is underlined by the fact that volatile non-hydrocarbon gases like N_2 , O_2 or Ar also form sII hydrate but feature a mesoporous microstructure (Kuhs et al., 2000a).

5.6.4 Mesoporous microstructure

The mesoporosity seems to be a function of the gas chemical composition in that only highly volatile gases feature that microstructure. But also, dense surfaces have been produced for methane-dominated, sI gas hydrate: Stern et al. (2003; 2004; 2005) and Klapproth et al. (2007) undertook gas hydrate formation experiments above the ice point and produced dense surfaces. Kuhs et al. (2000a) showed both dense and mesoporous hydrate surfaces for samples reacted below the ice point. The samples often show a uniform mesoporous microstructure, which sometimes is amended by dense parts. The mesoporous microstructure can in fact be used as a rapid mean of identifying gas hydrates in the scanning electron microscope as it uniquely is formed when gas hydrates are present in the sample. Indeed, estimates of the relative proportion of ice/water and gas hydrates (as identified by the mesoporosity) in the SEM compares very favorably with results from quantitative phase analysis by means of X-ray diffraction (Appendix IV).

5.6.5 Intrinsic dense microstructure

The dense microstructure was clearly observed in samples that were well preserved with little ice fractions. Accordingly, the SEM images should show the intrinsic and unaltered microstructure. For various reasons, it can be ruled out that the dense surface derives from ice of decomposed gas hydrate: Firstly, detailed microstructure studies were performed and the ice fractions of the samples TVG-10 as well as GC-2 established by diffraction are too low to account for the many SEM observations of dense material. Secondly, carbon signals as measured by SEM-mounted EDX units of dense samples cannot derive from ice, as water molecules do not contain carbon. Thirdly, decomposing gas hydrate does not form smooth

and dense surfaces but macropores of several μm in diameter, as shown in Bohrmann et al. (Appendix IV) from Hydrate Ridge samples. Such macropores are phenomena due to partial decomposition. Larger than those dissociation-derived macropores are intrinsic characteristics like gas-filled voids (Bohrmann et al., 1998), which are shown by aragonite precipitates that image the bubbles by the surface morphology (Bohrmann and Torres, 2006).

An alternative explanation for dense surface structure imaged by electron microscopy would be that they originate from mesopores filled with oil. Indeed, the co-occurrence of the dense hydrate microstructure with oil patches could support such a supposition. However, dense surfaces of sII gas hydrate were found also in specimen without any visible oil patches, indicating that the dense surface is truly intrinsic. In addition, the mesoporous microstructure is discernable in oil-stained sI gas hydrates retrieved from oil seeps in the Eastern Black Sea (unpublished data).

5.6.6 Gas hydrate and liquid hydrocarbons

SEM images show shimmering oil coatings on gas hydrate surfaces (Figure 5.5). Although the coexistence of oil and gas hydrate in the GOM is known since long (Brooks et al., 1984), the microscopic scale of the vicinity has not been explored so far. MacDonald et al. (2003) showed massive deposits of Bush Hill yellowish gas hydrates on a meter scale, which are colored by oil. Sassen et al. (2001c) report on oil-stained sediments with gas hydrates as vein-fillings from Atwater Valley (Block GC425) in the GOM. Liquid crude oil is described to occur as fluid inclusions and along fractures within the crystalline gas hydrate (Sassen et al., 2001c). Our work shows that oil diffuses through gas hydrate occurrences, as can be inferred macroscopically from Figure 5.2 and massive decolorization of gas hydrate deposits (MacDonald et al., 1994; 2003) as well as microscopically from Figure 5.5.

The presence of hydrocarbons outside the gas hydrate crystal structure is relevant for hydrate characterization. In interpreting chemical data from hydrate-associated light hydrocarbons, it normally is assumed that those gases are entrapped in the hydrate cages, i.e. as crystal-bound guest molecules (Sassen et al., 1994, 2001b; Chen and Cathles, 2003; MacDonald et al., 2004, 2005). These data are commonly used to deduce the crystal structure and the thermodynamic stability and, on those grounds, to estimate the abundances of hydrates in a region (Sassen et al., 2001d). Our SEM images show that oil sticks to the hydrate surface. As it turns out that heavy hydrocarbons occur along with the hydrates, the question arises whether light hydrocarbons also accompany petroleum and hydrates, for instance by being sequestered in long-chained hydrocarbons, without being included in the structure. One possibility would be that volatile hydrocarbon molecules stick to the hydrate surface by adsorption (e.g., Larsen et al., 1998). Liquid hydrocarbons are visible by FE-SEM, but gaseous hydrocarbons cannot be detected. The cage filling of the hydrate structures by distinct gas species can be best obtained from Raman spectroscopy (e.g., Hester et al., 2007b; Chazallon et al., 2007; Bourry et al., 2009). Also, gas exchange reactions in the cages can be traced by Raman measurements (Murshed and Kuhs, 2007).

5.6 Conclusions

The electron microscopically depicted microstructure of gas hydrates from the Green Canyon (GC415) and Bush Hill (GC185) features smooth and dense surfaces. Mesopores

are not discernable in these samples. These hydrates form sII gas hydrate, proved by XRD, and comprise 70–80% methane and 20–30% C₂–C₄ hydrocarbons.

There is clear evidence that hydrocarbons with relatively low volatility tend to form dense gas hydrate microstructures, while methane and light non-hydrocarbons gases often form mesoporous hydrates. This suggests that the volatility of the gases plays a significant role for the microstructural appearance and supports also the earlier finding that a mesoporous microstructure is a characteristic signature of more volatile gas hydrates, in particular of methane hydrate (Kuhs et al., 2004a). Dense microstructures are less readily assigned to a certain structure type or composition as methane hydrate sometimes also can appear in a dense microstructural form (Stern et al., 2004, 2005; Klapproth et al., 2007).

Oil patches together with dense gas hydrate occur in direct contact with each other. Insight into the formation process and the detailed chemistry at the micro-scale cannot be deduced from the present data, however.

It will not be possible to relate the porous nature of hydrates to any specific geological phenomenon until a full understanding of its formation is achieved. However, in microstructural SEM work on gas hydrates the appearance of mesopores can still be used as an indicator for gas hydrates and – as we have shown here – to some extent also for their chemical nature.

Acknowledgements

We thank the shipboard scientific parties and crews on R/V Sonne SO 174 and R/V Meteor M67/2 for their help. Likewise, we thank the HASYLAB/Hamburg for beam time and support concerning the synchrotron XRD work. We thank two anonymous reviewers and Keith Hester for helpful comments and suggestions. S.A. Klapp thanks the Vollkammer Scholarship for funding as well as GLOMAR Graduate School for Marine Sciences. This is publication GEOTECH - 920 of the R&D-Programme GEOTECHNOLOGIEN funded by the German Ministry of Education and Research (BMBF) and German Research Foundation (DFG). Funding for this research was provided by the METRO grant 03G0604A (BMBF).

CHAPTER 6

MANUSCRIPT 4

NATURAL GAS HYDRATE INVESTIGATIONS BY SYNCHROTRON RADIATION X-RAY CRYO-TOMOGRAPHIC MICROSCOPY (SRXCTM)

M. Mangir Murshed¹, Stephan A. Klapp², Frieder Enzmann¹, Thore Szeder¹, Thomas Huthwelker³, Marco Stampanoni^{3,4}, Federica Marone³, Christoph Hintermüller³, Gerhard Bohrmann², Werner F. Kuhs⁵, Michael Kersten¹

published in *Geophysical Research Letters*, Vol. 35, L23612,
doi:10.1029/2008GL035460, 2008

¹Institut für Geowissenschaften, Johannes Gutenberg-Universität Mainz, Becherweg 21,
55099 Mainz, Germany

²MARUM / DFG Research Center and Cluster of Excellence, University of Bremen, P.O.
330440, D-28334 Bremen, Germany

³Swiss Light Source, Paul Scherrer Institut, Villigen, Switzerland

⁴Institute for Biomedical Engineering, University of Zurich and ETH Zurich,
Zurich, Switzerland

⁵GZG, Abteilung Kristallographie, Universität Göttingen, Goldschmidtstr.1, 37077
Göttingen, Germany

6.1 Abstract

We report the 3D microstructure analyses of natural gas hydrates sampled from Gulf of Mexico. The samples were characterized by synchrotron radiation X-ray cryo-tomographic microscopy (SRXCTM) using the 'TOMCAT' beam line at the Swiss Light Source (SLS). The SRXCTM demonstrates its applicability to unlock some microscopic features of the marine hydrates, in particular of crystallite size and grain boundary network. The gas hydrate domains are surrounded by a network of pores of typically a few micrometers, which are largely due to decomposition. Out of the SRXCTM data, the porosity, total volume of the voids, the void surface area and number of the total gas-filled voids have been calculated. The results reveal the capability of SRXCTM to access the 3D microstructure which is of fundamental importance to model the petrophysical properties of natural gas hydrates.

6.2 Introduction

Clathrate hydrates are non-stoichiometric crystalline inclusion compounds built of a framework of hydrogen bonded water molecules that offers suitable cavities occupied by guest molecules such as methane and ethane (Sloan and Koh, 2008). Hydrates of hydrocarbons are stable in a wide range of oceanic and permafrost environments (Max et al.,

2006; Sloan and Koh, 2008). Gas hydrate deposits in sediments have been reported from more than 100 locations worldwide (Kvenvolden and Lorenson, 2001). The deposits are estimated to contain hydrocarbons (mainly methane), and thus pose a potential jeopardy to climate, as methane is a greenhouse gas. But also, the recovery even of a fraction of the estimated amount would provide a substantial energy resource. Besides, gas hydrates are of major concern to the oil and gas industries for their ability to block the pipelines (Sloan and Koh, 2008).

Natural gas hydrates have been recovered from various deep-sea sites during the Ocean Drilling Program (ODP) and the Integrated Ocean Drilling Program (IODP) campaigns (Tréhu et al., 2003), as well as from continental drillings (Dallimore and Collett, 2005) and individual ship expeditions (Bohrmann and Spiess, 2008). However, our overall knowledge of some fundamental properties of marine gas hydrates is surprisingly limited. One reason is the precarious preservation of the retrieved samples and the difficulties of characterization in situ. If recovered without pressure maintaining devices, gas hydrate will start decomposing (Heeschen et al., 2007). It is therefore important to sub-sample gas hydrate pieces from the inner core of a larger hydrate lump, which seems to be pristine and unaffected from decomposition. A good sample preservation is essential to study the concentration, texture, and geometry of voids (probably filled with gases) or to explore the crystallite size, the size distribution and grain boundary topology as well as the distribution and nature of embedded or surrounding minerals. An inspection of the pore structure by image analysis may provide a substantial appreciation of the role of porosity on the macroscopic properties of gas hydrates relevant to geophysical and engineering concerns. Despite the importance of these issues for a complete petrophysical investigation, means of characterization are limited in particular for the three-dimensional visualization of the microstructure. Many insights were achieved by cryo Scanning Electron Microscopy (cryo-SEM) (Staykova et al., 2003; Kuhs et al., 2004a; Stern et al., 2004; Appendix IV), which allowed a detailed 2D inspection down to a few micrometers. However, the possibilities of SEMs are limited in identifying the size and shape of crystallites (Klapp et al., 2007), in particular when gas hydrates are seen in their sub- μm porous form (Kuhs et al., 2000a). Moreover, the 2D imaging techniques cannot constrain higher-order geometrical attributes such as the connectivity of pore-networks (Higgins, 2000). X-ray computerized tomography (X-ray CT) overcomes the problem providing full volumetric (3D) information. The X-ray attenuation contrast enables even to distinguish crystallites and establish their spatial distribution in the samples as shown below.

X-ray CT is a non-destructive and non-invasive tool providing good spatial and time resolution to visualize hydrate formation and decomposition (Mikami et al., 2000; Gupta et al., 2006; Kneafsey et al., 2007). The number of studies on gas hydrates by X-ray CT is, however, small using tube-type X-ray sources with limited resolution (e.g., 350 μm (Mikami et al., 2000) and 2000 μm (Uchida et al., 2000) pixel size). In contrast, synchrotron based X-ray tomographic microscopy at TOMCAT offers pixel sizes down to a few hundred nanometers (e.g., 370 nm–6 μm) along with cryo-facilities. In this paper we show that synchrotron radiation X-ray cryo-tomographic microscopy (SRXCTM) is a well-suited tool to analyze natural gas hydrate samples collected from shallow-buried sediments of the Gulf of Mexico with a significantly improved resolution over conventional X-ray CT. To the best of our knowledge, this is the first tomographic report of marine gas hydrates analyzed using a synchrotron microtomography beamline; the pixel size was set here to 1.4 μm . The obtained SRXCTM images demonstrate the feasibility of the method for a variety of missing information such as

internal surface area, the individual volume of each inclusion and the morphology of the voids of natural gases in a specified volume. Likewise, it can give access to the crystallite shapes, crystallite size distribution and grain boundary network topology, quantities which are of prime importance for understanding any coarsening processes taking place in gas hydrates as a function of time.

6.3 Sampling and Methods

6.3.1 Hydrate Retrieval and Preservation

The sample investigated in this study was retrieved during the R/V Meteor cruise M67 at the Chapopote Asphalt volcano (Bohrmann and Spiess, 2008) in the Gulf of Mexico by conventional gravity coring. The gas hydrates were found in the upper first meter of Core GeoB 10618. Gas composition analysis of the hydrate revealed methane by far as the dominant gas suggesting structure I type hydrate (sl), which was confirmed by X-ray powder diffraction (unpublished data). The gravity core was recovered at latitude 21°53.95'N and longitude 93°26.21'E in 2903 m water depth, where the water temperature was 4.4°C. Preservation pressure was not maintained during the ascent of the corer; therefore the gas hydrate partially decomposed. As a consequence, the samples contain ice from the decomposition of gas hydrate as well as frozen interstitial water. To avoid further decomposition the samples were stored in liquid nitrogen (LN2) soon after the recovery and, all subsequent transfers and investigations were performed at temperatures of hydrate stability conditions. Under LN2 condition, a lump (~1 cm³) of the samples was crushed into sub-samples (~mm), and two pieces of the sub-samples (~2 mm) were put into the sample holder.

6.3.2 Experimental Setup

A detailed description of the polyamide-cup sample holder and the setup of SRXCTM compatible to the beamline station is available elsewhere (Miedaner, 2007). In short, cold nitrogen gas was flowed around a sample chamber made of plexiglass. A PT-100 resistor element (2 × 2.3 × 0.9 mm, Greisinger Electronics) was placed just below the sample chamber to record the actual temperature. For cooling, a flow of cold nitrogen gas (153 K) was directed from the standard nozzle of a CryojetXL (Oxford Instruments) onto the top of the sample holder. An additional flow (2 L/min) of dry shielding nitrogen protected the cryo-jet from icing due to water condensation inside the nozzle and the sample from ice formation. The position of the cryojet was readjusted to the rotational axis of the sample holder until no temperature fluctuation was detectable during a 180° rotation.

6.3.3 Data Acquisition and Processing

SRXCTM data have been acquired at the TOMCAT beam line of the SLS (Stampanoni et al., 2006). The monochromatic X-ray beam ($\Delta E/E = 2.5\%$ at 10 keV, [Ru/C]100 multilayer monochromator) was tailored by a slit system to a profile of 1.4 mm² to confine irradiation to the region of interest (ROI). The beam energy (8–11 keV) was optimized to enhance the contrast among hydrate, ice, and the surrounding matrix. After penetration of the sample, X-rays were converted into visible light by a thin Ce-doped YAG scintillator screen (Crismatec Saint Gobain, Nemours, France). Projection images were further magnified by microscope

optics and digitized by a high-resolution CCD-camera (PCO2000, PCO GmbH, Germany). The optical magnification was set to 10 \times , and 2 \times “on-chip binning” was selected to improve the signal-to-noise ratio, resulting in isotropic voxels of 1.4 μm in the reconstructed images. For our tomogram, 1001 projections were acquired at an integration time ranging from 180 to 642 ms for each projection. The reconstruction of the ROI was performed on a highly optimized FFT transformations and gridding procedures in a few minutes.

Post processing of the reconstructed raw data was carried out with the mathematical software MATLAB $\text{\textcircled{R}}$. 3D segmentation was based on K-means clustering (Spath, 1985), whereby clusters were merged according to corresponding features (e.g., gas-filled voids, gas hydrates, frozen water, salt inclusions and mineral grains). The spatial position of clusters influenced the process of feature formation (spatial neighbourhood relationships). Based on these results, parameters like porosity, surfaces, and volumes were calculated for the whole dataset and single objects.

6.4 Results and Discussion

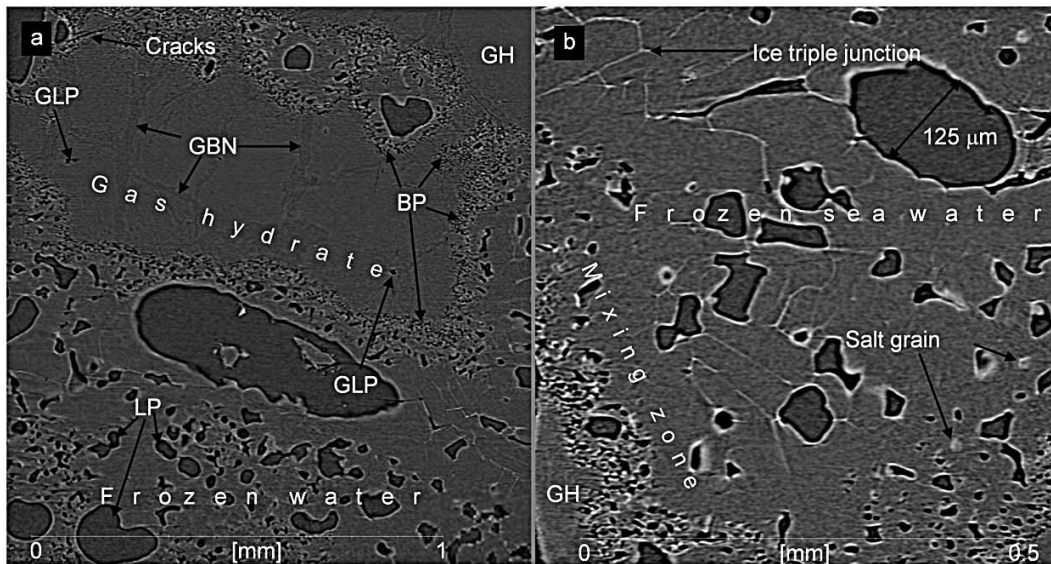


Figure 6.1: 2D slices of the computerized tomography images ($1024 \times 1024 \times 1024$ voxels with 1.4 μm length) of gas hydrate samples obtained from the Gulf of Mexico. (a) The image displays the characteristic feature of gas hydrate (GH) surrounded by micrometer-sized boundary pore (BP) that clearly discriminate GH from frozen water. The large pores (LP) are prevalent within the frozen water; while some pores ($\sim\mu\text{m}$) also occur within the gas hydrates shown as GLP. Grain boundary network (GBN) of gas hydrate crystallites is also seen in 2D slices. (b) Salt inclusions as frozen brines at the grain boundaries of ice and as discrete small salt grains. The mixing zone represents the frozen ice originating from seawater and decomposition of gas hydrates.

The SRXCTM 3D images of the gas hydrate sub-samples from Chapopote asphalt volcano are shown in Figures 6.1 and 6.2. The investigated specimen was sub-sampled manually under LN₂ to remove sediment as much as possible. The images therefore do not display any sediment particles. In some cases, cracks are seen (Figure 6.1a), which could be formed either ex situ due to fragility during contraction in LN₂ (Abegg et al., 2007), or in situ due to hydraulic fractures. Gravity coring preserves the sediment texture, and we assume the former cause for this type of cracks.

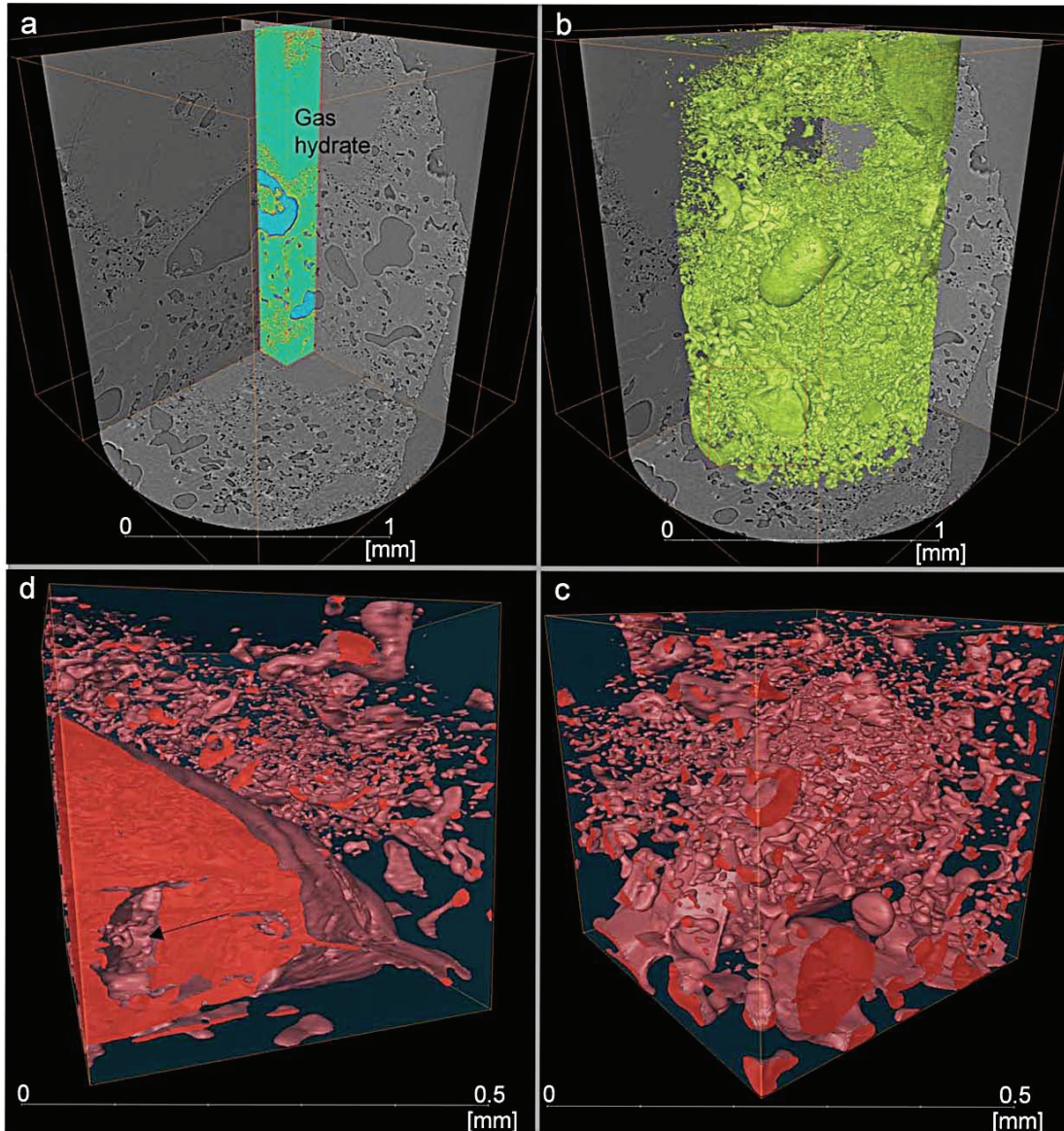


Figure 6.2: 3D computerized tomography images of the gas hydrate samples recovered from the Gulf of Mexico. **(a)** The porous feature is shown simultaneously by a coloured tetragonal volume texture (vortex) in 3D and grey-scale snapshots in 2D. Definite color discrimination is clear between gas hydrates and pore networks. The yellowish-red boundaries appear due to edge enhancement effects. **(b)** The pore network is displayed within a cylindrical cropped portion of Figure 6.2a. **(c)** Enlarged 3D view of the marked cubic portion (orange) of Figure 6.2b depicting nodular morphology of the pores and their interconnectivities. **(d)** A different directional (xyz) view of Figure 6.2c showing the intestinal channel networks (arrow).

Spatial distribution of salt inclusions is helpful to distinguish the type of ice originating from either quenched or interstitial seawater, or the decomposition of gas hydrates, because hydrate is composed of pure water and contains no salt. Regions of frozen brines are identified by SRXCTM, pointing to juxtaposition of the gas hydrate sample with seawater. To what extent ice derives from quenched seawater or dissociating gas hydrate cannot be answered satisfactorily. Triple junctions marked by frozen brine suggest frozen seawater, whereas macro-porous ice (Appendix IV) bordering the hydrate regions probably mixed with hydrate water, characterized by their boundary pores (BP in Figure 6.1), is likely to originate from decomposing gas hydrate. Occasionally, diffuse appearances of salt occur within the macro-

porous ice, suggesting mixing of the hydrate and seawater prior to quenching in LN₂. In our sample, the salt inclusions are minute, however, with a concentration high enough to make a significant absorption contrast. They are found at grain boundaries of ice and are frequently cladding the large pores (LP in Figure 6.1) within this ice, formed from the quenched seawater.

The gas hydrate domains are surrounded by porous matrix. By analogy with SEM images (Kuhs et al., 2004a; Appendix IV) we can identify areas surrounded by a micrometer-sized porous network as gas hydrate regions. These SEM investigations have established that gas hydrates show a typical feature of sub- μm -sized porosity (Kuhs et al., 2000a). The broad bands with lower density segmenting the gas hydrate regions can be assigned to these sub- μm porous regions. The size of the segments is in the same order of magnitude as the crystallite size of marine gas hydrates (Klapp et al., 2007); thus we ascribe these segments to individual crystallites. The sub- μm pores cannot be resolved within our spatial resolution limit at present. However, for the first time the spatial distribution of the sub- μm porous regions has been identified suggesting that they occur mainly along the grain-boundary network.

The sub- μm porous patches, which we ascribe to gas hydrate regions, are limited by a distinctive zone between the gas hydrate and the frozen ice phase (Figure 6.1). Within this boundary zone, pores are larger than the sub- μm -sized gas hydrate pores but are smaller than the fewer larger pores within the ice phase; their average diameter is about 2–4 μm . These boundary pores (BP) are uniformly distributed around the zones of gas hydrate. The interface between the boundary wall and the hydrates most probably marks the active decomposition front (Figure 6.1) just immediately before the sample was quenched in LN₂ (Appendix IV).

Large pores (LP) of tens to hundreds micrometer in size are quite frequent within the frozen water (Figures 6.1a and 6.1b). These pores were known from earlier SEM assessments (Appendix IV); here we see that in the third dimension these pores are of arbitrary shape and distribution. They probably arise from gas bubbles discharged from the partial decomposition of the sample while retrieving from the sea floor. The LP, being present in the ice phase only, most likely represent gas bubbles in former water derived from decomposed gas hydrate. Accordingly, regions with a concentric sequence of BP and LP provide good evidence for the previous presence of gas hydrates in this area for recovered samples. It should be noted that, in agreement with earlier work (Heeschen et al., 2007), individual pores ($\sim\mu\text{m}$) can also be occasionally found within the gas hydrate (Figure 6.1a).

Irrespective of size and location, most of the pores are interconnected forming nodular channel networks (Figures 6.2b and 6.2c). The channels have no defined shape and preferred orientation as visualized from the 3D imagery. Figure 6.2d depicts a large cavity, which is crossed by small channels (see arrow). The nature of this phenomenon is unclear, but it demonstrates that the channel networks must be mantled by slightly denser material like ice or brines.

The porous feature of the sample is characterized by some computations within the cylindrical volume ($2.3 \times 10^9 \mu\text{m}^3$) analyzed. The calculated porosity (gas-filled voids to ice/GH/substance volume) is 29%, total volume of the voids $6.7 \times 10^8 \mu\text{m}^3$, and the void surface area (= inner surface area) $1.15 \times 10^8 \mu\text{m}^2$. The number of the total calculated gas-filled voids is 51,074 (minimum size >10 connected voxels) of which the biggest interconnected void (internal channel volume assuming that all the voids are completely gas-filled/free) covers 26% of the total volume, i.e., $\sim 89\%$ of the total void volume is intercon-

nected. The smaller voids (<10 connected voxels) may also be interconnected; however, a calculation was not performed due to statistical noise of the raw data and edge enhancement effects. It is important to note that the voids and the pores do not mirror the truly intrinsic volume, as the sample partially decomposed.

6.5 Conclusion

The SRXCTM 3D images of the as-preserved specimen demonstrate the spatial relation among gas hydrates, frozen water, pores and their connectivity, and salt or frozen brine inclusions. The pore properties have been characterized along with some surface features. Pore studies of a fully-preserved sample, representative of the marine settings, by the SRXCTM will provide helpful information to understand the unusual seismic signals in porous rocks containing gas hydrates (Gerner et al., 2007) and may eventually lead to better estimation of the gas hydrates (e.g., Ecker et al., 2000). Likewise, the 3D gas hydrate crystallite arrangements will give valuable insights into possible coarsening or ripening process; understanding these processes may help provide an estimation of the formation age of gas hydrates (Klapp et al., 2007). Further work on time-resolved tomography (4D-tomography) might lead to a better understanding of decomposition scenarios under marine and permafrost conditions, also including the effect of self-preservation (Stern et al., 2003; Kuhs et al., 2004b).

Acknowledgments

The authors gratefully acknowledge the technical support provided by G. Mikuljan at PSI-SLS. Thanks are due to S. McDonald for his helpful discussions and practical support during the experiments. The help of the crew and captain of the R/V Meteor during cruise M67 is gratefully appreciated. We sincerely acknowledge DFG via the SFB-641 (TROPEIS) for partial financial support of this research. SAK thanks the Vollkammer scholarship for support and the Glomar Graduate School for Marine Science. This is publication GEOTECH-338 of the R&D Programme GEOTECHNOLOGIEN (METRO, grant 03G0604A (BMBF)).

CHAPTER 7

MANUSCRIPT 5

MIXED GAS HYDRATE STRUCTURES ON THE CHAPOPOTE ASPHALT VOLCANO, SOUTHERN GULF OF MEXICO

Manuscript in preparation

Stephan A. Klapp^{1,*}, Mangir M. Murshed², Thomas Pape¹, Helmut Klein²,
Gerhard Bohrmann¹, Werner F. Kuhs², Peter G. Brewer³

¹ MARUM – Center for Marine Environmental Sciences and Department of Geoscience,
University of Bremen, P.O. 330440, D-28334 Bremen, Germany

² Abteilung Kristallographie, Geowissenschaftliches Zentrum der Universität
Göttingen, Goldschmidtstrasse 1, D-37077 Göttingen, Germany

³ Monterey Bay Aquarium Research Institute, 7700 Sandholdt Road, Moss Landing,
CA 95039-9644, USA.

Keywords: gas hydrates; coexistence; structure I, structure II; Gulf of Mexico; Chapopote asphalt volcano; crystallite sizes; Laser-Raman; X-ray diffraction

7.1 Abstract

In underwater hydrocarbon seepage environments, gas hydrates are considered to play a significant role as shallow gas reservoirs and buffers for light hydrocarbon expulsion. Here we report on mixed hydrate structures from the Chapopote asphalt volcano in the southern Gulf of Mexico and discuss several options on how a mixture of sI and sII may arrive in nature. Gas hydrates were found within the matrix and pores of the asphalts extruded at the seafloor. Two of three hydrate pieces comprised only sI gas hydrate, formed mostly from methane. One piece comprised an intimate mixture of both structure I (sI) and structure II (sII) gas hydrate, with sII representing ca. 25 wt.% and sI ca. 75 wt.% of the present hydrate phase. The two structures were closely associated within individual grain agglomerates. The crystallites of sII were significantly larger than of sI, suggesting differences in the nucleation density or different ages of the crystallites. The coexistence of the two structures may be a result of one or of a combination of several independent processes: i) de-mixing into two hydrate structures from the gas phase, which provides an additional degree of freedom for lowering the free energy in the system; ii) from fractionated crystallization with a changing gas composition during crystallization; iii) simultaneous crystallization of separated gas bubbles with different compositions and water. It is possible that after the hydrate nucleated a transformation occurred from sII to sI, ceasing when a thermodynamically stable state was reached. The presented work may affect future assessments of natural hydrate deposits at thermogenic gas systems, as it shows that different crystallographic structures are encountered in closed systems on short length scales.

7.2 Introduction

Light hydrocarbons are frequent in marine sediments, where they originate from microbial or thermocatalytic decomposition of organic matter. Marine gas hydrates are an important pool in hydrocarbon seepage systems (Judd and Hovland, 2007), as they form from light hydrocarbons and therefore are a factor in the selective removal and fractionation of hydrocarbons from a reservoir (Chen and Cathles III, 2003). Pressure and temperature conditions required to form gas hydrates are met in permafrost sediments or in marine sediments in several hundred meters water depth. Hydrate-forming gases must at least locally and temporarily exceed solubility for hydrates to nucleate. Typically, gas hydrates crystallize either to the crystallographic structure type I or II (sI, sII, respectively), depending on the proportions of the present hydrate formers. sI hydrate has a cubic crystal structure and comprises 2 small cages, whereof each cage is formed from 12 pentagon planes (5^{12}), and 6 large cages, $5^{12}6^2$. sII consists of 16 small cages (SC) and eight large cages (LC). Unlike sI, the LC in sII are larger, having 4 instead of 2 hexagon planes in addition to the 12 pentagons ($5^{12}6^4$) and therefore can incorporate larger gas molecules.

Until recently, it seemed that a co-occurrence of different gas hydrate structures were unlikely to encounter in nature. It was assumed that the composition of different hydrate forming gas molecules in a given feeding gas would result in one hydrate structure and because it was unknown that a reordering of the crystal structure could occur in the case of gas hydrates. However, in hydrates from Lake Baikal sI and sII were found, occurring within the same stratigraphic horizon, implying that they formed simultaneously (Kida et al., 2006). A third hydrate structure (sH), previously only known from laboratory experiments (Ripmeester et al., 1987), was intimately associated to sII hydrate at a hydrocarbon seep at the Barkley Canyon site in the northeast Pacific (Lu et al., 2007). Lu and coworkers draw the conclusion that due to the actual hydrocarbon composition, the molecules would neither fit only into the sH clathrate cages nor only into the sII cages, therefore the hydrocarbon composition resulted in a coexistence of sH and sII. A miscibility gap, i.e. simultaneous crystallization from the gas phase into two structures which remained stable, was also observed in a laboratory experiment (Murshed & Kuhs, 2009).

Here we report on intimately associated sI/sII hydrate structures from the Chapopote asphalt volcano (short: Chapopote). A previous description of the gas hydrates from the Chapopote reported sI hydrate but indicated that the gas chemical composition of the bulk samples strongly suggests that minor fractions of sII should be present as well (Chapter 5; MacDonald et al., 2004). The interpretation of the data is partly hypothetical, which is due to the fact that many controls accounting for closely associated hydrate structures are unknown, particularly in unusual geological systems like on the Chapopote asphalt volcano. Therefore, the present study is an approach to critically assess several options of how composite hydrate structures may coexist in complex environments.

7.3. The Chapopote asphalt volcano

The Chapopote is located in the Campeche Knolls area in the Southern Gulf of Mexico. It is an elevation of about 400 m in almost 3000 m below sea level (mbsl), formed by salt diapirism (Bohrmann and Schenck, 2004; Ding et al., 2008; MacDonald et al., 2004). Salt tectonics opened pathways for hydrocarbons from deep-seated reservoirs, which results in

expulsion of viscous hydrocarbons like asphalts and heavy petroleum as well as light hydrocarbons, forming gas hydrates in shallow sediments. The asphalts are viscous, ductile and gas-laden (Brüning et al., submitted). Copious gas-filled cavities up to the size of several centimeters are embedded into the asphalt matrix, evoking gas hydrates nested in the asphalt medium (Bohrmann & Spiess, 2008). The hydrocarbon-laden sediments show evidence for anaerobic oxidation of methane in the upper 6 mbsf (AOM; Naehr et al., 2009; Orphan et al., 2001), where methane is microbially consumed (Boetius et al., 2000; Bohrmann & Spiess, 2008) and therefore locally depleted in the residual gas. The asphalt samples are highly diverse in their gaseous hydrocarbon content. Individual sections of asphalts containing gas bubbles showed a heterogeneous distribution of C₁ to C₅ hydrocarbons (Bohrmann & Spiess, 2008). In addition to AOM, the heterogeneity in hydrocarbon composition is supposed to be related to biodegradation of long-chained hydrocarbons (F. Schubotz, pers. comm. Dec. 2007).

7.4 Materials and methods

7.4.1 Sample origin and preservation

The gas hydrate samples presented in this study were recovered from at 21°53.95 N / 93°26.21 W at the Chapopote. They were part of one gravity core (GeoB10618), which was retrieved from the upper first meter of asphalt-covered sediment in ca. 2904 mbsl. The temperature at the sea floor was 4.4 °C. Images of asphalt and gas hydrate from the gravity core are shown in Figure 7.1, the gas hydrate was embedded in the asphalt matrix. The maximum vertical distance of the two samples was 40 cm. During recovery the gravity corer with the hydrates left the zone of gas hydrate stability between about 620 mbsl (sI) and ca. 380 mbsl (sII). Immediately upon recovery onboard the hydrate specimens were quenched in liquid nitrogen (LN₂; -196 °C). The hydrates could have started decomposition during the ascent; thus shore-based analyses were done only on central parts of the gravity core where decomposition set in late. Two gas hydrate samples – named CT2 and CT6 – were analyzed for mineralogical characterizations.



Figure 7.1: Gas hydrate and asphalt bearing gravity core GeoB 10618. Gas hydrates were found within the asphalt and inside pores embedded in the asphalt.

7.4.2 Laser Raman analyses of gas hydrates

For Raman spectroscopy, a Horiba Jobin Yvon HR800 UV Micro-Raman spectrometer was used. The system was equipped with an air-cooled Ar-laser working at 488 nm with a laser power of less than 20 mW and a long distance objective with 50x magnification. The spectral positions were corrected employing the Si-peak, which was measured against the Rayleigh line. A detailed description of the laser Raman spectrometer and the measuring conditions can be found in Murshed and Kuhs (2009). The spectrometer is furnished with a cooling stage where the hydrate samples are investigated at LN₂ temperature and atmospheric pressure. These conditions allow for investigations over several hours on the same specimen. The sample stage can be moved in lateral (X, Y) and horizontal directions (Z) allowing for a spatial resolution. The focus spot has a diameter of about 1.1 μm and a depth resolution of about 15 μm. The spectra were baseline corrected and fitted with the *dmfit* software (Massiot et al., 2002).

7.4.3 X-ray diffraction

Diffraction techniques were used both for quantitative phase analyses as well as for crystal size measurements (Bragg tomography). X-ray diffraction measurements were conducted at the high-energy synchrotron beam line BW5 at the 'Hamburger Synchrotronstrahlungslabor' (HASYLAB) at the 'Deutsches Elektronen-Synchrotron' (DESY) in Hamburg, Germany. The beam energy was about 100 kV and the wavelength about 0.12 Å. The Bragg reflections were recorded on a *mar345* 2D detector serving both for phase analyses and grain size measurements.

8.4.3.1 Phase analysis

To define the quantitative fractions of gas hydrate structures as well as ice in the samples the 2D diffraction pattern were integrated (Hammersley et al., 1996) and processed using the Rietveld refinement method (Larson and van Dreele, 2004) within the GSAS software environment (Toby, 2001). More details on the data analyses are given in Murshed and Kuhs (2009) and Appendix IV. The phase fractions are given in wt%.

8.4.3.2 Crystallite size analyses

Crystallite sizes were obtained by applying the Moving Area Detector Method (Bunge et al., 2002; Klein et al., 2004) on gas hydrates (Chapter 3). In total, four measurements of three subsamples of the gas hydrates were done for crystallite size inspections. One analysis was performed on a subsample from CT6 and three measurements were done on two subsamples from CT2. Thereof, two crystallite size scans were done on one and the same subsample of CT2 which contained the two hydrate structures sI and sII. The same volume of the specimen was scanned twice, once scanning only sI and once scanning only sII hydrate. The third measurement of CT2 and the only measurements of CT6 were done in sections that contained entirely sI hydrate. For the crystallite size scans of sI hydrate the Bragg reflection (321) was used because it gives a very strong signal. For sII the reflection (400)

was used because no other planes (either of sl or sll) have the same diffraction angle and therefore the signals on the detector are well separated.

8.4.4 Gas chemistry

The gas of the dissolved hydrates was collected in headspace vials and analyzed with a two-channel gas chromatograph (Agilent Technologies, 6890N). C₁ to C₅ hydrocarbons were analyzed with a capillary column (OPTIMA-5; 0.32 mm ID, 50 m length) connected to a flame ionisation detector. In addition, permanent gas constituents (O₂, N₂, CO₂) as well as methane and ethane were determined using a molecular sieve stainless steel column coupled to a thermal conductivity detector. For the scope of the present work we understand C₁ to C₅ hydrocarbons as light hydrocarbons. Abundances of these compounds are given as relative portion of the sum of C₁ to C₅ hydrocarbons in mol%.

7.5. Results

7.5.1 Crystallographic hydrate phases

The crystallographic phase analyses show that one piece of CT2 comprised both sl and sll (Figure 7.2), whereas in a second piece of CT2 and in sample CT6 only sl and no sll were found. Beside the hydrate structures, fractions of ice were identified in all samples, as evidenced from the typical ice peaks (100), (002) and (101). The presence of sl hydrate was indicated by the characteristic peaks (321), (320) and (210). The presence of sll hydrate was shown by the strong (531) and (440) signal. However, sll hydrate was not the dominant hydrate phase in the sample CT2 and the strong (531) peak lies close to (410) reflection of sl hydrate. sll could be clearly identified by the (400) and (111) reflections, which are not overlain by any other phases which could have been present in the sample.

The fraction of sl in CT2 is 62 wt.%, that of sll 19 % and the balance is comprised of ice (Table 7.1). The sample CT6 and the second piece of CT2 comprised only sl gas hydrate and ice.

Table 7.1: Synchrotron X-ray diffraction results (in wt.%)

Sample		GH sl	GH sll	Ice h
Phases				
CT2	mixed structure subsample	61.8	19.2	19.0
	pure sl subsample ^a	72.9	0.0	27.1
CT6	pure sl subsample ^a	66.9	0.0	33.1
Crystallite sizes [µm]				
CT2	mixed structure subsample	172	381	
	pure sl subsample ^b	±57	±45	
CT6	pure sl subsample ^b	227		
		±50		
		187		
		±55		

a: results from Chapter 5; b: results from Chapter 4

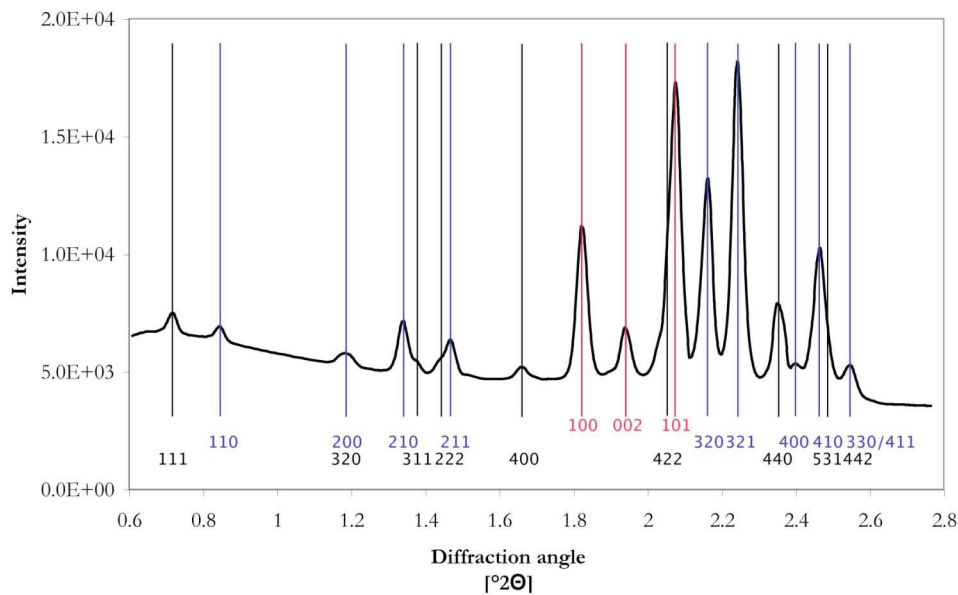


Figure 7.2: XRD pattern of the mixed structure sample GeoB 10618, CT2. The peak positions of the diffraction angles from the two gas hydrate structures and ice I_h are indicated (red: Ice I_h ; blue: gas hydrate structure I; black: gas hydrate structure II). For grain size analyses, the peaks (321) (sI) and (400) (sII) were used.

7.5.2 Raman spectra

Raman measurements were done on several small grains of the sample CT6 and at multiple positions on two grains from the sample CT2, where the two structures sI and sII were identified by XRD. The Raman spectra show that methane is the dominant hydrate former, amended by ethane, propane and butane isomers.

The Raman results show that in the sample CT2 two hydrate structures co-occur within the same crystal agglomerates. In the grains from CT6 a single structure, either sI or sII, was found in each grain. Figures 3 and 4 show microscopic images of two grains from CT2 and the positions where the measurements were done. The locations were chosen in order to find transitions of crystallographic structures. The structure and cage filling varies at different positions within the grain. The relative ratio of the SC and LC for the C—H stretching bands of methane can help to identify the crystal structure, if the C—C stretching of other hydrate forming components in the sample is considered.

The grain shown in Figure 7.3 comprises sI and sII. The grain was systematically mapped in three dimensions, here the Raman spectra of 9 positions of the same Z-horizon are depicted over the C—H stretching section of the spectrum ($2840 - 2960 \text{ cm}^{-1}$). In positions 2 and 3 (Figure 7.3), the intensities of the C—H stretching for methane in the LC were about thrice of the C—H stretching in the SC. As the unit cell of sI hydrate comprises three times as many LC than SC, the spectrum points to sI hydrate at these positions with methane being almost the only hydrate forming gas. The peak position for methane in the LC was 2902.6 , of the SC it was 2914.5 cm^{-1} (Table 7.2).

At the positions 1, 4, 6, 7, 8 and 9 (Figure 7.3), the intensity of the C—H stretching for methane in the LC was about half of the stretching the SC, matching the ratio of the respective cage numbers in the unit cell of sII. Also, C—H stretching for ethane and light hydrocarbons were discernable in the spectra of these positions, suggesting that sII hydrate is present there. The ratios of the C—H stretching in the SC and LC slightly changed at those

Table 7.2: Raman-spectroscopy: Center of peak positions (cm^{-1}) of the C–H Raman stretch frequencies of methane in the sl and sII hydrate samples. The spectra were measured at 113 K and ambient pressure.

Pure sl		Mixed (sl + sII)	
MLC	MSC	MLC	MSC
2902.6	2914.5	2902 – 2903	2912– 2914.5

MLC = methane in the large cage; MSC = methane in the small cage

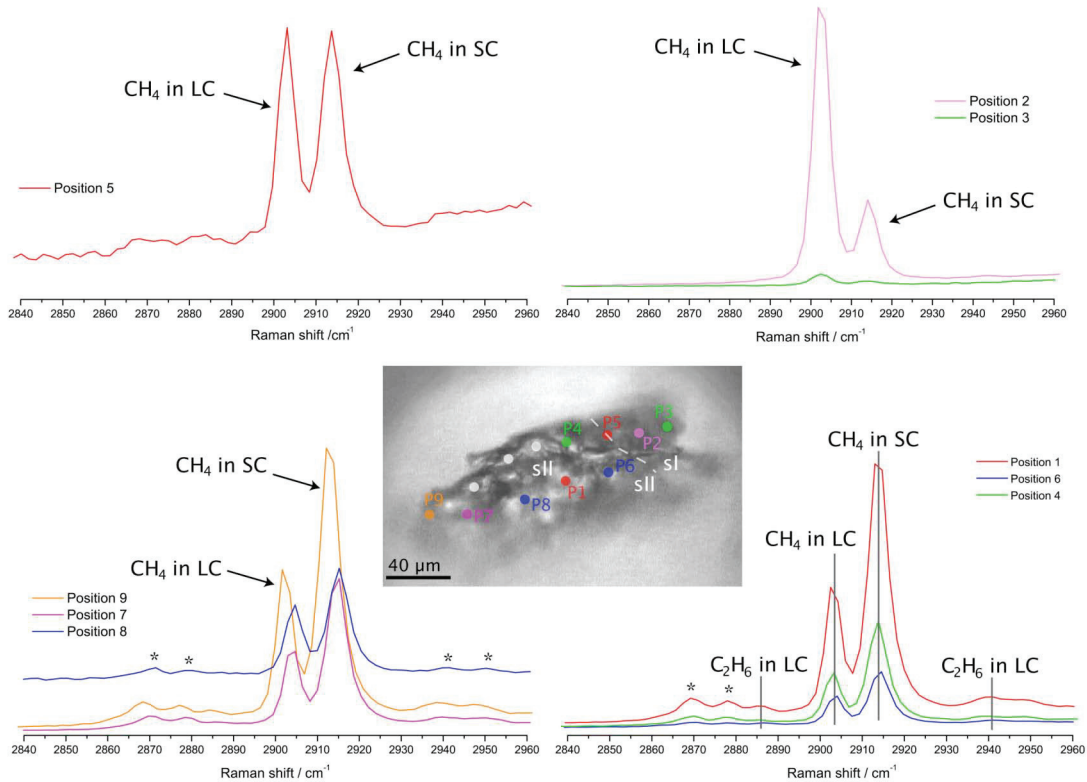


Figure 7.3: Grain from the mixed gas hydrate structure sample CT2. Raman spectra of different positions of the grain are shown in corresponding colors. The transition between sl and sII is indicated as a dashed line running through Position 5. The ordinates of the spectra (not shown) return the Raman intensity.

positions in Figure 7.3, as did the intensities of ethane and higher light hydrocarbons, indicating that the LC of sII was filled not only by methane but also by other gases.

Position 5 (Figure 7.3) was located along the transition from one structure to the other. On either side of position 5 was another structure, indicated by different ratios of the C–H stretching for methane, and at position 5 the C–H stretching had the same intensity for both cages, such that no crystallographic structure could be attributed.

Figure 7.4 shows another grain from CT2. Different hydrate structures were identified in this crystallite agglomerate as well. At position 1 of the grain (Figure 7.4) the ratio of SC and LC for the C–H stretching bands of methane changed significantly over short distances in the depth/ Z-direction of the grain (Figure 7.5A, B). The step size for the depth micro-mapping was 10 μm . On the surface of the grain, which was arbitrarily oriented, the intensities of the C–H stretching of methane in the LC were about thrice of the C–H stretching in the SC, so here the spectrum points to sl hydrate on the surface of position 1, with methane being almost the only hydrate forming gas. The intensity changes of the relative ratio of the

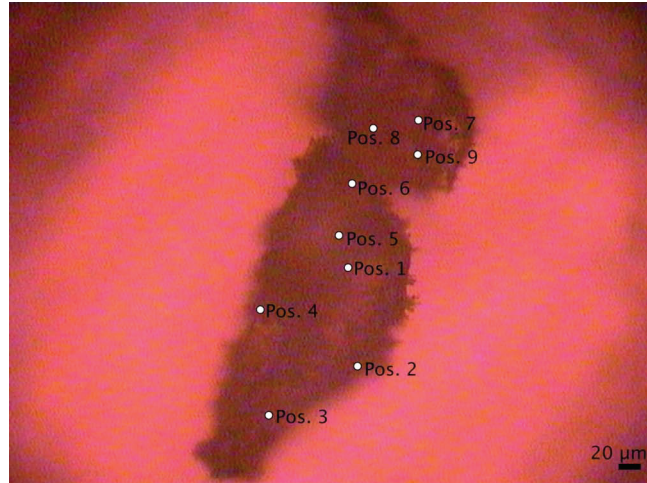


Figure 7.4: Microscopic image of a gas hydrate grain from sample CT2. Raman-measurements were done at the indicated sampling positions.

SC and LC for the C—H stretching bands over depth below the surface of the grain at position 1 are documented in Figure 7.5B. The intensities of the peaks were integrated, accounting for a discernable offset between the visual ratio of the peak heights in Figure 7.5A and the ratio of the peak areas, which is given in Figure 7.5B. The ratio changed dramatically over the depth of 200 μm and strongly indicates that a transition occurred from one structure to the other ca. 80 to about 100 μm below the surface of the grain. At about 90 μm in depth the integrated peak intensities were about equal; at this sample depth the structure transition occurred and no discrete crystal structure could be attributed.

Figure 7.6A shows Raman spectra in the C—H stretching range for the positions 1, 2, 3 and 4 (see Figure 7.4) at 200 μm depth (referring to Figure 7.5A). At Positions 1 and 4 the stretching for the SC had higher intensities than the LC, pointing to sII hydrate; at Position 3 the LC intensities were higher than of the SC, suggesting sI hydrate. At Position 2 no intensi-

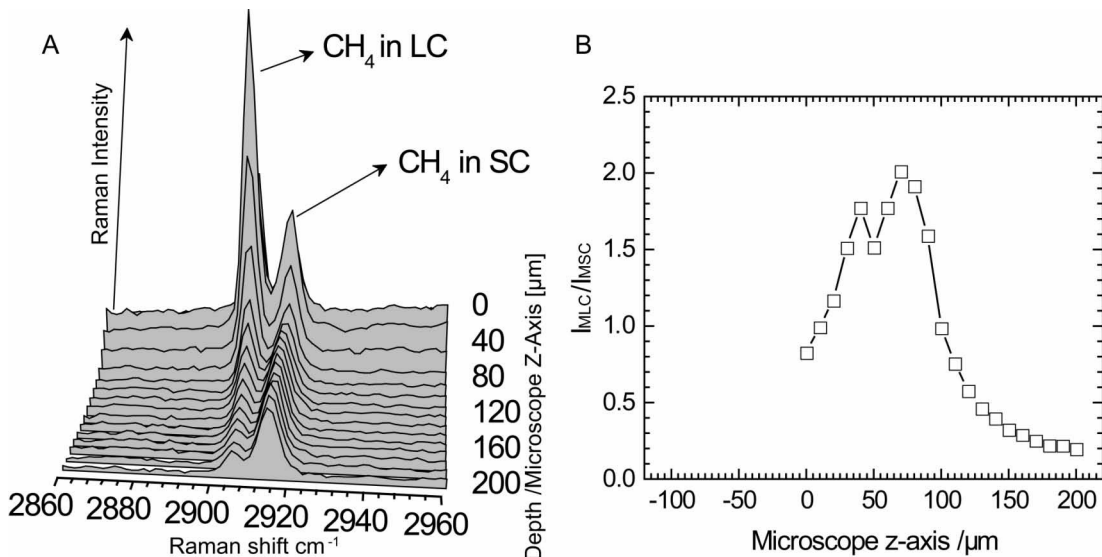


Figure 7.5: Raman spectra taken at Pos. 1 (see Fig. 4). **A.** Variations in the focal depth of the sample revealed changes in the ratio of the small and large cage for the intensities of the C-H stretching bands of methane. The relative ratio of large to small cage changes from 3:1 at the surface ($Z=0$) to about 1:2 at the bottom of the sample ($z=200 \mu\text{m}$). **B.** Ratio of relative intensities of small and large cage for C-H stretching of methane.

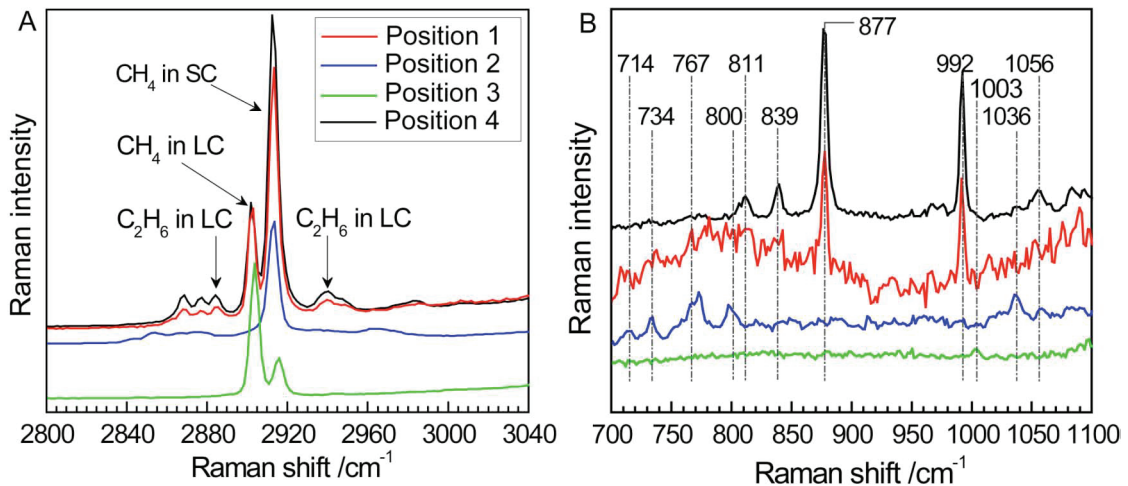


Figure 7.6: Raman spectra from Pos. 1, 2, 3 and 4 (see Fig. 4). **A.** C-H stretching of methane and ethane in the small and large cages. **B.** Section of lower wave numbers in the Raman spectra of sample positions from 5A. Frequencies at 811 cm^{-1} (*i*-C₄H₁₀, sII5¹²6⁴), 839 cm^{-1} , 877 cm^{-1} (CHv, sII5¹²6⁴) and 992 cm^{-1} (CHv, sII5¹²6⁴) are assigned to C—C stretching bands of *iso*-butane, *n*-butane, propane and ethane in the large cages of sII hydrates. Frequency at 1003 cm^{-1} represents C—C stretching vibration of ethane in the sI hydrates. The C—C stretching bands between 700 and 1100 cm^{-1} show C₂ through C₄ hydrocarbon homologues in the LC of sII at Pos. 1 and 4.

ties above background were recorded at the C—H stretching wave number for the LC of methane, only the SC was filled by methane there. The relative peak intensities of the C—H stretching of methane in the SC and LC and of ethane differed at positions 1 and 4. Relatively lower intensities for methane in the LC and higher intensities at the C—H stretching bands of ethane at Position 4 indicated that at that position more ethane than at Position 1 was incorporated in the LC of sII. This means that at each of those positions, the hydrocarbon incorporation into the hydrate differed irrespective of the crystal structure, and that different crystal structures occurred at those positions.

Vibrations of the C—C stretching at lower wave numbers are given in Figure 7.6B. The Figure shows that also *iso*-butane, *n*-butane, propane and ethane were enclathrated in the LC of sII hydrates at the positions 1 and 4 but not at Positions 2 and 3 (Figure 7.4). That points to inhomogeneous distributions of hydrocarbons within hydrates of the same structure and even in the same grain agglomerate over comparatively short distances. At wave number 1003 cm^{-1} , low-intensity C—C stretching of ethane was discernable in the LC of sI hydrate (Figure 7.6B). For position 2, the deficiency of methane in the LC (Figure 7.6A) coincided with an absence of ethane but presence of small amounts of higher hydrocarbons (Figure 7.6B) which we ascribe to C₅ isomers and larger molecules, but which at present cannot be assigned to discrete compounds.

Ratios of C—H stretching for methane between LC and SC varied among the positions 5, 6, 7, 8 and 9 as well (Figure 7.7A). The varying ratios indicate that the cage filling by methane was not the same for the hydrate at these different positions. Alternating maximum peak intensities for the SC and LC also point to different hydrate structures. Judging from relative peak heights, positions 5, 7 and 9 seemed to feature sI gas hydrate, while at position 6 sII hydrate seemed to be present. For position 8 a clear distinction was not possible, as the two peaks had almost identical peak heights, suggesting that not all cages of neither sI nor sII were filled to a degree that a certain structure type could be ascribed. No ethane could be identified from the wavelength of the C—H stretching bands for ethane at position 8, but it was discernable at position 6.

Figure 7.7B shows Raman C—H stretching spectra of three different grains from the sample CT6. At each location methane seemed to be the dominant guest molecule both in the LC and SC of sl hydrate. Small ethane fractions were present in the grains 1 and 2 (Figure 7.7B, inlet).

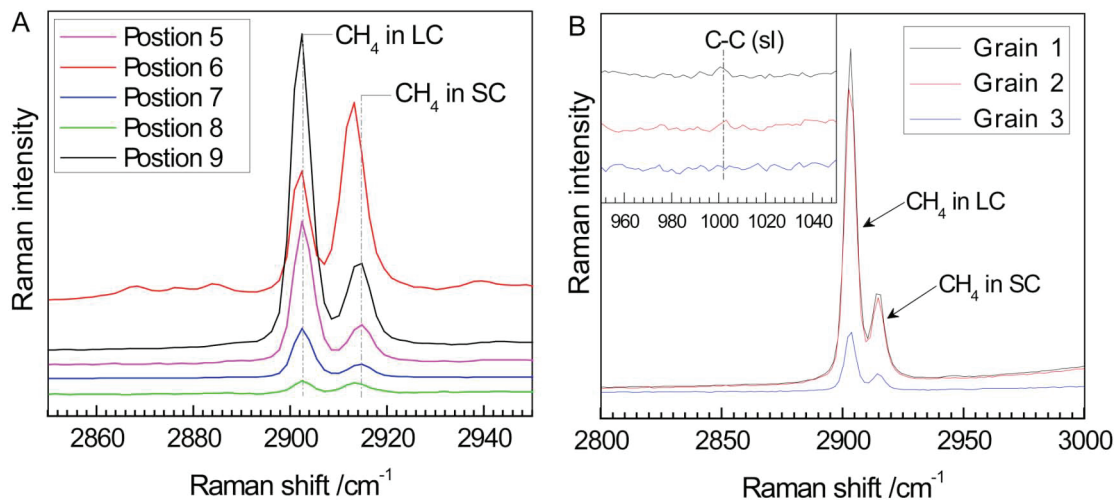


Figure 7.7: C—H-stretching of methane in the small and large cages. **A.** Sample CT2, positions 5, 6, 7, 8, 9 (see Fig. 4). **B.** Sample CT6. Signals for three different grains from the sample. The inlet shows the C—C stretching of ethane in sl hydrate.

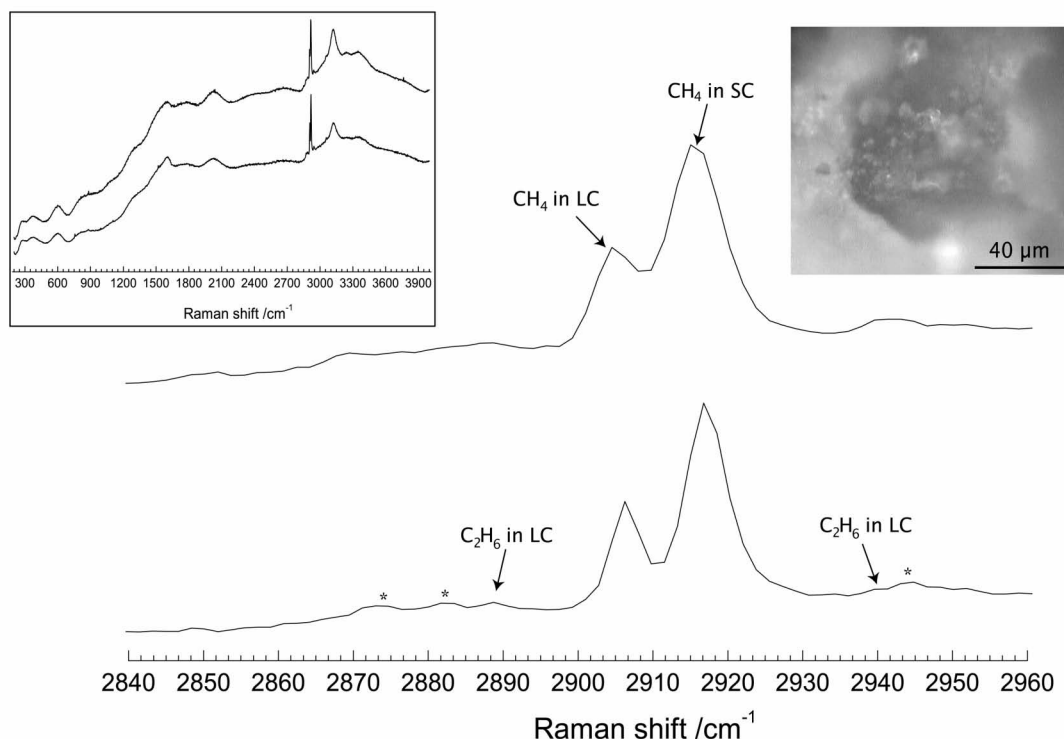


Figure 7.8: Grain from sample CT6 (see inlet). The peak ratios of the C—H stretching for methane indicate sl hydrate. C—H stretching for ethane, propane, butane are also present (see Fig. 5A). The spectra are fluorescence and elevated background intensities (left inlet, spectra from 200 – 3900 cm^{-1}). The two spectra were measured in the grain center with a vertical offset (Z-axis) of 30 μm .

Figure 7.8 depicts Raman two spectra of a fourth grain from CT6. In this grain (inlet on the right) the ratios of the methane stretching and the C—H stretching of ethane and higher light hydrocarbons indicated sII hydrate. The inlet on the left shows larger spectra from this grain. The high background rising from ca. 900 to 1400 cm^{-1} was due to fluorescence and a result of the presence of numerous hydrocarbon derivatives of multiple chain length in the asphalt sample.

7.5.3 Crystallite sizes

The crystallite sizes of the two gas hydrate structures sI and sII in the mixed hydrate sample CT2 had differently shaped distributions. The distribution of sI was skewed to smaller crystallite sizes (Figure 7.9A) and had an arithmetic mean of $172 \pm 57 \mu\text{m}$ (Table 7.1). The distribution of sII hydrate crystallites was skewed towards larger sizes (Figure 7.9B) with an arithmetic average value of $381 \pm 45 \mu\text{m}$. The two other samples, which had been identified as pure sI hydrates (Table 7.1; Figure 7.9C), had mean crystallite sizes in the same range as for the sI crystallites in the mixed structure sample: in the pure sI subsample from CT2 the arithmetic mean was $227 \pm 50 \mu\text{m}$, in CT6 it was $187 \pm 55 \mu\text{m}$. The crystallite size distribution of CT6 was also shaped towards smaller crystallite sizes (Chapter 4), similar to the sI distribution of the mixed sample.

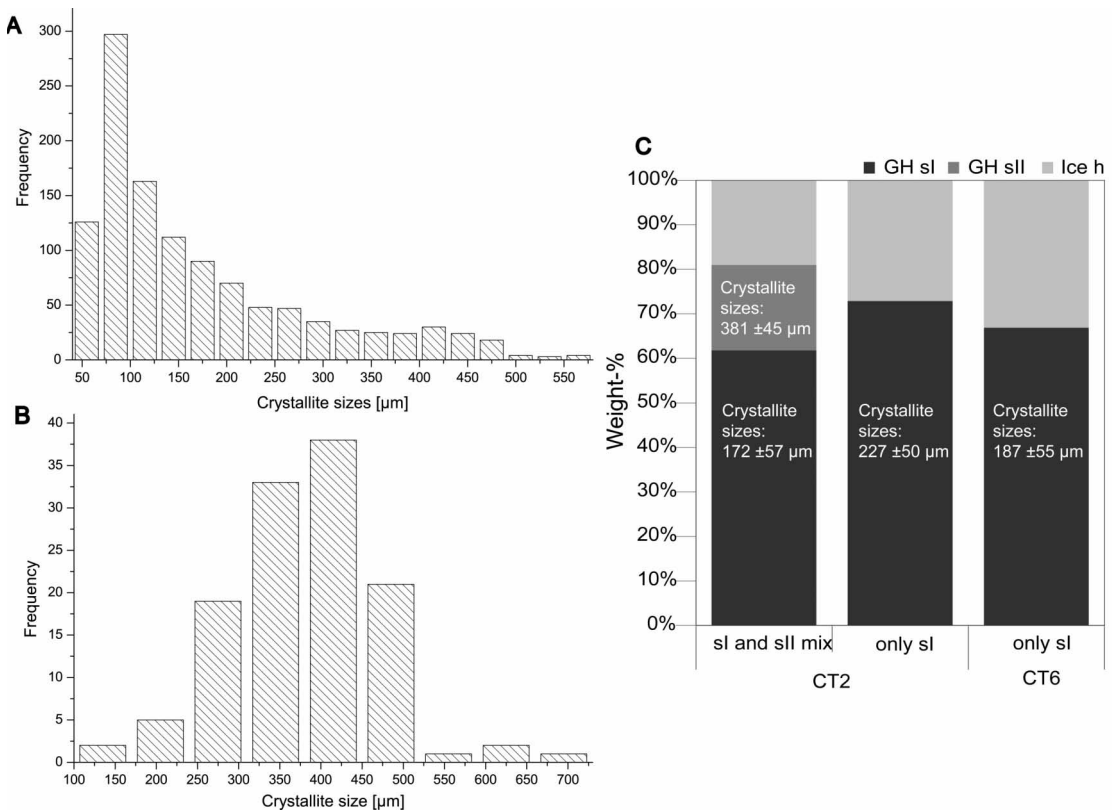


Figure 7.9: Size distributions of sI and sII gas hydrate crystallites from the mixed structure sample from CT2. **A**. Distribution of sI hydrate crystallites; **B**. Distribution of sII crystallites; **C**. Bar chart on the crystallographic structure and respective arithmetic mean crystallite sizes. Quantitative phase fractions are in weight percent.

7.5.4 Gas chromatography

Methane was the major component of the hydrate forming hydrocarbons, as it was present in all subsamples with more than 94 mol% (Table 7.3). Highest fractions of methane were present in the sample CT6 (98%). The fractions of C₂ to C₅ hydrocarbons amounted to 2.0 mol%. CT2 yielded different proportions of hydrocarbons for each of the two pieces: Piece 1 had a methane fraction of 97.6%, in Piece 2 it was 94.2%. Also, ethane, propane and butane isomers had different proportions in the two pieces (Table 7.3). The mol fraction of C₂-C₅ hydrocarbons in Piece 1 is 2.4%, in Piece 2 it is 5.8%. The C₁/C₂-C₅ ratio was at around 50 for the sample CT6, 41 for Piece 1 of CT2 and 16 for Piece 2, indicating a predominantly thermogenic origin of light hydrocarbons.

The average gas chemistry results of the different specimens were first reported in Chapter 5. Here, the detailed chemical composition of subsamples is given in order to better understand the heterogeneity of the gas composition of the coexisting sl and sll.

7.6 Discussion

Previous reports of natural gas hydrates described mostly the occurrence of one hydrate structure at a geological site. This is due to the fact that at most studied hydrate locations methane is the prevailing hydrate forming gas (Hester & Brewer, 2009, and references therein; Kvenvolden, 1993) or, like in the oil seeping sites in the northern Gulf of Mexico, the chemical mix of thermogenic hydrocarbons favors the precipitation of sll hydrates (e.g., Brooks et al., 1984; Sassen et al., 2001a). The following discussion of two intimately connected gas hydrate structures at the Chapopote will be guided by the question, why and how different hydrate structures occur on relatively short distances and why the gases do not combine to one structure.

Table 7.3: Gas chemistry (in mol%)

	CH ₄	C ₂ H ₆	C ₃ H ₈	<i>i</i> -C ₄ H ₁₀	<i>n</i> -C ₄ H ₁₀	C ₅ - Deriv. 1	C ₅ - Deriv. 2	<i>n</i> -C ₅	C ₁ /C ₂
CT6	98.252	1.607	0.060	0.009	0.035	0.001	0.017	0.018	56
	97.888	1.740	0.224	0.037	0.072	0.002	0.019	0.017	46
	98.045	1.621	0.196	0.043	0.063	0.002	0.015	0.014	50
	98.135	1.595	0.159	0.029	0.057	0.002	0.011	0.012	53
	97.971	1.707	0.195	0.037	0.065	0.002	0.011	0.012	48
mean	98.058	1.654	0.167	0.031	0.058	0.002	0.015	0.014	51
stddev	0.127	0.058	0.057	0.012	0.013	0.000	0.003	0.003	3
CT2									
piece 1	97.555	1.827	0.390	0.066	0.121	b.d.l.	0.041	b.d.l.	40
	97.655	0.529	1.228	0.201	0.328	b.d.l.	0.058	b.d.l.	42
mean	97.605	1.178	0.809	0.134	0.224		0.049		41
stddev	0.050	0.649	0.419	0.068	0.103		0.009		1
piece 2	93.721	2.723	2.438	0.349	0.690	b.d.l.	0.079	b.d.l.	15
	94.220	2.465	2.291	0.330	0.630	b.d.l.	0.064	b.d.l.	16
	94.509	2.646	1.923	0.271	0.590	b.d.l.	0.061	b.d.l.	17
mean	94.150	2.612	2.218	0.316	0.637		0.068		16
stddev	0.325	0.108	0.217	0.033	0.041		0.008		1

b.d.l.: below detection limit

7.6.1 Heterogeneity of the hydrate-forming gases with respect to hydrate crystallization

The coexistence of sI and sII hydrate at the K-2 mud volcano in the Kukuy Canyon in Lake Baikal is explained by changes in the gas feed from the depth of the Kukuy Canyon (Kida et al., 2006). The hydrocarbons at the K-2 mud volcano are supposed to originate both from thermogenic and biogenic sources (Kida et al., 2006). In contrast, hydrocarbons from the Chapopote are only of thermogenic origin as evidenced by stable carbon isotopes of hydrocarbons (MacDonald et al., 2004). A fractionation of the gases from deep reservoirs may happen in shallow sediments depths close to the seafloor by depletion of methane during AOM in combination with seawater sulfate reduction (Boetius et al., 2000; Bohrmann & Spiess, 2008). Also, biodegradation of oil and asphalts of different ages (MacDonald et al., 2004) is supposed to account for locally different hydrocarbon compositions in gas bubbles embedded in the asphalts (Bohrmann & Spiess, 2008; F. Schubotz, pers. comm., Dec. 2007).

It appears important to consider the scales, on which molecular fractionation of gases can occur, as even if gases from different origins had mixed during the upward migration, it would have been unlikely that the gas mixing accounts for the different hydrate structures occurring on such small distances as observed here. Spaces in the asphalt can be considered as secluded cavities or reactors, where the gas hydrate crystals form from the available gas. Therefore it is likely that for each such gas-laden cavity the separation into sI and sII hydrate happens during or even after the crystallization. This option is supported by the findings of the close spatial association of sI/sII hydrate.

7.6.2 Separation into sI and sII during crystallization

The pores in the asphalt, which are formed from intrusion of gas bubbles into the viscous and ductile asphalt (see Figure 7.1; Bohrmann & Spiess, 2008; Brüning et al., submitted), effectively cut off the bubbles from gas supply from below and form a closed system. Such a closed system seems to be important for a co-occurrence of two structures, as it was shown at high gas flux seeps that a fractionation of the gas occurs during the hydrate nucleation from the feeding gas, and that not all gas is incorporated into gas hydrate (e.g., Haeckel et al., 2004; Appendix III). The incipient hydrate structure tends to incorporate less volatile hydrocarbons (Ballard & Sloan, 2001). In this closed system gas and water are limited, which means that the nucleation and subsequent growth of the incipient hydrate structure denudes the ambient gas mixture successively of the gases which are favorably incorporated into the incipient hydrate (Hester et al., 2007a).

Three models on how a co-occurrence of sI and sII might evolve are discussed here; it is likely that a combination of these end-member models was realized on the Chapopote, rather than a single option.

7.6.2.1 De-mixing: Crystallization into two hydrate structures from the gas phase

sII hydrate is the favored hydrate structure for the measured gas composition of the sample CT2 (Table 3, Pieces 1 and 2) (CSMGem flash calculation basing on Sloan & Koh, 2007; P=290 bar; T=4.4 °C). For the gas composition of CT6 the flash calculation returns sI hydrate formation, applying a suggested water content of 11.11 mol% (Sloan & Koh, 2007;

C.A. Koh, pers. comm.). Assuming excess water (40.0 mol%), the model suggests a de-mixing into sI and sII coming directly from the vapor phase. This demonstrates that slight shifts in the water availability have great impact on the incipient hydrate formation, even though the actual water fraction in the asphalt pores cannot be reconstructed. For CT2, sII was the only calculated structure irrespective of the water content. But instead of pure sII we found a sI dominated mix of the two structures, or only sI (Figure 7.9). It should be noted that during hydrate formation there is always a fractionation between the feeding gas and the hydrate-bound gas (Ballard & Sloan, 2001; Appendix III). In the calculations reported here it was assumed that the gas composition of the hydrate is the same as the composition of the feeding gas, as the original gas composition is unknown. Therefore these calculations serve purely as an approximation. Given that for CT2 higher hydrocarbons are preferably incorporated into the hydrate phase, it is consequent to assume that the remaining gas phase approximates a composition similar to CT6 and a de-mixing into two structures may commence. In fact, an incipient de-mixing would be energetically favorable as that process lowers the free Gibbs energy in the system. As both sI and sII comprise the same SC (5^{12}) but different LC ($5^{12}6^2$, $5^{12}6^4$, respectively), two incipient structures provide one more degree of freedom compared to one structure. De-mixed hydrates of sI and sII were also found in recent laboratory experiments of methane-ethane sI/sII hydrate lasting almost 6 months (95 mol% methane; 50 bar; -3 °C) (Murshed & Kuhs, 2009). Also, the co-occurrence of sII and sH at Barkley Canyon was attributed to the circumstance that the gases due to their relative composition could not be incorporated into either of the two crystal structures alone (Lu et al., 2007), suggesting that miscibility gaps in the precipitation of different hydrate structures from a mix of hydrocarbons are stable in natural settings.

Other than stable miscibility gaps, metastable sI/sII co-occurrences have been observed repeatedly (e.g., Klapproth et al., 2003; Ohno et al., 2009; Schicks et al., 2006; Yeon et al., 2006). In those studies it was reported that the metastable structure transforms into the more stable structure after the nucleation with the speed depending on the degree of gas redistribution as well as the water molecule re-arrangement (Ohno, et al., 2009) and therefore also on the gas composition of the feeding gas. It was predicted that sI and sII hydrate of methane and ethane with compositions close to the structural transition points can coexist in a metastable state (Ballard & Sloan, 2001; Subramanian et al., 2000a, 2000b), which was confirmed by laboratory experiments (Ohno et al., 2009; Yeon et al., 2006).

For the Chapopote, it seems likely that during nucleation of hydrate the hydrocarbons de-mixed into two structures occurred and that a miscibility gap exists, providing the lowest free energy in the system. These findings are supported by the close association of the two structures within the samples.

7.6.2.2 Zoning of gas hydrate crystals

Assuming that during the subsequent growth of a seed crystal in a cavity less volatile hydrocarbons are preferably consumed (Sloan & Koh, 2007) and given that such a cavity is disconnected from gas supply, then outside of the hydrate phase less volatiles become denuded and subsequently more volatile hydrocarbons (like methane) are relatively enriched. Like for garnets (e.g., Ginibre et al., 2007) or feldspars (e.g., Triebold et al., 2006), the reason for chemical zoning lays in the lack of certain components for the material at the rim of the crystal. In the case of the Chapopote mixed hydrates, ethane and higher hydrocarbons

would be lacking after the reaction started. Subsequent formation and accumulation of gas hydrate at the surface of the growing crystal will result in an increase of the methane concentration from the center towards the rim. During the growth on the surface of the rim, the chemical composition of the hydrate favors a structure transition, which can be tracked by Raman measurements (Murshed & Kuhs, 2007; Ohno et al., 2009; Figure 7.5).

Yet, chemical zoning is known particularly from solid solution series minerals but it can also occur between different minerals like calcite and dolomite (Chave, 1952). Those minerals do not have the same spacegroup but the topology of the structures is similar and therefore provide a template for oriented growth. However, the topologies of sI and sII hydrates are different and the same (cubic) crystal system is insufficient for crystallization to a continuous gradient single crystal. Therefore, “zoning” in the case of sI/sII hydrate may not be understood as a templated growth with a fixed orientational relationship between the two structures. Instead, “riming” better describes the arbitrarily relationship without templated growth at the surface of preexisting crystals. Dedicated laboratory experiments with a change in the feeding gas composition in the course of the experiments probably would be a good way to start an investigation on chemical zoning – or riming – of gas hydrates.

7.6.2.3 Several seed crystals form, resulting in fractionation during crystallization

For the previous two sections on the separation into sI and sII during crystallization some assumptions needed to be made. In the case of the de-mixing (Section 8.6.2.1), it is assumed that the hydrocarbons in the feeding gas were homogeneously distributed prior to the nucleation. Also, in the case of zoning (or riming; Section 8.6.2.2) it is assumed that the hydrocarbons in the vapor phase outside the hydrate phase were homogeneously dispersed prior to fractionated crystallization. However, depths profiles of the sediments at Chapopote showed that hydrocarbons were very heterogeneously distributed due to AOM and biodegradation (Bohrmann & Spiess, 2008). Gas bubbles with different gas compositions intruding into the asphalt layer may form individual reactors within a shared cavity in the asphalt (see Hester et al., 2007a), complicating the two previously described options. This is because gas bubbles together with water form a solid skin of hydrate at the gas-water interface (e.g., Mori and Mochizuki, 1997; Smelik and King, 1997; Rheder et al., 2002), given that the P, T conditions are within the hydrate stability horizon. The nucleation of hydrate on the bubble surface occurs immediately and the hydrate skins around the bubbles form almost instantaneously after the gas bubbles got into contact with water (Rehder et al., 2002; Brewer et al., 2002). Therefore, at least for large cavities in the asphalt (i.e., on a centimeter range), it is uncertain whether these cavities were formed originally from a single gas bubble with a homogenous gas composition or rather filled by several gas bubbles, each of which covered by a hydrate skin on the surface.

The scheme in Figure 7.10 shows how the crystallization of water and different gas bubbles may commence, resulting in different gas hydrate structures. A single cavity in the asphalt is shown in Figure 7.10A, into which several gas bubbles intrude. The hydrate skin separates the gas inside the bubble from the water (Figure 7.10B). In Figure 7.10B it is assumed that the cavity is closed and neither gas nor water leave or enter the cavity. Topham (1984) suggested that the necessary water supply for the internal hydrate formation inside of a gas bubble is supplied by capillary action across the bubble surface. In fact, it is likely that the hydrate subsequently grows inwards to the center of the bubble sustained by permeation

of water through the hydrate layer (Figure 7.10C, D). Gas molecules most likely do not diffuse outward through the hydrate rim of the bubble, as the water in the asphalt cavities must have been super-saturated. Hydrates only form and are stable in aqueous solution if the ambient gas concentration exceeds the solubility (Kvenvolden, 1993). Instead, it is more likely that water molecules diffuse through the skin and combine with the gas inside the bubble (McGinnis et al., 2006). Sun et al. (2007) report from laboratory closed system experiments (i.e., without adding of gas or water) that the hydrate shell cracked within minutes upon hydrate formation (Figure 7.10E) and that the hydrate formation continued after complete freezing of the surface (Figure 7.10F). Ribeiro and Lage (2008) suggest that the porous microstructure of solid methane hydrates (Kuhs et al., 2000a; 2004a; Staykova et al., 2003) may be present also during the advancing hydrate crystallization at the bubble surfaces and could potentially have aided the diffusion of water.

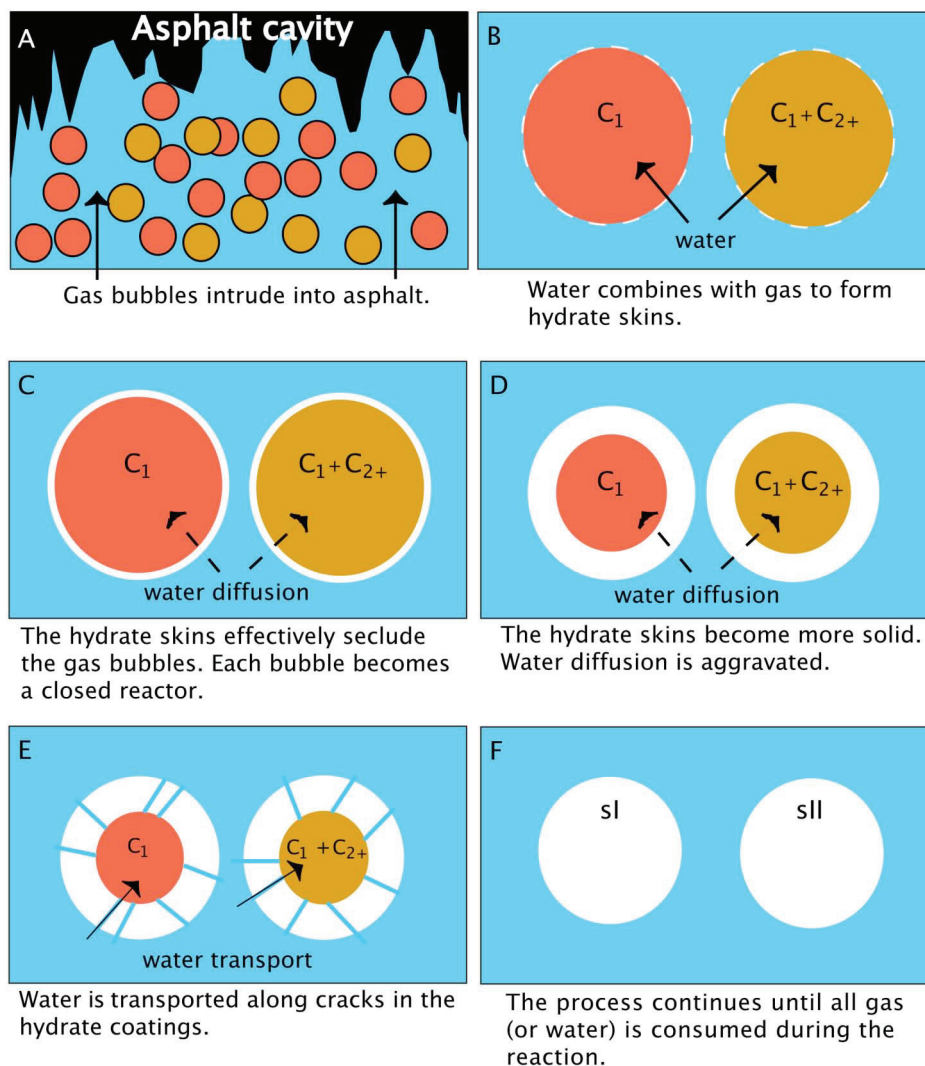


Figure 7.10: Model of the fractionation during crystallization. The hydrate structure is determined by the gas chemical composition of the originating gas bubble. Here, methane dominated gas (C_1) is shown in red; a gas mixture of methane and other light molecular weight hydrocarbons is colored in brown (C_1+C_{2+}). After the intrusion into a cavity in the viscous asphalt (A.), the bubbles and water form a hydrate skin (B.), which subsequently hampers an exchange of gas between the bubble and the saturated surrounding water in the asphalt cavity (C.). Water diffuses inside of the bubble (C.; D.), until the hydrate rim racks open (E.; Sun et al., 2007), and water reacts with the remaining gas and forms solid hydrate crystals (F.).

The hydrate skins separate gases in different bubbles (Hester et al., 2007a). Within a bubble, hydrate crystallites will grow independently from one another as long as there is sufficient gas and water in the system (e.g., Schicks et al., 2006; Tohidi et al., 2001). Assuming that gas bubbles have different gas chemical compositions and transform into hydrate, sI and sII crystals will coexist depending on differences in the gas composition of the original bubble. This derivation is confirmed by our Raman results, as we found gas hydrate of different structures neighboring within the samples (Figures 3; 5; 6; see Figure 7.4). Also, salt crusts at grain boundaries of gas hydrates visualized by micro-computer-tomography (Chapter 6) indicate that dissolved ions were expelled from the water during gas hydrate formation.

The assessment of possible options on the coexistence of sI and sII in the cavities of the asphalts is further complicated by drawing an analogy to so-called air hydrates. Nucleation of hydrate crystallites from air bubbles have been observed in deep polar ice sheets (Shoji und Langway, 1982). For those hydrates it is unclear whether one so-called air hydrate crystallizes from one air bubble (Ohno et al., 2004; Salamatin et al., 2003) or whether many crystallites can form simultaneously from a single air bubble (Kipfstuhl et al., 2001; Pauer et al., 2000). Answering this question seems relevant for the hydrates in the asphalts, as the crystallization of several hydrate crystals from one bubble might be accompanied by a fractionation of the hydrocarbons in the hydrate phase. The reaction from air bubbles to air hydrates happens within a few hours (Kuhns et al., 2000b) and therefore takes a bit longer than reported from the liquid water experiments by Sun et al. (2007).

7.6.3 Fractionation after crystallization

7.6.3.1 sI crystals trapped in sII

Laboratory experiments simulating natural conditions demonstrated that hydrates of both sI and sII, which form at the gas-water interface, grow to surface crystals (Makogon, 1994). Smelik and King (1997) showed how hydrate surface crystals trapped other crystals, increasing the thickness of the hydrate layer. Although the authors conducted their experiments with just one hydrate structure at a time, they observed this phenomenon for both structures I and II (Smelik & King, 1997). This might explain how hydrate crystallites are trapped between crystals of another structure. In fact, different crystallite sizes and size distributions can also be a result of sandwiched crystals between others. If a trapped crystallite has a different crystallographic structure than the encasing crystals, much energy is needed for the agglomerate to recrystallize to a single crystal (Humphreys & Hatherly, 2004). The gases in the hydrate cages of the trapped crystal have a different composition, such that for a recrystallization of two structures gas molecules need to be exported and replaced by others (Ohno et al., 2009). The only possibility to exchange gases from trapped crystals would be by diffusion through the encasing crystals. The energy demand for such processes is likely to be comparatively big, but during grain coarsening processes, each successive step must be energetically favorable (Lasaga, 1998; Lifshitz & Slyzov, 1961).

Consequently, if encasing crystals of another structure retard the regrowth of sandwiched crystals, it is reasonable to assume that the different structures have diverse crystallite sizes and size distributions. In fact, the smaller crystallite sizes of sI versus sII hydrate (Figure 7.9) and the skewed sI distributions towards smaller crystallites (Figure 7.9A; Chapter 4) support the interpretation of trapped crystals. On the other hand, the proportions of the hydrate phases do not allow for trapping of crystals as the only reason for the coexistence of two

hydrate structures (Figure 7.9C). By far not all of the much larger fraction of sI could be trapped in sII hydrate. Also, the scanned sI crystallites in sample CT6 were small and skewed towards small crystallite sizes without any sII detected. Therefore, trapping of crystals cannot be the dominant reason for the co-occurrence.

7.6.3.2 Coarsening of crystallites

Crystallite size distribution growing in steady-state and following normal grain growth (e.g., no effect of shear stress, mechanical work ect.) are shaped in a normal distribution, which can be slightly skewed towards larger crystallite sizes (Humphreys & Hatherly, 2004; Ricard & Bercovici, 2009). Freshly flocculated methane hydrates have crystallite sizes of ca. 15 μm (Staykova et al., 2003) and up to 40 μm (Klapp et al., 2007). The arithmetic means of the sI hydrate crystallites from Chapopote suggest that the crystallites grew up to the size of ca. 200 μm (Figure 7.9A, C), given that the initial crystallites were smaller, but the distributions of the sI crystallites from the sI/sII co-occurrence sample in CT2 as well as of the sI crystallites from CT6 (Chapter 4) are not shaped in a normal distribution but skewed towards small crystallite sizes (see Figure 7.9A). This suggests that the crystallites did not grow normally: In normal grain growth, the shape of the normal distribution stays constant while just the average mean value increases. Instead, at the mixed structure sample from Chapopote only the sII crystallite sizes are shaped in a normal distribution, slightly shifted to larger crystallite sizes (see Ricard & Bercovici, 2009). This circumstance allows for the following two interpretations: Either, the sII crystallites formed prior to the sI crystallites and therefore, the sII crystals had more space and time to grow. Then, the sI crystals nucleated in the limited inter-spaces between the already existing sII crystallites.

Alternatively, sII gas hydrate could have faster crystal growth rates, accounting for the size difference. The cause for that will likely be the formation of the LC, as the SC is the same for both structures, or the ratios of SC and LC in the two structures. Larger guest molecules, which are incorporated into the LC are less volatile, which is also the reason why less sub-cooling is required to shift such gases into the gas hydrate stability horizon. It might be that this also accounts for a faster crystal growth rate. The relation between the crystal growth rate and the nucleation rate needs to be investigated in more detail. However, Klapproth et al. (2003) and Murshed & Kuhs (2009) found faster nucleation rates of sII, parts of which later transformed into sI, which suggests that a relation may exist fostering sII crystal growth.

7.7 Conclusions

The Chapopote asphalt volcano is a thermogenic hydrocarbon seep in the southern Gulf of Mexico, where sI and sII hydrate structures are intimately associated in asphalt pockets. Various possible causes are presented which may explain the co-occurrence of sI and sII on short spatial distances. It is possible if not likely, that a combination of the following reasons accounted for the coexistence of the structures and the crystallite sizes.

- a) The separation into sI and sII occurred during the hydrate crystallization: the two hydrate structures crystallized directly from the gas phase, providing one more degree of freedom for lowering the free energy.

b) Preferred incorporation of less volatile compounds into the incipient hydrate crystals effected the chemical riming of the hydrates in that new hydrate formed from the remaining gas phase on the surface of preexisting hydrate crystals.

c) Hydrate skins secluded the gas bubbles from each other, which intruded into cavities in the asphalt. Each gas bubble crystallized independently to solid gas hydrate. Due to different gas compositions of the bubbles, different structures emerged.

d) Different crystallite sizes are predominantly the result of the higher nucleation density of sII and/or of its faster formation at the present P,T condition and gas compositions.

If our interpretation of the processes is correct, similar situations of complex hydrate structure associations might be found at other thermogenic gas seeps, where the P,T conditions and gas compositions favor the precipitation of sII and allow for sI. Therefore, it would be mandatory that the hydrates formed in a closed-system, where gases could neither be imported nor exported. The discovery of intimate sI/sII hydrate coexistence at a natural deposit sheds new light on gas hydrate occurrence at thermogenic gas seeps. Intimate hydrate structure associations formed from different gas molecules need to be considered in hydrate abundance estimations, in which the masses of hydrocarbon species incorporated in the hydrate lattice is calculated on the basis of the cage occupancy.

Acknowledgements

We thank Heidrun Sowa and Lars Raue for support at the HASYLAB and Burkhard Schmidt for help at the Raman spectrometer. We thank the captains and crews of the R/V METEOR (Cruise M67/2). Credits go to HASYLAB at DESY for providing beam time and support. S.A. Klapp thanks GLOMAR graduate school for Marine Sciences and the Vollkammer scholarship for support. This work was funded by the *German Research Foundation* (DFG) and the German Ministry of Education and Research (BMBF) in the program GEOTECHNOLOGIEN (Grants 03G064A, 03G0605B) of which it is publication number GEOTECH-xxxx. This study received additional funding through the DFG-Research Center / Excellence Cluster "The Oceans in the Earth System".

CHAPTER 8

MANUSCRIPT 6

HIGH-INTENSITY GAS SEEPAGE FEEDS SHALLOW GAS HYDRATE DEPOSITS IN THE EASTERN BLACK SEA

Submitted to *Earth and Planetary Science Letters*, June 25th 2009

Thomas Pape^{a*}, André Bahr^{a,b}, Stephan A. Klapp^a,
Friedrich Abegg^{a,b}, Gerhard Bohrmann^a

^a MARUM – Center for Marine Environmental Sciences and Department of
Geosciences, University of Bremen, Klagenfurter Strasse, D-28334 Bremen, Germany

^b IFM-GEOMAR Leibniz-Institute of Marine Sciences, Wischhofstrasse 1-3,
D-24148 Kiel, Germany

8.1 Abstract

Submarine gas hydrates are a major global reservoir of the potent greenhouse gas methane and other low-molecular-weight hydrocarbons. Current assessments of global hydrate-bound carbon vary considerably by at least one order of magnitude, due to the technical efforts required for direct hydrate quantifications. Thus, a strong need for accurate hydrate quantification in near-surface sediments is evident.

For the assessment of hydrate quantities in surface sediments of a highly active seepage site, we performed high-resolution sampling at the Batumi seep area in the eastern Black Sea. Sediments in pressure cores recovered with the Dynamic Autoclave Piston Corer and in gravity cores represented a succession of late glacial to Holocene Black Sea sediments. Quantitative pressure core degassing yielded volumetric gas/bulk sediment ratios of up to 20.3, which prove gas hydrates presence. In gravity cores, hydrates were absent in top sediments belonging to the Black Sea Unit 1 (coccolith ooze), but occurred as cm-sized layers of massive aggregates in deeper sections of Unit 2 (sapropel). In Unit 3 (lacustrine mud), disseminated gas hydrates occurred throughout the entire section recovered. Nominal methane concentrations in different Units in the pressure cores were calculated by comparison of gas/sediment relationships in the different cores. Nominal methane concentrations surpassed methane equilibrium concentrations in Units 2 and 3, resulting in constant hydrate fractions of 6% of pore volume in Unit 2 and mean values of 27% pore volume (11.5 to 43.2%, $n = 5$) in Unit 3. For the entire study area covering about 0.5 km² of seafloor, currently about 14.2 kt of hydrate-bound methane accumulate in sediments down to 265 cm subbottom depth. We conclude that the release of hydrate-bound carbon from this area and similar settings by decomposition or upfloating is an important factor for altering the Black Sea carbon budget.

Keywords: Black Sea, gas hydrate, methane, pressure core, autoclave technology, in situ gas volumes

8.2 Introduction

Atmospheric methane is one of the primary greenhouse gases accounting for about 18% of the radiative forcing (Forster et al., 2007) with marine seeps being a major natural source contributing about 31 to 48% to global methane emission (Etiope and Ciccioli, 2009; Etiope et al., 2008b). However, in particular for the Black Sea it was shown that almost all of the methane emitted from the seafloor into deep waters is dissolved and oxidized microbially in the water column (Kessler et al., 2006; Reeburgh et al., 1991) and therefore do not reach the atmosphere. For instance, for hydrocarbon seeps in the Northwestern Black Sea it was observed that only methane ejected close to the sea surface can escape conversion and enter the atmosphere (Schmale et al., 2005).

Effective mechanisms to transfer substantial amounts of hydrate-bound hydrocarbons from the deep sea directly via the sea-atmosphere boundary into the atmosphere might be i) the floating upward of massive hydrate aggregates (Suess et al., 2001), when hydrate buoyancy exceeds sediment load and chunks of near-surface hydrates suddenly detach from the seafloor (MacDonald et al., 1994; Paull et al., 1995) or ii) gas-bursts of rapidly dissociating hydrates (e.g., Dickens, 1999; Rothwell et al., 1998). Since shallow-buried hydrates are involved in both processes, in this study we aim to shed light on the abundance and distribution of hydrates in shallow deposits of a high-intensity seepage site in the Black Sea, with relevance for the assessment of hydrate inventories in similar geological settings worldwide.

Natural gas hydrates are ice-like substances, composed of gas molecules, such as low-molecular weight hydrocarbons (LMWHC), and cage-forming water molecules (Kvenvolden, 1988; Kvenvolden and Lorenson, 2001; Sloan and Koh, 2007). As gas hydrates are only stable in a restricted pressure-temperature (P/T) field, precipitation of submarine hydrates is confined to sites on continental margins and in deeper waters. Moreover, hydrate formation only takes place if concentrations of hydrate-forming guest molecules exceed solubilities (Sloan and Koh, 2007) and is additionally affected by the pore water activity (Dickens and Quinby-Hunt, 1997; Lu and Matsumoto, 2005). Sulfate penetration into the sea floor promotes the anaerobic oxidation of methane (AOM) in interstitial waters in the top sediment layers (Barnes and Goldberg, 1976; Reeburgh, 1976), thus, gas hydrates are usually restricted to sediments below the sulfate zone (Bhatnagar et al., 2007; Jørgensen and Kasten, 2006). In consequence, shallow-buried hydrates (here defined as < 2.65 m below sea floor (bsf) as the maximum penetration depth of our sampling tool) in marine sediments only occur at high-intensity seepage sites, such as cold seeps or mud volcanoes (Judd et al., 2002; Judd and Hovland, 2007 and refs. therein) where they serve as control factor for the flux of LMWHC into the overlying water column.

In particular near-surface deposits play an important role for the extent of hydrate accumulations, as they can be rapidly shifted outside the hydrate stability field due to alterations in pressure-temperature (P/T) conditions, which is expected to be most intense close to the sediment – water interface, or declining hydrocarbon supply. As a result, hydrates disintegrate while releasing LMWHC masses into overlying sediments and the hydrosphere. With respect to their sensitivity to physico-chemical changes and formidable carbon storage capacity past perturbations in the global carbon cycles and climate (Beerling and Berner, 2002; Dickens, 2003; Hesselbo et al., 2000; Kennett et al., 2003), as well as sediment destabilization on continental margins (Mienert et al., 2005) were related to extensive gas hydrate dissociation. However, current estimates of global hydrate-bound carbon vary between ~0.5 to

2.5×10^9 kt (Milkov, 2004) and $\sim 56 \times 10^9$ kt (Klauda and Sandler, 2005) due to the technical efforts required for direct hydrate quantifications. Pressure sampling tools, inhibiting gas loss related to decompression, are the only means to accurately determine gas and hydrate abundances in submarine deposits (Dickens et al., 1997b; Milkov et al., 2004).

The Black Sea basin comprises the world's largest surface reservoir of dissolved methane (9.6×10^4 kt) (Reeburgh et al., 1991), which is primarily supplied from seeps and decomposing hydrates (Kessler et al., 2006). Since shallow-buried gas hydrates precipitate at areas of high methane flux from below (Bhatnagar et al., 2007; Borowski et al., 1996), we investigated an known area of intense gas seepage (Nikolovska et al., 2008) and hydrate recoveries (Klaucke et al., 2006) in the eastern Black Sea.

In 2007 we performed high-resolution pressure core sampling with our Dynamic Autoclave Piston Corer (DAPC; Abegg et al., 2008) in order to constrain calculations of gas hydrate volumes in shallow sediments for the entire Batumi seep area. In this study we present for the first time in situ hydrate and LMWHC inventories for a confined high-intensity seepage area. In addition, high resolution calculations allowed for assignment of vertical hydrate distributions and nominal gas concentrations in distinct layers of late glacial to Holocene deposits.

8.3 Geological setting

The area investigated is located on the continental slope offshore Georgia in the eastern Black Sea (Figure 8.1). This region is characterized by a series of W-E trending canyons and ridges formed by diapiric activity (Tugolesov et al., 1985), which is related to the active compressional deformation caused by the northward movement of the Arabian plate and westward movement of the Anatolian Block (Meredith and Egan, 2002). On top of such a ridge a large hydrocarbon seepage area, the Batumi seep area (Klaucke et al., 2006), is located in permanent anoxic waters in about 830 to 860 m below sea level (bsl). The area comprises several sites of focused expulsion of bubble forming free gas (Nikolovska et al., 2008) and seismic profiling showed that the distinct seepages are in most cases related to fluid migration along tectonic faults fed by free gas accumulations beneath the base of the gas hydrate stability zone (BGHS; Wagner-Friedrichs, 2007). Strong acoustic backscatter anomalies in a seafloor area of approx. 0.5 km^2 (Figure 8.1) were interpreted as shallow reflectors indicating seepage-associated features (Klaucke et al., 2006), such as gas enrichments and methane-derived authigenic carbonates. During investigations of the Batumi seep area in 2004 and 2005, shallowest hydrates in gravity cores were found at about 25 cmbsf (Klaucke et al., 2006).

8.4 Materials and Methods

An expedition (M72/3, Legs a and b) to the Batumi seep area was conducted with the R/V METEOR and the remotely operated vehicle (ROV) 'MARUM-QUEST' (MARUM, University of Bremen) in spring 2007.

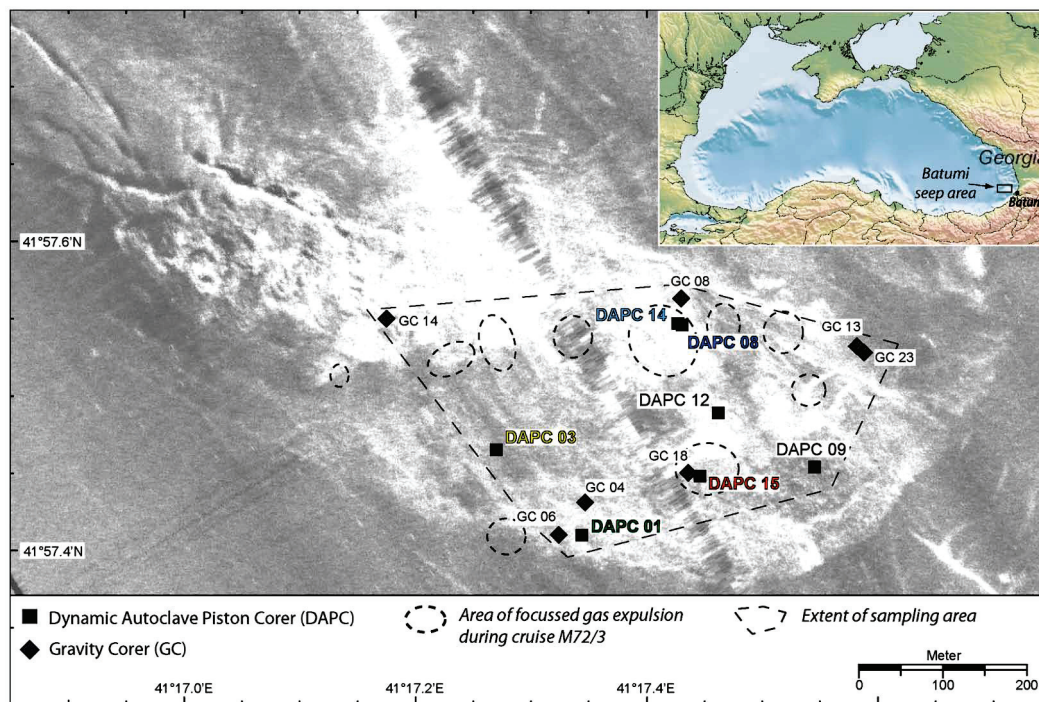


Figure 8.1: Map of the Batumi seep area indicating sampling positions of pressure cores (DAPC) and gravity cores (GC) in spring 2007. Different colors used for selected DAPC stations correspond to those in Figure 8.6. The sampled area covers about 0.243 km². Dashed circles indicate areas of focussed gas expulsion based on hydroacoustic plume imaging (Nikolovska et al., 2008).

Underneath a sidescan sonar mosaic illustrating seafloor backscatter intensities recorded in an area of about 0.5 km² seafloor in fall 2004 (adopted from Klaucke et al., 2006) is shown. High backscatter intensities interpreted as indications for intense seepage activity are displayed by lighter shades, whereas low backscatter intensities or shadows are illustrated in dark tones. The dark vertical strip is the poorly imaged zone beneath the ship's track.

Insert: Location of the Batumi seep area in the eastern Black Sea basin, off Georgia.

8.4.1 Sampling procedure

Pressurized and non-pressurized sediment cores were lifted from the seafloor (~850 m bsl) with 1 m s⁻¹, resulting in approx. 15 min recovery time. An acoustic transponder system mounted on the wire 50 m above the sampling tools was used for high-precision underwater positioning, except for station DAPC 09 (ship's position; Table 8.1).

8.4.1.1 Pressurized sediment cores

For determinations of true gas volumes in near-surface sediment, pressurized sediment cores were sampled with the Dynamic Autoclave Piston Corer (DAPC; Abegg et al., 2008), which is technically based on a conventional Piston corer (Kullenberg, 1947). The system is equipped with a gas-tight pressure chamber and a core cutting barrel (2.65 m length, liner inner diameter 8.25 cm) with a maximum core volume of 14,166 mL. The DAPC is released by a trigger weight and penetrates the seafloor in a free fall mode.

Immediately upon recovery, a PC-operated pressure sensor was connected to the DAPC pressure chamber for continuously monitoring the pressure. The gas contained in the pressure chamber was released incrementally via a 'gas manifold', which is an assembly of gas tight valves and valve-activated ports for gas sub-sampling, pressure monitoring and gas

quantification, as modified after Dickens et al. (2003). Quantification of released gas from the pressure chamber was carried out on deck at atmospheric pressure and ambient temperature (8 to 12 °C) using a 'gas catcher' consisting of two inverted plastic cylinders (Dickens et al., 2003; Heeschen et al., 2007). Repeatedly, after releasing of a certain gas volume, each time two gas-sub-samples were taken and transferred into glass serum vials. The glass serum vials were pre-filled with a sealing solution and sealed with butyl stoppers, and after introduction of the gas sampled stored at -20 °C until analysis of chemical composition and stable isotope composition of methane. Subsequent to degassing, the core liner containing the depressurized sediment core was removed from the DAPC pressure chamber for lithological descriptions.

Table 8.1: List of sediment cores taken at the Batumi seep area in spring 2007. Recovery pressure P_{rec} as maximum P at the initial stage of the degassing procedure.

Station No. GeoB	Running no.	Lat. N° (°)	Long. E° (°)	Water depth (m)	Core length (cm)	Recovery Pressure (P_{rec}) (bar)
<u>pressurized cores</u>						
11901	DAPC 01	41:57.410	41:17.344	851	264	68.3
11906	DAPC 03	41:57.465	41:17.270	843	83	64.3
11918	DAPC 08	41:57.547	41:17.427	840	233	84.4
11920	DAPC 09	41:57.454	41:17.545	844	259	71.3
11937	DAPC 12	41:57.489	41:17.462	842	41	49.3
11951	DAPC 14	41:57.546	41:17.431	840	137	80.6
11958	DAPC 15	41:57.448	41:17.446	847	146	87.3
<u>non-pressurized cores</u>						
11925	GC 04	41:57.431	41:17.347	844	215	
11927	GC 06	41:57.410	41:17.324	856	413	
11936	GC 08	41:57.563	41:17.430	844	193	
11946	GC 13	41:57.532	41:17.582	842	302	
11949	GC 14	41:57.550	41:17.175	842	n.d.	
11956	GC 18	41:57.450	41:17.436	843	96	
11975	GC 23	41:57.528	41:17.588	844	304	

DAPC: Dynamic Autoclave Piston Corer; GC: Gravity Corer; n.d. = not determined.

8.4.1.2 Non-pressurized sediment cores

Non-pressurized sediment cores for i) lithological descriptions and ii) X-ray computerized tomographic imaging were recovered using a conventional gravity corer equipped with a core cutting barrel of 3 m or 6 m length. In order to assure rapid access to hydrate pieces, plastic hoses were used as liners. For CT analysis, sediment cores recovered with PVC-liners were cut into segments and frozen in liquid nitrogen to preserve hydrate distributions and sediment texture.

8.4.2 Analysis

Chemical compositions of individual gas sub-samples were determined onboard within 48 h upon recovery with a two-channel gas chromatograph (GC; Flame Ionization Detector and Thermal Conductivity Detector). O₂ and N₂ contributed less than 2 mol-% and represented most likely artifacts introduced during the sub-sampling and analytical procedure. Calibrations and performance checks of the analytical system were conducted daily using commercial pure gas standards and gas mixtures (Air Liquide, Germany). The coefficient of variation

determined for the analytical procedure was lower than 2%. Compositions are given in mol-% assuming $\sum(C_1-C_3 \text{ LMWHC}) = 100\%$.

Stable carbon isotope signatures ($^{13}\text{C}/^{12}\text{C}$) of methane were determined at the MARUM (University of Bremen) by GC-Isotope-Ratio-Mass-Spectrometry (GC-IRMS) using a Trace GC Ultra (Finnigan) connected via a GC Combustion III line to a DELTA plus XP isotope mass spectrometer (both ThermoFinnigan). Isotopic values are reported in δ -notation in parts per mil (‰), relative to the Vienna PeeDee Belemnite (V-PDB) standard for carbon isotopes and to standard mean ocean water (SMOW) for hydrogen isotopes.

X-ray computerized tomography (CT)-scanning of a frozen core segment prepared from gravity core GC 13 was performed during the cruise as described in Abegg et al. (2007). The scanning procedure was performed with a mobile General Electric (GE) Pro Speed SC Power CT scanner analyzing 1 mm slices with a 512×512 data matrix.

8.4.3 Calculations

8.4.3.1. Nominal gas in situ volumes and methane concentrations

Nominal gas in situ volumes confined to the Black Sea stratigraphic Units 1 and 2 (V_{gU1} , V_{gU2}) were calculated for each DAPC core using total gas volumes (V_{gt}) relative to the respective volumes of Unit 1 and Unit 2 sediments in DAPC 09 and 12. Those two cores were devoid of Unit 3 sediments and also lacked substantial hydrate amounts (see Figure 8.2b, Figure 8.4).

The specific gas volumes contained in Unit 1 and Unit 2 (V_{gU1} , V_{gU2}) as well as potential occurrences of isolated gas hydrate layers in deeper Unit 2 sections could not be resolved. Yet, specific nominal gas (nC_{gUx}) and methane (nC_{CH4Ux}) concentrations in Unit 1 and 2 sediments were presumed to be similar in all cores, irrespective of their specific thicknesses, depths of the sulfate zone, and distance to discrete seepages. Individual gas concentrations in Unit 3 (V_{gU3}) of each core were calculated according to

$$V_{gU3} = V_{gt} - (V_{gU1} + V_{gU2})$$

We did not analyze for e.g., H_2S , CO , and noble gases, which are most likely present in the gas in minor amounts. As an educated guess we therefore suppose 97 vol.-% of the released gas to constitute of methane.

Unit-specific pore fluid masses (m_{pfUx}) were calculated using unit-specific sediment volumes (V_{sUx}) as well as average sediment porosities (ϕ_{Ux}), and pore fluid in situ densities (ρ_{pfUx}), respectively, adopted from Haeckel et al. (2008). For calculations of unit-specific methane in situ concentrations (nC_{CH4Ux}), unit-specific methane masses (m_{CH4Ux}) were divided by the respective pore fluid masses (m_{pfUx}).

8.4.3.2. Theoretical methane in situ solubilities

Theoretical unit-specific methane in situ solubilities were calculated with regard to absence (s_{gp} ; Duan and Mao, 2006) or presence of hydrates (s_{ghp} ; Tishchenko et al., 2005).

8.4.3.3. Hydrate volumes

The concentration of hydrate-bound and/or free methane, i.e. concentration surpassing equilibrium (C_{CH4hb}) in Unit 2 and 3 of each core, was calculated by subtracting the concentration of dissolved CH_4 ($S_{ghp} = C_{CH4diss}$) from the unit-specific methane concentration (nC_{CH4Ux}) according to Dickens et al. (1997). Since the study area is located within the gas hydrate stability zone (GHSZ; Figure 8.5), this non-dissolved methane ($C_{CH4hbUx}$) is considered to predominantly exist in the hydrate phase, although emissions of bubble-forming free gas from the into bottom waters were observed as well. The hydrate fraction occupying the pore space of Units 2 and 3 in each pressure core were calculated by converting $C_{CH4hbUx}$ into hydrate volumes according to Heeschen et al. (2007).

8.4.3.4. Phase boundaries of gas hydrate stabilities

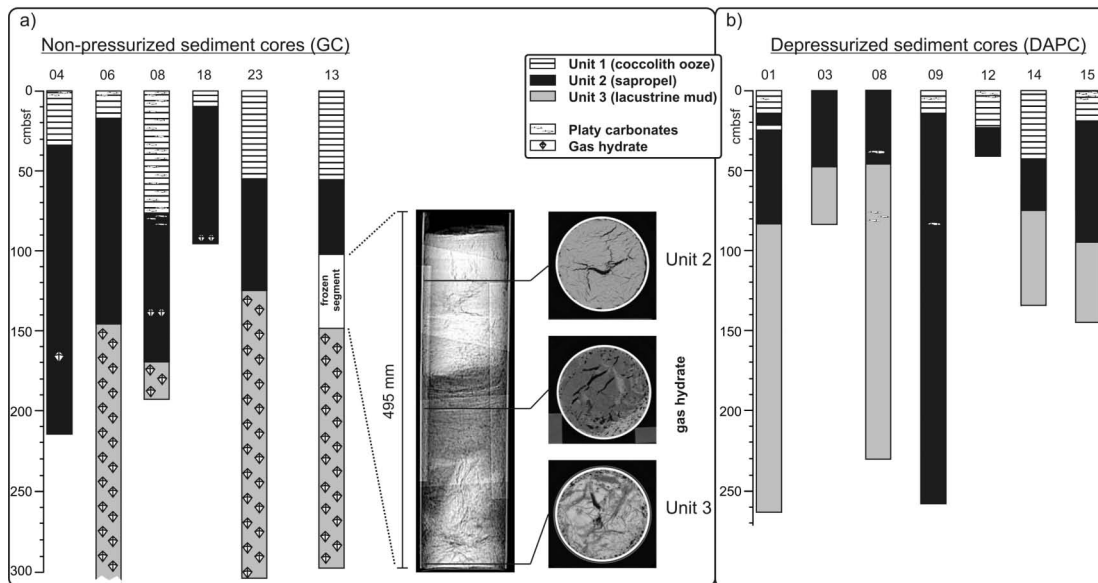
A phase diagram of gas hydrate structure I (sl) was calculated using the CSMGem software package (Sloan and Koh, 2007) and Heriot-Watt-Hydrate software (Masoudi and Tohidi, 2005; Østergaard et al., 2005) loaded with LMWHC compositions (see section 8.5.2.) and average interstitial water salinities for late glacial to Holocene deposits deduced from Leonov (2005) and Manheim and Chan (1974). Prevalence of sl hydrate at the Batumi seep area was inferred from the LMWHC composition in the hydrate phase and confirmed by cryo X-ray diffractometry (unpublished results).

8.5 Results and Discussions

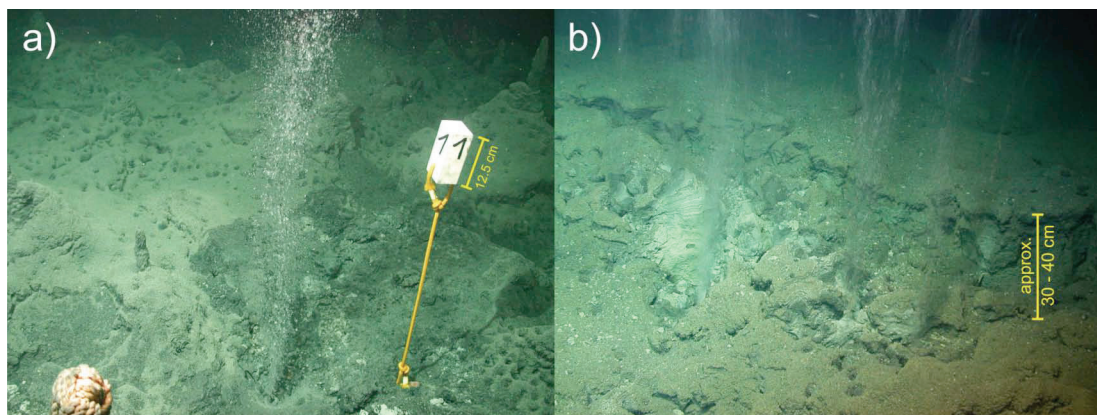
8.5.1 Composition of sediments

Sediments retrieved by both DAPC and GC were used for lithological descriptions. Core lengths varied between 96 and 413 cm for gravity cores (Figure 8.2a) and between 41 and 264 cm for depressurized DAPC cores (Figure 8.2b), respectively. The cores comprised the typical basinal succession of Holocene hemipelagic sediments, i.e. laminated coccolith ooze (Unit 1; Ross and Degens, 1974) and sapropelic sediments (Unit 2), overlying late glacial to early Holocene lacustrine mud (Unit 3). Sporadic but vigorous seepage activity is likely to cause the considerable spatial variations in the depository regime since at least 8.0 kyrs (Lamy et al., 2006) indicated by strongly differing recoveries of the marine Units 1 and 2, as well as a rough local seafloor topography observed during ROV-based visual documentation (Figures 8.3a and 8.3b).

Irrespective of specific thicknesses of the overlying sediments, near-surface hydrates confirming high methane flux from below (e.g., Bhatnagar et al., 2008; Tréhu et al., 2006b) in the Batumi seep area, were found disseminated in high density in Unit 3 of gravity cores (Figure 8.2a). In GC 04 and 08, which were taken away from sites of focused seepage, hydrates occurred additionally in deeper sections of Unit 2, where they formed distinct massive layers. However, in most cores (GC 06, 13, 18 and 23) hydrates appeared near the base of the sapropel. Such a vertical hydrate distribution is corroborated by computerized tomography imaging (see core segment GC 13), and by the observation that highest volumetric gas/sediment ratios were obtained for cores containing relatively high portions of Unit 3 material (Figure 8.4, Table 8.2), as well as by pore fluid chlorinity-based modeling results (Haeckel et al., 2008).



Figures 8.2a and b: Lithological compositions of non-pressurized sediment cores (GC) and pressurized sediment cores (DAPC) from the Batumi seep area. Assignments of lithological units adopted from Ross and Degens (1974). Gas hydrates present as distinct massive layers in Unit 2 and disseminated in Unit 3. For core GC 13 taken less than 15 m apart from GC 23, a frozen core segment (98 to 147.5 cmbsf) was visualized by computerized X-ray tomography. Note the absence of sediments belonging to Unit 3 in DAPC cores 09 and 12. Dark grey = gas hydrates; light grey = sediment devoid of gas hydrate. Hydrate is present in high density in the depths interval from 116 to 128 cmbsf covering the transition from Unit 2 to Unit 3. Orientated voids in sediments and gas hydrates are illustrated in darkish colors.



Figures 8.3: Sea floor impressions from the Batumi seep area in the eastern Black Sea during ROV observations in spring 2007. **(a)** Intense focused gas stream supplying bubbles of variable size from a cm- to dm-sized orifice within the rugged seafloor. Smaller potential gas outlets exist right in the front and in the background. Left in front a sampling tool's handle operated by the ROV manipulator is observable. For scale refer to marker buoy no. 1 (12.5 cm in height) in the right section of the picture. **(b)** Sharp sediment rupture of approx. 30 to 40 cm in height, which was potentially caused by hydrate detachment and uncovered strongly disturbed sediments. Packages of layered sediments are discernible at the left section of the rupture. Curtains of tiny bubbles are ejected into bottom waters from several outlets at the base of the rupture.

8.5.2 Gas volumes and hydrocarbon compositions

Gas in situ volumes were gathered for seven DAPC cores and yielded between 3.7 and 20.3 L gas per L wet sediment (Table 2). The highest volumetric gas/sediment ratio was determined for core DAPC 08, which was taken close to focused seepage (Figure 8.1) and

contained highest portions of Unit 3 material. Notably, core DAPC 14 taken at the same site close to DAPC 08, yielded only 14.1 L gas per L sediment, because less Unit 3 material, which supposedly included highest specific gas concentrations was recovered (Figure 8.4). Average LMWHC compositions of gas samples taken during degassing of DAPC cores were dominated by methane (99.9601 mol-% of C₁ to C₃ LMWHC, followed by ethane (0.0390 mol-%) and propane (0.0009 mol-%; Table 3). Methane stable isotopic values ($\delta^{13}\text{C} \sim -51$ VPDB; $\delta^2\text{H} \sim -152$ to -190 SMOW) and the LMWHC composition ($\text{C}_1/(\text{C}_2 + \text{C}_3) = 2108$ to 3383) suggest that the near-surface gas at the Batumi seep area is supplied from both biogenic and thermogenic sources (Whiticar, 1999).

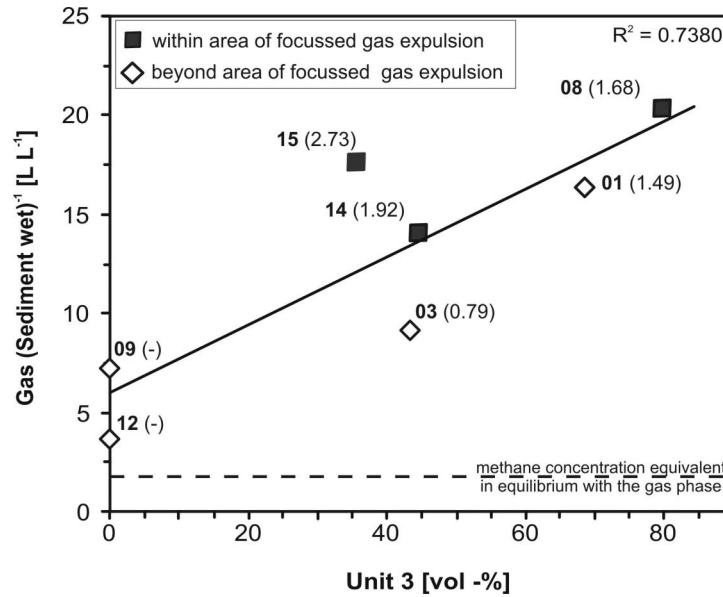


Figure 8.4: Volume portion of Unit 3 material in pressure cores vs. volumetric gas/sediment ratio. Numbers in bold denote DAPC station numbers, whereas numbers in brackets indicate nominal CH₄ concentrations in Unit 3 pore space (in mM). ‘Methane concentration equivalent’ in equilibrium with the gas phase $\approx 1.8 \text{ L}_{\text{gas}} (\text{L}_{\text{wet sediment}})^{-1}$. Volumetric gas/sediment ratios exceeding the methane concentration equivalent indicate hydrate precipitates in the core.

Table 8.2: Specifics of pressure cores recovered by DAPC from the Batumi seep area. Total core volume [V_{st}] after gas release, total accumulated gas volumes [V_{gt}], calculated volumetric gas / sediment ratios [V_{gt} / V_{st}], and specific wet sediment volumes of lithological Units [V_{SUx}].

Pressure core	Vol. core	Vol. gas	Vol. gas /	Vol. sediment	Vol. sediment	Vol. sediment
	V _{st} (mL)	V _{gt} (mL)	Vol. sediment	Unit 1	Unit 2	Unit 3
		released *)	V _{gt} / V _{st} (L / L)	V _{SU1} (mL)	V _{SU2} (mL)	V _{SU3} (mL)
DAPC 01	14 112	231 200	16.4	801.8	3635.0	9675.6
DAPC 03	4437	40 700	9.2	n.p.	2512.4	1924.4
DAPC 08	12 455	253 200	20.3	106.9	2405.5	9942.8
DAPC 09	13 845	100 550	7.3	748.4	13 069.8	n.p.
DAPC 12	2192	8000	3.7	1229.5	962.2	n.p.
DAPC 14	7323	103 250	14.1	2245.2	1817.5	3260.8
DAPC 15	7805	137 450	17.6	1069.1	3955.8	2779.7

n.p. = not present

*) total gas volumes include sum of gas and sediment–water suspension extruded through tubings of the degassing manifold

Table 8.3: Average proportions of C₁ to C₃ hydrocarbons (mol-% of C₁ to C₃) and molecular ratios in gas released from pressure cores taken at the Batumi seep area.

Pressure core	C ₁	C ₂	C ₃	C ₁ / C ₂	C ₁ / C ₃
DAPC 01	99.9656	0.0337	0.0007	2967	141 550
DAPC 03	99.9519	0.0474	0.0007	2108	144 813
DAPC 08	99.9693	0.0296	0.0012	3383	85 597
DAPC 09	99.9543	0.0448	0.0009	2231	116 839
DAPC 12	99.9571	0.0415	0.0014	2407	73 896
DAPC 14	99.9565	0.0427	0.0008	2343	119 153
DAPC 15	99.9661	0.0330	0.0009	3026	110 186
mean	99.9601	0.0390	0.0009	2638	113 148

8.5.3 Gas hydrate stability fields

Calculations of phase boundaries strongly suggest that gas hydrate structure I (sI) is the stable hydrate structure at the Batumi seep area. The phase diagram for sI hydrates shown in (Figure 8.5) demonstrates that the study area is well located within the hydrate stability field. Parameters determined in spring 2007 (R/V meteor cruise M72/3) were: bottom water temperature 8.96 °C; salinity 20.97; gas chemical composition as stated below. For assessing the base of the gas hydrate stability zone (BGHSZ), we considered a geothermal gradient of 40 mK m⁻¹ (Kutas et al., 2004) as more accurate temperature data are unavailable for the region investigated to the best of our knowledge. Based on these assumptions the BGHSZ at the Batumi seep area was calculated to be located in approx. 60 mbsf (Figure 8.5). The pore water salinity in general decreases with increasing depth from sea bottom towards the lacustrine sediments belonging to Unit 3 (Leonov, 2005; Manheim and Chan, 1974), which should result in an increase in pore water activity and hydrate stability with depth (Dickens and Quinby-Hunt, 1997) for these strata.

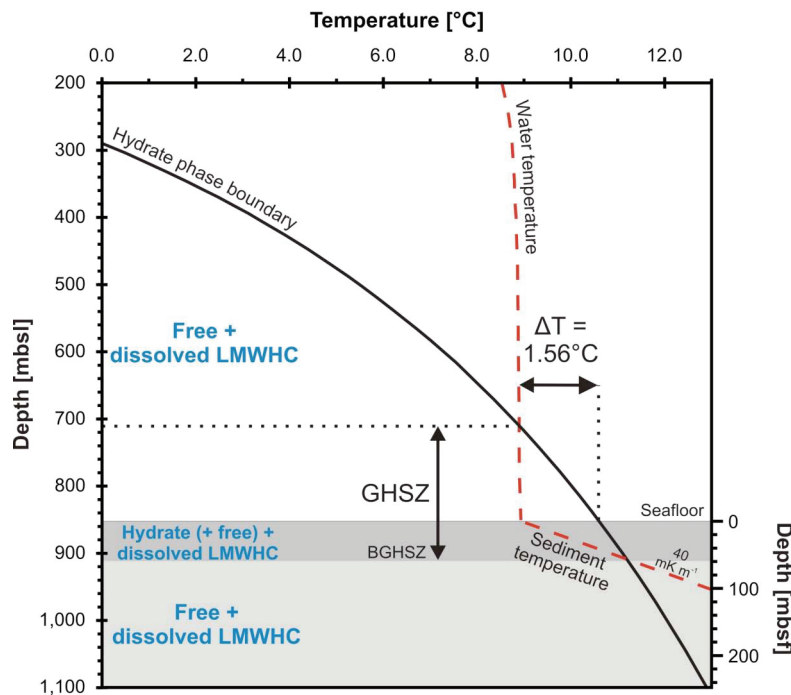


Figure 8.5: Phase boundaries of nominal gas hydrate stabilities calculated for structure I gas hydrate at the Batumi seep area.

8.5.4. Methane masses in sediments

In order to evaluate total LMWHC masses stored in Batumi seep near-surface deposits we calculated quantities of both dissolved and hydrate-bound methane in the specific lithological units. Nominal methane in situ concentration in Unit 1 ($nC_{CH_4U1} = 26.6$ mM) was lower than the theoretical methane solubility in equilibrium with the gas phase (108.5 mM), while the corresponding value in Unit 2 ($nC_{CH_4U2} = 460.8$ mM) exceeded the methane equilibrium concentration in the presence of a hydrate phase (93.9 mM) considerably, substantiating hydrate occurrences in Unit 2. Remarkably, nC_{CH_4U1} is at least by three orders of magnitude higher than the CH_4 concentration between approx. 10 to 13 μ M measured by ex situ approaches for near-bottom waters in the central Black Sea (Kessler et al., 2006; Reeburgh et al., 1991) and interstitial waters in surface sediments from deep non-seep sites in the western Black Sea basin (Jørgensen et al., 2001; Schubert et al., 2006).

The occurrence of authigenic carbonates (Figure 8.2a) as by-product of the sulphate-dependent AOM (Peckmann et al., 2001; Ritger et al., 1987) indicates (sub-)recent methane consumption in top sediments. Those carbonates were preferentially found in Unit 1 material and, less frequently, in Unit 2 down to about 80 cmbsf. As the sulfate zone currently appears to be restricted to the upper 25 cm subbottom depth (Haeckel et al., 2008), which again supports high methane flux from below (Borowski et al., 1996; Castellini et al., 2006), AOM does not take place in deeper Unit 2 sections, but results in reduction in methane concentrations down to nC_{CH_4U1} values below the theoretical methane solubility. Taking these features into account, the resulting steep horizontal gas concentration gradients between the gas-charged seep deposits and adjacent non-seep sediments along with high densities of seep-associated methane-derived authigenic carbonates are an explanation for the sharp boundaries of backscatter anomalies reflecting the Batumi seep area (Figure 8.1).

8.5.5 Unit-specific methane concentrations

Individual methane volumes attributed to Unit 1 and Unit 2 material ($nV_{CH_4Ux} = nC_{CH_4Ux} \times V_{pfUx}$) in each pressure core were subtracted from total core methane volumes (V_{CH_4Ut}), to obtain methane in situ concentrations entailed in Unit 3 (nC_{CH_4U3}). Values for nC_{CH_4U3} ranged between 1,492 and 2,728 mM (Table 4), except for core DAPC 03 (794 mM), and highest concentrations were observed for cores retrieved from sites close to focused seepage (DAPC 08, 14, 15). The nC_{CH_4U3} of the very adjacent cores DAPC 08 and 14 were similar (Figure 8.1; Figure 8.6), although different volumetric gas/sediment ratios were released during degassing, corroborating the reliability of our approach. nC_{CH_4U3} values may be over-estimated to some extent as we cannot distinguish isolated hydrate layers in Unit 2, which were observed in three out of six gravity cores. However, it is consequent to assume that the nominal excess methane in Unit 2 ($C_{hbU2} = 367$ mM) and Unit 3 (Figure 8.6; Table 4) calculated in this study is predominantly derived from hydrates, which were found in all gravity cores in depths > 90 cmbsf (Figure 8.2a). However, it also cannot be excluded that subordinate volumes of the LMWHC released from the pressure cores initially occurred in the free gas phase, as virulent gas bubble emissions from the seafloor were documented during ROV dives.

nC_{CH_4U3} values in the pressure cores from the Batumi seep area are in the same range as maximum values reported for much deeper sediments from the Blake Ridge (2.0 M; Dickens

et al., 1997b), Peru Trench (0.4 M; Dickens et al., 2003), Hydrate Ridge (3.1 M; Milkov et al., 2003b), and Cascadia Margin (3.8 M; Riedel et al., 2006). Other than deep subsurface sediments, shallow deposits in our study area are strongly affected by steep vertical concentration gradients due to the anaerobic oxidation of hydrocarbons (Krüger et al., 2005) and upward diffusion into the water column (Kessler et al., 2006; Reeburgh et al., 1991). Additionally, nC_{CH_4U3} in most of our cores was higher than methane in situ concentrations calculated for shallow sediment underneath the sulfate zone from two sites at the Northern Gulf of Mexico ($\leq 1.0 \text{ mol kg}^{-1}$; Heeschen et al., 2007). This indicates that at the Batumi seep area comparably high LMWHC amounts are stored in near-surface hydrates.

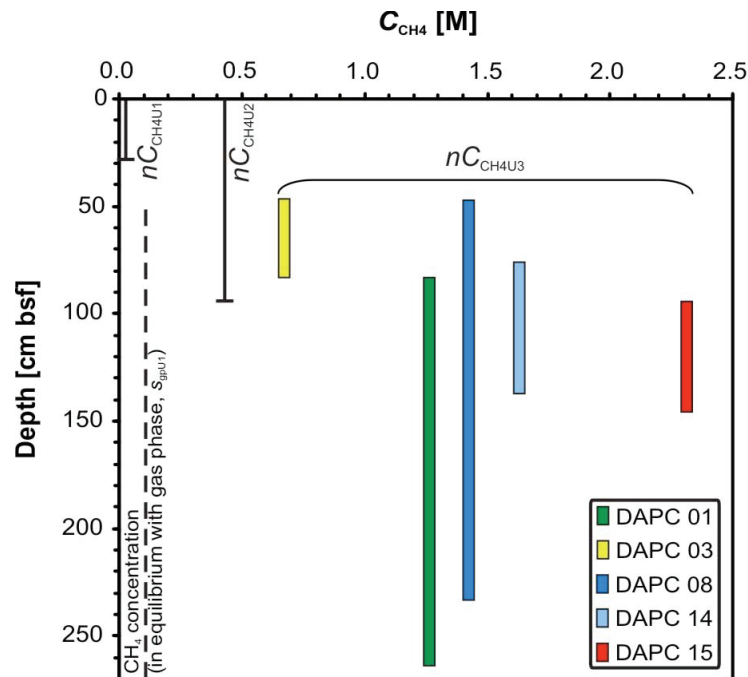


Figure 8.6: Nominal methane in situ concentrations nC_{CH_4U3} in Unit 3 sediment segments (colored bars) as function of depth. Calculations for DAPC 08 and 14 (very close to each other) revealed similar Unit 3-specific methane concentrations irrespective of different core recoveries and thicknesses of Units 1 to 3. Bar length nC_{CH_4U1} (26.6 mM) and nC_{CH_4U2} (460.8 mM) indicates maximum thickness of Unit 1 and Unit 2 in pressure cores. CH_4 concentration in equilibrium with gas phase, $s_{gpU1} = 108.5 \text{ mM}$.

8.5.6 Volumes of shallow gas hydrates

Calculations of unit-specific hydrate fractions using excess methane concentrations in Unit 2 and 3 revealed that hydrates filled about 6.0% of pore volume (pv) in Unit 2 and between 11.5%pv (DAPC 03, off area of focused gas ebullition) and 43.2%pv (DAPC 15, within area of focused gas seepage) in Unit 3 (mean 26.7%, $n = 5$; Table 4). hydrate densities in Unit 3 calculated for our pressure cores meet those reported for sections below the sulfate zone in three near-surface sediment cores recovered in 2005 (Haeckel et al., 2008). Average hydrate fractions obtained for Unit 3 sediments in our pressure cores were higher than those reported from pressure coring at other hydrate-bearing sites, like Hydrate Ridge (mean $\sim 11\%$ pv; Milkov et al., 2003b), the Northern Gulf of Mexico (max. 18%pv; Heeschen et al., 2007), or Blake Ridge (max. 9%pv; Dickens et al., 1997b). With respect to the presence of hydrates in all gravity cores $> 90 \text{ cmbsf}$ and the relatively high methane concentrations, it can be concluded that near-surface hydrates in high density in Unit 3 are characteristic for

the Batumi seep area. Such hydrate accumulations require substantial LMWHC volumes exceeding those being dissolved in interstitial water (Haeckel et al., 2004) and, consequently, resulted from hydrocarbons in the gas phase, which likely migrated upward from greater depths through the GHSZ.

Table 8.4: Total volume (V_{CH4t}), nominal methane in situ concentrations [nC_{CH4U3}] and concentrations of excess methane [C_{hbU3}] in Unit 3, as well as contents of gas hydrates in Units 2 and 3.

Pressure core (DAPC)	Unit		01	03	08	09	12	14	15	mean
Volume CH₄*)	V_{CH4t}	mL	224 264	39 479	245 604	97 534	7760	100 153	133 327	
Conc. CH₄ Unit 3 **)	nC_{CH4U3}	mmol kg ⁻¹	1462.5	778.3	1645.9	n.p.	n.p.	1885.2	2674.4	
Conc. CH₄ Unit 3 **)	nC_{CH4U3}	mM	1491.9	794.0	1679.0	n.p.	n.p.	1923.1	2728.3	
Conc. excess CH₄ Unit 3 ***)	$nC_{hbCH4U3}$	mmol kg ⁻¹	1369.7	685.5	1553.1	n.p.	n.p.	1792.4	2581.6	
Conc. excess CH₄ Unit 3	$nC_{hbCH4U3}$	mM	1397.3	699.3	1584.4	n.p.	n.p.	1828.5	2633.6	
Mass excess CH₄ Unit 2	$m_{hbCH4U2}$	g	15.40	10.65	10.19	55.50	4.08	7.70	16.76	17.18
Mass excess CH₄ Unit 3	$m_{hbCH4U3}$	G	132.30	13.17	154.16	n.p.	n.p.	58.35	71.64	85.92
Volume GH Unit 2	V_{GHU2}	L	0.157	0.109	0.104	0.567	0.042	0.079	0.171	
Volume GH Unit 3	V_{GHU3}	L	1.352	0.135	1.575	n.p.	n.p.	0.596	0.732	
Fraction GH Unit 3	f_{GHU3PV}	% pv	22.9	11.5	26.0	n.p.	n.p.	30.0	43.2	26.7
Fraction GH Unit 3	f_{GHU3CV}	% cv	14.0	7.0	15.8	n.p.	n.p.	18.3	26.3	16.3

GH = gas hydrate; n.p. = not present; pv = pore volume, cv = core volume

*) assuming a CH₄ fraction of 97 vol-% of the entire gas (see section 3.3.1)

**) Nominal CH₄ in situ concentrations in Units 1 and 2 (nC_{CH4U1} , nC_{CH4U2}) based on gas volumes of DAPC 09 and 12 devoid of Unit 3 (see Table 2; Figure 4).

***) Excess CH₄ concentration (C_{hbUx}) indicates the difference between nC_{CH4Ux} and s_{ghpUx} . Nominal excess CH₄ concentrations in sediments belonging to Unit 2 (C_{hbU2}) were 359.3 [mM], resulting in nominal hydrate fractions of $f_{GHU2PV} = 6.0\%$ of pore volume and $f_{GHU2CV} = 4.3\%$ of core volume, respectively.

8.5.7 Hydrate-bound low-molecular weight hydrocarbons in shallow gas hydrates of the Batumi seep area

Overall volumes of C₁ to C₃ hydrocarbons and gas hydrates were calculated using average thicknesses of Unit 1 (0 to 30 cm) and Unit 2 (30 to 106 cm) deposits and assuming that

8. High-intensity gas seepage feeds shallow gas hydrate deposits in the eastern Black Sea

the remaining sediment recovered belonged to Unit 3 (106 to 265 cmbsf; maximal core recovery). Additionally, minimum, mean, and maximum concentrations of hydrate-bound methane (C_{hbUx} ; Table 5) and molecular ratios (C_1/C_2 ; C_1/C_3 ; Table 3) were considered. We extrapolate that on average a total of 7.501 kt of C_1 to C_3 hydrocarbons is accumulating in near-surface deposits of the sampled area (0.234 km² seafloor area; 569,835 m³; Table 8.5, Figure 8.1). For the seafloor area characterized by high-backscatter (0.5 km² seafloor area; 1,172,500 m³) C_1 to C_3 hydrocarbons in surface sediments would account for 15.435 kt. Hydrocarbons bound in shallow hydrates account for about 6.921 (14.241) kt methane, 2.624 (5.398×10^{-3}) kt ethane, and 0.061 (0.126×10^{-3}) kt propane. This amount of hydrate-bound methane is about 350 times the annual flux of dissolved methane calculated for a selected central section of the Batumi seep area (0.31 km²; Haeckel et al., 2008) and approx. 0.3% of methane considered to be annually emitted from Black Sea seeps and decomposing hydrates (Kessler et al., 2006).

Table 8.5: Hydrate-bound and overall C_1 to C_3 -hydrocarbons stored in Batumi seep area surface sediments. The sampled area covers about 0.234 km² of seafloor while the area characterized by backscatter anomalies includes 0.5 km² seafloor (Klaucke et al., 2006).

Seafloor area	Hydrate-bound hydrocarbons				Total hydrocarbons			
	CH ₄ (kt)	C ₂ H ₆ (*10 ⁻³ kt)	C ₃ H ₈ (*10 ⁻³ kt)	$\Sigma(C_1-C_3)$ (kt)	CH ₄ (kt)	C ₂ H ₆ (*10 ⁻³ kt)	C ₃ H ₈ (*10 ⁻³ kt)	$\Sigma(C_1-C_3)$ (kt)
Sampled area 569,835 m³								
Unit 1	n.p.	n.p.	n.p.	n.p.	0.026	0.010	0.000	0.026
Unit 2	0.785	0.298	0.007	0.785	0.986	0.374	0.009	0.986
Unit 3 (min)	2.635	0.999	0.023	2.636	2.989	1.133	0.026	2.990
Unit 3 (mean)	6.136	2.326	0.054	6.138	6.487	2.459	0.057	6.490
Unit 3 (max)	9.922	3.761	0.088	9.926	10.270	3.893	0.091	10.274
Total (min)	3.420	1.296	0.030	3.421	4.000	1.516	0.035	4.002
Total (mean)	6.921	2.624	0.061	6.924	7.499	2.843	0.066	7.501
Total (max)	10.707	4.059	0.095	10.711	11.282	4.277	0.100	11.286
'Backscatter' area 1,172,500 m³								
Unit 1	n.p.	n.p.	n.p.	n.p.	0.054	0.020	0.000	0.054
Unit 2	1.615	0.612	0.014	1.616	2.028	0.769	0.018	2.029
Unit 3 (min)	5.421	2.055	0.048	5.423	6.150	2.331	0.054	6.152
Unit 3 (mean)	12.625	4.786	0.112	12.630	13.348	5.060	0.118	13.353
Unit 3 (max)	20.416	7.739	0.180	20.424	21.132	8.011	0.187	21.140
Total (min)	7.037	2.667	0.062	7.039	8.231	3.120	0.073	8.234
Total (mean)	14.241	5.398	0.126	14.246	15.429	5.849	0.136	15.435
Total (max)	22.031	8.352	0.195	22.040	23.213	8.800	0.205	23.222

n.p. = not present

8.5.8 Geological implications

According to hydrate dissociation temperature (T_{diss}) and pressure (P_{diss}) calculated for sl hydrates at the Batumi seep area (Figure 8.5), a warming of near-surface sediments by more than 1.56 °C, or a decrease of in situ hydrostatic pressure ($P_{hydrostat}$) by more than 13 bars, or a combination of both in lesser extent would be required to shift the GHSZ and to induce hydrate dissociation. Paleoenvironmental investigations suggested that bottom water temperature changes in the Black Sea deep basin were reduced to approx 1-2 °C even during

severe climate shifts associated with the deglacial and early Holocene (Bahr et al., 2008). Thus, in the absence of major variation in the Black Sea level, stable P/T-conditions at the seafloor can be assumed for the mid and late Holocene. On the other hand, glacial-interglacial sea level variations with a proposed amplitude of up to 155 m (Ryan et al., 2003) and subsequent changes in bottom water chemistry (Bahr et al., 2008), related to the evolution from a freshwater lake to a marine-influenced marginal sea might have severely affected hydrate stability at the Batumi seep area.

Even under stable environmental conditions, seafloor detachment and upfloating of hydrate pieces as observed at Bush Hill, Northern Gulf of Mexico, and the Hydrate Ridge, Cascadia Margin, can transfer considerable LMWHC quantities into the hydrosphere and potentially to the atmosphere (MacDonald et al., 1994; Suess et al., 2001). Abrupt rafting of near-surface hydrate clumps is likely to contribute to the rough topography observed during Batumi seep seafloor documentation (Figures 8.3a and 3b). LMWHC export from hydrate detachments is hardly quantifiable, but should play a prominent role for the Black Sea carbon budget, as numbers of seep sites are documented within the GHSZ. These are characterized by strong backscatter anomalies (Figure 8.1; Klauke et al., 2006) indicating gas-laden near-surface sediments. As shown here, the correlation of true LMWHC inventories in shallow deposits and seafloor hydroacoustic anomalies serves as a model for interpreting backscatter maps from other LMWHC emitting sites.

The copious hydrate density and the continuing gas discharge are likely to induce a near-surface self-sealing process and to promote episodic upfloating of hydrate masses. The loss is counterbalanced by the formation of fresh hydrates sourced by diffusion from below and bubble dissolution (Haeckel et al., 2008) recharging the deposits. Smaller hydrate crystal sizes compared to those found at Hydrate Ridge indicate a relatively short residence time of LMWHC in the hydrate phase (Chapter 4).

Based on the exceptionally high gas hydrate concentrations found in the shallow subsurface of the Batumi seep area it is likely that the total amount of potentially labile shallow hydrate deposits in the Black Sea and elsewhere are considerably underestimated since the shallow gas hydrate inventory at other high-intensity seepage sites has not been comprehensively accessed yet. This type of geological settings might therefore represent a dynamic hydrocarbon pool of far bigger importance for the biogeochemical carbon cycle than estimated so far.

8.6 Conclusions

Pressure core sampling at a restricted area in the eastern Black Sea, the Batumi seep area, provided new data with respect to vertical distributions of near-surface gas hydrate, their stability and dynamic response to environmental changes, and total amounts of hydrate-bound hydrocarbons:

1. Sediments sampled at the Batumi seep area within the gas hydrate stability zone (GHSZ) belonged to the Holocene to late glacial Black Sea Units 1 to 3. Gas hydrates in gravity cores occurred in deeper sections of Unit 2 as massive aggregates and were finely disseminated over the entire Unit 3. X-ray computerized tomography scanning on a frozen core segment illustrated dense hydrate accumulations close to the Unit 2 – Unit 3.

2. Methane in situ concentrations in near-surface sediments were obtained by pressure core sampling and quantitative degassing. Nominal methane concentrations calculated for the distinct Black Sea units revealed steep concentration gradients with concentrations exceeding solubilities in Unit 2 and 3 in accord with the observed presence of hydrates in these units. Although anaerobic oxidation of hydrocarbons is likely to proceed in top sediments, strong backscatter anomalies as reported earlier (Klaucke et al., 2006) from this sites are most probably caused by elevated gas concentrations along with the presence of methane-derived authigenic carbonates.

3. To the best of our knowledge, total masses of hydrate-bound gases in near-surface deposits of a confined seepage area are presented for the first time. In the uppermost sediment body of the Batumi seep area (0.5 km² seafloor area; 0 to 265 cmbsf; 1,172,500 m³) about 14.241 kt of methane, 5.398 t of ethane, 0.126 t of propane, corresponding to approx. 10.7 kt of hydrate-bound carbon are currently accumulating. Unit-specific calculations of nominal hydrate volumes revealed that pore volume in Unit 2 is filled by about 6% hydrate while the pore volume in Unit 3 is occupied by 27% hydrate. Such high hydrate densities are fuelled by light hydrocarbons in the gas phase passing through the GHSZ.

4. Hydrate-bound methane constituted > 99.96 mol-% of C₁ to C₃ hydrocarbons. Stable carbon and hydrogen isotopic compositions of methane ($\delta^{13}\text{C-CH}_4 \sim -51$ VPDB; $\delta^2\text{H-CH}_4 \sim -152$ to -190 SMOW) and molecular compositions ($\text{C}_1/\text{C}_{2+} = 2638$) point to admixture of hydrocarbons supplied from biogenic and thermogenic sources.

5. Phase calculations indicated preferential precipitation of hydrate structure sI at the Batumi seep area. At this site, the hydrostatic pressure P_{hydr} is about 13 bars below dissociation pressure P_{diss} for sI hydrates and bottom water temperature T_{bw} is about 1.56 °C lower than dissociation temperature T_{diss} . Hence, short-term changes of P/T-conditions shifting the Batumi seep area in about 840 m bsl off the GHSZ are not likely to occur under present conditions but might be of relevance on glacial/interglacial timescales.

6. Episodic detachment of hydrate chunks is considered to account for the rugged seafloor topography. This process along with rapid hydrate floating towards the sea surface, as already observed in other regions, might provide an effective mechanism for transferring light hydrocarbons including methane to the atmosphere.

Acknowledgments

We thank the captain and crew of R/V METEOR cruise M72/3 for their excellent support. We are grateful for technical support by H.-J. Hohnberg, A.H. Mai, K. Dehning, G. von Halem (MARUM, Bremen), E. Kozlova (MSU, Moscow, Russia), J. Rethemeyer, S. Kusch (AWI, Bremerhaven), and C. Graef. Comments by H. Sahling (MARUM) greatly improved the quality of an earlier version of the manuscript. This is contribution GEOTECH-XXX of the R&D program GEOTECHNOLOGIEN funded by the German Ministry of Education and Research (BMBF) and the German Research Foundation (DFG), collaborative project METRO (grant 03G0604A), and through DFG-Research Center / Excellence Cluster "The Ocean in the Earth System". S.A.K. thanks the GLOMAR graduate school and the Vollkammer Scholarship for financial support.

CHAPTER 9

CONCLUSIONS AND PERSPECTIVES

9.1 Conclusions

The presented thesis contributes to the understanding of gas hydrates as minerals at high gas flux sites in marine environments. It shows that the microstructure of gas hydrates is affected and in some cases constrained by controls which are diagnostic for the respective geological setting. Five important outcomes on submarine gas hydrate occurrences are addressed.

9.1.1 sl/sII structure co-occurrence

The co-occurrence of two structures can be an energetically favored state of gas hydrates in nature as shown from the hydrates at the Chapopote asphalt volcano. Direct crystallization into sl/sII is kinetically advantageous as one additional degree of freedom is provided during the nucleation of three cage types: the SC (the same both for sl and sII), the LC-sl and the LC-sII. The availability of three instead of two cage types could also be relevant during rapid formation of gas hydrates at other high gas flux seepage sites. However, the preferred formation of sII hydrate from C_2 — C_5 hydrocarbons seems to be a key factor in the permanent coexistence of sl and sII. A closed system or at least an impermeable layer provides the necessary environment for the relative depletion and enrichment of the guests for two hydrate structures. If the gas, from which the coexistence emerges, occurs as bulk gas, de-mixing into two structures is likely. Intrusion of many gas bubbles into a cavity results in structure coexistence if the bubbles are coated by hydrate skins and crystallize independently from other bubbles as single hydrate reactors.

It is quite possible that crystal structures co-occur at more geological locations. Such locations need to be thermogenic seeps, characterized by C_1 — C_5 hydrocarbon seepage and impermeable surface layers. At Chapopote both structures are within hydrate stability. Similar conditions are not given at the Bush Hill in the northern GOM, because the site conditions are outside the GHSZ of methane dominated sl hydrates. Therefore sII is the prevailing hydrate structure at Bush Hill. The presented results show that hydrate occurrence at thermogenic gas seeps are more complex than previously thought. Structure coexistences should be considered in future quantifications of gas hydrate masses of thermogenic hydrocarbon seeps.

9.1.2 Relation between the gas chemical composition, crystallographic structure and microstructure

Relatively large hydrocarbon guests such as C_3H_8 or C_4H_{10} which are built into sII have a lower vapor pressure compared to smaller molecules and less subcooling is required for hydrate nucleation from those gases. This thesis shows that this is reflected in the microstructural appearance of the hydrate surfaces, as sII hydrates formed from methane and significant portions of C_2 through C_4 hydrocarbons have a dense, i.e. non-porous surface (Chapter 5). Because of the low subcooling required to shift those hydrocarbons into the GHSZ, dense hydrates in consequence are thermodynamically more stable than hydrates

requiring more subcooling. Instead, submarine sl hydrates formed mostly from methane have a porous microstructure, comprising an almost monodisperse fabric of many small pores. The microstructural observations are most likely related to the volatility of the hydrate forming gases, as C₂–C₄ hydrocarbons forming sl hydrate are less mobile than methane and other volatile hydrate guests. Therefore, the surfaces of hydrates from less volatiles are less active in respect to sublimation and re-sublimation (W.F. Kuhs, pers. comm., Dec. 2007), resulting in a dense appearance.

There is indication that different absorption contrasts in gas hydrates imaged by μ -computer tomography can help identifying hydrates of different densities. This aspect, however, arose near the end of the present thesis and might be investigated in more detail in future research.

9.1.3 Crystallite sizes and size distributions of hydrates

When this thesis started, the understanding of gas hydrate crystallites was that natural and synthetic hydrates are quite different in size. The assumption was that most likely Ostwald ripening of crystallites was the reason for the differences. The results and interpretations presented here demonstrate that also the sizes of marine gas hydrate crystals differ significantly, and also the grain size distributions indicate diverse grain size evolutions. The arithmetical mean crystallite sizes presented here varied between 190 and 400 μm . Ripening of crystals is the major control of crystal size evolution, but it is not the only one. Instead, the results demonstrate that the environment has a significant impact on the gas hydrate crystallites and evolution of size distributions:

Gas hydrates in the Black Sea are a good example for the domination of Ostwald ripening in the grain size evolution: Shallow hydrates from two different oil seeps (Colkheti Seep and Pechori Mound, offshore Georgia) were exposed to similar formation and site conditions, therefore it is consequent to argue that the grain size evolution must have been similar. In fact, the crystallites had almost the same arithmetical mean size and size distributions. Also, at the Batumi gas seep area the gas hydrates had the same formation conditions. They were retrieved from shallow depths of two different high-intensity gushers. It turned out that the investigated samples had almost the same arithmetical mean crystallite size and were shaped normally.

Gas hydrates from the Bush Hill in the northern Gulf of Mexico are a good example that Ostwald ripening might not be the only factor in grain size evolution: Grain sizes of Bush Hill hydrates were distributed normally indicating normal grain growth, but despite close spatial vicinity of the hydrate pieces the mean crystallite sizes of two samples were almost 100 μm different, which demonstrates that grain size controls act on short distances. Ostwald ripening works by diffusive mass transfer between grains but the diffusive transfer can be hampered by impurities between the crystals. Oil stains were found on the grain boundaries of Bush Hill hydrates, suggesting that oil might act as an inhibitor in terms of mass transfer between grains.

In addition to oil, salts in the grain boundary network can work as retarders for grain growth. Salt crystals were found on the surfaces of grains and in the grain boundary networks between grains. A good example for the effect of salts in the grain size evolution is a gas hydrate piece from the Indian gas hydrate expedition 01 in the Krishna-Godawari basin, which stems from a horizon where salt brines were found (Collett et al., 2008a).

The hydrate structure can have an effect on the mean grain sizes. This becomes apparent when two structures are present. Different hydrate structures of the Chapopote asphalt volcano were diverse in both arithmetic mean crystallite size and size distributions and demonstrated that even within the same sample volume crystallites of two co-occurring structures can be very distinctive: sl crystallite size distributions were skewed to smaller sizes; the sll crystals were quite large and skewed to larger crystal sizes. sll must have higher growth rates and/or a higher nucleation density, given that both structures formed simultaneously.

In short, the results of this thesis demonstrate that for a submarine gas hydrate crystal size evolution the underlying process is normal grain growth or Ostwald ripening, which can be superimposed by retardation due to impurities in the grain boundary network. Hydrate crystallites in submarine settings are several hundred μm in size. Two basic different consequences can be deduced from this:

1. In order to retard or even prevent hydrate crystal regrowth (not hydrate nucleation), admixing of certain components to the system may provide useful. That could be beneficial for operating gas pipelines or for any technical applications where hydrates are involved.
2. The sizes of hydrate crystals in combination with the size distribution can be used as a proxy to draw a qualitative conclusion whether a hydrate deposit is relatively old or young. However, all factors which affect the crystal size evolution need to be considered. What is desirable is a database with worldwide hydrate crystallite size information related to geological information (see Section 9.2).

9.1.4 Dissociation of gas hydrates

μ -computer tomography (μCT) has proven to be a suitable technique to image the diagenetic state of gas hydrate specimen. Ice originating both from frozen pore or seawater and from decomposing hydrate could be differentiated. This technique allows to visualize the degree of gas hydrate dissociation in higher precision. Until today, only the hydrate/ice phase fractions in combination with SEM were used to describe the genetic state. The presented work shows from microstructure inspection in 3D that ice can also derive from in situ formation water, which was frozen during the sample storage in liquid nitrogen. μCT therefore can help to further improve the assessment of the state of hydrate decomposition.

9.1.5 Gas hydrate occurrence at a constrained seep site and possible transport mechanisms to the sea surface

Pressure coring of shallow sediments in the Batumi seep area provided new data on the vertical distributions of gas hydrates, the total amount of hydrate-bound hydrocarbons, the hydrate stability and potential response to environmental changes. The restricted uppermost sediment body of the Batumi seeps of 1,172,500 m^3 (0.5 km^2 seafloor area; 0 to 265 cm below seafloor) hosts approximately 10.7 kt of hydrate-bound carbon, comprising more than 99.96 mol% methane. The hydrates prevail as sl. Hydrate decomposition would set in at a pressure drop of ca. 13 bar or at a temperature rise of ca. 1.56 $^{\circ}\text{C}$, which is unlikely to occur in short timescales. However, changes in the P,T conditions in the Black Sea are known to have occurred on glacial/interglacial timescales. Hydrate detachment from the seafloor is known from Hydrate Ridge and the Gulf of Mexico and is considered as an effective mecha-

nism for transporting hydrate-bound volatiles including hydrocarbons to the atmosphere. At the Batumi seep area sporadic loosening of shallow hydrate chunks is considered to account for the rugged seafloor topography. That could mean that hydrocarbons and gas hydrates from the Batumi seeps site reach the atmosphere.

9.2 Perspectives

9.2.1 Porosity and grain boundaries of different hydrate structures

It was shown in this study that the porosity or dense microstructure of gas hydrates could not be interpreted without information about the gas chemistry forming the hydrates and the crystal structures. sII hydrates with low methane fractions (60-70 mol%) were found in water depths where methane-rich sI hydrate would not be stable. For a basic understanding it is relevant to see in how far the microstructure changes if multiple crystallographic structures co-occur. A working hypothesis could be that within a single specimen comprising sI and sII, sII with less volatile guests would have a dense, non-porous surface and sI would be formed predominantly by methane and would have a porous microstructure. That would imply that the two structures could be distinguished by SEM without much difficulty. The Barkley Canyon in the northeastern Pacific could be a location to start these investigations, as the thermogenic hydrocarbons (Pohlman et al., 2005) have a composition which crystallizes into different hydrate structures and structure mixes. Hydrates from the Chapopote may not be suitable for this particular investigation as the presented results show that the hydrate mix has only a small fraction of sII. This fraction might be too small for a systematic microstructure inspection assessing differences in porosity of sI and sII.

Understanding the three-dimensional intergrowth of different hydrate structures is fundamental to fully comprehend the co-occurrence of different structures. μ -computer tomography will be an important technology to address this question: different X-ray absorption contrasts in gas hydrates observed by μ -computer tomography were attributed to both grain boundary networks and different hydrate densities. For hydrocarbon gas hydrate, the density difference between sI and sII is about 0.02 – 0.15 g/cm³. A future perspective is to refine the current contrast imaging for μ -computer tomography such that density differences of less than 0.1 g/cm³ in the density range of gas hydrates (0.9 to 1.1 g/cm³) can be resolved.

9.2.2 Crystallite sizes

This thesis demonstrates that crystallite sizes and size distributions reflect the formation and growth conditions of the hydrate. Therefore, hydrate crystallite sizes can serve as valuable information in characterizing seep systems and associated hydrate deposits. In order to approach a quantitative understanding of the major control of grain sizes – normal grain growth – further information on the varying factors affecting grain growth and more data on crystal sizes is needed. Suggestions how to systematically obtain this information include:

- Extending a crystallite size distribution database (started in Chapter 4) by including the respective thermodynamic settings, gas chemical and crystal structure data, and pore water compositions at the individual hydrate-bearing sites. If a sample originates from shallow sediments at a gas seepage site, information on the gas flux will be helpful to compare the effect of gas fluxes on crystallite sizes. Additionally, further microstructure data should be included into the database, such as SEM and μ CT data.

- Data acquisition: In addition to Synchrotron beamlines, laboratory diffractometers can also be used for crystallite size measurements; but an area detector and a mobile sample stage are necessary. Two thoughts on laboratory diffractometry are mentioned here:
 - The sizes of hydrate crystals can be inferred from the spot sizes of individual crystallite reflections on Debye-Scherrer-reflections (Rodriguez-Navarro et al., 2006).
 - The area detector could be used to measure the actual lengths of crystallites in a certain direction. Using laboratory diffractometers, that would imply that either the detector or the sample or both need to be moved in a certain relation (H. Klein, pers. comm., Dec. 2007; Dec. 2008).

In addition to diffraction techniques, X-ray tomography can be used to obtain crystallite size information as grain boundaries can be inferred from grain boundary networks. Furthermore, this technique allows visualizing the crystal shapes and determining whether the crystal growth was hampered by impurities between grains.
- Improving knowledge on ripening and annealing of crystals in a comparatively early stage after the formation by a dual approach:
 - Conduct in situ seafloor experiments with constrained P,T parameters and sampling intervals: freshly formed hydrates should remain at the seafloor for at least several weeks or months, as recent experiments performed in the framework of the thesis (unpublished data) showed that the sampling material still comprised mostly hydrate-coated bubbles four days after the experiment.
 - In addition, laboratory studies simulating natural conditions could focus on the influence of ions (York & Firoozabadi, 2009) typically found in pore waters, higher hydrocarbons, or other retarders on crystal growth. For retarding crystal growth, it would be interesting to analyze the effect of polymers such as PVCap on crystal growth. PVCap (poly-*N*-vinylcaprolactam) is frequently used as a kinetic inhibitor for hydrate nucleation.

9.2.3 Co-occurrence of two structures

For the coexistence of sI and sII at the Chapopote, it is still unanswered whether the coexistence is due to crystallization of individual gas bubbles or whether bulk gas de-mixed into two incipient structures or whether both happened on different lengths scales. Answering this question is fundamental to understanding the hydrate structure coexistence and might be transferred to other geological sites. Several starting points are given here to address it:

- Kinetics of the formation in re-enacted experiments (for instance by neutron diffraction): Simulating the situation on the Chapopote by using similar hydrocarbon compositions and applying the location specific P,T conditions, the kinetics of the reaction could reveal whether initially one or two hydrate phases form. Also, in case one structure forms first, the measurements may show whether de-mixing into two structures occurs, depending on the duration of the measurement.
- Zoning or riming, i.e., a structural change accompanying an altered gas feed from the rim towards the center of a grain might be a reason for the sI/sII coexistence. To learn more about zoning of hydrates, in laboratory studies water can be set under gas pressure to form hydrates. In the course of the experiment the feeding gas would be ex-

changed. In those experiments possible gas exchange reactions within the hydrate need to be considered as gases might not only form new hydrate on the surface of existing crystals but could also exchange guests in the preexisting hydrates.

9.2.4 Hydrate transport through water by means of seafloor rafting

Seafloor rafting of gas hydrates is considered as an effective transport mechanism allowing hydrate-bound hydrocarbons to break the sea surface. Since the effect of seeping gases on climate might be significant (Denman et al., 2007; Westbrook et al., 2009), hydrocarbons from a sufficient amount of dissociating hydrate pieces floating on the water surface will have an effect on climate, too. An unanswered question is, what is the contribution of up-floating gas hydrate chunks to the climate?

It would be hard to quantify the volume of detached gas hydrate chunks, accordingly a first step would be to develop ideas how to approach this problem at all:

- Finding and specifying parameters which make gas hydrate seafloor detachment more likely, such as near-surface deposits, hydrates cropping out at the seafloor and high gas flux from below setting hydrate caps under pressure.
- Calculating the volume of hydrate that dissociates during floating depending on time lapse and traveled distance (Brewer et al., 2002; Paull et al., 2003). Such calculations, however, can only be rough approximations and need to be size-normalized. The changing P,T field as well as the effect of anomalous self preservation need to be considered in those calculations. ROV-supported open water experiments may provide field data for the calculations.
- Considering in how far long-term observatories such as deep-sea landers (Pfannkuche & Linke, 2003) or cameras (MacDonald et al., 2005) can be used for analyzing hydrate detachment from the seafloor.

REFERENCES

- Abegg, F., G. Bohrmann, W.F. Kuhs (2006) 21. Data Report: Shapes and structures of gas hydrates imaged by computed tomographic analyses, ODP Leg 204, Hydrate Ridge, in: A.M. Tréhu, Bohrmann, G., Torres, M.E., and Colwell, F.S. (Eds), Proceedings of the Ocean Drilling Program, Scientific Results Volume 204, 11 pp.
- Abegg, F., G. Bohrmann, J. Freitag, W. Kuhs (2007) Fabric of gas hydrate in sediments from Hydrate Ridge - results from ODP Leg 204 samples, *Geo-Marine Letters*, 27, 269-277.
- Abegg, F., H.J. Hohnberg, T. Pape, G. Bohrmann, J. Freitag (2008) Development and application of pressure-core-sampling systems for the investigation of gas- and gas-hydrate-bearing sediments, *Deep Sea Research Part I: Oceanographic Research Papers*, 55, 1590-1599.
- Akhmetzhanov, A.M., M. Ivanov, N.H. Kenyon, A. Mazzini (2007) Deep-water cold seeps, sedimentary environments and ecosystems of the Black and Tyrrhenian Seas and Gulf of Cadiz, UNESCO, Preliminary results of investigations during the TTR-15 cruise of RV Professor Logachev, June-August, 2005. IOC Technical Series No. 72, 99 pp.
- Allmann, R., A. Kern (2002) Röntgenpulverdiffraktometrie: Rechnergestützte Auswertung, Phasenanalyse und Strukturbestimmung, Springer, Berlin, 278 pp.
- Anderson, B.J., J.W. Wilder, M. Kurihara, M.D. White, G.J. Moridis, S.J. Wilson, M. Pooladi-Darvish, Y. Masuda, T.S. Collett, R.B. Hunter, H. Narita, K. Rose, R. Boswell (2008) Analysis of modular dynamic formation test results from the Mount Elbert 01 stratigraphic test well, Milne Point Unit, North Slope Alaska, in: P. Englezos, J. Ripmeester (Eds) Proceedings of the 6th International Conference on Gas Hydrates (ICGH 2008) Vancouver, British Columbia, Canada, July 6-10, 2008, 1 DVD.
- Archer, D., B. Buffett (2005) Time-dependent response of the global ocean clathrate reservoir to climate and anthropogenic forcing, *Geochemistry Geophysics Geosystems*, 6, Q03002, doi:10.1029/2004GC000854.
- Austin, N.J., B. Evans (2007) Paleowattmeters: A scaling relation for dynamically recrystallized grain size, *Geology*, 35, 343-346.
- Bahr, A., F. Lamy, H.W. Arz, C. Major, O. Kwiecien, G. Wefer (2008) Abrupt changes of temperature and water chemistry in the late Pleistocene and early Holocene Black Sea, *Geochemistry, Geophysics, Geosystems*, 9, Q01004, doi:10.1029/2007GC001683.
- Ballard, A.L., E.D. Sloan (2001) Hydrate phase diagrams for methane plus ethane plus propane mixtures, *Chemical Engineering Science*, 56, 6883-6895.
- Bangs, N.L.B., R.J. Musgrave, A.M. Tréhu (2005) Upward shifts in the southern Hydrate Ridge gas hydrate stability zone following postglacial warming, offshore Oregon, *Journal of Geophysical Research*, 110, B03102, doi:10.1029/2004JB003293.
- Barnes, R.O., E.D. Goldberg (1976) Methane production and consumption in anaerobic marine sediments, *Geology*, 4, 297-300.
- Bartolini, C., R.T. Buffler, A. Cantú-Chapa (2002) Western Gulf of Mexico Basin: Tectonics, Sedimentary Basins, and Petroleum Systems, AAPG Memoir No. 75, American Association of Petroleum Geologists, 480 pp.
- Beerling, D.J., R.A. Berner (2002) Biogeochemical constraints on the Triassic-Jurassic boundary carbon cycle event, *Global Biogeochemical Cycles*, 16, 1036, doi:10.1029/2001GB001637.
- Bernard, B.B., J.M. Brooks, W.M. Sackett (1976) Natural gas seepage in the Gulf of Mexico, *Earth and Planetary Science Letters*, 31, 48-54.
- Bhatnagar, G., W.G. Chapman, G.R. Dickens, B. Dugan, G.J. Hirasaki (2007) Generalization of gas hydrate distribution and saturation in marine sediments by scaling of thermodynamic and transport processes. *American Journal of Science*, 307, 861-900.
- Bhatnagar, G., W.G. Chapman, G.R. Dickens, B. Dugan, G.J. Hirasaki (2008) Sulfate-methane transition as a proxy for average methane hydrate saturation in marine sediments, *Geophysical Research Letters*, 35, L03611, doi:10.1029/2007GL032500.

- Bialas, J., J. Greinert, P. Linke, O. Pfannkuche (2007) FS Sonne Fahrtbericht / Cruise Report SO 191 New Vents "Puaretanga Hou" Wellington - Napier - Auckland 11.01. - 23.03.2007, Berichte aus dem Leibniz-Institut für Meereswissenschaften an der Christian-Albrechts-Universität zu Kiel Nr. 9, April 2007, 191 pp.
- Boetius, A., K. Ravenschlag, C.J. Schubert, D. Rickert, F. Widdel, A. Gieseke, R. Amann, B.B. Jørgensen, U. Witte, O. Pfannkuche (2000) A marine microbial consortium apparently mediating anaerobic oxidation of methane, *Nature*, 407, 623-626.
- Bohrmann, G., J. Greinert, E. Suess, M. Torres (1998) Authigenic carbonates from the Cascadia subduction zone and their relation to gas hydrate stability, *Geology*, 26, 647-650.
- Bohrmann, G., K. Heeschen, C. Jung, W. Weinrebe, B. Baranov, B. Cailleau, R. Heath, V. Hühnerbach, M. Hort, D. Masson, I. Trummer (2002) Widespread fluid expulsion along the seafloor of the Costa Rica convergent margin, *Terra Nova*, 14, 69-79.
- Bohrmann, G., M.K. Ivanov, J.P. Foucher, V. Spiess, J. Bialas, J. Greinert, W. Weinrebe, F. Abegg, G. Aloisi, Y. Artemov, V. Blinova, M. Drews, F. Heidersdorf, A. Krabbenhöft, I. Klauke, S. Krastel, T. Leder, I. Polikarpov, M. Saburova, O. Schmale, R. Seifert, A. Volkonskaya, M. Zillmer (2003) Mud volcanoes and gas hydrates in the Black Sea: new data from Dvurechenskii and Odessa mud volcanoes, *Geo-Marine Letters*, 23, 239-249.
- Bohrmann, G., S. Schenck (2004) RV SONNE cruise report SO174, OTEGA II, Balboa - Corpus Christi - Miami (1 October - 12 November, 2003) GEOMAR Report, 117, Kiel, 130 pp.
- Bohrmann, G., M.E. Torres (2006) Gas hydrates in marine sediments, in: H.D. Schulz, M. Zabel (Eds) *Marine Geochemistry*, Springer, Heidelberg, pp. 481- 512.
- Bohrmann, G., T. Pape, and cruise participants (2007) Report and preliminary results of R/V Meteor cruise M72/3, Istanbul - Trabzon - Istanbul, 17 March - 23 April, 2007. Marine gas hydrates of the Eastern Black Sea, Berichte, Fachbereich Geowissenschaften, Universität Bremen, No. 261, Bremen, 176 pp.
- Bohrmann, G., V. Spiess, and cruise participants (2008) Report and preliminary results of R/V Meteor Cruise M67/2a and 2b, Balboa - Tampico - Bridgetown, 15 March - 24 April, 2006. Fluid seepage in the Gulf of Mexico, Berichte, Fachbereich Geowissenschaften, Universität Bremen, No. 263, Bremen, 119 pp.
- Bohrmann, G., and cruise participants (2008) Report and preliminary results of R/V Meteor Cruise M74/3, Fujairah - Male, 31 October - 28 November, 2007. Cold Seeps of the Makran Subduction Zone (Continental Margin of Pakistan) Berichte, Fachbereich Geowissenschaften, Universität Bremen, No. 266, Bremen, 161 pp.
- Borowski, W.S., C.K. Paull, W. Ussler III (1996) Marine pore-water sulfate profiles indicate in situ methane flux from underlying gas hydrate, *Geology*, 24, 655-658.
- Bourry, C., B. Chazallon, J.L. Charlou, J. Pierre Donval, L. Ruffine, P. Henry, L. Geli, M.N. Cagatay, S. Inan, M. Moreau (2009) Free gas and gas hydrates from the Sea of Marmara, Turkey: Chemical and structural characterization, *Chemical Geology*, 264, 197-206.
- Brewer, P.G., G. Friederich, E.T. Peltzer, F.M. Orr, Jr. (1999) Direct Experiments on the Ocean Disposal of Fossil Fuel CO₂, *Science*, 284, 943-945.
- Brewer, P.G., C. Paull, E.T. Peltzer, W. Ussler, G. Rehder, G. Friederich (2002) Measurements of the fate of gas hydrates during transit through the ocean water column, *Geophysical Research Letters*, 29, 2081, doi:2010.1029/2002gl014727.
- Brewer, P.G., G. Malby, J.D. Pasteris, S.N. White, E.T. Peltzer, B. Wopenka, J. Freeman, M.O. Brown, M. O. (2004) Development of a laser Raman spectrometer for deep-ocean science, *Deep Sea Research Part I: Oceanographic Research Papers*, 51, 739-753.
- Brooks, J.M., M.C. Kennicutt, II, R.R. Fay, T.J. McDonald, R. Sassen (1984) Thermogenic Gas Hydrates in the Gulf of Mexico, *Science*, 225, 409-411.
- Brüning, M., H. Sahling, F. Ding, I.R. MacDonald, G. Bohrmann (submitted) Origin, distribution, and alteration of asphalts at Chapopote Knoll, Southern Gulf of Mexico, *Marine and Petroleum Geology*.
- Buffett, B., D. Archer (2004) Global inventory of methane clathrate: sensitivity to changes in the deep ocean, *Earth and Planetary Science Letters*, 227, 185-199.

- Buffett, B.A. (2000) Clathrate hydrates, *Annual Review of Earth and Planetary Sciences*, 28, 477-507.
- Bunge, H.J., L. Wcislak, H. Klein, U. Garbe, J.R. Schneider (2002) Texture and microstructure analysis with high-energy synchrotron radiation, *Textures of Materials, Parts 1 and 2, Materials Science Forum* 408-4, pp. 137-142.
- Bunge, H.J., L. Wcislak, H. Klein, U. Garbe, J.R. Schneider (2003) Texture and microstructure imaging in six dimensions with high-energy synchrotron radiation, *Journal of Applied Crystallography*, 36, 1240-1255.
- Cady, G.H. (1983) Composition of Clathrate Gas Hydrates of H₂S, S_Xe, SO₂, Cl₂, CH₃Cl, CH₃Br, CHClF₂, CCl₂F₂, and C₃H₈, *Journal of Physical Chemistry*, 87, 4437-4441.
- Camps, A.P., A.E. Milodowski, C.A. Rochelle, M.A. Lovell, J.F. Williams, P.D. Jackson (2008) Cryogenic-SEM Investigations of CO₂ Hydrate Morphologies, in: P. Englezos, J. Ripmeester (Eds) *Proceedings of the 6th International Conference on Gas Hydrates (ICGH 2008) Vancouver, British Columbia, Canada, July 6-10, 2008*, 1 DVD.
- Castellini, D.G., G.R. Dickens, G.T. Snyder, C.D. Ruppel (2006) Barium cycling in shallow sediment above active mud volcanoes in the Gulf of Mexico, *Chemical Geology*, 226, 1-30.
- Chapman, R., J. Pohlman, R. Coffin, J. Chanton, L. Lapham (2004) Thermogenic gas hydrates in the northern Cascadia margin, *EOS*, 85, 361-368.
- Charlou, J.L., J.P. Donval, Y. Fouquet, H. Ondreas, J. Knoery, P. Cochonat, D. Levaché, Y. Poirier, P. Jean-Baptiste, E. Fourré, B. Chazallon, The ZAIROV Leg 2 Scientific Party (2004) Physical and chemical characterization of gas hydrates and associated methane plumes in the Congo-Angola Basin, *Chemical Geology*, 205, 405-425.
- Chave, K.E. (1952) A Solid Solution between Calcite and Dolomite, *The Journal of Geology* 60, 190-192.
- Chazallon, B., C. Focsa, J.L. Charlou, C. Bourry, J.P. Donval (2007) A comparative Raman spectroscopic study of natural gas hydrates collected at different geological sites, *Chemical Geology*, 244, 175-185.
- Chen, D.F., L.M. Cathles III (2003) A kinetic model for the pattern and amounts of hydrate precipitated from a gas steam: Application to the Bush Hill vent site, Green Canyon Block 185, Gulf of Mexico, *Journal of Geophysical Research*, 108, B1, 2058, doi: 10.1029/2001JB001597.
- Chen, D.F., Cathles III, L.M. and Roberts, H.H., (2004) The geochemical signatures of variable gas venting at gas hydrate sites, *Marine and Petroleum Geology*, 21, 317-326.
- Chou, I.M., A. Sharma, R.C. Burruss, J.F. Shu, H.K. Mao, R.J. Hemley, A.F. Goncharov, L.A. Stern, S.H. Kirby (2000) Transformations in methane hydrates, *Proceedings of the National Academy of Sciences of the United States of America*, 97, 13484-13487.
- Chun, J.-H., Y.-I. Kwon, H.-Y. Lee, H.-J. Kim, J.-H. Kim, Y.-S. Park, C.-W. Jeon, J.-W. Lee, G.-O. An, B.-K. Son, J. Ko, B.-J. Ryu, D. Sunwoo, J.-H. Oh, Y. Lee, T.-J. Cheong, J.-Y. Lee, N.-K. Kang (2008) Shallow gas hydrate in deep sea sediments in the Ulleung Back-Arc Basin, offshore Korea, in: P. Englezos, J. Ripmeester (Eds) *Proceedings of the 6th International Conference on Gas Hydrates (ICGH 2008) Vancouver, British Columbia, Canada, July 6-10, 2008*, 1 DVD.
- Circone, S., L.A. Stern, S.H. Kirby, W.B. Durham, B.C. Chakoumakos, C.J. Rawn, A.J. Rondinone, Y. Ishii (2003) CO₂-Hydrate: Synthesis, Composition, Structure, Dissociation Behavior, and a Comparison to Structure I CH₄ Hydrate, *Journal of Physical Chemistry B*, 107, 5529-5539.
- Circone, S., S.H. Kirby, L.A. Stern (2005) Direct measurement of methane hydrate composition along the hydrate equilibrium boundary, *Journal of Physical Chemistry B*, 109, 9468-9475.
- Claypool, G.E., I.R. Kaplan (1974) The Origin and Distribution of Methane in Marine Sediments, in: I.R. Kaplan (Ed) *Natural Gases in Marine Sediments* 3, Plenum Press, New York, pp. 99-140.
- Claypool, G.E., K.A. Kvenvolden (1983) Methane and other hydrocarbon gases in marine sediment, *Annual Review of Earth and Planetary Sciences*, 11, 299-327.

- Clennell, M.B., M. Hovland, J.S. Booth, P. Henry, W.J. Winters (1999) Formation of natural gas hydrates in marine sediments. 1. Conceptual model of gas hydrate growth conditioned by host sediment properties, *Journal of Geophysical Research*, 104, 22,985-23,003.
- Collett, T.S., V.A Kuuskraa (1998) Hydrates contain vast store of world gas resources, *Oil and Gas Journal*, 96, 90-95.
- Collett, T. (2002) Energy resource potential of natural gas hydrates, *AAPG Bulletin*, 86, 1971-1992.
- Collett, T., M. Riedel, J. Cochran, R. Boswell, J. Presley, P. Kumar, A. Sathe, A. Sethi, M. Lall, V. Siball (2008a) National Gas Hydrate Program Expedition 01 Initial Reports, U.S. Geological Survey and Directorate General of Hydrocarbons, Ministry of Petroleum & Natural Gas (India), 1 DVD.
- Collett, T.S., W.F. Agena, M.W. Lee, M.V. Zyrianova, K.J. Bird, T.C. Charpentier, D.W. Houseknecht, T.R. Klett, R.M. Pollastro, C.J. Schenk (2008b) Assessment of gas hydrate resources on the North Slope, Alaska, 2008: U.S. Geological Survey Fact Sheet 2008-3073, 4 pp. (http://pubs.usgs.gov/fs/2008/3073/pdf/FS08-3073_508.pdf).
- Dallimore, S.R., T.S. Collett (Eds) (2005) Scientific results from the Mallik 2002 Gas Hydrate Production Research Well Program, Mackenzie Delta, Northwest Territories, Canada, Geological Survey of Canada, Bulletin, 585.
- Davidson, D.W., M.K. El-Defrawy, M.O. Fuglem, A.S. Judge (1978) Natural Gas Hydrates in Northern Canada, *Proceedings of the International Conference on Permafrost*, 3 (1) 937-943.
- Davy, H. (1811) The Bakerian Lecture: On some of the combinations of oxymuriatic gas and oxygene, and on the chemical relations of these principles, to inflammable bodies, *Philosophical Transactions of the Royal Society (London)* 101, 1-35.
- Denman, K.L., G. Brasseur, A. Chidthaisong, P. Ciais, P.M. Cox, R.E. Dickinson, D. Hauglustaine, C. Heinze, E. Holland, D. Jacob, U. Lohmann, S. Ramachandran, P.L. da Silva Dias, S.C. Wofsy and X. Zhang (2007) Couplings Between Changes in the Climate System and Biogeochemistry, in: Solomon, S., D. Qin, M. Manning, Z. Chen, M. Marquis, K.B. Averyt, M. Tignor and H.L. Miller (Eds) *Climate Change 2007: The Physical Science Basis. Contribution of Working Group I to the Fourth Assessment Report of the Intergovernmental Panel on Climate Change*, Cambridge University Press, Cambridge, UK and New York, NY, USA.
- Devlin, J.P. (2000) Preferential deuterium bonding at the ice surface: A probe of surface water molecule mobility, *Journal of Chemical Physics*, 112, 5527-5529.
- Dickens, G.R., M.M. Castillo, J.C.G. Walker (1997a) A blast of gas in the latest Paleocene: Simulating first-order effects of massive dissociation of oceanic methane hydrate, *Geology*, 25, 259-262.
- Dickens, G.R., C.R. Paull, P. Wallace, the ODP Leg 164 scientific party (1997b) Direct measurement of *in situ* methane quantities in a large gas-hydrate reservoir, *Nature*, 385, 426-428.
- Dickens, G.R., M.S. Quinby-Hunt (1997) Methane hydrate stability in pore water: A simple theoretical approach for geophysical applications, *Journal of Geophysical Research*, 102, 773-783.
- Dickens, G.R. (1999) Carbon cycle: The blast in the past, *Nature*, 401, 752-755.
- Dickens, G.R. (2003) Rethinking the global carbon cycle with a large, dynamic and microbially mediated gas hydrate capacitor, *Earth and Planetary Science Letters*, 213, 169-183.
- Dickens, G.R., D. Schroeder, K.-U. Hinrichs, and the Leg 201 Scientific Party (2003) The pressure core sampler (PCS) on ODP Leg 201: General operations and gas releases, in: S. D'Hondt, B.B. Jørgensen, D.J. Miller (Eds) *Proceedings of the Ocean Drilling Program, Initial Reports Volume 201*.
- Ding, F., V. Spiess, M. Brüning, N. Fekete, H. Keil, G. Bohrmann (2008) A conceptual model for hydrocarbon accumulation and seepage processes around Chapopote asphalt site, southern Gulf of Mexico: From high resolution seismic point of view, *Journal of Geophysical Research*, 113 B08404, doi:10.1029/2007bj005484.

- Doherty, R.D., D.A. Hughes, F.J. Humphreys, J.J. Jonas, D.J. Jensen, M.E. Kassner, W.E. King, T.R. McNelley, H.J. McQueen, A.D. Rollett (1997) Current issues in recrystallization: a review, *Materials Science and Engineering: A*, 238, 219-274.
- Donoghue, P.C.J., S. Bengtson, X.-p. Dong, N.J. Gostling, T. Huldgren, J.A. Cunningham, C. Yin, Z. Yue, F. Peng, M. Stampanoni (2006) Synchrotron X-ray tomographic microscopy of fossil embryos, *Nature*, 442, 680-683.
- Duan, Z., S. Mao (2006) A thermodynamic model for calculating methane solubility, density and gas phase composition of methane-bearing aqueous fluids from 273 to 523 K and from 1 to 2000 bar, *Geochimica et Cosmochimica Acta*, 70, 3369-3386.
- Dunlap, W.A., J.R. Hooper (1990) Gas Hydrate Influence on Deepwater Slope Stability, *AAPG Bulletin*, 74, 971.
- Durham, W.B., S.H. Kirby, L.A. Stern, W. Zhang (2003) The strength and rheology of methane clathrate hydrate, *Journal of Geophysical Research*, 108, 2182-2193.
- Ecker, C., J. Dvorkin, and A. M. Nur (2000) Estimating the amount of gas hydrate and free gas from marine seismic data, *Geophysics*, 65, 565-573.
- Englezos, P., J. Ripmeester (Eds) (2008) Proceedings of the 6th International Conference on Gas Hydrates (ICGH 2008) Vancouver, British Columbia, Canada, July 6-10, 2008, 1 DVD.
- Ersland, G., J. Husebø, A. Graue, B.A. Baldwin, J. Howard, J. Stevens (in press) Measuring gas hydrate formation and exchange with CO₂ in Bentheim sandstone using MRI tomography, *Chemical Engineering Journal*, In Press, Corrected Proof; doi:10.1016/j.cej.2008.12.028.
- Etiopie, G., A. Feyzullayev, C.L. Baciú (2008a) Terrestrial methane seeps and mud volcanoes: A global perspective of gas origin, *Marine and Petroleum Geology*, 26, 333-344.
- Etiopie, G., K.R. Lassey, R.W. Klusman, E. Boschi (2008b) Reappraisal of the fossil methane budget and related emission from geologic sources, *Geophysical Research Letters* 35, L09307, doi:10.1029/2008GL033623.
- Etiopie, G., P. Ciccioli (2009) Earth's Degassing: A Missing Ethane and Propane Source, *Science*, 323, 478.
- Evans, J.C., H.J. Bernstein (1956) Intensity in the Raman effect. 5. The effect of intermolecular interaction on the Raman spectrum of carbon disulphide, *Canadian Journal of Chemistry-Revue Canadienne De Chimie*, 34, 1127-1133.
- Falenty, A., G. Genov, W.F. Kuhs (2007) From ice to CO₂ hydrates and back - Study of nucleation and initial growth using scanning electron microscopy, in: W.F. Kuhs (Ed) Proceedings of the 11th International Conference on the Physics and Chemistry of Ice. Special Publication No. 311, Royal Society of Chemistry, Cambridge, UK, pp. 171-179.
- Falenty, A., W.F. Kuhs (2008) The formation and decomposition kinetics of gas hydrates at sub-zero temperatures, in: P. Englezos, J. Ripmeester (Eds) Proceedings of the 6th International Conference on Gas Hydrates (ICGH 2008) Vancouver, British Columbia, Canada, July 6-10, 2008, 1 DVD.
- Faraday, M. (1823) On fluid chlorine, *Philosophical Transactions of the Royal Society (London)* 113, 160-165.
- Feseker, T., J.P. Foucher, F. Harmegnies (2008) Fluid flow or mud eruptions. Sediment temperature distributions on Hakon Mosby mud volcano, SW Barents Sea slope, *Marine Geology*, 247, 194-207.
- Fisher, C.R., I.R.M. Donald, R. Sassen, C.M. Young, S.A. Macko, S. Hourdez, R.S. Carney, S. Joye, E. McMullin (2000) Methane ice worms: *Hesiocaeca methanicola* colonizing fossil fuel reserves, *Naturwissenschaften*, 87, 184-187.
- Forster, P., V. Ramaswamy, P. Artaxo, T. Berntsen, R. Betts, D.W. Fahey, J. Haywood, J. Lean, D.C. Lowe, G. Myhre, J. Nganga, R. Prinn, G. Raga, M. Schulz, R. Van Dorland (2007) Changes in Atmospheric Constituents and in Radiative Forcing, in: Solomon, S., D. Qin, M. Manning, Z. Chen, M. Marquis, K.B. Averyt, M. Tignor, H.L. Miller (eds) *Climate Change 2007: The Physical Science Basis. Contribution of Working Group I to the Fourth Assessment Report of the Intergovernmental Panel on Climate Change*, Cambridge University Press, Cambridge, UK and New York, NY, USA.

- Freifeld, B. M., T. J. Kneafsey, L. Tomutsa, L. A. Stern, and S. H. Kirby (2002) Use of computed tomographic data for analyzing the thermodynamics of a dissociating porous sand/hydrate mixture, Proceedings of the 4th International Conference in Gas Hydrates, May 19-23 2002, Yokohama, Japan.
- Freifeld, B.M., T.J. Kneafsey, F.R. Rack (2006) On-site geological core analysis using a portable X-ray computed tomographic system, in: Rothwell, R.G. (ed) New techniques in sediment core analysis, Geological Society, London, Special Publications, 267, 165-178.
- Friis, E.M., P.R. Crane, K.R. Pedersen, S. Bengtson, P.C.J. Donoghue, G.W. Grimm, M. Stampanoni (2007) Phase-contrast X-ray microtomography links Cretaceous seeds with Gnetales and Bennettiales, *Nature*, 450, 549-552.
- Garrison, L.E., R.G. Martin (1973) Geologic structures in the Gulf of Mexico Basin, US Geological Survey Professional Paper, 773, US Government Printing Office, Washington.
- Genov, G., W.F. Kuhs, D.K. Staykova, E. Goreschnik, A.N. Salamatina (2004) Experimental studies on the formation of porous gas hydrates, *American Mineralogist*, 89, 1228-1239.
- Gerner, A., E. H. Saenger, and S. A. Shapiro (2007) Attenuation of P waves due to interlayer fluid flow in hydrate-bearing sediments, *Journal of Geophysical Engineering*, 4, 394-403.
- Ginibre, C., G. Worner, A. Kronz (2007) Crystal Zoning as an Archive for Magma Evolution, *Elements* 3, 261-266.
- Ginsburg, G.D., R.A. Guseynov, A.A. Dadashev, G.A. Ivanova, S.A. Kazantsev, V.A. Soloviev, Y.V. Telepnev, R.E. Askerinasirov, A.D. Yesikov, V.I. Maltseva, Y.G. Mashirov, I.Y. Shabaeva (1992) Gaseous hydrates of the Southern Caspian, *International Geology Review*, 43, 765-782.
- Ginsburg, G.D., V.A. Soloviev, R.E. Cranston, T.D. Lorenson, K.A. Kvenvolden (1993) Gas hydrates from the continental-slope, offshore Sakhalin Island, Okhotsk Sea, *Geo-Marine Letters*, 13, 41-48.
- Goldstein, J., D. Newbury, D. Joy, C. Lyman, P. Echlin, E. Lifshin, L. Sawyer, J. Michael (2003) *Scanning Electron Microscopy and X-Ray Microanalysis*, Kluwer Academic/Plenum Publishers, New York, 689 pp.
- Greinert, J., Y. Artemov, V. Egorov, M. De Batist, D. McGinnis (2006) 1300-m-high rising bubbles from mud volcanoes at 2080m in the Black Sea: Hydroacoustic characteristics and temporal variability, *Earth and Planetary Science Letters*, 244, 1-15.
- Gupta, A., T. J. Kneafsey, G. J. Mordis, Y. Seol, M. B. Kowalsky, and E. D. Sloan, Jr. (2006) Composite thermal conductivity in a large heterogeneous porous methane hydrate sample, *Journal of Physical Chemistry B*, 110, 16384-16392.
- Haackel, M., E. Suess, K. Wallmann, D. Rickert (2004) Rising methane gas bubbles form massive hydrate layers at the seafloor, *Geochimica et Cosmochimica Acta*, 68, 4335-4345.
- Haackel, M., A. Reitz, I. Klauke, H. Sahling (2008) Methane budget of a large gas hydrate province offshore Georgia, Black Sea, in: P. Englezos, J. Ripmeester (Eds) Proceedings of the 6th International Conference on Gas Hydrates (ICGH 2008) Vancouver, British Columbia, Canada, July 6-10, 2008, 1 DVD.
- Hammerschmidt, E.G. (1934) Formation of gas hydrates in natural gas transmission lines, *Industrial and Engineering Chemistry*, 26, 851-855.
- Hammersley, A.P., S.O. Svensson, M. Hanfland, A.N. Fitch, D. Hausermann (1996) Two-dimensional detector software: From real detector to idealised image or two-theta scan, *High Pressure Research*, 14, 235-248.
- Han, X., E. Suess, Y. Huang, N. Wu, G. Bohrmann, X. Su, A. Eisenhauer, G. Rehder, Y. Fang (2008) Jiulong methane reef: Microbial mediation of seep carbonates in the South China Sea, *Marine Geology*, 249, 243-256.
- Heeschen, K., M. Haackel, I. Klauke, G. Bohrmann (submitted) New near-surface gas hydrate occurrences investigated in the eastern Black Sea using two complementary methods, *Geophysical Research Letters*.

- Heeschen, K.U., H.J. Hohnberg, M. Haeckel, F. Abegg, M. Drews, G. Bohrmann (2007) In situ hydrocarbon concentrations from pressurized cores in surface sediments, Northern Gulf of Mexico, *Marine Chemistry*, 107, 498-515.
- Henriet, J.-P., J. Mienert (Eds) (1998) Gas Hydrates Relevance to World margin stability and climate change, The Geological Society, London, 338 pp.
- Herzberg, G. (1945) Molecular Spectra and Molecular Structure: Infrared and Raman of Polyatomic Molecules, *Molecular Spectra and Molecular Structure: Infrared and Raman of Polyatomic Molecules*, Van Nostrand, Princeton, New Jersey, USA, 676 pp.
- Hesselbo, S.P., D.R. Gröcke, H.C. Jenkyns, C.J. Bjerrum, P. Farrimond, H.S. Morgans Bell, O.R. Green (2000) Massive dissociation of gas hydrate during a Jurassic oceanic anoxic event, *Nature*, 406, 392-395.
- Hester, K.C., R.M. Dunk, P.M. Walz, E.T. Peltzer, E.D. Sloan, P.G. Brewer (2007a) Direct measurements of multi-component hydrates on the seafloor: Pathways to growth, *Fluid Phase Equilibria*, 261, 396-406.
- Hester, K.C., R.M. Dunk, S.N. White, P.G. Brewer, E.T. Peltzer, E.D. Sloan (2007b) Gas hydrate measurements at Hydrate Ridge using Raman spectroscopy, *Geochimica et Cosmochimica Acta*, 71, 2947-2959.
- Hester, K.C., P.G. Brewer (2009) Clathrate Hydrates in Nature, *Annual Review of Marine Science*, 1, 303-327.
- Higgins, M. (2000) Measurement of crystal size distributions. *American Mineralogist*, 85, 1105-1116.
- Holland, M., P. Schultheiss, J. Roberts, M. Druce (2008) Observed gas hydrate morphologies in marine sediments, in: P. Englezos, J. Ripmeester (Eds) Proceedings of the 6th International Conference on Gas Hydrates (ICGH 2008) Vancouver, British Columbia, Canada, July 6-10, 2008, 1 DVD.
- House, K.Z., D.P. Schrag, C.F. Harvey, K.S. Lackner (2006) Permanent carbon dioxide storage in deep-sea sediments, *Proceedings of the National Academy of Sciences of the United States of America*, 103, 12291-12295.
- Humphreys, F.J., M. Hatherly (2004) Recrystallization and Related Annealing Phenomena, Elsevier, Oxford, UK, 628 pp.
- Humphris, C.C. (1979) Salt movement on continental slope, northern Gulf of Mexico, *AAPG Bulletin*, 63, 782-798.
- Husebø, J., A. Graue, B. Kvamme, J. Stevens, J.J. Howard, B.A. Baldwin (2008) Experimental investigation of methane release from hydrate formation in sandstone through both hydrate dissociation and CO₂ sequestration, in: P. Englezos, J. Ripmeester (Eds) Proceedings of the 6th International Conference on Gas Hydrates (ICGH 2008) Vancouver, British Columbia, Canada, July 6-10, 2008, 1 DVD.
- HWHYD, 2005. HWHYD Heriot-Watt-Hydrate Version 1.1. Multiphase hydrate and PVT prediction software for Microsoft® Windows® operating systems. Centre for Gas Hydrate Research, Institute of Petroleum Engineering, Heriot-Watt-University, Edinburgh, UK.
- Jähne B, Henz G, and Dietrich W. (1987) Measurement of the diffusion coefficients of sparingly soluble gases in water, *Journal of Geophysical Research* 92, 10,767–10,776.
- Jones, K.W., H. Feng, S. Tomov, W.J. Winters, M. Prodanovic, D. Mahajan (2007) Characterization of methane hydrate host sediments using synchrotron-computed microtomography (CMT) *Journal of Petroleum Science and Engineering*, 56, 136-145.
- Jørgensen, B.B., A. Weber, J. Zopfi (2001) Sulfate reduction and anaerobic methane oxidation in Black Sea sediments, *Deep-Sea Research I*, 48, 2097-2120.
- Jørgensen, B.B., S. Kasten (2006) Sulfur cycling and methane oxidation, in: H.D. Schulz, M. Zabel (Eds) *Marine Geochemistry*, Springer, Heidelberg, pp. 271-310.
- Judd, A.G. (2002) The global importance and context of methane escape from the seabed, 7th International Conference on Gas in Marine Sediments/NATO Advanced Research Workshop on Seafloor Hydrocarbon Seeps, Springer-Verlag, 147-154 pp.

- Judd, A.G., M. Hovland, L.I. Dimitrov, S. Garcia Gil, V. Jukes (2002) The geological methane budget at Continental Margins and its influence on climate change, *Geofluids*, 2, 109-126.
- Judd, A.G. (2004) Natural seabed gas seeps as sources of atmospheric methane, *Environmental Geology*, 46, 988-996.
- Judd, A.G., M. Hovland (2007) *Seabed fluid flow. The Impact on Geology, Biology, and the Marine Environment*, Cambridge University Press, Cambridge, 492 pp.
- Kashchiev, D., A. Firoozabadi (2002) Driving force for crystallization of gas hydrates, *Journal of Crystal Growth*, 241, 220-230.
- Katz, M.E., D.K. Pak, G.R. Dickens, K.G. Miller (1999) The source and fate of massive carbon input during the latest Paleocene thermal maximum, *Science*, 286, 1531-1533.
- Kennett, J.P., K.G. Cannariato, I.L. Hendy, R.J. Behl (2000) Carbon isotopic evidence for methane hydrate instability during quaternary interstadials, *Science*, 288, 128-133.
- Kennett, J.P., K.G. Cannariato, I.L. Hendy, R.J. Behl (2003) Methane hydrates in Quaternary climate change: the clathrate gun hypothesis, AGU books board, 216 pp.
- Kennicutt II, M.C., J.M. Brooks, R.R. Bidigare, G.J. Denoux (1988) Gulf of Mexico hydrocarbon seep communities - I. Regional distribution of hydrocarbon seepage and associated fauna, *Deep-Sea Research I*, 35, 1639-1651.
- Kessler, J.D., W.S. Reeburgh, J. Southon, R. Seifert, W. Michaelis, S.C. Tyler (2006) Basin-wide estimates of the input of methane from seeps and clathrates to the Black Sea, *Earth and Planetary Science Letters*, 243, 366-375.
- Kida, M., O. Khlystov, T. Zemskaya, N. Takahashi, H. Minami, H. Sakagami, A. Krylov, A. Hachikubo, S. Yamashita, H. Shoji, J. Poort, L. Naudts (2006) Coexistence of structure I and II gas hydrates in Lake Baikal suggesting gas sources from microbial and thermogenic origin, *Geophysical Research Letters*, 33, L24603, doi:24610.21029/22006GL028296.
- Kida, M., A. Hachikubo, H. Sakagami, H. Minami, A. Krylov, S. Yamashita, N. Takahashi, H. Shoji, O. Khlystov, J. Poort, H. Narita (2009) Natural gas hydrates with locally different cage occupancies and hydration numbers in Lake Baikal, *Geochemistry Geophysics Geosystems*, 10, Q05003, doi:05010.01029/02009gc002473.
- Killops, S., V. Killops (2004) *An Introduction to Organic Geochemistry*, Blackwell Science, 408 pp.
- Kipfstuhl, S., F. Pauer, W.F. Kuhs, H. Shoji (2001) Air bubbles and clathrate hydrates in the transition zone of the NGRIP deep ice core, *Geophysical Research Letters*, 28, 591-594.
- Kirchner, M.T., R. Boese, W.E. Billups, L.R. Norman (2004) Gas Hydrate Single-Crystal Structure Analyses, *Journal of the American Chemical Society*, 126, 9407-9412.
- Klapp, S.A., H. Klein, W.F. Kuhs (2007) First determination of gas hydrate crystallite size distributions using high-energy synchrotron radiation, *Geophysical Research Letters*, 34, L13608, DOI:13610.11029/12006GL029134.
- Klapproth, A. (2002) *Strukturuntersuchungen an Methan- und Kohlenstoffdioxid-Clathrat-Hydraten*, PhD thesis, Universität Göttingen, Germany.
- Klapproth, A., E. Goreschnik, D. Staykova, H. Klein, W.F. Kuhs (2003) Structural studies of gas hydrates, *Canadian Journal of Physics*, 81, 503-518.
- Klapproth, A., K.S. Techmer, S.A. Klapp, M.M. Murshed, W.F. Kuhs (2007) Microstructure of Gas Hydrates in Porous Media, in: W.F. Kuhs (Ed) *Proceedings of the 11th International Conference on the Physics and Chemistry of Ice*. Special Publication No. 311, Royal Society of Chemistry, Cambridge, UK, pp. 321-328.
- Klaucke, I., H. Sahling, W. Weinrebe, V. Blinova, D. Bürk, N. Lursmanashvili, G. Bohrmann (2006) Acoustic investigations of cold seeps offshore Georgia, eastern Black Sea, *Marine Geology*, 231, 51-67.
- Klauda, J.B., S.I. Sandler (2005) Global distribution of methane hydrate in ocean sediment, *Energy & Fuels*, 19, 459-470.
- Klein, H., A. Preusser, H.J. Bunge, L. Raue (2004) Recrystallization texture and microstructure in Ni and AlMg1Mn1 determined with high-energy synchrotron radiation, *Recrystallization and Grain Growth*, Parts 1 and 2, *Materials Science Forum* 467-470, pp. 1379-1384.

- Kneafsey, T. J., L. Tomutsa, G. J. Moridis, Y. Seol, B. M. Freifeld, C. E. Taylor, and A. Gupta (2005) Methane hydrate formation and dissociation in a partially saturated sand – measurements and observations, Proceedings of the 5th International Conference on Gas Hydrates, June 13-16 2005, Trondheim, Norway.
- Kneafsey, T.J., L. Tomutsa, G.J. Moridis, Y. Seol, B.M. Freifeld, C.E. Taylor, A. Gupta (2007) Methane hydrate formation and dissociation in a partially saturated core-scale sand sample, *Journal of Petroleum Science and Engineering*, 56, 108-126.
- Koh, C.A. (2002) Towards a fundamental understanding of natural gas hydrates, *Chemical Society Reviews*, 31, 157-167.
- Kopf, A.J. (2002) Significance of mud volcanism, *Reviews of Geophysics*, 40, doi:10.1029/2000rg000093.
- Kopf, A.J. (2003) Global methane emission through mud volcanoes and its past and present impact on the Earth's climate, *International Journal of Earth Sciences*, 92, 806-816.
- Krüger, M., T. Treude, H. Wolters, K. Nauhaus, A. Boetius (2005) Microbial methane turnover in different marine habitats, *Palaeogeography, Palaeoclimatology, Palaeoecology*, 227, 6-17.
- Kuhs, W.F., R. Dorwarth, D. Londono, J.L. Finney (1992) In-situ study on composition and structure of Ar-clathrate, in: N. Maeno, T. Hondoh (Eds) *Physics and Chemistry of Ice*, Hokkaido University Press, Sapporo, pp. 126-130.
- Kuhs, W.F., B. Chazallon, P.G. Radaelli, F. Pauer (1997) Cage occupancy and compressibility of deuterated N-2-clathrate hydrate by neutron diffraction, *Journal of Inclusion Phenomena and Molecular Recognition in Chemistry*, 29, 65-77.
- Kuhs, W.F., A. Klapproth, F. Gotthardt, K.S. Techmer, T. Heinrichs (2000a) The formation of meso- and macroporous gas hydrates, *Geophysical Research Letters*, 27, 2929-2932.
- Kuhs, W.F., A. Klapproth, B. Chazallon (2000b) Chemical physics of air clathrate hydrates, in: T. Hondoh (Ed) *Physics of Ice Core Records*, Hokkaido University Press, Sapporo, pp. 373-392.
- Kuhs, W.F., G. Genov, E. Goreschnik, A. Zeller, K.S. Techmer, G. Bohrmann (2004a) The Impact of Porous Microstructures of Gas Hydrates on Their Macroscopic Properties, *International Journal of Offshore and Polar Engineering*, 14, 305-309.
- Kuhs, W.F., G. Genov, D.K. Staykova, T. Hansen (2004b) Ice perfection and onset of anomalous preservation of gas hydrates, *Physical Chemistry Chemical Physics*, 6, 4917-4920.
- Kuhs, W.F., T.C. Hansen (2006) Time-resolved Neutron Diffraction Studies with Emphasis on Water Ices and Gas Hydrates, *Reviews in Mineralogy & Geochemistry*, 63, 171-204.
- Kuhs, W.F., D.K. Staykova, A.N. Salamatin (2006) Formation of Methane Hydrate from Polydisperse Ice Powders, *The Journal of Physical Chemistry B*, 110, 13,283-13,295.
- Kullenberg, B. (1947) The piston core sampler, *Svenska Hydrografisk-Biologiska Kommissionens Skrifter*, 1, 1-46.
- Kutas, R.I., S.I. Paliy, O.M. Rusakov (2004) Deep faults, heat flow and gas leakage in the northern Black Sea, *Geo-Marine Letters*, 24, 163-168.
- Kvenvolden, K.A. (1988) Methane hydrate - a major reservoir of carbon in the shallow geosphere?, *Chemical Geology*, 71, 41-51.
- Kvenvolden, K.A. (1993) Gas hydrates - global perspective and global change, *Reviews of Geophysics*, 31, 173-187.
- Kvenvolden, K.A., G.D. Ginsburg, V.A. Soloviev (1993) Worldwide distribution of subaquatic gas hydrates, *Geo-Marine Letters*, 13, 32-40.
- Kvenvolden, K.A. (1995) A review of the geochemistry of methane in natural gas hydrate, *Organic Geochemistry*, 23, 997-1008.
- Kvenvolden, K.A. (1998) A primer on the geological occurrence of gas hydrate, in: Henriot, J.P., J. Mienert (Eds) *Gas Hydrates: Relevance to World Margin Stability and Climate Change*, Special Publications 137, Geological Society, London, pp. 9-30.
- Kvenvolden, K.A. (1999) Potential effects of gas hydrate on human welfare, *Proceedings of the National Academy of Sciences of the United States of America*, 96, 3420-3426.

- Kvenvolden, K.A., T.D. Lorenson (2001) Global occurrence of natural gas hydrates, in: Paull, C.K., W.P. Dillon (Eds) *Natural gas hydrates: Occurrence, distribution, and detection*, Geophysical Monograph 124, American Geophysical Union, Washington D.C., pp. 3-18.
- Kvenvolden, K.A. (2002) Methane hydrate in the global organic carbon cycle, *Terra Nova*, 14, 302-306.
- Lackner, K.S. (2003) Climate change: A Guide to CO₂ Sequestration, *Science*, 300, 1677-1678.
- Lamy, F., H.W. Arz, G.C. Bond, A. Bahr, J. Pätzold (2006) Multicentennial-scale hydrological changes in the Black Sea and northern Red Sea during the Holocene and the Arctic/North Atlantic Oscillation, *Paleoceanography*, 21, PA1008, doi:10.1029/2005PA001184.
- Larsen, R., C.A. Knight, and E.D. Sloan, 1998. Clathrate hydrate growth and inhibition, *Fluid Phase Equilibria*, 150-151, 353-360.
- Larson, A.C., R.B. von Dreele (2004) General Structure Analysis System (GSAS) Los Alamos National Laboratory Report LAUR 86-748, Los Alamos National Laboratory, Los Alamos, p. 231.
- Lasaga, A.C. (1998) *Kinetic Theory in the Earth Sciences*, Princeton University Press, Princeton, New Jersey; Chichester, West Sussex, 811 pp.
- Leadbetter, A.J., R.C. Ward, J.W. Clark, P.A. Tucker, T. Matsuo, H. Suga (1985) The equilibrium low-temperature structure of ice, *Journal of Chemical Physics*, 82, 424-428.
- Lee, H., J. Lee, D.Y. Kim, J. Park, Y. Seo, H. Zeng, I.L. Moudrakovski, C.I. Ratcliffe, J.A. Ripmeester (2005) Tuning clathrate hydrates for hydrogen storage, *Nature*, 434, 743-746.
- Legagneux, L. (2003) *Evolution de la microphysique du manteau neigeux. Surface spécifique et métamorphisme*, PhD thesis, Université Joseph-Fourier, Grenoble, France.
- Leifer, I., A.G. Judd (2002) Oceanic methane layers: the hydrocarbon seep bubble deposition hypothesis, *Terra Nova*, 14, 417-424.
- Leifer, I., R.K. Patro (2002) The bubble mechanism for methane transport from the shallow sea bed to the surface: A review and sensitivity study, *Continental Shelf Research*, 22, 2409-2428.
- Leifer, I., I. MacDonald (2003) Dynamics of the gas flux from shallow gas hydrate deposits: interaction between oily hydrate bubbles and the oceanic environment, *Earth and Planetary Science Letters*, 210, 411-424.
- Leonov, A.V. (2005) Variations in the Black Sea water salinity from its latest salinization to the present state: Estimation based on mathematical modeling, *Water Resources*, 32, 134-144.
- Lifshitz, I.M., V.V. Slyozov (1961) The kinetics of precipitation from supersaturated solid solutions, *Journal of Physics and Chemistry of Solids*, 19, 35-50.
- Long, D.A. (1977) *Raman Spectroscopy*, McGraw-Hill, New York, 276 pp.
- Longhi, J. (2006) Phase equilibrium in the system CO₂-H₂O: Application to Mars, *Journal of Geophysical Research*, 111, E06011, DOI: 06010.01029/02005JE002552.
- Lu, H., R. Matsumoto (2005) Experimental studies on the possible influences of composition changes of pore water on the stability conditions of methane hydrate in marine sediments, *Marine Chemistry*, 93, 149-157.
- Lu, H., Y.-T. Seo, J.-W. Lee, I. Moudrakovski, J.A. Ripmeester, N.R. Chapman, R.B. Coffin, G. Gardner, J. Pohlman (2007) Complex gas hydrate from the Cascadia margin, *Nature*, 445, 303-306.
- Luff, R., K. Wallmann (2003) Fluid flow, methane fluxes, carbonate precipitation and biogeochemical turnover in gas hydrate-bearing sediments at Hydrate Ridge, Cascadia Margin: numerical modeling and mass balances, *Geochimica et Cosmochimica Acta*, 67, 3403-3421.
- MacDonald, I.R., G.S. Boland, J.S. Baker, J.M. Brooks, M.C. Kennicutt II, R.R. Bidigare (1989) Gulf of Mexico hydrocarbon seep communities, *Marine Biology*, 101, 235-247.

- Macdonald, I.R., N.L. Guinasso, R. Sassen, J.M. Brooks, L. Lee, K.T. Scott (1994) Gas hydrate that breaches the sea floor on the continental slope of the Gulf of Mexico, *Geology*, 22, 699-702.
- MacDonald, I.R., J.F. Reilly Jr., S.E. Best, R. Venkataramaiah, R. Sassen, N.L. Guinasso Jr., J. Amos (1996) Remote sensing inventory of active oil seeps and chemosynthetic communities in the northern Gulf of Mexico, in: D. Schumacher, M.A. Abrams (Eds) *Hydrocarbon migration and its near-surface expression* 66, AAPG Memoir, pp. 27-37.
- MacDonald, I.R., W.W. Sager, M.B. Peccini (2003) Gas hydrate and chemosynthetic biota in mounded bathymetry at mid-slope hydrocarbon seeps: Northern Gulf of Mexico, *Marine Geology*, 198, 133-158.
- MacDonald, I.R., G. Bohrmann, E. Escobar, F. Abegg, P. Blanchon, V. Blinova, W. Brückmann, M. Drews, A. Eisenhauer, X. Han, K. Heeschen, F. Meier, C. Mortera, T. Naehr, B. Orcutt, B. Bernard, J. Brooks, M. de Farágo (2004) Asphalt volcanism and chemosynthetic life in the Campeche Knolls, Gulf of Mexico, *Science*, 304, 999-1002.
- MacDonald, I.R., L.C. Bender, M. Vardaro, B. Bernard, J.M. Brooks (2005) Thermal and visual time-series at a seafloor gas hydrate deposit on the Gulf of Mexico slope, *Earth and Planetary Science Letters*, 233, 45-59.
- Macgregor, D.S. (1993) Relationships between seepage, tectonics and subsurface petroleum reserves, *Marine and Petroleum Geology*, 10, 606-619.
- Magoon, L.B., T.L. Hudson, H.E. Cook (2002) Pimienta-Tambra – A giant supercharged petroleum system in the southern Gulf of Mexico, Onshore and Offshore Mexico, in: C. Bartolini, R.T. Buffler, A. Cantú-Chapa (Eds) *The western Gulf of Mexico Basin: Tectonics, sedimentary basins, and petroleum systems*, AAPG Memoir No. 75, pp. 83-125.
- Maini, B.B., P.R. Bishnoi (1981) Experimental Investigation of Hydrate Formation Behavior of a Natural Gas Bubbles in a Simulated Deep Sea Environment, *Chemical Engineering Science*, 36, 183-189.
- Makogon, Y.F. (1965) Hydrate formation in the gas-bearing beds under permafrost conditions, *Gazovaia Promyshlennost*, 5, 14-15.
- Makogon, Y.F., F.A. Trebin, A.A. Trofimuk, V.P. Tsarev, N. Cherskii (1971) Detection of A Pool of Natural Gas in a Solid (Hydrated Gas) State, *Doklady Akademii Nauk SSSR*, 196, 203-206.
- Makogon, Y.F. (1994) Russia's Contribution to the Study of Gas Hydrates, *Annals of the New York Academy of Sciences*, 715, 119-145.
- Malone, R.D. (1985) Gas Hydrates. DOE Topical Report, DOE/METC report DOE/METTTC/SP-218 (DE85001986) 35 pp.
- Manheim, F.T., K.M. Chan (1974) Interstitial waters of Black Sea sediments: New data and review, in: Degens, E.T., D.A. Ross (Eds) *The Black Sea - Geology, chemistry and biology* Memoir 20, The American Association of Petroleum Geologists, Tulsa, Oklahoma, USA, pp. 155-180.
- Mao, W.L., H. Mao (2004) Hydrogen storage in molecular compounds, *Proceedings of the National Academy of Sciences of the United States of America*, 101, 708-710.
- Masoudi, R., B. Tohidi, A. Danesh, A.C. Todd (2004) A new approach in modelling phase equilibria and gas solubility in electrolyte solutions and its applications to gas hydrates, *Fluid Phase Equilibria*, 215, 163-174.
- Masoudi, R., B. Tohidi (2005) Estimating the hydrate stability zone in the presence of salts and/or organic inhibitors using water partial pressure, *Journal of Petroleum Science and Engineering*, 46, 23-36.
- Massiot, D., F. Fayon, M. Capron, I. King, S.L. Calvé, B. Alonso, J.-O. Durand, B. Bujoli, Z. Gan, G. Hoatson (2002) Modelling one- and two-dimensional solid-state NMR spectra, *Magnetic Resonance in Chemistry*, 40, 70-76.
- Matsumoto, R., Uchida, T., Waseda, A., Takeya, S., Hirano, T., Yamada, K., Maeda, Y. Okui, T. (2000) Occurrence, structure and composition of natural gas hydrates recovered from the Blake Ridge, ODP Leg 164, Northwest Atlantic, *Proceedings of the Ocean Drilling Program, Scientific results*, 164, 13–28.

- Matsumoto, R. (Ed) (2009) Methane Hydrate (Part I): Occurrence, Origin, and Environmental Impact, *Journal of Geography* Vol. 118 No. 1.
- Max, M.D. (2002) Hydrate desalination or water purification, U.S. Patent No. 20020003111, Marine Desalination Systems, L.L.C., USA.
- Max, M.D. (2006) Hydrate desalination for water purification, U.S. Patent No. 6991722, Marine Desalination Systems, L.L.C., USA.
- Max, M.D., H.K. Johnsen, W.P. Dillon (2006) Economic geology of natural gas hydrate, coastal systems and continental margins. Springer, Dordrecht, 341 pp.
- McClusky, S., S. Balassanian, A. Barka, C. Demir, S. Ergintav, I. Georgiev, O. Gurkan, M. Hamburger, K. Hurst, H. Kahle, K. Kastens, G. Kekelidze, R. King, V. Kotzev, O. Lenk, S. Mahmoud, A. Mishin, M. Nadariya, A. Ouzounis, D. Paradissis, Y. Peter, M. Prilepin, R. Reilinger, I. Sanli, H. Seeger, A. Tealeb, M.N. Toksoz, G. Veis (2000) Global Positioning System constraints on plate kinematics and dynamics in the eastern Mediterranean and Caucasus, *Journal of Geophysical Research*, 105, 5695-5719.
- McCreery (2000) Raman Spectroscopy for Chemical Analysis, John Wiley & Sons, Inc., 448 pp.
- McGinnis, D.F., J. Greinert, Y. Artemov, S.E. Beaubien, A. Wuest (2006) Fate of rising methane bubbles in stratified waters: How much methane reaches the atmosphere?, *Journal of Geophysical Research*, 111, C09007, doi:10.1029/2005JC003183.
- Medalia, O., I. Weber, A.S. Frangakis, D. Nicastro, G. Gerisch, W. Baumeister (2002) Macromolecular Architecture in Eukaryotic Cells Visualized by Cryoelectron Tomography, *Science*, 298, 1209-1213.
- Meredith, D.J., S.S. Egan (2002) The geological and geodynamic evolution of the eastern Black Sea basin: insights from 2-D and 3-D tectonic modelling, *Tectonophysics*, 350, 157-179.
- Miedaner, M. M. (2007) Characterization of inclusions and their distribution in natural and artificial ice samples by synchrotron cryo micro tomography (SCXRTM), PhD thesis, Johannes Gutenberg University Mainz, Germany.
- Mienert, J., M. Vanneste, S. Bünz, K. Andreassen, H. Hafliðason, H.P. Sejrup (2005) Ocean warming and gas hydrate stability on the mid-Norwegian margin at the Storrega Slide, *Marine and Petroleum Geology*, 22, 233-244.
- Mikami, J., Y. Masuda, T. Uchida, T. Satoh and T. Hondoh (2000) Dissociation of Natural Gas Hydrates Observed by X-ray CT Scanner, in *Gas Hydrates: Challenges for the Future*, *Annals of the New York Academy of Science*, 912, 1011-1020.
- Milkov, A.V., R. Sassen, T.V. Apanasovich, F.G. Dadashev (2003a) Global gas flux from mud volcanoes: a significant source of fossil methane in the atmosphere and the ocean, *Geophysical Research Letters*, 30, 9.1-9.4.
- Milkov, A.V., G.E. Claypool, Y.-J. Lee, W. Xu, G.R. Dickens, W.S. Borowski, ODP Science Party (2003b) In situ methane concentrations at Hydrate Ridge, offshore Oregon: New constraints on the global gas hydrate inventory from an active margin, *Geology*, 31, 833-836.
- Milkov, A.V., G.R. Dickens, G.E. Claypool, Y.-J. Lee, W.S. Borowski, M.E. Torres, W. Xu, H. Tomaru, A.M. Tréhu, P. Schultheiss (2004) Co-existence of gas hydrate, free gas, and brine within the regional gas hydrate stability zone at Hydrate Ridge (Oregon margin): evidence from prolonged degassing of a pressurized core, *Earth and Planetary Science Letters*, 222, 829-843.
- Milkov, A.V. (2004) Global estimates of hydrate-bound gas in marine sediments: how much is really out there?, *Earth-Science Reviews*, 66, 183-197.
- Milkov, A.V. (2005) Molecular and stable isotope composition of natural gas hydrates: A revised global dataset and basic interpretations in the context of geological settings, *Organic Geochemistry*, 36, 681-702.
- Milkov, A.V., G.E. Claypool, Y.-J. Lee, R. Sassen (2005) Gas Hydrate systems at Hydrate Ridge offshore Oregon inferred from molecular and isotopic properties of hydrate-bound and void gases, *Geochimica et Cosmochimica Acta*, 69, 1007-1026.
- Milton, D.J. (1974) Carbon Dioxide Hydrate and Floods on Mars, *Science*, 183, 654-656.
- Mori, Y.H., T. Mochizuki (1997) Mass transport across clathrate hydrate films - a capillary permeation model, *Chemical Engineering Science*, 52, 3613-3616.

- Moudrakovski, I.L., C.I. Ratcliffe, J.A. Ripmeester (2001) Probing transient hydrate structure with hyperpolarized ^{129}Xe NMR spectroscopy: a metastable structure II hydrate of Xe, *Angewandte Chemie, International Edition*, 40, 3890-3892.
- Murshed, M.M., W.F. Kuhs (2007) Hydrate phase transformations imposed by gas exchange, in: W.F. Kuhs (Ed) *Proceedings of the 11th International Conference on the Physics and Chemistry of Ice. Special Publication No. 311*, Royal Society of Chemistry, Cambridge, UK, pp. 427 – 433.
- Murshed, M.M., W.F. Kuhs (2009) Kinetic Studies of Methane-Ethane Mixed Gas Hydrates by Neutron Diffraction and Raman Spectroscopy, *Journal of Physical Chemistry B*, 113, 5172-5180.
- Murshed, M.M., B.C. Schmidt, W.F. Kuhs (submitted) Kinetics of Methane-Ethane Gas Replacement in Clathrate-Hydrates Studied by Time-Resolved Neutron Diffraction and Raman Spectroscopy, *Journal of Physical Chemistry B*.
- Naehr, T.H., D. Birgel, G. Bohrmann, I.R. MacDonald, S. Kasten (2009) Biogeochemical controls on authigenic carbonate formation at the Chapopote "asphalt volcano", Bay of Campeche, *Chemical Geology*, 266, 399-411.
- Nielsen, J.A., D. McMorrow (2001) *Elements of Modern X-ray Physics*, John Wiley and Sons Ltd., Chichester, UK, 318 pp.
- Nikolovska, A., H. Sahling, G. Bohrmann (2008) Novel hydro-acoustic methodology for detection, localization and quantification of gas bubbles rising from the seafloor at gas seeps from the eastern Black Sea, *Geochemistry Geophysics Geosystems*, 9, Q10010, doi:10.1029/2008GC002118.
- Nisbet, E.G., D.J.W. Piper (1998) Giant submarine landslides, *Nature*, 392, 329-330.
- Ohmura, R., W. Shimada, T. Uchida, Y.H. Mori, S. Takeya, J. Nagao, H. Minagawa, T. Ebinuma, H. Narita (2004) Clathrate hydrate crystal growth in liquid water saturated with a hydrate-forming substance: variations in crystal morphology, *Philosophical Magazine*, 84, 1-16.
- Ohno, H., V.Y. Lipenkov, T. Hondoh (2004) Air bubble to clathrate hydrate transformation in polar ice sheets: A reconsideration based on the new data from Dome Fuji ice core, *Geophysical Research Letters*, 31, L21401, doi:21410.21029/22004gl021151.
- Ohno, H., T.A. Strobel, S.F. Dec, E.D. Sloan, C.A. Koh (2009) Raman Studies of Methane-Ethane Hydrate Metastability, *Journal of Physical Chemistry A*, 113, 1711-1716.
- Orphan, V.J., C.H. House, K.-U. Hinrichs, K.D. McKeegan, E.F. DeLong (2001) Methane-consuming Archaea revealed by directly coupled isotopic and phylogenetic analysis, *Science*, 293, 484-487.
- Osegovic, J.P., M.D. Max (2005) Compound clathrate hydrate on Titan's surface, *Journal of Geophysical Research*, 110, E08004, doi:08010.01029/02005JE002435.
- Østergaard, K.K., R. Anderson, M. Llamedo, B. Tohidi (2002) Hydrate phase equilibria in porous media: effect of pore size and salinity, *Terra Nova*, 14, 307-312.
- Østergaard, K.K., R. Masoudi, B. Tohidi, A. Danesh, A.C. Todd (2005) A general correlation for predicting the suppression of hydrate dissociation temperature in the presence of thermodynamic inhibitors, *Journal of Petroleum Science and Engineering*, 48, 70-80.
- Pape, T., M. Blumenberg, R. Seifert, G. Bohrmann, W. Michaelis (2008) Marine methane biogeochemistry of the Black Sea: A review, in: Dilek, Y., H. Furnes, K. Muehlenbachs (Eds) *Links Between Geological Processes, Microbial Activities & Evolution of Life*, Springer Science + Business Media B.V., pp. 281-311.
- Pape, T., A. Bahr, F. Abegg, H.J. Hohnberg, M. Zabel, S. Kasten, G. Bohrmann (submitted) Thermogenic hydrocarbons feeding gas hydrates in shallow deposits of the Amsterdam mud volcano, Anaximander Mountains, Northeastern Mediterranean Sea, *Geo-Marine Letters*.
- Pauer, F., S. Kipfstuhl, W.F. Kuhs, H. Shoji (1999) Air clathrate crystals from the GRIP deep ice core, Greenland: a number-, size- and shape-distribution study, *Journal of Glaciology*, 45, 22-30.
- Pauer, F., S. Kipfstuhl, W.F. Kuhs, H. Shoji (2000) Classification of air clathrates found in polar ice sheets, *Zeitschrift für Polarforschung*, 66, 31-38.
- Paull, C.K., W.I. Ussler, W.S. Borowski, F.N. Spiess (1995) Methane-rich plumes on the Carolina continental rise: Associations with gas hydrates, *Geology*, 23, 89-92.

- Paull, C.K., P.G. Brewer, W. Ussler III, E.T. Peltzer, G. Rehder, D. Clague (2003) An experiment demonstrating that marine slumping is a mechanism to transfer methane from seafloor gas-hydrate deposits into the upper ocean and Atmosphere, *Geo-Marine Letters*, 22, 198-203.
- Paull, C.K., W.R. Normark, W. Ussler III, D.W. Caress, R. Keaten (2008) Association among active seafloor deformation, mound formation, and gas hydrate growth and accumulation within the seafloor of the Santa Monica Basin, offshore California, *Marine Geology*, 250, 258-275.
- Pecher, I.A., C.R. Ranero, R. von Huene, T.A. Minshull, S.C. Singh (1998) The nature and distribution of bottom simulating reflectors at the Costa Rican convergent margin, *Geophysical Journal International*, 133, 219-229.
- Pecher, I.A., N. Kukowski, C. Huebscher, J. Greinert, J. Bialas, G.W. Group (2001) The link between bottom-simulating reflectors and methane flux into the gas hydrate stability zone - new evidence from Lima Basin, Peru Margin, *Earth and Planetary Science Letters*, 185, 343-354.
- Peckmann, J., A. Reimer, U. Luth, C. Luth, B.T. Hansen, C. Heinicke, J. Hoefs, J. Reitner (2001) Methane-derived carbonates and authigenic pyrite from the northwestern Black Sea, *Marine Geology*, 177, 129-150.
- Perry, R.H., D.W. Green (1997) *Perry's Chemical Engineers' Handbook*, McGraw-Hill, 2581 pp. Online version available at: http://knovel.com/web/portal/browse/display?_EXT_KNOVEL_DISPLAY_bookid=48&VerticalID=0.
- Pfannkuche, O., P. Linke (2003) GEOMAR Landers as Long-Term Deep-Sea Observatories, *Sea Technology*, 44, 50-55.
- Pohlman, J.W., E.A. Canuel, N.R. Chapman, G.D. Spence, M.J. Whiticar, R.B. Coffin (2005) The origin of thermogenic gas hydrates on the northern Cascadia Margin as inferred from isotopic ($^{13}\text{C}/^{12}\text{C}$ and D/H) and molecular composition of hydrate and vent gas, *Organic Geochemistry*, 36, 703-716.
- PowderCell (2006) PowderCell 2.3 - Pulverdiffraktogramme aus Einkristalldaten und Anpassung experimenteller Beugungsaufnahmen. Online available at: http://www.bam.de/de/service/publikationen/powder_cell_a.htm (in this version since 29 March 2006).
- Prasad, P.S.R., K. Shiva Prasad, Y. Sowjanya, K. Sain (2008) Laser micro Raman investigations on gas hydrates, *Current Science*, 94, 1495-1499.
- Priest, J., E. Kingston, C. Clayton, P. Schultheiss, M. Druce (2008) The structure of hydrate bearing fine grained marine sediments, in: P. Englezos, J. Ripmeester (Eds) *Proceedings of the 6th International Conference on Gas Hydrates (ICGH 2008)* Vancouver, British Columbia, Canada, July 6-10, 2008, 1 DVD.
- Priestley, J. (1790) *Experiments and Observations on Different Kinds of Acid and Other Natural Branches of Natural Philosophy Connected with the Subject*, Printed by T. Pearson, Vol. 3.
- Rawn, C.J., A.J. Rondinone, B.C. Chakoumakos, S.L. Marshall, L.A. Stern, S. Circone, S.H. Kirby, C.Y. Jones, B.H. Toby, Y. Ishii (2002) Neutron powder diffraction studies as a function of temperature of structure II hydrate formed from a methane + ethane gas mixture. *Proceedings of the 4th International Conference on Gas Hydrates*, Yokohama, Japan, 595-603.
- Rawn, C.J., R. Sassen, S.M. Ulrich, T.J. Phelps, B.C. Chakoumakos, E.A. Payzant (2008) Low temperature X-Ray Diffraction studies of natural gas hydrate samples from the Gulf of Mexico, in: P. Englezos, J. Ripmeester (Eds) *Proceedings of the 6th International Conference on Gas Hydrates (ICGH 2008)* Vancouver, British Columbia, Canada, July 6-10, 2008, 1 DVD.
- Reeburgh, W.S. (1976) Methane consumption in Cariaco Trench waters and sediments, *Earth and Planetary Science Letters*, 28, 337-344.
- Reeburgh, W.S., B.B. Ward, S.C. Whalen, K.A. Sandbeck, K.A. Kilpatrick, L.J. Kerkhof (1991) Black Sea methane geochemistry, *Deep-Sea Research*, 38, S1189-S1210.
- Rehder, G., P.W. Brewer, E.T. Peltzer, G. Friederich (2002) Enhanced lifetime of methane bubble streams within the deep ocean, *Geophysical Research Letters*, 29, doi:10.1029/2001/gl013966.

- Rehder, G., S.H. Kirby, W.B. Durham, L.A. Stern, E.T. Peltzer, J. Pinkston, P.G. Brewer (2004) Dissolution rates of pure methane hydrate and carbon-dioxide hydrate in undersaturated seawater at 1000-m depth, *Geochimica et Cosmochimica Acta*, 68, 285-292.
- Rehder, G., I. Leifer, P.G. Brewer, G. Friederich, E.T. Peltzer (2009) Controls on methane bubble dissolution inside and outside the hydrate stability field from open ocean field experiments and numerical modeling, *Marine Chemistry*, 114, 19-30.
- Reilly II, J.F., E.K. Biegert, J.M. Brooks, I.R. MacDonald (1996) Geologic Controls on the Distribution of Chemosynthetic Communities in the Gulf of Mexico, in: D. Schumacher, M.A. Abrams (Eds) *Hydrocarbon migration and its near-surface expression*, AAPG Memoir 66, pp. 39-62.
- Reitz, A., M. Haeckel, K. Wallmann, C. Hensen, K. Heeschen (2007) Origin of salt-enriched pore fluids in the northern Gulf of Mexico, *Earth and Planetary Science Letters*, 259, 266-282.
- Ribeiro Jr, C.P., P.L.C. Lage (2008) Modelling of hydrate formation kinetics: State-of-the-art and future directions, *Chemical Engineering Science*, 63, 2007-2034.
- Ricard, Y., D. Bercovici (2009) A continuum theory of grain size evolution and damage, *Journal of Geophysical Research*, 114, B01204, doi:10.1029/2007JB005491.
- Riedel, M., T.S. Collett, M.J. Malone, Exploration Scientists (2006) *Proceedings of the Integrated Ocean Drilling Program, Volume 311 Expedition Reports Cascadia Margin Gas Hydrates, Expedition 311 of the riserless drilling platform Balboa, Panama, to Victoria, British Columbia (Canada) Sites U1325-U1329, 28 August-28 October 2005*, 311, Integrated Ocean Drilling Program Management International, Inc., for the Integrated Ocean Drilling Program.
- Ripmeester, J.A., C.I. Ratcliffe (1988) Low-Temperature Cross-Polarization/Magic Angle Spinning ^{13}C NMR of Solid Methane Hydrates: Structure, Cage Occupancy, and Hydration Number, *Journal of Physical Chemistry*, 92, 337-339.
- Ripmeester, J.A., J.S. Tse, C.I. Ratcliffe, B.M. Powell (1987) A new clathrate hydrate structure, *Nature*, 325, 135-136.
- Ritger, S., B. Carson, E. Suess (1987) Methane-derived authigenic carbonates formed by subduction-induced pore-water expulsion along the Oregon/Washington margin, *Geological Society of America Bulletin*, 98, 147-156.
- Roberts, H.H., P. Aharon (1994) Hydrocarbon-derived carbonate buildups of the northern Gulf of Mexico continental slope: A review of submersible investigations, *Geo-Marine Letters*, 14, 135-148.
- Roberts, H.H., R.S. Carney (1997) Evidence of episodic fluid, gas, and sediment venting on the northern Gulf of Mexico continental slope, *Economic Geology*, 92, 863-879.
- Rochelle, C.A., A.P. Camps, D. Long, A. Milodowski, K. Bateman, D. Gunn, P. Jackson, M.A. Lovell, J. Rees (2009) Can CO_2 hydrate assist in the underground storage of carbon dioxide?, *Geological Society, London, Special Publications*, 319, 171-183.
- Rodriguez-Navarro, A.B., P. Alvarez-Lloret, M. Ortega-Huertas, M. Rodriguez-Gallego (2006) Automatic crystal size determination in the micrometer range from spotty X-ray diffraction rings of powder samples, *Journal of the American Ceramic Society*, 89, 2232-2238.
- Ross, D.A., E.T. Degens (1974) Recent sediments of Black Sea, in: E.T. Degens, D.A. Ross (Eds) *The Black Sea - Geology, Chemistry and Biology*, American Association of Petroleum Geologists, Tulsa, Oklahoma, USA, pp. 183-199.
- Rothwell, R.G., J. Thomson, G. Kähler (1998) Low-sea-level emplacement of a very large Late Pleistocene "megaturbidite" in the western Mediterranean Sea, *Nature*, 392, 377-379.
- Rowan, M.G., M.P.A. Jackson, B.D. Trudgill (1999) Salt-related fault families and fault welds in the northern Gulf of Mexico, *AAPG Bulletin* 83, 1454-1484.
- Ruppel, C. (2000) Thermal state of the gas hydrate reservoir, in: M.D. Max (Ed) *Natural gas hydrate in oceanic and permafrost environments*, Kluwer Academic Publications, Dordrecht, pp. 29-42.
- Ruppel, C., G.R. Dickens, D.G. Castellini, W. Gilhooly, D. Lizarralde (2005) Heat and salt inhibition of gas hydrate formation in the northern Gulf of Mexico, *Geophysical Research Letters*, 32, L04605, doi:10.1029/2004GL021909.

- Ryan, W.B.F., C. Major, G. Lericolais, S.L. Goldstein (2003) Catastrophic flooding of the Black Sea, *Annual Reviews in Earth and Planetary Sciences*, 31, 525-554.
- Ryu, B.-J., M. Riedel, J.-H. Kim, R.D. Hyndman, Y.-J. Lee, B.-H. Chung, I.-S. Kim (2009) Gas hydrates in the western deep-water Ulleung Basin, East Sea of Korea, *Marine and Petroleum Geology*, 26, 1483-1498.
- Sager, W.W., I.R. MacDonald, R. Hou (2003) Geophysical signatures of mud mounds at hydrocarbon seeps on the Louisiana continental slope, northern Gulf of Mexico, *Marine Geology*, 198, 97-132.
- Sahling, H., D. Rickert, R.W. Lee, P. Linke, E. Suess (2002) Macrofaunal community structure and sulfide flux at gas hydrate deposits from the Cascadia convergent margin, NE Pacific, *Marine Ecology-Progress Series*, 231, 121-138.
- Sahling, H., S.V. Galkin, A. Salyuk, J. Greinert, H. Foerstel, D. Piepenburg, E. Suess (2003) Depth-related structure and ecological significance of cold-seep communities - a case study from the Sea of Okhotsk, *Deep-Sea Research Part I. Oceanographic Research Papers*, 50, 1391-1409.
- Sahling, H., G. Bohrmann, V. Spiess, J. Bialas, M. Breitzke, M. Ivanov, S. Kasten, S. Krastel, R. Schneider (2008) Pockmarks in the Northern Congo Fan area, SW Africa: Complex seafloor features shaped by fluid flow, *Marine Geology*, 249, 206-225.
- Salamantin, A.N., V.Y. Lipenkov, T. Hondoh (2003) Air-hydrate crystal growth in polar ice, *Journal of Crystal Growth*, 257, 412-426.
- Santamaría-Orozco, D., B. Horsfield, R. di Primio, D.H. Welte (1998) Influence of maturity on distributions of benzo- and dibenzothiophenes in Tithonian source rocks and crude oils, Sonda de Campeche, Mexico, *Organic Geochemistry*, 28, 423-439.
- Sassen, R., I.R. Mac Donald, A.G. Requejo, N.L. Guinasso Jr, M.C. Kennicutt II, S.T. Sweet, J.M. Brooks (1994) Organic geochemistry of sediments from chemosynthetic communities, Gulf of Mexico slope, *Geo-Marine Letters*, 14, 110-119.
- Sassen, R., S. Joye, S.T. Sweet, D.A. DeFreitas, A.V. Milkov, I.R. MacDonald (1999) Thermogenic gas hydrates and hydrocarbon gases in complex chemosynthetic communities, Gulf of Mexico continental slope, *Organic Geochemistry*, 30, 485-497.
- Sassen, R., S.T. Sweet, A.V. Milkov, D.A. DeFreitas, M.C. Kennicutt (2001a) Thermogenic vent gas and gas hydrate in the Gulf of Mexico slope: Is gas hydrate decomposition significant?, *Geology*, 29, 107-110.
- Sassen, R., Losh, S.L., Cathles III, L., Roberts, H.H., Whelan, J.K., Milkov, A.V., Sweet, S.T., DeFreitas, D.A. (2001b) Massive vein-filling gas hydrate: relation to ongoing gas migration from the deep subsurface in the Gulf of Mexico. *Marine and Petroleum Geology*, 18, 551-560.
- Sassen, R., Sweet, S.T., DeFreitas, D.A., Morelos, J.A., Milkov, A.V. (2001c) Gas hydrate and crude oil from the Mississippi Fan Foldbelt, downdip Gulf of Mexico Salt Basin: significance to petroleum system. *Organic Geochemistry*, 32, 999-1008.
- Sassen, R., S.T. Sweet, A.V. Milkov, D.A. DeFreitas, M.C. Kennicutt II, H.H. Roberts (2001d) Stability of thermogenic gas hydrates in the Gulf of Mexico: Constraints on models of climate change, in: Paull, C.K. and W.P. Dillon (Eds) *Natural gas hydrates: Occurrence, distribution, and detection*. Geophysical Monograph. American Geophysical Union, Washington D.C., 131-143 pp.
- Sauter, E.J., S.I. Muyakshin, J.L. Charlou, M. Schluter, A. Boetius, K. Jerosch, E. Damm, J.P. Foucher, M. Klages (2006) Methane discharge from a deep-sea submarine mud volcano into the upper water column by gas hydrate-coated methane bubbles, *Earth and Planetary Science Letters*, 243, 354-365.
- Schicks, J.M., R. Naumann, J. Erzinger, K.C. Hester, C.A. Koh, E.D. Sloan (2006) Phase Transitions in Mixed Gas Hydrates: Experimental Observations versus Calculated Data, *Journal of Physical Chemistry B*, 110, 11468-11474.
- Schmale, O., J. Greinert, G. Rehder (2005) Methane emission from high-intensity marine gas seeps in the Black Sea into the atmosphere, *Geophysical Research Letters*, 32, L07609, doi:10.1029/2004gl021138.
- Schoell, M. (1988) Multiple origins of methane in the earth, *Chemical Geology*, 71, 1-10.
- Schubert, C.J., E. Durisch-Kaier, L. Klausner, F. Vazquez, B. Wehrli, C. Holzner, R. Kipfer, O. Schmale, J. Greinert, M.M.M. Kuypers (2006) Recent studies on sources and sinks

- of methane in the Black Sea, in: L.N. Neretin (Ed) Past and Present Water Column Anoxia, Springer, Dordrecht, pp. 419-441.
- Shiple, T.H., B.M. Didyk (1982) Occurrence of Methane Hydrates Offshore Southern Mexico, Initial Report of the Deep Sea Drilling Project GPO: Washington, D.C., 66, 547-555.
- Shoji, H., C.C. Langway (1982) Air hydrate inclusions in fresh ice core, *Nature*, 298, 548-550.
- Skovborg, P., H.J. Ng, P. Rasmussen, U. Mohn (1993) Measurements of induction times for the formation of methane and ethane gas hydrates, *Chemical Engineering Science*, 48, 445-453.
- Sloan, E.D., C.A. Koh (2007) Clathrate hydrates of natural gases, CRC Press, 119, Boca Raton, 752 pp.
- Smelik, E.A., H.E. King (1997) Crystal-growth studies of natural gas clathrate hydrates using a pressurized optical cell, *American Mineralogist*, 82, 88-98.
- Solomon, E.A., M. Kastner, I.R. MacDonald, I. Leifer (2009) Considerable methane fluxes to the atmosphere from hydrocarbon seeps in the Gulf of Mexico, *Nature Geoscience*, 2, 561-565.
- Spath, H. (eds) (1985) Spath Cluster Dissection and Analysis—Theory, FORTRAN Programs, Examples, translated by J. Goldschmidt, Halsted Press, New York, 226 pp.
- Stampanoni, M., A. Groso, A. Isenegger, G. Mikuljan, Q. Chen, A. Bertrand, S. Henein, R. Betemps, U. Frommherz, P. Böhler, D. Meister, M. Lange, R. Abela (2006) Trends in synchrotron-based tomographic imaging: the SLS experience, in: U. Bonse (Ed) Developments in X-Ray Tomography V. Proc. of SPIE Vol. 6318, 63180M, doi: 10.1117/12.679497.
- Starostenko, V., V. Buryanov, I. Makarenko, O. Rusakov, R. Stephenson, A. Nikishin, G. Georgiev, M. Gerasimov, R. Dimitriu, O. Legostaeva, V. Pehelarov, C. Sava (2004) Topography of the crust-mantle boundary beneath the Black Sea Basin, *Tectonophysics*, 381, 211-233.
- Staykova, D.K., W.F. Kuhs, A.N. Salamantin, T. Hansen (2003) Formation of porous gas hydrates from ice powders: diffraction experiments and multi-stage model, *Journal of Physical Chemistry B*, 107, 10299-10311.
- Stern, L.A., S.H. Kirby, W.B. Durham (1996) Peculiarities of Methane Clathrate Hydrate Formation and Solid-State Deformation, Including Possible Superheating of Water Ice, *Science*, 273, 1843-1848.
- Stern, L.A., S. Circone, S.H. Kirby, W.B. Durham (2001) Anomalous Preservation of Pure Methane Hydrate at 1 atm, *Journal of Physical Chemistry B*, 105, 1756-1762.
- Stern, L.A., S. Circone, S.H. Kirby, W.B. Durham (2002) Reply to "Comments on "Anomalous Preservation of Pure Methane Hydrate at 1 atm", *Journal of Physical Chemistry B*, 106, 228-230.
- Stern, L.A., S.H. Kirby, S. Circone, W.B. Durham (2004) Scanning Electron Microscopy investigations of laboratory-grown gas clathrate hydrates formed from melting ice, and comparison to natural hydrates, *American Mineralogist*, 89, 1162-1174.
- Stern, L.A., S.H. Kirby, W.B. Durham (2005) Scanning electron microscope imaging of grain structure and phase distribution within gas-hydrate-bearing intervals from JAPEx/JNOCGSC et al. Mallik 5L-38: what can we learn from comparisons with laboratory-synthesized samples?, in: S.R. Dallimore, T.S. Collett (Eds) Scientific Results from the Mallik 2002 Gas Hydrate Production Research Well Program, Mackenzie Delta, Northwest Territories, Canada 585, Geological Survey of Canada, Bulletin, pp. 19.
- Stern, L.A., S.H. Kirby (2007) Grain and pore structure imaging of gas hydrate from core MD02-2569 (Mississippi Canyon, Gulf of Mexico): A first look by Scanning Electron Microscopy (SEM) Chapter 12, in: W.J. Winters, T.D. Lorenson, C.K. Paull (Eds) Initial report of the IMAGES VIII/PAGE 127 gas hydrate and paleoclimate cruise on the RV Marion Dufresne in the Gulf of Mexico, 2–18 July 2002 Open-File Report 2004–1358, U.S. Geological Survey, p. 8.
- Stern, L.A., S.H. Kirby (2008) Natural gas hydrates up close: a comparison of grain characteristics of samples from marine and permafrost environments as revealed by cryogenic SEM, in: P. Englezos, J. Ripmeester (Eds) Proceedings of the 6th

- International Conference on Gas Hydrates (ICGH 2008) Vancouver, British Columbia, Canada, July 6-10, 2008, 1 DVD.
- Stern, L.A., T.D. Lorenson, J.C. Pinkston (in press) Gas hydrate characterization and grain-scale imaging of recovered cores from the BPXA-DOE-USGS Mount Elbert Gas Hydrate Stratigraphic Test Well, Milne Point, Alaska, *Marine and Petroleum Geology*, In Press, Accepted Manuscript.
- Stevens, J.C., J.J. Howard, B.A. Baldwin, G. Ersland, J. Husebø, A. Graue (2008) Experimental hydrate formation and gas production scenarios based on CO₂ sequestration, in: P. Englezos, J. Ripmeester (Eds) *Proceedings of the 6th International Conference on Gas Hydrates (ICGH 2008) Vancouver, British Columbia, Canada, July 6-10, 2008, 1 DVD.*
- Strobel, T.A., C.J. Taylor, K.C. Hester, S.F. Dec, C.A. Koh, K.T. Miller, E.D. Sloan (2006) Molecular hydrogen storage in binary THF-H₂ clathrate hydrates, *Journal of Physical Chemistry B*, 110, 17, 121-17, 125.
- Subramanian, S., R.A. Kini, S.F. Dec, E.D. Sloan Jr. (2000a) Evidence of structure II hydrate formation from methane+ethane mixtures, *Chemical Engineering Science*, 55, 1981-1999.
- Subramanian, S., A.L. Ballard, R.A. Kini, S.F. Dec, E.D. Sloan (2000b) Structural transitions in methane plus ethane gas hydrates - Part I: upper transition point and applications, *Chemical Engineering Science*, 55, 5763-5771.
- Subramanian, S., E.D. Sloan (2002) Trends in vibrational frequencies of guests trapped in clathrate hydrate cages, *Journal of Physical Chemistry B*, 106, 4348-4355.
- Suess, E., M.E. Torres, G. Bohrmann, R.W. Collier, J. Greinert, L. Linke, G. Rehder, A. Tréhu, K. Wallmann, G. Winckler, E. Zuleger (1999) Gas hydrate destabilization: enhanced dewatering, benthic material turnover and large methane plumes at the Cascadia convergent margin, *Earth and Planetary Science Letters*, 170, 1-15.
- Suess, E., M.E. Torres, G. Bohrmann, R.W. Collier, D. Rickert, C. Goldfinger, P. Linke, A. Heuser, H. Sahling, K. Heeschen, C. Jung, K. Nakamura, J. Greinert, O. Pfannkuche, A. Tréhu, G. Klinkhammer, M.C. Whiticar, A. Eisenhauer, B. Teichert, E. Elvert (2001) Sea floor methane hydrates at Hydrate Ridge, Cascadia Margin, in: Paull, C.K., W.P. Dillon (Eds) *Natural gas hydrates: Occurrence, distribution, and detection*, Geophysical Monograph 124, American Geophysical Union, Washington D.C., pp. 87-98.
- Suess, E., G. Bohrmann, D. Rickert, W.F. Kuhs, M.E. Torres, A. Tréhu, P. Linke (2002) Properties and fabric of near-surface methane hydrates at Hydrate Ridge, Cascadia Margin, *Fourth International Conference on Gas Hydrates*, Yokohama, May 19-23, 2002, 740-744.
- Sum, A.K., R.C. Burruss, J. E. D. Sloan (1997) Measurement of Clathrate Hydrates via Raman Spectroscopy, *Journal of Physical Chemistry B*, 101, 7371-7377.
- Sun, C.Y., Chen, G.-J., Ma, C.-F., Huang, Q., Luo, H., Li, Q.-P. (2007) The growth kinetics of hydrate film on the surface of gas bubble suspended in water or aqueous surfactant solution, *Journal of Crystal Growth*, 306, 491-499.
- Sun, R., Z. Duan (2007) An accurate model to predict the thermodynamic stability of methane hydrate and methane solubility in marine environments, *Chemical Geology*, 244, 248-262.
- Susilo, R. (2008) Methane storage and transport via structure H clathrate hydrate, PhD thesis, University of British Columbia, Canada.
- Takahashi, H., T. Yonezawa, Y. Takedomi, (2001) Exploration for Natural Gas Hydrate in Nankai-Trough Wells Offshore Japan, *Journal of the Japanese Association for Petroleum Technology*, 66, 652-665.
- Takeya, S., W. Shimada, Y. Kamata, T. Ebinuma, T. Uchida, J. Nagao, H. Narita (2001) In Situ X-ray Diffraction Measurements of the Self-Preservation Effect of CH₄ Hydrate, *Journal of Physical Chemistry A*, 105, 9756-9759.
- Takeya, S., Y. Kamata, T. Uchida, J. Nagao, T. Ebinuma, H. Narita, A. Hori, T. Hondoh (2003) Coexistence of structure I and II hydrates formed from a mixture of methane and ethane gases, *Canadian Journal of Physics*, 81, 479-484.
- Techmer, K.S., T. Heinrichs, W.F. Kuhs (2005) Cryo-electron microscopic studies on the structures and composition of Mallik gas-hydrate-bearing samples, in: S.R.

- Dallimore, T.S. Collett (Eds) Scientific Results from JAPEX/JNOC/GSC et al., Mallik as Hydrate Production Research Well Program, Mackenzie Delta, Northwest Territories, Canada, Geological Survey of Canada Bulletin 585, pp. 12.
- Tishchenko, P., C. Hensen, K. Wallmann, C.S. Wong (2005) Calculation of the stability and solubility of methane hydrate in seawater, *Chemical Geology*, 219, 37-52.
- Tissot, B.P., D.H. Welte (1984) *Petroleum formation and occurrence*, Springer, New York, NY, 699 pp.
- Tobie, G., J.I. Lunine, C. Sotin (2006) Episodic outgassing as the origin of atmospheric methane on Titan, *Nature*, 440, 61-64.
- Toby, B.H. (2001) *EXPGUI*, a graphical user interface for GSAS, *Journal of Applied Crystallography*, 34, 210-213.
- Tohidi, B., R. Anderson, M.B. Clennell, R.W. Burgass, A.B. Biderkab (2001) Visual observation of gas-hydrate formation and dissociation in synthetic porous media by means of glass micromodels, *Geology*, 29, 867-870.
- Topham, D.R. (1984) The Formation of Gas Hydrates on Bubbles of Hydrocarbon Gases Rising in Seawater, *Chemical Engineering Science*, 39, 821-828.
- Torres, M.E., J. McManus, D.E. Hammond, M.A. de Angelis, K.U. Heeschen, S.L. Colbert, M.D. Tryon, K.M. Brown, E. Suess (2002) Fluid and chemical fluxes in and out of sediments hosting methane hydrate deposits on Hydrate Ridge, OR, I: Hydrological provinces, *Earth and Planetary Science Letters*, 201, 525-540.
- Torres, M.E., K. Wallmann, A.M. Tréhu, G. Bohrmann, W.S. Borowski, H. Tomaru (2004) Gas hydrate growth, methane transport, and chloride enrichment at the southern summit of Hydrate Ridge, Cascadia margin off Oregon, *Earth and Planetary Science Letters*, 226, 225-241.
- Tréhu, A.M., M.E. Torres, G.F. Moore, E. Suess, G. Bohrmann (1999) Temporal and spatial evolution of a gas hydrate-bearing accretionary ridge on the Oregon continental margin, *Geology*, 27, 939-942.
- Tréhu, A. M., G. Bohrmann, F. R. Rack, M. E. Torres and ODP Leg 204 Shipboard Scientific Party (2003) Proceedings of the Ocean Drilling Program Initial Reports, 204: College Station, TX (Ocean Drilling Program). doi:10.2973/odp.proc.ir.204.2003
- Tréhu, A.M., P.E. Long, M.E. Torres, G. Bohrmann, R.F. R., T.S. Collett, D.S. Goldberg, A.V. Milkov, M. Riedel, P. Schultheiss, N.L. Bangs, S.R. Barr, W.S. Borowski, G.E. Claypool, M.E. Delwiche, G.R. Dickens, E. Gracia, G. Guerin, M. Holland, J.E. Johnson, Y.-J. Lee, C.-S. Liu, X. Su, B. Teichert, H. Tomaru, M. Vanneste, M. Watanabe, J.L. Weinberger (2004) Three-dimensional distribution of gas hydrate beneath southern Hydrate Ridge: constraints from ODP Leg 204, *Earth and Planetary Science Letters*, 222, 845-862.
- Tréhu, A.M., C. Ruppel, M. Holland, G.R. Dickens, M.E. Torres, T.S. Collett, D. Goldberg, M. Riedel, P. Schultheiss (2006a) Gas Hydrates in Marine Sediments: Lessons from Scientific Ocean Drilling, *Oceanography*, 19, 124-142.
- Tréhu, A.M., G. Bohrmann, M.E. Torres, F.S. Colwell (Eds) (2006b) Proceedings of the Ocean Drilling Program (ODP) 204, Scientific Results, College Station, TX (Ocean Drilling Program) doi:10.2973/odp.proc.sr.204.2006.
- Triebold, S., A. Kronz, G. Wörner (2006) Anorthite-calibrated backscattered electron profiles, trace elements, and growth textures in feldspars from the Teide-Pico Viejo volcanic complex (Tenerife) *Journal of Volcanology and Geothermal Research*, 154, 117-130.
- Tugolesov, D.A., A.S. Gorshkov, L.B. Meysner, V.V. Soloviov, E.M. Khakhalev, Y.V. Akilova, G.P. Akentieva, T.I. Gabidulina, S.A. Kolomeytseva, T.Y. Kochneva, I.G. Pereturina, I.N. Plashihina (1985) *Tectonics of the Mesozoic Sediments of the Black Sea Basin*, Nedra, Moscow, 215 pp.
- Tulk, C., J. Ripmeester, D. Klug (2000) The application of Raman spectroscopy to the study of gas hydrates, *Annals of the New York Academy of Sciences*, 912, 859-872.
- Tulk, C.A., J.F. Wright, C.I. Ratcliffe, J.A. Ripmeester (1999) Storage and handling of natural gas hydrate, in: S.R. Dallimore, T. Uchida, T.S. Collett (Eds) Scientific Results from JAPEX/JNOC/GSC Mallik 2L-38 Gas Hydrate Research Well, Mackenzie Delta, Northwest Territories, Canada Geological Survey of Canada, Bulletin 544, pp. 263-267.

- Uchida, T., S. Dallimore, and J. Mikami (2000) Occurrences of natural gas hydrates beneath the permafrost zone in Mackenzie Delta visual and X ray CT imagery, *Annals of the New York Academy of Science*, 912, 1021-1033.
- Uchida, T., S. Takeya, Y. Kamata, I.Y. Ikeda, J. Nagao, T. Ebinuma, H. Narita, O. Zatsepina, B.A. Buffett (2002) Spectroscopic observations and thermodynamic calculations on clathrate hydrates of mixed gas containing methane and ethane: Determination of structure, composition and cage occupancy, *Journal of Physical Chemistry B*, 106, 48, 12426-12431.
- Uchida, T., S. Takeya, Y. Kamata, R. Ohmura, H. Narita (2007) Spectroscopic Measurements on Binary, Ternary, and Quaternary Mixed-Gas Molecules in Clathrate Structures, *Industrial & Engineering Chemistry Research*, 46, 5080-5087.
- Udachin, K.A., H. Lu, G.D. Enright, C.I. Ratcliffe, J.A. Ripmeester, N.R. Chapman, M. Riedel, G. Spence (2007) Single Crystals of Naturally Occurring Gas Hydrates: The Structures of Methane and Mixed Hydrocarbon Hydrates, *Angewandte Chemie International Edition*, 46, 8220-8222.
- Ussler III, W., C.K. Paull (2001) Ion exclusion associated with marine gas hydrate deposits, in: Paull, C.K., W.P. Dillon (Eds) *Natural gas hydrates: Occurrence, distribution, and detection*, Geophysical Monograph 124, American Geophysical Union, Washington D.C., pp. 41-52.
- van der Waals, J.H., J.C. Platteeuw (1959) Clathrate solutions, *Advances in Chemical Physics*, 11, 1-58.
- Von Stackelberg, M., H.R. Müller (1951) On the Structure of Gas Hydrates, *Journal of Chemical Physics*, 19, 1319-1320.
- von Stackelberg, M., H.R. Müller (1954) Feste Gashydrate II, *Zeitschrift für Elektrochemie*, 58, 25-39.
- Wagner, C. (1961) Theorie der Alterung von Niederschlägen durch Umlösen (Ostwaldreifung) *Zeitschrift für Elektrochemie*, 65, 581-591.
- Wagner-Friedrichs, M. (2007) Seafloor seepage in the Black Sea: mud volcanoes, seeps and diapiric structures imaged by acoustic methods, Ph.D. thesis, University of Bremen, Germany.
- Wallmann, K., M. Drews, G. Aloisi, G. Bohrmann (2006a) Methane discharge into the Black Sea and the global ocean via fluid flow through submarine mud volcanoes, *Earth and Planetary Science Letters*, 248, 545-560.
- Wallmann, K., G. Aloisi, M. Haeckel, A. Obzhairov, G. Pavlova, P. Tishchenko (2006b) Kinetics of organic matter degradation, microbial methane generation, and gas hydrate formation in anoxic marine sediments, *Geochimica et Cosmochimica Acta*, 70, 3905-3927.
- Walsh, M.R., S.H. Hancock, S.J. Wilson, S.L. Patil, G.J. Moridis, R. Boswell, T.S. Collett, C.A. Koh, E.D. Sloan (2009) Preliminary report on the commercial viability of gas production from natural gas hydrates, *Energy Economics*, 31, 815-823.
- Wang, B., A.P. Cote, H. Furukawa, M. O'Keeffe, O.M. Yaghi (2008) Colossal cages in zeolitic imidazolate frameworks as selective carbon dioxide reservoirs, *Nature*, 453, 207-211.
- Watkins, J.S., J.W. Ladd, R.T. Buffler, F.J. Shaub, M.H. Housto, J.L. Worzel (1978) Occurrence and evolution of salt in deep Gulf of Mexico, in: A.H. Bouma, G.T. Moore, J.M. Coleman (Eds) *Framework, facies and oil-trapping characteristics of the upper continental margin*, AAPG studies in Geology 7, 43-65.
- WBGU (2006) "Die Zukunft der Meere - zu warm, zu hoch, zu sauer", Wissenschaftlicher Beirat der Bundesregierung Globale Umweltveränderungen, Berlin, 53 pp.
- Wcislak, L., H.J. Bunge, H. Klein, U. Garbe, J.R. Schneider (2003) High-resolution texture imaging with hard synchrotron radiation in the moving area detector technique, *Nuclear Instruments & Methods in Physics Research (Section B) Beam Interactions with Materials and Atoms*, 199, 38-43.
- Westbrook, G.K., K.E. Thatcher, E.J. Rohling, A.M. Piotrowski, H. Pälike, A.H. Osborne, E.G. Nisbet, T.A. Minshull, M. Lanoisellé, R.H. James, V. Hühnerbach, D. Green, R.E. Fisher, A.J. Crocker, A. Chabert, C. Bolton, A. Beszczynska-Möller, C. Berndt, A. Aquilina (2009) Escape of methane gas from the seabed along the West

- Spitsbergen continental margin, *Geophysical Research Letters*, 36, L15608, doi:15610.11029/12009GL039191.
- Whelan, J., Eglinton, L., Cathles III, L., Losh, S. and Roberts, H., 2005. Surface and subsurface manifestations of gas movement through a N-S transect of the Gulf of Mexico. *Marine and Petroleum Geology*, 22, 479-497.
- Whiticar, M.J., E. Faber, M. Schoell (1986) Biogenic methane formation in marine and freshwater environments: CO₂ reduction vs. acetate fermentation - isotope evidence, *Geochimica et Cosmochimica Acta*, 50, 693-709.
- Whiticar, M.J., M. Hovland, M. Kastner, J.C. Sample (1995) Organic geochemistry of gases, fluids, and hydrates at the Cascadia accretionary margin, in: Carson, B., G.K. Westbrook, R.J. Musgrave, E. Suess (Eds) *Proceedings of the Ocean Drilling Program, Scientific Results 146 (Pt. 1)*.
- Whiticar, M.J. (1999) Carbon and hydrogen isotope systematics of bacterial formation and oxidation of methane, *Chemical Geology*, 161, 291-314.
- Wilcox, W.I., D.B. Carson, D.L. Katz (1941) Natural Gas Hydrates, *Industrial & Engineering Chemistry Research*, 33, 662-665.
- Wilson, L.D., C.A. Tulk, J.A. Ripmeester (2002) Instrumental Techniques for the Investigation of Methane Hydrates: Cross-Calibrating NMR and Raman Spectroscopic Data, *Fourth International Conference on Gas Hydrates*, May 19-23, Yokohama, Japan, pp. 614-618.
- Worrall, D.M., S. Snelson (1989) Evolution of the northern Gulf of Mexico, with emphasis on Cenozoic growth faulting and the role of salt, in: Bally, A.W., A.R. Palmer (Eds) *The geology of North America: an overview: GSA Decade of North American Geology*, v.A., pp. 97-138.
- Xu, W. (2004) Modeling dynamic marine gas hydrate systems, *American Mineralogist*, 89, 1271-1279.
- Yamamoto, A., Y. Yamanaka, E. Tajika (2009) Modeling of methane bubbles released from large sea-floor area: Condition required for methane emission to the atmosphere, *Earth and Planetary Science Letters*, 284, 590-598.
- Yefremova, A.G., B.P. Zhizhchenko (1974) Occurrence of Crystal Hydrates of Gases in the Sediments of Modern Marine Basins, *Doklady Akademii Nauk SSSR (Translation)* 214, 1179-1181.
- Yeon, S.H., J. Seol, H. Lee (2006) Structure transition and swapping pattern of clathrate hydrates driven by external guest molecules, *Journal of the American Chemical Society*, 128, 12388-12389.
- Yoon, J.H., T. Kawamura, Y. Yamamoto, T. Komai (2004) Transformation of Methane Hydrate to Carbon Dioxide Hydrate: In Situ Raman Spectroscopic Observations, *Journal of Physical Chemistry A*, 108, 5057-5059.
- York, J.D., A. Firoozabadi (2009) Effect of Brine on Hydrate Antiagglomeration, *Energy & Fuels*, 23, 2937-2946.
- Zachos, J.C., G.R. Dickens, R.E. Zeebe (2008) An early Cenozoic perspective on greenhouse warming and carbon-cycle dynamics, *Nature*, 451, 279-283.
- Zeebe, R.E., J.C. Zachos, G.R. Dickens (2009) Carbon dioxide forcing alone insufficient to explain Palaeocene-Eocene Thermal Maximum warming, *Nature Geoscience*, 2, 576-580.
- Zhang, H., S. Yang, N. Wu, X. Su, M. Holland, P. Schultheiss, K. Rose, H. Bultler, G. Humphrey (2007) Successful and surprising results for China's first gas hydrate drilling expedition, *Fire in the Ice*, US-DOE-NETL Methane Hydrate Newsletter (www.netl.doe.gov/technologies/oil-gas/publications/Hydrates/Newsletter/HMNewsFall07.pdf) Fall 2007, 6-9.

ACKNOWLEDGEMENTS

Without the support and help of so many I would have never succeeded in this work. I am very grateful to many people including the following:

First of all, I would sincerely like to thank Prof. Dr. Gerhard Bohrmann (Marum) for giving me the opportunity to design my research project in his group. He had faith in me, allowed much freedom and let me establish and cultivate collaborations with partners both home and abroad. He offered me guidance, assistance and friendship and left no doubt that he wanted me to succeed in this work.

To Prof. Dr. Werner F. Kuhs (Göttingen), for supporting me throughout my academic career till this day. Also, I would like to thank him for his patience, which I tried a lot, and for the many creative discussions and enlightening insights on gas hydrates he shared with me.

To Dr. Thomas Pape (Marum), for his inspiring ideas, for counsel and advice on countless questions, for sharing his understanding of scientific practice with me and for being a great friend.

To Dr. Peter G. Brewer, for showing me how to recognize connections and realize which questions matter, for his patience and for hosting me as a member in his lab at MBARI.

To 'GLOMAR – Graduate school of Marine Sciences', including Prof. Dr. Dierk Hebbeln, Dr. Uta Brathauer and Dr. Philipp Assmy for the enormous support and education.

To Dieter Vollkammer, head of the 'HGM Energy GmbH' in Bremen for my scholarship.

To the 'MARUM – Center for Marine and Environmental Sciences', for giving me the opportunity to conduct my research here.

To Dr. Mangir M. Murshed (Göttingen), for the numerous conversations on Raman spectroscopy and scientific theory as well as culture and music, and for helping me out more than once.

To PD Dr. Helmut Klein and Susanne Hemes (both Göttingen), for the successful and thriving beam times in Hamburg.

To Dr. Frieder Enzmann (Mainz), for introducing me into a whole new micro-cosmos.

To Peter Walz, Dr. Keith C. Hester, Dr. Edward T. Peltzer and Xin Zhang for many stimulating discussions, for the tremendous support and for making my stay at MBARI successful.

To Dr. Thomas Huthwelker, for his energetic support and inventive solutions during the beam times at the Swiss Light Source.

To Dr. André Bahr (now Kiel) and Prof. Dr. Janet Rethemeyer (now Cologne), for the many productive discussions on the Black Sea, the great time together on METEOR and for being great friends.

To Dr. Thore Szeder (then Mainz), for the ingenious idea to use μ CT at the SLS for gas hydrates.

To Markus Brüning and Katharina Jantzen, for our efficient and smooth cooperation as PhD student representatives, and for sharing almost the whole PhD time with me. They became dear friends.

To the 'AG Bohrmann', including Angelika Rinkel, Greta Ohling, Dr. Heiko Sahling, Dr. Antonie Haas, Dr. Fritz Abegg, Miriam Römer, David Fischer, PD Dr. Sabine Kasten, Jürgen Hohnberg, Gregor von Halem, Dr. Akihiro Hiruta and Jan-Hendrik Körber and all our guests, for creating a very welcoming and comfortable atmosphere forming a relaxed, open-minded and scientifically stimulating environment.

The scientific colleagues and technical staff in Göttingen, including PD Dr. Heidrun Sowa, Dr. Kirsten S. Techmer, Dr. Sérgio H. Faria, Eberhard Hensel and Heiner Bartels. They always made me feel warm and relaxed and provided a comfortable, efficient scientific atmosphere.

To Dr. Barbara Teichert (Münster), for her generous help with the Indian hydrate sample.

To the secretaries of our group – this goes extra – Angelika Rinkel, Greta Ohling and Gabi Rathmeyer for the tremendous support far beyond administrative issues.

To the technical, administrative and PR support at the MARUM and Department of Geosciences, including the MARUM-workshop, Carmen Murken, Gabi Ratmeyer, Volker Diekamp, Albert Gerdes and Kirsten Achenbach.

To the Captains and Crews of the R/V METEOR Cruises M70/3, M72/3a+b, M74/3 and of R/V POINT LOBOS in September 2008, and to the ROV pilots.

To the scientific and technical support at the HASYLAB beamlines HARWII 2 and BW5 as well as at the TOMCAT beamline at the SLS, including Dr. Rajmund Mokso, Dr. Marco Stampanoni (both SLS) and Rüdiger Nowak (HASYLAB).

To the student helpers, including David Wangner (Marum) and Elena Efuni (Mainz), for disburdening me a lot.

To all other colleagues from different institutes, who contributed in different ways to the success of this work, including Marilena Calarco, Dr. Tomas Feseker, Dr. Matthias Haeckel, Dr. Matthias Held, Dr. Sepp Kipfstuhl, Dr. Ian R. MacDonald, Dr. Lars Raue, PD Dr. Burkhard Schmidt, Dr. Jens-Oliver Schwarz and Dr. Caterina E. Tommaseo.

Also, I thank my wonderful wife Jessica for her great support over the last years, for her understanding when I was working long hours and for her genuine interest in my research – she now is halfway a gas hydrate researcher herself.

I am grateful to my family and friends outside geosciences for their faith in me accomplishing this goal, and for their still growing curiosity in my field of study.

Appendices

Appendix I: Feseker et al., in press

Appendix II: Sahling et al., in press

Appendix III: Pape et al., submitted in revised form (Abstract)

Appendix IV: Bohrmann et al., 2007

Appendix V: Klapp et al., 2009



Contents lists available at ScienceDirect

Marine and Petroleum Geology

journal homepage: www.elsevier.com/locate/marpetgeo

The thermal structure of the Dvurechenskii mud volcano and its implications for gas hydrate stability and eruption dynamics

T. Feseker^{a,b,*}, T. Pape^c, K. Wallmann^d, S.A. Klapp^c, F. Schmidt-Schierhorn^c, G. Bohrmann^c

^a Max-Planck-Institute for Marine Microbiology, Bremen, Germany

^b Ifremer, Department of Marine Geosciences, Brest, France

^c MARUM – Center for Marine Environmental Sciences and Faculty of Geosciences, University of Bremen, Germany

^d IFM-GEOMAR, Leibniz Institute of Marine Sciences, Kiel, Germany

ARTICLE INFO

Article history:

Received 26 May 2008

Received in revised form

22 January 2009

Accepted 26 January 2009

Available online xxx

Keywords:

Black Sea

Mud volcano

Temperature measurements

Gas hydrates

ABSTRACT

The sediment temperature distribution at mud volcanoes provides insights into their activity and into the occurrence of gas hydrates. If ambient pressure and temperature conditions are close to the limits of the gas hydrate stability field, the sediment temperature distribution not only limits the occurrence of gas hydrates, but is itself influenced by heat production and consumption related to the formation and dissociation of gas hydrates. Located in the Sorokin Trough in the northern Black Sea, the Dvurechenskii mud volcano (DMV) was in the focus of detailed investigations during the M72/2 and M73/3a cruises of the German *R/V Meteor* and the *ROV Quest 4000 m* in February and March 2007. A large number of in-situ sediment temperature measurements were conducted from the ROV and with a sensor-equipped gravity corer. Gas hydrates were sampled in pressurized cores using a dynamic autoclave piston corer (DAPC). The thermal structure of the DMV suggests a regime of fluid flow at rates decreasing from the summit towards the edges of the mud volcano, accompanied by intermittent mud expulsion at the summit. Modeled gas hydrate dissociation temperatures reveal that the gas hydrates at the DMV are very close to the stability limits. Changes in heat flow due to variable seepage rates probably do not result in changes in sediment temperature but are compensated by gas hydrate dissociation and formation.

© 2009 Published by Elsevier Ltd.

1. Introduction

Submarine mud volcanoes are geological structures related to the emission of gas, pore water seepage and mud expulsion at the sea floor (Dimitrov, 2002; Kopf, 2002). They are considered one of the most important natural sources of methane emission to the hydrosphere and atmosphere (e.g. Dimitrov, 2003; Kvenvolden and Rogers, 2005), but to quantify the role of mud volcanoes in global budgets, it is important to understand their activity (cf. Wallmann et al., 2006b). Since the ascent of warm mud and fluids creates temperature anomalies close to the sea floor, detection and quantification of these anomalies in turn provides information on the nature and strength of mud volcano activity (e.g. de Beer et al., 2006; Feseker et al., 2008).

The Dvurechenskii mud volcano (DMV) was in the focus of intense research during the cruise M52/1 (MARGASCH) of the German *R/V Meteor* in 2003. Measurements revealed elevated sediment temperatures of up to 16.5 °C at the center of the mud

volcano against a background water temperature of around 9.1 °C (Bohrmann et al., 2003). Gas hydrates were found in all gravity cores recovered from an area covering the entire DMV plateau (Blinova et al., 2003; Bohrmann et al., 2003). During the same cruise, unusually high pore water salinity was observed at the center of the DMV (Bohrmann et al., 2003; Aloisi et al., 2004; Wallmann et al., 2006b), which causes a substantial shift of the gas hydrate stability limit towards lower temperatures and suggests that gas hydrates at the DMV are very close to the stability limit. With respect to variable intensities of gas bubble emissions into the water column, Greinert et al. (2006) suggested strong variability in the mud volcano activity, which point to dynamic fluid movement in the subsurface. Based on geochemical analyses of pore water samples, Aloisi et al. (2004) concluded that the high-salinity fluids that are expelled at DMV originate from source depths of around 3 km below the seabed and are subjected to alteration due to shallow gas hydrate formation. They presented simple transport models that pointed to flow rates between 0.25 m per year at the center of the mud volcano and 0.08 m per year at the edge.

More recently, the DMV was once more investigated in great detail during the cruises M72 and M72/3a of *R/V Meteor* and the *ROV Quest 4000 m* in February and March 2007. For the first time, an

* Corresponding author. IFM-GEOMAR, Wischhofstr. 1-3, D-24143 Kiel, Germany.
E-mail address: tfeseker@ifm-geomar.de (T. Feseker).

ROV was used for visual sea floor observations and precisely positioned in-situ measurements and sampling at this mud volcano. Winch-operated tools such as a gravity corer equipped with temperature sensors and a dynamic autoclave piston corer were used to obtain additional in-situ measurements and samples. Based on the results of these two cruises, this paper presents a detailed analysis of the temperature distribution in the sediments and bottom water at the DMV, its relation to the presence of gas hydrates, and its implications for the nature of the activity of this mud volcano.

2. Geological setting

The DMV is located in the Sorokin Trough on the northern margin of the Black Sea, SE of the Crimean Peninsula (Fig. 1). The Sorokin Trough is a 150 km long and 50 km wide NE–SW oriented depression. Towards the S, the depression is bounded by the Cretaceous–Eocene Tetyaev and Shatsky uplifts, gradually narrowing to the NE (Belousov et al., 1988). With water depths ranging between 600 and 2100 m, it is one of the deepest troughs in the eastern basin of the Black Sea.

The Sorokin Trough formed the fore-deep basin of the Crimean Alpine range in Oligocene–Lower Miocene (Maikopian) times and was filled with up to 5 km of Maikopian clays (Maikopian Shale Formation), covered by up to 3 km of Quaternary sediments (e.g. Woodside et al., 1997; Limonov et al., 1997; Ivanov et al., 1998). The organic-rich Maikopian formation is considered to serve as hydrocarbon source rock for widespread areas in the Black Sea. Due to the northward movement of the rigid blocks of the Tetyaev Rise and Shatsky Ridge, the region is subject to a compressional tectonic regime that resulted in diapiric folding of the Maikopian shales (Woodside et al., 1997). The diapirs disrupted by numerous faults, which sometimes continue into the Quaternary sediments or reach the sea floor (Woodside et al., 1997; Limonov et al., 1997; Ivanov et al., 1998) and are suggested to act as pathways for fluids (Krastel

et al., 2003). The mud volcanoes in the Sorokin Trough are mostly located on the flanks of the Maikopian diapirs (Ivanov et al., 1998) and may be the result of focused flow from the diapirs to the sea floor (Krastel et al., 2003). In contrast to the conical shape of the Sevastopol mud volcano (Wagner-Friedrichs et al., 2008), the Vodyanitskii mud volcano (Sahling et al., in press), and other mud volcanoes in the vicinity, the DMV is characterized by a nearly flat top at a water depth of around 2055 m (Figs. 2 and 5), which indicates relatively high fluidity of the expelled mud (Brown, 1990).

3. Methods

3.1. Temperature measurements

In-situ temperature measurements from the DMV were obtained during two cruises M72/2 and M72/3a (Bohrmann et al., 2007) of *R/V Meteor* in February and March 2007 using a gravity corer and a temperature lance operated by the *ROV Quest 4000 m* (MARUM, Bremen). The 6-m-long gravity corer was equipped with five to six autonomous temperature loggers mounted on outriggers that were welded to the corer barrel. Measuring at a resolution of 0.0006 °C, the accuracy of these sensors is better than 0.002 °C within a calibration range from –2 to 35 °C. While the relative distance between individual sensors could always be measured accurately when the instrument was on deck, the absolute depths of the measurements below the seabed had to be estimated from mud smear on the gravity corer or on the cable. Particularly at the center of the mud volcano, the extremely soft consistency of the sediments led to over-penetration of the instrument, which made it very difficult to estimate the penetration depth. For each deployment, the corer was left in the sediment for a period of 5–10 min, during which the loggers recorded temperature measurements at a time interval of 5 s. The sediment temperatures were calculated by extrapolation from these equilibration curves. A transponder (POSIDONIA, IXSEA) was attached to the cable 50–100 m above the

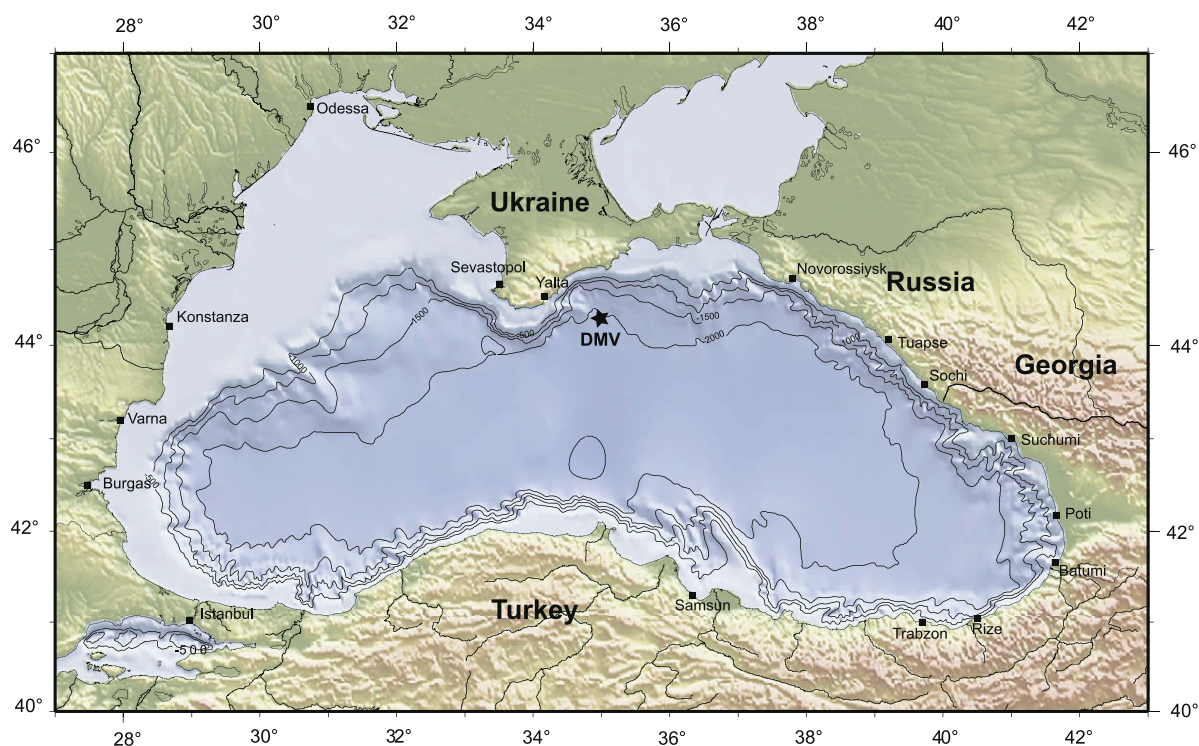


Fig. 1. The Dvurechenskii mud volcano (DMV) is located on the northern margin of the Black Sea, SE of the Crimean peninsula.

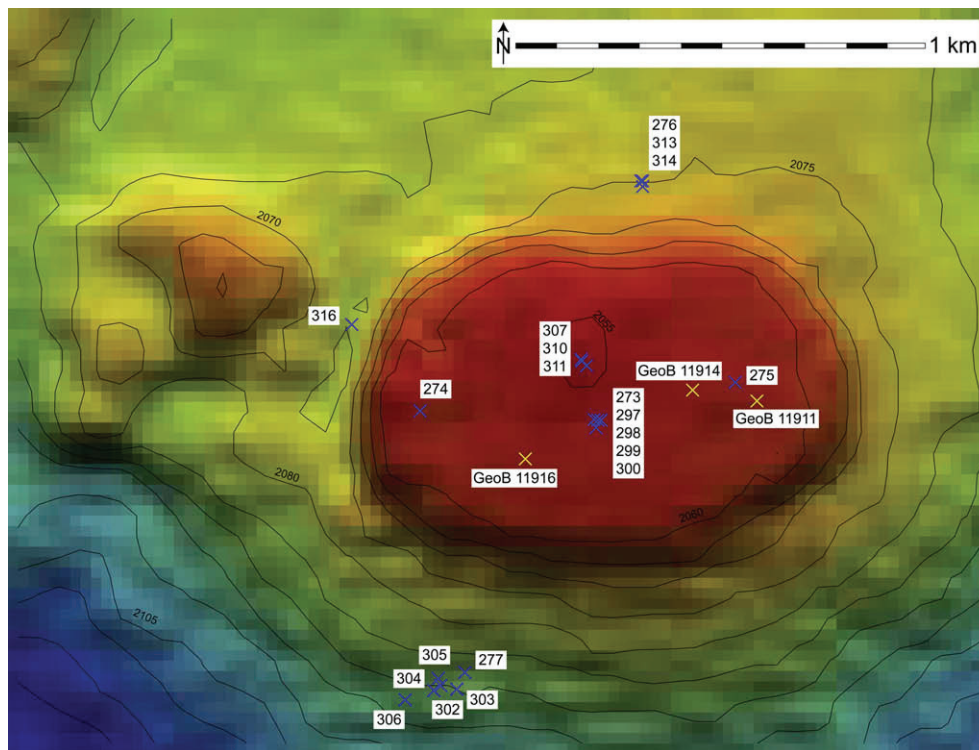


Fig. 2. Shaded bathymetry of the DMV with an isobath interval of 5 m. The blue crosses indicate the positions of in-situ sediment temperature measurements using the gravity corer during M72/2. The yellow crosses denote DAPC stations carried out during M72/3a. Labels indicate station numbers. The positions of the gravity corer stations are listed in Table 1.

gravity corer for each deployment to improve the accuracy of underwater positioning. The remaining error of the instrument position at the sea floor is estimated to be less than 20 m.

In addition to the gravity corer equipped with temperature sensors, a new ROV-operated short temperature lance (ROV lance) was used on M72/2 during three dives (dives 147, 150, and 151) to obtain in-situ sediment temperature measurements. The ROV lance consists of a 0.8-m-long plastic rod with eight temperature sensors distributed over the lower 0.55 m. All temperature sensors were connected to a data logger attached to the upper end of the rod, which turned the ROV lance into a fully autonomous instrument. Resolution and precision of the temperature measurements are identical to those of the autonomous loggers mentioned above. During each dive, temperature readings from all sensors were recorded at a time interval of 10 s while the ROV was in the water. For each station, the ROV lance remained in the sediment for at least 7 min. After the dives, the sediment temperatures were calculated through extrapolation from the equilibration process in the same way as for the measurements using the gravity corer. The measurements using the ROV lance were continued during two dives (dives 159 and 160) in the course of leg M72/3a.

The same autonomous temperature loggers used on the gravity corer were also attached to the frame of the ROV *Quest 4000 m* during the cruise M72/2 to obtain highly accurate water temperature measurements. For dive 147, a single logger was placed at a height of 0.63 m above the bottom of the ROV. An additional logger was placed at a height of 1.25 m above the bottom for dives 150 and 151. Both loggers recorded temperature measurements at an interval of 5 s while the ROV was in the water. After the dives, the measurements were georeferenced using the ROV dive navigation log. For all times when the altitude of the ROV was less than 30 m above the sea floor, the water depth at the position of the ROV was calculated as the sum of the immersion and the altitude. However, as these parameters had not been calibrated for the

density profile of the water column in the working area, there was an offset between the calculated water depths and the multibeam map that was compensated for by adding 14.8 m to the values calculated from the ROV navigation data.

3.2. Gas chemistry and calculation of gas hydrate stability limits

For retrieval of the gas contained in near-surface sediments of the DMV, pressurized sediment cores were recovered using a Dynamic Autoclave Piston Corer (DAPC) (Abegg et al., 2008). The DAPC is operated similar to a conventional piston corer, but is additionally equipped with a gas-tight pressure chamber which enables the recovery of sediment cores of up to 2.65 m in length under in-situ pressure. Immediately upon recovery, the gas contained in the DAPC pressure chamber was released incrementally via a gas manifold modified after (Dickens et al., 2003), and quantified by use of a gas catcher (Dickens et al., 2003; Heeschen et al., 2007). Gas samples were taken at selected time points of the degassing procedure and stored in glass serum vials until gas chemical analysis. Abundances of C₁–C₆ hydrocarbons, oxygen, nitrogen and carbon dioxide in individual gas samples were analysed by gas chromatography. Concentrations stated for individual hydrocarbons and carbon dioxide are average values calculated for total gas released from the pressure core.

Gas hydrate stability curves mark the boundaries of the hydrate phase and a phase of free gas and water. The stability curves for the near-surface sediments at DMV were calculated using the software HWHYD, developed at the Centre for Gas Hydrate Research, Heriot-Watt University, U.K., in 2005 (Masoudi and Tohidi, 2005; Østergaard et al., 2005). The software was loaded with gas chemical compositions derived from degassing of DAPC cores and different values of salinity taken from Bohrmann et al. (2003) and Aloisi et al. (2004). For comparison, the phase boundaries were also calculated for ambient conditions (chlorinity 830 mM, salinity 51 PSU, no

sulfate) following the Pitzer approach as described by Tishchenko et al. (2005). In the following, the term ‘methane hydrate’ refers to theoretical structure-I hydrates incorporating pure methane, while the term ‘gas hydrates’ denotes hydrates enclosing hydrocarbons and carbon dioxide in specific composition as determined in this study for shallow DMV deposits.

3.3. Geochemical pore water analyses and calculation of gas hydrate inventory

Gas hydrates were dissociated in the DAPC cores under controlled conditions over a period of several days. Wet sediment samples were taken for the determination of water contents and sediment porosity after hydrate dissociation was completed. The pore water was extracted by squeezing at a pressure of 4 bar and a temperature of 10 °C (Wallmann et al., 2006a). Chloride, sulfate and bromide concentrations in the pore water samples were determined by ion-chromatography (Wallmann et al., 2006a). Wet sediment samples were freeze-dried to determine the contents of water and dry solids in weight percent. The porosity ϕ^* of the sediment samples after hydrate melting, i. e. the volume fraction of pore water in wet sediments, was calculated as:

$$\phi^* = \frac{\frac{M_W}{\rho_W}}{\frac{M_W}{\rho_W} + \frac{M_S}{\rho_S}} \quad (1)$$

where M_W and M_S are the contents of pore water and dry solids in weight percent, respectively, and ρ_W and ρ_S are the densities of salt-free pore water (1.0 g/cm³) and the sediment grains (2.5 g/cm³), respectively.

Dissolved salts are diluted by H₂O released from hydrates dissociating upon core retrieval. The decrease in dissolved chloride may thus be used to calculate the hydrate inventory (Ussler and Paull, 2001). The chloride concentration after hydrate dissociation (c_{Cl}^*) is related to the in-situ chloride concentration prior to hydrate melting (c_{Cl}) by:

$$c_{Cl}^* = c_{Cl} \frac{\phi}{\phi^*} = c_{Cl} \frac{\phi}{\phi + R} \quad (2)$$

where ϕ is the in-situ porosity or, in other words, the volume of pore water per unit volume of bulk sediment prior to melting, and R is the ratio of the volume of H₂O produced by hydrate dissociation per unit volume of bulk sediment.

The in-situ porosity ϕ is thus calculated from the measured porosity and chloride data and the estimated in-situ chloride concentration c_{Cl} as:

$$\phi = \frac{c_{Cl}^* \cdot \phi^*}{c_{Cl}} \quad (3)$$

The ratio R is derived from the water balance as:

$$R = \phi^* - \phi = \phi^* \left(1 - \frac{c_{Cl}}{c_{Cl}^*} \right) \quad (4)$$

The amount of methane bound in hydrate per unit volume of bulk sediment (H in mol/cm³) is finally calculated from R applying the density of water released during hydrate melting ($\rho_W = 1.0$ g/cm³), the molecular weight of water ($m_W = 18$ g/mol), and the average molar H₂O/CH₄ ratio of structure-I hydrate ($r = 5.9$; Ussler and Paull, 2001):

$$H = \frac{R \cdot \rho_W}{m_W \cdot r} = \phi^* \left(1 - \frac{c_{Cl}}{c_{Cl}^*} \right) \frac{\rho_W}{m_W \cdot r} \quad (5)$$

The hydrate concentration in terms of volume of hydrate per unit volume of bulk sediment (c_H in cm³/cm³) is calculated from H applying the average molecular weight ($m_H = 122.2$ g/mol) and density ($\rho_H = 0.9$ g/cm³; Ussler and Paull, 2001) of methane hydrates:

$$c_H = \frac{H \cdot m_H}{\rho_H} \quad (6)$$

4. Results

4.1. In-situ temperature measurements using the gravity corer

In-situ sediment temperature profiles were measured during 20 deployments of the gravity corer at seven different targets on the DMV (Fig. 2). The stations are listed in Table 1, and the corresponding results of the measurements are listed in Table 2. All temperature measurements on the flanks of the mud volcano revealed linear profiles. The results from multiple measurements at the same targets agreed very well with each other. The lowest temperature gradients of around 0.037 °C/m were found on the southern flank (Fig. 3a). Slightly higher temperature gradients of 0.052 and 0.057 °C/m were measured on the northern and western flanks, respectively (Fig. 3b).

Seven temperature profiles from the plateau of the DMV but away from the summit are compiled in Fig. 3c. The corresponding temperature gradients varied between 0.186 °C/m at station 274 close to the western edge, 0.354 °C/m at station 275 in the eastern part of the plateau, and from 0.764 to 0.880 °C/m at stations 298 through 300 close to the geometrical center of the mud volcano, where two other deployments (stations 273 and 297) with more weight on the gravity corer revealed a nearly constant temperature of 16.274–16.372 °C with no apparent gradient below sediment depths of 10 m. The results of all five deployments close to the geometrical center agreed very well with each other and could be combined to a full temperature profile covering an interval of 1.7–14 m below the sea floor (mbsf).

Due to the very soft sediment, the gravity corer over-penetrated during all three deployments at the summit of the DMV, even when the weight of the head was reduced to around 200 kg.

Table 1

Positions of sediment temperature measurements using the gravity corer. The positions are also shown on the bathymetric map in Fig. 2. The results of the measurements are listed in Table 2 and shown in Fig. 3.

Station no.	Date	Time [UTC]	Latitude N	Longitude E	Depth [m]
273	27/02/2007	10:24	44°16.947'	034°58.929'	2056
274	27/02/2007	13:13	44°16.959'	034°58.596'	2057
275	27/02/2007	15:36	44°16.997'	034°59.175'	2057
276	27/02/2007	18:02	44°17.263'	034°59.002'	2075
277	27/02/2007	20:20	44°16.614'	034°58.679'	2075
297	02/03/2007	21:52	44°16.948'	034°58.916'	2054
298	03/03/2007	00:57	44°16.947'	034°58.923'	2054
299	03/03/2007	03:10	44°16.937'	034°58.920'	2054
300	03/03/2007	05:36	44°16.937'	034°58.920'	2054
302	03/03/2007	23:15	44°16.590'	034°58.621'	2089
303	04/03/2007	01:56	44°16.592'	034°58.664'	2089
304	04/03/2007	05:11	44°16.597'	034°58.634'	2086
305	04/03/2007	08:27	44°16.606'	034°58.630'	2086
306	04/03/2007	11:05	44°16.578'	034°58.569'	2086
307	04/03/2007	15:27	44°17.027'	034°58.892'	2050
310	06/03/2007	08:25	44°17.025'	034°58.893'	2055
311	06/03/2007	11:10	44°17.019'	034°58.902'	2052
313	06/03/2007	14:42	44°17.263'	034°59.005'	2075
314	06/03/2007	17:45	44°17.255'	034°59.005'	2075
316	06/03/2007	21:14	44°17.073'	034°58.471'	2081
318	07/03/2007	03:15	44°16.970'	034°58.910'	2041

Table 2

In-situ sediment temperatures measured using the gravity corer. For each sensor, the distance Δz between the sensor and the tip of the gravity corer is given in the last row of the table. The estimated penetration depth also refers to the tip of the gravity corer, such that the sensor depth may be calculated by subtracting Δz from the penetration depth. The positions of the stations are listed in Table 1 and shown in Fig. 2.

Station no.	Temperature [°C]						Penetration depth [m]
	T1	T2	T3	T4	T5	T6	
273	16.317	16.330	16.351	16.361	16.315	16.218	14
274	10.609	10.374	10.191	10.055	9.856	9.712	7
275	12.882	12.621	12.260	12.011	11.638	11.177	10
276	9.313	9.262	9.205	9.148	9.114	9.119	4
277	9.264	9.222	9.186	9.155	9.120	9.117	4.5
297	16.372	16.353	16.354	16.375	16.380	16.274	14.5
298	15.645	14.951	14.267	13.353	12.502	11.404	7
299	15.853	15.489	14.719	13.863	12.998	12.051	7.7
300	15.997	15.710	14.956	14.102	13.226	12.313	8
302	9.218	9.176	9.142	9.112	9.115	9.117	3.2
303	9.225	9.183	9.149	9.113	9.120	9.117	3.5
304	9.267	9.225	9.188	9.157	9.118	9.117	4.5
305	9.263	9.224	9.186	9.157	9.125	9.117	4.5
306	9.259	9.222	9.187	9.157	9.116	–	4.5
307	16.766	16.794	16.795	16.811	16.828	–	68
310	17.520	17.469	17.802	18.481	19.684	20.534	7.2
311	17.173	17.018	16.899	16.865	16.885	16.986	13
313	9.311	9.253	9.210	9.138	9.114	9.115	4
314	9.317	–	9.205	9.148	9.114	9.114	4
316	9.337	9.266	9.210	9.153	9.114	9.115	4
Δz [m]	0.43	1.47	2.42	3.4	4.3	5.25	

Consequently, the absolute depth of the measured temperature profiles was difficult to estimate and is subjected to an error in the order of up to several meters. According to station 307 (Fig. 3d), the sediment temperature decreased from 16.828 to 16.766 °C between

63.7 and 67.6 mbsf with a mean gradient of -0.016 °C/m, while the other two deployments revealed higher temperatures at less than 14 mbsf: At station 310, the sediment temperature decreased from 20.534 to 17.469 °C between 2 and 5.8 mbsf, corresponding to

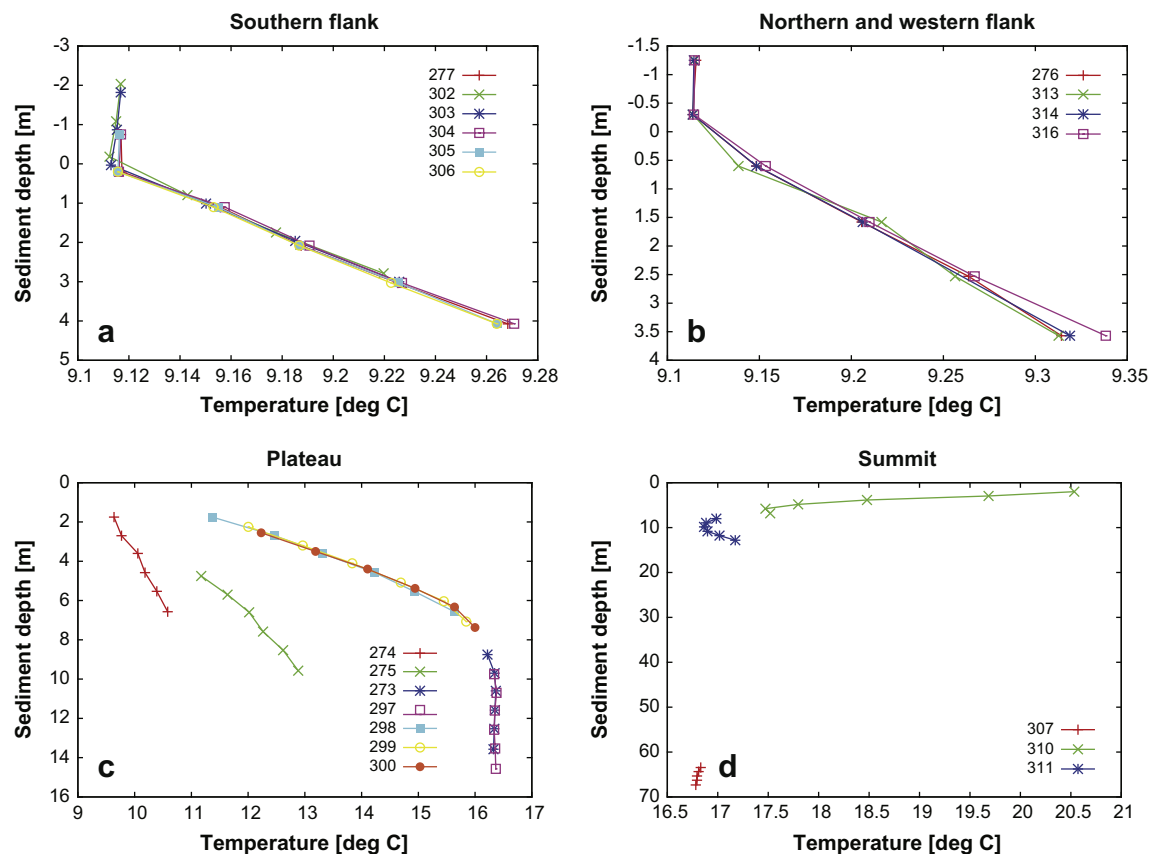


Fig. 3. In-situ sediment temperature profiles from the southern flank (a), the northern and western flank (b), the plateau (c), and the summit (d) of the DMV. The corresponding locations are illustrated in Fig. 2.

a mean gradient of $-0.847\text{ }^{\circ}\text{C/m}$. Below, the temperature increased again slightly to $17.520\text{ }^{\circ}\text{C}$ at 6.8 mbsf. At station 311, the sediment temperature decreased from 16.986 at 7.8 mbsf to $16.865\text{ }^{\circ}\text{C}$ at 9.6 mbsf, which corresponds to a gradient of around $-0.066\text{ }^{\circ}\text{C/m}$. Below this relative minimum, the temperature increased by around $0.106\text{ }^{\circ}\text{C/m}$ – $17.173\text{ }^{\circ}\text{C}$ at 12.6 mbsf. Thus, the two shallower temperature profiles from the summit both point to higher sediment temperatures close to the seabed than at 60 mbsf. This is consistent with the time series of the temperature measurements during the deployment of the gravity corer at station 307 (Fig. 4), which shows an increase in temperature during heaving just before the instrument leaves the sediment. Part of this temperature increase, however, may have been caused by friction.

4.2. In-situ temperature measurements during ROV dives

In-situ temperature measurements using the ROV-operated short temperature lance were conducted in the course of three dives during cruise leg M72/2 and two additional dives during cruise leg M72/3. Bottom water temperature measurements were obtained using autonomous temperature loggers mounted on the frame of the ROV during three dives of the first cruise leg. For comparison, the data were projected on two transect lines across the mud volcano, which are shown in Fig. 5. The microbathymetry compiled from the ROV navigation data for parts of the two transect lines revealed that the flanks of the mud volcano are slightly steeper and that the summit is less pronounced than suggested by the multibeam map (Fig. 6).

Focussing on the summit of the DMV, the ROV-operated short temperature lance was used to measure shallow in-situ sediment temperature profiles at 54 locations on the plateau and at two locations on the flanks. The locations of all measurements are

shown in Fig. 5. All of the shallow temperature profiles were linear. The corresponding temperature gradients ranged between 11.020 and $0.025\text{ }^{\circ}\text{C/m}$ and decreased rapidly from the summit towards the flanks of the mud volcano (Fig. 6).

Fig. 6 shows water temperature measurements obtained from the sensor mounted close to the bottom of the ROV, which were recorded within a distance of 10 m from the transect lines and while the ROV was at the sea floor. Thus the height of the sensor was about 0.63 m above the seabed. For comparison, the normal water temperature as a function of depth was extracted from data recorded when the ROV was moving through the water column away from the mud volcano. Fig. 6 shows that the normal water temperature increased with depth and that the water depth of the plateau (2055 m) corresponded to values of approximately $9.114\text{ }^{\circ}\text{C}$. At the summit of the DMV, however, the measurements revealed a positive bottom water temperature anomaly of more than $+0.01\text{ }^{\circ}\text{C}$ and a second anomaly of around $0.008\text{ }^{\circ}\text{C}$ was found at the northern edge of the plateau.

4.3. Gas samples from pressurized sediment cores

Three DAPC stations (GeoB 11911, 11914 and 11916) were carried out on the plateau of the DMV away from the summit (Fig. 2). Amounts of gas associated to shallow deposits of the DMV were retrieved during on-board degassing of the pressure cores. All pressure cores achieved nearly full penetration (up to 256 cm core length) and recovered the typical mud breccia including clasts presumably Maikopian (Oligocene/Lower Miocene) in age (Bohrmann et al., 2007).

The average distribution of low molecular-weight hydrocarbons and carbon dioxide released during degassing of the three pressure cores was strongly dominated by methane (99.0868 mol-%),

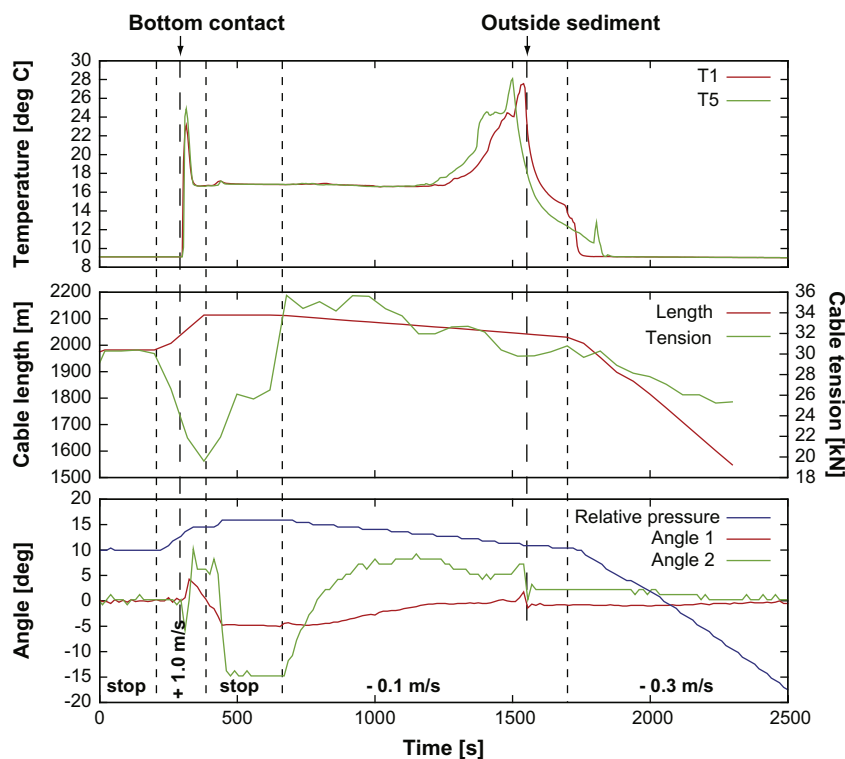


Fig. 4. Synopsis of the temperature records from the sensors T1 and T5 (top), length and tension of the cable (middle), and the data from the tilt and pressure sensor (bottom) during the deployment of the gravity corer at station 307. Sensor T5 was mounted 3.87 m above sensor T1. The sampling intervals were 5 s for temperature, 15 s for tilt and pressure, and 60 s for winch data.

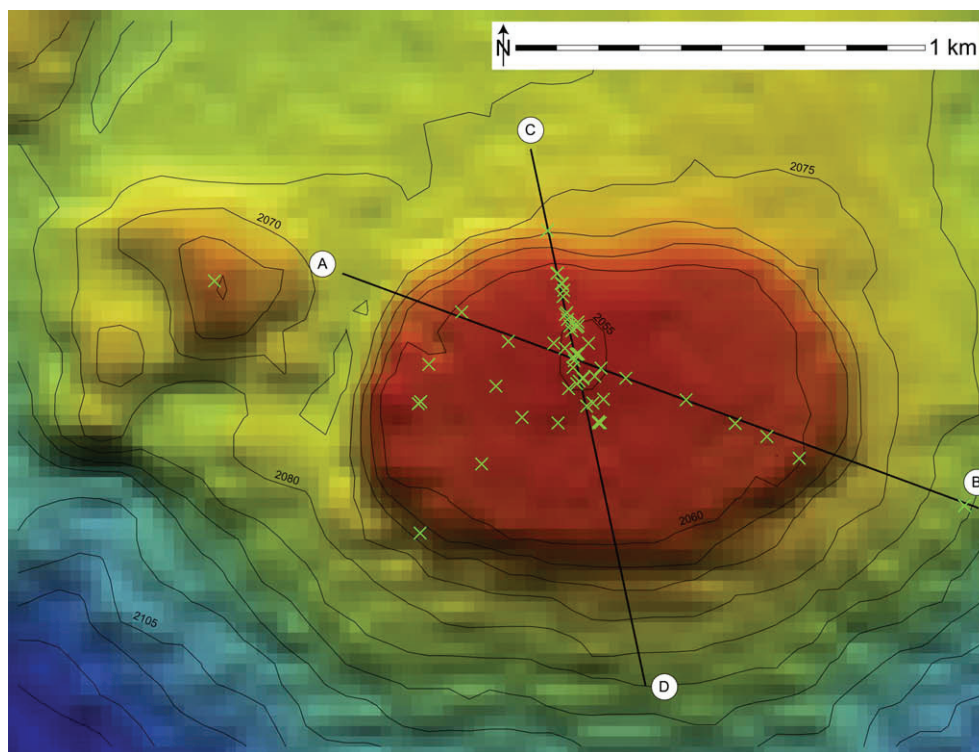


Fig. 5. Shaded bathymetry of the DMV with an isobath interval of 5 m. The crosses show the positions of in-situ sediment temperature measurements using ROV lance. The lines AB and CD show the positions of the transect lines used in Fig. 6.

followed by ethane (0.0557 mol-%), propane (0.0004 mol-%), and carbon dioxide (0.8569 mol-%) (Table 3). The resulting mean molecular ratio ($C_1/C_{2+} = 1760$) suggests that low molecular-weight hydrocarbons in shallow deposits of the DMV are predominantly sourced by microbial activity (Bernard et al., 1976).

4.4. Gas hydrate stability

The phase diagram in Fig. 7 shows the stability curves calculated using the software Heriot-Watt-Hydrate (HWHYD) software and following the Pitzer approach. At the water depth of the DMV all curves plot in a very small temperature range between about 16.5 °C and 17.0 °C, except for the stability curve calculated with the Black Sea bottom water chlorinity. The Pitzer approach, using pure methane as the only hydrate former, reveals the lowest temperature at a given water depth. Considering the site-specific composition of low molecular-weight hydrocarbons and CO₂ (HWHYD software) shows slightly elevated temperatures at the same depth. However, for the same gas composition, the curves vary due to different pore water chlorinities or salt ions, respectively, as assumed from previous studies (e.g. Bohrmann et al., 2003; Aloisi et al., 2004; Wallmann et al., 2006b).

4.5. In-situ porosity and concentrations of methane hydrates in DMV sediments

At station GeoB 11911, chloride was depleted only at the sediment surface due to the diffusive exchange with the overlying Black Sea bottom water (Fig. 8). The concentration reached a plateau value of 830 mM below sediment depths of 100 cm. Dissolved chloride was, however, significantly depleted below sediment depths of 150 cm at stations GeoB 11914 and GeoB 11916. The chloride depletion was accompanied by a strong increase in

sediment porosity (Fig. 8). The in-situ chloride concentration c_{Cl} in hydrate-bearing sediments (GeoB 11914 and GeoB 11916) may be estimated as 830 mM from the dissolved chloride values in the overlying hydrate-free sediment horizons and the chloride concentration measured in the hydrate-free sediment core GeoB 11911 (Fig. 8).

Methane hydrate concentrations are below the detection limit of the chloride method in core GeoB 11911. In cores GeoB 11914 and GeoB 11916, hydrate appears below a sediment depth of 150 cm and approaches concentrations of 1.7 mmol CH₄/cm³ or 0.23 cm³ of hydrate per cm³ of bulk sediment at 200–250 cm sediment depth (Fig. 9). The in-situ porosity of hydrate-bearing sediments is much lower than the porosity determined after hydrate melting. It is also lower than the porosity in the overlying hydrate-free sediment layers (Figs. 8 and 9). The decrease in in-situ porosity from around 0.65 in hydrate-free surface sediments to around 0.55 in the underlying hydrate-bearing layers indicates that the available pore space is partly clogged by hydrates. However, the total porosity calculated as sum of the pore space filled by water and hydrates ($\phi + c_H$) increases to more than 0.7 in the hydrate-bearing layer. This increase strongly suggests that sediment grains are pushed aside by hydrate formation. Thus, hydrate formation induces, both, the creation of new pore space by sediment grain displacement and the clogging of available pore space.

5. Discussion

5.1. Sediment temperature distribution

The in-situ measurements using the ROV lance and the gravity corer both revealed very high sediment temperatures at the summit of the DMV and showed a rapid decrease in near-surface temperature gradient away from the summit. Assuming a thermal

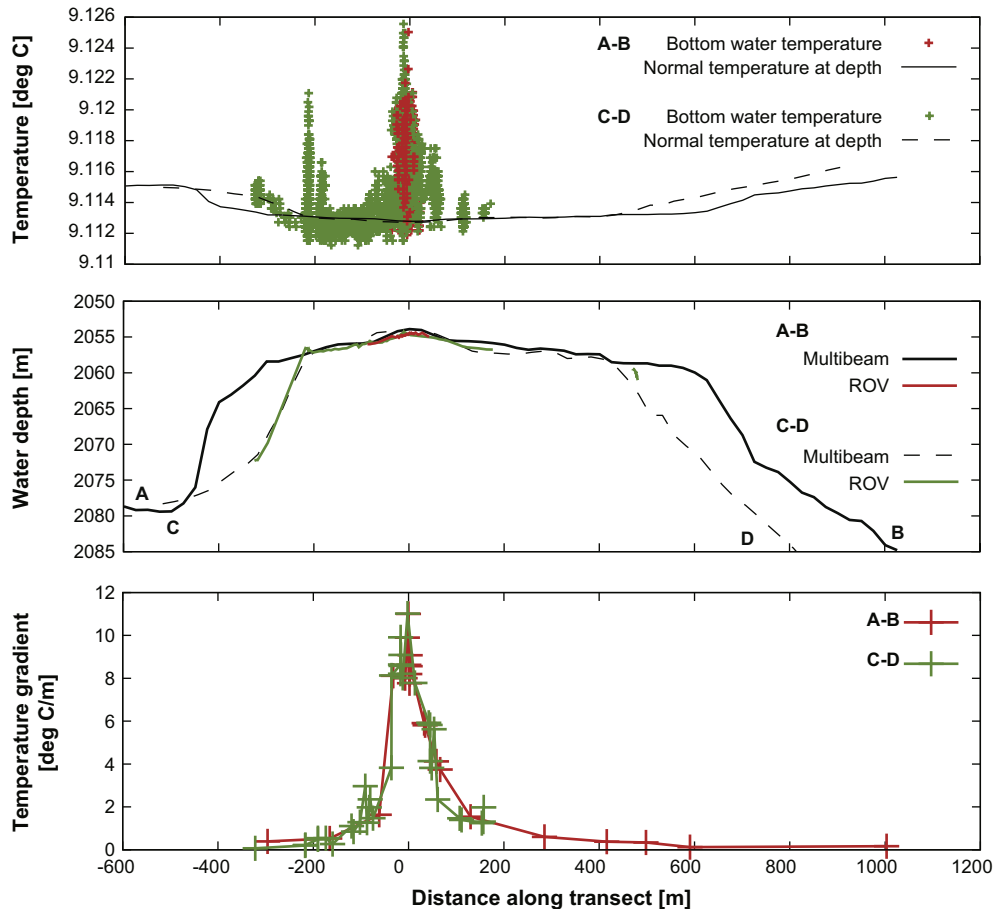


Fig. 6. Bottom water temperature (top), bathymetry (middle), and near-surface sediment temperature gradient (bottom) along transect lines AB and CD across the center of the DMV. The location of the transect lines is shown in Fig. 5.

conductivity of $1 \text{ W}/(\text{m}^\circ\text{C})$ for the near-surface sediments, the highest temperature gradient at the summit corresponds to a heat flow of $11,020 \text{ mW}/\text{m}^2$, which is more than four times greater than the maximum value reported previously by Kutas and Poort (2008). The mean temperature gradient measured at the southern flank is equivalent to a heat flow of $37 \text{ mW}/\text{m}^2$ and falls within the range of regional background values (Kutas and Poort, 2008).

The high sediment temperature gradients at the summit coincided with an area of elevated bottom water temperatures. Within a distance of approximately 50 m from the highest point of the mud volcano, the seawater was up to 0.014°C warmer than the normal

water temperature at that depth (Fig. 6). While the location and extent of this anomaly appear to be comparable to previous observations by Bohrmann et al. (2003), the magnitude described here is around five times larger, which may be related to the fact that the measurements were conducted closer to the sea floor. A

Table 3

Distributions of low molecular-weight hydrocarbons (C_1 to $i\text{-C}_4$) and carbon dioxide in gas retrieved by degassing of pressure cores from the DMV. Values given in mol-% of $\Sigma\text{C}_1\text{-C}_4$, CO_2 . Note: Presumably due to a small leakage of the sampling device, pressure and total gas volume of core GeoB 11911 contained in the pressure chamber upon recovery were lower than expected. This pressure loss suggests that core GeoB 11911 was devoid of substantial amounts of gas hydrate, which is consistent with the results obtained by the Pitzer model. Due to compositional trends in the course of core degassing, the composition of residual gas in the pressure chamber of GeoB 11911 probably differs slightly from that initially associated to the sampled sediments. Accordingly, mean values were calculated for cores GeoB 11914 and 11916, only.

	CH_4	C_2H_6	C_3H_8	$i\text{-C}_4\text{H}_{10}$	CO_2	C_1/C_{2+}
GeoB 11911	(98.6441)	(0.0560)	(0.0004)	(0.0000)	(1.2995)	(1750)
GeoB 11914	99.1442	0.0542	0.0005	0.0000	0.8012	1814
GeoB 11916	99.4720	0.0569	0.0004	0.0006	0.4700	1715
Mean	99.3081	0.0556	0.0005	0.0003	0.6356	1765

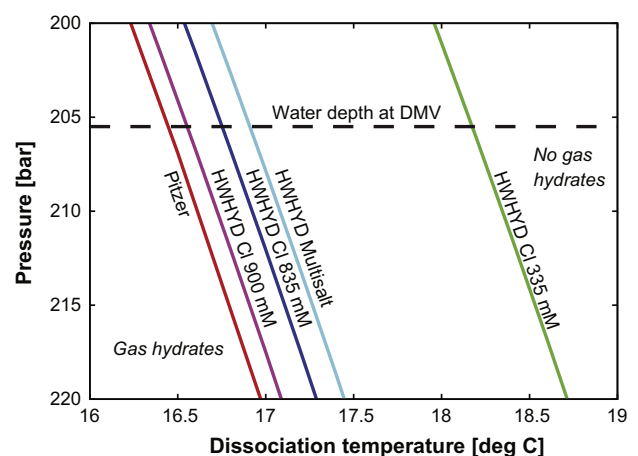


Fig. 7. Gas hydrate stability curves calculated following the Pitzer approach (red) and using the HWHYD software with chloride concentrations of 335 mM (green), 835 mM (dark blue), and 900 mM (purple). The light blue line labeled 'HWHYD Multisalt' shows the stability limit for a chloride concentration of 835 mM, and taking into account salts formed by Mg^{2+} , Ca^{2+} , and K^+ in addition to Na^{2+} .

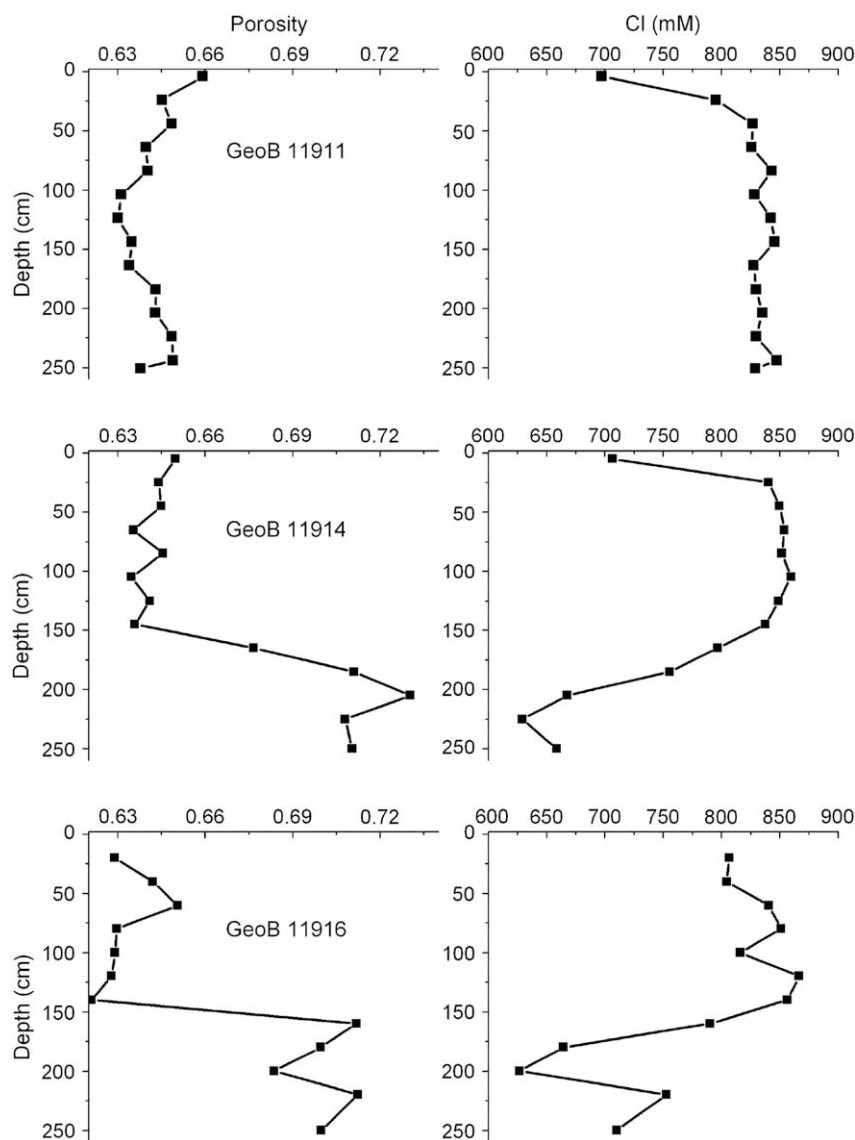


Fig. 8. Porosity and dissolved chloride measured in DAPC samples from the DMV.

second anomaly at the northwestern edge of the plateau could not be related to elevated sediment temperatures (Fig. 6, transect C–D).

According to Bohrmann et al. (2003), the sediment temperatures at the DMV did not exceed 16.5 °C in 2003. Kutas and Poort (2008) reported a maximum temperature of 20.17 °C at 2.5 mbsf measured during a cruise in 2005 at a station slightly west of the geometric center. In this study, the highest temperature value was 20.534 °C, measured at 2 mbsf at the summit. However, it is not clear whether these differences are related to temporal or spatial variability. In fact, the combination of the shallow and deep measurements presented here suggests even higher temperatures at 1–2 mbsf at the summit: The gradient at the upper end of the profile recorded at station 310 was still negative (−0.847 °C/m at 2 mbsf, Fig. 3d), pointing to a further temperature increase towards the sea floor, and all shallow measurements at the summit showed high gradients of around 8–11 °C/m (Fig. 6), such that temperatures of more than 20 °C could already be reached below 1 mbsf. A similar sediment temperature distribution was reported from the Håkon Mosby mud volcano on the Barents Sea slope, where very high temperatures were measured close to the seabed at the active

center of the mud volcano, while the sediment temperatures below were much lower (Feseker et al., 2008). These locally very limited shallow sediment temperature maxima could be explained by short phases of mud eruption, during which an isolated volume of warm mud reaches the sea floor very rapidly and cooler sediment from the surroundings filled the void in the conduit below, leaving the warm mud at the sediment surface completely detached from its warm source at depth.

The increase in temperature gradient towards the summit also resembles observations from other mud volcanoes (e.g. Håkon Mosby mud volcano, de Beer et al., 2006; Feseker et al., 2008) and suggests upward fluid flow at high rates at the summit and low rates closer to the edge of the plateau, as described previously for the DMV by Aloisi et al. (2004). This interpretation is consistent with the observed bottom water temperature anomaly at the summit.

Based on geochemical analyses of the mud volcano fluids, Aloisi et al. (2004) concluded that the temperature at the source of the DMV is around 100 °C, corresponding to a depth of about 2.5–3 km. Considering the highest near-surface sediment temperatures

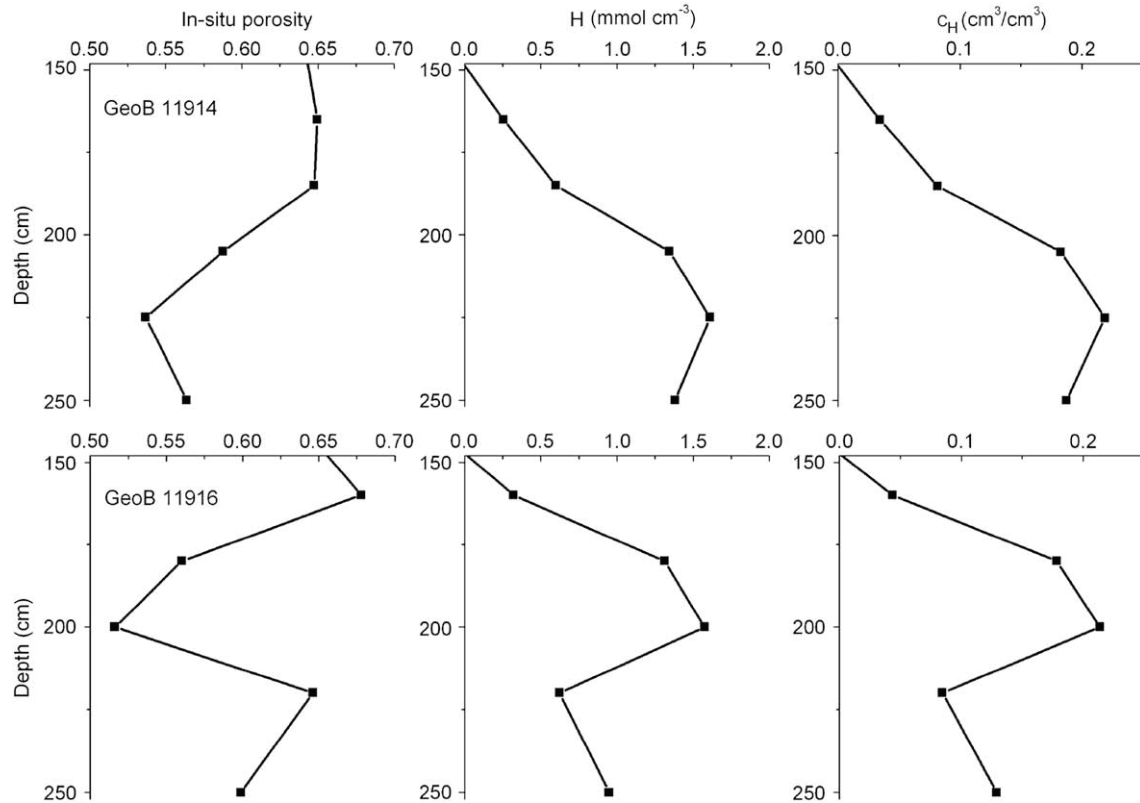


Fig. 9. In-situ porosity and hydrate concentrations (H : methane bound in hydrates in mmol of CH_4 per cm^3 of bulk sediment; c_H : hydrate concentration in cm^3 of hydrate per cm^3 of bulk sediment) in hydrate-bearing cores.

reported here, this implies that the fluids and the mud lose nearly 80 percent of their initial heat to the surrounding sediments during the ascent.

5.2. Gas hydrate stability models

At the water depth of the DMV (2055 m), the gas hydrate dissociation temperatures predicted by the HWHYD software for the mean measured gas composition and chlorinities of 355 mM and 900 mM (Fig. 7) were approx. 0.5°C higher than those given by Bohrmann et al. (2003), who assumed pure methane hydrates. The shift to warmer temperatures could thus be related to small fractions of higher low molecular-weight hydrocarbons and CO_2 filling the hydrate cages (Sloan and Koh, 2007). Taking into account the concentrations of Mg^{2+} , Ca^{2+} , and K^+ in addition to chlorinity resulted in an additional shift to warmer temperatures compared to the stability curve calculated for the same chlorinity but neglecting all components other than Na^{2+} . It turns out that with a theoretical presence of pure chloride, gas hydrate is less stable than when the same total salinity is composed of additional ions. The changes, however, are minor, because the stability is quite similar to the curve for pure methane.

The Pitzer approach returns a marginally more limited methane hydrate stability boundary, i.e. slightly colder temperatures at a given pressure, than the curves generated by HWHYD software, which is based on gas chemistry and salinity. By that, it fits well into the data set from HWHYD models, which consider also minor fractions of other hydrocarbons and CO_2 . Yet, the abundances of other gas species are small, and consequently, the differences in predicted dissociation temperature at the ambient pressure at the

DMV are not more than 0.5°C . Accordingly, for the conditions encountered at the DMV both methods are useful for predicting the occurrence of gas hydrates in the subsurface.

5.3. Total methane inventory in DMV sediments

Methane occurs not only as hydrate but also in the dissolved phase. The concentration of methane in highly saline solutions in the presence of structure-I hydrate was calculated applying the Pitzer approach (Tishchenko et al., 2005). For ambient conditions in DMV surface sediments ($T = 16.5^\circ\text{C}$, $p = 210$ bar, $c_{\text{Cl}} = 830$ mM, salinity: 51, no sulfate), structure-I methane hydrate has a solubility of 123 mmol/kg or 118 mmol/dm³ (Tishchenko et al., 2005). Reactive transport modeling showed that the DMV pore fluids reach saturation with respect to methane hydrate already at shallow sediment depths of only ≈ 100 cm (Wallmann et al., 2006b). The total inventory of dissolved methane in the sampled sediments is thus estimated considering the in-situ porosity ϕ and assuming a constant methane concentration of 118 mM at 100–250 cm depths and a reduced concentration of ≈ 60 mM at 0–100 cm depths. The corresponding hydrate-bound CH_4 inventories are calculated by multiplying c_H and ϕ (Table 4).

It should be noted that the methane inventories listed in Table 4 are minimum estimates since methane occurring as free gas is not considered. Moreover, the estimated in-situ chloride concentration may be too low. It is possible that salts excluded during hydrate formation accumulate in the pore fluids (Haackel et al., 2004; Torres et al., 2004). The calculations presented here were based on the assumption that the excluded salts were flushed from the hydrate-bearing sediments by upward fluid flow and diffusion. The

hydrate inventory could, however, be much larger than the values estimated here if a significant fraction of the excluded salts remains in the hydrate-bearing sediments.

5.4. Gas hydrates and sediment temperature – a ‘gas hydrate thermostat’

The hydrocarbon composition of gas recovered by pressure coring resembled that previously reported for gas and gas hydrates associated to sediments sampled by gravity coring within the DMV area (Blinova et al., 2003). Hence, it may be assumed that the compositions of gas (Blinova et al., 2003, and this study) and fluids (Aloisi et al., 2004, and this study) have not changed significantly since 2003. However, in contrast to the results presented here, the sediment temperatures in 2003 appeared to be lower (Bohrmann et al., 2003) and gas hydrates were found in all gravity cores covering large parts of the DMV area (Blinova et al., 2003). Thus, the presence or absence of gas hydrates in shallow deposits of the DMV could be primarily controlled by the temperature regime.

Converting the temperature time series recorded by the sensors T1 and T5 while heaving the gravity corer through the sediment at station 307 into a continuous temperature profile illustrates the relationship between sediment temperature and gas hydrates at the DMV (Fig. 10): Below 30 mbsf, the resulting temperature profiles reflect the gas hydrate dissociation temperature and show no indications for frictional heat. Above 30 mbsf, the profiles show much higher temperatures than the conventional profiles from stations 310 and 311, while the general shape is similar. The deviation of the upper parts of the profiles could be related to frictional heat during heaving, which was compensated by the dissociation of gas hydrates in the lower part of the profile. Outside the upper 30 m of the sediment column at the summit, all measured temperatures fall within the gas hydrate stability zone (GHSZ).

Thus, if gas hydrate dissociation effectively compensates the frictional heat of the gravity corer moving through hydrate-bearing sediments, it may also be possible that gas hydrate formation and dissociation compensate changes in heat flow caused by variations in fluid seepage through hydrate-bearing sediments within the GHSZ. According to data compiled by Sloan and Koh (2007), the dissociation energy of gas hydrate is around 55 kJ/mol. For a hydrate occupancy of 23% of the total volume, corresponding to a concentration of 1.7 mmol CH₄/cm³ (this study), the energy required to dissociate all gas hydrates in the sediment is:

$$\Delta Q = 5.5 \times 10^4 \frac{\text{J}}{\text{mol}} \times 1700 \frac{\text{mol}}{\text{m}^3} = 9.35 \times 10^7 \frac{\text{J}}{\text{m}^3} \quad (7)$$

where ΔQ is the energy consumed by gas hydrate dissociation per m³ of sediment. Applying the same amount of heat to a hydrate-free volume of bulk sediment would result in a temperature increase of:

$$\Delta T = \frac{\Delta Q}{\rho c} = \frac{9.35 \times 10^7 \frac{\text{J}}{\text{m}^3}}{1678 \frac{\text{kg}}{\text{m}^3} \times 2630.4 \frac{\text{J}}{\text{kg} \cdot \text{C}}} \approx 21.18^\circ \text{C} \quad (8)$$

where ΔT is the calculated temperature change, and $\rho = 1678 \text{ kg/m}^3$ and $c = 2630.4 \text{ J/kg}^\circ\text{C}$ are the density and the

Table 4

Methane inventory (mmol/cm²) in DAPC cores GeoB 11911, GeoB 11914 and GeoB 11916. Inventories are calculated integrating the concentrations of dissolved and hydrate-bound methane over the entire length of the sediment cores (0–250 cm).

	GeoB 11911	GeoB 11914	GeoB 11916
Dissolved CH ₄	16	15	15
CH ₄ bound in hydrate	0	105	96

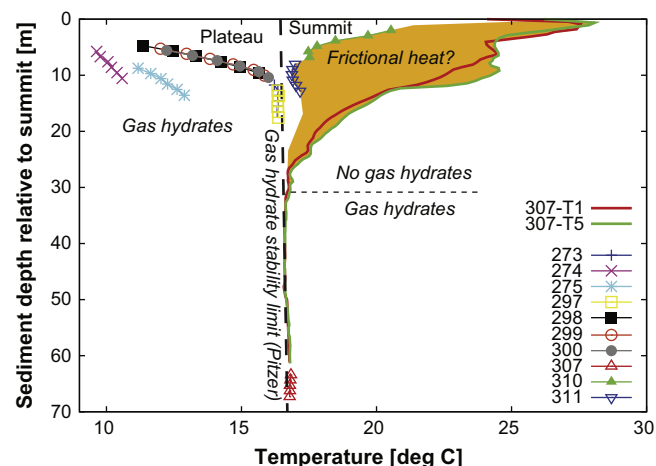


Fig. 10. Sediment temperature distribution and gas hydrate stability at the DMV. The temperature time series recorded by the sensors T1 and T5 while heaving the gravity corer through the sediment at station 307 were converted into continuous temperature profiles, assuming a constant velocity. Below 30 mbsf, the resulting profile reflects the gas hydrate dissociation temperature. Above 30 mbsf, the profile shows much higher temperatures than the conventional profiles from stations 310 and 311, while the general shape is comparable. The deviation of the upper part of the profile could be related to frictional heat during heaving, which was compensated by the dissociation of gas hydrates in the lower part of the profile. Away from the summit, all measured temperatures fall within the gas hydrate stability field.

specific heat of the bulk sediment, respectively, assuming a porosity of 0.6. The magnitude of ΔT reveals the enormous potential of gas hydrate-bearing sediments to buffer changes in heat flow.

Since heat is consumed during hydrate dissociation and produced during hydrate formation, it may be assumed that the sediment temperatures in the GHSZ are generally stabilized by this negative feedback. A ‘gas hydrate thermostat’ may be established providing negative feedback on sediment temperature. Any increase in seepage of warm fluid through hydrate-free sediments leads to a temperature increase. In sediments within the GHSZ at the DMV, an increase in fluid seepage will cause the dissociation of gas hydrates, while the temperature remains unchanged. On the other hand, when new gas hydrates are formed during phases of reduced seepage, the heat of formation would stabilize the sediment temperature just below the dissociation temperature. Hence, variable gas flares observed above the DMV (Greiner et al., 2006) could be explained by fluctuating seepage rates. In contrast to fluid seepage through hydrate-bearing sediments, the increase in heat flow associated with the ascent of warm, hydrate-free mud could not be compensated immediately by gas hydrate dissociation, which supports the interpretation of a recent mud eruption at the summit of the DMV.

6. Conclusions

The distribution of sediment temperatures at the DMV provides indications for both fluid seepage and mud eruptions. Increasing temperature gradients from the edges of the plateau towards the summit point to low rates of fluid seepage at the edges and higher rates at the summit. The high sediment temperatures close to the seabed at the summit, however, are probably the result of short, rapid mud expulsion.

Gas hydrate dissociation temperatures were calculated using (i) the HWHYD software and hydrocarbon compositions determined from pressurized cores and (ii) following the Pitzer approach. Both methods yielded very similar results for the depth range of the DMV and showed that the gas hydrates in the near-surface sediments are very close to the stability limit. According to the

temperature measurements, the only compartment beyond the gas hydrate stability zone at the DMV comprises the upper 30 m of the sediment column at the summit. At any other place within the mud volcano structure, the temperatures in shallow sediments allow for gas hydrate precipitation as predicted by both methods.

Based on the chloride depletion from gas hydrate dissociation in DAPC cores, the gas hydrate content of the sampled sediments was estimated at around 23% of the volume. In-situ sediment temperature measurements suggest that the gas hydrate at the DMV may compensate changes in heat flow due to changes in seepage rates, establishing a 'gas hydrate thermostat'.

Acknowledgements

The authors would like to acknowledge the Captain and crew of R/V *Meteor* as well as the team operating the ROV *Quest 4000 m* for their invaluable support at sea. Steffen Gauger (FIELAX GmbH, Bremerhaven) evaluated the positioning of all instruments at the sea floor and the navigation logs of the ROV dives. We are grateful to H.-J. Hohnberg for the development and the deployments of the DAPC, A.H. Mai (MARUM, Bremen) for support during maintenance of the DAPC, J. Rethemeyer and S. Kusch (AWI, Bremerhaven) for assistance during DAPC handling and gas chemical analysis. E. Kozlova (MSU, Moscow) provided lithological descriptions of DAPC cores (M72/3a). S.A.K. thanks the Vollkammer Scholarship for financial support. T.F. is grateful for financial support from the Max Planck Society. Two anonymous reviewers helped to improve the first version of this manuscript.

This is publication no. GEOTECH – 1220 of the R&D programme GEOTECHNOLOGIEN funded by the German Ministry of Education and Research (BMBF) and the German Research Foundation (DFG), project METRO (grant O3G0604A). This study received additional funding from Wintershall Holding AG (Germany) and through the DFG-Research Center/Excellence Cluster "The Ocean in the Earth System".

References

- Abegg, F., Hohnberg, H.-J., Pape, T., Bohrmann, G., Freitag, J., 2008. Development and application of pressure core sampling systems for the investigation of gas and gas hydrate bearing sediments. *Deep Sea Research Part I: Oceanographic Research Papers* 55 (11), 1590–1599.
- Aloisi, G., Drews, M., Wallmann, K., Bohrmann, G., 2004. Fluid expulsion from the Dvurechenskii mud volcano (Black Sea): part I. Fluid sources and relevance to Li, B, Sr, I and dissolved inorganic nitrogen cycles. *Earth and Planetary Science Letters* 225 (3–4), 347–363.
- Belousov, V.V., Volvovskiy, B.S., Arkhipov, I.V., Buryanova, B.V., Evsyukov, Y.D., Goncharov, V.P., Gordienko, V.V., Ismagilov, D.E., Kislov, G.K., Kogan, L.L., Kondyurin, A.V., Kozlov, V.N., Lebedev, L.L., Lokholatnikov, V.M., Malovitsky, Y.E., Moskalenko, V.N., Neprochnov, Y.R., Otisty, B.K., Rusakov, O.M., Shimkus, K.M., Shlezinger, A.E., Sochelnikov, V.V., Sollogub, V.B., Solovyev, V.D., Starostenko, V.I., Starovoitov, A.F., Terekhov, A.A., Volvovskiy, I.S., Zhigunov, A.S., Zolotarev, V.G., 1988. Structure and evolution of the Earth's crust and upper mantle of the Black Sea. *Bolletino di Geofisica. Teorica ed Applicata. (Bulletin of Geophysics. Theory and Application)* 30 (117–118), 109–196.
- Bernard, B.B., Brooks, J.M., Sackett, W.M., 1976. Natural gas seepage in the Gulf of Mexico. *Earth and Planetary Science Letters* 31 (1), 48–54.
- Blinova, V.N., Ivanov, M.K., Bohrmann, G., 2003. Hydrocarbon gases in deposits from mud volcanoes in the Sorokin Trough, north-eastern Black Sea. *Geo-Marine Letters* 23 (3–4), 250–257.
- Bohrmann, G., Ivanov, M., Foucher, J.-P., Spiess, V., Bialas, J., Greinert, J., Weinrebe, W., Abegg, F., Aloisi, G., Artemov, Y., Blinova, V., Drews, M., Heidersdorf, F., Krabbenhöft, A., Klaucke, I., Krastel, S., Leder, T., Polikarpov, I., Saburova, M., Schmale, O., Seifert, R., Volkonskaya, A., Zillmer, M., 2003. Mud volcanoes and gas hydrates in the Black Sea: new data from Dvurechenskii and Odessa mud volcanoes. *Geo-Marine Letters* 23 (3–4), 239–249.
- Bohrmann, G., Pape, T., cruise participants, 2007. Report and preliminary results of R/V METEOR cruise M72/3, Istanbul – Trabzon – Istanbul, 17 March – 23 April, 2007. In: *Marine Gas Hydrates in the Black Sea*, vol. 261. *Berichte, Fachbereich Geowissenschaften, Universität Bremen*, Bremen.
- Brown, K.M., 1990. The nature and hydrogeologic significance of mud diapirs and diatremes for accretionary systems. *Journal of Geophysical Research* 95, 8969–8982.
- de Beer, D., Sauter, E., Niemann, H., Kaul, N., Foucher, J.-P., Witte, U., Schlüter, M., Boetius, A., 2006. In situ fluxes and zonation of microbial activity in surface sediments of the Håkon Mosby mud volcano. *Limnology and Oceanography* 52 (3), 1315–1331.
- Dickens, G.R., Schroeder, D., Hinrichs, K.-U., Party atLS, 2003. The pressure core sampler (PCS) on ODP Leg 201: general operations and gas releases. In: D'Hondt, S., Jørgensen, B.B., Miller, D.J. (Eds.), *Proceedings of the Ocean Drilling Program, Initial Reports*, vol. 201.
- Dimitrov, L.I., 2002. Mud volcanoes – the most important pathway for degassing deeply buried sediments. *Earth-Science Reviews* 59 (1–4), 49–76.
- Dimitrov, L.I., 2003. Mud volcanoes – a significant source of atmospheric methane. *Geo-Marine Letters* 23 (3–4), 155–161.
- Feseker, T., Foucher, J.P., Harmegnies, F., 2008. Fluid flow or mud eruptions? Sediment temperature distributions on Håkon Mosby mud volcano, SW Barents Sea slope. *Marine Geology* 247 (3–4), 194–207.
- Greinert, J., Artemov, Y., Egorov, V., De Batist, M., McGinnis, D., 2006. 1300-m-high rising bubbles from mud volcanoes at 2080 m in the black sea: hydroacoustic characteristics and temporal variability. *Earth and Planetary Science Letters* 244 (1–2), 1–15.
- Haeckel, M., Suess, E., Wallmann, K., Rickert, D., 2004. Rising methane gas bubbles form massive hydrate layers at the sea floor. *Geochimica et Cosmochimica Acta* 68 (21), 4335–4345.
- Heeschen, K.U., Hohnberg, H.-J., Haeckel, M., Abegg, F., Drews, M., Bohrmann, G., 2007. In situ hydrocarbon concentrations from pressurized cores in surface sediments, Northern Gulf of Mexico. *Marine Chemistry* 107, 498–515.
- Ivanov, M.K., Limonov, A.F., Woodside, J.M., 1998. Extensive deep fluid flux through the sea floor on the Crimean continental margin (Black Sea). In: Henriet, J.P., Mienert, J. (Eds.), *Gas Hydrates: Relevance to World Margin Stability and Climate Change*. Geological Society, London, Special Publications, vol. 137, pp. 177–193.
- Kopf, A.J., 2002. Significance of mud volcanism. *Reviews of Geophysics* 40 (2).
- Krastel, S., Spiess, V., Ivanov, M., Weinrebe, W., Bohrmann, G., Shashkin, P., Heidersdorf, F., 2003. Acoustic investigations of mud volcanoes in the Sorokin Trough, Black Sea. *Geo-Marine Letters* 23 (3–4), 230–238.
- Kutas, R.I., Poort, J., 2008. Regional and local geothermal conditions in the northern Black Sea. *International Journal of Earth Sciences* 97 (2), 353–363.
- Kvenvolden, K.A., Rogers, B.W., 2005. Gaia's breath—global methane exhalations. *Marine and Petroleum Geology* 22, 579–590.
- Limonov, A.F., van Weering, T.C.E., Kenyon, N.H., Ivanov, M.K., Meisner, L.B., 1997. Seabed morphology and gas venting in the Black Sea mud volcano area: observations with the MAK-1 deep-tow sidescan sonar and bottom profiler. *Marine Geology* 137 (1–2), 121–136.
- Masoudi, R., Tohidi, B., 2005. Estimating the hydrate stability zone in the presence of salts and/or organic inhibitors using water partial pressure. *Journal of Petroleum Science and Engineering* 46 (1–2), 23–36.
- Østergaard, K.K., Masoudi, R., Tohidi, B., Danesh, A., Todd, A.C., 2005. A general correlation for predicting the suppression of hydrate dissociation temperature in the presence of thermodynamic inhibitors. *Journal of Petroleum Science and Engineering* 48 (1–2), 70–80.
- Sahling, H., Bohrmann, G., Artemov, Y.G., Bahr, A., Brüning, M., Klapp, S.A., Iklaucke, I., Kozlova, E., Nikolovska, A., Pape, T., Reitz, A., Wallmann, K., Vodyanitskii mud volcano, Sorokin trough, Black Sea: Geological characterization and quantification of gas bubble streams. *Marine and Petroleum Geology*, in press. doi:10.1016/j.marpetgeo.2009.01.010.
- Sloan, E.D., Koh, C.A., 2007. *Clathrate Hydrates of Natural Gases*. CRC Press, Boca Raton.
- Tishchenko, P., Hensen, C., Wallmann, K., Wong, C.S., 2005. Calculation of the stability and solubility of methane hydrate in seawater. *Chemical Geology* 219 (1–4), 37–52.
- Torres, M.E., Wallmann, K., Trehu, A.M., Bohrmann, G., Borowski, W.S., Tomaru, H., 2004. Gas hydrate growth, methane transport, and chloride enrichment at the southern summit of Hydrate Ridge, Cascadia margin off Oregon. *Earth and Planetary Science Letters* 226 (1–2), 225–241.
- Ussler III, W., Paull, C.K., 2001. Ion exclusion associated with marine gas hydrate deposits. In: Paull, C.K., Dillon, W.P. (Eds.), *Natural Gas Hydrates – Occurrence, Distribution, and Detection*, vol. 124. American Geophysical Union, pp. 41–51.
- Wagner-Friedrichs, M., Krastel, S., Spiess, V., Ivanov, M., Bohrmann, G., Meisner, L., 2008. Three-dimensional seismic investigations of the Sevastopol mud volcano in correlation to gas/fluid migration pathways and indications for gas hydrate occurrences in the Sorokin Trough (Black Sea). *Geochemistry Geophysics Geosystems* 9 (5).
- Wallmann, K., Aloisi, G., Haeckel, M., Obzhairov, A., Pavlova, G., Tishchenko, P., 2006a. Kinetics of organic matter degradation, microbial methane generation, and gas hydrate formation in anoxic marine sediments. *Geochimica et Cosmochimica Acta* 70, 3905–3927.
- Wallmann, K., Drews, M., Aloisi, G., Bohrmann, G., 2006b. Methane discharge into the Black Sea and the global ocean via fluid flow through submarine mud volcanoes. *Earth and Planetary Science Letters* 248 (1–2), 544–559.
- Woodside, J.M., Ivanov, M.K., Limonov, A.F., 1997. Neotectonics and fluid flow through sea floor sediments in the Eastern Mediterranean and Black Seas. Parts I and II. In: *IOC Technical Series*, vol. 48. UNESCO.

Appendix II: Sahling et al., in press



Contents lists available at ScienceDirect

Marine and Petroleum Geology

journal homepage: www.elsevier.com/locate/marpetgeo

Vodyanitskii mud volcano, Sorokin trough, Black Sea: Geological characterization and quantification of gas bubble streams

Heiko Sahling^{a,*}, Gerhard Bohrmann^a, Yuriy G. Artemov^b, André Bahr^c, Markus Brüning^a, Stephan A. Klapp^a, Ingo Klaucke^c, Elena Kozlova^d, Aneta Nikolovska^a, Thomas Pape^a, Anja Reitz^c, Klaus Wallmann^c

^aMARUM – Center for Marine Environmental Sciences and Faculty of Geosciences, University of Bremen, Klagenfurter Strasse, 28359 Bremen, Germany

^bIBSS – Institute of Biology of the Southern Seas, National Academy of Sciences of Ukraine, Nakhimov Prosp. 2, IBSS, UA-99011, Sevastopol, Ukraine

^cIFM-GEOMAR – Leibniz-Institute of Marine Sciences, Wischhofstr. 1–3, 24148 Kiel, Germany

^dUNESCO-MSU Center for Marine Geosciences, Geological Faculty, Moscow State University, Vorobjevy Gory, Moscow 119899, Russia

ARTICLE INFO

Article history:

Received 14 May 2008

Received in revised form

15 December 2008

Accepted 6 January 2009

Available online xxx

Keywords:

Fluid seepage

Methane flux

Mud volcanism

Bubble emanation

ABSTRACT

Vodyanitskii mud volcano is located at a depth of about 2070 m in the Sorokin Trough, Black sea. It is a 500-m wide and 20-m high cone surrounded by a depression, which is typical of many mud volcanoes in the Black Sea. 75 kHz sidescan sonar show different generations of mud flows that include mud breccia, authigenic carbonates, and gas hydrates that were sampled by gravity coring. The fluids that flow through or erupt with the mud are enriched in chloride (up to $\sim 650 \text{ mmol L}^{-1}$ at $\sim 150\text{-cm}$ sediment depth) suggesting a deep source, which is similar to the fluids of the close-by Dvurechenskii mud volcano. Direct observation with the remotely operated vehicle QUEST revealed gas bubbles emanating at two distinct sites at the crest of the mud volcano, which confirms earlier observations of bubble-induced hydroacoustic anomalies in echosounder records. The sediments at the main bubble emission site show a thermal anomaly with temperatures at $\sim 60 \text{ cm}$ sediment depth that were $0.9 \text{ }^\circ\text{C}$ warmer than the bottom water. Chemical and isotopic analyses of the emanated gas revealed that it consisted primarily of methane (99.8%) and was of microbial origin ($\delta\text{D-CH}_4 = -170.8\text{‰}$ (SMOW), $\delta^{13}\text{C-CH}_4 = -61.0\text{‰}$ (V-PDB), $\delta^{13}\text{C-C}_2\text{H}_6 = -44.0\text{‰}$ (V-PDB)). The gas flux was estimated using the video observations of the ROV. Assuming that the flux is constant with time, about $0.9 \pm 0.5 \times 10^6 \text{ mol}$ of methane is released every year. This value is of the same order-of-magnitude as reported fluxes of dissolved methane released with pore water at other mud volcanoes. This suggests that bubble emanation is a significant pathway transporting methane from the sediments into the water column.

© 2009 Elsevier Ltd. All rights reserved.

1. Introduction

Gas bubbles rising from the seafloor into the water column have been described from many cold seeps in the deep sea but the associated gas flux remains largely unknown. At most sites, the existence of bubbles in the water column has been proposed based on hydroacoustic anomalies in echosounder records rather than on direct observations with unmanned or manned underwater vehicles. Evidence for bubbles streams has been found in a wide variety of deep-water geological settings, such as Hydrate Ridge at the Cascadia convergent margin (Heeschen et al., 2003; Torres et al., 2002), sediment-hosted vents in the Guaymas Basin (Merewether et al., 1985), hydrocarbon seeps associated to salt tectonics in the

Gulf of Mexico (MacDonald et al., 2002), the drift deposit Blake Ridge offshore South Carolina (Paull et al., 1995), Håkon Mosby mud volcano in the Norwegian Sea (Sauter et al., 2006), a pockmark on the Congo (Zaire) sediment fan (Charlou et al., 2004), the Sakhalin and Kamchatka continental slope in the Sea of Okhotsk (Cranston et al., 1992; Ginsburg et al., 1993; Obzhirov et al., 2004), the convergent margin offshore New Zealand (Lewis and Marshall, 1996), and numerous sites in the Black Sea (Egorov et al., 2003; Greinert et al., 2006; Klaucke et al., 2006; Naudts et al., 2006). However, the amount of gas escaping from the sediments has been estimated at only three deep-water sites, i.e. at Hydrate Ridge (Torres et al., 2002), at Håkon Mosby mud volcano (Sauter et al., 2006), and site GC 184 in the Gulf of Mexico (Leifer and MacDonald, 2003).

Submarine mud volcanoes are complex, positive seafloor structures occurring in a wide variety of geological settings as recently reviewed by Dimitrov (2002) and Kopf (2002). About 1000

* Corresponding author. Tel.: +49 (0) 421 218 65054; fax: +49 (0) 421 218 65099.
E-mail address: hsahling@marum.de (H. Sahling).

known or inferred submarine mud volcanoes are summarized in these reviews. They vary in size, shape, and activity reflecting their complex nature. In general, the activity of a mud volcano may be distinguished between an eruptive phase, when large amounts of mud and fluid are expelled and a quiescent period dominated by fluid flow, which includes the advective flow of pore water as well as the emanation of free gas. In addition, there might be a senescence phase without any fluid flow and mud eruptions in between. Only a few mud volcanoes have been investigated in detail so far. Håkon Mosby mud volcano is probably the best studied example at which the fluxes of bubbles (Sauter et al., 2006) and fluids (De Beer et al., 2006; Feseker et al., 2008) have been estimated. All other reported values concern the flux of dissolved methane that is released together with advecting pore water, including Dvurechenskii mud volcano in the Black Sea (Wallmann et al., 2006), Atalante and Cyclope at the Barbados convergent margin (Henry et al., 1996), and Mound Culebra at the Middle American convergent margin (Mau et al., 2006; Sahling et al., 2008b).

About 60 mud volcanoes are currently described in the Black Sea. Almost all of the mud volcanoes are presently active with respect to fluid flow as indicated by high concentrations of gas in the pore waters, the presence of gas hydrates in the sediments, and elevated heatflow values (Blinova et al., 2003; Bohrmann et al., 2003; Bouriak and Akhmetzhanov, 1998; Ivanov et al., 1996; Ivanov et al., 1998; Limonov et al., 1997; Wallmann et al., 2006; Woodside et al., 1997). In addition, bubble streams have been detected by echosounder at the mud volcanoes Dvurechenskii, Vodyanitskii and a Nameless Seep site (Greinert et al., 2006). The bubble streams cause backscatter anomalies in the echographs that are shaped like “flares”, a term that is widely used in the scientific literature to describe this phenomenon. The flare at Vodyanitskii mud volcano was found to be 1300-m high (Greinert et al., 2006). Subsequent modelling of the bubbles stream and the environmental conditions in the deep Black Sea showed that bubbles of a realistic size range can rise 1300 m high before they rise out of the hydrate stability zone and then rapidly dissolve completely in the water column (McGinnis et al., 2006).

The purpose of this study is to geologically characterize Vodyanitskii mud volcano, which is located in 2070-m water depth in the Sorokin Trough, using swath bathymetry, 75-kHz sidescan sonar, 18-kHz echosounder, and gravity coring. In addition, the remotely operated vehicle (ROV) QUEST was employed in order to visually document the bubbles escaping the seabed, and to deploy a temperature probe for geothermal measurements and a novel gas bubble sampler for pressure-tight gas sampling. We report on the presence of mud flows and the flow of chloride-rich warm fluids as well as the occurrence of gas hydrate and authigenic carbonates. Furthermore, the flux of gas bubbles was quantified based on ROV video images in order to provide data for improved methane flux estimations of a deep-water mud volcano.

2. Study area

The Black Sea is generally considered to be a result of back-arc extension related to the subduction of the Thetyan Ocean (e.g. Okay et al., 1994). Following the collision between the Eurasian and the Arabian plates since the Eocene, the tectonic setting changed to a compressional regime (Nikishin et al., 2003). Mud volcanoes have been described mainly in two areas of the Black Sea (Fig. 1), in the central western basin (Ivanov et al., 1996) and in the Sorokin Trough (Limonov et al., 1997; Woodside et al., 1997). The Sorokin Trough is considered as a foredeep of the Crimean Mountains. It is composed of two main sedimentary units (Woodside et al., 1997): a lower unit comprising the upper part of the Maikopian Formation (Oligocene-lower Miocene) and Pliocene deposits, and an upper unit consisting

of Quaternary deposits. The N–S compressional regime and the weight of the overburden lead to the protrusion of the clay- and organic-rich Maikopian Formation (Limonov et al., 1997).

In general, mud volcanoes occurring in the Sorokin Trough are connected to mud diapirs as revealed by reflection seismics (Krastel et al., 2003; Wagner-Friedrichs et al., 2008; Woodside et al., 1997). Vodyanitskii mud volcano is connected, like Dvurechenskii and NIOZ mud volcanoes (Fig. 1), to a diapiric ridge which protrudes to depths of less than 500 m below the seafloor. The ridge is composed of organic-rich clays from the Maikopian Formation and can be traced for about 40 km in the Sorokin Trough (Krastel et al., 2003; Wagner-Friedrichs, 2007; Woodside et al., 1997). Mud is transported to the seafloor along conduits, which appear as acoustically transparent zones in seismic profiles. These have been imaged at the Dvurechenskii (Krastel et al., 2003) and Vodyanitskii mud volcanoes (Wagner-Friedrichs, 2007).

3. Material and methods

This study is based on data obtained during the R/V METEOR cruise M72/3 in March–April, 2007 (Bohrmann et al., 2007). Bathymetric maps were produced using the ship's KONGSBERG SIMRAD EM 120 swath echosounder operating at 12 kHz. Raw data were processed with the CARAIBES IFREMER program and plotted with the public domain program, General Mapping Tool (GMT). Hydro-acoustic anomalies caused by gas bubbles (“flares”) were recorded using the primary frequency of 18 kHz of the ships parametric sediment echosounder system, PARASOUND, with a beam width of 4°. The system settings were optimized for bubble detection (Nikolovska et al., 2008). Sidescan sonar data were recorded about three weeks after the other data by the deep-towed sidescan sonar system DTS-1 (EDGETECH) described in Klaucke et al. (2006). It is a full digital chirp system operating around 75 kHz. The data were processed with the CARAIBES IFREMER software. The towfish position was determined by a layback method based on ship position, cable length, and ship speed. However, the backscatter map had to be shifted by about 50 m to match with the bathymetry.

Three gravity cores were taken at Vodyanitskii mud volcano: GeoB 11913 (44°17.621'N; 035°01.946'E), GeoB 11980 (44°17.659'N; 035°01.965'E), GeoB 11990 (44°17.623'N; 035°01.946'E). The sediment cores were immediately opened upon retrieval, gas hydrates extracted, and sub-samples taken for pore-water analyses. Pore water was separated from the sediments by squeezing through a 0.2 µm membrane filter. Dissolved chloride was determined via titration with AgNO₃. Rates of upward fluid flow were determined by applying a transport-reaction model running on MATHEMATICA Version 5.2 (Schmidt et al., 2005) and fitting the model to the measured pore-water concentration of chloride and lithium, which are known as conservative elements. Boundary conditions for the sediment surface (0 cm) were defined as the background concentration of the bottom water and the base of the respective cores (GeoB 11913 and 11990).

One ROV dive (No. 161, GeoB 11917) was conducted at Vodyanitskii mud volcano on 28 March, 2007. Accurate navigation was provided by a combination of the IxSEA POSIDONIA ultra-short baseline (USBL) positioning system with an RDI 1200 Hz Doppler Velocity Log (DVL). The search for gas emanations was carried out by flying with the ROV about 20 m above the seafloor while scanning the water column for backscatter signals caused by bubbles with the ROV-mounted KONGSBERG SIMRAD DT MS1000 horizontally looking sonar system operating at a frequency of 765 kHz (Nikolovska et al., 2008).

The estimation of bubble sizes, numbers, and rising velocity are based on the recorded images of two video cameras mounted on the ROV. The video sequences (PAL format, 25 frames per second)

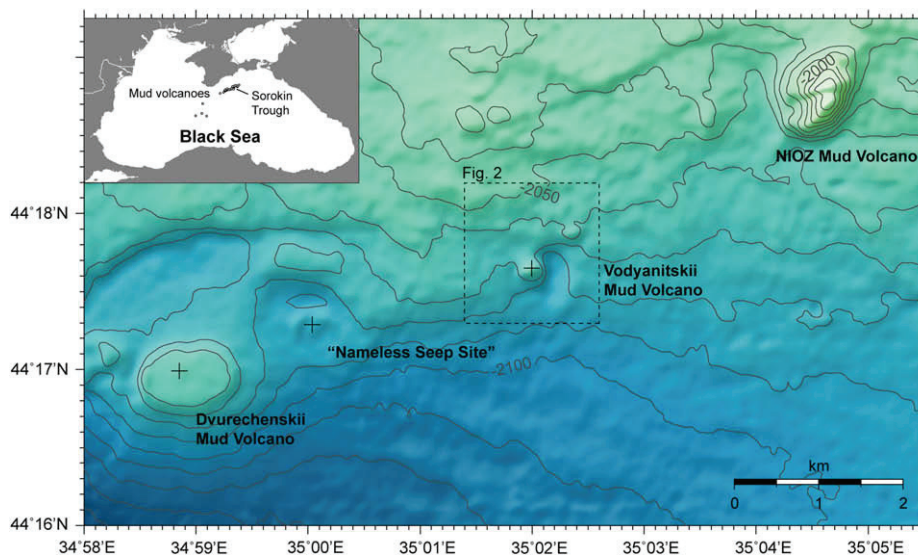


Fig. 1. Bathymetry of mud volcanoes in the Sorokin Trough (10-m contours). Crosses indicate the positions of published gas bubble streams (Greiner et al., 2006). The inset shows the location of mud volcanoes in the Black Sea (Ivanov et al., 1996; Woodside et al., 1997).

were replayed with the program ADOBE PREMIERE PRO. The frequency of bubbles crossing an arbitrary plane was estimated by replaying frame by frame of several 5 s intervals. The sizes of each bubble in the images and their rising velocity were calculated using the known size of the funnel of the gas bubble sampler (13-cm height, 16.2-cm outer diameter). The distance between funnel and camera was about 1 m. Only those bubbles that rose very close to the funnel were analysed in order to minimize errors due to inadequate scaling. Bubble sizes were estimated by exporting individual frames from the film sequence, which were then analysed using the public domain program IMAGEJ. The bubble volume was calculated assuming an ellipsoid with the two measured axes (major and minor) and a third axis, which is the arithmetic mean of the former two. The bubble rising velocity was calculated by measuring the number of frames it took a bubble to rise about 13 cm. The underwater images shown in this publication were taken with a 3 megapixel digital still camera.

Gas bubbles were collected using a novel gas bubble sampler consisting of a funnel, a pressure valve, a pressure gauge, and a gas cylinder. Prior to the dive, the gas cylinder is closed at atmospheric pressure. At the seafloor, bubbles are collected in the funnel and, subsequently, the pressure valve is opened and re-closed by the ROV's manipulators. By this method, the gas and gas hydrate are sucked into the cylinder by the pressure gradient. Upon retrieval, the gas is released and sub-samples are taken. The gas composition was analysed on board using a two-channel 6890 N (AGILENT TECHNOLOGIES) gas chromatograph. Low-molecular-weight hydrocarbons (C₁–C₆) were separated, detected, and quantified with a capillary column (OPTIMA-5; 5 μm film thickness; 0.32 mm inner diameter, 50 m length, carrier gas: He) connected to a flame ionisation detector. Permanent gases (O₂, N₂, CO₂) as well as C₁ and C₂ hydrocarbons were determined using a packed stainless steel column (molecular sieve, carrier gas: He) coupled to a thermal conductivity detector. Air contamination during sampling and analytical procedure were estimated to contribute to less than 2 vol-% of all volatiles. For onshore determinations of stable isotopic ratios (¹H/D, ¹²C/¹³C), gas samples were transferred into serum glass vials, which were pre-filled with NaCl-saturated water, sealed with butyl stoppers, and stored inverted in a cool room (4 °C). The isotopic ratios of volatile hydrocarbons were measured by gas-chromatograph-isotope-ratio-mass-spectrometry at a commercial laboratory (GCA, Sehnde, Germany).

Temperature measurements were carried out with a 80-cm long temperature probe (RBR Ltd., Canada). Eight sensors are equally spaced along a distance of 0.5 m. The values were autonomously recorded every 10 s. The sensors have an accuracy of 0.002 °C and were cross-calibrated with a hydrographic CTD_60-77 (SEA & SUN TECHNOLOGIES) mounted on the ROV, which has a precision of 0.0005 °C. The T-stick was pushed into the sediment by the ROV's manipulator and left for equilibration with the sediments for about 15 min. Equilibrium temperatures were calculated following the method given in Hartmann and Villinger (2002) and Villinger and Davis (1987) employing a self-written routine in MATLAB.

The hydrate stability conditions were calculated with the program HWHYD model developed at the Heriot–Watt University, U.K (Masoudi and Tohidi, 2005). The upper limit of hydrate stability was defined using the temperature vs. depth profile recorded by the CTD sensor mounted on the ROV.

4. Results

4.1. Hydroacoustic investigations and sediment core descriptions

Vodyanitskii mud volcano is situated on a gentle slope resulting in an asymmetric shape of the feature that is quite complex (Fig. 1). It consists of a cone about 500 m in diameter and 20-m height surrounded by a depression, which is most pronounced on its eastern side. The sidescan sonar image shows the characteristic configuration of a mud volcano (Fig. 2). The central crater-like crest is most likely the site where the mud flows erupted. It is surrounded by radial small-scale ridges and a concentric pattern of anomalous backscatter that we interpret as mudflows of different generations. The mud preferentially flowed downslope in SSE direction beyond the limit of the sidescan sonar survey. About 500 m NE of the Vodyanitskii mud volcano, another mud volcano-like structure can be distinguished, though much less apparent. It has a positive morphology of about 10 m with very slightly higher backscatter compared to the surrounding (Fig. 2). These are probably seafloor features of an old and inactive mud volcano, which is buried by the regular hemipelagic sedimentation, leading to an indistinct morphology and weak backscatter anomaly.

Sediment samples were taken at three gravity corer stations at the summit of Vodyanitskii mud volcano (Fig. 2). One core contained mud clasts whereas two cores recovered clay or sandy clay

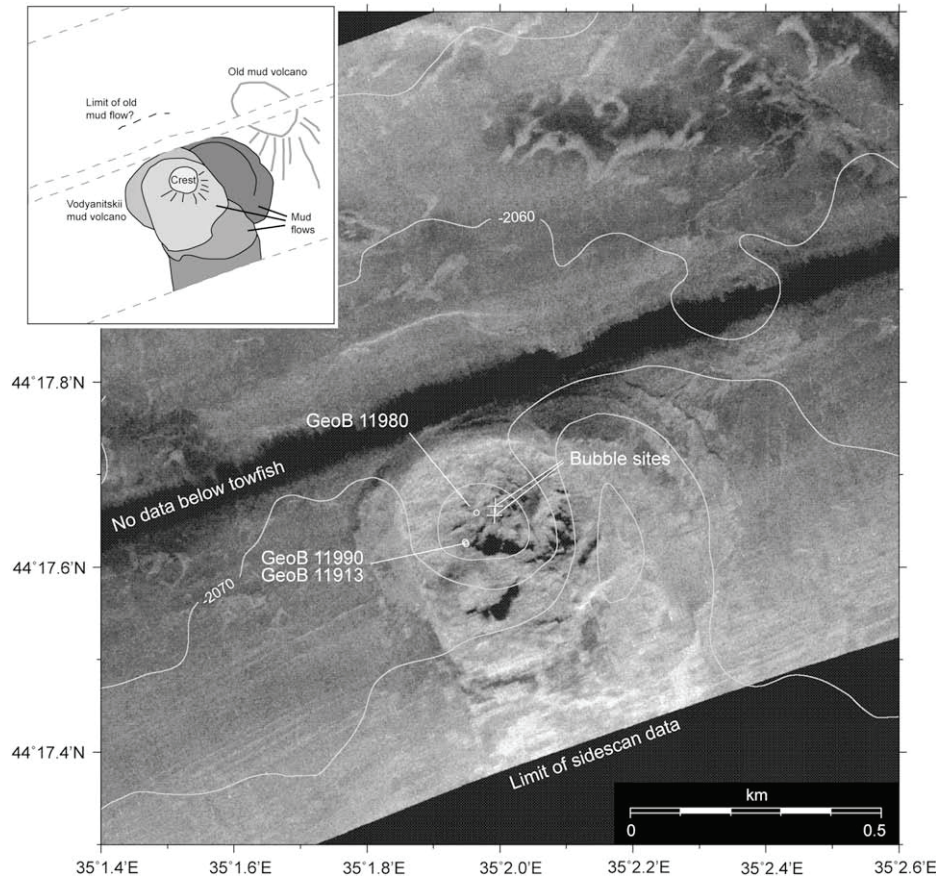


Fig. 2. Bathymetric contours draped over 75 kHz sidescan sonar profile (high backscatter in white) at Vodyanitskii mud volcano and a less distinct, probably old mud volcano. The inset shows the interpretation of the backscatter image. The locations of the two bubble streams detected by ROV *QUEST* and the gravity corer-sampling sites are indicated.

(Fig. 3). Gas hydrates were recovered in two cores at about 1.5 m sediment depths, which was generally the maximum penetration depth of the cores, suggesting that a layer of gas hydrate may have prevented the cores from deeper penetration. The gas hydrates occurred as chips and plates with broken edges and were up to 2 cm in size (Fig. 4A). Carbonates occurred in the upper 35 cm of two of the cores. Their shapes and sizes were up to 9 cm (Fig. 4B), typical for authigenic carbonates probably related to anaerobic oxidation of methane. In addition, the cores had a mousse-like texture below a depth of about 40 cm indicating a high gas content that expanded during the core recovery procedure. Analyses of the pore water extracted from the gravity corer GeoB 11913 and 11990 revealed increasing chlorinity with depth (Fig. 5). The linear chlorite profiles indicate that ex situ gas hydrate destabilisation did not occur, which would result in spikes of lower chloride concentrations.

In order to detect and localize gas bubble emission sites on Vodyanitskii mud volcano, a short survey with the ship's sediment echosounder PARASOUND was carried out. The ship crossed the mud volcano in different directions at a low speed of about 1 knot (Fig. 6A). The gas bubble streams are discernable as hydroacoustic anomalies ("flares") in the 18 kHz record (Fig. 7). The flares have different shapes as a result of crossing the rising bubble streams in various directions at variable distance to the actual source at the seafloor. In order to better localize the emanation sites, those segments of the ship track are marked in Fig. 6A, where the flares originate at the seafloor (segments 1–1', 3–3', and 4–4' in Fig. 7). As confirmed later by the ROV *QUEST*, two distinct bubble sites were found in the center of the marked area in Fig. 6A. Thus, flare

imaging is a successful approach to locate bubble emanation sites at the seafloor.

During the flare survey, the gas bubbles did not rise straight upwards but were deflected in a westerly direction. This is seen, for example, at the flare along profile 4–4' in Fig. 7, which shows that during bubbles rise, they horizontally moved in the direction the ship travelled (Fig. 6A). The deflection is probably caused by bottom currents, which can be roughly estimated from the echosounder records. Assuming a bubble rise velocity of about 25 cm s^{-1} (see below), it takes about 2700 s for a bubble to rise to a height of 680 m above the seafloor as shown in Fig. 7. For the bubble horizontal drift of about 130 m, this corresponds to a bottom current of about 4.8 cm s^{-1} .

4.2. Seafloor observations and sampling with ROV *QUEST*

During ROV *QUEST* dive no. 161 (GeoB 11917) at Vodyanitskii mud volcano we systematically surveyed large parts of the mud volcano and discovered two individual sites with bubble streams (Fig. 6B). At one site (bubble site #1), a comprehensive sampling program with push corer, temperature probe, and gas bubble sampler was carried out, whereas at a second site (bubble site #2) only video images were taken due to the failure of the ROV's manipulator and, subsequently, a dead vehicle due to an electrical short circuit (Bohrmann et al., 2007). Due to time constraints, the ROV travelled only about 150 m on the seafloor (bold lines in Fig. 6B). The observations revealed that along the bottom track, the entire surface of the mud volcano was homogeneously covered by soft mud with only slight undulations of the seafloor. We found, apart from

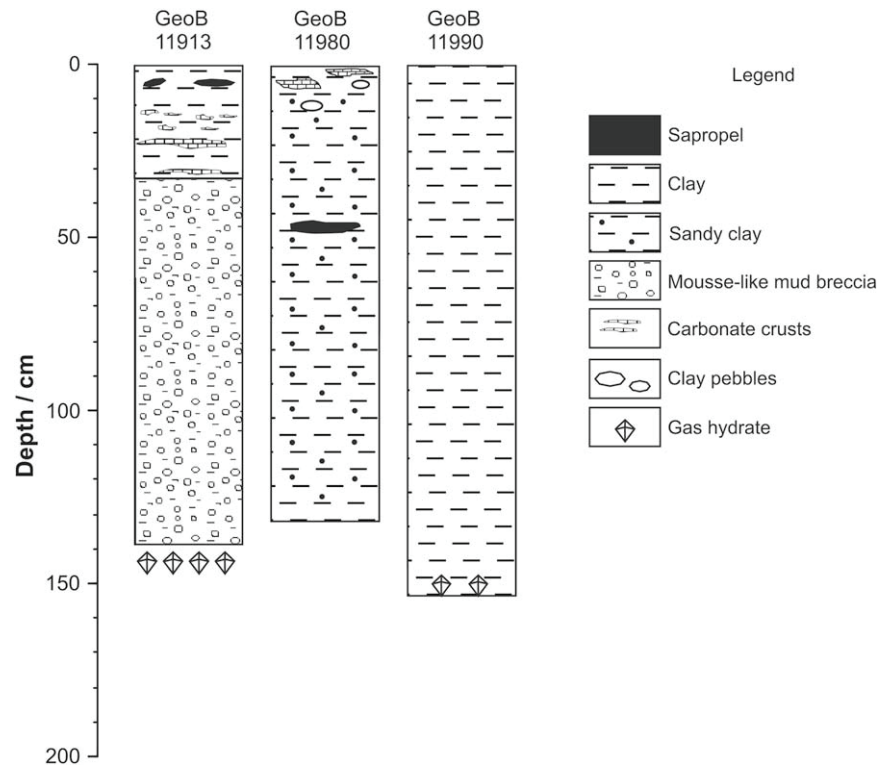


Fig. 3. Lithological descriptions of gravity corer retrieved from Vodyanitskii mud volcano. Two cores contained gas hydrates in the lowermost sediment sections around 1.5 m, in the case of GeoB 11913 in the core catcher.

the two sites with bubble escapes described below, only one additional site where the mud cover was interrupted. At one spot, two circular depressions each about 1-m in diameter were observed but as there were no indications for current fluid flow we did not study it in detail.

The seafloor at the bubble sites #1 and #2 was disturbed as shown in Fig. 8A and B, respectively. At bubble site #1, the bubbles rose from a slightly bulged seafloor that is located at the rim of a crater-like depression several meters in diameter. Bubbles were released from four distinct, small cracks in the seafloor. Three small outlets emanated single bubbles forming “bubble trains” whereas the main bubble conduit released a stream of bubbles. Bubble site #2 is located about 20 m north of site #1. The seafloor was slightly

arched upward similar to the small bulge at bubble site #1. Bubbles at site #2 emanated in about equal amounts from two conduits, which release very rapidly trains of bubbles.

Bubbles were collected from the main bubble stream at bubble site #1 using the gas bubble sampler (Fig. 9A). Upon collection in the funnel the bubbles remained as individual spheres and turned slightly opaque, suggesting the formation of gas hydrate at their gas–water interface. The bubble fabric of hydrate in the funnel was rather rigid, as it stayed largely intact when the funnel was shaken by the ROV’s manipulator and, after the sampling, rotated (Fig. 9B). The gas composition was analysed on board and revealed the dominance of methane (99.773% CH₄; 0.154% CO₂; 0.058% C₂H₆; 0.006% C₃H₈; 0.005% *i*-C₄H₁₀; 0.001% *n*-C₄H₁₀; 0.002% C₅-

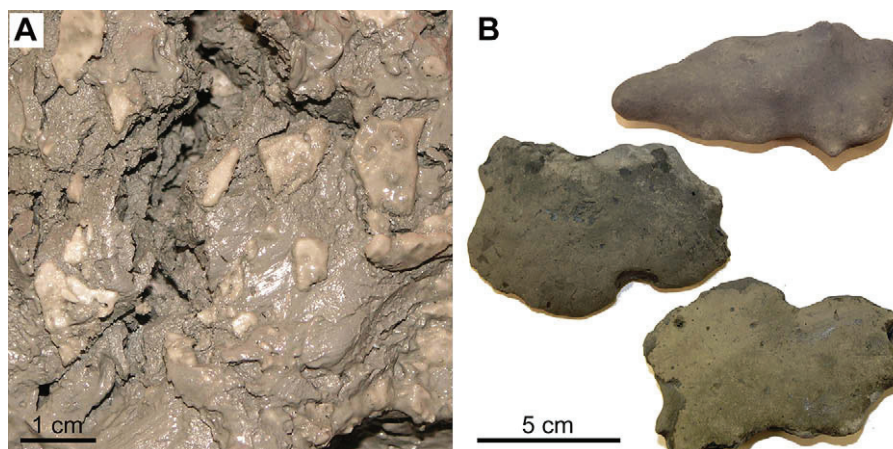


Fig. 4. (A) Chips of gas hydrates in the core catcher and (B) rounded carbonates found in the sediment interval 10–35 cm in core GeoB 11913 taken at Vodyanitskii mud volcano.

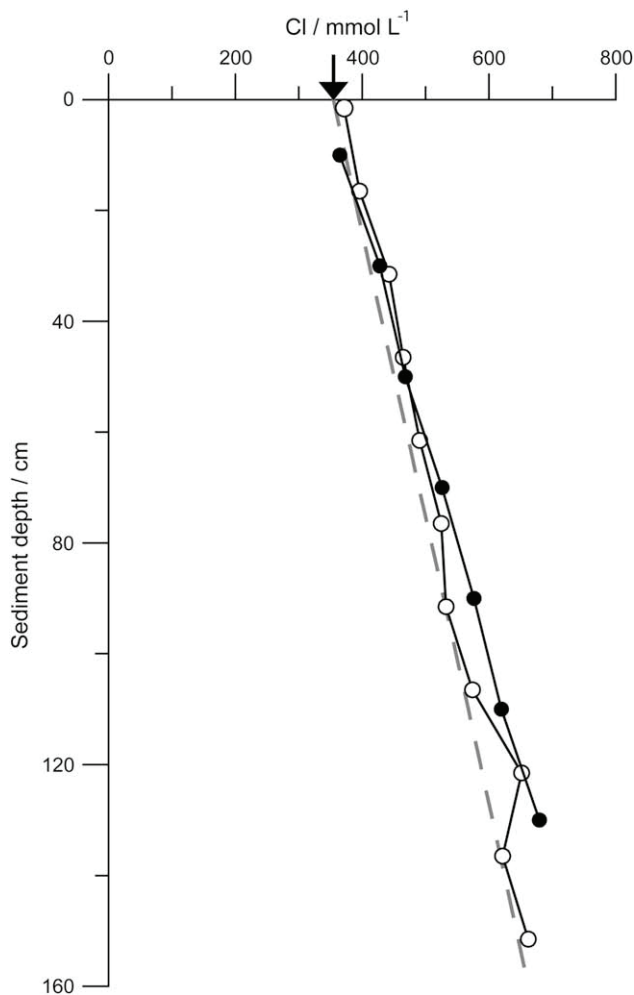


Fig. 5. Pore-water concentration of chloride in gravity cores GeoB 11913 (filled symbols) and 11990 (open symbols) taken at Vodyanitskii mud volcano. The dashed line represents the modelled Cl^- depth-profile considering a fluid advection rate of 0.2 cm yr^{-1} . The arrow on the x-axes represents the Black Sea bottom water concentration of chloride.

derivates); all values as mol-% of $\Sigma (\text{C}_1\text{--C}_6, \text{CO}_2)$. The onshore stable isotope analyses revealed a $\delta\text{D-CH}_4$ value of -170.8‰ (SMOW), a $\delta^{13}\text{C-CH}_4$ value of -61.0‰ (V-PDB), and a $\delta^{13}\text{C-C}_2\text{H}_6$ value of -44.0‰ (V-PDB).

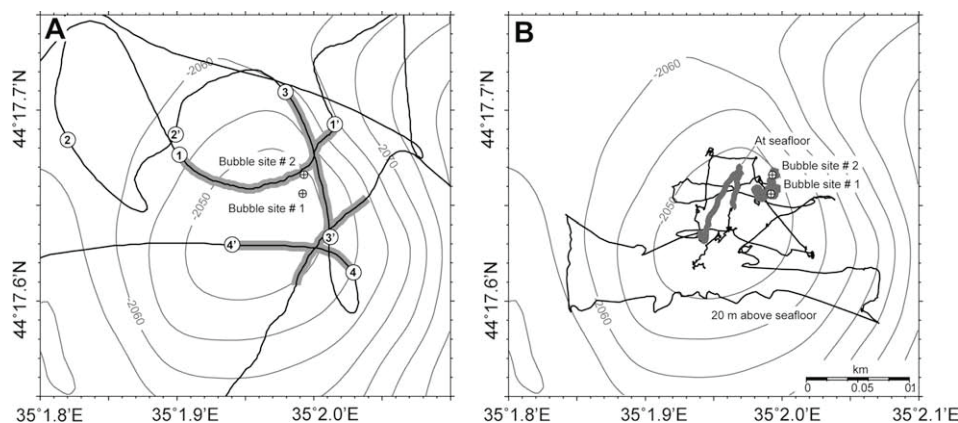


Fig. 6. (A) Ship track during the flare survey with the 18 kHz echosounder and the positions of the two bubble streams found by ROV QUEST at Vodyanitskii mud volcano. The segments marked with thick grey lines indicate hydroacoustic anomalies close to the seafloor as shown in Fig. 7. (B) ROV QUEST dive track (Dive 161, GeoB 11917). The ROV flew at the seafloor (thick lines) or about 20 m above the seafloor (thin lines) when searching for the gas bubble streams with the horizontally-looking sonar. Two bubble streams occur close together.

The gas emanation is associated with a remarkable temperature profile (Fig. 10). The temperature probe was pushed into the sediments at the main bubble outlet of bubble site #1 by the ROV's manipulator. It penetrated to a maximum depth of about 70 cm as judged from the size of the tool that remained above the seafloor. The temperature generally rose from bottom water values of about 9.1 to 9.9 °C at 70 cm sediment depths. The individual measurements scatter considerably indicating that non steady-state conditions prevail.

4.3. Estimation of bubble flux

In order to estimate the gas flux we measured the average size of the bubbles and counted the number of bubbles released from the seafloor per time unit. The average bubble size was estimated at the main outlet at bubble site #1. The bubbles appear ellipsoidal and elongated horizontally (Fig. 9A). The bubbles rose steadily and straight upward without significant wobbling or path oscillation. Their rise velocity was about $27 \pm 2 \text{ cm s}^{-1}$ ($n = 20$). On average, the equivalent spherical diameter was about $5.2 \pm 0.9 \text{ mm}$ (Fig. 11) with a volume of $80 \pm 45 \text{ mm}^3$ ($n = 396$). The number of bubbles rising from the seafloor through an arbitrary baseline was repeatedly measured for five-second intervals at all bubble vents. In total, about 1500 bubbles were released every minute at bubble site #1 with the majority escaping through the main vent (more than 1200 bubbles per minute). About 400 bubbles per minute emanated at bubble site #2. The temporal variability of the bubble flux was small within the observation period of about 1 h. We measured the quantity of released bubbles at the main outlet at site #1 12 times during 5 s intervals and found a constant flux that varied not more than 12% around the average value.

Calculation of the gas flux at bubble site #1 ($1500 \text{ bubbles min}^{-1}$) and #2 ($400 \text{ bubbles min}^{-1}$) and an average gas bubble volume of 80 mm^3 results in a gas volume released from the seafloor of about 0.12 and 0.032 L min^{-1} , respectively. These bubbles were observed at a water depth of about 2070 m, which corresponds to a hydrostatic pressure of about 205 MPa, and an ambient temperature of 9 °C . The molar volume of methane gas at these conditions is about $90 \text{ cm}^3 \text{ mol}^{-1}$ (Duan et al., 1992). Applying this value, the annual methane bubble flux is $0.9 \times 10^6 \text{ mol methane}$ from Vodyanitskii mud volcano assuming the gas flux remains constant.

Our approach of estimating the bubble flux is a first-order approximation and subject to errors. The counting of bubbles was rather straight forward and associated with minor uncertainties because bubbles were clearly identifiable in the video sequences. In contrast, large errors may be related to the estimation of the bubble

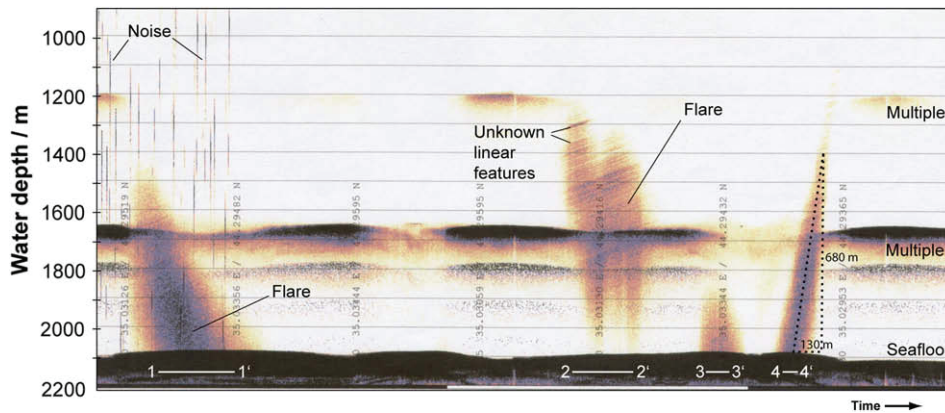


Fig. 7. Hydroacoustic anomalies due to bubble streams recorded during the flare survey (Fig. 6) using the 18 kHz signal of the PARASOUND echosounder at Vodyanitskii mud volcano. The ship crossed over the bubble streams several times in different directions. Those locations of the intervals marked by Arabic numbers are shown in Fig. 6A. Inclined linear patterns of unknown origin occur within the high backscatter of the flare ("unknown features"). The slope of the lineaments is about 50 cm s^{-1} , which is considerably higher than the observed rising speed of individual bubbles (see Discussion).

volume. The volume was calculated assuming that a bubble is an ellipsoid with the diameters a , b , and c . The major (a) and minor (b) axes of the bubbles were measured in the frame-grabbed images. The accuracy of this measurement is crucial and, therefore, was repeated for 396 different bubbles. Despite an ellipsoidal shape of the bubbles, the calculation of the volume greatly depends on which axis of rotation is chosen. In order to provide a conservative estimate, we used the arithmetic average of the major and minor axes as ellipsoid diameter c . This results in values that are about 10% smaller than values assuming rotation along the minor axis. The obtained bubble volumes with a median of 80 mm^3 have a large standard deviation of 45 mm^3 (Fig. 11). We assume that this large standard deviation might be a result of the natural variation in the bubble size population, bubble oscillation, and methodological uncertainties. Therefore, we propose that the error of the volume flux estimate is within the standard deviation of $\pm 45 \text{ mm}^3$, which corresponds to an uncertainty in the volume calculation of about 55%. Thus, we estimate the flux of methane as about $0.9 \pm 0.5 \times 10^6 \text{ mol yr}^{-1}$.

5. Discussion

5.1. Mud volcanism, mud flow, fluid advection

The morphologies of mud volcanoes in the Sorokin Trough are highly variable. For example, the mud volcanoes Dvurechenskii,

Vodyanitskii, and NIOZ shown in Fig. 1 are characterized by large differences in their shape ranging from a less than 20-m high flat-topped mud pie, a 20-m high cone surrounded by a depression to a nearly 100 m high cone, respectively. The variability has been attributed to, among others, the geometry of the feeder channel and the viscosity of the extruded material (Brown, 1990; Kopf, 2002).

The morphology of Vodyanitskii mud volcano is similar to numerous other mud volcanoes in the Black Sea characterized by one or more cones within a circular depression (Woodside et al., 1997). The shape may be explained by an initial violent eruption leading to a circular depression with subsequent less-violent eruptions of mud forming one or several cones in the depression (e.g., Sevastopol mud volcano; Wagner-Friedrichs et al., 2008). Despite the fact that most publications follow the concept that a violent eruption is the cause for depressions (see review in Judd and Hovland, 2007), we propose that an alternative explanation may be considered. The depression may be caused by a general subsidence of the mud volcano and its surrounding as a result of the loss of volume due to fluid flow in periods without mud eruptions. However, we stress that this is pure speculation due to two observations. Firstly, in the case of a violent eruption one may expect to find evidence of the extruded material in the vicinity of the depression, for which there is no indication in the sidescan sonar images. Secondly, one may expect to find a more or less

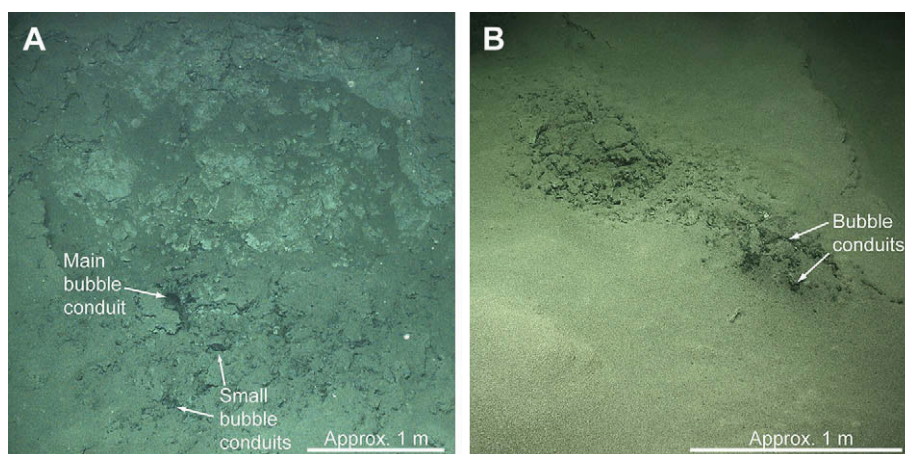


Fig. 8. Seafloor images at (A) bubble stream #1 and (B) bubble stream #2 at Vodyanitskii mud volcano. The seafloor is slightly bulged with cracks and holes from which bubbles emanate. The resolution of the images is not sufficient to show the bubbles.

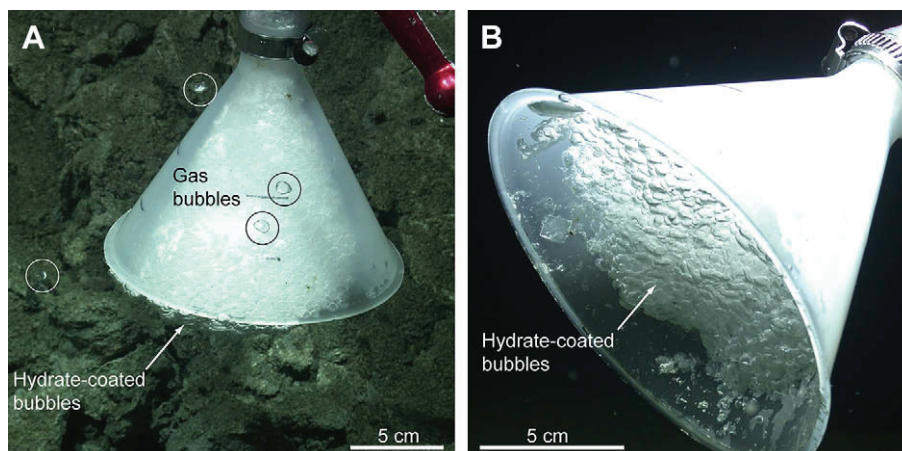


Fig. 9. Images of gas bubbles and the funnel of the gas bubble sampler at bubble stream #1 at Vodyanitskii mud volcano. (A) The bubbles are spherical and did not wobble noticeably while rising. Those bubbles that were caught by the funnel kept their shapes probably due to the formation of a hydrate skin. (B) Close-up of the framework of the hydrate-coated bubbles caught in the funnel.

recent example of a violent eruption on the seafloor, but this has, to our knowledge, not been reported from the seafloor in the Black Sea so far.

However, mud flows occur at Vodyanitskii mud volcano. The extruded mud has acoustic properties that differ from those of the surrounding basin sediments causing a distinct backscatter pattern in the sidescan sonar image (Fig. 2). The mud flows consist of clay, sandy clay, and mousse-like mud breccia (Fig. 3), the latter having a clayey matrix with mm-sized fragments of stiff clay and rocks, which are typical mud inclusions originating from the Maikopian Formation (Woodside et al., 1997). In contrast, the regular hemipelagic sediments of the Black Sea consist of finely laminated

coccolith ooze overlying a finely laminated sapropel in the upper decimetres (Ross and Degens, 1974). This lithological difference is probably the main reason for the difference in the backscatter characteristic between mud flows and background sediments (Fig. 2). The lack of the typical Holocene sediment units on top of the mud flows suggest that these must have erupted recently.

In addition, authigenic carbonates likely contribute to the acoustic properties of the sediments. Carbonates were present in two of the three cores within the uppermost few decimetres of the sediments (Figs. 3 and 4B). We interpret these carbonates as authigenic precipitations as a result of the anaerobic oxidation of methane, which are widespread at seeps and mud volcanoes in the Black Sea (Bahr et al., in press; Mazzini et al., 2004; Mazzini et al., 2008; Peckmann et al., 2001; Reitner et al., 2005). However, it is unlikely that gas hydrates that were found at a depth of about 1.5 m in the cores, contributed to the high backscatter. Studies with the same DTS-1 sidescan sonar system operating at 75 kHz indicate that it does not penetrate to these depths (Sahling et al., 2008a).

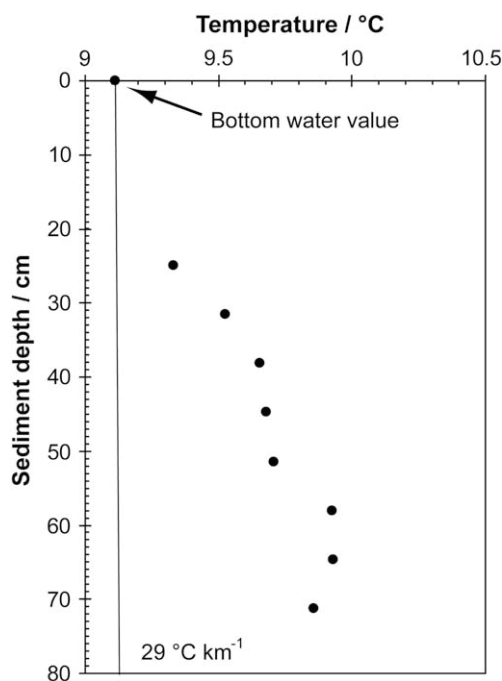


Fig. 10. The bottom water temperature and equilibrium temperatures obtained by the ROV-operated temperature probe at bubble site #1 at Vodyanitskii mud volcano. The temperatures scatter considerably but there is a clear increase with depth. For comparison, the geothermal gradient of 29 °C km^{-1} is shown, which is the typical value for sediments not influenced by mud volcanism in the Sorokin Trough (Bohrmann et al., 2003).

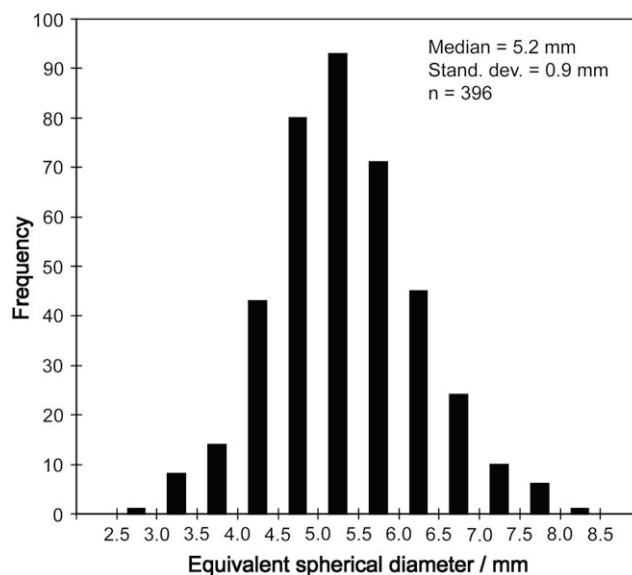


Fig. 11. Frequency distribution of bubble diameters based on video analyses. The measured minor and major diameters were recalculated to equivalent spherical diameters.

The findings are in agreement with earlier sidescan sonar studies at Black Sea mud volcanoes attributing most of the backscatter characteristics of mud flows to mud clasts, breccia, and carbonates (Akhmanov, 1996; Ivanov et al., 1996; Limonov et al., 1997; Woodside et al., 1997).

Mud volcanoes are complex three-phase flow systems with eruption of mud as well as emanation of pore water and gas bubbles. An increase of chlorinity with depth as observed in the sediments of Vodyanitskii mud volcano (Fig. 5), can either be produced by advection of high-salinity pore water as described by Aloisi et al. (2004) for the nearby Dvurechenskii mud volcano. Alternatively it can arise due to the equilibration of a recently deposited mud flow (clay in a high-salinity fluid) with the overlying bottom water (Feseker et al., 2008). Both processes can lead to similar geochemical profiles. Even though the overall trend of increasing chloride concentration with depth at Vodyanitskii mud volcano is similar to that of the nearby Dvurechenskii mud volcano (Aloisi et al., 2004; Wallmann et al., 2006) their fluid flow velocities are considerably different. Dvurechenskii mud volcano shows relatively high advection rates of 10–20 cm yr⁻¹ whereas Vodyanitskii mud volcano shows rather low advection rates of 0.2 cm yr⁻¹. Still the profile might have been produced by this low fluid advection rates as discussed earlier in Wallmann et al. (2006) or, alternatively, by the elapse of sufficiently more time since the last mud flow occurred (Feseker et al., 2008) compared to Dvurechenskii mud volcano.

In general, the presence of chloride-rich fluids at both mud volcanoes indicates a deep source of the fluids. Aloisi et al. (2004) discusses in detail the chemical and isotopic composition of fluids at Dvurechenskii mud volcano. They conclude that alteration of silicate phases is the most likely source of the high-salinity fluids and that the fluids had equilibrated with the sediments at temperatures of roughly 100 °C, which is encountered at a sediment depth of about 3 km in the Sorokin Trough. In addition, they regard gas hydrate formation in the shallow subsurface as a process that probably contributes to enhance the salinity of the seeping fluids. The spatial proximity of Vodyanitskii and Dvurechenskii mud volcano, their common connection to the diapiric ridge (Wagner-Friedrichs, 2007), and their distinct high-chlorinity fluids suggest, therefore, that the fluids at Vodyanitskii mud volcano have a similar deep origin as those expelled at Dvurechenskii mud volcano.

5.2. Gas bubble streams

Gas bubble streams are probably constantly released at Vodyanitskii mud volcano. Aside from this study conducted in March 2007, additional evidence of bubbles causing hydroacoustic anomalies in the echosounder has been found previously during five cruises that took place in 2003 and 2004 (Greinert et al., 2006). The position of the bubble sites #1 and #2 that we located at the seafloor using the USBL navigation of ROV QUEST is about the same location as shown by Greinert et al. (2006). The distance between both positions is less than 40 m, which is within the range of uncertainty taking into account the errors of two different GPS navigation systems on different ships in different years as well as the inaccuracy of the underwater USBL navigation system.

Greinert et al. (2006) used the echosounder-recorded flare height and backscatter strength as a relative measure for the amount of emanated gas. Unfortunately, our results are not directly comparable because we used a different echosounder system and we spent little time to the detection and mapping of the flares. In addition, bottom currents that were not detected during earlier surveys were encountered. The rising bubbles are significantly deflected by these currents in a westerly direction. As we did not

systematically searched for the shallowest evidence of bubbles, which can be expected in a region west of the emanation sites (Figs. 6 and 7), we are not able to estimate the maximum rising height of bubbles in the water column. Our data show that they rose at least to a water depth of about 1200 m (Fig. 7), which is 870 m above the seafloor. However, we do not know whether or not the bubbles rose as high as 1300 m, as reported by Greinert et al. (2006). In conclusion, we take the fact that bubble streams have been documented during six cruises in a four-year time interval as strong evidence for a continuous process but that fluctuations in the amount of released gas are likely.

Analysis of the gas samples revealed that methane is the dominant constituent and that low-molecular-weight hydrocarbons are mainly of microbial origin. The molecular ratio (C₁/(C₂ + C₃) = 1546), as well as the stable carbon isotopic signatures ($\delta^{13}\text{C-CH}_4 = -61.0\text{‰}$; $\delta^{13}\text{C-C}_2\text{H}_6 = -44.0\text{‰}$) indicate that microbial production is the primary source of methane and ethane at Vodyanitskii mud volcano (Bernard et al., 1976; Milkov, 2005). In addition, the $\delta^{13}\text{C-CH}_4$ and $\delta\text{D-CH}_4$ (-171‰) are in the range of values that are characteristic for microbial methanogenesis by carbonate reduction (Whiticar et al., 1986). Microbial activity may be mainly expected at sediment depth shallower than ~3 km, given the regular geothermal gradient of 29 °C km⁻¹ in the Sorokin Trough (Bohrmann et al., 2003) and considering upper temperature limits of thermophilic methanogens (Orphan et al., 2003). The source depth of the majority of low-molecular-weight hydrocarbons is, thus, most likely shallower than that of the liquid fluid.

Volatile hydrocarbons are produced by the microbial fermentation of organic matter that migrates upwards in the sediments and accumulate below the lower limit of the gas hydrate stability zone, which is generally considered as a barrier. This concept is in agreement with seismic data that show amplitude anomalies that can be indicative of free gas at constant depths of about 300 ms TWT (~250 m) beneath the seafloor in the Sorokin Trough (Krstel et al., 2003). High reflection patches have also been found at the respective depths below Dvurechenskii and Vodyanitskii mud volcano (Krstel et al., 2003; Wagner-Friedrichs, 2007). This is slightly shallower than the theoretical depth of the base of the hydrate stability zone of ~350 m assuming a geothermal gradient of 29 °C km⁻¹, as illustrated in Fig. 12.

Several mechanisms have been envisaged to explain how free gas from below the gas hydrate stability zone is transported to the seafloor where it is released as bubble streams into the water column. For example, hydrate formation may be hampered by the availability of water (Ginsburg and Soloviev, 1997) or due to high pore-water salinity (Haecckel et al., 2004; Liu and Flemings, 2006; Torres et al., 2004). Furthermore, methane may be transported by the advection of warm fluids within gas chimneys (Wood et al., 2002). At Vodyanitskii mud volcano the combined effect of high-chlorinity fluids and local temperature anomalies are the most likely causes that allow gas bubbles to transit the stability zone without forming hydrate. The fluids at Vodyanitskii mud volcano are, like those at Dvurechenskii mud volcano, chloride-rich, which reduces the stability of gas hydrate compared to the bottom water conditions (Bohrmann et al., 2003). This is shown in Fig. 12 where the hydrate stability field at chloride concentrations of 900 mmol L⁻¹ is plotted, which is about 200 mmol L⁻¹ more than the maximum value found at 130 cm sediment depths at Vodyanitskii mud volcano (Fig. 5). However, the influence of the salt on the thickness of the hydrate stability zone in the sediments is small; it decreases by ~50 m (Fig. 12).

We found elevated temperatures in the sediments at the bubble site, which we interpret as temperature anomalies at Vodyanitskii mud volcano. Before discussing these measurements any further, we have to consider that potentially they may be disturbed due to

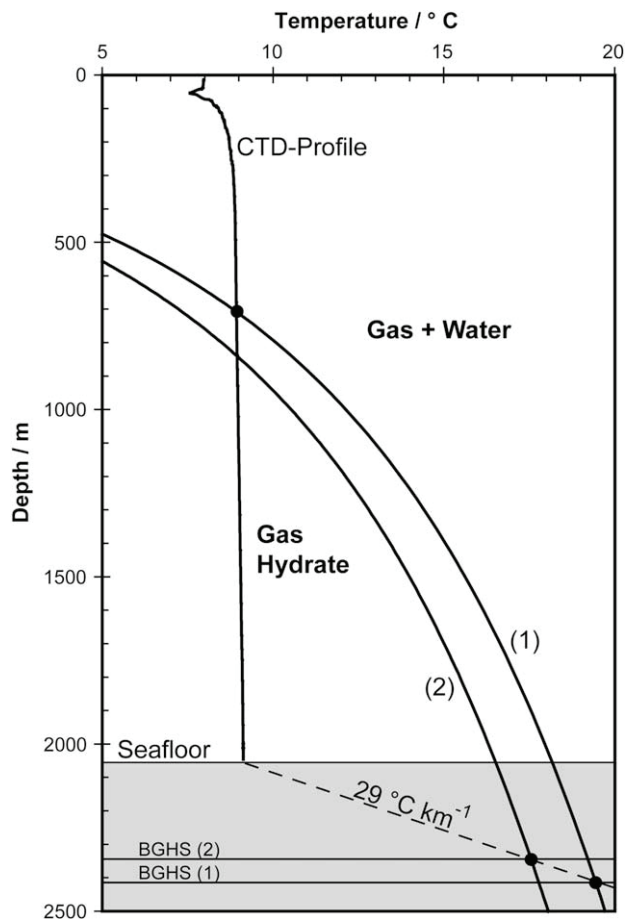


Fig. 12. Hydrate stability fields calculated for the methane-dominated gas composition as analysed from the gas bubble sampler. The stability fields were calculated for chloride concentrations of (1) 355 and (2) 900 mmol L⁻¹, which are the respective values for typical Black Sea bottom water (Bohrmann et al., 2003) and a chloride-rich deep fluid (Aloisi et al., 2004).

the spontaneous formation of hydrate around the temperature sensors, which is an exothermic reaction. However, hydrate formation would be expected to cause considerable variance in the temperature profile of each sensor during the deployment period, which was not apparent (data not shown). Thus, we regard the data as real and suggest that the temperatures were elevated due to the ascending mud, pore water, and/or gas bubbles. As we measured the profile in the sediments percolated by bubbles, we hypothesize that the rising bubbles and/or the water dragged with these bubbles are responsible for the observed temperature anomalies. The locally elevated temperature may facilitate the ascent of gas through the hydrate stability zone. However, further measurements are needed to investigate the interaction between temperature on one hand and fluid and mud flow on the other.

5.3. Fate of bubbles

Upon release of a bubble from the seafloor into the water column, its composition changes due to exchange of gases across the gas-water interface. In general, methane is transported into the surrounding methane-depleted water causing bubble shrinkage. The fraction of methane that is released from the bubble to the water depends on the release depth, bubble size, dissolved gas concentration, temperature, surface-active substances, and bulk fluid motions. Several bubble models have been developed in order to describe these

complex processes (Artemov et al., 2007; Leifer and Patro, 2002; McGinnis et al., 2006). The model of McGinnis et al. (2006) was explicitly adapted to the environmental conditions encountered at Vodyanitskii and Dvurechenskii mud volcanoes taking into account the decreased methane dissolution rates due to the formation of a hydrate skin around the bubbles (Rehder et al., 2002).

Our observation at the gas outlets at Vodyanitskii mud volcano with the ROV *QUEST* is generally consistent with the McGinnis et al. (2006) model. In summary, the model shows that the immediate formation of a hydrate rim around bubbles in the size range of 6–9.5 mm diameter in 2000 m water depth can explain their long lifetime and rise through the water column, which is consistent with the flare heights of 800–1300 m above the mud volcanoes observed by Greinert et al. (2006). The model predicts that, at this height, the bubbles leave the hydrate stability field and dissolve completely in the water column. During our investigations, the bubbles observed at Vodyanitskii mud volcano are with a median diameter of 5 mm (Fig. 11) somewhat smaller than the size range that was assumed by McGinnis et al. (2006). However, an initial size of 5 mm is still sufficient to allow the bubble to rise several hundred meters above the seafloor, as we observed (Fig. 7) and is predicted by the model of McGinnis et al. (2006). We estimated an initial rise velocity that is higher than the assumed rising speed of McGinnis et al. (2006), with values of 27 compared to 21 cm s⁻¹, respectively, which also is high compared to values determined experimentally for clean bubbles (Clift et al., 1978) or based on hydroacoustic data (Artemov et al., 2007). This could indicate a bubble-induced upwelling of the water (Leifer et al., 2006). Upwelling flows were not considered in the McGinnis et al. (2006) model but have been shown important when considering rising heights and methane dissolution in other settings (Leifer et al., 2006; Leifer and Judd, 2002; Leifer and Patro, 2002). Unfortunately, we did not pay attention to potentially occurring bubble-induced upwelling while diving with the ROV *QUEST* on site, consequently, the significance of this process at Vodyanitskii mud volcano remains open. There is also evidence that plume upwelling from a deep-water site at Håkon Mosby mud volcano indeed leads to significant vertical movement of the water column (Sauter et al., 2006).

5.4. Estimation of bubble flux

Kessler et al. (2006) estimated the basin-wide input of methane from seeps and hydrates into the Black Sea on the basis of the natural radiocarbon content of methane and by a geochemical box model. Their methane flux values fall in the range 0.2–0.4 × 10¹² mol yr⁻¹, which is about five orders of magnitude higher than our study estimate for the bubble flux at Vodyanitskii mud volcano of about 0.9 ± 0.5 × 10⁶ mol yr⁻¹. This illustrates that bubble flux from mud volcanoes contributes only a small fraction to the total amount of methane fluxes from the seafloor to the water column, considering that about 60 mud volcanoes exist in the Black Sea (Ivanov et al., 1996; Krastel et al., 2003; Woodside et al., 1997). On the other hand, there is growing evidence that gas bubble streams are significant transport pathways of methane. For example, Artemov et al. (2007) estimated the methane bubble flux from 2200 sites in a 387.1 km² large area at the Dnieper paleo-delta in water depth between 66 and 832 m. The estimation is based on extensive echosounder surveys combined with a bubble flux model and revealed a methane flux value of 750 × 10⁶ mol yr⁻¹. Given the numerous sites with evidence of bubble streams along all Black Sea shelves and slopes (Egorov et al., 2003) and recent findings of additional sites (Klaucke et al., 2006; Nikolovska et al., 2008), it is to be expected that gas flux is an important phenomenon in the Black Sea.

The estimation of the bubble flux at Vodyanitskii mud volcano reveals that the flux of gaseous methane from seeps is in the same

order-of-magnitude as the flux of dissolved methane with advecting pore waters. The values of methane fluxes at mud volcanoes and other seeps at water depth close to or within the gas hydrate stability zone are summarized in Table 1. These values have been estimated using a variety of methods, such as pore-water modelling (Wallmann et al., 2006), video analyses of in situ observations (Leifer and MacDonald, 2003; Sauter et al., 2006; Torres et al., 2002), water column methane budgets (Heeschen et al., 2005; Mau et al., 2006), or the volume of mud flows that were deposited in a defined time interval (Kopf and Behrmann, 2000). The values span four orders of magnitude (Table 1). However, the upper values of dissolved methane flux have been adjusted downward by Wallmann et al. (2006) applying more appropriate boundary conditions in their re-calculations. As shown in Table 1 the values of the methane bubble flux range between about 0.9 and $6.3 \times 10^6 \text{ mol yr}^{-1}$ and are close to the flux of dissolved methane ranging between 0.07 and $6.38 \times 10^6 \text{ mol yr}^{-1}$. This comparison illustrates that the bubble flux is a significant transport pathway of methane from the sediments into the bottom water. Further, bubble flux transports methane far higher in the water column than diffusion, e.g., diffusion time scales are slow compared to microbial

degradation (Rehder et al., 1999) while bubble times scales are in the order of 10^3 s . Thus, the fate of bubble seep gas is distinct from dissolved seep gas. In addition, it suggests that a substantial fraction of the methane by-passes the benthic seep communities. Methane-oxidizing microorganisms (as well as sulfur-oxidizing bacteria and symbiont-harboring megafauna in oxic bottom waters) act as a benthic filter at many seeps, hindering the release of dissolved methane into the water column (Niemann et al., 2006). As it is unlikely that gaseous methane can be directly taken up by microorganisms, the benthic filter is inefficient for gas bubble streams.

6. Conclusion

A variety of methods including swath and single beam echosounder, sidescan sonar, gravity coring and ROV observation and sampling were carried out at Vodyanitskii mud volcano. The mud volcano shows evidence for mud flows, advection of chloride-rich, warm pore water and emanation of gas bubbles. Estimation of methane bubble flux suggests that this is a significant pathway transporting methane into the water column and by-passing benthic oxidation processes. The fate of free gas methane in the water column has been successfully modelled in a previous study (McGinnis et al., 2006) and showed that the lifetime of the bubbles in the water column is enhanced due to a hydrate skin but ultimately the bubbles dissolve and do not reach the winter mixed sea surface layer. The model is generally confirmed by our data based on in situ observation of the bubble streams with the ROV QUEST. However, the effect of bubble-induced upwelling is largely unknown and should be studied in the future.

With the order-of-magnitude estimation of the bubble flux at Vodyanitskii mud volcano we add a value to the very short list of quantifications of methane fluxes at deep-water mud volcanoes and other seep sites (Table 1). Comparison of these fluxes suggests that the bubble flux is in the same order-of-magnitude as the flux of dissolved methane transported with advecting pore water. More data are needed to better constrain the fluxes. Especially, there is a complete lack of knowledge on how much material and fluids are transported during violent phases of mud eruption.

Acknowledgements

We are grateful to the master and crew of R/V METEOR as well as the scientific-technical team operating the ROV QUEST for their professional assistance at sea. We would like to thank Tom Feseker for assistance with the temperature probe, Hans-Jürgen Hohnberg for constructing the gas bubble sampler, and Friederike Schmidt-Schierhorn for the analyses of the temperature data. We also acknowledge the constructive comments of the reviewers Jean-Luc Charlou and Ira Leifer as well as the special issue guest editor Adriano Mazzini, which improved the manuscript significantly. This is publication no. GEOTECH – 859 of the R&D programme GEOTECHNOLOGIEN funded by the German Ministry of Education and Research (BMBF) and the German Research Foundation (DFG), Grant (03G0604A). This study is also a contribution to the scientific program of the DFG-Research Center/Excellence Cluster “The Ocean in the Earth System”.

References

- Akhmanov, G.G., 1996. Lithology of mud breccia clasts from the Mediterranean Ridge. *Marine Geology* 132, 151–164.
- Aloisi, G., Drews, M., Wallmann, K., Bohrmann, G., 2004. Fluid expulsion from the Dvurechenskii mud volcano (Black Sea) Part I. Fluid sources and relevance to Li, B, Sr, I and dissolved inorganic nitrogen cycles. *Earth and Planetary Science Letters* 225, 347–363.

Table 1

Compilation of methane fluxes at deep-water mud volcanoes and other seep sites reported so far. Methane emanates as bubbles (gaseous), dissolved with advecting pore water (dissolved) or with mud (mud flow).

Methane flux in 10^6 mol yr^{-1}	Type	Area	References
Mud volcanoes			
0.9 (0.4–1.3)	Gaseous	Vodyanitskii mud volcano, Black Sea	This study
1.9	Dissolved	Dvurechenskii mud volcano, Black Sea	(Wallmann et al., 2006)
6.3 (2.5–11.4)	Gaseous	Håkon Mosby mud volcano, Norwegian Sea	(Sauter et al., 2006)
0.04–0.66	Dissolved	Håkon Mosby mud volcano, Norwegian Sea	(Sauter et al., 2006)
0.6	Dissolved	Mound Culebra, offshore Costa Rica	(Mau et al., 2006)
0.4	Dissolved	Mound 12, offshore Costa Rica	(Mau et al., 2006)
0.07	Dissolved	Mound 11, offshore Costa Rica	(Mau et al., 2006)
185	Dissolved	Atalante, offshore Barbados	(Henry et al., 1996)
6.5	Dissolved	Atalante, offshore Barbados	Recalculated by (Wallmann et al., 2006)
14	Dissolved	Cyclope, offshore Barbados	(Henry et al., 1996)
0.6	Dissolved	Cyclope, offshore Barbados	Recalculated by (Wallmann et al., 2006)
6.38–27.72	Mud flow	Milano, Hellenic Arc, Mediterranean Sea	(Kopf and Behrmann, 2000)
12.05–45.09	Mud flow	Napoli, Hellenic Arc, Mediterranean Sea	(Kopf and Behrmann, 2000)
0.2–0.7	Dissolved	Milano, Hellenic Arc, Mediterranean Sea	Recalculated by (Wallmann et al., 2006)
0.5–1.3	Dissolved	Napoli, Hellenic Arc, Mediterranean Sea	Recalculated by (Wallmann et al., 2006)
Other sites			
747	Gaseous	NW Black Sea shelf (66 – 832 m depth)	(Artemov et al., 2007)
1.97	Gaseous	GC185, Gulf of Mexico (525–550 m)	(Leifer and MacDonald, 2003)
2.19	Gaseous	North Hydrate Ridge, offshore Oregon	(Torres et al., 2002)
4.66	Gaseous	North Hydrate Ridge, offshore Oregon	(Heeschen et al., 2005)
3.5	Gaseous	South Hydrate Ridge, offshore Oregon	(Heeschen et al., 2005)

- Artemov, Y., Egorov, V.N., Polikarpov, G.G., Gulin, S.B., 2007. Methane emission to the hydro- and atmosphere by gas bubble streams in the Dnieper Paleo-Delta, Black Sea. *Marine Ecological Journal* 3 (6), 3–25.
- Bahr, A., Pape, T., Bohrmann, G., Mazzini, A., Haeckel, M., Reitz, A., Ivanov, M. Authigenic carbonate precipitates from the NE Black Sea: a mineralogical, geochemical, and lipid biomarker study. *International Journal of Earth Sciences*, in press, doi:10.1007/s00531-007-0264-1. Online first: <http://springerlink.metapress.com/content/h2616m763660008/fulltext.pdf>.
- Bernard, B.B., Brooks, J.M., Sackett, W.M., 1976. Natural gas seepage in the Gulf of Mexico. *Earth and Planetary Science Letters* 31, 48–54.
- Blinova, V., Ivanov, M.K., Bohrmann, G., 2003. Hydrocarbon gases in deposits from mud volcanoes in the Sorokin Trough, north-eastern Black Sea. *Geo-Marine Letters* 23, 250–257.
- Bohrmann, G., Ivanov, M.K., Foucher, J.P., Spiess, V., Bialas, J., Greinert, J., Weinrebe, W., Abegg, F., Aloisi, G., Artemov, Y., Blinova, V., Drews, M., Heidersdorf, F., Krabbenhöft, A., Klaucke, I., Krastel, S., Leder, T., Polikarpov, I., Saburova, M., Schmale, O., Seifert, R., Volkonskaya, A., Zillmer, M., 2003. Mud volcanoes and gas hydrates in the Black Sea: new data from Dvurechenskii and Odessa mud volcanoes. *Geo-Marine Letters* 23, 239–249.
- Bohrmann, G., Pape, T., and Cruise participants, 2007. Report and preliminary results of R/V METEOR Cruise M72/3, Istanbul-Trabzon-Istanbul, 17 March – 23 April, 2007. Marine gas hydrates of the Eastern Black Sea. *Berichte aus dem Fachbereich Geowissenschaften der Universität Bremen* No. 261, Bremen, Germany.
- Bourriak, S.V., Akhmetzhanov, A.M., 1998. Origin of gas hydrate accumulations on the continental slope of the Crimean from geophysical studies. *Special Publications*. In: Henriot, J.-P., Mienert, J. (Eds.), *Gas Hydrates: Relevance to World Margin Stability and Climate Change*. Geological Society, London, pp. 215–222.
- Brown, K.M., 1990. The nature and hydrogeologic significance of mud diapirs and diatremes for accretionary systems. *Journal of Geophysical Research* 95 (B6), 8969–8982.
- Charlou, J.L., Donval, J.P., Fouquet, Y., Ondreas, H., Cochonat, P., Levaché, D., Poirier, Y., Jean-Baptiste, P., Fourré, E., Chazallon, B., Party, and the ZAIROV Leg 2 Scientific Party, 2004. Physical and chemical characterization of gas hydrates and associated methane plumes on the Congo-Angola Basin. *Chemical Geology* 205, 405–425.
- Clift, R., Grace, J.R., Weber, M.E., 1978. *Bubble, Drops, and Particles*. Academic Press, New York, 380 pp.
- Cranston, R.E., Ginsburg, G.D., Soloviev, V.A., Lorenson, T.D., 1992. Gas venting and hydrate deposits in the Okhotsk Sea. *Bulletin of the Geological Society of Denmark* 41, 80–85.
- De Beer, D., Sauter, E., Niemann, H., Kaul, N., Foucher, J.-P., Witte, U., Schlüter, M., Boetius, A., 2006. In situ fluxes and zonation of microbial activity in surface sediments of the Håkon Mosby Mud Volcano. *Limnology and Oceanography* 51 (3), 1315–1331.
- Dimitrov, L.I., 2002. Mud volcanoes – the most important pathways for degassing deeply buried sediments. *Earth-Science Reviews* 59, 49–76.
- Duan, Z., Møller, N., Weare, J.H., 1992. An equation of state for the CH₄–CO₂–H₂O system: I. Pure systems from 0 to 1000 °C and 0 to 800 bar. *Geochimica et Cosmochimica Acta* 56, 2605–2617.
- Egorov, V.N., Polikarpov, G.G., Gulin, S.B., Artemov, Y.G., Stokozov, N.A., Kostova, S.K., 2003. Modern conception about forming-casting and ecological role of methane gas seeps from bottom of the Black Sea. *Marine Ecological Journal* 2 (3), 5–26.
- Feseker, T., Foucher, J.P., Harmegnies, F., 2008. Fluid flow or mud eruptions? Sediment temperature distributions on Håkon Mosby mud volcano, SW Barents Sea slope. *Marine Geology* 247, 194–207.
- Ginsburg, G.D., Soloviev, V.A., Cranston, R.E., Lorenson, T.D., Kvenvolden, K.A., 1993. Gas hydrates from the continental slope, offshore Sakhalin Island, Okhotsk Sea. *Geo-Marine Letters* 13, 41–48.
- Ginsburg, G.D., Soloviev, V.A., 1997. Methane migration within the submarine gas-hydrate stability zone under deep-water conditions. *Marine Geology* 137, 49–57.
- Greinert, J., Artemov, Y., Egorov, V., De Batist, M., McGinnis, D., 2006. 1300-m-high rising bubbles from mud volcanoes at 2028 m in the Black Sea: hydroacoustic characteristics and temporal variability. *Earth and Planetary Science Letters* 244, 1–15.
- Haeckel, M., Suess, E., Wallmann, K., Rickert, D., 2004. Rising methane gas bubbles form massive hydrate layers at the seafloor. *Geochimica et Cosmochimica Acta* 68 (21), 4335–4345.
- Hartmann, A., Villinger, H., 2002. Inversion of marine heat flow measurements by expansion of the temperature decay function. *Geophysical Journal International* 148 (3), 628–636.
- Heeschen, K., Tréhu, A., Collier, R.W., Suess, E., Rehder, G., 2003. Distribution and height of methane bubble plumes on the Cascadia Margin characterized by acoustic imaging. *Geophysical Research Letters* 30 (12), 1643, doi:10.1029/2003GL016974.
- Heeschen, K.U., Collier, R.W., DeAngelis, M.A., Suess, E., Rehder, G., Linke, P., Klinkhammer, G.P., 2005. Methane sources, distributions, and fluxes from cold vent sites at Hydrate Ridge, Cascadia Margin. *Global Biogeochemical Cycles* 19, GB2016, doi:10.1029/2004GB002266.
- Henry, P., Pichon, X.L., Lallemand, S., Lance, S., Martin, J., Foucher, J.-P., Fiala-Médioni, A., Rostek, F., Guilhaumou, N., Pranal, V., Castrec, M., 1996. Fluid flow in and around a mud volcano field seaward of the Barbados accretionary wedge: results from Manon cruise. *Journal of Geophysical Research* 101 (B9), 20297–20323.
- Ivanov, M.K., Limonov, A.F., van Weering, T.C.E., 1996. Comparative characteristics of the Black Sea and Mediterranean Ridge mud volcanoes. *Marine Geology* 132, 253–271.
- Ivanov, M.K., Limonov, A.F., Woodside, J.M., 1998. Extensive deep fluid flux through the sea floor on the Crimean continental margin. *Special Publications*. In: Henriot, J.-P., Mienert, J. (Eds.), *Gas Hydrates: Relevance to World Margin Stability and Climate Change*. Geological Society, London, pp. 195–213.
- Judd, A., Hovland, M., 2007. *Seabed Fluid Flow*. Cambridge University Press, Cambridge, 475 pp.
- Kessler, J.D., Reeburgh, W.S., Southon, J., Seifert, R., Michaelis, W., Tyler, S.C., 2006. Basin-wide estimates of the input of methane from seeps and clathrates to the Black Sea. *Earth and Planetary Science Letters* 243, 366–375.
- Klaucke, I., Sahling, H., Weinrebe, W., Blinova, V., Bürk, D., Lursmanashvili, N., Bohrmann, G., 2006. Acoustic investigations of cold seeps offshore Georgia, eastern Black Sea. *Marine Geology* 231 (1–4), 51–67.
- Kopf, A., Behrmann, J.H., 2000. Extrusion dynamics of mud volcanoes on the Mediterranean Ridge accretionary complex. *Special Publication of the In: Vendeville, G., Mart, Y., Vignerresse, J.-L. (Eds.), Salt, Shale and Igneous Diapirs in and Around Europe*. Geological Society, London, pp. 169–204.
- Kopf, A.J., 2002. Significance of mud volcanism. *Review of Geophysics* 40 (2), doi:10.1029/2000RG000093.
- Krastel, S., Spiess, V., Ivanov, M.K., Weinrebe, W., Bohrmann, G., Shashkin, P., Heidersdorf, F., 2003. Acoustic investigations of mud volcanoes in the Sorokin Trough, Black Sea. *Geo-Marine Letters* 23, 230–238.
- Leifer, I., Judd, A.G., 2002. Oceanic methane layers: the hydrocarbon seep bubble deposition hypothesis. *Terra Nova* 14, 417–424.
- Leifer, I., Patro, R.K., 2002. The bubble mechanism for methane transport from the shallow sea bed to the surface: a review and sensitivity study. *Continental Shelf Research* 22, 2409–2428.
- Leifer, I., MacDonald, I.R., 2003. Dynamics of gas flux from shallow gas hydrate deposits: interaction between oily hydrate bubbles and the oceanic environment. *Earth and Planetary Science Letters* 210, 411–424.
- Leifer, I., Luyendyk, B.P., Boles, J., Clark, J.F., 2006. Natural marine seepage blowout: Contribution to atmospheric methane. *Global Biogeochemical Cycles* 20, GB3008, doi:10.1029/2005GB002668.
- Lewis, K.B., Marshall, B.A., 1996. Seep faunas and other indicators of methane-rich dewatering on New Zealand convergent margins. *New Zealand Journal of Geology and Geophysics* 39, 181–200.
- Limonov, A.F., van Weering, T.C.E., Kenyon, N.H., Ivanov, M.K., Meisner, L.B., 1997. Seabed morphology and gas venting in the Black Sea mudvolcano area: Observations with the MAK-1 deep-tow sidescan sonar and bottom profiler. *Marine Geology* 137 (1/2), 121–136.
- Liu, X., Flemings, P.B., 2006. Passing gas through the gas hydrate stability zone at southern Hydrate Ridge, offshore Oregon. *Earth and Planetary Science Letters* 241, 211–226.
- MacDonald, I.R., Sassen, I.L.R., Stine, P., Mitchell, R., Guinasso, N.J., 2002. Transfer of hydrocarbons from natural seeps to the water column and atmosphere. *Geofluids* 2, 95–107.
- Masoudi, R., Tohidi, B., 2005. Estimating the hydrate stability zone in the presence of salts and/or organic inhibitors using water partial pressure. *Journal of Petroleum Science and Engineering* 46 (1–2), 23–36.
- Mau, S., Sahling, H., Rehder, G., Suess, E., Linke, P., Soeding, E., 2006. Estimates of methane output from mud extrusions at the erosive convergent margin off Costa Rica. *Marine Geology* 225, 129–144.
- Mazzini, A., Ivanov, M.K., Parnell, J., Stadnitskaia, A., Cronin, B.T., Poludetkina, E., Mazurenko, L., van Weering, T.C.E., 2004. Methane-related authigenic carbonates from the Black Sea: geochemical characterisation and relation to seeping fluids. *Marine Geology* 212, 153–181.
- Mazzini, A., Ivanov, M.K., Nermoen, A., Bahr, A., Bohrmann, G., Svensen, H., Planke, S., 2008. Complex plumbing systems in the near subsurface: geometries of authigenic carbonates from Dolgovskoy Mound (Black Sea) constrained by analogue experiments. *Marine and Petroleum Geology* 25 (6), 457–472.
- McGinnis, D.F., Greinert, J., Artemov, Y., Beaubien, S.E., Wüest, A., 2006. Fate of rising methane bubbles in stratified waters: How much methane reaches the atmosphere? *Journal of Geophysical Research* 111 (C09007), doi:10.1029/2005JC003183.
- Merewether, R., Olsson, M.S., Lonsdale, P., 1985. Acoustically detected hydrocarbon plumes rising from 2-km depths in Guaymas Basin, Gulf of California. *Journal of Geophysical Research* 90 (B4), 3075–3085.
- Milakov, A.V., 2005. Molecular and stable isotope compositions of natural gas hydrates: A revised global dataset and basic interpretations in the context of geological settings. *Organic Geochemistry* 36, 681–702.
- Naudts, L., Greinert, J., Artemov, Y., Staelens, P., Poort, J., Van Rensbergen, P., De Batist, M., 2006. Geological and morphological setting of 2778 methane seeps in the Dnepr paleo-delta, northwestern Black Sea. *Marine Geology* 227, 177–199.
- Niemann, H., Lösekann, T., De Beer, D., Elvert, M., Nadalig, T., Knittel, K., Amann, R., Sauter, E.J., Schlüter, M., Klages, M., Foucher, J.P., Boetius, A., 2006. Novel microbial communities of the Håkon Mosby mud volcano and their role as a methane sink. *Nature* 443, 854–858.
- Nikishin, A.M., Korotaev, M.V., Ershov, A.V., Brunet, M.-F., 2003. The Black Sea basin: tectonic history and Neogene-Quaternary rapid subsidence modelling. *Sedimentary Geology* 156 (1–4), 149–168.
- Nikolovska, A., Sahling, H., Bohrmann, G., 2008. Novel hydro-acoustic methodology for detection, localization and quantification of gas bubbles rising from the seafloor at cold seeps. *Geochemistry Geophysics Geosystems* 9, Q10010, doi:10.1029/2008GC002118.

- Obzhairov, A., Shakirov, R., Salyuk, A., Suess, E., Biebow, M., Salomatin, A., 2004. Relations between methane venting, geological structure and seismo-tectonics in the Okhotsk Sea. *Geo-Marine Letters* 24, 135–139.
- Okay, A.I., Celal Sengor, A.M., Görür, N., 1994. Kinematic history of the opening of the Black Sea and its effect on the surrounding regions. *Geology* 22, 267–270.
- Orphan, V.J., Goffredi, S.K., Delong, E.F., Boles, J.R., 2003. Geochemical influence on diversity and microbial processes in high temperature oil reservoirs. *Geomicrobiology Journal* 20, 295–311.
- Paull, C.K., Ussler, W.I., Borowski, W.S., Spiess, F.N., 1995. Methane-rich plumes on the Carolina continental rise: associations with gas hydrates. *Geology* 23 (1), 89–92.
- Peckmann, J., Reimer, A., Luth, U., Luth, C., Hansen, B.T., Heinicke, C., Hoefs, J., Reitner, J., 2001. Methane-derived carbonates and authigenic pyrite from the northwestern Black Sea. *Marine Geology* 177, 129–150.
- Rehder, G., Keir, R.S., Suess, E., Rhein, M., 1999. Methane in the northern Atlantic controlled by microbial oxidation and atmospheric history. *Geophysical Research Letters* 26 (5), 587–590.
- Rehder, G., Brewer, P.W., Peltzer, E.T., Friederich, G., 2002. Enhanced lifetime of methane bubble streams within the deep ocean. *Geophysical Research Letters* 29 (15), doi:10.1029/2001GL013966.
- Reitner, J., Peckmann, J., Reimer, A., Schumann, G., Thiel, V., 2005. Methane-derived carbonate build-ups and associated microbial communities at cold seeps on the lower Crimean shelf (Black Sea). *Facies* 51, 66–79.
- Ross, D.A., Degens, E.T., 1974. Recent sediments of Black Sea. In: Degens, E.T., Ross, D.A. (Eds.), *The Black Sea – Geology, Chemistry, and Biology*. American Association of Petroleum Geologists, pp. 183–199.
- Sahling, H., Bohrmann, G., Spiess, V., Bialas, J., Breitzke, M., Ivanov, M., Kasten, S., Krastel, S., Schneider, R., 2008a. Pockmarks in the Northern Congo Fan area, SW Africa: complex seafloor features shaped by fluid flow. *Marine Geology* 249 (3–4), 206–225.
- Sahling, H., Masson, D.G., Ranero, C.R., Hühnerbach, V., Weinrebe, W., Klauke, I., Bürk, D., Brückmann, W., Suess, E., 2008b. Fluid seepage at the continental margin offshore Costa Rica and southern Nicaragua. *Geochemistry Geophysics Geosystems*, Q05S05, doi:10.1029/2008GC001978.
- Sauter, E.J., Muyakshin, S.I., Charlou, J.-L., Schlüter, M., Boetius, A., Jerosch, K., Damm, E., Foucher, J.-P., Klages, M., 2006. Methane discharge from a deep-sea submarine mud volcano into the upper water column by gas hydrate-coated methane bubbles. *Earth and Planetary Science Letters* 243, 354–365.
- Schmidt, M., Hensen, C., Mörz, T., Müller, C., Grevemeyer, I., Wallmann, K., Mau, S., Kaul, N., 2005. Methane hydrate accumulation in “Mound 11” mud volcano, Costa Rica forearc. *Marine Geology* 216, 83–100.
- Torres, M.E., McManus, J., Hammond, D., de Angelis, M.A., Heeschen, K.U., Colbert, S.L., Tryon, M.D., Brown, K.M., Suess, E., 2002. Fluid and chemical fluxes in and out of sediments hosting methane hydrate deposits on Hydrate Ridge, OR, I: Hydrological provinces. *Earth and Planetary Science Letters* 201, 525–540.
- Torres, M.E., Wallmann, K., Tréhu, A.M., Bohrmann, G., Borowski, W.S., Tomaru, H., 2004. Gas hydrate growth, methane transport, and chloride enrichment at the southern summit of Hydrate Ridge, Cascadia margin off Oregon. *Earth and Planetary Science Letters* 226, 225–241.
- Villinger, H., Davis, E., 1987. A new reduction algorithm for marine heat flow measurements. *Journal of Geophysical Research* 92, 12846–12856.
- Wagner-Friedrichs, M., 2007. Seafloor Seepage in the Black Sea: Mud Volcanoes, Seeps and Diapiric Structures Imaged by Acoustic Methods. Ph.D. Thesis, University of Bremen, Bremen, 154 pp.
- Wagner-Friedrichs, M., Krastel, S., Spiess, V., Ivanov, M., Bohrmann, G., Meisner, L., 2008. 3D seismic investigations of the Sevastopol mud volcano in correlation to gas/fluid migration pathways and indications for gas hydrate occurrences in the Sorokin Trough (Black Sea). *Geochemistry Geophysics Geosystems* 9, Q05012, doi:10.1029/2007GC001685.
- Wallmann, K., Drews, M., Aloisi, G., Bohrmann, G., 2006. Methane discharge into the Black Sea and the global ocean via fluid flow through submarine mud volcanoes. *Earth and Planetary Science Letters* 248, 545–560.
- Whiticar, M.J., Faber, E., Schoell, M., 1986. Biogenic methane formation in marine and freshwater environments: CO₂ reduction vs. acetate fermentation – isotope evidence. *Geochimica et Cosmochimica Acta* 50, 693–709.
- Wood, W.T., Gettrust, J.F., Chapman, N.R., Spence, G.D., Hyndman, R.D., 2002. Decreased stability of methane hydrates in marine sediments owing to phase-boundary roughness. *Nature* 420, 656–660.
- Woodside, J.M., Ivanov, M.K., Limonov, A.F., 1997. Neotectonics and Fluid Flow Through Seafloor Sediments in the Eastern Mediterranean and Black Seas. Part I and II, vol. 48. UNESCO IOC Tech Ser, Paris.

Appendix III: Pape et al., submitted in revised form (Abstract)

MOLECULAR AND ISOTOPIC PARTITIONING OF LOW-MOLECULAR WEIGHT HYDROCARBONS DURING MIGRATION AND GAS HYDRATE PRECIPITATION IN DEPOSITS OF A HIGH-FLUX SEEPAGE SITE

Submitted in revised form to *Chemical Geology*

Thomas Pape^{1*}, André Bahr^{1,2}, Janet Rethemeyer³, John D. Kessler⁴, Heiko Sahling¹,
Kai-Uwe Hinrichs¹, Stephan A. Klapp¹, William S. Reeburgh⁵, Gerhard Bohrmann¹

A B S T R A C T Detailed knowledge on the extent of post-genetic modifications affecting shallow submarine hydrocarbons fueled from the deep subsurface is fundamental for evaluations of source and reservoir properties. We investigated gases from a submarine high-flux seepage site in the anoxic basin of the Eastern Black Sea in order to elucidate molecular and isotopic alterations of low-molecular-weight hydrocarbons (LMWHC) associated with upward migration through the sediment and precipitation of shallow-buried gas hydrates. For this, pressurized near-surface sediment cores and free gas venting from the seafloor were collected using autoclave technology at the Batumi seep area in about 845 m water depth within the gas hydrate stability zone (GHSZ).

Emanated gas bubbles and gas from core degassing and hydrate dissociation were strongly dominated by methane (> 99.85 mol-% of $\sum[C1 - C4, CO_2]$). Molecular ratios of LMWHC ($C1/[C2 + C3] > 1000$) and stable isotopic compositions of methane ($\delta^{13}C = -53.5\text{‰}$ V-PDB; D/H around -175‰ SMOW) indicated predominant microbial LMWHC formation and less important contribution from thermocatalytic processes. $C1/C2+$ ratios and stable isotopic compositions of LMWHC distinguished three gas types prevailing in the seepage area. Vent gas discharged into bottom waters was depleted in methane by >0.03 mol-% ($\sum[C1 - C4, CO_2]$) relative to the other gas types and the virtual lack of $^{14}C\text{-CH}_4$ indicated a negligible input of methane from degradation of fresh organic matter. Of all gas types analyzed, vent gas is least affected by molecular fractionation, thus, its origin from the deep subsurface rather than from decomposing hydrates in near-surface sediments is likely.

As a result of the anaerobic oxidation of methane (AOM), LMWHC in pressurized cores confined to top sediments included smaller methane portions [0.03 mol-% $\sum(C1 - C4, CO_2)$] than gas released from pressure cores additionally containing deeper sediments. LMWHC derived from such long cores and from decomposing hydrates contained highest proportions of methane due to preferential incorporation in hydrate lattices. In contrast, indications for stable carbon isotopic fractionations of methane during hydrate crystallization from vent gas were not found.

The molecular variations along with lithologic characteristics demonstrate hydrate accumulation in sediments below 90 cmbsf, which are most likely formed from ascending vent gas. Enrichments of $^{14}C\text{-CH}_4$ (1.4 pMC) in short cores compared to much lower abundances (max. 0.6 pMC) in gas from long cores and gas hydrates substantiates for the first time recent methanogenesis utilizing modern organic matter deposited in top sediments of a high-flux hydrocarbon seep area.

Keywords: Black Sea, gas hydrates, methane, fractionation, isotopes, methane radiocarbon

¹ MARUM – Center for Marine Environmental Sciences and Department of Geosciences, University of Bremen, Klagenfurter Strasse, D 28334 Bremen, Germany

² IFM-GEOMAR Leibniz-Institute of Marine Sciences, Wischhofstrasse 1-3, D-24148 Kiel, Germany

³ Alfred Wegener Institute for Polar and Marine Research, Am Handelshafen 12, D-27570 Bremerhaven, Germany

⁴ Department of Oceanography, Texas A&M University, College Station, Texas 77843-3146, USA

⁵ Department of Earth System Science, University of California Irvine, Irvine CA 92697-3100, USA

* Corresponding author: Tel.: +49-421-218-65053; fax: +49-421-218-8664
E-mail address: tpape@marum.de

Appendix IV: Bohrmann et al., 2007

Appearance and preservation of natural gas hydrate from Hydrate Ridge sampled during ODP Leg 204 drilling

Gerhard Bohrmann^{a,*}, Werner F. Kuhs^b, Stephan A. Klapp^{a,b}, Kirsten S. Techmer^b, Helmut Klein^b, M. Mangir Murshed^b, Fritz Abegg^a

^a *Fachbereich Geowissenschaften, Universität Bremen, Postfach 330440, 28334 Bremen, Germany*

^b *GZG, Abt. Kristallographie, Universität Göttingen, Goldschmidtstr. 1, 37077 Göttingen, Germany*

Received 27 May 2006; received in revised form 12 March 2007; accepted 12 May 2007

Abstract

The state of preservation of natural gas hydrate samples, recovered from 6 sites drilled during ODP Leg 204 at southern summit of Hydrate Ridge, Oregon Margin, has been investigated by X-ray diffraction (XRD) and cryo-scanning-electron-microscopy (cryo-SEM) techniques. A detailed characterization of the state of decomposition of gas hydrates is necessary since no pressurized autoclave tools were used for sampling and partial dissociation must have occurred during recovery prior to the quench and storage in liquid nitrogen. Samples from 16 distinct horizons have been investigated by synchrotron X-ray diffraction measurements at HASYLAB/ Hamburg. A full profile fitting analysis (“Rietveld method”) of synchrotron XRD data provides quantitative phase determinations of the major sample constituents such as gas hydrate structure I (sI), hexagonal ice (Ih) and quartz. The ice content (Ih) in each sample is related to frozen water composed of both original existing pore water and the water from decomposed hydrates. Hydrate contents as measured by diffraction vary between 0 and 68 wt.% in the samples we measured. Samples with low hydrate content usually show micro-structural features in cryo-SEM ascribed to extensive decomposition. Comparing the appearance of hydrates at different scales, the grade of preservation seems to be primarily correlated with the contiguous volume of the original existing hydrate; the dissociation front appears to be indicated by micrometer-sized pores in a dense ice matrix.

© 2007 Elsevier B.V. All rights reserved.

Keywords: gas hydrate; X-ray diffraction; Ocean Drilling Program; FE-SEM

1. Introduction

Natural gas hydrate occurs worldwide in oceanic sediments and polar areas, where temperature and pressure conditions of the gas hydrate stability field are reached and sufficient gas is available (Matsumoto et al., 2000; Kvenvolden and Lorenson, 2001; Bohrmann and Torres,

2006). Based on global estimates, although still uncertain, gas hydrates in ocean and permafrost areas are considered as significant reservoirs for natural gases (in particular methane) along with societal and economic points of view. Natural gas hydrates might therefore become a major hydrocarbon source which may help to meet the increasing demand due to global consumption of hydrocarbons (Max et al., 2006). Natural gas hydrates have also captured the attention of geologists as slope stability around continents seems to be influenced by the presence of hydrates in the pore space of margin deposits (Paull et al., 2003).

* Corresponding author. Tel.: +49 421 218 8639; fax: +49 421 218 8664.

E-mail address: gbohrmann@uni-bremen.de (G. Bohrmann).

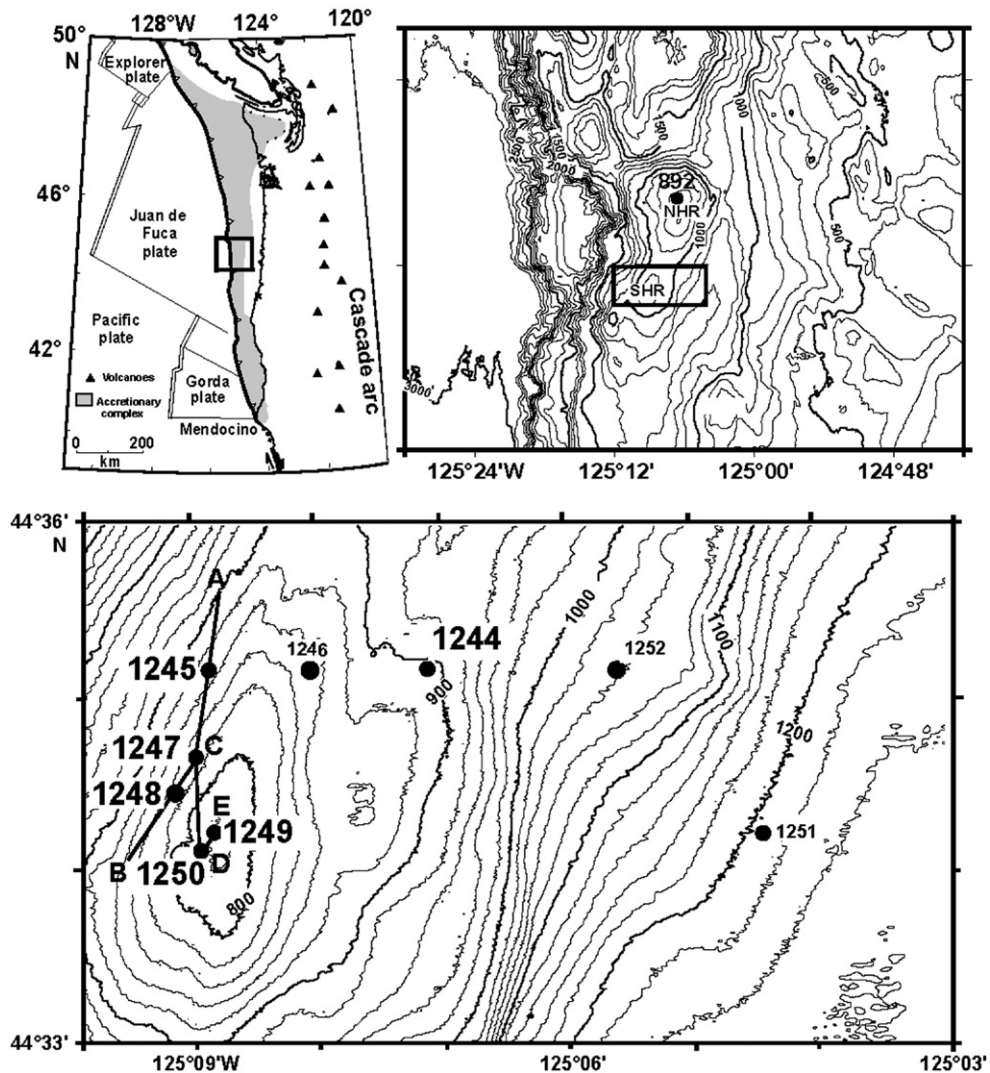


Fig. 1. Tectonic setting of the Cascadia subduction zone at the western margin of the Northamerican Plate (above left); location of the map (right) is indicated by the box. Bathymetric map of Hydrate Ridge and vicinity (above right) showing the area of a 3-D seismic survey at southern Hydrate Ridge (black box). Detailed bathymetric map (lower map) of the area of southern summit Hydrate Ridge indicating locations of ODP Leg 204 drill sites. Tracks of seismic profiles are shown and traced by letters A–E (from Tréhu et al., 2003).

Furthermore, the release of methane hydrates from large reservoirs could impact the atmospheric composition and thereby the global climate (Kennett et al., 2002).

Gas hydrates are ice-like crystalline compounds in which gases (carbon dioxide, methane, ethane etc.) are trapped within cages formed by water molecules (Sloan, 1998). From the pioneering X-ray crystallography work of von Stackelberg and Müller (1954), cubic hydrate structures I and II (sI and sII) were determined which both occur in natural marine deposits. A hexagonal clathrate hydrate designated as structure H was introduced by Ripmeester et al. (1987). Besides Nuclear Magnetic

Resonance (NMR) and Raman spectroscopy, X-ray diffraction can be used to identify the structure and determine the lattice parameters of hydrates. X-ray diffraction is the only method which can deliver absolute occupancies of the cages with gas molecules (Klapproth et al., 2003). In addition, XRD may be used to establish the relative amounts of ice, hydrate and other minerals in the gas hydrate samples to elucidate the degree of preservation.

This manuscript describes the use of synchrotron X-ray diffraction for the quantitative phase analysis of natural gas hydrate samples, from ODP drill sites at Hydrate Ridge, Oregon margin.

Quantitative phase analysis of gas hydrate samples is important, because without the use of proper autoclave tools, dissociation starts when gas hydrates are outside their p – T stability field resulting in the formation of ice or water. On the other hand, any seawater attached to the gas hydrate sample immediately converts into ice when liquid nitrogen is used for sample preservation. Ice from frozen seawater or as the end-product of dissociation and preserved hydrate cannot be easily distinguished through visual inspection and other methods must be used to differentiate between ice and hydrate. High-energy synchrotron X-ray diffraction offers both qualitative and quantitative analyses of all mineral phases present in a natural bulk sample. Due to its high spatial resolution and high penetration power it is far superior to conventional X-ray sources. Instead of a 1-dimensional detection as in most conventional X-ray diffractometers complete 2-D projections of the Debye–Scherrer cones are recorded in our synchrotron work. This is of crucial importance when larger crystallites occur in the sample (e.g. large ice crystallites as in our case), which frequently bias the conventionally recorded diffraction patterns leading to grossly erroneous phase fractions.

As an additional tool, cryo-scanning-electron-microscopy (cryo-SEM) explores the micro-structural and micro-chemical composition of the samples. The Energy Dispersive X-ray (EDX) detector, coupled with the cryo-SEM, detects constituents by their elemental composition with a spatial resolution of a few micro-

meters. By revealing details of the microstructure, cryo-SEM may also provide new insights into the dissociation processes taking place in recovered natural gas hydrate samples (Kuhns et al., 2004a). In addition, cryo-SEM helps to differentiate between ice originating from frozen seawater and from hydrate decomposition.

The determination of chemical composition, fabric, and grain size characteristics of gas hydrates in natural environments is still quite difficult due to the unknown extent of partial decomposition and ice formation that occurs during the recovery procedure. Assessing what is original and what is recovery-induced is important in order to interpret other geochemical and geophysical properties measured on recovered natural gas hydrate samples.

2. Gas hydrate on Hydrate Ridge

The gas hydrates investigated here were recovered during drilling on the southern Hydrate Ridge, a 30-km-long and 15-km-broad topographic high in the accretionary complex of the Cascadia subduction zone, located approximately 80 km west of the Oregon coast (Fig. 1). Ocean Drilling Program Leg 204 sampled the gas hydrate stability zone (GHSZ) from the seafloor to its base, which was indicated by a bottom-simulating reflector (BSR) in contrasting geological settings defined by a 3D seismic survey (Tréhu et al., 2003). By integrating results from pressure core sampler (PCS) measurements, chloride anomalies in the pore water, IR temperature logging on

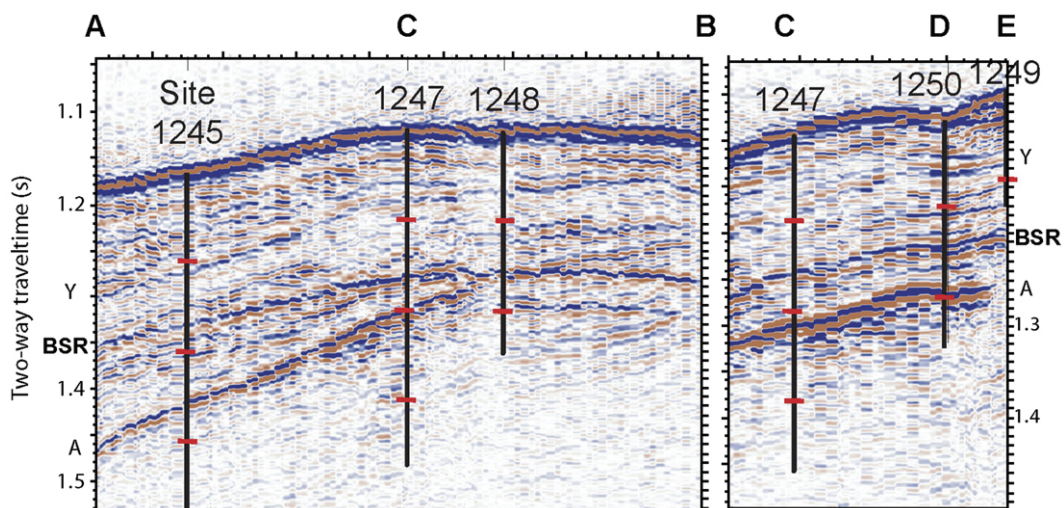


Fig. 2. North–south-trending slices from the 3-D seismic data that extend from the western flank to the summit of southern Hydrate Ridge (track lines are shown in the map of Fig. 1; from Tréhu et al., 2003). ODP drill sites are indicated. The position of the BSR marks the lower boundary of the gas hydrate stability field.

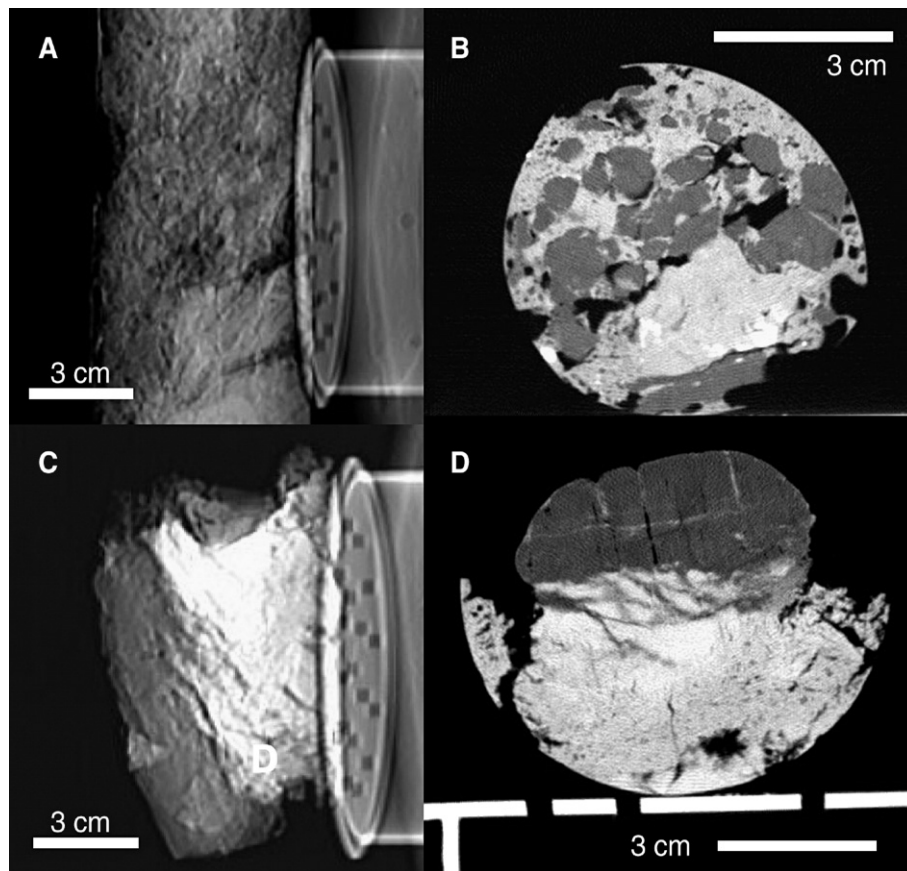


Fig. 3. CT images from both samples 1248C-8H-6, 68–67 cm (A and B) and 1247B-12H-2, 41–51 cm (C and D). CT images show dense material in white and less dense phases by darker color. Gas hydrate is represented by dark grey. Overview images of the entire core sections are shown left (A and C). CT slices are shown on the right side (B and D).

the catwalk and electrical resistivity data from logging-while-drilling, the problem of a very heterogeneous spatial distribution of gas hydrates within the GHSZ was overcome and quantitative estimates of the total amount and its spatial distribution on southern Hydrate Ridge were deduced (Tréhu et al., 2004). On average the gas hydrate content of the GHSZ between the BSR and the seafloor is generally 2% or less of the pore space, whereas some patchy zones of locally higher gas hydrate concentrations occur (Tréhu et al., 2004). High gas hydrate content of 30–40% of the pore space is restricted to the upper 30–40 m below the seafloor (mbsf) near the summit of southern Hydrate Ridge, where vigorous gas seepage occurs and gas hydrate is outcropping on the seafloor (Bohrmann et al., 1998; Suess et al., 1999, 2001). Based on a model that integrates gas hydrate growth, gaseous methane transport from below and chloride enrichment, Torres et al. (2004) calculated that a methane amount of 10^4 moles per day has to be supplied to the base

of the GHSZ. This supply of free gas is thought to occur preferentially at seismically imaged Horizon A, which is a high permeability gas-saturated sediment layer (Tréhu et al., 2004) that gets shallower towards the summit (Fig. 2).

A variety of gas hydrate textures were observed and sampled during the leg, providing new insight into the spatial distribution of gas hydrates on southern Hydrate Ridge. Based on their macroscopic geometry, samples were described as layers, massive (layers <10 cm in thickness) lenses, veins or veinlets, nodular features and disseminated hydrate grains that are distributed throughout the sediment matrix (Tréhu et al., 2003). A large collection of samples was investigated by X-ray computed tomography (CT) analyses of frozen whole-round samples, which showed that all hydrates had been present in layers with a variety of dip directions and angles within the sediment. Shallow hydrate layers parallel or sub-parallel to bedding are formed by gas injections parallel to stratification. Below 40 mbsf, hydrate layers are characterized by steeper dip angles of

Table 1

List of samples from ODP Leg 204 sites investigated in this study

ODP samples	Depth (mbsf)	No of measurements	Hydrate (%)	Ice (%)	Quartz (%)
1244C-8H-1, 47–52 cm	62.97	4	2.59±0.27	97.33±0.33	0.08±0.11
1244C-8H-1, 47–52 cm	62.97	3	1.33±0.09	98.43±0.05	0.24±0.11
1245B-6H-5, 60–78 cm	54.10	4	2.40±1.43	93.62±1.07	3.98±1.13
1247B-12H-2, 41–51 cm	93.01	4	43.88±3.71	54.53±3.82	1.60±0.29
1248C-1-CC, 0–14 cm	2.24	4	3.01±0.72	91.54±1.70	5.46±1.10
1248C-3X-3, 0–3 cm	21.83	4	1.34±0.58	96.88±0.61	1.80±0.49
1248C-8H-6, 68–87 cm	74.46	3	66.03±6.38	31.95±6.00	2.01±0.43
1248C-10H-1, 100–119 cm	87.00	2	6.64±1.33	92.89±1.19	0.47±0.14
1248C-10H-1, 100–119 cm	87.00	3	2.93±0.49	96.55±0.64	0.52±0.17
1248C 11H-5, 38–75 cm*	100.89	2	33.30±21.78	66.70±21.78	
1249C 1H-1, 0–25 cm*	0.12	2	0.00	100.00	
1249C-1H-CC, 0–10 cm	1.50	4	19.38±1.34	80.16±1.15	0.47±0.27
1249C-3H-1, 106–131 cm	5.89	3	7.48±1.73	84.58±2.31	7.94±0.57
1249F-5H-1, 64–70 cm	16.14	1	18.09	81.71	0.20
1250D-1H-3, 30–63 cm	1.66	4	2.89±1.00	96.71±1.71	0.61±0.49
1250D-1H-3, 30–63 cm*	1.66	3	1.35±0.09	97.90±0.03	0.75±0.10
1250D 1H-3, 30–63 cm	1.66	2	3.60±0.14	96.40±0.14	0.00
1250D-11H-3, 53–84 cm	78.01	4	34.45±3.87	64.60±3.58	0.97±0.36
1250D-11H-3, 53–84 cm	78.01	4	36.88±1.62	62.76±1.69	0.37±0.12
1250C 2H-CC, 0–1 cm*	5.06	2	27.50±38.89	72.50±38.89	
1250C-11H-3, 94–95 cm	86.35	4	7.09±1.01	92.78±1.08	0.14±0.06

Compositions (in weight %) of the samples are based on the synchrotron XRD data Rietveld analyses. Deviations given for the composition represent the spread from the average for different measured positions of the sample. Four samples marked by an asterisk correspond to uncrushed samples with very low quartz content, which, consequently, was not included in the Rietveld analysis.

30–90° and are interpreted as hydrate precipitates in open fractures or joints (Abegg et al., 2007).

3. Methods

During Leg 204 numerous gas hydrate samples were recovered as whole-rounds instantly after they were detected by IR imaging in the cores on the catwalk

(Tréhu et al., 2004) and preserved in liquid nitrogen for detailed shore-based studies. More than 60 whole-round samples were collected from 8 of 9 drill sites. Whole-round sections with variable sizes, around 5–20 cm in length, were first investigated by CT analyses (Fig. 3) which imaged the fabric and the appearance of the gas hydrate within the host sediment (Abegg et al., 2006). Based on the CT-image information we selected 16

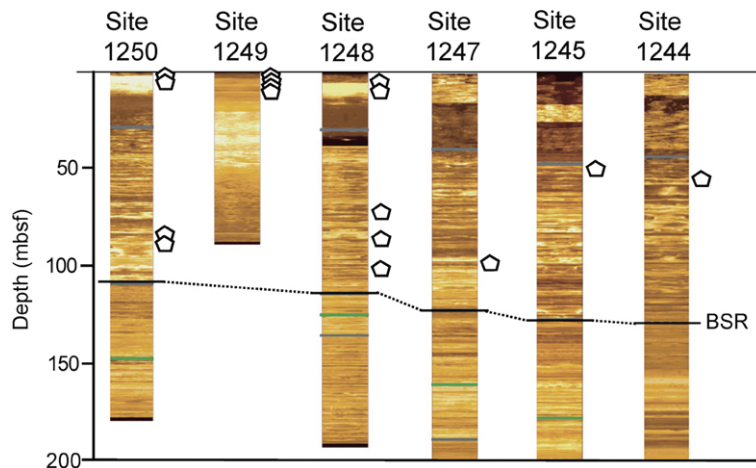


Fig. 4. ODP Leg 204 drill sites represented by logging-while-drilling electrical resistivity records from the uppermost 200 m below seafloor (light shades represent higher resistivity). Gas hydrate samples presented in this paper are shown by pentagon symbols.

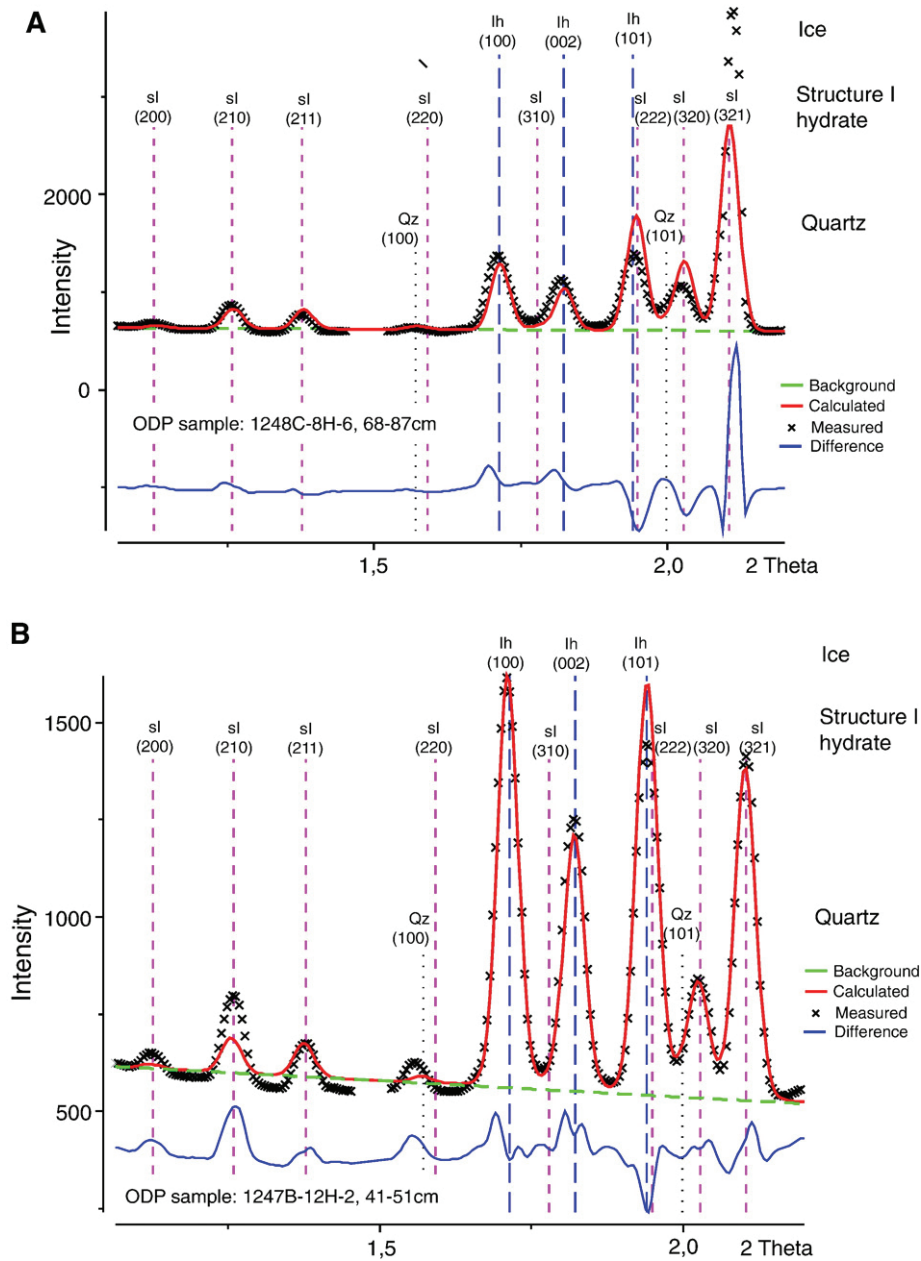


Fig. 5. XRD records from high-energy synchrotron radiation measured at HASYLAB/Hamburg and calculated models based on Rietveld analyses. Major peaks of hydrate, ice and quartz are shown from samples documenting distinct differences in gas hydrate amounts. From sample 1248C-8H-6, 68–67 cm (panel A) 68% structure I hydrate was calculated whereas sample 1247B-12H-2, 41–51 cm yields 45% gas hydrate (panel B).

samples from different horizons, all with some promise for containing gas hydrates (Table 1, Fig. 4). Working under liquid nitrogen in a cold laboratory at $-20\text{ }^{\circ}\text{C}$ (to avoid the condensation of water vapour from the atmosphere) we dissected pure hydrate/ice parts and cleaned the samples from attached sediment particles. Of these 16 cleaned sub-samples 13 were crushed to sub-millimeter size and filled into aluminium vials of

7 mm diameter and 40 mm length. Samples from four depth horizons were split into two sub-samples each (see Table 1). One set of sub-samples from each horizon was left intact and placed in aluminium vials of 7 mm diameter filling most of the vial's cross-section.

For XRD analysis we used high-energy synchrotron radiation at the beamline BW5 at DESY-HASYLAB in Hamburg. In contrast to in-house X-ray techniques,

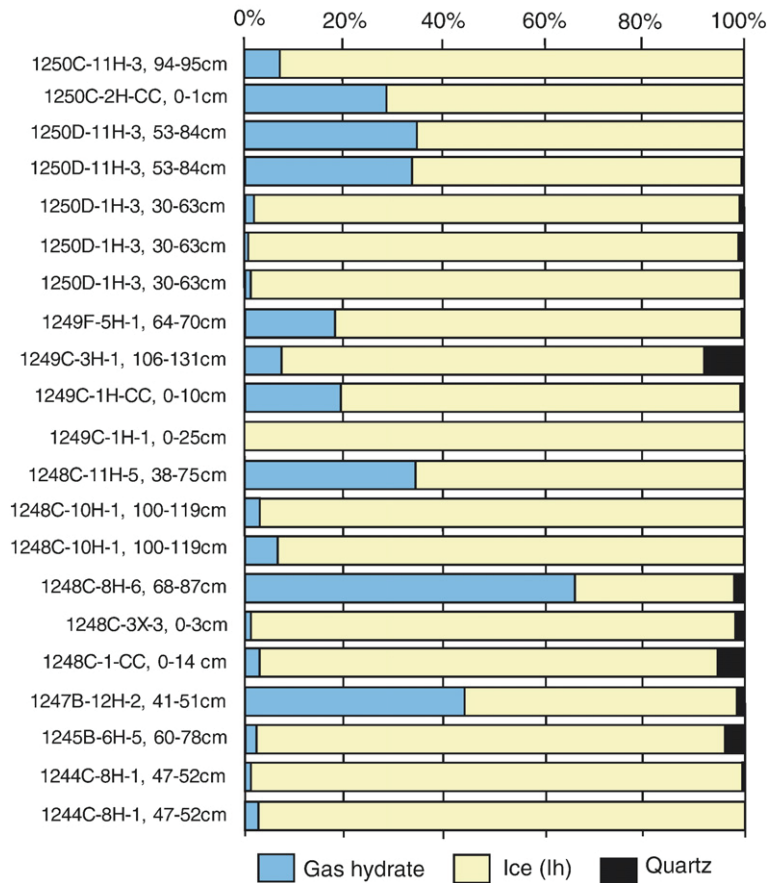


Fig. 6. Bar chart of gas hydrate, ice and quartz amounts calculated in 21 samples from 16 depth levels of frozen ODP samples which have been identified as gas hydrate samples onboard the JOIDES Resolution.

synchrotron X-ray diffraction provides better resolution, because of high radiation flux (5×10^{10} photons/s/mm² at 100 keV), high collimation, i.e. small angular divergence of the beam, and wide tunability in energy/wavelength (sub eV to hundreds of keV). A monochromatized and collimated photon beam of about 100 keV (wavelength ~ 0.124 Å) was used as an incident X-ray beam with a size of 1 mm² at the sample position. For the X-ray measurements, samples were placed in the cylindrical aluminium vials described above. The sample was held at a temperature of 70 K at ambient pressure. The small beam size allows for spatially resolved measurements to obtain information on internal sample variability. Consequently, one has to measure at several positions, or move the sample during data collection. Here, usually 2–4 areas within each sample were investigated without translating (but rotating) the sample during data collection (Table 1). The typical distance between two measured positions was 10 mm.

A two-dimensional (2-D) image plate detector (mar345) placed 120 cm away from the sample was used permitting interception of the X-ray powder diffraction cones as

complete Debye–Scherrer rings. Using the FIT2D program (Hammersley et al., 1996) these rings were integrated to yield a conventional one-dimensional (1-D) 2-theta pattern. In the 2-D images, some Debye–Scherrer rings show individual Bragg spots scattered within the ring width. These spots are distinct due to their high peak intensity compared to any other point (~ 10 times higher) within the ring width. Clearly, they represent the Bragg reflections of large crystallites of a particular phase (ice Ih or sI hydrate). The resulting 1-D powder pattern shows spikes sitting on an otherwise smooth integrated Bragg peak. Moreover, as other lattice planes of these large crystallites are not necessarily in reflection position, the Rietveld method will tend to produce a lower quality of fit. In certain cases it may hamper a reasonable refinement altogether. The problem can be addressed by masking outliers before integration. The resulting peaks in the 2-theta patterns will then not show any abrupt change in intensity. The “MASK” tool of the FIT2D program was used for this purpose, which allowed manually selected outlying points to be ignored in further treatments enabling a more meaningful profile fit.

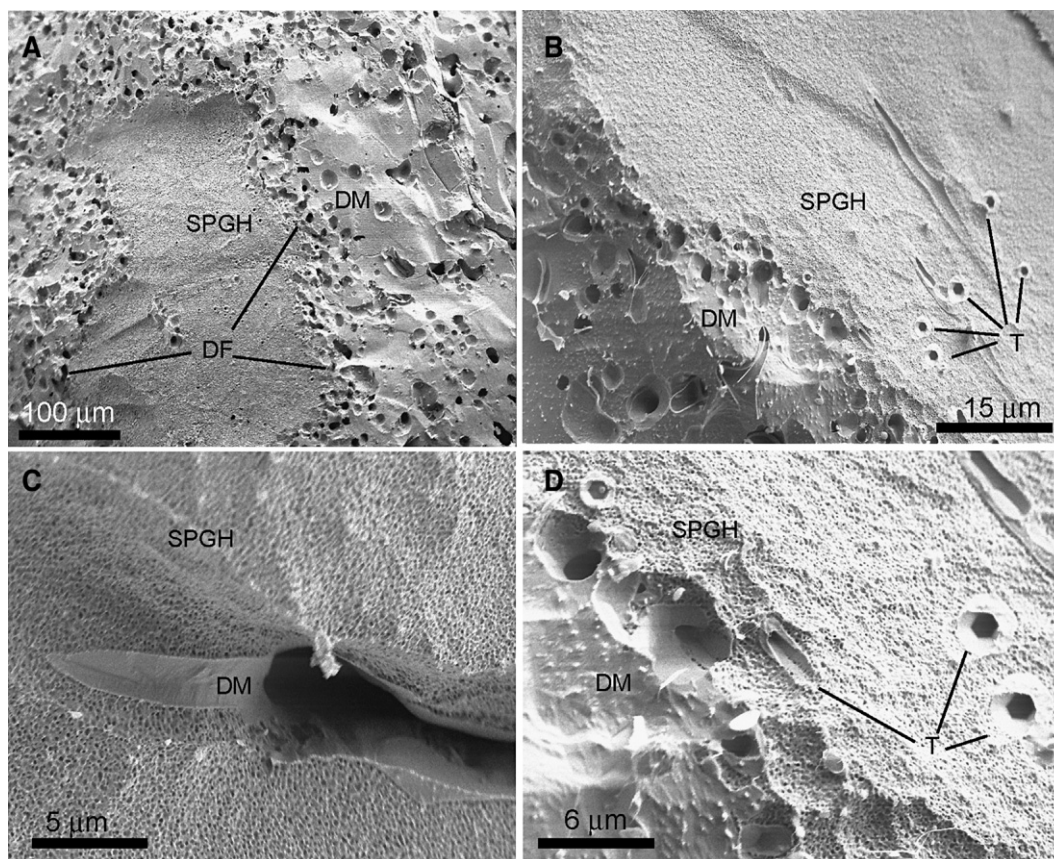


Fig. 7. FE-SEM images from ODP Leg 204 gas hydrate samples. A. Overview of an area characterized by sub-micrometer-sized porosity (SPGH) surrounded by dense material (DM) that contains pores 5–20 μm in size. Those pores are concentrated in certain areas and seem to be more frequent near the contact to sub-micrometer-porous patches (Sample 1249C-1H-CC). B. Image of the transition from a sub-micrometer-sized porosity (SPGH) area to the dense material (DM) is shown. Single tube pores (T) with hexagonal shape are typical for SPGH parts. C. Large pore in sub-micrometer-porous gas hydrate (SPGH). Note that the contact is lined by dense material (DM). D. Detail of higher magnification of image B. B–D are from sample 1247B-12H-2, 41–51 cm. Decomposition front (DF).

Phase fractions of the samples are then obtained from a full-pattern profile fitting (Rietveld refinement) using the GSAS software (Larson and Von Dreele, 2000) and are summarized in Table 1. The starting parameters for the sl hydrate (space group Pm-3n) refinements are taken from Klapproth (2002). During refinements, general parameters such as the scale factor, background parameters, the zero point and the profile parameters are optimized. The cell parameters of ice Ih and quartz are kept fixed, while the cell parameter of sl hydrate slightly varies around a value of ~ 11.88 (1) \AA .

In addition to XRD analyses, few samples were investigated by cryo-SEM. We used a Field-Emission SEM (FE-SEM; LEO Gemini 1530), which is dedicated to work at low acceleration voltages. The FE-SEM is equipped with a nitrogen-cooled sample stage in the vacuum chamber, which allows a study of samples at temperatures as low as -185 $^{\circ}\text{C}$. Samples were moved onto the liquid nitrogen cooled sample holder within a liquid nitrogen bath and then

transferred through a cryo-preparation chamber (without receiving a metal coating) into the vacuum chamber (10^{-5} mbar) of the SEM. A low acceleration voltage (<2 keV) was used during imaging to minimize sample alteration or beam damage. This allowed us to investigate the surface of the samples in detail down to several tens of nm resolution. In order to obtain qualitative elemental analyses the instrument is equipped with an energy dispersive X-ray sensor (EDX). Images were stored in digital format. Further details of the FE-SEM used for studies of gas hydrates were described in earlier publications (Kuhs et al., 2004a; Techmer et al., 2005).

4. Results

4.1. Synchrotron X-ray diffraction

X-ray diffraction analyses of all samples (Table 1) revealed that the gas hydrate phase in each sample is cubic

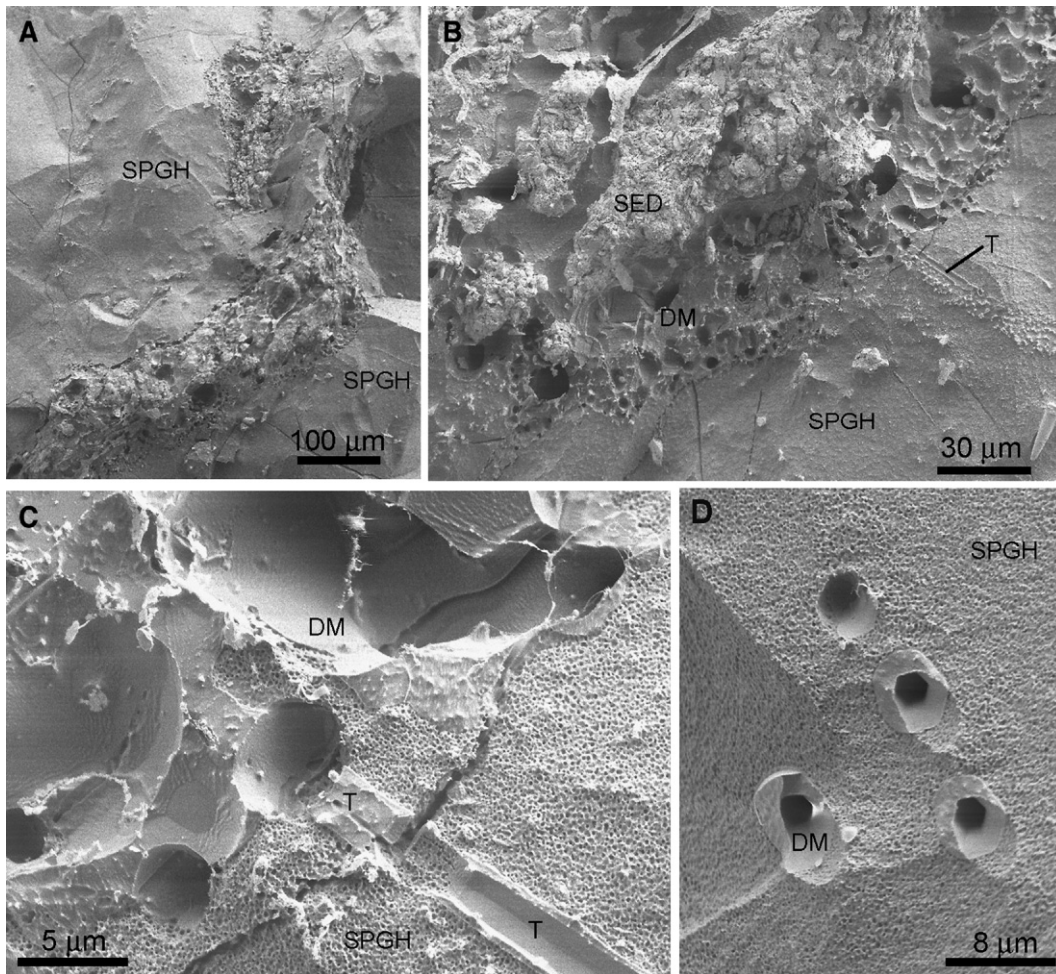


Fig. 8. FE-SEM images from ODP Leg 204 gas hydrate samples. A. Image of dominantly sub-micrometer-porous gas hydrate (SPGH) containing domains of sediment (SED). The sub-micrometer-sized porosity is not visible under low magnification. B. Transition between a sub-micrometer-porous area (SPGH) and sediment-dominated region (SED). Dense material (DM) yielding pores of a few micrometer in diameter are intercalated. C. Detail from B shows the distinct transition from sub-micrometer-porous gas hydrate (SPGH) to dense material (DM). The single tube pore (T) from the gas hydrate is ending in a pore within the dense material. D. Four single tubes of dense material with clear hexagonal shapes within the inner vug. Images A–C are from sample 1248C-8H-6, 68–67 cm; image D is taken from sample 1247B-12H-2, 41–51 cm.

sI hydrate. This is demonstrated by the presence of the three most intense sI-peaks (222), (320), (321) in the 2θ scans (Fig. 5). The hexagonal ice Ih phase in this example is by far the major fraction, which is clearly indicated by the dominant intensities of the three major ice Ih peaks (100), (002), (101) (Fig. 5). A third mineral phase is identified as quartz as documented by its (101) and (100) reflections (Fig. 5). In total, we performed 66 analyses from 16 gas hydrate samples of various depths at Sites 1244, 1245 and 1247–1250. In most cases we ran 3–4 measurements for each sub-sample. In some particular cases, i.e. from 4 samples, we measured a second set of uncrushed sub-samples in order to check the local compositional variations (Table 1).

The synchrotron XRD data Rietveld analysis provides quantitative phase fractions of the constituents present in each sample, which are listed in Table 1 and shown in Fig. 6. For the crushed samples, the amount of Ih ice varies between 32 and 98% in each sample, with 83% as a nominal average for the measured samples. It is therefore clear that ice Ih is the most abundant phase in the collected samples, despite the fact that the samples were selected for their high gas hydrate content. The sI hydrate phase fraction varies between 0 and 66% with a nominal averaged value of 15%. Eight of thirteen crushed samples contain a low amount (between 1 and 7%) of gas hydrate and only five samples showed gas hydrate contents of 20–68% along with a lower

concentration of ice Ih (30–75%). As expected based on the sample preparation procedure, quartz is only a minor constituent (the nominal average content of the samples is around 1.6%) and varies between 1.1 and 7.9% (Fig. 6). Results from the four measurements with uncrushed samples revealed an inhomogeneous distribution of gas hydrate and ice within the sample. In particular, samples with higher gas hydrate contents (about 30 wt.%) show significant local differences in the gas hydrate and ice proportions.

4.2. FE-SEM observations

Optical studies on microstructures have been carried out on a few samples with different gas hydrate concentrations (Figs. 7 and 8). From these samples the highest amount of gas hydrate (68%) was analyzed in sample 1248C-8H-6, 68–67 cm and the lowest concentration of 3.1% was found in sample 1248C-1-CC, 0–14 cm. Sample 1247B-12H-2, 41–51 cm reaches gas hydrate concentration of 43.8%, which is a medium value between the other two samples. As it was shown in other natural and synthetic gas hydrate samples, the samples studied here show a characteristic sub-micrometer-sized porosity, which can be used as a rapid visual aid in identifying gas hydrates (Kuhs et al., 2000, 2004a; Klapproth et al., 2007).

Pore sizes typically vary between 100 and 400 nm in diameter (Figs. 7C, D, and 8C, D), and are homogeneously distributed over large areas in samples of high gas hydrate concentration. The porosity is about 15% with pores that show no preferred orientation and are rarely inter-

connected as evidenced by specific surface area measurements (Kuhs et al., 2004a). In the sample of low gas hydrate concentration just two very small areas of sub-micrometer-sized porosity were found and in the sample of medium gas hydrate concentration, sub-micrometer-sized porous patches are repeatedly observed. Next to sub-micrometer-sized porous areas, dense material was observed with few larger pores of tens of micrometers in diameter. Those pores are often concentrated in certain domains and are particularly frequent in dense material that surrounds patches of sub-micrometer-sized porosity. As shown in Fig. 7A the size distribution of the pores in this area is fairly homogenous, whereas farther away the pores reveal more variable, mostly larger pore sizes. The dense material containing some micrometer-sized pores was repeatedly identified as ice by EDX. From synthetic gas hydrate samples we know that the sub-micrometer-porous material is representative for gas hydrates (Kuhs et al., 2000, 2004a). This permits us to retrace the decomposition front between gas hydrate and the (now frozen) water at the moment of quenching in liquid nitrogen and allows us to visually estimate the size of patches of un-decomposed hydrates in the SEM samples as discussed below.

Within areas of sub-micrometer-sized porosity, tubes of 2–4 μm in diameter with dense walls occur, which in all cases show a hexagonal cross-section (Figs. 7A, D and 8D). Most of the neighbouring long tubes appear to be aligned parallel to each other. Investigations of the change from areas of sub-micrometer porosity to dense areas revealed that some of the tubes end in larger pores within the dense material (Fig. 8). Contacts to sediment

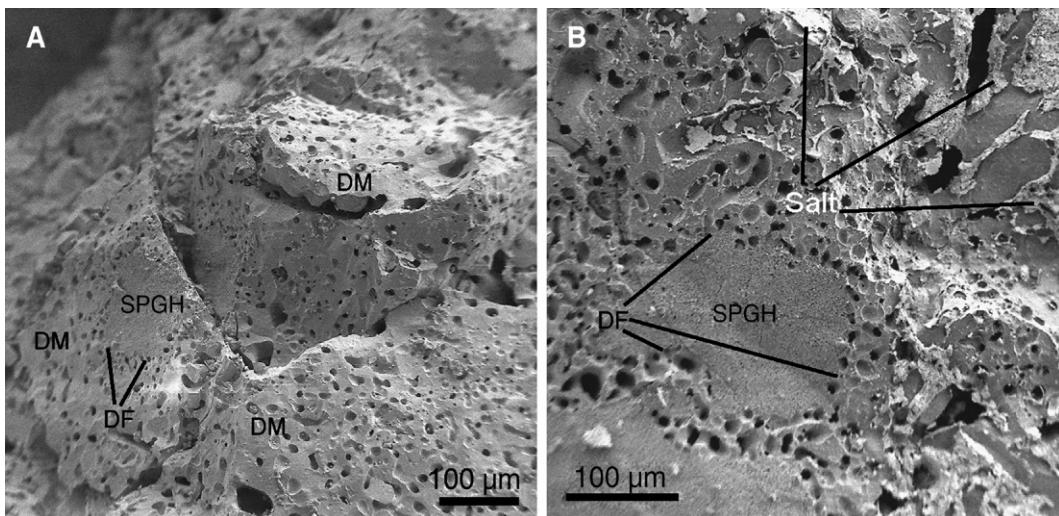


Fig. 9. FE-SEM images from ODP Leg 204 gas hydrate samples. A. Large-scale image of a small patch of sub-micrometer-porous gas hydrate (SPGH), surrounded by dense material (DM) with fewer and larger pores (tens of micrometers). The decomposition front (DF) of the gas hydrate is marked (sample 1249C-1H-CC, 0–10 cm). B. Sub-micrometer-porous gas hydrate (SPGH) with direct contact to a matrix of dense material (DM) on a decomposition front (DF). Salt crusts in the right hand side of the picture are labeled (sample 1248C-8H-6, 68–87 cm).

domains are mostly represented by dense material containing some micrometer-sized pores (Fig. 8A and B).

Figs. 7A and 9A and B show patches of sub-micrometer-sized pores which are surrounded by dense material. Fig. 9A depicts a small, single patch which is entirely encircled by a large area of dense material. The dense material is directly connected to the sub-micrometer-sized porous patch; also, no crusts of any kind are visible which might help retracing the origin of the dense material to external sources such as seawater. In Fig. 9B crusts are visible in the image which was identified as salt crusts from, presumably, seawater, by EDX-measurements. On the other hand, sub-micrometer-sized porous areas are embedded within dense material with fewer and larger pores. No sub-micrometer-sized porous patches were found with areas of salt crusts.

5. Discussion

Kim et al. (2005) observed sI hydrate in one sample collected from the Site 1249 on ODP Leg 204. Structure I hydrate was also postulated by gas analyses of distinct hydrate samples during the work onboard the JOIDES Resolution (Tréhu et al., 2003). The adopted cell parameter of 11.88(1) Å, measured at 70 K, is comparable to the earlier reports on natural gas hydrates as well as synthetic ones. For instance, Kim et al. (2005) obtained the cell parameter as 11.8615 ± 0.015 Å, measured at 123 K, while Kirchner et al. (2004) reported 11.877(3) Å for pure synthetic methane hydrate from a single crystal XRD measurement. Measurements at different locations (10 mm apart) of the same sub-sample do not show any substantial differences in cell parameter, but yield slightly different phase fractions (Table 1). Thus it appears, that all recovered gas hydrate here is of structure I, but that it occurs in different proportions relative to other phases such as ice (Table 1), indicating sample heterogeneity at a mm scale.

5.1. Distinction between gas hydrate and ice

SEM imaging within the matrix of gas hydrates shows areas of sub-micrometer-sized pores that represent the hydrate phase, which is therefore distinguishable from the ice (Kuhs et al., 2000, 2004a; Stern et al., 2004; Techmer et al., 2005; Stern et al., 2005). The gas hydrates studied here show comparable pore structures with pore diameters less than 1 µm. Such sub-micrometer-sized pores were reported from natural gas hydrate samples from the Black Sea, from the SW African Margin and from near-surface gas hydrates from Hydrate Ridge and from the Mallik drill site (Kuhs et al., 2004a; Techmer et al., 2005). The porosity is also known from laboratory-synthesized gas hydrates, specifi-

cally from those that formed from gas reacted with water/ice to form hydrates (Staykova et al., 2003; Genov et al., 2004; Kuhs et al., 2006). Straight tubiform pores with the dense walls were exclusively found within the sub-micrometer-scale porous gas hydrate domains. However, the hexagonal shape of the tubes in cross-sections indicates that the dense material of the wall represents frozen water since normal ice crystallizes in hexagonal lattice. Accordingly, using the EDX detector we were unable to detect any carbon in the material of the dense walls, which suggests that the dense material probably does not consist of gas hydrate, as was shown for samples from the Mallik drill site (Techmer et al., 2005).

Large patches of sub-micrometer-sized pores are particularly well preserved in samples with high amounts of gas hydrate. On the other hand a large proportion of ice coincides with a widespread occurrence of dense material. The appearance of gas hydrates under the SEM shows the typical feature: the sub-micrometer-sized porous material is always surrounded by dense material (Fig. 7A). This includes large pores several tens of micrometers in size, which are always surrounded by dense material (Fig. 8C). This was observed in all samples and is a good argument, that the dense material is dominantly frozen water. Local variations of the ice and gas hydrate fractions from XRD measurements of uncrushed samples agree well with SEM observations. Consequently, we can assume that by and large the dense material is mostly composed of ice. The possibility that some of the hydrates investigated here also show dense surface areas cannot be excluded, however. Dense hydrates were described in other investigations (Stern et al., 2004; Techmer et al., 2005). In the samples from the Hydrate Ridge, no dense gas hydrate as indicated by carbon signals from the EDX detector could be found. In addition, the arrangements of micrometer-sized pores (Figs. 7 and 8) and the distribution of the pores within the dense material most probably represent former gas bubbles in water that froze during the rapid quench in liquid nitrogen. Those bubbles were potentially frozen with the surrounding water. They are recognizable as cavities covered by thin ice layers.

5.2. Decomposition of gas hydrate and its detection

Decomposition of gas hydrate starts on free surfaces or interfaces of gas hydrates with sediment or along the surface of large pores that originally exist between sediment grains. Discrete rounded patches of sub-micrometer-sized porous gas hydrate are consequently decomposed around their periphery. The boundary between porous and dense material represents most probably the active decomposition surface, just immediately before the sample was frozen in

liquid nitrogen. Consequently, only large and massive pieces of gas hydrate will be preserved as gas hydrates patches whereas similar amounts of gas hydrate which occur disseminated in the sediment will decompose during retrieval within the drill string. This is indicated by small gas hydrate patches which are situated within large areas of ice originating from hydrate decomposition. Ice originating from quenched seawater can be identified by the presence of salt crusts. Micro-structurally identical salt crusts were obtained by us in laboratory experiments for rapidly quenched sea water. Such salt precipitates cannot be observed in frozen hydrate water, because hydrate is composed of pure water and contains no salt. The patchy distribution of ice and gas hydrates seen in SEM is confirmed by the varying proportions of gas hydrate and ice at different locations in uncrushed samples.

Hydrate dissociation itself is an endothermic reaction consuming a considerable amount of heat, which could lead to a simultaneous freezing of the water released by the dissociation process. In addition to gas hydrate decomposition, gas expansion and gas exsolution are further processes that can cause a temperature decrease in sediment cores during their ascent from seabed to the surface. Consequently, decreasing temperatures induced by any process could probably lead to the formation of ice in the ascending sediments. Temperature measurements taken by the Temperature, Pressure and Conductivity (TPC) tool during the ascent of cores revealed at least sharply-defined cooling anomalies with ΔT up to ~ 4 °C measured on top of the TPC tool (Ussler et al., 2006). This may indicate even lower cooling temperatures in small areas around gas hydrates inside such cores. The spot-like temperature decreases could induce local ice formation and contribute to the self-preservation effect of hydrates which is observed at temperatures below 0 °C (Yakushev and Ito, 1992; Stern et al., 2003). This effect allows gas hydrates to exist for some time outside its normal p-T conditions of stability. The thermal limits of the preservation window and the effects of pressure variations were investigated on many pure samples of structure I as well as on mixed hydrate samples (sI and sII) by Stern et al. (2003; Kuhs et al., 2004b; Circone et al., 2005). This effect was first observed in laboratory experiments on both natural and laboratory-made gas hydrate (Davidson et al., 1986), and is suggested as a basis for a commercial scheme for methane hydrate storage and transport (Gudmundson and Borrehaug, 1996).

6. Conclusion

Preservation of gas hydrates from ODP samples from conventional APC cores, without using autoclave coring

systems, seems to be unsatisfactory due to widespread and advanced dissociation of the hydrate. Typically, samples we investigated from ODP drill sites are decomposed up to 85% and are converted to hexagonal ice. Only a few samples revealed gas hydrate concentrations more than 15% going up in rare cases to 70% of the selected sample. High gas hydrate contents can only be expected when the starting material consists of massive gas hydrates which are considerably more resistant to decomposition than thin hydrate layers, veinlets or disseminated hydrate crystals. The distribution of gas hydrates in partially decomposed samples was found to vary at scales of mm to cm.

Gas hydrate samples frozen in liquid nitrogen show many features of hydrate decomposition. Results from FE-SEM studies are in agreement with XRD conclusions. Gas hydrate domains seem to be represented by sub-micrometer-sized porosity, whereas on this scale the frozen water appears dense in FE-SEM images containing, however, many pores of larger size. These pores are probably caused by methane bubbles discharged from outer surfaces of decomposing hydrates which were frozen during quenching in liquid nitrogen. Hydrate decomposition was obviously ongoing before the process was stopped in the liquid nitrogen bath. We cannot exclude that some of the ice was formed directly by the cooling effect of hydrate decomposition during the ascent of the core to the surface within the drill hole and above, before the sample was quenched in liquid nitrogen.

Acknowledgements

We thank Till Heinrich (GZG Abt. Angewandte Geologie) for his help during the SEM investigations as well as Doreteya K. Staykova, Torben Seidel and Marion Calcagnotto (GZG Abt. Kristallographie) for their help in the XRD work. Likewise, we thank the HASYLAB/Hamburg for beam time and support concerning the synchrotron XRD work. This research used data provided by the Ocean Drilling Program (ODP), which is sponsored by the US National Science Foundation and participating countries under management of Joint Oceanographic Institutions (JOI). We thank two anonymous reviewers for their helpful comments and recommendations. This is publication GEOTECH-278 of the R&D-Programme GEOTECHNOLOGIEN funded by the German Ministry of Education and Research (BMBF) and German Research Foundation (DFG). Funding for this research was provided by the Deutsche Forschungsgemeinschaft (DFG grants BO 1049/7 and Ku 920/13). This is publication no. 423 of the Research Center Ocean Margins of the University of Bremen.

References

- Abegg, F., Bohrmann, G., Kuhs, W., 2006. Data report: shapes and structures of gas hydrates imaged by computed tomographic-analyses, ODP Leg 204, Hydrate Ridge. In: Tréhu, A., Bohrmann, G., Colwell, F.S., Torres, M. (Eds.), Results, vol. 204, pp. 1–8. [Online]. Available from World Wide Web.: http://www-odp.tamu.edu/publications/204_SR/122/122.htm.
- Abegg, F., Bohrmann, G., Freitag, J., Kuhs, W., 2007. Fabric of gas hydrate in sediments from the Hydrate Ridge — results from ODP 204 samples. *Geo Mar. Lett.* 27, 269–277.
- Bohrmann, G., Torres, M., 2006. Gas hydrates in marine sediments. In: Schulz, H.D., Zabel, M. (Eds.), *Marine Geochemistry*. Springer, pp. 481–512.
- Bohrmann, G., Greinert, J., Suess, E., Torres, M., 1998. Authigenic carbonates from the Cascadia subduction zone and their relation to gas hydrate stability. *Geology* 26, 647–650.
- Circone, S., Kirby, S.H., Stern, L.A., 2005. Thermal regulation of methane hydrate dissociation: implications for gas production models. *Energy Fuels* 19, 2357–2363.
- Davidson, D.W., Garg, S.K., Gough, S.R., Handa, Y.P., Ratcliffe, C.I., Ripmeester, J.A., Tse, J.S., 1986. Laboratory analysis of a naturally occurring gas hydrate from sediment of the Gulf of Mexico. *Geochim. Cosmochim. Acta* 50, 619–623.
- Genov, G., Kuhs, W.F., Staykova, D.K., Goreshnik, E., Salamatin, A.N., 2004. Experimental studies on the formation of porous gas hydrates. *Am. Mineral.* 89, 1228–1239.
- Gudmundson, J., Borrehaug, A., 1996. Frozen hydrate for transport of natural gas. *Proc. 2nd Int. Conf. on Natural Gas Hydrates*, Toulouse, pp. 415–422.
- Hammersley, A.P., Svensson, S.O., Hanfland, M., Fitch, A.N., Häusermann, D., 1996. Two-dimensional detector software: from real detector to idealised image or two-theta scan. *High Press. Res.* 14, 235–248.
- Kennett, J.P., Cannariato, K.G., Hendy, I.L., Behl, R.J., 2002. Methane Hydrates in Quaternary Climate Change: The Clathrate Gun Hypothesis. American Geophysical Union, Washington D.C.
- Kim, D., Uhm, T., Lee, H., Lee, Y., Ryu, B., Kim, J., 2005. Compositional and structural identification of natural gas hydrates collected at Sites 1249 on Ocean Drilling Program Leg 204. *Korea J. Chem. Eng.* 22 (4), 569–572.
- Kirchner, M.T., Boese, R., Billups, W.E., Norman, L.R., 2004. Gas hydrate single-crystal structure analyses. *J. Am. Chem. Soc.* 126, 9407–9412.
- Klapproth, A., 2002. Strukturuntersuchungen an Methan- und Kohlenstoffdioxid-Clathrat-Hydraten. Ph.D. dissertation, Georg-August-Universität Göttingen.
- Klapproth, A., Goreshnik, E., Staykova, D., Klein, H., Kuhs, W.F., 2003. Structural studies of gas hydrates. *Can. J. Phys.* 81, 503–518.
- Klapproth, A., Techmer, K.S., Klapp, S.A., Murshed, M.M., Kuhs, W.F., 2007. Microstructures of gas hydrates in porous media. *Proc. Int. Conf. Physics and Chemistry of Ice*, Bremerhaven, July 23–28, 2006. Royal Society of Chemistry. RSC Publishing, pp. 321–328.
- Kuhs, W.F., Klapproth, A., Gotthardt, F., Techmer, K., Heinrichs, T., 2000. The formation of micro- and macroporous gas hydrates. *Geophys. Res. Lett.* 27, 2929–2932.
- Kuhs, W.F., Genov, G.Y., Goreshnik, E., Zeller, A., Techmer, K., Bohrmann, G., 2004a. The impact of porous microstructures of gas hydrates on their macroscopic properties. *Int. J. Offshore Polar Eng.* 14, 305–309.
- Kuhs, W.F., Genov, G., Staykova, D.K., Hansen, T.C., 2004b. Ice perfection and onset of anomalous preservation of gas hydrates. *Phys. Chem. Chem. Phys.* 6, 4917–4920.
- Kuhs, W.F., Staykova, D.K., Salamatin, A.N., 2006. Formation of methane hydrate from polydisperse ice powders. *J. Phys. Chem., B* 110, 13283–13295.
- Kvenvolden, K.A., Lorenson, T.D., 2001. The global occurrence of natural gas hydrates. In: Paull, C. (Ed.), *Natural Gas Hydrates: Occurrence, Distribution, and Detection*. Geophysical Monograph, vol. 124. American Geophysical Union, pp. 3–18.
- Larson, A.C., Von Dreele, R.B., 2000. General Structure Analysis System (GSAS). Los Alamos National Laboratory Report LAUR, pp. 86–748.
- Matsumoto, R., Uchida, T., Waseda, A., Uchida, T., Takeya, S., Hirano, T., Yamada, K., Maeda, Y., Okui, T., 2000. Occurrence, structure, and composition of natural gas hydrate recovered from the Blake Ridge, northwest Atlantic. *Proc. Ocean Drill. Program Sci. Results* 164, 13–28.
- Max, M.D., Johns, H.K., Dillon, W.P., 2006. Economic geology of natural gas hydrate. *Coastal Systems and Continental Margins*. Springer. 340 p.
- Paull, C.K., Ussler III., W., Dillon, W.P., 2003. Potential role of gas hydrate decomposition in generating submarine slope failures. In: Max, M.D. (Ed.), *Natural Gas Hydrate in Oceanic and Permafrost Environments*, pp. 149–156.
- Ripmeester, J.A., Tse, J.A., Ratcliffe, C.I., Powell, B.M., 1987. A new clathrate hydrate structure. *Nature* 325, 135–136.
- Sloan, E.D.J., 1998. *Clathrate Hydrate of Natural Gases*, (second edition). Marcel Dekker Inc., Publisher, New York. 705 pp.
- Staykova, D.K., Kuhs, W.F., Salamatin, A.N., Hansen, T., 2003. Formation of porous gas hydrates from ice powders: diffraction experiments and multistage model. *J. Phys. Chem., B* 107, 10299–10311.
- Stern, L., Cicerone, S., Kirby, S., Durham, W., 2003. Temperature, pressure, and compositional effects on anomalous or “self” preservation of gas hydrate. *Can. J. Phys.* 81 (1–2), 271–283.
- Stern, L., Kirby, S.H., Circone, S., Durham, W.B., 2004. Scanning electron microscopy investigations of laboratory-grown gas clathrate hydrates formed from melting ice and comparison to natural hydrates. *Am. Mineral.* 89, 1162–1175.
- Stern, L.A., Kirby, S.H., Durham, W.B., 2005. Scanning electron microscope imaging of grain structure and phase distribution within gas-hydrate-bearing intervals from JAPEX/JNOC/GSC et al. Mallik 5L-38: what can we learn from comparisons with laboratory-synthesized samples? In: Dallimore, S.R., Collett, T.S. (Eds.), *Scientific Results from the Mallik 2002 Gas Hydrate Production Research Well Program*, Mackenzie Delta, Northwest Territories, Canada. Geological Survey of Canada, Bulletin, vol. 585. 19 p.
- Suess, E., Torres, M.E., Bohrmann, G., Collier, R.W., Greinert, J., Linke, L., Rehder, G., Tréhu, A., Wallmann, K., Winckler, G., Zuleger, E., 1999. Gas hydrate destabilization: enhanced dewatering, benthic material turnover and large methane plumes at the Cascadia convergent margin. *Earth Planet. Sci. Lett.* 170, 1–15.
- Suess, E., Torres, M.E., Bohrmann, G., Collier, R.W., Rickert, D., Goldfinger, C., Linke, P., Heuser, A., Sahling, H., Heeschen, K., Jung, C., Nakamura, K., Greinert, J., Pfannkuche, O., Tréhu, A., Klinkhammer, G., Whiticar, M.C., Eisenhauer, A., Teichert, B., Elvert, E., 2001. Sea floor methane hydrates at Hydrate Ridge, Cascadia Margin. In: Paull, C., Dillon, W.P. (Eds.), *Natural Gas Hydrates: Occurrence, Distribution, and Detection*. Geophysical Monograph, vol. 124. American Geophysical Union, pp. 87–98.
- Techmer, K.S., Heinrichs, T., Kuhs, W.F., 2005. Cryo-electron microscopic studies of structures and composition of Mallik gas-hydrate-bearing samples. In: Dallimore, S.R., Collett, T.S. (Eds.), *Scientific Results from the Mallik 2002 Gas Hydrate Production*

- Research Well Program, Mackenzie Delta, Northwest Territories, Canada. Geological Survey of Canada, Bulletin, vol. 585. 12 p.
- Torres, M.E., Wallmann, K., Tréhu, A.M., Bohrmann, G., Borowski, W.S., Tomaru, H., 2004. Gas hydrate growth, methane transport, and chloride enrichment at the southern summit of Hydrate Ridge, Cascadia margin off Oregon. *Earth Planet. Sci. Lett.* 226, 225–241.
- Tréhu, A.M., Bohrmann, G., Rack, F.R., Torres, M.E., et al., 2003. Proc. ODP, Init. Repts., 204 [CD-ROM]. Available from: Ocean Drilling Program, Texas A&M University, College Station TX 77845-9547, USA.
- Tréhu, A.M., Long, P.E., Torres, M.E., Bohrmann, G., R., R.F., Collett, T.S., Goldberg, D.S., Milkov, A.V., Riedel, M., Schultheiss, P., Bangs, N.L., Barr, S.R., Borowski, W.S., Claypool, G.E., Delwiche, M.E., Dickens, G.R., Gracia, E., Guerin, G., Holland, M., Johnson, J.E., Lee, Y.-J., Liu, C.-S., Su, X., Teichert, B., Tomaru, H., Vanneste, M., Watanabe, M., Weinberger, J.L., 2004. Three-dimensional distribution of gas hydrate beneath southern Hydrate Ridge: constraints from ODP Leg 204. *Earth Planet. Sci. Lett.* 222, 845–862.
- Ussler III, W., Paull, C.K., McGill, P., Schroeder, D., Ferrell, D., 2006. Data report: a test of the temperature, pressure, and conductivity tool prototype at Hydrate Ridge. In: Tréhu, A.M., Bohrmann, G., Torres, M.E., Colwell, F.S. (Eds.), *Proc. ODP, Sci. Results*, vol. 204, pp. 1–41. doi:10.2973/odp.proc.sr.204.112.2006. College Station, TX (Ocean Drilling Program).
- von Stackelberg, M., Müller, H.R., 1954. Feste Gashydrate II: Struktur und Raumchemie. *Z. Elektrochem.* 58, 25–39.
- Yakushev, V.S., Istomin, V.A., 1992. In: Maeno, N., Hondoh, T. (Eds.), *Gas-hydrate self-preservation effect*. Hokkaido University Press, Sapporo, pp. 136–140.

Appendix V: Klapp et al., 2009

Gas hydrate crystallite size investigations with high-energy synchrotron radiation

S. A. KLAPP^{1,2}, H. KLEIN¹ & W. F. KUHS^{1*}

¹*Abteilung Kristallographie, Geowissenschaftliches Zentrum der Universität Göttingen
Goldschmidtstrasse 1; D-37077 Göttingen, Germany*

²*Present address: MARUM, Center for Marine Environmental Sciences,
University of Bremen, D-28359 Bremen, Germany*

**Corresponding author (e-mail: wkuhs1@gwdg.de)*

Abstract: The grain sizes of gas hydrate crystallites are largely unknown in natural samples. Single grains are hardly detectable with electron or optical microscopy. For the first time, we have used high-energy synchrotron diffraction to determine grain sizes of six natural gas hydrates retrieved from the Bush Hill region in the Gulf of Mexico and from ODP Leg 204 at the Hydrate Ridge offshore Oregon from varying depth between 1 and 101 metres below seafloor. High-energy synchrotron radiation provides high photon fluxes as well as high penetration depth and thus allows for investigation of bulk sediment samples. Gas hydrate grain sizes were measured at the Beam Line BW 5 at the HASYLAB/Hamburg. A 'moving area detector method', originally developed for material science applications, was used to obtain both spatial and orientation information about gas hydrate grains within the sample. The gas hydrate crystal sizes appeared to be (log-)normally distributed in the natural samples. All mean grain sizes lay in the range from 300 to 600 μm with a tendency for bigger grains to occur in greater depth. Laboratory-produced methane hydrate, aged for 3 weeks, showed half a log-normal curve with a mean grain size value of *c.* 40 μm . The grains appeared to be globular shaped.

The grain sizes of gas hydrate crystallites are largely unknown in natural samples despite their possible importance for our understanding of gas hydrate formation and the physical properties of gas hydrate aggregates. Grain sizes and shapes of gas hydrates yield insights for geosciences, glaciology and chemistry. The understanding of gas hydrate crystal growth could be significantly enhanced by knowing the typical sizes of gas hydrate crystals. This information may also help in understanding possible time-dependent continued growth processes; gas hydrate crystal growth might resemble a ripening process similar to Ostwald ripening (Lifshitz & Slyozov 1961; Wagner 1961). In such a process, large grains grow at the expense of smaller grains in order to minimize the free energy within a system. This happens both because of the higher solubility of smaller particles compared with larger particles (Wagner 1961) and because the grain boundary energy of larger particles is relatively less than that of smaller particles. The ripening of crystals will be a function of time, thus larger grains might be older than smaller grains assuming that the initial grain size was similar (i.e. the formation conditions are similar). Therefore, grain size information may well contribute to

evaluating the formation ages of gas hydrates once the formation processes and conditions have been established. Knowing the size of gas hydrate crystals also helps in understanding the processes taking place on grain boundaries, e.g. mass transport and diffusion. Many kinetic and thermodynamic considerations involve surface processes and depend on the available surface area (Lasaga 1998), e.g. gas exchange reactions that result in readjustment of the composition and cage filling of gas hydrates in response to changing environmental and physical conditions. The application of these considerations to gas hydrates will require knowledge of the grain size. This information is scarce for gas hydrates. In particular, statistically representative quantitative grain size information is unavailable.

In this study, grains are understood to be represented as single crystals, separated by grain boundaries. To explore the nature of these single grains, a sample of artificial gas hydrate, sieved to provide a particle size range between 200 and 400 μm and comprising single grains or agglomerates, was investigated.

Some grain size information on synthetic methane hydrates was reported in an earlier study

by Klapproth (2002), who estimated the typical crystal size to be 15 μm using X-ray diffractometric techniques. The samples were produced from ice and methane gas by the methods described by Kuhs *et al.* (1992) & Stern *et al.* (1996). Although difficult, Staykova *et al.* (2003) investigated methane hydrates (synthesized in a similar way, using a well-defined particle size and shape for the initial ice particles) using scanning electron microscopy (SEM), which is possible in the case of synthetic hydrates. Boundaries between hydrate crystallites are difficult to identify; only some freely grown euhedral hydrate crystals could be measured to have a size of 30–40 μm . Since these visual measurements were too few to have statistical significance, we have to assume that synthetic methane hydrate crystals, fabricated as described by Kuhs *et al.* (1992) & Stern *et al.* (1996), are typically 15 μm in size with individual crystals going up to at least 40 μm .

One objective of this study is to use a sample with a known particle size constrained between 200 to 400 μm to test the application of synchrotron techniques for determining the particle size of gas hydrates. Results within the order of magnitude as reported by Klapproth (2002) & Staykova *et al.* (2003) are expected for the measurement of the synthetic sample. The results within the anticipated range should underline the reliability and precision of the technique and serve also as a calibration.

The six natural samples investigated were from two different locations. One sample originates from the Bush Hill region in the Gulf of Mexico and was retrieved from the seafloor during the *RV Sonne* Cruise SO 174 in 2003 (Bohrmann & Schenck 2004). The other five natural samples are from Hydrate Ridge at the Cascadia Margin offshore Oregon. These samples were obtained from four different drilling sites of the ODP Leg 204 and originate from varying depths between 1 and 101 m below the seafloor (mbsf) (Shipboard Scientific Party 2002).

To enable good evaluation of the measurements, natural samples with considerable amounts of gas hydrate were chosen. A pre-selection was done based on 'on-the-catwalk' observations after sample recovery and computer-tomography (Abegg *et al.* 2006). For the purpose of this work, samples containing sufficiently large volumes of dense gas hydrate were needed, that is samples containing discrete nodules or lenses as described by Abegg *et al.* (2007). Bohrmann *et al.* (2007) also undertook quantitative phase analysis and scanning electron microscopy on some of the samples investigated in this study. Based on their results, samples with high proportions of gas hydrate were finally selected and used in this work.

Experimental methods

The grain sizes of one synthetic sample and six natural samples were investigated. The synthetic sample was prepared as in previous laboratory investigations on synthetic hydrates (Kuhs *et al.* 1992 & Stern *et al.* 1996) using ice grains ($\leq 400 \mu\text{m}$) and methane gas at a pressure of 60 bar for 3.5 weeks. During this time the temperature was raised in steps from -5 to $+2^\circ\text{C}$ each step being taken after the gas consumption at the previous temperature step had almost ceased.

Because the objective for investigating the natural samples was to evaluate the sizes of individual gas hydrate crystals, it was therefore important not to change the state of the samples (e.g. by crushing the sample). Consequently, small pieces of intact material about about 1 cm^2 in size were measured.

The grain sizes of gas hydrates were measured by imaging the length of the crystals with high-energy synchrotron radiation. Initially, however, the specimens were investigated with a cryo-scanning electron microscope. We used a field-emission scanning electron microscope (FE-SEM; Zeiss Leo 1530 Gemini). The FE-SEM is designed for work at low acceleration voltages of less than 2 kV, which is important for ice or gas hydrates in order to minimize sample alteration due to beam damage (Kuhs *et al.* 2004; Stern *et al.* 2004). During the measurements, the samples were placed on a liquid-nitrogen cooled sample stage inside a vacuum chamber at temperatures of about 90 K (-188°C) and a pressure of about 1×10^{-6} bar. The uncoated pieces of gas hydrate bearing samples with dimensions of about $0.5 \times 0.5 \times 0.5$ cm were examined in the cryo-SEM. The SEM instrument was equipped with a thin-window energy-dispersive X-ray microanalysis (EDX) detector allowing for microchemical analyses of low-Z elements.

The goal of SEM-imaging was to define the grain boundaries between gas hydrates on the surface of the specimen. Gas hydrate could be distinguished from other phases like ice and sediments by the presence of typical homogeneously distributed micropores within the gas hydrate phase. Submicrometre-sized micropores were described by Kuhs *et al.* (2000, 2004) & Techmer *et al.* (2005) within the gas hydrate phase as a typical feature and can be regarded as a potential tool for identifying gas hydrates. The pores are not fully connected and have diameters ranging from 200 to 400 nm in methane hydrate (Kuhs *et al.* 2000).

For the synchrotron measurements, pieces of pure hydrate/ice parts were broken off each of the six natural samples and then fixed into aluminium cans of 7 mm inner diameter and 40 mm length in an arbitrary orientation. In order to measure the

natural sizes of the grains, only large pieces coming close to the inner diameter of the cans were selected. The gas hydrate grain sizes were measured at the Beam Line BW 5 at the Hamburg Synchrotron Laboratory (HASYLAB) of the Deutsche Elektronen Synchrotron (DESY). High-energy synchrotron radiation provides a short X-ray wavelength and thus allows investigating bulk sediments up to some centimetres thickness (for a wavelength of *c.* 0.12 Å) in X-ray diffraction experiments. This depth of penetration is essential because the samples are 7 mm thick and are also located in a cryostat with Al shields (Fig. 1). Since the crystal sizes of natural samples were unknown, but expected to be quite small, a particularly good angular and spatial resolution was needed. This is provided by high collimation, i.e. parallel radiation of the high-energy synchrotron radiation and a high photon flux allowing small beam diameters.

During measurements, the cryostat stage was cooled by a closed cycle helium system to temperatures of 70 K (−208 °C). A Lake Shore (Cryotronics Inc.) controller was used to regulate the temperature of the sample. A vacuum of about

1×10^{-5} bar between the sample can and the shields of the cryostat insulates the sample from external heat.

The grain size measurements were performed with the synchrotron radiation using the moving area detector method, which was developed for material science purposes such as metals or ceramics (Bunge *et al.* 2002; Klein *et al.* 2004). It enables the simultaneous measurement of the grain sizes of many crystals in a single sample in relatively short time, and the measurement of grain sizes of many crystallites in one run gives statistically significant results. The diffracted Debye–Scherrer cones of individual crystal planes of sample crystallites are imaged as rings on a two-dimensional image plate detector. For this study, a *mar345* image plate detector was used. A diffraction image of a gas hydrate sample is shown in Figure 2.

The Debye–Scherrer ring corresponding to the gas hydrate structure I (321)-reflex is used for grain size measurements in the moving area detector method, because it is strong and does not overlap with other phases. In order to exclude all other reflections except the gas hydrate (321)-reflex,

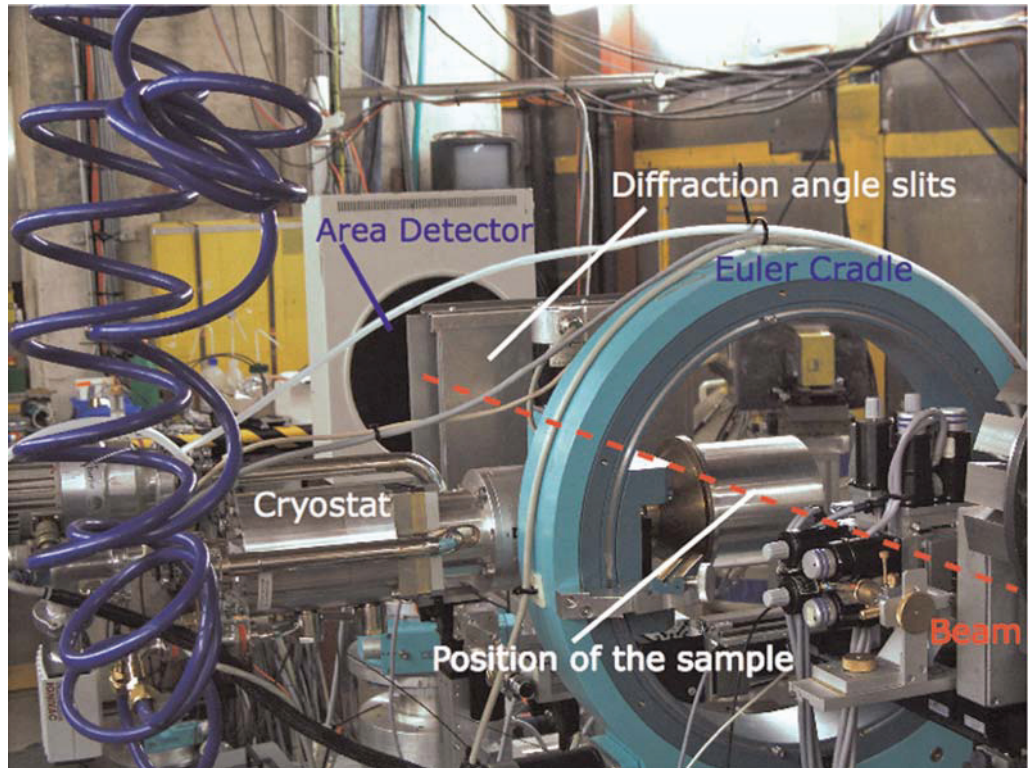


Fig. 1. Set up at BW5, the photograph is taken parallel to the beam direction. The gas hydrate sample is stored during measurements in a cylindrical (7.7 mm diameter) size aluminium can which is located within the cryostat.

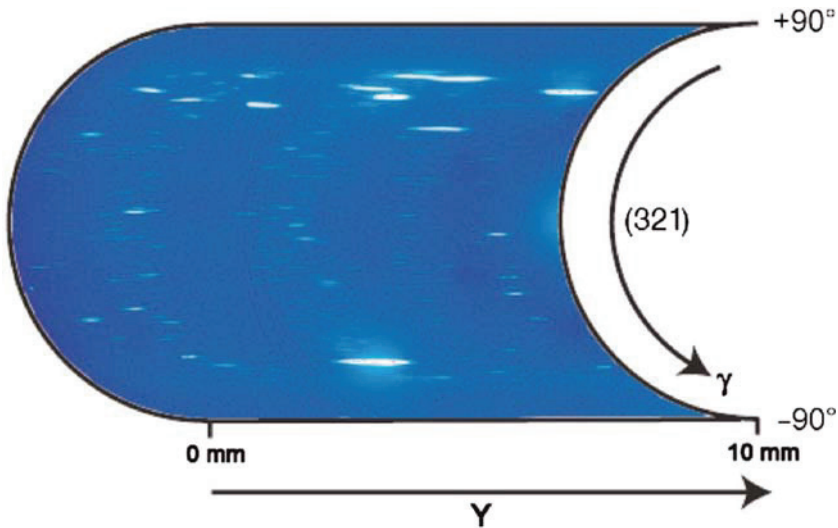


Fig. 4. Detector image of a sample (204 1249C-1H-CC, 0–10 cm). The streaks correspond to individual crystals; only reflections from the crystal plane (321) are recorded. The sample was scanned 10 mm in the y -direction. The total exposure time for this image was 85 min; the beam energy was 100 keV.

However, gas hydrates are weak scatterers unlike technical materials such as metals, for which the Moving Area Detector Method was developed (Bunge *et al.* 2003). The detector image processing and the measurement of the streaks are the most time-consuming steps in the data treatment process, because two challenges need to be met. First, the weak scattering of the synchrotron radiation by the gas hydrate crystal planes results in low intensities. Consequently, the data processing needs to enhance the contrast between background and reflections. Second, by enhancing the displayed intensity, artefacts on the image plate detector become more prominent and start to resemble features from true reflections. Artefacts are pixels with higher than background intensities, which do not belong to gas hydrate reflections. Unlike true reflections, they are not extended into the scanning direction or have a gradual increase in intensity towards the centre of the reflection.

The problems were solved in three succeeding steps for each individual sample. First, the background noise of the raw data from the synchrotron beamline was reduced by the image processing software. In the next step, objects with high intensities were counted and measured on the whole detector image of the sample. By doing that, intense gas hydrate reflections were measured, but not artefacts or weak gas hydrate reflections. To include streaks of gas hydrates with low intensities, small-scale areas of interest (AOIs) were drawn into the image encircling gas hydrate streaks. For these AOIs, the intensity threshold was decreased, which

allowed the objects to be added to the results. In a third step, the results were double-checked to determine if a measured object was a gas hydrate reflection or an artefact. This was done by switching between a results list and the corresponding objects in the images.

A reflected crystallite on the detector of just one pixel is equivalent to about $6 \mu\text{m}$ of crystal size. Theoretically, a crystal of that size could be imaged on the screen; practically, streak lengths starting at four pixels (which is equivalent to $24 \mu\text{m}$) are included in the data. This was done to ensure that all artefacts are kept out of the data.

Results

Gas hydrates were found in all samples by cryo-SEM. Areas of gas hydrate content could be identified both by carbon detected in the EDX analysis and as patches of sub-micrometre pore sizes (Fig. 5a, b); these pores are typically seen in gas hydrates and are well described features of gas hydrate occurrences (Kuhs *et al.* 2000; Techmer *et al.* 2005). These pores are not fully connected and have similar pore diameters (Kuhs *et al.* 2004). Boundaries between the gas hydrates and surrounding phases are indicated by a sharp change in the pore size. Dense material surrounding patches of sub-micrometre sized gas hydrate have fewer pores; also, these pores are of the order of tens of micrometres in diameter. EDX analysis detected no carbon signal in the dense parts of the

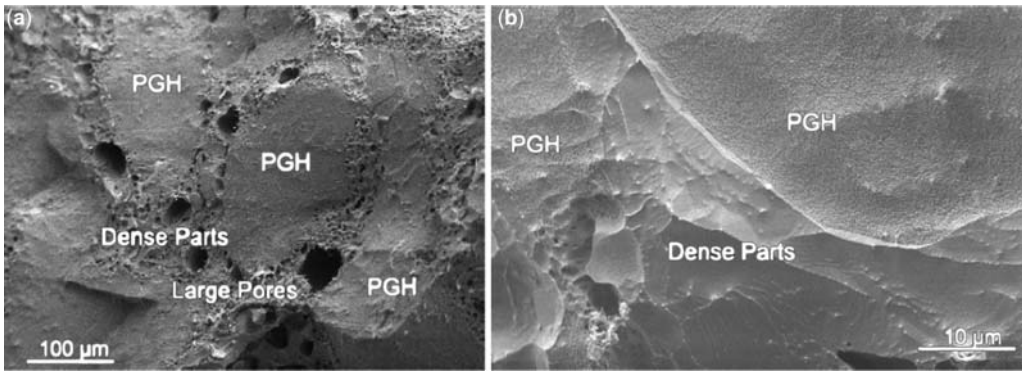


Fig. 5. Images of gas hydrate samples. (a) Overview of patches of gas hydrate (PGH), characterized by sub-micrometre-sized pores. The patches are surrounded by dense ice parts containing larger pores of tens of micrometre size in diameter. No information can be obtained about the actual size of the hydrate crystallites within the patches, nor is it certain that larger pores within the dense matrix are forming grain boundaries between gas hydrate grains. Sample ODP 204 1247B-12H-2, 41–51 cm. (b) Boundary between dense ice parts and sub-micrometre sized porous gas hydrate in the synthetic methane hydrate sample. Such clear boundaries are generally scarce and can hardly be found in natural samples.

samples (Fig. 5b). Bohrmann *et al.* (2007) describe these parts as ice, frozen from porewater during quenching in liquid nitrogen upon sample recovery. Although gas hydrates are detectable in electron microscopy, grain boundaries between single crystals are usually not clearly imaged. Patches of gas hydrate can be partially covered by crusts of salt or sediments. Most important, however, is that no boundaries are discernable within the sub-micrometre-sized patches of gas hydrate. This is why high-energy synchrotron radiation was applied as an alternative method.

The grain sizes measured by synchrotron radiation were collected and plotted as histograms. Different data sets from one sample, coming from measurements with different ω -positions as explained above, are summarized as follows. For the natural samples, the total number of counts for each sample varies and lies in the range of a few hundred to about 600. This does not include the

sample that was tilted 90° , since due to the shorter distances fewer crystals were scanned. This also accounts for the increased standard deviation of the corresponding results (Table 1). Although the distributions of the crystal sizes from natural samples look normally distributed (Fig. 6a, b), they cannot be mathematically fitted due to the number of streaks measured, which would allow both normal and log-normal fitting. The mean value was calculated by dividing the sum of all crystal sizes of a sample through the frequency of occurrence. For all natural samples, the crystals are about 300–600 μm in diameter as measured by the location scan method. Table 1 gives the crystal sizes for the gas hydrates of the seven different samples. Figure 7 displays the crystal size *v.* depth.

The synthetic gas hydrate sample was prepared in a way that most of the ice reacted with the methane gas to form methane hydrate. The sample was fully

Table 1. Crystal sizes of measured samples

Sample-ID	Depth (mbsf)	Location-scan-method	
		Size (μm)	Standard deviation (μm)
204 1248C-8H-6, 68–87 cm	74.46	361	79
204 1247B-12H-2, 41–51 cm	93.01	592	374
204 1249C-1H-CC, 0–10 cm	1.5	373	134
204 1248C 11H-5 (no tilt)	100.89	517	176
204 1248C 11H-5 (90° tilted)	100.89	569	342
204 1250C 2H-CC 0-1 cm	5.06	451	132
Bush Hill, TVG 10 GH 1	Seafloor	301	114
CH4-Hydrate	Synthetic	43	24

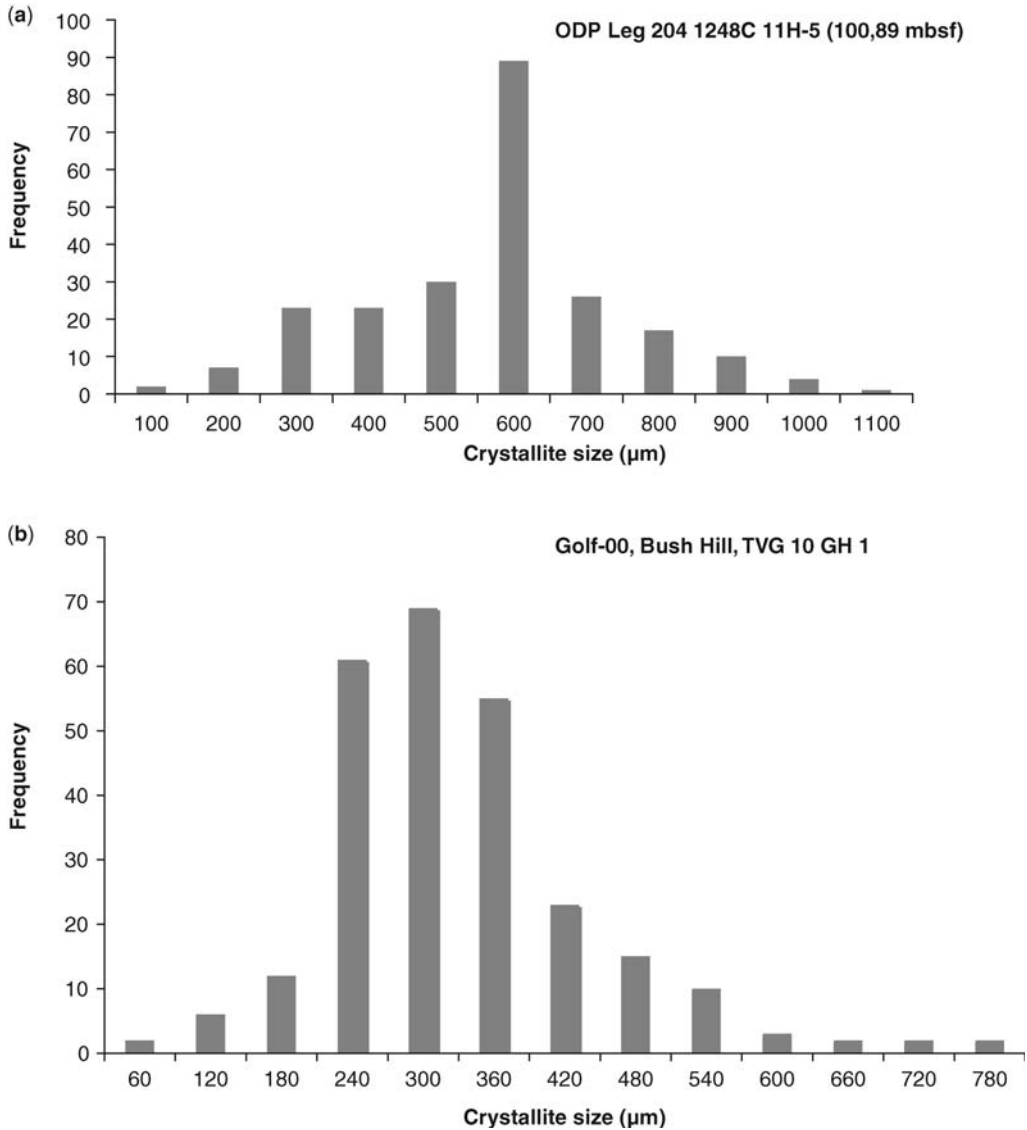


Fig. 6. Examples of grain size distributions. (a) Sample ODP 204 1248C 11H-5 (100.89 mbsf). The crystallite sizes appear to be normally distributed with a mean size of 517 μm . (b) Sample Gulf of Mexico, Bush Hill, TVG 10 GH 1 (seafloor). The crystallite sizes appear to be normally distributed with a mean size of 301 μm . (c) Synthetic methane hydrate sample. The size distribution is shaped like half a normal distribution; the mean grain size is 43 μm assuming a log-normal distribution.

reacted and thus essentially free of ice. A large number of crystallites were measured in one run as a consequence of the distinctly smaller grain sizes as compared with the natural samples (Fig. 6c). However, although the sizes of the individual grains, which were measured with synchrotron radiation, is a sieved fraction of 200–400 μm , the actual crystal sizes came out as well below these sizes with

a mean value of *c.* 40 μm . This shows that the crystal sizes lay in the range of 15–50 μm , as described by Klapproth (2002) & Staykova *et al.* (2003).

The crystal size distribution of the synthetic sample, unlike the natural samples, is shaped as half a log-normal distribution (Fig. 6c). Since the crystals were freshly prepared in the laboratory, the initial grain size is quite small with a mean

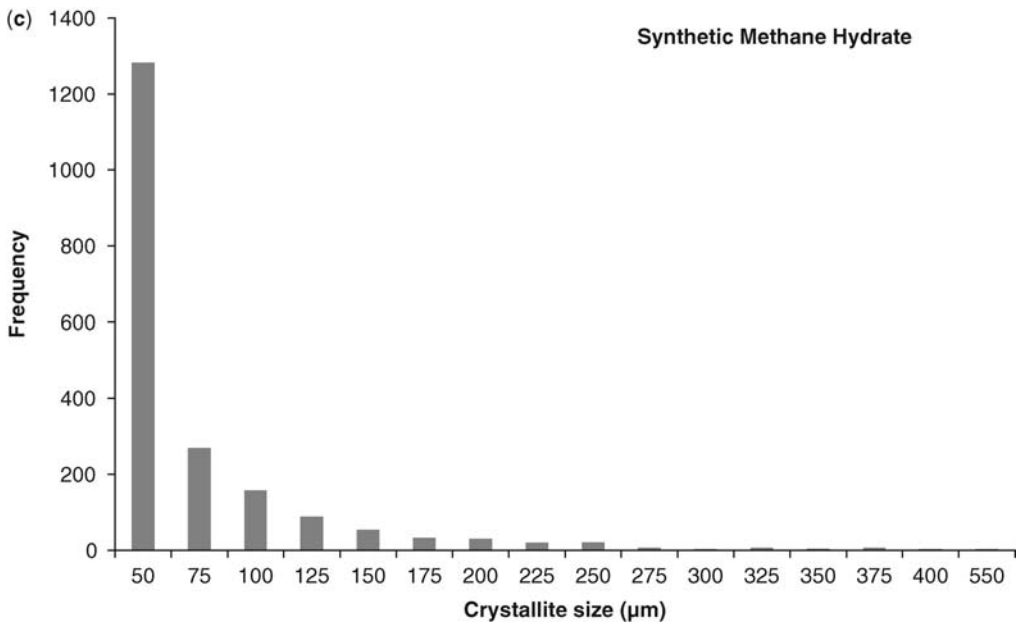


Fig. 6. (Continued).

size of about 40 µm, which is close to the detection limit of the measurements, as explained above.

Discussion

Exploring the nature of gas hydrate crystal growth and of processes involving surfaces of gas hydrate crystals requires information about the actual size of crystallites. Scanning electron microscopy is an effective tool for investigating gas hydrates when it comes to observation of the hydrate surface, like studying the microstructure or phenomena related to the decomposition of gas hydrates. Gas hydrate patches could be identified by sub-micrometre-sized pores and EDX analysis. The patches are surrounded by a dense matrix, which could lead to the impression that a single patch is a single grain. Actually, single grains, which are connected to crystal agglomerates, will have the same appearance in scanning electron microscopic images; also, the patches are likely to be shaped by partial decomposition of gas hydrates during retrieval. Accordingly, single patches of hydrate cannot necessarily be addressed as single gas hydrate crystals. However, crystals, which are attached to each other, can be distinguished by different orientation of the crystals. This is used by synchrotron measurements.

The moving area detector method is already regularly applied to materials such as metals or ceramics (e.g. Bunge *et al.* 2003; Klein *et al.* 2004) and, as shown here, it can successfully be used also

for gas hydrates. Previous studies on laboratory-made hydrates that revealed sizes of 15–40 µm (Klapproth 2002; Staykova *et al.* 2003) were confirmed by the moving area detector method with high-energy synchrotron radiation (Table 1).

Repeated measurement series of a sample turned by 90° indicates that the crystallites are not elongated into a preferred direction or orientation. This gives confidence that the samples are of globular shape, meaning that they have about the same extensions into the two orthogonal, measured directions. The synchrotron radiation measurements on hundreds of crystals indicate that the sizes of six different natural samples, ranging between 300 and 600 µm, are actually much larger than that of the synthetic sample.

Conclusions

The moving area detector method, applied to high-energy synchrotron radiation, is suggested as a new tool for the investigation of both synthetic and natural gas hydrates.

The grain sizes of natural and freshly laboratory-prepared samples differ by about an order of magnitude. Whether this is predominantly a consequence of some ripening process within the natural gas hydrates or due to different initial growth processes must remain an open question at this stage. In any case, some caveats need to be formulated concerning the relevance of physical properties of gas

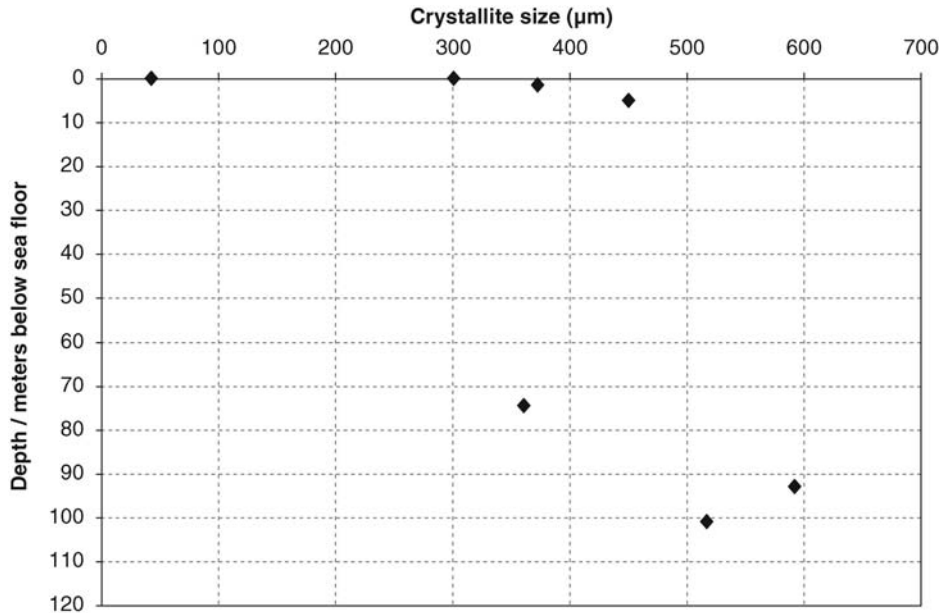


Fig. 7. Mean crystallite size v. depth: no clear correlation of size with depth is present, although larger grains tend to occur in greater depth.

hydrates measured on synthetic samples in applications on natural samples. Judging from the marine samples investigated, surface processes like diffusion or other kinds of mass transport, including mechanical properties, may take place differently in nature than observed in laboratory experiments.

Moreover, the results of this study suggest that growth and ripening of gas hydrate crystals could well take place in oceanic environments. Exploring the time involved for the ripening could lead to the approximate determination of the age of the gas hydrates. Such ripening processes have been observed in air hydrates enclosed in deep ice cores of Arctic and Antarctic ice sheets (Kipfstuhl *et al.* 2001). The primary crystallites are small with a typical crystallite size of a few tens of micrometres, which then transform into one single crystal of typically a few hundred micrometres; as the ice cores are dated, the time-scales of re-growth processes may be obtained by further analyses.

We thank Gerhard Bohrmann from MARUM, Center for Marine Environmental Sciences, in Bremen for providing the samples. Credit is also given to Andrea Preusser and Lars Raue for support at the HASYLAB and Kirsten Techmer for help at the FE-SEM (all GZG Göttingen). We thank the Deutsche Forschungsgemeinschaft for funding and HASYLAB at DESY for providing beam time and support. This work was funded by the Deutsche

Forschungsgemeinschaft and the German Ministry of Education and Research in the programme Geotechnologien, of which this is publication no. GEOTECH-322.

References

- ABEGG, F., BOHRMANN, G., FREITAG, J. & KUHS, W. F. 2007. Fabric of gas hydrate in sediments from the Hydrate Ridge – results from ODP 204 samples. *Geo-Marine Letters*, **27**, 269–277, doi: 10.1007/s00367-007-0080-4.
- ABEGG, F., BOHRMANN, G. & KUHS, W. F. 2006. Data report: Shapes and structures of gas hydrates imaged by computed tomographic-analyses, ODP Leg 204, Hydrate Ridge. In: TRÉHU, A., BOHRMANN, G., COLWELL, F. S. & TORRES, M. (eds) *Proceedings of ODP, Scientific Results*, **204**, 1–8. World Wide Web Address: http://www-odp.tamu.edu/publications/204_SR/122/122.htm.
- BOHRMANN, G. & SCHENCK, S. 2004. *GEOMAR Cruise Report SO 174, OTEGA II, RV 'SONNE'*. GEOMAR Report, Kiel.
- BOHRMANN, G., KUHS, W. F. *ET AL.* 2007. Appearance and preservation of natural gas hydrate from Hydrate Ridge sampled during ODP Leg 204 drilling. *Marine Geology*, **244**, 1–14.
- BUNGE, H. J., WCISLAK, L., KLEIN, H., GARBE, U., NOWAK, R. & SCHNEIDER, J. R. 2002. Orientation imaging of crystals in polycrystalline materials. *Advanced Engineering Materials*, **4**, 300–305.
- BUNGE, H. J., WCISLAK, L., KLEIN, H., GARBE, U. & SCHNEIDER, J. R. 2003. Texture and microstructure

- imaging in six dimensions with high-energy synchrotron radiation. *Journal of Applied Crystallography*, **36**, 1240–1255.
- KIPFSTUHL, S., PAUER, F. & KUHS, W. F. 2001. Air bubbles and clathrates in the transition zone of the NGRIP deep ice core. *Geophysical Research Letters*, **28**, 591–594.
- KLAPPROTH, A. 2002. *Strukturuntersuchungen an Methan- und Kohlenstoffdioxid-Clathrat-Hydraten*. Ph.D. dissertation, Georg-August-Universität, Göttingen.
- KLEIN, C. 2004. mar345dtb. User's Guide. Version 4.3. World Wide Web Address: <http://www.marresearch.com/mar345dtb/mar345dtb.htm> [online in this version since 28 October 2004, downloaded March 2006].
- KLEIN, H., PREUSSER, A., BUNGE, H. J. & RAUE, L. 2004. Recrystallisation texture and microstructure in Ni and AlMg1Mn1 determined with high-energy synchrotron radiation. In: *Proceedings of the 2nd International Conference on Recrystallization and Grain Growth*. Material Science Forum, **467–470**, 1379–1384.
- KUHS, W. F., DORWARTH, R., LONDONO, D. & FINNEY, J. L. 1992. *In-situ* study on composition and structure of Ar-clathrate. In: MAENO, N. & HONDOH, T. (eds) *Physics and Chemistry of Ice*. Hokkaido University Press, Sapporo, 126–130.
- KUHS, W. F., GENOV, G. Y., GORESHNIK, E., ZELLER, A., TECHMER, K. & BOHRMANN, G. 2004. The impact of porous microstructures of gas hydrates on their macroscopic properties. *International Journal of Offshore and Polar Engineering*, **14**, 305–309.
- KUHS, W. F., KLAPPROTH, A., GOTTHARDT, F., TECHMER, K. & HEINRICHS, T. 2000. The formation of meso- and macroporous gas hydrates. *Geophysical Research Letters*, **27**, 2929–2932.
- LASAGA, A. C. 1998. *Kinetic Theory in the Earth Sciences*. Princeton Series in Geochemistry. Princeton University Press, Princeton, NJ, 811.
- LIFSHITZ, I. M. & SLYOZOV, V. V. 1961. The kinetics of precipitation from supersaturated solid solution. *Journal of Physics and Chemistry of Solids*, **19**, 35–50.
- MEDIA CYBENETICS, INC. 2002. *Image-Pro Plus. Version for Windows. Start-Up Guide*.
- SHIPBOARD SCIENTIFIC PARTY. 2002. Preliminary report. ODP Prelim. Report **204**. World Wide Web Address: http://www-odp.tamu.edu/publications/prelim/204_prel/204toc.html (accessed 15 June 2006).
- STAYKOVA, D. K., KUHS, W. F., SALAMATIN, A. N. & HANSEN, T. 2003. Formation of porous gas hydrates from ice powders: Diffraction experiments and multi-stage model. *Journal of Physical Chemistry B*, **107**, 10299–10311.
- STERN, L., KIRBY, S. H. & DURHAM, W. B. 1996. Peculiarities of methane clathrate hydrate formation and solid-state deformation, including a possible superheating of water ice. *Science*, **273**, 1843–1848.
- STERN, L. A., KIRBY, S. H., CIRCONI, S. & DURHAM, W. B. 2004. Scanning electron microscopy investigations of laboratory-grown gas clathrate hydrates formed from melting ice, and comparison to natural hydrates. *American Mineralogist*, **89**, 1162–1175.
- TECHMER, K., HEINRICHS, T. & KUHS, W. F. 2005. Cryo-electron microscopic studies on the structures and composition of Mallik gas-hydrate-bearing samples. In: DALLIMORE, S. R. & COLLETT, T. S. (eds) *Scientific Results from JAPEX/JNOC/GSC et al. Mallik as Hydrate Production Research Well Program, Mackenzie Delta, Northwest Territories, Canada*. Geological Survey of Canada Bulletin, **585**.
- WAGNER, C. 1961. Theorie der Alterung von Niederschlägen durch Umlösen (Ostwald-Reifung). *Zeitschrift für Elektrochemie*, **65**, 581–591.